Domination in double layered fuzzy graphs

Cite as: AIP Conference Proceedings **2112**, 020117 (2019); https://doi.org/10.1063/1.5112302
Published Online: 24 June 2019

A. Kirupa, and J. Jesintha Rosline

Domination In Double Layered Fuzzy Graphs

A. Kirupa[1,a)] and J. Jesintha Rosline [2,b)]

[1]Research Scholar,
P.G. and Research Department of Mathematics,
Loyola College, Chennai -34, Tamil Nadu, India.

[2]Assitant Professor,
Department of Mathematics,
SRMIST, Kattankulathur -603203, Tamil Nadu, India.

[a)]Corresponding author: mariakiruba@gmail.com
[b)]jesintharosline.j@ktr.srmuniv.ac.in

Abstract: In this paper, we study various domination concepts like domination, 2-domination, edge domination, perfect edge domination, strong domination, split domination, perfect domination and double domination in double layered fuzzy graphs. We further investigate some of its properties.

Keywords: Fuzzy graph, Domination in Fuzzy graph, double layered fuzzy graph, domination in double layered fuzzy graphs, Perfect domination, split domination, double domination.

INTRODUCTION

Fuzzy set theory was first introduced by L.A Zadeh in 1965[15]. Although the first definition of a fuzzy graph using fuzzy relations on fuzzy sets was given by Kaufman, Azriel Rosenfeld developed the theory of fuzzy graph in 1975[4]. It has enormous application in the field of engineering and technology and has proved to be a useful tool for solving many problems in various fields. In was during 1962, the concept of domination in graphs was introduced by Ore and Berge and further studied by Cockayne and Hedetniemi[20]. Domination in fuzzy graph was first introduced by A. Somasundaram and S. Somasundaram[6]. A. Nagoor Gani and K. Prasanna Devi, introduced 2–Domination in Fuzzy Graphs[10]. About Independent domination and Irredundance in Fuzzy Graph is studied by A. Nagoor Gani and P. Vadivel[11]. Perfect Domination set and some interesting results with new parameters is being worked by S. Revathi, P.J. Jayalakshmi, C.V.R. Harinarayanan[12]. Muneera R.V.N. Srinivas rao made a detailed analysis on edge domination in domination of fuzzy graphs and fuzzy trees[7]. In 2014 the double layered fuzzy graph (DLFG)[1] was introduced by T. Pathinathan and J. Jesintha Rosline, and the matrix representation of double layered fuzzy graph[3] and its properties are also studied by them. A. Nagoor Gani along with K. Prasanna devi in 2015 introduced 2-Domination in Fuzzy Graph[10]. The structural core of double layered fuzzy graph was introduced by J.J. Rosline, J.J. and T. Pathinathan[16], and they extremely contributed in triple layered fuzzy graph and studied the relationship between the triple layered with the parental graph using in 2015[2].

Through this paper, we study various Domination in Double Layered Fuzzy Graphs. We verify Domination, edge domination, perfect edge domination, Perfect Domination, split Domination, 2-domination and double domination in double layered fuzzy graphs with example and each of its fuzzy cardinality number is also discussed. Properties and theorem are guaranteed with relevant proofs.

BASIC PRELIMINARIES

In this section, we provide few basic definitions and notations related to fuzzy graphs and dominations.

Fuzzy Graph

A fuzzy graph G is a pair of functions $G:(\sigma,\mu)$ where σ is a fuzzy subset of a non empty set S and μ is a symmetric fuzzy relation on σ. The underlying crisp graph of $G:(\sigma,\mu)$ is denoted by $G^*:(\sigma^*,\mu^*)$. G is a set with two functions, $\sigma: V \to [0,1]$ and $\mu: E \to [0,1]$ such that $(u,v) = \sigma(u) \wedge \sigma(v)$. The order and size of a fuzzy graph $G:(\sigma,\mu)$ are defined to be $p = \sum \sigma(x)$, where $x \in V$, and $q = \sum \mu(xy)$ where $xy \in E$. An edge $e = xy$ is called effective edge if $\mu(x,y) = \sigma(x) \wedge \sigma(y)$.

The 11th National Conference on Mathematical Techniques and Applications
AIP Conf. Proc. 2112, 020117-1–020117-7; https://doi.org/10.1063/1.5112302
Published by AIP Publishing. 978-0-7354-1844-8/$30.00

Dominating Set

Given a fuzzy graph $G:(\sigma,\mu)$. D is said to be dominating set of G if there exist a subset D of σ in which $\sigma - D$ is adjacent to some vertex in D. The fuzzy cardinality of $D \subseteq \sigma$ of $G:(\sigma,\mu)$ is defined as $\sum \sigma(x)$ where $x \in D$. The minimum scalar cardinality taken over all dominating set in G is the cardinality number $\gamma(G)$.

Perfect Domination Set

A set $D \subseteq \sigma$ is called a perfect dominating set of G if for each vertex x not in D, v is adjacent to exactly one vertex of D. The minimum scalar cardinality over all perfect dominating set is called the perfect domination number $\gamma_{pf}(G)$.

Edge Domination Set

Given a fuzzy graph $G:(\sigma,\mu)$ on (V, E). Let the fuzzy relation φ on μ of is said to be an edge domination set in G if for every edge in $\mu \setminus \varphi$ is adjacent to at least one effective edge in φ. The scalar cardinality of a minimum edge dominating set of G is called the edge domination number of G and its denoted by $\gamma'(G)$.

Perfect Edge Domination Set

Given a fuzzy graph $G:(\sigma,\mu)$ on (V, E). An edge dominating set φ of a fuzzy graph is said to be a perfect edge dominating set if every edge of $\mu - \varphi$ is adjacent to exactly one edge in φ. The minimum fuzzy cardinality of the perfect edge dominating sets is the perfect edge domination set. Its minimum scalar cardinality is the perfect dominating number of G and it is denoted by $\gamma_{pf}{}'(G)$.

2-Dominating Set

Let the given fuzzy graph be $G:(\sigma,\mu)$. For every $x \in \sigma - D$ if there exist at least two strong neighbours in D, then the subset $D \subseteq \sigma$ is called as 2-dominating set of G. Its scalar cardinality of a minimum dominating set over all 2-dominating set is called as 2-domination number of a fuzzy graph G and it is denoted by $\gamma_2(G)$.

Strong Dominating Set

An arc (x,y)in a fuzzy graph $G:(\sigma,\mu)$ is $\alpha - strong$ if $\mu(x,y) > CONN_{G-(x,y)}(x,y)$. An arc$(x,y)$in a fuzzy graph G is $\beta - strong$ if $\mu(x,y) = CONN_{G-(x,y)}(x,y)$. Thus an edge (x,y) is a strong edge if it is either $\alpha - strong$ or $\beta - strong$. If arc (x,y) is strong then y is strong neighborhood of x and is denoted by $N_s(x)$. A set sD of nodes of a fuzzy graph $G:(\sigma,\mu)$ is a strong dominating set of G, if no proper subset of sD is a dominating set. $\sigma - sD$ is a strong neighbour of some node in sD. Minimum strong dominated set of a fuzzy graph G is defined as a strong dominating set which has minimum number of nodes. Strong dominating number $\gamma_s(G)$ of G is defined as the number of scalar cardinality of a minimum strong dominating set.

Split Dominating Set

Let D be a dominating set of G**.** A subgraph $\langle \sigma \setminus D \rangle$ induced by $\sigma \setminus D$ is disconnected. The split domination number of G is defined as scalar cardinality of minimum taken over all the split dominating set in G. Its dominating number is denoted by $\gamma_{sp}(G)$.

Double Dominating Set

A set $D \subseteq \sigma$ is called a double dominating set of G if every vertex in σ is dominated by at least two vertices in D. The double domination number of G is defined as minimum scalar cardinality taken over all the double dominating set in G. It is denoted by $\gamma_{dd}(G)$.

Double Layered Fuzzy Graph

Let $G:(\sigma,\mu)$ be a fuzzy graph with the underlying crisp graph $G^*:(\sigma^*,\mu^*)$. The pair $DL(G):(\sigma_{DL},\mu_{DL})$ is defined as follows. The node set of $DL(G)$ be $\sigma^* \cup \mu^*$. The fuzzy subset σ_{DL} is defined as

$$\sigma_{DL} = \begin{cases} \sigma(u) if\ u \in \sigma^* \\ \mu(uv) if\ uv \in \mu^* \end{cases}$$

The fuzzy relation μ_{DL} on $\sigma^* \cup \mu^*$ is defined as

$$\mu_{DL} = \begin{cases} \mu(uv)\ if\ u,v \in \sigma^* \\ \mu(e_i) \wedge \mu(e_j) \text{ if the edge } e_i \text{ and } e_j \text{ have node in common between them} \\ \sigma(u_i) \wedge \mu(e_i) \text{ if } u_i \in \sigma^* \text{ and } e_i \in \mu^* \text{ and each } e_i \text{is incident with single } u_i \text{ either clockwise or anticlockwise} \\ 0\ otherwise \end{cases}$$

By definition $\mu_{DL}(u,v) \leq \sigma_{DL}(u) \wedge \sigma_{DL}(v)$ for all u, v in $\sigma^* \cup \mu^*$. Here μ_{DL} is a fuzzy relation on the fuzzy subset σ_{DL}. Hence the pair $DL(G):(\sigma_{DL},\mu_{DL})$is defined as double layered fuzzy graph (DLFG) or 3-D Fuzzy Graph.

Dominations in Double Layered Fuzzy Graph

Consider a double layered fuzzy graph $DL(G):(\sigma_{DL},\mu_{DL})$ such that $\sigma_{DL} = \{a,b,c,D,E,F\}$
$\mu_{DL} = \{(a,b),(a,c),(a,D),(b,c),(D,E),(D,F),(E,F),(b,E),(c,F)\}$

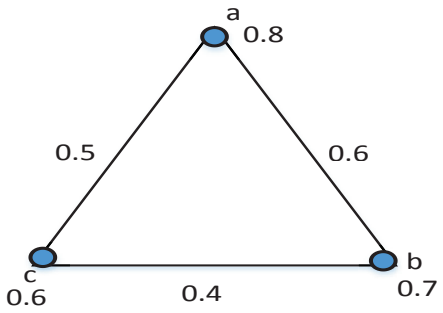

Figure 1: A Fuzzy Graph $G:(\sigma,\mu)$.

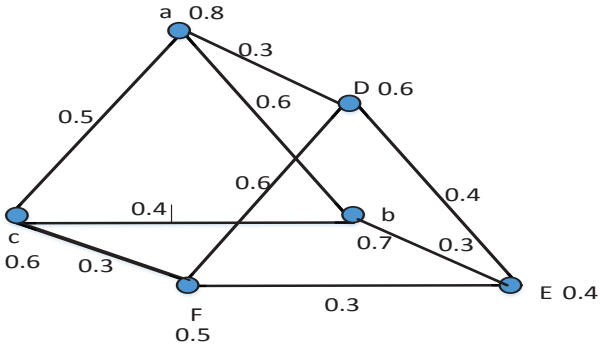

Figure 2: A Double Layered Fuzzy Graph $G:(\sigma,\mu)$.

Varying Results on Domination in Double Layered Fuzzy Graph

Result 1

Dominating set of DLFG of the figure 2:
Set of all possible dominating set for DLFG for n=3 vertices.
$DD = \{(a,c),(D,b),(c,E),(a,D,E),(a,E,F),(c,D,E),(a,b,E,F),(a,b,D,E,F)\}$
$V - DD = \{(b,D,E,F),(a,c,E,F),(b,c,D\ F),(b,c,F),(b,c,D),(a,b,F),(c,D)(c)\}$
Fuzzy cardinality of DD = {0.9, 1.3, 0.8, 1.4, 1.3, 1.3, 2.1, 2.7}
Minimum cardinality is 0.8 for$\{c,E\}$. Therefore DD of DLFG is $\{c,E\}$ and $V - DD = \{a,b,D,F\}$
The domination number of DD is $\gamma(DL(G)) = 2$.

Theorem: For a DLFG G, a dominating set DD of $DL(G)$ is a minimal dominating set if and only if each $x \in DD$ one of the following 2 conditions holds good

(i) $N(x) \cap DD = \emptyset$

(ii) There is a vertex $y \in {}^{\sigma_{DL}}/_{DD} \ni N(y) \cap DD = \{x\}$

Proof: Let DD be a minimal dominating set and an $x \in DD$. Then $DD_x = DD/\{x\}$ is not a dominating set and hence there exist $y \in {}^{\sigma}/_{DD_x}$ such that y is not dominated by any element of DD_x.
If $y = x$, we get $N(x) \cap DD = \emptyset$
and if $x \neq y$, we get a vertex $y \in {}^{\sigma_{DL}}/_{DD} \ni N(y) \cap DD = \{x\}$.
Then the converse is obviously true.

Illustration:

From Figure 2,
Let $c \in DD$ from $DD = \{c,E\}$
Then, $\sigma_{DL} - DD = \{a,b,D,F\}$
$N(c) \cap DD = \{a,b,F\} \cap \{c,E\} = \emptyset$
If $a \in {}^{\sigma_{DL}}/_{DD} \ni N\{a\} \cap DD$
$\Longrightarrow \{D,b,c\} \cap \{c,E\} = \{c\}$.

Result 2

2 - Domination set DD of DLFG for the figure 2:
Set of all Strong arcs of DLFG is $\{DE, bE, FE, DF, cF\}$
Strong Neighbors N = $\{b, c\ D, E, F\}$
Set of all possible 2- dominating set for DLFG for n=3 vertices
$2DD = \{(b,c,D,E,F),(b,c,D,F),(b,c,D),(c,E,F),(b,D,F)\ \}$
$V - 2DD = \{(a),(a,F),(a,E,F),(a,b,D),(a,c,E)\}$. Each of $x \in V - 2DD$ has at least 2 strong neighbors, in which with minimum scalar cardinality is $\gamma_2(DL(G)) = 3$.

Remark: Independent set of DLFG

No 2 nodes of the DLFG have no strong arc between them, hence no fuzzy independent set exist. The independent domination number $i(DL(G)) = 0$.

Result 3

Edge domination set of DLFG for the figure 2:
Let the edges of DLFG $\mu_{DL} = \{e_1, e_2, e_3, e_4, e_5, e_6, e_7, e_8, e_9\}$
Effective edges $\{e_4, e_5, e_6, e_7, e_8, e_9\}$
The set of all edge domination set of DLFG
$eDD = \{(e_1,e_5),(e_3,e_7),(e_1,e_5,e_9),(e_1,e_3,e_4,e_9),(e_2,e_3,e_5,e_8,e_9)\ (e_1,e_3,e_5,e_7,e_8,e_9)\}$
$\mu_{DL} - eDD = \{(e_2,e_3,e_4,e_6,e_7,e_8,e_9),(e_1,e_2,e_4,e_5,e_6,e_8,e_9),(e_2,e_3,e_4,e_6,e_7,e_8),(e_2,e_5,e_6,e_7,e_8),$
$(e_1,e_4,e_6,e_7),\ (e_2,e_4,e_6)\}$. Every edge is adjacent to at least one effective edge in eDD. Minimum edge domination number is $\gamma'(DL(G)) = 2$ for the $eDD = (e_1,e_5)$.

Result4

Perfect edge domination set of DLFG for the figure 2:
The set of possible perfect edge domination set of $DL(G)$is $pfDD = \{e_2, e_6\}$
$\mu_{DL} - pfDD = = \{e_1, e_3, e_4, e_5, e_7, e_8, e_9\}$. Every edge is adjacent to exactly one in $pfDD$. Minimum fuzzy cardinality number is defined as perfect edge domination number $\gamma_{pf}(DL(G)) = 2$.

Theorem: $\gamma'\big(DL(G)\big) = \gamma_{pf}\big(DL(G)\big)$, where $DL(G)$ is a double layered fuzzy graph.

Proof: Let $DL(G)$: (σ_{DL}, μ_{DL}) is the double layered fuzzy graph. As the edge domination set consist of edges dominated by one or more than one effective edge of $\mu_{DL} - eDD$. And perfect edge domination set consist of edges dominated by exactly one effective edge of $pfDD$.

Since edge domination with one or more than one adjacency and the with minimum fuzzy membership value of the $DL(G)$ is $\gamma'\big(DL(G)\big) = 2$. Even though perfect domination set says only one exact edge adjacency in μ_{DL} for every in $\mu_{DL} - pfDD$, its scalar cardinality fuzzy value of the $pfDD$ is also 2.

Thus, we have proved $\gamma'\big(DL(G)\big) = \gamma_{pf}\big(DL(G)\big)$.

Result 5

Strong dominating set of $DL(G)$ for the figure 2:
A set sD of nodes of $DL(G)$ is a strong dominating set of $DL(G)$ if no proper subset of sD is a dominating set. $DD - sD$ is a strong neighbour of some node in sD.
The set of all possible $DD = \{(a, E), (D, b), (c, E), (a, D, E), (a, E, F), (c, D, E), (a, b, E, F), (a, b, D, E, F)\}$
The set of all possible $sD = \{(a, E), (b, D), (c, E)\}$
The minimum scalar cardinality of sD is $\{c, E\}$ with membership value 1.
Its strong dominating number is $\gamma_s\big(DL(G)\big) = 2$.

Theorem: For any double layered fuzzy graph $DL(G)$, $\gamma_s\big(DL(G)\big) = \gamma(DL(G))$.

Proof: Let $DL(G)$: (σ_{DL}, μ_{DL}) be a $3 - D$ fuzzy graph.
As the node set of dominating set says every vertex of $\sigma_{DL} - DD$ is adjacent to D. And its minimum fuzzy membership value, the dominating number is $\gamma(DL(G))$.
As the node set of strong dominating set says there should not be any proper subset from the dominating set DD. Therefore, finding a set of cardinality value of dominating set and the minimum scalar cardinality is c said to be strong dominating set of $DL(G)$.

$$\sum \sigma_{DL}(sDD) = \sum \sigma_{DL}(DD)$$
$$\Longrightarrow \gamma_s\big(DL(G)\big) = \gamma(DL(G)).$$

Result 6

Split domination set of DLFG for the figure 2:
Subgraphs induced by ${}^{\sigma_{DL}}/_{DD}$ is $\langle {}^{\sigma_{DL}}/_{DD} \rangle$
The set of all possible subgraphs induced is
$\langle {}^{\sigma_{DL}}/_{DD} \rangle = \{(b, D, E, F), (a, c, E, F), (a, b, F), (b, c, F), (b, c, E), (c, E)(E, F)(c, D), (b), (F)\}$.
The minimum scalar cardinality is defined as split domination number of DLFG. $\gamma_s(DL(G)) = 2$.

Proposition

Let DD be minimum domination set of a double layered fuzzy graph $DL(G)$.
If $|DD| \geq \left|\frac{\sigma_{DL}}{2}\right|$, then $\gamma(DD) \geq \gamma\langle {}^{\sigma_{DL}}/_{DD} \rangle$

From the figure 1: We have the sets $DD = \{c, E\}$ and ${}^{\sigma_{DL}}/_{DD} = \{a, b, D, F\}$.
$\rho(DD) = 1$ and $\rho\big({}^{\sigma_{DL}}/_{DD}\big) = 2.6$. It is proven that the above proposition does not satisfy for double layered fuzzy graphs.
However, this result always holds for any crisp graph.

Proposition

If $\gamma(DD) < \gamma\langle {}^{\sigma_{DL}}/_{DD}\rangle$, then any $x \in DD$ dominates two or more vertices of ${}^{\sigma_{DL}}/_{DD}$, where D is a minimum dominating set.

From the figure 2: the set $DD = \{c, E\}$ is a dominating set of D(G).
$\rho(DD) = 1$ and $\rho\left({}^{\sigma_{DL}}/_{DD}\right) = 2.6$.
Therofore $\rho(DD) < \rho\left({}^{\sigma_{DL}}/_{DD}\right)$.
The vertex $c \in DD$ is adjacent to $\{a, b, F\} \in {}^{\sigma_{DL}}/_{DD}$ and $E \in DD$ is adjacent to $\{b, D, E\} \in {}^{\sigma_{DL}}/_{DD}$.

Result 7

Double domination set of DLFG for the figure:
Set of all possible double domination set of DLFG is $dDD = \{(a, b, c, E, F), (b, c, F, E), (a, c, D, E, f)\}$. Each vertex in σ_{DL} is dominated by at least two vertices in dDD. The minimum fuzzy cardinality taken over all dDD is double domination number $\gamma_{dd}(DL(G)) = 4$ for$\{b, c, F, E\}$ with the membership value is 2.2.

Proposition

For a double layered fuzzy graph $DL(G)$of order p. If there exists $x \in DD$ such that *x* has at least two neighbours in $DL(G)$ and for each $y \in N_{DL(G)}(x)$, y has at aleast one neighbor, then $\gamma_{dd}(DL(G)) \leq p - \sigma_{DL}$.

Proof:
For every $a \in \sigma_{DL}$ with at least two neighbours. Then $DD = \sigma_{DL} \backslash \{a\}$is a dominating set. Since each $b \in N_{DL(G)}$ has at least one neighbour, then we have $\gamma_{dd}(DL(G)) \leq p - \sigma_{DL}(a)$.
From the fig 2,
We have $\rho(dDD) = 2.2$ and $p = 3.1 - 0.6$, also $\sigma_{DL}(a)$= 0.6.
$\Longrightarrow 2.2 \leq 2.5$.
Hence the above proposition is proved.

Theorem: For any double layered fuzzy graph $DL(G)$ without isolated vertex, $\gamma_{dd}(DL(G) \geq \frac{4p-2q}{3}$.

Proof: Let us consider a double layered fuzzy graph $DL(G)$ without isolated vertex. Let dDD be the double dominating set of $DL(G)$if every vertex of σ_{DL} is dominated by at least two vertices in dDD. And $\gamma_{dd}(DL(G))$ as its double domination number of $DL(G)$ being with minimum scalar cardinality among all possible sets of double domination.
Thus, We have this inequality $\gamma_{dd}(DL(G)) \geq \frac{4p-2q}{3}$ holds good for any $DL(G)$.
As a counter example from the figure 2,
We have $\gamma_{dd}(DL(G)) = 2.2$, $p = 3.1, q = 3.4$.
satisfying the inequality $\gamma_{dd}(DL(G)) \geq \frac{4p-2q}{3}$
i.e., $2.2 \geq \frac{12.4-6.8}{3}$, which is clearly greater than *2.2*.

CONCLUSION

Throughout this paper, we have introduced varying domination into double layered fuzzy graph and identified the relation between them in form of propositions and results. As findings, theorem have been proved in dominations for double layered fuzzy graphs.

FURTHER DIRECTIONS

The concept of domination in graph is very rich in both theoretical developments and applications. Further works could be continued in domination with different parameters for any double layered fuzzy graphs.

REFERENCES

1. T. Pathinathan and J.Jesintha Rosline, "Double layered fuzzy graph", Annals of Pure and Applied Mathematics, 8(1), pp.135-143 (2014).
2. J.J Rosline, J.J. and T. Pathinathan, "Triple Layered Fuzzy Graph", Int. J. Fuzzy Mathematical Arhive, 8(1), pp.36-42, (2015).
3. T. Pathinathan and J.J Rosline, "Matrix representation of double layered fuzzy graph and its properties", Annals of Pure and Applied Mathematics, 8(2), pp.51-58, (2014).
4. A. Rosenfled, Fuzzy graphs, L.A Zadeh, K.S. Fu, K. Tanaka and M. Shimura, (editors), "In Fuzzy sets and their applications to cognitive and decision processes", Academic press, (New York 1975), pp. 77-95.
5. A. Nagoorgani and K. Radha, "The degree of a vertex in some fuzzy graphs", Internal Journal of Algorithms, Computing and Mathematics, 2(3), pp. 107- 116, (2009).
6. A. Somasundaram and S. Somasundaram, "Domination in fuzzy graph-I", Elsevier publishers, pp. 787-791, (1998).
7. A. Muneera and R.S. Rao, "On Domination of fuzzy graphs and fuzzy Trees", International Journal of Pure and applied Mathematics, 113(8), pp. 210-219, (2017).
8. O.T. Manjusha, O.T. and M.S. Sunitha, "Notes on domination in fuzzy graphs", Journal of Intelligent & Fuzzy Systems, 27(6), pp. 3205-3212, (2014).
9. Benjier H Arriola, "A note on some domination of fuzzy graphs", Ear East Journal of Applied Mathamatics, pp. 113-123, (2017).
10. A. Nagoor Gani and K. Prasanna Devi, "2–Domination in Fuzzy Graphs", International Journal Fuzzy Mathematical Archive", pp. 119-124, (2015).
11. A. Nagoor Gani and P. Vadivel, "A Study on Domination, Independent Domination and Irredundance in Fuzzy Graph", Applied Mathematical Science, 2317-2325 (2011).
12. S. Revathi, P.J.Jayalakshmi, and C.V.R.Harinarayanan Assistant P, "Perfect Domination Sets in Fuzzy Graph", IOSR Journal of Mathematics, 43-47 (2013).
13. A.Nagoorgani and M. Basheed Ahamed, "Order and size in fuzzy graphs", Bulletin of Pure and Applied Sciences, 22E(1),145 – 148 (2003).
14. T.W. Haynes, S.T. Hedetniemi, P.J. Slater, "Fundamentals of Domination in Graphs", (CRC PressNew York, Jan 1998).
15. L.A. Zadeh, "Fuzzy Sets", Information and Control 8, pp. 338-353 (1965).
16. J.Jesintha Rosline and T.Pathinathan, "Structural core graph of double layered fuzzy graph", Intern.J.Fuzzy Mathematical Archive, 8(2), pp. 59 – 67 (2015).
17. P. Bhattacharya, "Some Remarks on Fuzzy Graphs", Pattern Recognition Letters, 6, pp. 297-302 (1987).
18. K. R. Butani, "On Automorphisms of fuzzy graphs", Pattern Recognition Letters 9, pp. 159-162 (1989).
19. A. Nagoorgani and J. Malarvizhi, "Some aspects of total fuzzy graph", Proceedings of international conference on mathematical methods and computation, (Tiruchirappalli 2009), pp. 168 – 179.
20. E.J. Cockayne and S.T. Hedetnieme, "Towards a theory of domination in graphs", Netwroks 7, pp. 247-261(1977).
21. A. Nagoorgani and K. Radha, "The degree of a vertex in some fuzzy graphs", International Journal of Algorithm, Computing and Mathemtics, 2(3), pp.107-116 (2009).
22. A. Nagoorgani and M. Basheed Ahamed, "Order and size in fuzzy graphs", Bulletin of Pure and Applied Sciences, 22E(1), pp.145-148 (2003).

Available online at www.sciencedirect.com

ScienceDirect

Materials Today: Proceedings 8 (2019) 28–36

materialstoday: PROCEEDINGS

www.materialstoday.com/proceedings

ICMEE 2018

Synthesis, Growth and Characterization of $[DAMS]_2[CdI_4]$ single crystal [DAMS =4-N, N-dimethylamino-N-methyl-stilbazolium iodide]

A. Karolin Martina, J.Arul Martin Mani, J.Reena Priya, N.S. Nirmala Jothi*, and P. Sagayaraj

Department of Physics, Loyola College, Chennai – 600 034, India.

Abstract

The hybrid complex of inorganic-organic $[DAMS]_2[CdI_4]$ [[DAMS =4-N, N-dimethylamino-N-methyl-stilbazolium iodide] was synthesized by metathesization of the 4-N,N-dimethylamino -N-methyl stilbazolium iodide [DAMS.I^-] salt with cadmium acetate. The $[DAMS]_2[CdI_4]$ single crystals were grown by slow evaporation method using methanol as solvent. The single crystal X-ray diffraction analysis was carried out and the cell parameters a = 11.0569(3) Å, b = 12.8526(3) Å, c = 14.1427(4) Å, α = 73.7240(10)°, β = 73.9810(10)°, γ = 83.6640(10)° and Volume1853.17 (9) $Å^3$ were determined. The presence of functional groups and their corresponding vibrational modes are evaluated by FT-IR spectrum. The linear optical properties are investigated by UV-vis absorption. The melting point and thermal behavior of $[DAMS]_2[CdI_4]$ were investigated by Thermogravimetric / Differential Thermal Analysis [TG/DTA].

Selection and peer-review under responsibility of the scientific committee of the Materials For Energy and Environment.

Keywords: Single crystal XRD; Slow evaporation method; Thermal stability.

* Corresponding author. Tel.:+91-9444481558; fax: 91-44 28175566.
E-mail address: jmjnirmala@yahoo.co.in

Selection and peer-review under responsibility of the scientific committee of the Materials For Energy and Environment.

1. Introduction

The ability to combine the organic and inorganic compound with in one single molecule scale, have made the preparation of inorganic-organic hybrid compounds a focus area of chemistry and materials science. Second order nonlinear optical (NLO) response, magnetism, luminescence are some special properties exhibited by these crystals with interesting structure. [1-3]. Amoung the organic crystals, the organic stilbazolium salt 4-N, N – dimethylamino -4'-N'-methyl stillbozolium toysylate (DAST) is well known and potential material for electro optic application. This ionic organic material DAST has been investigated by many researchers for their use in optical applications. [4-5]. It has the advantages that the alignment of ionic chromophore can be controlled in a polar structure by changing the counter ion. Also it is an interesting material for phase-matched parametric interactions such as frequency doubling and optic parametric oscillations in the near infrared. [6] By changing the counter anion in the DAST structure, many derivatives has been developed and investigated. Here the hybrid organic-inorganic structure has been synthesized which has, organic cationic chromophore and inorganic anion. [7-8]. In this article we report synthesis, structural, optical and thermal properties of the grown crystal, which has potential application in the field of optics. [9] 4-dimthylamino benzaldehyde is a well-known chromophore exhibiting a large molecular hyperpolarizability (β) and large conjugation system, which will be beneficial to the exhibition on second order NLO property and luminescence [10-12]. As the effectiveness in solubility control is an important features of anion, an appropriate solubility of the crystal is required for the crystal growth from the solution. The properties will be varied according to the anion exchange and the new compounds with large NLO properties and with easy crystalline ability formed, is an interesting investigation. [13,14].

This crystal has been grown by slow evaporation method using methanol as solvent .In this present study cadmium atom was bonded to 4 iodine atoms to form a distorted tetrahedron, which was surrounded by DAMS cations. There is interaction between the 2 adjacent antiparallelly arrayed DAMS cations. The grown crystal has been subjected to single crystal XRD, FTIR, UV and thermal analysis.

2. Materials and method

In this work, slow evaporation method is used for synthesis and cell parameters values are found to be slightly different from that synthesized by solvothermal method [15]. ($[DAMS]_2[CdI_4]$) was prepared by metathesization reaction of the DAMS [4-N, N-dimethylamino-N-methyl-stilbazolium iodide] with Cadmium acetate. DAMS was synthesized by the condensation of 1,4-dimethyl pyridinium iodide (2.35g/10ml), methanol(30ml) and dimethylamino benzaldhyde (1.46g/12ml) in the presence of piperidine (0.2ml). The above mixture was refluxed for nearly a day and then cooled to room temperature. The product was filtered and recrystallized from methanol for about 6 times and stirred for 24 hours. The product appeared as a white precipitate which was later dried in an oven at 100^0 C for 8 hours.

Fig. 1. Photograph of as grown crystal $[DAMS]_2[CdI_4]$

During the next stage, the metathesization reaction was carried out by the following procedure. DAMS as synthesized is dissolved in Millipore water and simultaneously Cadmium acetate was dissolved in Millipore water by heating at 70 °C. These two hot solutions were mixed and heated for 30 min at 70 °C and then allowed to cool naturally to room temperature. A red precipitate was obtained as a result of exchange reaction between anion and

cation. The purity of $[DAMS]_2[CdI_4]$ was further improved by successive re-crystallization from methanol. $[DAMS]_2$ $[CdI_4]$ crystals with size up to 4 x 4 x 3 mm^3 are grown within a period of 4-5 weeks. The photograph of as grown crystal is shown in Fig. 1

3. Result and discussion

3.1. Single crystal x-ray diffraction analysis

The structural analysis of $[DAMS]_2[CdI_4]$ single crystal was carried out using Bruker APEX-II CCD' single crystal X-ray diffractometer. The XRD data was monitored at 293(2) K. The structural elucidation of precursors and refinements were performed using the SHELXL program. The Semi-empirical from equivalents influences the absorption correction and the structure was solved by Full-matrix least-squares and the refinements by using F2 taking all the unique refinements. The experimental conditions supporting the data and refinement for the $[DAMS]_2[CdI_4]$ is given in the table:1 This crystal $[DAMS]_2[CdI_4]$ belongs to the triclinic family with space group P-1 Centro symmetric and the cell parameters are very similar to that of DAST reported by Marder et all.[4]. The hydrogen atoms causing the H-bonds were located from the different Fourier and refined with isotropic thermal parameters while the non-hydrogen atoms were refined with anisotropic thermal parameters. The atomic co-ordinates and equivalent isotropic displacement parameters, bond length and bond angles, anisotropic displacement parameters, the hydrogen co-ordinates and isotropic displacement parameters of the$[DAMS]_2[CdI_4]$ are listed in table 2 -3respectively.

Fig: 2 shows the molecular structure of the hybrid compound. Fig: 3 show the crystal packing along *c* direction. It is clear that the cadmium atom is bonded to four iodine atoms in a distorted tetrahedron geometry, which is surrounded by DAMS cations. The DAMS cations can be divided into two groups between which the molecular planes are perpendicular to each other. It is interesting to note that the dipole directions of two adjacent DAMS cations are contrary to each other, that is, they are antiparallelly arrayed. [16,17]

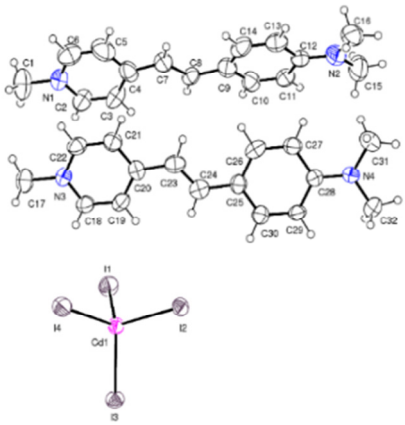

Fig.2 ORTEP diagram of $[DAMS]_2[CdI_4]$ crystal

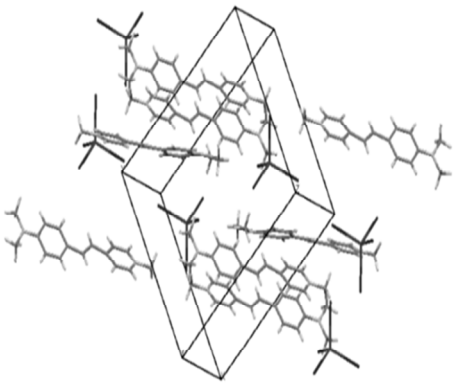

Fig.3 The crystal packing diagram of $[DAMS]_2[CdI_4]$

Table 1. Crystal data and structure refinement for $[DAMS]_2[CdI_4]$

Identification code	$[DAMS]_2[CdI_4]$	
Empirical formula	$C_{32}\ H_{38}\ Cd\ I_4\ N_4$	
Formula weight	1098.66	
Temperature	293(2) K	
Wavelength	0.71073 Å	
Crystal system	Triclinic	
Space group	P-1	
Unit cell dimensions	a = 11.0569(3) Å	α= 73.7240(10)°
	b = 12.8526(3) Å	β= 73.9810(10)°.
	c = 14.1427(4) Å	γ = 83.6640(10)°.
Volume	1853.17(9) $Å^3$	
Z	2	
Density (calculated)	1.969 Mg/m^3	
Absorption coefficient	3.947 mm^{-1}	
F(000)	1036	
Crystal size	0.150 x 0.100 x 0.100 mm^3	
Theta range for data collection	2.391 to 25.000°.	
Index ranges	-13<=h<=13, -15<=k<=15, -16<=l<=16	
Reflections collected	35805	
Independent reflections	6508 [R (int) = 0.0350]	
Completeness to theta = 25.000°	99.9 %	
Absorption correction	Semi-empirical from equivalents	
Max. and min. transmission	0.7456 and 0.6212	
Refinement method	Full-matrix least-squares on F^2	
Data / restraints / parameters	6508 / 70 / 389	
Goodness-of-fit on F^2	1.068	
Final R indices [I>2sigma(I)]	R1 = 0.0313, wR2 = 0.0509	
R indices (all data)	R1 = 0.0558, wR2 = 0.0622	
Extinction coefficient	n/a	
Largest diff. peak and hole	1.019 and -1.003 e.$Å^{-3}$	

For the same crystal grown by solvothermal method, the cell parameters are parameters a = 12.9849(19) Å, b = 13.1935(13) Å, c = 13.8792(10) Å, α= 106.798(10)°, β= 109.827(6)°, γ = 108.206(9)° and Volume 1906.0 (4) $Å^3$ [15]. The cell parameter values and bond angles for the same crystal are completely different when grown by slow evaporation method.

Table 2. Anisotropic displacement parameters ($Å^2 x\ 10^3$) for $[DAMS]_2[CdI_4]$. The anisotropic displacement factor exponent takes the form: $-2\pi^2[\ h^2\ a^{*2}U^{11} + ...\ + 2\ h\ k\ a^*\ b^*\ U^{12}\ ]$

	U^{11}	U^{22}	U^{33}	U^{23}	U^{13}	U^{12}
C(1)	153(8)	91(6)	107(7)	-46(5)	-80(6)	37(6)
C(2)	74(5)	53(4)	107(6)	-22(4)	-37(5)	-1(4)
C(3)	60(5)	85(5)	107(6)	-46(5)	-40(4)	15(4)
C(4)	80(5)	78(5)	57(4)	-12(4)	-6(4)	15(4)
C(5)	111(7)	60(5)	104(7)	1(5)	-15(6)	-21(5)
C(6)	82(6)	81(6)	114(7)	-36(5)	-25(5)	-22(5)
C(9)	65(5)	89(5)	51(4)	-19(4)	-6(3)	8(4)
C(10)	76(5)	59(4)	70(5)	-15(4)	-15(4)	6(4)
C(11)	58(4)	64(4)	71(4)	-26(4)	-18(4)	-3(3)
C(12)	48(4)	58(4)	54(4)	-17(3)	-5(3)	-4(3)
C(13)	63(4)	74(5)	74(5)	-29(4)	-9(4)	-15(4)
C(14)	56(4)	125(7)	65(5)	-42(5)	-19(4)	-7(4)
C(15)	120(8)	111(7)	128(8)	4(6)	-73(7)	-19(6)
C(16)	81(6)	67(5)	128(7)	4(5)	-9(5)	-1(4)
C(17)	85(5)	57(4)	81(5)	-18(4)	-40(4)	13(4)
C(18)	50(4)	57(4)	65(4)	-9(3)	-13(3)	-8(3)
C(19)	46(4)	74(4)	71(4)	-21(4)	-22(3)	-2(3)
C(20)	67(4)	46(3)	48(4)	-17(3)	-18(3)	6(3)
C(21)	61(4)	46(3)	66(4)	-11(3)	-17(3)	-9(3)
C(22)	50(4)	54(4)	73(4)	-15(3)	-14(3)	-10(3)
C(23)	58(4)	62(4)	71(5)	-22(3)	-9(4)	-13(3)
C(24)	61(4)	59(4)	64(4)	-29(3)	-13(3)	-3(3)
C(25)	59(4)	54(4)	53(4)	-18(3)	-20(3)	3(3)
C(26)	41(4)	74(4)	74(5)	-34(4)	-10(3)	-1(3)
C(27)	51(4)	57(4)	61(4)	-10(3)	-7(3)	-7(3)
C(28)	48(4)	39(3)	53(4)	-16(3)	-12(3)	0(3)
C(29)	39(3)	54(4)	59(4)	-12(3)	-7(3)	-7(3)
C(30)	57(4)	49(3)	59(4)	-16(3)	-17(3)	2(3)
C(31)	81(5)	87(5)	76(5)	13(4)	-12(4)	-18(4)
C(32)	57(4)	86(5)	84(5)	-9(4)	-30(4)	-3(4)
N(1)	69(4)	63(4)	68(4)	-30(3)	-28(3)	12(3)
N(2)	79(4)	66(4)	82(4)	-8(3)	-21(3)	-13(3)
N(3)	49(3)	51(3)	56(3)	-19(2)	-20(2)	5(2)
N(4)	48(3)	56(3)	57(3)	-3(3)	-9(3)	-5(2)
Cd(1)	48(1)	42(1)	50(1)	-9(1)	-15(1)	-5(1)
I(1)	70(1)	76(1)	73(1)	-28(1)	-12(1)	19(1)
I(2)	58(1)	41(1)	66(1)	-1(1)	-21(1)	-6(1)
I(3)	52(1)	51(1)	67(1)	-11(1)	-12(1)	-13(1)
I(4)	71(1)	78(1)	62(1)	-14(1)	-23(1)	-29(1)
C(7)	75(6)	60(6)	65(6)	-17(5)	-26(5)	-16(5)
C(8)	52(6)	67(7)	58(6)	-25(5)	-19(4)	-5(5)
C(7')	62(9)	67(9)	61(9)	-28(8)	-29(8)	-2(8)
C(8')	62(10)	82(10)	58(9)	-18(9)	-25(8)	-3(9)

Table 3. Hydrogen coordinates (x 10^4) and isotropic displacement parameters ($Å^2$x 10^3) for $[DAMS]_2[CdI_4]$

	x	y	z	U(eq)
H(1A)	4824	4107	998	160
H(1B)	4462	3220	567	160
H(1C)	3518	3562	1490	160
H(2)	6188	3541	1947	90
H(3)	7089	2289	3030	93
H(5)	4705	153	3106	117
H(6)	3856	1452	2039	106
H(10)	8581	107	5538	84
H(11)	9445	-1172	6640	75
H(13)	7816	-3478	6051	83
H(14)	6958	-2173	4963	93
H(15A)	10319	-3604	8135	176
H(15B)	10696	-2528	7281	176
H(15C)	9462	-2551	8159	176
H(16A)	9595	-4818	7759	153
H(16B)	8265	-4554	7538	153
H(16C)	9465	-4589	6643	153
H(17A)	6839	2668	-1092	108
H(17B)	7559	3603	-998	108
H(17C)	8181	2960	-1813	108
H(18)	9781	2915	-760	70
H(19)	10722	1732	382	74
H(21)	7692	-94	1324	69
H(22)	6847	1100	158	71
H(23)	9269	-664	2250	77
H(24)	11501	334	1391	71
H(26)	9942	-1771	3540	73
H(27)	10846	-2919	4738	70
H(29)	14200	-1627	3160	62
H(30)	13266	-493	2002	65
H(31A)	13070	-4332	6017	133
H(31B)	11750	-3787	5935	133
H(31C)	12466	-4480	5184	133
H(32A)	14704	-3467	5345	114
H(32B)	14973	-3151	4153	114
H(32C)	14665	-2244	4739	114
H(7)	6131	-626	3927	76
H(8)	7536	792	4334	67
H(7')	7324	1033	4171	70
H(8')	6397	-806	4163	79

3.1 FT-IR analysis

Vibrational spectroscopy has been extensively used to understand the factors contributing to the linear electro-optic effect from the vibrational modes in organic materials and to provide deeper knowledge regarding the intermolecular interaction nonlinear response and the hyper polarizability, molecular architecture and their relationship could also be studied. [14] The stilbazolium cation group comprise the vinyl group vibrations, phenyl ring vibrations and methyl group vibrations while the tosylate anion group encompass the sulfonate group and skeletal vibrations. The FTIR spectrum recorded using BRUKER IFS 66V FT-IR spectrometer. The measurement was done with KBr method for the wavelength range 400-4000 cm^{-1} and shown in figure: 4. The peak seen around 3036cm^{-1} C-H stretching vibrations of stilbene derivative, 2904 cm^{-1} derivative, alkyl C-H stretch, 1591 cm^{-1} trans stilbene C=C stretching, 821 cm^{-1}1,4distribution aromatic vibration, 962 cm^{-1}1,2 substituted pyridinium ring and 530 cm^{-1} is due to the phenyl ring C-H out of plane bending. The peak at 1160 cm^{-1} S=O Stretch of sulfonate group. [6].Various atomic molecular vibration are listed in Table 4.

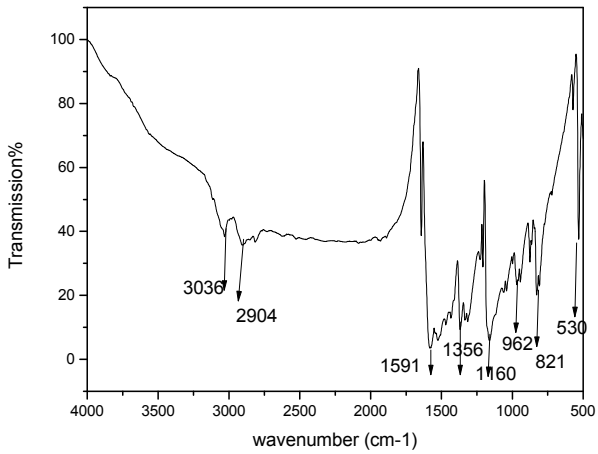

Fig.4. FT-IR spectrum of for $[DAMS]_2[CdI_4]$ crystal

Table 4. FTIR wavenumber assignment for $[DAMS]_2[CdI_4]$

S.No	Wavenumber cm^{-1}	Assignment
1	3036	C-H stretching vibrations of stilbene derivative
2	1160	S=O Stretch of sulfonate group
3	2904	alkyl C-H stretch
4	1591	stibence C=C stretching
5	962	1,2 substituted pyridinium ring
6	821	1,4 distribution aromatic vibration
7	530	phenyl ring C-H out of plane bending

3.3 *UV-Vis absorption analysis*

Figure. 5 shows the absorption spectrum of $[DAMS]_2[CdI_4]$ in solid phase using KAPPA APEX-II spectrophotometer recording in a wavelength region 200-1100 nm. The optical absorption spectrum of $[DAMS]_2[CdI_4]$ dissolved in methanol it is well known that when the DAST and its derivatives are dissolved in methanol, it leads to dissociated state generating free cations and anions. [19] The UV cut – off wavelength is found to be 450 nm. It is very useful to identify the optical absorption or transmission window and cut-off wavelength of the crystal. Also it is useful to understand its electronic states, when interacting with linear light. Absence of absorption in the region is between 545 and 1093 nm.

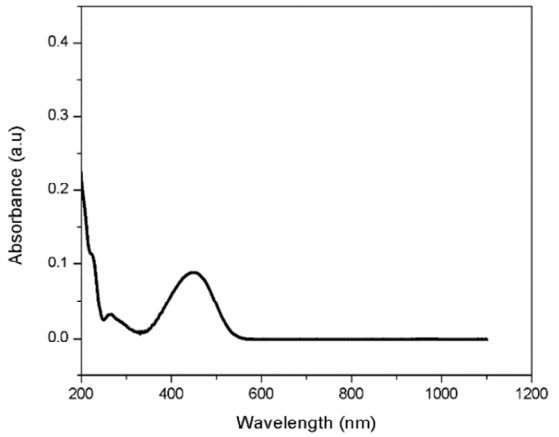

Fig.5 optical absorption spectrum of $[DAMS]_2[CdI_4]$

3.4 Thermal analysis

The thermal behavior of $[DAMS]_2[CdI_4]$ grown crystal was investigated by Thermogravimetric / Differential Thermal Analysis [TG/DTA] using carried between 28°C and 1000 °C at a heating rate of 15°C min^{-1} using the instrument Perkin-Elmer TGA-7 spectrometer. From the TG/DTA thermogram figure: 6. The TGA curve reveals the three distinct weight loss stages occurred on sample: the first one at 319.34°C connected with 3% mass loss was due to the removal of moisture absorbed by the compound. The 74% mass loss 433.83°C is indicative for the decomposition of pyridine moiety. DTA curve shows one main endothermic at 269.81◦C which corresponds to melting point and three exothermic peaks at 319.34, 395.51 and 498.30 °C indicating the major decomposition of materials.

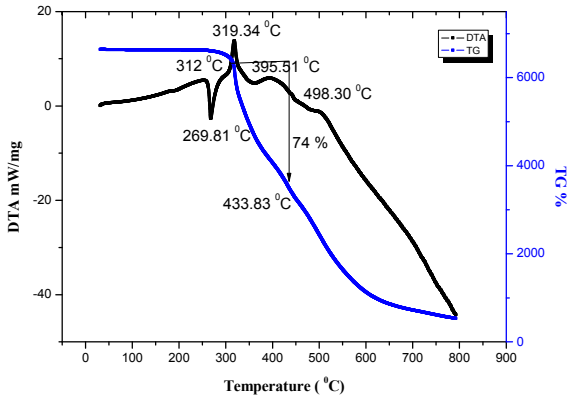

Fig.6. TG/DTA thermogram of $[DAMS]_2[CdI_4]$

4. Conclusion

The growth of the single crystal $[DAMS]_2[CdI_4]$ was achieved by slow evaporation method. The present study demonstrates the enhancement in the size of the crystal achieved through proper choice of solvent and growth conditions. The cell parameters of the grown crystals are determined using single crystal X-ray diffraction analysis. The presence of functional groups in the sample is verified using FT-IR analysis. The UV cut – off wavelength is found to be 450 nm. It is very useful to identify the optical absorption or transmission window and cut-off wavelength of the crystal. Thermal studies indicate that the sample was thermally more stable than DAST and a few other DAST derivatives.

References

[1] Mitzi, D.B. J. C. S., Dalton Trans. 2001, 1.
[2] Mitzi, D.B. Prog. Inorg. Chem. 1999, 48, 1.
[3] Qin, J.; Dai, C.; Liu, D.; Chen, C.; Wu, B.; Yang, C.; Zhan, C.Co ord. Chem. Rev. 1999, 188, 23.
[4] S. R. Marder, J. W. Perry, and W. P. Schaefer, "Synthesis of organic salts with large second-order optical nonlinearities," Science 245, 626–628 (1989).
[5] F. Pan, G. Knopfle, Ch. Bosshard, S. Follonier, R. Spreiter, M.S. Wong, P.Gunter,¨Appl. Phys. Lett. 69 [1996] 13.
[6] Y. Mori, Y. Takahashi, T. Iwai, M. Yoshimura, Y.K. Yap, T. Sasaki, Jpn. J. Appl. Phys. 39 [2000] L1006.
[7] Y.Li, J.Zhang, G.Zhang, L.Wu.Fu, Y.Wu, J.Cryst.Growth 327 [2011]127-132.
[8] Qin, J.; Dai, C.; Liu, D.; Chen, C.; Wu, B.; Yang, C.; Zhan, C. Coord. Chem. Rev. 1999,188, 23.
[9] Jiang, M.; Fang, Q. Adv. Mater. 1999, 11, 1147.
[10] S.R.Marder, J.W.Perry, W.P Schaefer, Science 245 (1989) 626.
[11] V.Alan, M.Blanchard-Desce, I.Ledoux-Rak, J.Zyss, Journal Chemical Society, Chemical communications 353 (2000).
[12] J.Ogawa,S.Okada,Z.Glavcheva,H.Nakanishi, Journal of Crystal Growth 310 (2008) 836.
[13] Ogawa, M.; Kuroda, K. Chem. Rev. 1995, 95, 399.
[14] P´ecaut, J.; Le Fur, Y.; Levy, J.; Masse, P.R. J. Mater. Chem 1993, 3, 333.
[15] Peng Ren,Jingui Qin,Chuangtian Chen,Deqing Zhang and Huanming Hu Journal of Chemical Crystallography, Vol.34.No,4. April (2004).
[16] Lacroix, P.G. Chem. Mater. 2001, 13, 3495.
[17] Lacroix, P.G.; Clement, R.; Nakatani, K.; Delaire, J. A.; Zyss,J.; Ledoux, I. Science 1994, 263, 658.
[18] C.Bosshard, R.Spreiter,I.Degiorgi and P.Gunter,Phys.Rev.B,66(2002) 205107.
[19] R.Macchi, E.Cariati, D.Marinotto, D.Roberto, E.Tordin, R.Ugo, R.Bozio. M,Cozzuol, D.Pedron, G.Mattei, J.Mater, Chem. 20 (2010) 1885-1890.

Available online at www.sciencedirect.com

ScienceDirect

Materials Today: Proceedings 8 (2019) 207–213

materialstoday: PROCEEDINGS

www.materialstoday.com/proceedings

ICMEE 2018

A Featural Analysis of Aluminium Doped SnO_2 and Bare SnO_2 Thin Films Grown on FTO Substrates

J. Kethzy Agnes [a], D.J. Sharmila[a], B. Praveen[a], K. Pugazhendhi[a], P. Naveen Kumar[a], J. Madhavan[a] and J. Merline Shyla[a]*

[a] *Department of Physics, Loyola Institute of Frontier Energy (LIFE), Loyola College, Chennai, India .email: jmshyla@gmail.com*

Abstract

Nanomaterials when developed as thin films exhibit better properties compared to nanoparticles. Tin oxide with its outstanding properties such as wide band gap, low electrical resistivity, and good chemical stability is a versatile material in the field of nanomaterials. Metal doped SnO_2 in addition exhibits enhanced properties. We report herein the preparation and analysis of the important properties of Al doped and pure SnO_2 thin films through a simple sol-gel process and subsequent spin coating on FTO substrates. Microstructural characterization of the thin films was carried out for comparative evaluation of their physical properties. The as-grown thin films were studied using powder XRD technique and the crystallite sizes were estimated for Al doped and bare SnO_2 thin films. The surface morphologies of the as-synthesized thin films were examined using High Resolution Scanning Electron Microscope. The observed images indicated lesser agglomeration and good homogeneity in the case of Al doped SnO_2 thin films in comparison with its pure counterpart. The surface area, pore volume and pore radius of the samples were determined using BET analysis. The Fourier Transform Infrared Spectroscopy evidenced the presence of the various functional groups related to the materials of the films.

Selection and peer-review under responsibility of the scientific committee of the Materials For Energy and Environment.

Keywords: SnO_2 thin films; Al doped SnO_2; sol gel; spin coating; microstructural study

* Corresponding author. Tel.: +91- 94442 39551; Fax: 91- 44-28175566.
E-mail address: jmshyla@gmail.com

Selection and peer-review under responsibility of the scientific committee of the Materials For Energy and Environment.

1. Introduction

From the beginning of this century, there has been a continuous quest for revolutionary approaches for the renovation of exciting scientific routes. Nanotechnology with its uncommonly gifted properties has accomplished itself in all technological applications. Reduced dimensional nanostructured material has taken nanotechnology up a notch. Thin films play an invigorate role in the development and study of collective nanomaterials as the result of their exciting properties and enhanced device performance [1]. Plurality of nanostructured materials assembled on thin films lifts up the functionality of device in comparison with their individual entities. Thin films are cheaper to manufacture owing to low material cost and energy expenditure. Thin films help to achieve ordered distribution and controlled orientation making them preferable for mass production of devices.

In the field of nanomaterials, oxides play a dominant role.They can adopt a vast number of structural geometries with an electronic structure that can exhibit metallic, semiconductor or insulator characteristics. Oxides are employed in the manufacture of sensors, piezoelectric devices, fuel cells, microelectronic circuits, coatings for the passivation of surfaces against corrosion, and as catalysts [2]. Tin oxide (SnO_2) was one of the first considered yet frequently used for various applications. Tin oxide is known to exhibit a low electrical resistance with high optical transparency [3] in the visible range of the electromagnetic spectrum. Although they are transparent in the visible range, they are highly reflective for infrared light [4]. It is this property which makes it useful as an energy conserving material. SnO_2 an n-type wide band gap semiconductor [5], possesses high conductivity due to intrinsic defects [6]. Thus, tin oxide has been much investigated and it is found that this semiconductor oxide, displays excellent potential for a wide range of applications [7].

Doping facilitates in ameliorating the chemical, physical and electrical properties by the addition of the dopant in lattices of metal oxide [2]. Dopants such as Fe, Cr, Al, Cu, etc. lead to an increase in the surface area of the metal oxide making it more reactive for absorption [8]. Some transition metal elements have close ionic radius parameter to that of Sn^{4+}, which means these elements can easily penetrate into SnO_2 crystal lattice or substitute Sn^{4+} position in crystal. Al^{3+} has been the most used dopant element due to its small ionic radius and low material cost. The substitution of Sn^{4+} by Al^{3+} ions in the SnO_2 system creates oxygen vacancies due to the charge imbalance, generating free electrons in the conduction band making it favorable for photovoltaic application [9]. Doping with Al can induce a change from n-type to p-type as the Al-content is increased in the Al-doped SnO_2 system [10].

Fluorine Doped Tin Oxide (FTO) coated glass substrate has many excellent properties [11] such as electrical conductivity and optical transparency, high visibility to near IR light transmission, uniform transmission homogeneity and reflection in the infrared range which benefits the initial nucleation and subsequent growth of high quality SnO_2 films on FTO substrate [12] making it a good candidate for transparent conductive oxide [13].

Various methods have been developed for the synthesis of thin films, most of which are based on bottom up process. Sol-gel method is more supple and offers many advantages, such as excellent film homogeneity, well-defined film thickness, simple and low-cost processing, low- temperature processing, and most significantly, the ability to produce fine films [14]. Spin coating is imperative for fabrication of ultra-thin, ultra-high density thin films.

Here, we present the investigation undertaken on simple and environment friendly processed SnO_2 and Al doped SnO_2 thin films. The nanoparticles were synthesized by a simple sol-gel route and made into thin film by spin coating the prepared nanoparticles on FTO substrate. We report the superior behavior of Al doped SnO_2 over pure SnO_2 on account of doping by carrying out microstructural characterization such as X-ray Diffraction, Fourier Transformed Infrared Spectroscopy, High Resolution Scanning Electron Microscopy and BET analysis**.**

2. Experimental details

2.1. Synthesis Procedure

All the chemicals used in this process were of analytical grade and used without any further purification. In a typical synthesis process of SnO_2 thin film 2.25 grams of Tin(II)chloride dihydrate ($SnCl_2.2H_2O$) and 1.26 g of Oxalic acid ($C_2H_2O_2$) are dissolved in a mixture of 10 ml of deionized water & 10 ml of Isopropyl Alcohol(C_3H_8O), under magnetic stirring for half an hour . Then 5 ml of Ammonia (NH_3) is added dropwise to the solution and subjected to continuous stirring for 24 hours to form the resulting product. Ammonia is added to maintain the pH value and aids in formation of sol [15]. The semi-solid colloidal fluid was taken from the solution to be seated on the FTO substrate. The FTO substrates were gently cleaned and further subjected to ultra-sonication to remove any kind of impurities. The product is coated on FTO substrate for 60 seconds under 4500 rpm in a spin coater. The desired thickness of the film is achieved by repeated deposition. The coated FTO substrate is annealed in the furnace at 400˚ C for 4 hours to crystallize the thin film.

For the synthesis of Al doped SnO_2 thin films, 0.02 g of Aluminum Chloride Hexahydrate ($AlCl_3.6H_2O$) was additionally added to the mixture under continuous stirring for half an hour, prior to the addition of ammonia and is followed by the same procedure as in the preparation of SnO_2 thin films. .

2.2. *Characterization techniques*

The X- ray diffraction (XRD) patterns of the as-prepared pure and Al doped SnO_2 thin films were studied using a Phillip PW 1800 X-ray diffractometer with Cu Kα radiation of wavelength 1.5405Å.The morphology of the samples were examined by a High Resolution Scanning Electron Microscope (HITACHI S-4800). Fourier Transformed Infrared (FTIR) spectra of the samples were recorded using a Perkin Elmer R×1 spectrometer ranging from 4000 to 400 cm^{-1}, respectively. BET (Brunauer-Emmett-Teller) surface area and BJH (Barrett-Joyner-Halenda) pore size distribution were measured by Micromeritics ASAP 2020 porosimeter.

3. Results and Discussion

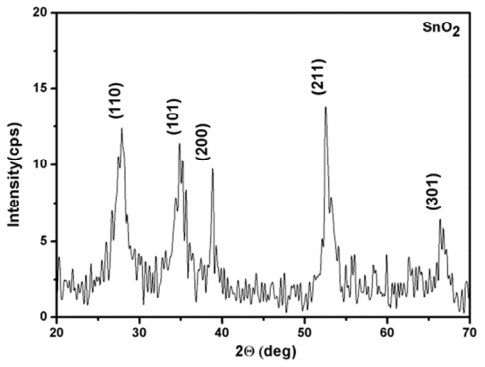

Fig. 1. (a) XRD pattern of SnO_2

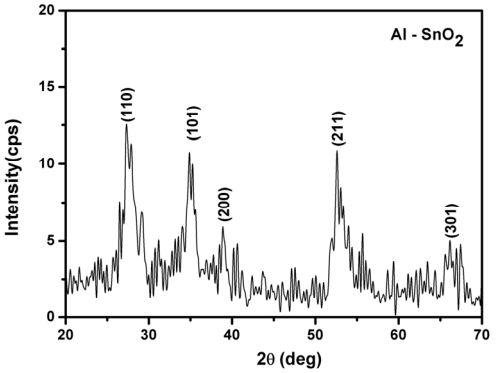

Fig. 1. (b) XRD pattern of Al-SnO_2

Figure 1. (a) and (b) show the typical XRD patterns of SnO_2 and Al doped SnO_2 films respectively. All the diffraction peaks are in good accordance with the tetragonal cassiterite SnO_2 (JCPDS file No: 41-1445) [16]. No characteristics peaks from other impurities are observed. A small shift in the peak values of Al-SnO_2 films indicates Al doping. This is due to the difference in the ionic radii of Sn^{4+} and Al^{3+} resulting in small changes in the crystal micro-structure [13]. From most intensity diffraction peaks along the planes (110), (101), (211), we observe that the synthesized films are poly-crystalline in nature. Crystallite size D is calculated using Scherer's formula

$$D = \frac{0.89\lambda}{\beta \cos\theta}$$

where λ is wavelength of incident X-ray,β is full width at half maximum (FWHM) intensity and θ is Bragg's diffraction angle. The average crystallite size calculated is found to be 24.76 nm and 23.85 nm for bare and Al doped SnO_2 films [18]. Al doping reduces the size of SnO_2 nanoparticles since the metallic ion doping inhibits the crystal growth of SnO_2 [19].

Micrograms from High Resolution Scanning Electron Microscopy (HRSEM) are presented in Fig 2. (a) and (b). The morphology of the thin films is studied at high magnification. The aggregates exhibit an irregular spherical structure in both cases. The dark spots indicate a moderate level of agglomeration in the samples [20]. It is clearly visible in the case of Al doped SnO_2 observed by HRSEM images, that the addition of Al decreases the size of the nanoparticles which agrees well with the XRD results [10].

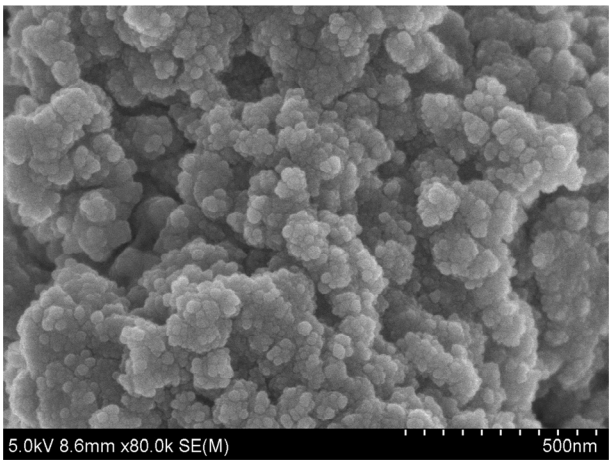

Fig. 2. (a) SEM image of SnO_2

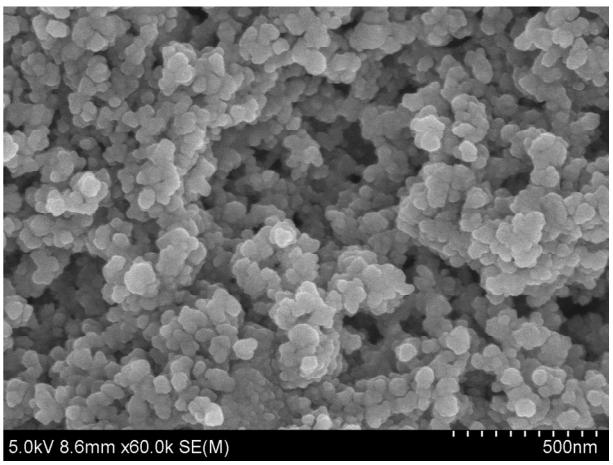

Fig. 2. (b) SEM image of Al-SnO_2

FT-IR spectral measurements for Al doped and bare SnO_2 thin films deposited on FTO substrates are shown in Figure 3 (a) and (b). The sol-gel derived Al doped and bare SnO_2 films contains no other residual species such as chlorine or propoxy groups making sol -gel one of the feasible methods for the preparation of thin films [10].The low transmittance υ_1 attributes to the O-H bond stretching vibrations of H_2O molecule adsorbed [21]. A sharp peak υ_2 is due to carbon dioxide absorbed while exposing the films in atmosphere [10] while υ_3 is designated to CO vibration. The peak υ_4 attributes to the bending vibrations of adsorbed water molecules [22]. A peak υ_5 is caused by vibration of Sn-O-Sn in SnO_2 molecule. The small peak υ_6 ascribes to Al-O bond stretching vibration [23] .

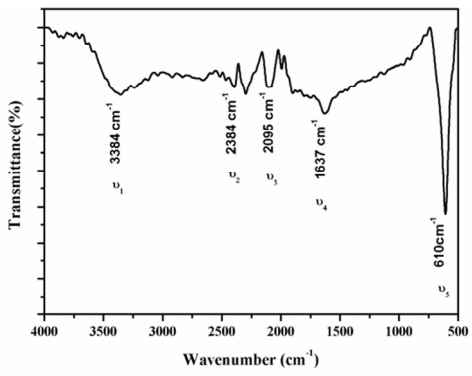

Fig. 3. (a) FT-IR spectrum of SnO_2

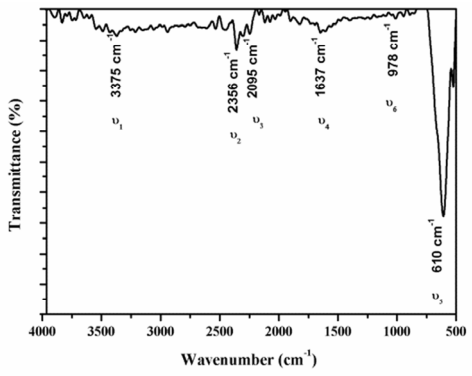

Fig. 3. (b) FT-IR spectrum of Al- SnO_2

The Brunauer-Emmett-Teller (BET) analysis of the as-prepared SnO_2 and Al doped SnO_2 thin films has been performed and the N_2 adsorption-desorption curve is shown in Fig. 4. (a) and (b) and the parameters are summarized in Table.1. The nitrogen adsorption-desorption isotherms of pure and Al doped SnO_2 shows that they are of type IV with a distinct hysteresis loop observed according to IUPAC classification which is an indication of porous structures. Hysteresis loop observed in the plot is associated with the filling and emptying of mesopores by capillary condensation [21]. A characteristic hysteresis loop can be observed in the plot at higher relative pressures, indicating the presence of mesopores in both the films [24]. A surface area of 19.547 $m^2 g^{-1}$ and 20.862 $m^2 g^{-1}$ for pure and Al doped SnO_2 is inferred.

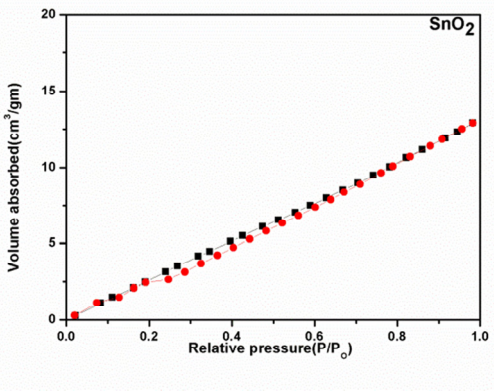

Fig. 4. (a) N_2 adsorption-desorption curve of SnO_2

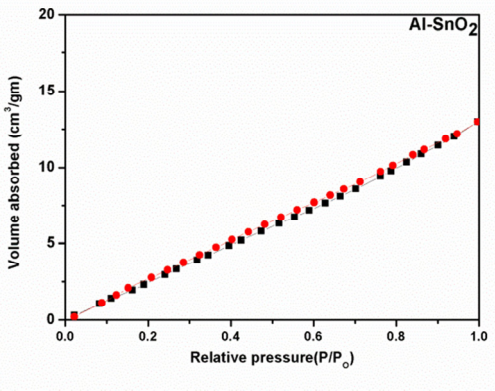

Fig. 4. (b) N_2 adsorption-desorption curve of Al-SnO_2

Table 1. Parameters obtained from BET analysis

Parameters	SnO_2	Al - SnO_2
Pore radius (nm)	1.791	1.551
Pore volume (cc/g)	0.017	0.026
Surface Area (m^2/g)	19.547	20.862

It is clear from Table 1 that on incorporation of Al^{3+}, the particle size and the pore radius reduces suggesting that the dopant influences the grain growth and the porosity of pure SnO_2 material. The high surface area and the mesoporous nature of the material is expected to be beneficial for absorbing of incident particles [25] making Al-SnO_2 thin films a better candidate for photovoltaic applications.

4. Conclusions

To summarize, high quality pure and Al doped SnO_2 nanocrystalline thin film on FTO substrate has been prepared by sol gel method using spin coating technique. The microstructural and morphological properties of the as-prepared films are studied. The observed XRD pattern shows that the particles exhibit tetragonal phase. The crystallite size of the particles decreased by Al dopant which supports the data derived from SEM images. The FT-IR spectra confirm the various functional groups present. From BET analysis, we deduce that the Al doping increases the surface area that favors many device fabrication opportunities. Comparing the properties of the pure SnO_2 and Al doped SnO_2 thin films on FTO substrate, Al doped SnO_2 thin films emerged as a promising foundation for fabricating gas sensing and photovoltaic devices and can be extended to a wide range of applications owing to its enhanced properties.

5. Acknowledgement

The funding extended by the Loyola College - Times of India Research Grants (6LCTOI1421F002) towards this work is gratefully acknowledged.

References

[1] L. Hu, D.S. Hecht, G. Gru, Carbon Nanotube Thin Films : Fabrication , Properties , and Applications, Chem. Rev. 110 (2010) 5790–5844. doi:10.1021/cr9002962.

[2] M.J.A. Fernández-garcia, Rodriguez, Metal Oxide Nanoparticles, Nanomater. Inorg. Bioinorg. Perspect. (2007) 60. doi:10.1002/0470862106.ia377.

[3] F. Li, J. Xu, X. Yu, L. Chen, J. Zhu, Z. Yang, X. Xin, One-step solid-state reaction synthesis and gas sensing property of tin oxide nanoparticles, Sensors Actuators B …. 81 (2002) 165–169. http://www.sciencedirect.com/science/article/pii/S0925400501009479.

[4] M. Khechba, A. Bouabellou, F.C. Hanini, S. Touati, Effect of Al doping on the structural and optical properties of SnO 2 thin films elaborated by sol-gel technique, 7 (2017) 72–75.

[5] S. Luo, J. Fan, W. Liu, M. Zhang, Z. Song, C. Lin, X. Wu, P.K. Chu, Synthesis and low-temperature photoluminescence properties of SnO 2 nanowires and nanobelts, Nanotechnology. 17 (2006) 1695–1699. doi:10.1088/0957-4484/17/6/025.

[6] H. Search, C. Journals, A. Contact, M. Iopscience, I.P. Address, Evolution of the doping regimes in the Al-doped SnO 2 nanoparticles prepared by a F H Arag on, 95301 (n.d.). doi:10.1088/0953-8984/27/9/095301.

[7] A.C. Fernandez, P. Sakthivel, J. Jesudurai, Et Al., A Novel Approach towards Gas Sensing Through A.C.Conductivity of Tin Oxide-Aluminum Oxide Composite ,3(6):, 3 (2014).

[8] S.M. Ali, S.T. Hussain, S.A. Bakar, Effect of doping on the Structural and Optical Properties of SnO 2 Thin Films fabricated by Aerosol Assisted Chemical Vapor Deposition Effect of doping on the Structural and Optical Properties of SnO 2 Thin Films fabricated by Aerosol Assisted Chemical Va, (2013). doi:10.1088/1742-6596/439/1/012013.

[9] P. Kumar, C. Panda, M. Kar, Evolution of the doping regimes in the Al-doped SnO 2 nanoparticles prepared by a F H Arag on, (n.d.). doi:10.1088/0953-8984/27/9/095301.

[10] S.F. Ahmed, S.K.P.K. Ghosh, K.K. Chattopadhyay, Effect of Al doping on the conductivity type inversion and electro-optical properties of SnO 2 thin films synthesized by sol-gel technique, (2006) 241–247. doi:10.1007/s10971-006-7808-x.

[11] M. Shokooh-saremi, The influence of Al doping on the electrical , optical and structural properties of SnO 2 transparent conducting films deposited by the spray pyrolysis technique, 1248 (2004) 0–6. doi:10.1088/0022-3727/37/8/014.

[12] K.B. Kumar, P. Raji, Synthesis and Characterization of Nano Zinc Oxide by Sol Gel Spin coating, 3 (2011) 48–52.

[13] N. Kumari, A. Ghosh, S. Tewari, A. Bhattacharjee, Synthesis , structural and optical properties of Al doped SnO 2 nanoparticles, 88 (2014) 65–70. doi:10.1007/s12648-013-0387-0.

[14] N.A. Dahham, A. Esmaeel, N.A. Abed, Effect of Al doping on the Structural properties of SnO2 thin films prepared by (sol-gel) method, 21 (2016) 155–161.

[15] A.E. Danks, S.R. Hall, Z. Schnepp, The evolution of "sol–gel" chemistry as a technique for materials synthesis, Mater. Horiz. 3 (2016) 91–112. doi:10.1039/C5MH00260E.

[16] D.M. Qu, P.X. Yan, J.B. Chang, D. Yan, J.Z. Liu, G.H. Yue, R.F. Zhuo, H.T. Feng, Nanowires and nanowire-nanosheet junctions of SnO2 nanostructures, Mater. Lett. 61 (2007) 2255–2258. doi:10.1016/j.matlet.2006.08.058.

[17] J. Wu, D. Zeng, S. Zhang, Mesoporous Al-doped SnO 2 nanotubes with enhanced gas-sensing properties fabricated by electrospinning, (2013) 257–262. doi:10.5162/sensor2013/B4.4.

[18] M. Benhaliliba, C.E. Benouis, Y.S. Ocak, Nanostructured Al Doped SnO 2 Films Grown onto ITO Substrate via Spray Pyrolysis Route, 1 (2011) 272–276.

[19] K. Suematsu, N. Ma, M. Yuasa, RSC Advances incorporation of Al for the detection of, (2015) 86347–86354. doi:10.1039/C5RA17556A.

[20] P.S. Kolhe, P.M. Koinkar, N. Maiti, K.M. Sonawane, Synthesis of Ag doped SnO2 thin fi lms for the evaluation of H2S gas sensing properties, Phys. B Phys. Condens. Matter. 524 (2017) 90–96. doi:10.1016/j.physb.2017.07.056.

[21] S. Blessi, M.M.L. Sonia, B. Francis, S. Pauline, S. Pauline, CODEN (USA): PCHHAX Effect of aluminium substitution in porous tin dioxide nanoparticles, 8 (2016) 488–492.

[22] M.M. Rashad, A.A. Ismail, I. Osama, I.A. Ibrahim, A.H.T. Kandil, Photocatalytic decomposition of dyes using ZnO doped SnO2nanoparticles prepared by solvothermal method, Arab. J. Chem. 7 (2014) 71–77. doi:10.1016/j.arabjc.2013.08.016.

[23] A.R. Razeghizadeh, L. Zalaghi, I. Kazeminezhad, V. Rafee, Growth and Optical Properties Investigation of Pure and Al- doped SnO 2 Nanostructures by Sol-Gel Method, (n.d.) 1–9.

[24] Y.F. Wang, W.X. Zhao, X.F. Li, D.J. Li, Engineered interfacial and configuration design of double layered SnO2@TiO2-ZnO nanoplates ternary heterostructures for efficient dye-sensitized solar cells, Electrochim. Acta. 151 (2015) 399–406. doi:10.1016/j.electacta.2014.11.059.

[25] L. Qi, D.P. Birnie, Templated titania films with meso- and macroporosities, Mater. Lett. 61 (2007) 2191–2194. doi:10.1016/j.matlet.2006.08.076.

Available online at www.sciencedirect.com

ScienceDirect

Materials Today: Proceedings 8 (2019) 412–418

materialstoday: PROCEEDINGS

www.materialstoday.com/proceedings

ICMEE 2018

Structural and Optical Analysis of 1D Zinc Oxide Nanoparticles Synthesized Via Hydrothermal Method

Mahendiran M[a,b], A. Asha[a,b], J. Madhavan[a] M. Victor Antony Raj[a, b]*

[a]*Department of Physics, Loyola College, Chennai, India.*
[b]*Loyola Institute of Frontier Energy (LIFE), Loyola College, Chennai, India.*

Abstract

Nano sized zinc oxide was synthesized by simple hydrothermal method using zinc acetate dihydrate as a transition metal precursor in the presence of NaOH. The synthesized nanoparticles were characterized by X-ray Diffraction (XRD), High resolution scanning electron microscope (HR-SEM), UV-Visible spectroscopy (UV-Vis) Fourier Transform Infrared Spectroscopy (FT-IR) and Dielectric studies. From the XRD analysis of ZnO the hexagonal crystalline structure was found based on which the crystal size and lattice parameters were calculated. The HR-SEM shows the morphology of ZnO nanoparticles. A UV-Visible spectrum helps to find the band gap of zinc oxide. The FT-IR studies show a prominent peak at 447 cm^{-1} which indicates the formation of ZnO bond. The dielectric loss and dielectric constant have high values at low frequency. The high ac resistance shows the presence of space charge polarization, which plays an important role in the electrical property of ZnO.

Selection and peer-review under responsibility of the scientific committee of the Materials For Energy and Environment.

Keywords: 1D ZnO nanoparticles, Hydrothermal, visible light, FT-IR, Dielectric

1. Introduction:

ZnO is a transition metal which is an important crystalline functional semiconductor. It is a direct band gap of semiconducting material and an excitation binding energy (E_g) of around 60MeV at room temperature. Zinc oxide

* Corresponding author. Phone: +91-9976249172 ; Fax: +91-44-28175566
E-mail address: vicvad2003@yahoo.co.in

Selection and peer-review under responsibility of the scientific committee of the Materials For Energy and Environment.

is an II-VI semiconductor with a variety of interesting chemical and physical properties. Metal oxides with specific properties are currently establishing new research areas. It is widely accepted that the morphology, crystal structure and size of nanomaterials mainly depend on the method of preparation. Synthesis of ZnO with tunable size and morphology can be done by using the methods of zinc oxidation, chemical vapour deposition (CVD), sol-gel, co-precipitation, and hydrothermal method. Among all these methods, hydrothermal method is the best method to synthesize highly pure and advanced nanostructures, whose surface properties can be controlled. Zinc oxide is a compound of great interest, since it has hexagonal (wurtzite) structured nano rods. It has attracted a lot of researchers, because it is non-toxic, inexpensive and has an extensive range of applications in solar cells, gas sensors, light emitting diodes (LEDs), transducers, photocatalytic devices and various photonic and optoelectronic devices which are used for information Storage. Due to the large surface to volume ratio, nanoparticles contain a large number of vacancies. Size and surface effects are both significant at the nanoscale to control these vacancies. The presence of a large number of vacancies greatly helps in the elimination of photo-generated electrons, which in turn affects the luminescence properties of the nanoparticles. Therefore, it is essential to control the surface of nanoparticles to achieve improved optical properties.

2. Experimental detail:

Initially, 4.388 g (0.2 M) of Zinc Acetate dehydrate (Zn $(CH_3COO)_2$. $2H_2O$) was dissolved in 100 mL of deionized water and the solution was stirred for 2h till a transparent solution was obtained. Then, 0.8g (1M) of NaOH was dissolved in 20 mL of deionized water and was added drop by drop to the above solution and stirred for 1h till the pH of the solution becomes 7. The solution was then transferred into a 150 mL Teflon lined autoclave and kept in a furnace. The temperature of the furnace was maintained at 180˚C for 8h and then slowly cooled to room temperature naturally. After this process, the obtained product was centrifuged at a rate of 3000 rpm and washed five times with deionized water and ethanol. The white precipitate was then dried in a furnace at 150˚C for 3h. The dried white precipitate was finally grounded to get the required Zinc oxide (ZnO) nanoparticles.

3. Characterization

Phase identification of the obtained powder was performed with a X-ray Diffraction instrument. The morphology of the sample was carried out by high resolution scanning electron microscope (HR-SEM). The optical absorption of the sample was observed with the help of UV-Vis spectroscopy. The chemical elements in the prepared nanoparticles were determined by using Fourier transform infrared (FT-IR) spectroscopy. Dielectric studies can reveal the electrical properties of the sample.

4. Results and Discussions:

4.1 Structural Study:

Fig 4.1 shows the X-ray Diffraction (XRD) patterns of the pure zinc oxide (ZnO) nanoparticles synthesized by simple hydrothermal method. The diffraction peaks are indexed to hexagonal Structure (JCPDS NO 36-1451). The sharp and strong diffraction peaks demonstrate that the products are well crystallized. The diffraction peaks present at 31.7°, 34.4°, 36.1°, 47.5°, 56.6°, 62.8°, 66.4°, 67.9, and 69.1 can be respectively indexed to (1 0 0), (0 0 2), (1 0 1), (1 0 2), (1 1 0), (1 0 3), (2 0 0), (1 1 2), and (2 0 1) of ZnO planes. The average particle size (D) of the zinc oxide (ZnO) nanocrystals can be obtained using the Debye Scherrer formula,

$$D=0.94\lambda/ \beta \cos\theta \ldots\ldots\ldots\ldots (1)$$

Where D is the mean particle size, β is the full width at half maximum of the diffraction line, θ is the Bragg angle of diffraction and λ is the wavelength of the X-ray radiation. From the full width at half maximum of the (1 0 0)

diffraction peak the particle size can be calculated. In this case, the average particles size is found to be 55 nm. The lattice parameters calculated from the (100) diffraction peak are a=3.252Å, c=5.643.

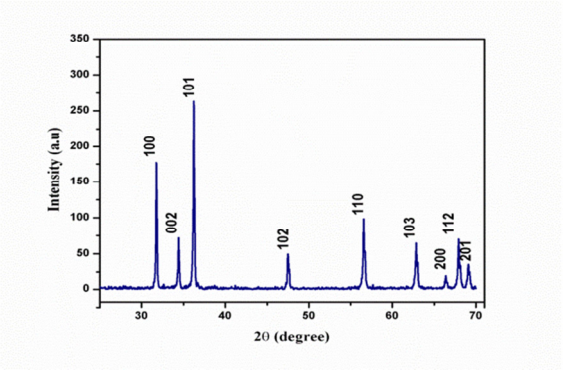

Figure 4.1: X-ray Diffraction Analysis (XRD)

4.2 HR-SEM (High Resolution Scanning Electron Microscope)

The morphology of the synthesized zinc oxide (ZnO) nanopowders are examined by the high resolution scanning electron microscope (HR-SEM). It shows several morphology and shape such as hexagonal disks, spheroidal structure elongated porous hexagonal nano rod and flower like structure, spindle like structure. Further increasing the temperature results in shape variation. Fig 4.2 shows the HR-SEM images of ZnO, it can be confirmed that the synthesized powder shows the nanoparticles shape.

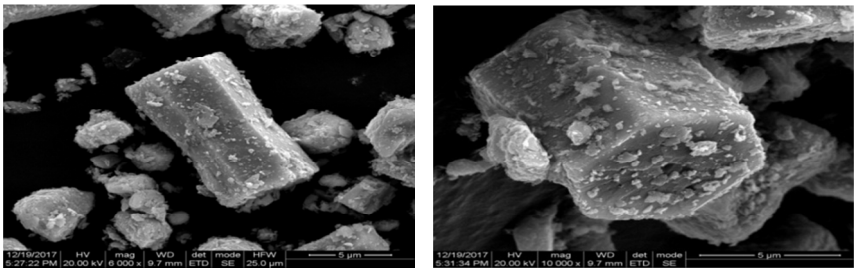

Figure 4.2: HR-SEM analysis of ZnO

This shows the ZnO nanorods obtained for pH 7 got hexagonal structure. Well defined nanorods like morphology study has found out the synthesized ZnO are in form of rod like structure. The EDX spectrum of pure ZnO nanoparticles Fig. 4.3 confirms the presence and formation of pure ZnO nanoparticles. The nanorods contain only elements of Zn and O without any other impurities was indicated by the pattern.

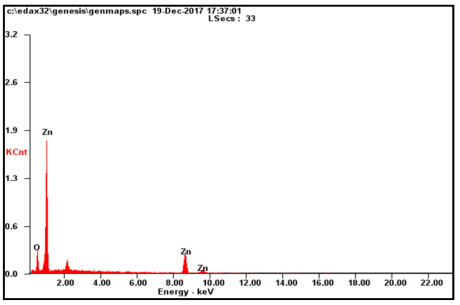

Figure 4.3: EDAX analysis of ZnO

4.3 UV-Vis studies

The optical absorption band gap energy is determined by using Kubelka- Munk Function,

$$\left(h\nu F(R\infty)\right)^2 = A(h\nu - E_g) \quad \ldots\ldots\ldots\ldots (2)$$

Where h is Planck's constant, ν is the frequency of vibration, E_g is the energy gap, A is the proportionality constant and F (R∞) is the function of reflectance and can be expressed as,

$$F(R\infty) = \frac{(1-R)^2}{2R} \quad \ldots\ldots\ldots\ldots (3)$$

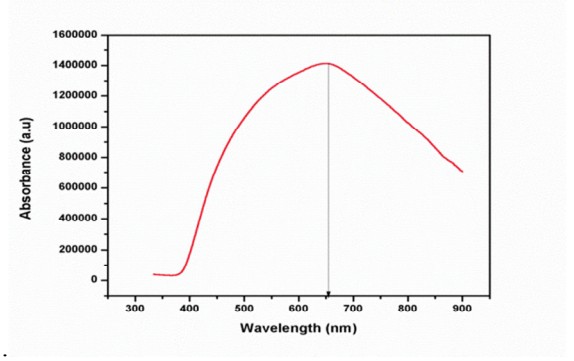

Figure 4.3: Reflectance spectra of Pure ZnO nanoparticles

The reflectance spectra of pure ZnO nanoparticles are shown in Fig 4.3. The Kubelka – Munk plot is plotted between (hν F(R∞))^2 and hν (eV). The optical band gap of pure ZnO can be found out by extrapolating the linear portion of the energy axis at zero reflectance. The Kubelka – Munk plot for the pure ZnO nanoparticles is shown in Fig 4.4 respectively. The optical band gap of pure ZnO nanoparticles was found to be 3.027 Ev.

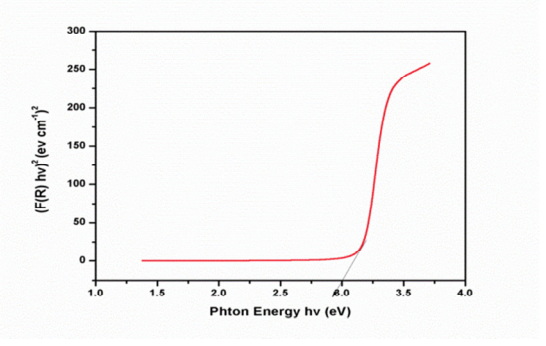

Figure 4.4: The Kubelka-Munk plot of ZnO nanoparticles

4.4 FT-IR: (Fourier Transform Infrared Spectroscopy)

The chemical composition of the synthesized ZnO nanoparticles was examined by (FT-IR) spectroscopy. FT-IR spectra are generally used to characterize compounds.

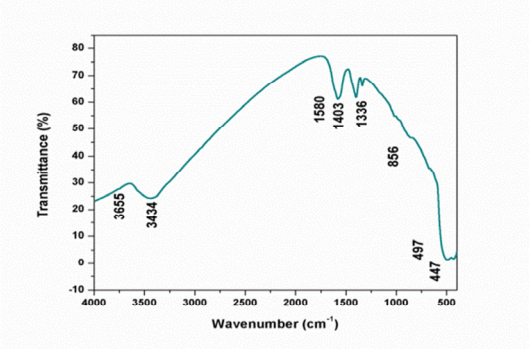

Figure 4.5: Fourier Transform Infrared Spectroscopy (FT-IR)

They give information about the functional groups, molecular geometry and inter / intra molecular interactions present in compounds. The FT-IR spectra shown in Fig. 4.5, the wavenumber is taken between 400 to 4000 cm^{-1}. It shows well-defined peaks appearing at 447 cm^{-1}, 1580 cm^{-1} and 3434cm^{-1}. The occurrence of a strong peak at 447 cm^{-1} is due to the Zn-O stretching vibration. The bond at 1403 cm^{-1} corresponds to the asymmetric stretching mode of C=O. The other two peaks appearing at 1580 cm^{-1} and 3434 cm^{-1} are originated due to the bending vibration of the absorbed surface water O-H stretching mode. The spectra reveal the nature of elements in the synthesized ZnO nanoparticles.

4.5 Dielectric studies:

The energy storing property of the dielectric material leads to the fabrication of capacitors, which is the most important component in any electrical circuit. The dielectric phenomenon arises from the interaction of electric field with different charged particles such as electrons, ions, protons and electron shells. Materials with more dielectric constants are very convenient for fabrication of high-value capacitors. The dielectric constant (ε) consists of two components. A real permittivity or relative dielectric constant, normally called as dielectric constant of the test material (ε_r) and an imaginary permittivity or dielectric loss (ε_i). Dielectric constant of the material (ε_r) is calculated using the following equation,

$$\boldsymbol{\varepsilon_r = \frac{tC_p}{A\varepsilon_0} = \frac{tC_p}{\pi r^2 \varepsilon_0}} \quad \textbf{..... (4)}$$

Where‘t’ is the thickness, C_p is the parallel capacitance, ε_0 is the relative permittivity and r is the radius. Fig 4.6 shows that the dielectric constant has high values in the low frequency region and thereafter its values decrease with the applied frequency. The high values of ε_r at low frequencies may be due to the existence of all the four polarizations, namely orientation, ionic, electronic and space charge polarization. The low values at higher frequencies may be due to the gradual loss of these polarizations. The variation of dielectric loss with frequency is shown in Fig. 4.7**.** The ac electrical conductivity can be determined using the relation,

$$\sigma_{ac} = \omega\, \varepsilon_o\, \varepsilon_r \tan\delta \quad \text{..... (5)}$$

Where $\omega = 2\pi f$, in which, f is the frequency. The variation of frequency with ac conductivity is shown in Fig. 4.8. From the high values of ac conductivity at low frequencies, it can be said that the space charge polarization plays an important role in the electrical properties of the sample.

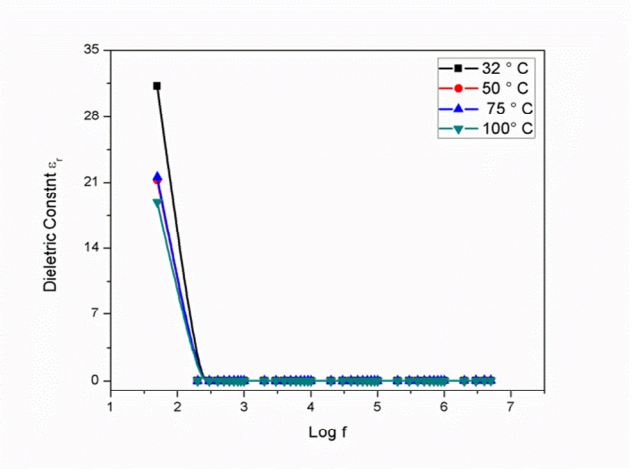

Figure 4.6: Dielectric Constsnt

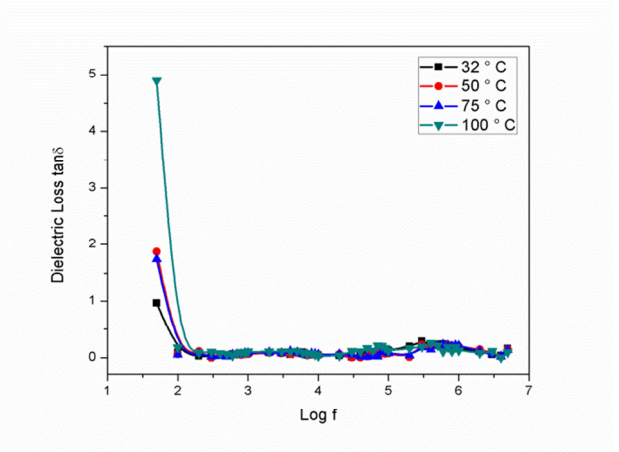

Figure 4.7: Dielectric Loss

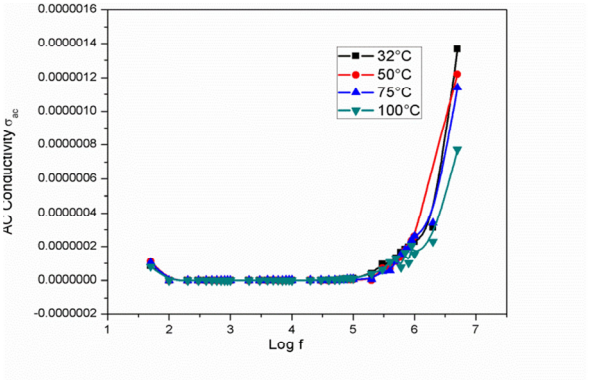

Figure 4.8: AC conductivity

4.5 Conclusions

In this work, zinc oxide nanoparticles were successfully synthesized by using a simple hydrothermal method and characterized. The X-ray diffraction showed the particle structure and also used to calculate the average crystal size, which is 55 nm. The high resolution scanning electron microscope shows the nanorod shape and hexagonal structure. Fourier transform infrared spectroscopy showed the chemical composition of the material and the Zn-O stretching vibration. From the UV-Visible spectrometry, it was found that the zinc oxide nanomaterials had a direct band gap of 3.027eV and thus their optical properties were also studied. The dielectric constant, dielectric loss and ac conductivity obtained from the dielectric studies showed the electric properties of the zinc oxide nanoparticles.

References

1. Randeep Lamba, Ahmad Umar, Prof., S.K. Mehta, Sushil Kumar Kansal, Prof "ZnO doped SnO2 nanoparticles heterojunction photo-catalyst for environmental remediation", Journal of Alloys and Compounds, S0925-8388(15)30916-6.
2. N. Kumaresana, K. Ramamurthia*, R. Ramesh Babub, K. Sethuramanc, S. Moorthy Babud "Hydrothermally Grown ZnO Nanoparticles for Effective Photocatalytic Activity", Applied surface science, S0169-4332(16)32975-0.
3. J.N. Hasnidawani [1,a*], H.N. Azlina [1,b], H. Norita[1,c], N.N. Bonnia[2,d], S. Ratim[2,e] and E.S. Ali[2,f] "Synthesis of ZnO Nanostructures Using Sol-Gel Method", procedia chemistry 19 (2016) 211-216.
4. Sa Liang a,1, Lianfeng Zhu b,1, Guosheng Gai b, Youwei Yao c, Jue Huang c, Xuewen Ji d, Xiaoming Zhou a, Dongyun Zhang a, Peixin Zhang a,* "Synthesis of morphology-controlled ZnO microstructures viaa microwave-assisted hydrothermal method and their gas-sensing property", Ultrasonics Sonochemistry 21 (2014) 1335–1342.
5. Juan Xiea,b, Hu Wanga,b,, Ming Duana, Liehui Zhanga, "Synthesis and photocatalysis properties of ZnO structures with different morphologies via hydrothermal method", Applied Surface Science 257 (2011) 6358–6363.
6. Mohd Mubashshir Hasan Farooqi, Rajneesh K. Srivastava "Structural, optical and photoconductivity study of ZnO nanoparticles synthesized by annealing of ZnS nanoparticles", Journal of Alloys and Compounds, S0925-8388(16)32643-3.
7. Gaurav Hitkari, Sandhya Singh, Gajanan Pandey * "Structural, optical and photocatalytic study of ZnO and ZnO–ZnS synthesized by chemical method", Nano-Structures & Nano-Objects 12 (2017) 1–9.
8. Kun Xu, Changzhen Liu, Rui Chen, Xiaoxiang Fang, Xiuling Wu, Jie Liu "Structural and room temperature ferromagnetic properties of Ni doped ZnO nanoparticles via low temperature hydrothermal method", Physics of Condensed Matter, S0921-4526(16)30296-4.
9. Prakash Chand, Anurag Gaur ⇑, Ashavani Kumar "Structural and optical properties of ZnO nanoparticles synthesized at different pH values", Journal of Alloys and Compounds 539 (2012) 174–178.
10. Dinesh Varshney Kavita Verma Sonam Dwivedi "Structural and dielectric studies of hexagonal ZnO nanoparticles", Optik - International Journal for Light and Electron Optics, S0030-4026(15)00885-2.
11. Radhika S., Jesty Thomas "Solar light driven photocatalytic degradation of organic pollutants using ZnO nanorods coupled with photosensitive molecules", Environmental Chemical Engineering, S2213-3437(17)30398-6.
12. Donghwan Lee a, Taeho Kang a, Yoon-Young Choi b, and Seong-Geun Oh a, "Preparation of electron buffer layer with crystalline ZnO nanoparticles in inverted organic photovoltaic cells", Journal of Physical and Chemistry of Solids, S0022-3697(16)31273-2.
13. Pijus Kanti Samantaa, Abhijit Sahab, Tapanendu Kamilya "Morphological and optical property of spherical ZnO nanoparticles", Optik 126 (2015) 1740–1743.

Available online at www.sciencedirect.com

ScienceDirect

Materials Today: Proceedings 8 (2019) 435–443

materialstoday: PROCEEDINGS

www.materialstoday.com/proceedings

ICMEE 2018

Experimental and Theoretical Studies of Glycine Zinc Sulphate: An Adequate NLO Single Crystal

A Shiny Febena[a], M Victor Antony Raj[a,b], J Madhavan[a,*]

[a]*Department of Physics, Loyola College, Chennai -34.*
[b]*Loyola Institute of Frontier Energy (LIFE), Loyola College, Chennai-34.*

Abstract

The present work deals with the synthesis, growth, characterization and DFT studies of a nonlinear optical material Glycine Zinc Sulphate (GZS). Crystals have been grown by slow evaporation technique. XRD analysis confirmed that the crystal belongs to orthorhombic structure with lattice parameters a = 8.340 Å, b = 8.279 Å, c = 12.522 Å and space group orthorhombic $Pca2_1$. Presence of various functional groups in GZS and protonation of the ions were confirmed by the Fourier Transform infrared spectroscopy (FT-IR) analysis. The optimized molecular geometry of GZS was calculated using density functional theory (DFT). The optical energy band gap was calculated to be 4.55 eV from optical absorption studies. TGA/DTA studies show the thermal stability of the grown crystals. Micro hardness studies reveal that the grown crystal possesses good mechanical strength. The SHG efficiency of GZS is three times higher than KDP.

Selection and peer-review under responsibility of the scientific committee of the Materials For Energy and Environment.

Keywords: GZS; DFT; FT-IR; TGA/DTA; SHG; KDP.

1. Introduction

Nonlinear optical applications find a variety of applications to perform functions like frequency conversion, light modulation, optical switching, optical memory storage and optical second harmonic generation. The new

* Corresponding author. Phone: +91-9840479638 ; Fax: +91-44-28175566
E-mail address: jmadhavang@yahoo.com

Selection and peer-review under responsibility of the scientific committee of the Materials For Energy and Environment.

development technique for the fabrication and single crystal growth of nonlinear optical materials has dramatically contributed to this evolution. On account of the large flexibility for molecular design and higher nonlinear optical efficiency, there has been much progress in basic research on organic and semi organic NLO materials. In this respect, amino acids are interesting materials for NLO applications. The significance of amino acids in NLO applications is due to the fact that all the amino acids have chiral symmetry and crystallize in non-centrosymmetric space groups. Also, some of the amino acids are used as dopants and they enhance the material properties like nonlinear optical and ferroelectric properties.

Amino acids are interesting organic materials for NLO applications as they contain donor carboxylic (COOH) group and the proton acceptor amino group (NH2) group in them, called as zwitter ions. Out of 20 amino acids Glycine is the simplest of all. Glycine family crystals have been subjected to extensive research by several researchers for their efficient NLO properties. Attempts were made to grow a crystal from organic-inorganic complexes in which the high optical nonlinearity of a purely organic compound is combined with the favorable mechanical and thermal properties of inorganic materials [1–6].

In current study, a potential semi-organic nonlinear optical single crystal of Glycine Zinc Sulphate (molecular weight 236.54 g/mol) has been grown by slow evaporation solution growth technique at room temperature. The Glycine Zinc Sulphate crystallizes in orthorhombic crystal system with Pca21 space group. The grown crystal was confirmed by XRD and FT-IR analyses. The molecular structure and spectroscopic properties of Glycine Zinc Sulphate (GZS) have been studied at the DFT/B3LYP level with 6-31G (d, p) basis set were calculated and discussed in detail.

2. Experimental Details

2.1Material Synthesis and Crystal Growth

Glycine Zinc Sulphate (GZS) was synthesized by dissolving equimolar ratio of high purity Glycine [NH2CH2COOH] and Zinc Sulphate, with distilled water as the solvent. The chemical reaction is

$$\mathbf{ZnSO_4.\ H_2O + NH_2CH_2COOH \rightarrow Zn\ [NH_2CH_2COOH]\ SO_4\ .\ H_2O}$$

Prior to growth, GZS was recrystallized several times to yield the purified material. Before crystal growth, the solubility of Glycine Zinc Sulphate in water was measured as a function of temperature in the range 30 and 50 °C. The saturated solution, prepared in room temperature with excess of solute was magnetically stirred and equilibrated for nearly 3 hours before the sample was taken. Solubility was then measured gravimetrically. The GZS has positive solubility gradient. The solubility curve obtained was shown in Fig. 1. As the solubility is higher in water, attempts were made to grow bulk single crystals of the synthesized material using water as the solvent. A saturated solution of GZS was taken and the solution was filtered and kept undisturbed for evaporation in a dust free environment. After a period of 40 days, good quality single crystal of size 14 x 9 x 6 mm^3 was harvested. The photograph of the as grown crystal is shown in Fig. 2.

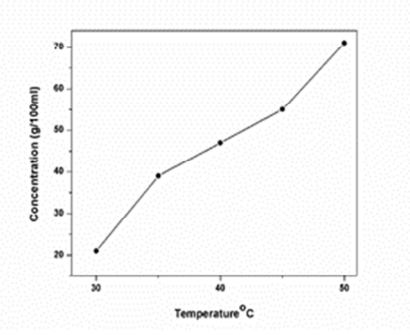

Fig. 1. The Solubility Curve

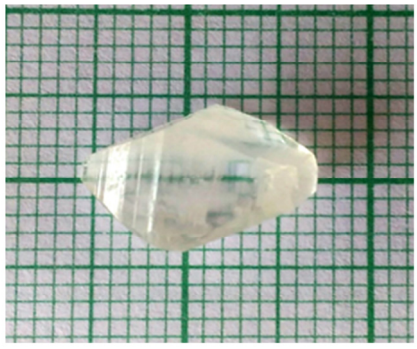

Fig 2 Photograph of GZS crystal

3. Results and Discussion

3.1. Powder X-Ray Diffraction Analysis

To test the crystallinity of the sample, Powder X-Ray Diffraction patterns were obtained at room temperature using a Rich-Seifert powder x-ray diffractometer with CuKα radiation (λ = 1.5418 Å) was used at a scan speed of 0.02°/s. The grown crystals were of high degree of crystallinity which can be revealed from the sharp and high intensity peaks. The sharp and well defined Bragg's peak at specific 2θ angles in the pattern attest the proper orientation of the crystallite, purity and perfection of the grown crystal, this manifests that the grown crystals belong to single crystal class. Experimental and theoretically simulated powder XRD pattern of GZS single crystal with indexed peak is given in Fig. 3 and Fig. 4. The crystal data is given in Table 1.

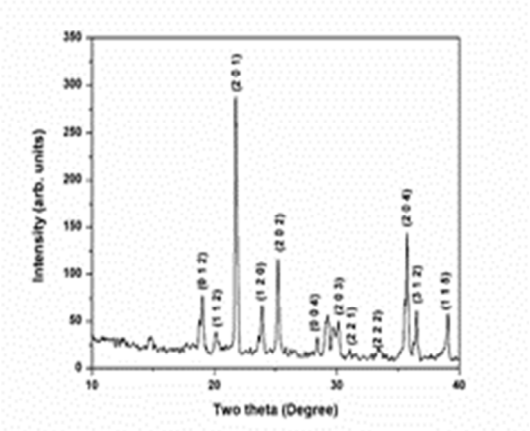

Fig. 3. Powder XRD spectrum of GZS

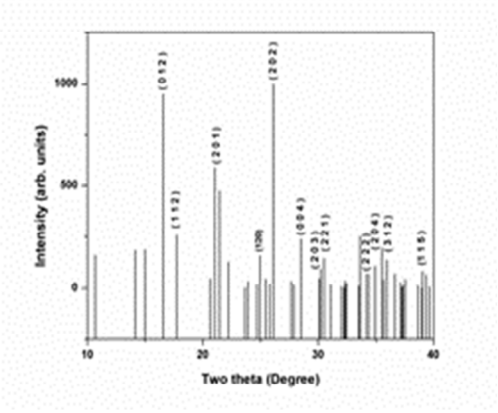

Fig. 4. Theoretically simulated Powder XRD spectrum

Table 1. Crystal parameters of GZS

Empirical Formula	$C_2H_{11}NO_9SZn$
Crystal system	Orthorhombic
Space group	$Pca2_1$
Unit cell dimensions	a = 8.340 Å
	b = 8.279 Å
	c = 12.522 Å
	α= β =γ=90°
Cell volume	864.6 $Å^3$

3.2. Computational details

The density functional theory (DFT) with B3LYP level theory using 6-31G(d, p) basis set in Gaussian-09 have been used for theoretical calculations. The structure optimization and the geometry optimization for the complexes has been done using the DFT method with the functional B3LYP and basis set 6-31G (d, p) [7,8].

3.3. Molecular Geometry

The optimized molecular structure of GZS is shown in Figure 5. Detailed description of vibrational modes can be given by means of normal coordinate analysis. The internal coordinates describe the position of the atoms in terms

of distances, angles and dihedral angles with respect to an origin atom. The symmetry coordinates are constructed using the set of internal coordinates.

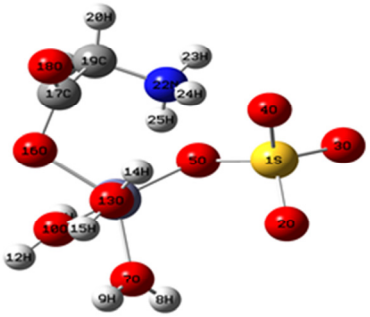

Fig. 5. Atomic numbering system adapted for GZS molecule

3.4. Vibrational assignments

The molecule GZS belongs to Cs point group symmetry. The title molecule (GZS) has 25 atoms. It has 69 normal vibrational modes. 47 of these modes should be in-plane symmetric (A′) and 22 out-of-plane symmetric (A″) with respect to the reflection on the symmetry plane. The fundamental modes are distributed among the symmetry species as

$$\Gamma\ 3N\text{-}6 = 47A' \quad \text{(in-plane)} + 22A'' \quad \text{(out-of-plane) respectively}$$

The detailed vibrational assignments of fundamentals often made on the basis of the unscaled frequencies by assuming the observed frequencies so that they are in the same order as the calculated ones. The infrared spectral analysis was carried out to understand the chemical bonding and it provides useful information regarding the molecular structure of the compound. Fourier transform infrared spectrum was taken for the powdered sample of GZS in the wavelength of 400–4000 cm^{-1} following KBr pellet technique as shown in Fig. 6.

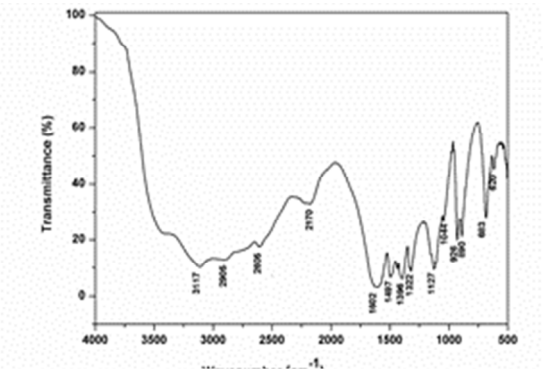

Fig. 6. FT-IR Spectrum of GZS

The most important feature of carboxylic group is a single band which is observed usually between 1650 and 1550 cm^{-1} (asymmetric stretching mode) and around 1440 cm^{-1} (symmetric stretching mode) [9,10]. In the present

study, the peaks at 1648 cm^{-1} (theoretical) and 1602 cm^{-1} (experimental) of GZS crystal are in agreement with the band values of asymmetric modes of vibration.

The COO- deformation coupled with rocking mode appears as a very strong band at 533 cm^{-1} which is in agreement with the theoretical value 539 cm^{-1} rocking in-plane and out-of-plane deformation vibrations are observed as medium-to-strong bands in the region 760-400 cm^{-1} [11].

Table 2. Experimental and Calculated B3LYP/6-31 G (d, p) level of vibrational frequencies of GZS

No.	Frequency (cm^{-1})		Spectroscopic assignment	Force constant	Reduced mass
	B3LYP	Expt.			
1.	507.6478	504	COO^- opd+CCl st	0.2355	1.5511
2.	533.6512	539	COO^- d+opd	0.7908	4.7133
3.	659.1552	620	COO^- roc ipd	0.2750	1.0741
4.	676.5270	683	COO^- opd	1.2114	4.4923
5.	833.8694	890	CH opb	7.2064	17.5903
6.	957.7089	929	R asy d	1.4737	2.7271
7.	1018.4878	1044	NH_2 t	1.6838	2.7551
8.	1103.4815	1127	CN st	2.1408	2.9840
9.	1451.1042	1436	COO^- sym st	1.5010	1.2099
10.	1506.4586	1497	NH_3^+ sym d+CN st	1.7983	1.3449
11.	1648.4421	1602	NH_3^+ asy d	1.7230	1.0762

The vibrational bands observed between 1400 and 1650 cm^{-1} are due to C-C stretching vibrations in benzene derivations [12]. The carbon-carbon stretching modes of the phenyl group are expected in the range from 1650 to 1200 cm^{-1}. In general, the bands of stretching are observed at 1600-1400 cm^{-1}.The ring C=C and C-C stretching vibrations, known as semicircle stretching occurs in the region 1625-1400 cm^{-1} and 1380-1280 cm^{-1}. In the present work the C-C stretching vibrations in benzene derivations are observed at 1436 cm^{-1}, 1497 cm^{-1} and 1602 cm^{-1} .The corresponding theoretical assignments are at 1451 cm^{-1}, 1506 cm^{-1} and 1648 cm^{-1} which is consistent with the experimentally observed values. The detailed vibrational assignments of fundamental modes, force constant and reduced mass of GZS by DFT methods are reported in Table 2.

3.5. Hyper Polarizability

The nonlinear response, linear polarizability and first order hyperpolarizability can be related as a Taylor expansion [13]. The calculated first order hyperpolarizability values for GZS molecule are given in Table 3. The calculated first order hyperpolarizability of GZS is 3.6434 x 10-30 e.s.u. The result indicates that intermolecular hydrogen bonds have a substantial influence on the first hyperpolarizability.

3.6. HOMO-LUMO Energy gap

The highest occupied molecular orbital (HOMO) and lowest unoccupied molecular orbital (LUMO) are referred to as Frontier molecular orbitals (FMOs) and it can provide more useful details on optical and excited state properties [14,15].

Table. 3. Calculated Hyperpolarizability

	B3LYP/ 6-31G
	Dipole Moment in Debye
μ_{tot}	16.1894
	Polarizability in esu
α_o	6.5417×10^{-31}
	Hyperpolarizability in esu
β_{xxx}	-70.8917068
β_{xxy}	-115.6153578
β_{xyy}	-17.5513275
β_{yyy}	-214.4878355
β_{xxz}	22.1289043
β_{xyz}	15.1888649
β_{yyz}	1.0861532
β_{xzz}	-70.4969638
β_{yzz}	-75.1296562
β_{zzz}	-16.5954812
β_{tot}	3.6434×10^{-30}

It can provide qualitative indication of the molecular excitations and charge transfer interactions that play an essential role in NLO response. The HOMO–LUMO energy gap and the molecular electrostatic potential in the crystal was simulated using the DFT method at the B3LYP/6-31G basis set [16]. The small energy gap of FMOs plays a significant role in chemical reactivity, optical polarizability, chemical hardness and softness of the appropriate molecule. The calculated energies of HOMO and LUMO are -0.267 a.u and -0.161 a.u respectively and the energy gap of GZS is found to be 0.106 a.u. This lower energy gap reveals the high chemical reactivity and chemical softness of the grown crystal. Moreover, this decrease in energy gap facilitates more responsible for the large polarity of the grown crystal and more NLO active because of eventual charge transfer that takes place within the molecule. HOMO–LUMO plot of GZS molecule is shown in Fig. 7.

HOMO energy (B3LYP) = -0.267 a.u.
LUMO energy (B3LYP) = 0.161 a.u.
HOMO–LUMO energy gap (B3LYP) = 0.106 a.u.

The LUMO as an electron acceptor represents the ability to obtain an electron and HOMO represents ability to donate an electron. The strong charge transfer interaction through π-conjugated bridge results in substantial ground state donor–acceptor mixing and the appearance of a charge transfer band in the electron absorption spectrum.

3.7. SHG Efficiency

The SHG measurement of GZS crystals were carried out by passing the output of Nd: YAG Quanta ray laser emitting 1064 nm, generating about 6 mJ/pulse. KDP was used as the reference material. The measured amplitude of second harmonic signal (532 nm) for KDP is 91.66 mW and for GZS is 278.32 mW for the same laser input pulse of 6.2 mJ. Thus, it is observed that the SHG efficiency of the grown GZS crystal is 3 times that of the standard KDP crystal.

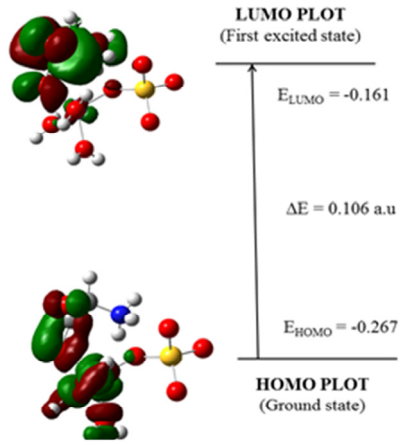

Fig. 7. HOMO-LUMO energy gap

3.8. Optical absorption spectrum

The optical property of the GZS crystal was assessed by using UV-Visible spectrometer. The specimen was subjected to transmission measurements in the spectral region of 200 – 1200 nm. Optical absorption spectrum of grown crystal of GZS is shown in Fig. 8.

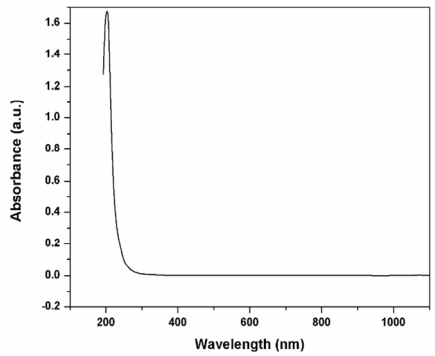

Fig. 8. Optical absorption spectrum

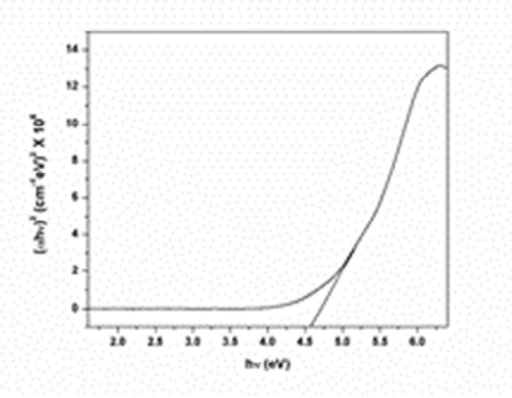

Fig. 9. Optical band gap

From the spectrum, it is evident that the GZS crystal has good transparency and the lower cutoff wavelength of the crystal is found to be 240 nm which is one of the key requirements for having efficient NLO character [15] and shows that the crystal possesses good optical transparency for SHG. The band gap value was determined using Tauc's a graph plotted between photon energy and ($\alpha h\nu^2$). Where α is the absorption co-efficient and h is the energy of the incident photon from the Fig. 9. The band gap energy is found to be 4.55 eV.

3.9. Thermal studies

To analyze the thermal stability, melting point and phase transition of Glycine Zinc Sulphate (GZS), Thermo gravimetric (TG) and Differential Thermal Analyses (DTA) for GZS were carried out by NETZSCH STA 409C thermal analyzer. The percentage of weight loss of the samples as a function of temperature is measured in TGA. The TGA curve also shows the different stages of weight loss. A steady weight loss of 51.45 % was observed in the range of 181 – 315 °C. The second stage occurs in the temperature range 315 – 520 °C with a weight loss of 17.4%. Third weight loss step occurs from 520°C. A residue of 16.36 % remains after 910 °C. The TGA trace clearly indicates that the compound is thermal stable up to 181°C. The thermal studies affirm the grown crystal may be exploited for NLO applications. TGA and DTA curve of GZS crystal is shown in Fig.10.

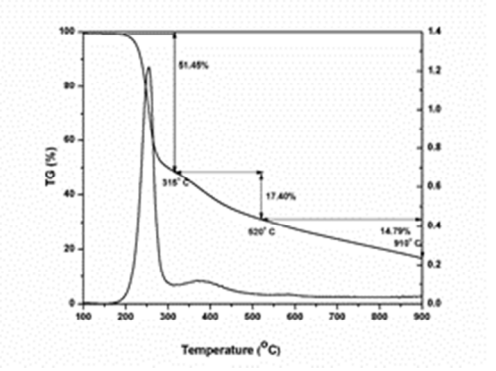

Fig. 10. TG/DTA of GZS crystal

4. Conclusion

In this study, we have reported the growth and characterization of Glycine Zinc Sulphate (GZS). The structural characterization of the synthesized compound was made by using the X-ray analyses and spectroscopic methods. FT-IR and thermal analysis were performed to study the molecular vibration and thermal behavior respectively. The first hyperpolarizability of the compound studied has been calculated by B3LYP method. The calculated HOMO and LUMO along with their plot has been presented for understanding of charge transfer occurring within the molecule and molecular energy gap was found as 0.106 a. u. Optical absorption spectrum was recorded for the given crystal and the band gap energy is found to be 4.55 eV. The SHG efficiency of the grown GZS crystal is 3 times that of the standard KDP crystal which indicates the use of GZS crystals for application in nonlinear optical devices.

Acknowledgements

The authors acknowledge University Grants Commission (UGC), India, for funding this research project-F.No.4-4/2015-16 (MRP/UGC-SERO).

References

[1] A.C. Peter, M. Vimalan, P. Sagayaraj, J. Madhavan, Thermal , optical , mechanical and electrical properties of a novel NLO active L -phenylalanine L -phenylalaninium perchlorate single crystals, Phys. B Phys. Condens. Matter. 405 (2010) 65–71. doi:10.1016/j.physb.2009.08.035.

[2] K. Ambujam, K. Rajarajan, S. Selvakumar, J. Madhavan, Growth and characterization of gel grown single crystals of bis-glycine hydrogen chloride (BGHC), 29 (2007) 657–662. doi:10.1016/j.optmat.2005.11.008.

[3] G.P. Joseph, N. Melikechi, J. Philip, J. Madhavan, P. Sagayaraj, Studies on the electrical , linear and nonlinear optical properties of Manganese mercury thiocyanate bis-dimethyl sulfoxide , an efficient NLO crystal, 404 (2009) 295–299. doi:10.1016/j.physb.2008.10.055.

[4] S. Senthil, S. Pari, G.P. Joseph, P. Sagayaraj, J. Madhavan, Thermal , mechanical , electrical , linear and nonlinear optical properties of a nonlinear optical L -ornithine monohydrochloride single crystal, 404 (2009) 2336–2339. doi:10.1016/j.physb.2009.04.053.

[5] S. Senthil, S. Pari, R.J. Xavier, J. Madhavan, Optik Linear and nonlinear optical properties of N- (3-nitrophenyl) acetamide single crystals, Opt. - Int. J. Light Electron Opt. 123 (2012) 104–108. doi:10.1016/j.ijleo.2011.03.007.

[6] S. Sathiskumar, T. Balakrishnan, K. Ramamurthi, Growth and characterization of semiorganic single crystal of bis-glycine manganese chloride, Opt. - Int. J. Light Electron Opt. (2015) 1–7. doi:10.1016/j.ijleo.2015.12.033.

[7] C.J. John, M. Amalanathan, A.R. Twinkle, P. Srinivasan, I.H. Joe, Vibrational spectra and first order hyperpolarizability studies of dimethyl amino pyridinium 4-nitrophenolate 4-nitrophenol, Spectrochim. Acta Part A Mol. Biomol. Spectrosc. (2011). doi:10.1016/j.saa.2011.05.086.

[8] Frisch, M.J., Trucks, G.W., Schlegel, H.B., et al., (2004) Gaussian 03, revision E. 01, Gaussian Inc., Wallingford CT., (2004) 2004.

[9] Socrates G., Infrared and Raman Characteristic Group Frequency, third ed., Wiley, New York, 2001., (2001) 2001.

[10] T.J. Beaula, A. Packiavathi, D. Manimaran, I.H. Joe, V.K. Rastogi, V.B. Jothy, Quantum Chemical Computations , Vibrational Spectroscopic Analysis and Antimicrobial studies of 2 , 3-Pyrazinedicarboxylic Acid, Spectrochim. ACTA PART A Mol. Biomol. Spectrosc. (2014). doi:10.1016/j.saa.2014.11.034.

[11] Dollish F.R., Fateley W.G., Bentley F.F., Characteristic Raman Frequencies of Organic Compounds, John Wiley & Sons, New York, 1997., (1997) 1997.

[12] J. Senthil Kumar, M. Arivazhagan, P. Thangaraju, Vibrational spectra, NLO analysis, and HOMO-LUMO studies of 2-chloro-6-fluorobenzoic acid and 3,4-dichlorobenzoic acid by density functional method, Spectrochim. Acta - Part A Mol. Biomol. Spectrosc. 147 (2015) 235–244. doi:10.1016/j.saa.2015.03.058.

[13] T. Yakhanthip, S. Jungsuttiwong, S. Namuangruk, N. Kungwan, V. Promarak, T. Sudyoadsuk, P. Kochpradist, Theoretical Investigation of Novel Carbazole-Fluorene based D- p -A Conjugated Organic Dyes as Dye-Sensitizer in Dye-Sensitized Solar Cells (DSCs), (2011) 2–10. doi:10.1002/jcc.

[14] R.G. Parr, C. Hill, N. Carolina, Electrophilicity Index, (1999) 1922–1924.

[15] Y.G. Yu, R.M. Wentzcovitch, Density functional study of vibrational and thermodynamic properties of ringwoodite, 111 (2006) 1–8. doi:10.1029/2006JB004282.

[16] C. Structures, I.A. Re, J. Nishida, S. Tsukaguchi, Y. Yamashita, Full paper, (2012) 1–8. doi:10.1002/chem.201200591.

Available online at www.sciencedirect.com

ScienceDirect

Materials Today: Proceedings 8 (2019) 162–168

materialstoday: PROCEEDINGS

www.materialstoday.com/proceedings

ICMEE 2018

Surfactant Free Hydrothermal Synthesis, Structural and Dielectric Studies of One-Dimensional β $-MnO_2$ Nanorods

Mohamed Racik. K[a]. K, P. Prabakaran[a], J. Madhavan[a], M.Victor Antony Raj[a,b]*

[a.] Department of Physics, Loyola College, Chennai-600 034, Tamilnadu, India.
[b.] Loyola Institute of Frontier Energy (LIFE), Loyola College, Chennai, India.

Abstract

An n-type semiconductor, MnO_2 has drawn fabulous attention due to their significant relevance in supercapacitors. In this paper, one-dimensional (1-D) nanostructured β $-MnO_2$ nanorods have been synthesized via a facile one-step hydrothermal method without any surfactant. The crystallographic information of the as-prepared products was established by powder X-ray diffraction (XRD). Average crystalline size of the sample estimated using Scherer formula and Williamson–Hall analysis were found to be 32 nm and 35 nm respectively. The functional groups present in the sample were examined using FTIR spectroscopy. The morphological analysis and elemental composition of the as prepared β $-MnO_2$ was performed in terms of high resolution scanning electron microscopy (HRSEM) and energy dispersive X-ray spectroscopy (EDX). Dielectric studies were carried out in a Hioki make LCR Hi-Tester 3250 at a temperature of 300K over a wide range of frequencies from 50 Hz to 5 MHz. The dielectric constant and dielectric loss factor were found to decrease rapidly in the low frequency region and became almost constant in the high frequency region. The ac conductivity values show weak frequency at lower applied frequencies and exhibits strong frequency dependence at higher frequencies.

Selection and peer-review under responsibility of the scientific committee of the Materials For Energy and Environment.

Keywords: β $-MnO_2$ nanorod; hydrothermal synthesis; HRSEM; dielectric studies.

* Corresponding author. Tel.: +91-9976249172
E-mail address: vicvad2003@yahoo.co.in.

Selection and peer-review under responsibility of the scientific committee of the Materials For Energy and Environment.

1. INTRODUCTION

One dimensional MnO_2 nanostructures have been considered as an idyllic electrode material for electrochemical energy storage devices, such as lithium-ion batteries [1-3], high-capacity lithium ion batteries [4], and supercapacitors [5-8], due to their key advantages of low cost, superior performance in energy capacity and environmental friendliness. So far, various efforts have been conducted to fabricate MnO_2 nanostructures and a variety of approaches have been established, including coprecipitation [9], sol-gel [10], microwave process [11], simple reduction [12], solid-phase process, hydrothermal method [8], etc. Among these approaches, hydrothermal chemical route has attracted more consideration because it is easily controlled on the shape of materials, which are simple processed and in large scale. For example, Li et al. [13] utilized hydrothermal route to achieve 3D urchinlike β-MnO_2 constructed of self-assembled nanorods; MnO_2 nanomaterials were prepared via hydrothermal treatment and investigated for catalytic and electrochemical properties by Qiu et al. [14].

Crystallite size and lattice strain are dynamic structural parameters of materials and hence their correct determination is very important. Over the years, for X-ray diffraction (XRD) line profile analysis Williamson-Hall (W-H) method has been commonly used to determine the crystallite size and lattice strain of the samples [15,16]. Dielectric spectroscopy is an essential tool to study the dielectric properties of the material with the advantage of manual control over temperature and frequency. The dielectric constant and dielectric loss measurement as a function of frequency and applying temperature gives more information about the polarization mechanism, conduction process, phase transition and influence of impurities [17]. On the combining of DC conductivity with the AC conductivity data obtained from the dielectric studies will help to understand the information on impurities, defect formation, and conduction nature of a sample [18].

In this work, β-MnO_2 nanorods were synthesized through one-step hydrothermal route without any surfactant. Structural, Morphological and dielectric properties of β-MnO_2 nanorods were studied with help of powder X-ray diffraction (XRD), FTIR spectroscopy, high resolution scanning electron microscopy (HRSEM), energy dispersive X-ray spectroscopy (EDX) and LCR HI tester.

2. EXPERIMENTAL

All the reagents used in the experiments were analytically pure and were purchased from Merck India Company and were used without further purification. The synthetic procedures are as follows:

2.1 Preparation of β-MnO_2 nanorods

β -MnO_2 nanorods were synthesized via simple and cost effective hydrothermal method. Typically, $MnSO_4 \cdot H_2O$ (0.008 mol) and urea were put into deionized water to form a homogeneous solution. Then, the above solution was transferred into a 100ml Teflon-lined stainless steel autoclave and maintained at 150 ºC for 24h. After completion of the reaction, the resulting products were centrifuged, washed with deionized water and finally dried at 60 ºC.

2.2 Characterization

X-ray diffraction (XRD) patterns were recorded using a D8 Discover (Bruker) X-ray diffractometer with Cu Kα radiation. Fourier transform infrared (FT-IR, Bruker) spectra were recorded on a spectrometer with a diamond ATR in the range of 400 - 4000 cm^{-1}. High resolution scanning electron microscope (HRSEM) images were obtained using FEI Quanta 200 scanning electron microscopy integrated with energy dispersive X-ray (EDX). The frequency dependent dielectric studies were calibrated using a computer controlled LCR-meter (HIOKI- 3552) at the AC voltage of 1.0 V.

3. RESULTS AND DISCUSSION

3.1 Powder XRD analysis

The phase and purity of the resulting materials were tested by XRD analysis. The XRD patterns of the sample are shown in Fig. 1. In MnO_2 samples all the diffraction peaks at about 28.68°, 37.44°, 40.89°, 42.86°, 56.70°, 59.35° and 72.78° can be indexed to (110), (101), (200), (111), (211), (220) and (301) respectively, which can be indexed to the pure tetragonal phase of β-MnO_2 (JCPDS 24-0735, a = b =4.42 Å, c= 2.868 Å) with the space group of P42/mnm without any impurity peaks [19].

The analysis of the crystallite size has been carried out using the broadening of the XRD peaks. Crystallite size has been calculated using Scherrer's formulae and Williamson- Hall plot. We have calculated the crystallite size by the above two methods to compare their sizes in two different methods. The crystallite size can be calculated by using the Debye–Scherrer formula is given as:

$$D = \frac{K\lambda}{\beta \cos\theta} \tag{1}$$

where D is the average crystallite size, λ is the X-ray wavelength, β is the full width at half maximum, k is the shape factor, θ is the diffraction angle of Bragg and k is often assigned a value of 0.89, which depends on several factors, including the Miller index of the reflecting plane and the shape of the crystal. The average crystallite size calculated from Scherrer formula is 32 nm.

Williamson-Hall (W-H) relation the strain was assumed to be uniform in all crystallographic direction, β_{hkl} is given by

$$\beta_{hkl} = \left(\frac{K\lambda}{D\cos\theta}\right) + 4\varepsilon \tan\theta \tag{2}$$

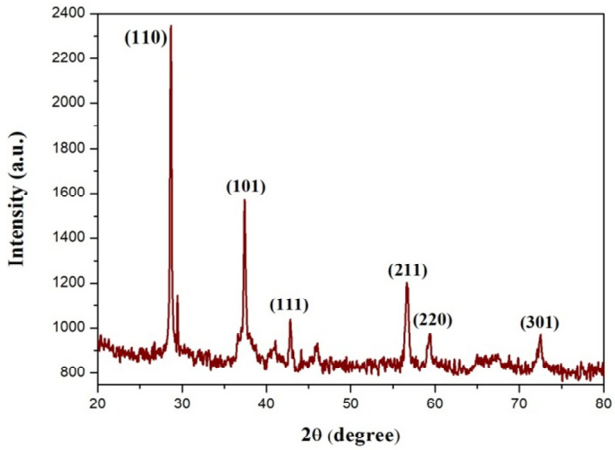

Fig. 1: XRD pattern of β –MnO_2 nanorods

Rearranging Eqn. (2) gives

$$\beta_{hkl}\cos\theta = \left(\frac{K\lambda}{D}\right) + 4\varepsilon \sin\theta \tag{3}$$

Here D and ε corresponds to the crystallite size value and dimension value (microstrain) respectively. To make Williamson-Hall analysis, a plot is drawn with 4sinθ along the x-axis and $\beta_{hkl}\cos\theta$ along the y-axis for all orientation peaks of β –MnO_2 as shown in Fig. 2. From the linear fit to the data, the crystalline size was estimated from the y-intercept and the strain (ε) from the slope of the fit [20]. The crystallite size and lattice strain estimated from the Williamson-Hall (W-H) method is 33.25 nm and 0.00070 respectively

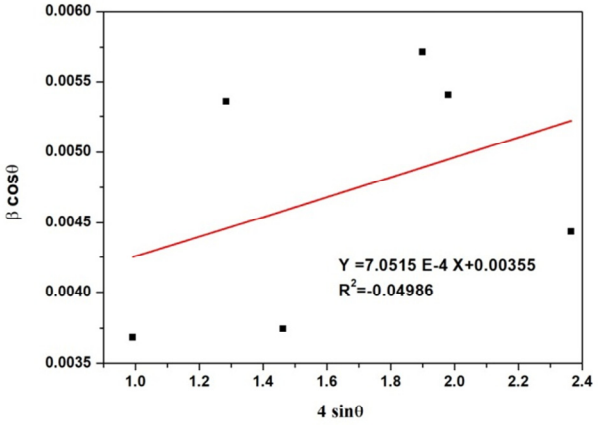

Fig. 2: Williamson –Hall plot of β –MnO_2 nanorods

3.2 Fourier transform infrared (FT-IR) spectroscopy analysis

The FT-IR spectroscopy is a right beneficial technique to deduce the molecular dynamics. The FT-IR absorption bands of the crystalline materials are usually assigned to the vibration of ions in the crystal lattice. The FT-IR spectra of the samples are recorded at room temperature in the range of 400 to 4000 cm^{-1}. The bands appearing at 3432 and 1627 cm^{-1} correspond to the O–H vibrating mode of traces of absorbed water. The bands located at 538, and 434 cm^{-1} can be ascribed to the Mn–O vibrations of β –MnO_2 products. The FTIR spectra in Fig.3 agree well with the results reported in the literature [21].

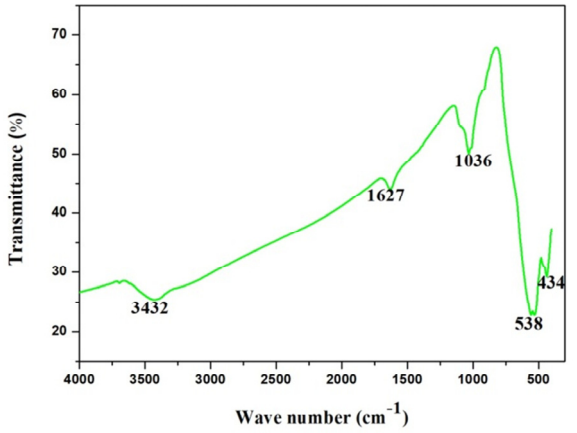

Fig. 3: FT-IR spaectra of β –MnO_2 nanorods

3.2 HRSEM and EDAX analysis

The structural morphologies of the as-prepared β –MnO_2 sample were inspected by HRSEM analysis. Fig. 4(a) shows that β –MnO_2 with nanorod-like shape with a diameter of 32 nm and length of 1.5–2.0 mm and HRSEM images exhibits pyramid-like top end of the nanorods. The chemical compositions of all the samples were studied by energy dispersive spectroscopy (EDS) analysis. EDX analysis of the β –MnO_2 sample (Fig. 4(b)) confirms the presence of manganese (Mn) and oxygen (O) originated from manganese oxide.

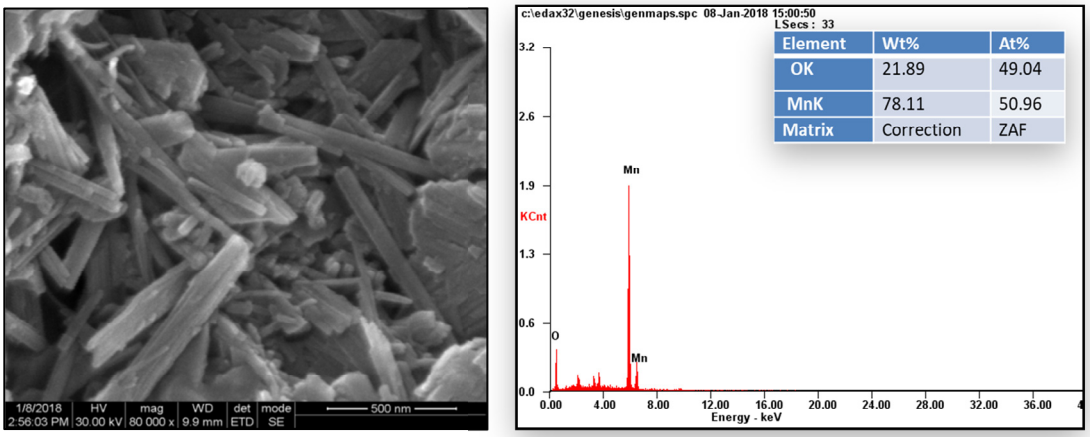

Fig. 4(a): HRSEM images and 4(b)EDX specra of β –MnO_2 nanorods

3.4 Dielectric studies

Fig. 5 shows the plot of dielectric constant versus applied frequency for β –MnO_2 sample. It is mainly observed that the dielectric constant values decreases with increasing applied frequency and then reaches almost a constant value in the higher frequency region. This result also shows that dielectric constant values increases with an increase in the temperatures. The decrease in the dielectric constant is due to quite less electronic polarization. Dipolar polarization is also predictable to decrease with different temperature as it is inversely proportional to temperature. The contribution to polarizability of the space charge depends on the purity of the nanoparticles. At lower temperature and high frequency, we may take it as small. However, it is significant in the low frequency region. As the temperature increases, the contribution of the space charge effect towards polarization may have a tendency to increase [22].

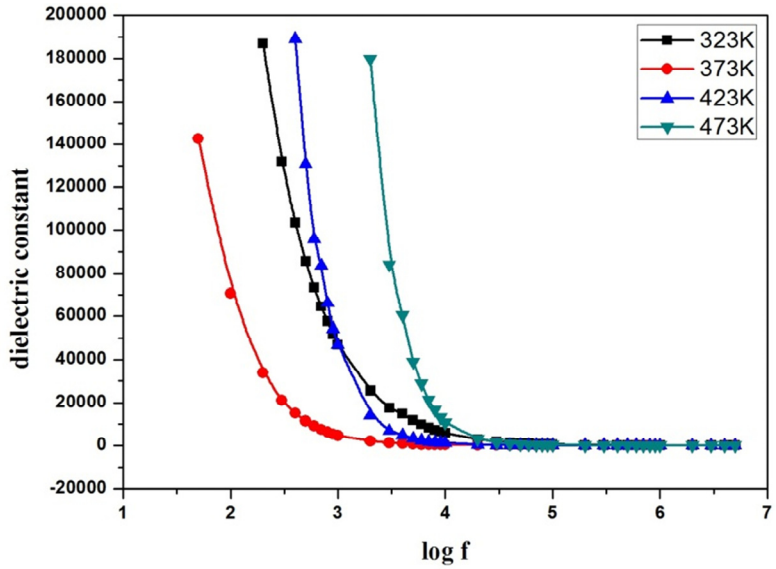

Fig. 5: Variation of dielectric constant vs frequency for β –MnO_2 nanorods

The dielectric loss measured as a function of applied frequency at different temperatures is shown in Figure 6**.** These plots suggest that the dielectric loss of the sample is strongly dependent on the frequency of the applied field, similar to that of the dielectric constant. The dielectric loss values decreases with an increase in the frequency at almost all the temperatures. In the low frequency region, high energy loss is observed, which may be due to the space charge, dielectric polarization and rotation direction polarization taking place in the low frequency range [23].

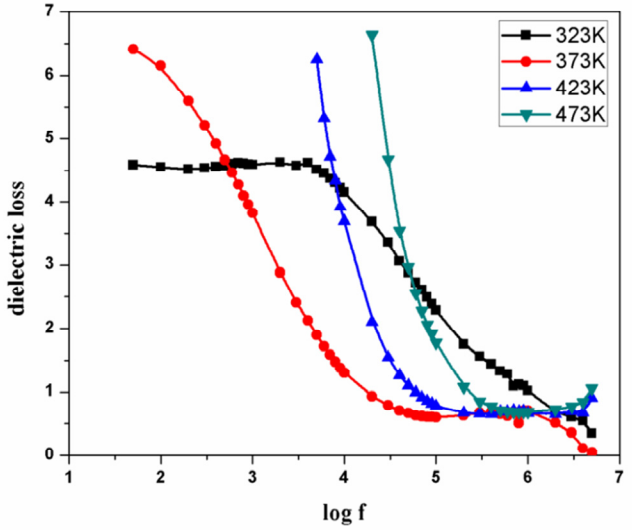

Fig. 6: Variation of dielectric loss vs frequency for β –MnO_2 nanorods

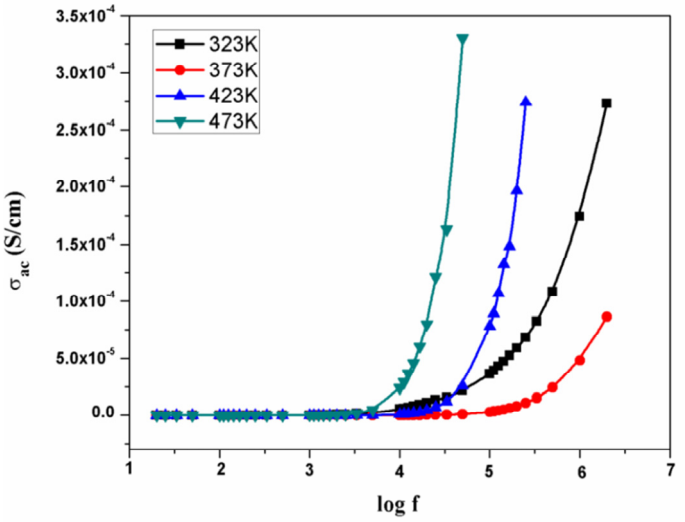

Fig. 7: Variation of ac conductivity vs frequency for β –MnO_2 nanorods

Fig.7 shows the conductivity graph for β –MnO_2 nanorods as function of frequency and temperature. AC conductivity of the sample also follows a common pattern in which the conductivity distribution produces a low frequency plateau and increase with frequency by following the power law. The phenomenon has been described to relaxation caused by the atomic or electronic polarization. Such motion can involve in hopping or tunnelling between equilibrium sites. [24]

4. CONCLUSION

In summary, the β –MnO_2 nanorods have been successfully synthesized by a one-step hydrothermal method which avoided the usage of any toxic reduced agent. Powder XRD pattern has been indexed for the pure tetragonal phase of β-MnO_2 with the space group of P42/mnm (136). X-ray peak broadening analysis was used to evaluate the crystallite size and lattice strain by the Williamson-Hall (W-H) method as 33.25 nm and 0.00070 respectively. The FT-IR absorption bands of the nanocrystalline β –MnO_2 nanorods confirmed the Mn–O vibrations. HRSEM images have been confirmed that β –MnO_2 with nanorod-like shape with a diameter of 32 nm and length of 1.5–2.0 mm. The dielectric constant and dielectric loss of the material decreases with increasing the frequency. In higher frequencies, dielectric constant and dielectric loss are almost constant compared to the lower frequency values.

REFERENCES

1. A.Debart, A. J. Paterson, J. Bao and P. G. Bruce, Angewandte Chemie-International Edition, Vol. 47, No. 24, 2008, pp. 4521-4524.
2. A.K. Thapa, Y. Hidaka, H. Hagiwara, S. Ida and T. Ishihara, Journal of the Electrochemical Society, Vol. 158, No. 12, 2011, pp. A1483-A1489.
3. A.K. Thapa and T. Ishihara, Journal of Power Sources, Vol. 196, No. 16, 2011, pp. 7016-7020.
4. B.Li, G. Rong, Y. Xie, L. Huang and C. Feng, Inorganic Chemistry, Vol. 45, No. 16, 2006, pp. 6404- 6410.
5. X.Lang, A. Hirata, T. Fujita and M. Chen, Nature Nanotechnology, Vol. 6, No. 4, 2011, pp. 232-236.
6. W.Wei, X. Cui, W. Chen and D. G. Ivey, Chemical Society Reviews, Vol. 40, No. 3, 2011, pp. 1697-1721.
7. W. Li, G. Li, J. Sun, R. Zou, K. Xu, Y. Sun, Z. Chen, J. Yang and J. Hu, Nanoscale, Vol. 5, No. 7, 2013, pp. 2901-2908.
8. W. Li, Q. Liu, Y. Sun, J. Sun, R. Zou, G. Li, X. Hu, G. Song, G. Ma, J. Yang, Z. Chen and J. Hu, Journal of Materials Chemistry, Vol. 22, No. 30, 2012, pp. 14864- 14867.
9. T. Brousse, M. Toupin, R. Dugas, L. Athouel, O. Crosnier and D. Belanger, Journal of the Electrochemical Society, Vol. 153, No. 12, 2006, pp. A2171-A2180.
10. X. Wang, A. Yuan and Y. Wang, Journal of Power Sources, Vol. 172, No. 2, 2007, pp. 1007-1011.
11. T. T. Truong, Y. Liu, Y. Ren, L. Trahey and Y. Sun, Acs Nano, Vol. 6, No. 9, 2012, pp. 8067-8077.
12. P. Ragupathy, D. H. Park, G. Campet, H. N. Vasan, S.-J. Hwang, J.-H. Choy and N. Munichandraiah, Journal of Physical Chemistry C, Vol. 113, No. 15, 2009, pp. 6303-6309.
13. W. N. Li, J. K. Yuan, X. F. Shen, S. Gomez-Mower, L. P. Xu, S. Sithambaram, M. Aindow and S. L. Suib, Advanced Functional Materials, Vol. 16, No. 9, 2006, pp. 1247-1253.
14. G. Qiu, H. Huang, S. Dharmarathna, E. Benbow, L. Stafford and S. L. Suib, Chemistry of Materials, Vol. 23, No. 17, 2011, pp. 3892-3901.
15. G.K. Williamson, W.H. Hall, X-ray line broadening from filed aluminium and wolfram, Acta Metall. 1 (1953) 22–31.
16. H.P. Klug, L.E. Alexander, X-ray Diffraction Procedures for Polycrystalline and Amorphous Materials, Second ed., Wiley, New York, 1974.
17. D. B. Sirdeshmukh, L. Sirdeshmukh, K. G. Subhadra, Micro and Macro properties of solids: Thermal, mechanical and dielectric properties, Springer-Verlag, Berlin, Heidelberg, 2006.
18. I. S. Zheludev, Physics of crystalline dielectrics: Electrical properties, Plenum Press, 1971.
19. Y. L. Yang and M. C. Gupta, Nano Lett., 2005, 5, 2131–2134.
20. S. Anand, A. Persis Amaliya, M. Asisi Janifer and S. Pauline, Modern Electronic Materials, 3 (2017) 168–173.
21. R.Z. Yang, Z.X. Wang, L. Dai, L.Q. Chen, Mater. Chem. Phys. 93 (2005) 149.
22. M. Maria Lumina Sonia, S. Anand, S. Blessi, S. Pauline, A. Manikandan, Ceramics International (2018) doi:10.1016/j.ceramint.2018.08.317.
23. Sagadevan S , Appl Nanosci. 4: (2014) 325-329.
24. M. Maria Lumina Sonia, S. Anand, V. Maria Vinosel, M. Asisi Janifer, S. Pauline, A. Manikandan, Journal of Magnetism and Magnetic Materials,466(2018) 238-251.

Available online at www.sciencedirect.com

ScienceDirect

Materials Today: Proceedings 8 (2019) 470–475

materialstoday: PROCEEDINGS

www.materialstoday.com/proceedings

ICMEE 2018

Structural, Optical and Thermal Behaviour of L-Phenylalanine L-Phenylalaninium Perchlorate (LPAPCl) A Nonlinear Optical Single Crystal

R. Vincent Femilaa[1], M. Victor Antony Raj[1,2] and J. Madhavan[1]*

[1]*Department of Physics, Loyola College, Chennai, India*
[2]Loyola Institute of Frontier Energy (LIFE), Loyola College, Chennai, India.

Abstract

L-Phenylalanine L-Phenylalaninium Perchlorate (LPAPCl) - a nonlinear optical (NLO) single crystal is grown at room temperature using slow evaporation technique. The crystal found to be orthorhombic crystal system having non-centrosymmetry with $P2_12_12_1$ space group. Powder X-ray Diffraction (XRD) pattern was compared with the simulated results. HOMO-LUMO analysis describes the energetic behaviour of LPAPCl. From the UV-Vis study, the band gap (E_g) is found to be 4.068eV. TGA curve indicates three states of weight loss. The weight loss observed in the TGA trace coincided with the DTA trace. The dielectric constant and loss for different frequencies were studied for the title compound.

Selection and peer-review under responsibility of the scientific committee of the Materials For Energy and Environment.

Keywords: NLO ; LPAPCl ; XRD ; HOMO ; LUMO ; UV-Vis ; TGA ; DTA.

* Corresponding author. Tel.: 9840479638
E-mail address: jmadhavang@yahoo.com

Selection and peer-review under responsibility of the scientific committee of the Materials For Energy and Environment.

1. Introduction

Crystal design technique for assembling the materials and development of novel molecular is a nifty concern.the molecular engineering of new materials provides many structure and bonding schemes. Semiorganic nonlinear optical (NLO) crystals are attracting a great deal of attention due to their high NLO coefficient, high mechanical strength and high damage threshold compared to the organic NLO crystals. For this nonlinear optical material, the crystal engineering exhibits a large NLO efficiency on the amino acid group, which ensures convenient, mechanical, thermal and optical stabilities based on the anchorage of organic molecules **[1]**. Recently, the interesting materials for NLO applications, complexes of amino acids have been explored. The importance of amino acids in NLO applications is due to the fact of chiral symmetry of all the amino acids **[2]**.Nonlinear optical materials influence laser technology, optical communication and optical storage technology. New materials exhibiting nonlinear optical (NLO) effects for developing optical devices like optical modulators and frequency-doubling devices have been explored **[3]**. In the present work, a NLO material named L -Phenylalanine L-Phenylalaninium Perchlorate (LPAPCl) is synthesized and grown using L-phenylalanine and perchloric acid. Phenylalanine is one among the three naturally occurring aromatic amino acids where the other two are tryptophan and tyrosine. All the three are essential amino acids which must be provided in the diet for vertebrates **[4].** Using a slow evaporation technique, the LPAPCl crystals are grown and the characterizations such as XRD, UV-Vis absorption spectroscopy, thermal studies are performed and the results are reported.

2. Experimental Procedure

To prepare an aqueous solution of LPAPCl, a stoichiometric amount of L-phenylalanine and perchloric acid are taken in the ratio 2:1 and is dissolved in the double distilled water. To produce LPAPCl, L-phenylalanine and perchloric acid will undergo the following chemical reaction in deionized water.

$$2(C_9H_{11}NO_2) + HClO_4 \longrightarrow C_9H_{11}NO_2 . C_9H_{12}NO_2^{+} . ClO_4^{-}$$

By evaporating the solvent, the synthesized salt of LPAPCl is obtained from the solution by collecting the precipitate formed at the bottom of the container. Solubility corresponds to saturation i.e. to equilibrium between a solid and its solution at a given temperature and pressure. This states that the chemical potential of the solute in the saturated solution and its respective pure solid are thermodynamically equal.

The solubility and temperature determines the growth rate of the crystal. The amount of material available for the growth is governed by the solubility data and this defines the total size limit. The driving force for the rate of crystal growth is the supersaturation (defined from the solvent and the solubility factors). The essential criterion for the material to grow as a crystal is the determination of the solubility in a particular solvent.

Repetition of crystallization process further purifies the synthesized salt of LPAPCl. The temperature bath comprises a 250ml glass beaker with 100ml of deionized water in it. 30°C will be set as the initial temperature of the bath. An acrylic sheet containing a hole at the center is used to close the beaker through which a spindle from an electric motor placed on the top of the sheet is introduced into the solution. The solution is then stirred using a Teflon paddle. The saturation of the solution is confirmed by adding the synthesized salt in small amounts and stirring the solution continuously using a motorized stirrer until the precipitate forms. To have a uniform temperature and concentration throughout the entire volume of the solution, the stirring is further continued. Gravimetrically, the equilibrium concentration of the solution is analyzed from attainment of the saturation. Using a warmed pipette, a 20ml of the clear supernatant liquid is withdrawn and is poured into a clean, dry and weighed empty Petri dish. The solution is kept in a heating mantle for slow evaporation until the solvent evaporates completely. By weighing the Petri dish along with salt, the mass of LPAPCl in 20ml of solution is determined and hence it also determines the amount of LPAPCl salt (in gram) which is dissolved in 100 ml of water. The solubility of LPAPCl is estimated by repeating the procedure for various temperatures such as 30, 35, 40, 45 and 50°C. The solubility curve of LPAPCl is shown in the Fig. 1(a).After a period of 35−40 days, good optical quality crystals of dimension up to 22 x 5 x 5 mm^3 is harvested by seeding the supersaturated solution and evaporating the solvent. Fig. 1(b) shows the photograph of the as grown crystal of LPAPCl.

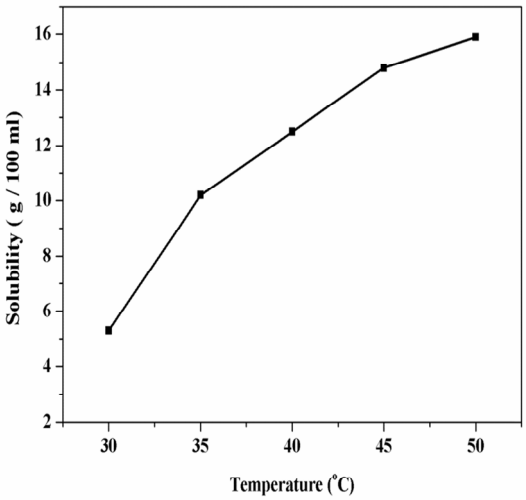

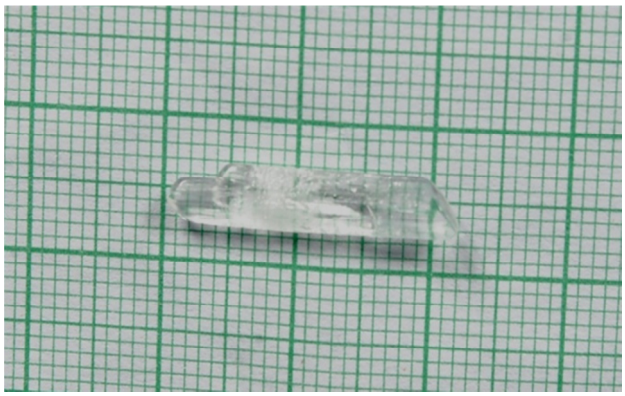

Fig. 1. (a) Solubility curve of LPAPCl**;** (b) Photograph of as grown LPAPCl single crystal

3. Characterization

3.1 Single crystal XRD Analysis

A single crystal X-ray diffraction study is performed for the grown crystal using ENRAF NONIUS CAD 4 single crystal X-ray diffractometer at room temperature with MoKα radiation (λ=0.71073 Å). It is observed that the crystal belongs to the orthorhombic crystal system having non-centrosymmetry with $P2_12_12_1$ space group and the lattice parameter values are a=5.3907(11) Å, b=12.680(2) Å and c=29.152(5) Å. Table 1 gives the crystal data and structural refinement data.

Table 1. Crystal parameters of LPAPCl

Empirical Formula	$C_{18}H_{23}Cl_1N_2O_8$	
Formula weight	430.830	
Wave length	0.71073 Å	
Crystal system, Space group	Orthorhombic, $P2_12_12_1$	
Unit cell dimensions	a =5.3907(11) b =12.680(2) c = 29.152(5)	α = β = γ = 90°

3.2 Powder X-ray Diffraction

A powder X-ray diffraction study is performed for the grown crystal using RICH SIEFERT X-ray Diffractometer at room temperature along with CuKα (Kα = 1.5406) radiation. Fig. 2(a) and Fig. 2(b) shows the experimental and theoretically simulated XRD pattern of LPAPCl single crystal with its indexed peaks respectively. Both the XRD patterns are almost similar in comparison.

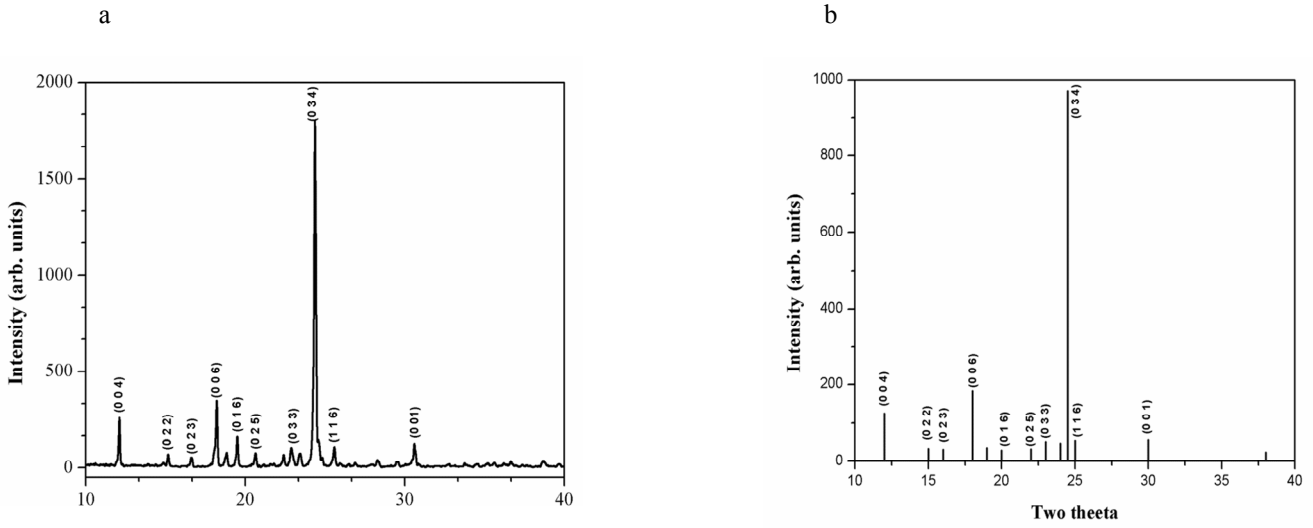

Fig. 2. (a) Experimentally obtained powder XRD pattern of LPAPCl ; (b) Theoretically simulated powder XRD pattern of LPAPCl

3.3 HOMO-LUMO Gap

The HOMO, LUMO, the frontier molecular orbitals and the frontier orbital energy gap are the important parameters for electronic studies which exemplifies the reactivity and kinetic stability of the molecules. From HOMO-LUMO analysis, the energetic behavior of LPAPCl is evaluated and the energies of HOMO and LUMO orbital energy gaps using B3LYP/ 6-31 G (d,p) are clearly shown in Fig. 3. The transition from the ground state to the first excited state corresponds the electronic absorption and is mainly described by an excitation of electron from the highest occupied molecular orbital (HOMO) to the lowest unoccupied molecular orbital (LUMO). Here, the ionization potential relates the HOMO energy and electron affinity relates the LUMO energy. 0.19892 a.u (5.39471 eV) is found to be the energy gap value.

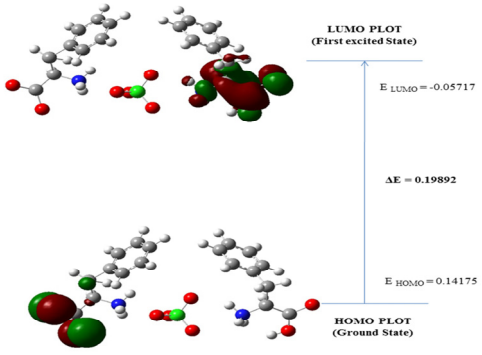

Fig. 3. HOMO – LUMO plot of LPAPCl molecule

3.4 UV-Vis study

Using the VARIAN CARY 5E model spectrophotometer, the UV-Vis analysis of LPAPCl crystal is carried out between the range 200nm and 1100nm covering the near ultra violet and visible regions. Fig. 4(a) shows the UV-Vis optical absorption spectrum of LPAPCl crystal and the cut-off wavelength is observed to be 240nm. In the entire visible region the crystal has got almost less than 0.2 unit of absorption. LPAPCl crystal has got a wide optical transmission window which is an encouraging optical property and is of vital importance for NLO materials. The transmission window in the UV and visible region enables good optical transmission of Nd: YAG laser for its second harmonic frequencies **[5]**. A graph has been plotted using Tauc relation which estimates the band gap values and is clearly shown in Fig. 4(b). The band gap value is determined to be 4.068 eV.

a b

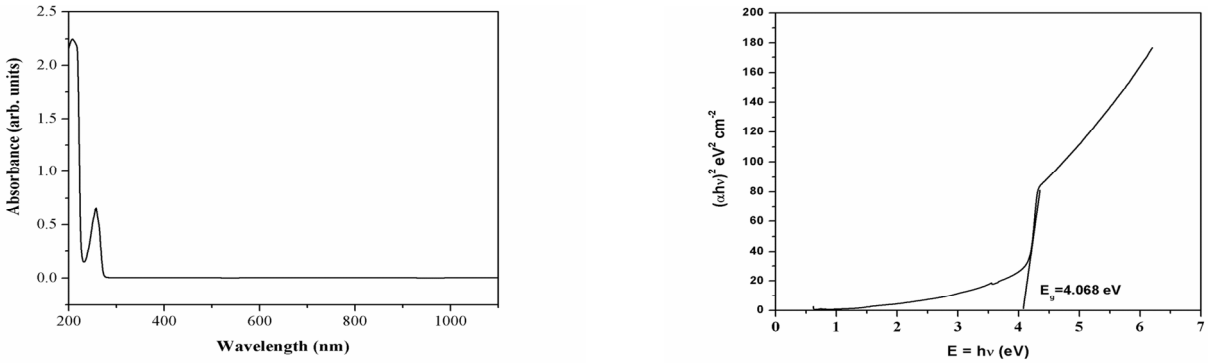

Fig. 4. (a) Optical Absorption spectrum of LPAPCl; (b) Energy band gap of LPAPCl

3.5 Thermal analysis

Fig. 5 shows the TGA and DTA thermogram of LPAPCl crystal. TGA curve indicates the three states of weight loss. Due to the elimination of volatile substances, probably carbon dioxide, ammonia and oxides of chlorine a major weight loss occurs which started at about 200°C and ended at 260°C. This corresponds to about 55.36% of the sample. The temperature beyond 100°C has no evidence for any physically adsorbed water on the surface of the crystal or any entrapped water in the crystal lattice. The melting of the sample is confirmed at 200°C. 21.66% of the sample corresponds to the second weight loss which started at 260°C and ended at 450°C. 12.78% is the final and third weight loss of the sample. After 910°C, a residue of 10% remains. The weight loss that observed in the TGA trace coincides to the DTA trace.

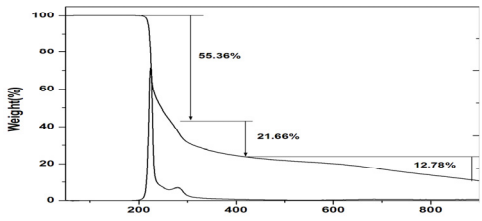

Fig. 5. TG- DTA curves of LPAPCl single crystal

4. Conclusion

The single crystal of LPAPCl of appreciable size was grown at room temperature using slow evaporation technique, and the grown crystal was confirmed by the powder XRD. The value of HOMO-LUMO energy gap was determined to be 5.3947eV. In the entire visible and infrared region, the crystal has got a very low absorption with the lower UV cut off around 240nm, an essential consideration for NLO crystals revealed from the theoretical studies. The material was found to have its optical band gap at the value of 4.068eV. DTA trace coincided with the observed weight loss in the TGA trace.

Acknowledgements

The authors acknowledge University Grants Commission (UGC), India, for funding this research project-F.No.4-4/2015-16 (MRP/UGC-SERO).

References

[1] A.Cyrac Peter, M.Vimalan, P.Sagayaraj, J.Madhavan, Physica B 405 (2010) 65–71.
[2] V.Siva Shankar, R.Siddheswaran, R.Sankar, R.Jayavel, P.Murugakoothan, Materials Letters 63 (2009) 363–365.
[3] R.Surekha, R.Gunaseelan, P.Sagayaraj and K.Ambujam, Cryst Eng Comm, 16 (2014) 7979–7989.
[4] Beulah J.M. Rajkumar, V.Ramakrishnan, Spectrochimica Acta Part A 58 (2002) 1923–1934.
[5] P.Rajesh, P.Ramasamyx, Spectrochimica Acta Part A 74 (2002) 210–213.

Available online at www.sciencedirect.com

ScienceDirect

Materials Today: Proceedings 8 (2019) 492–501

materialstoday: PROCEEDINGS

www.materialstoday.com/proceedings

ICMEE 2018

Growth and Characterization of Nonlinear Optical Crystal L-Isoleucine D-Norleucine: A DFT Approach

P Vinnarasi[a], M Victor Antony Raj[a,b], J Madhavan[a,] *

[a]*Department of Physics, Loyola College, Chennai -34.*
[b]*Loyola Institute of Frontier Energy (LIFE), Loyola College, Chennai-34.*

Abstract

Single crystals of L-Isoleucine D-Norleucine (LIDN) of size 21mm x 6mm x 4mm have been grown by slow evaporation technique at ambient temperature. The structure of the grown crystal is determined by powder X-ray diffraction technique (PXRD). It is found that the crystal belongs to the monoclinic system with P2 space group. Functional groups of the crystallized molecules were determined by FT-IR analyses. The LIDN crystallizes in noncentrosymmetric structure, which is an essential criterion for second harmonic generation. The molecular geometry, highest occupied molecular orbital (HOMO), lowest unoccupied molecular orbital (LUMO) and first order hyper polarizability properties of the title compound have been computed with the help of density functional theory (B3LYP) with 6-31 G(d, p) as basis set.

Selection and peer-review under responsibility of the scientific committee of the Materials For Energy and Environment.

Keywords: LIDN; PXRD; FT-IR; HOMO; LUMO

1. Introduction

Materials with large second-order optical nonlinearities, lower cutoff wavelength and stable physicochemical performance are needed in order to realize many of photonic and optoelectronic applications. Considerable efforts are currently made to develop new organic materials with large second-order nonlinear optical (NLO) susceptibilities [1]. It has been generally understood that the second-order molecular nonlinearity can be enhanced by large delocalized π-electron systems with strong donor and acceptor groups. During the last several years, according to the idea of combining the inorganic distorted polyhedron with the asymmetric conjugate organic

* Corresponding author. Tel.: 9840479638.
*E-mail address:*jmadhavang@gmail.com.

Selection and peer-review under responsibility of the scientific committee of the Materials For Energy and Environment.

molecules, semiorganic materials have been attracting a great deal of attention in the NLO field, because such materials have the potential for combining the high optical nonlinearity and chemical flexibility of organics with thermal stabilities and excellent transmittance of inorganics [2]. The importance of amino acids in NLO applications is due to the fact that all the amino acids have chiral symmetry and crystallize in noncentrosymmetric space groups [3]. Many numbers of natural amino acids are individually exhibiting the nonlinear optical properties because they are characterized by chiral carbons, a proton-donating carboxyl group and the proton-accepting amino group. The crystal structures of amino acids and their complexes have provided a wealth of interesting information to the patterns of their aggregation and the effect of other molecules and ions on their interactions and molecular properties. Among them, L-Isoleucine is both glucogenic and ketogenic amino acid. This is one of the amino acids having branched hydrocarbons side chains. It is non-polar and aliphatic in nature. Norleucine is better known as 2-amino hexanoic acid or amino cupric acid although not a naturally occurring amino acid, it is a structural isomer of Leucine and Isoleucine, both essential amino acids, and Leucine has been isolated from wool, wheat and haemoglobin. The present work deals with the growth and detailed vibrational spectral investigation of LIDNL to explicate the correlation between the molecular structure and NLO property, charge transfer interaction between HOMO-LUMO, bond length and first hyperpolarizability aided by using B3LYP levels with 6-31G(d, p) technique based on DFT computation.

2. Experimental Details

Stoichiometric amounts of L-Isoleucine and D-Norleucine taken in 1:1 ratio were dissolved in double distilled water to prepare the aqueous solution of LIDNL.

$$C_6H_{13}NO_2 + C_6H_{13}NO_2 \longrightarrow C_{12}H_{26}N_2O_4$$

Synthesized salt of LIDNL was obtained from the solution by evaporating the solvent and collecting the precipitate formed at the bottom of the container having the solution. The solubility of LIDNL was measured at 30, 35, 40, 45, 50 and 55 °C and the variation of solubility (g LIDNL / 100 ml H_2O) with temperature is shown in Fig.1. The solution was saturated at 40 °C and seed crystals were formed due to spontaneous nucleation. Transparent good quality seed crystals free from macro defects were used for growth experiments. Single crystals of size 21 x 6 x 4 mm^3 were grown in 50 days and the photograph of the as grown crystal of LIDNL is shown in Fig. 2.

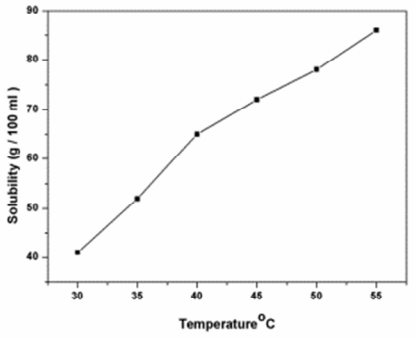

Fig. 1. Solubility Curve of LIDNL

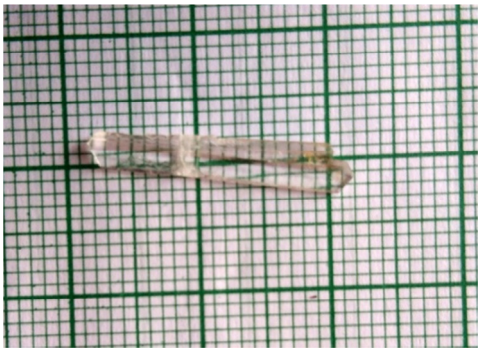

Fig. 2. Photograph of as grown LIDNL crystal

3. Results and discussion

3.1. Powder X-ray diffraction studies

The structural properties of the single crystal of LIDNL have been studied by X-ray powder diffraction technique. Powder X-ray diffraction studies of the grown crystals were carried out, using Rich Siefert & Co X-ray diffractometer with CuK_α (λ = 1.5418 Å) radiation. Fig. 3 shows the Powder XRD pattern of LIDNL crystal. The

diffraction patterns of the crystal were indexed by least square fit method. The lattice parameter values of LIDNL crystal were calculated and are well matched with the reported literature. The lattice parameters are shown in Table 1.

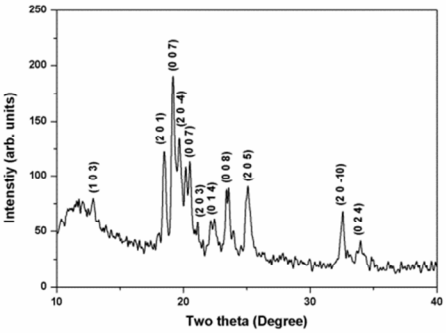

Table.1. Crystal data of LIDNL crystal

Empirical Formula	$C_{12}H_{26}N_2O_4$
Crystal System	Monoclinic
a (Å)	10.012
b (Å)	4.7227
c (Å)	30.335
β°	98.38
Volume (Å^3)	1419.1
Space group	$P2_1$

Fig. 3. Powder XRD pattern of LIDNL crystal

3.2. Computational methods

Quantum Chemical Density Functional Theoretical (DFT) computations were performed using closed-shell Becke–Lee–Yang–Parr hybrid exchange-correlation three-parameter functional (B3LYP) in combination with 6-31G (d, p) basis set to derive the complete geometry optimizations and normal-mode analysis on isolated entities. The atom numbering scheme adopted in this study is given in Fig. 4.

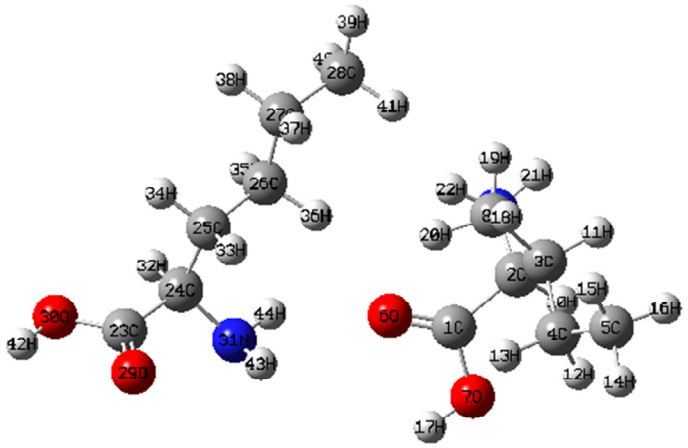

Fig. 4. Atomic numbering for ab initio computations of LIDNL molecule

Above said task was achieved using Gaussian03W [4] program package, invoking gradient geometry optimization. The optimized geometries corresponding to the minimum potential energy surface have been obtained by solving Self-Consistent field (SCF) equation iteratively. The absence of imaginary values of wave numbers on the calculated vibrational spectrum confirms that the structure deduced corresponds to minimum energy.

3.3. Molecular geometry

The optimized geometric parameters (bond lengths and bond angles) of the title component were given in Table 2 and 3 using B3LYP with 6-31G+ (d, p) basis set.

Table.2. Selected bond lengths of LIDNL molecule

Atoms	Bond length (Å)	Atoms	Bond length (Å)
O30-H42	0.974771	C26-C27	1.504399
O30-C23	1.378551	C28-H39	1.118157
C23-C24	1.523315	C8-H19	1.116568
C24-H32	1.148295	H20-C8	1.116316
C23-O29	1.235246	H13-C4	1.12667
C24-C25	1.542723	C4-C5	1.497753
N31-H43	0.979010	H19-H21	3.958526
C25-H33	1.124807	C8-H18	1.118512
C26-H35	1.123478	H37-H21	7.386328
C26-H36	1.127714	H39-H41	1.810102

Table.3. Selected bond lengths of LIDNL molecule

Atoms	Bond Angle (degree)	Atoms	Bond Angle (degree)
H42-C30-C23	109.64683	H35-C26-H36	107.31253
O29-C23-C24	129.31184	H33-C23-H34	107.59352
H32-C24-C25	108.27988	H43-N31-H44	108.56136
C24-N31-H44	109.64124	H32-C24-C23	107.92719
H44-N31-H43	108.56136	O29-C23-C24	129.31184
H34-C25-C26	109.88196	C24-C23-O30	113.52917
C26-C25-H33	109.81778	O30-C23-O29	117.14720
H35-C26-C27	109.47935	N31-C24-H32	107.15225
H39-C28-H40	108.48396	H40-C28-H41	108.27487

3.4. Hyperpolarizability studies

In order to allow the second harmonic generation (SHG) process, the materials must possess an absolute value of the susceptibility $\chi^{(2)}$ which is a bulk property and generally is associated with non-centrosymmetric crystalline structures. From a microscopic point of view, the description of the bulk property $\chi^{(2)}$ is analogous to the molecular response named first hyperpolarizability (β). It is common that some organic molecules own absolute β values. Some of these molecules tend to crystallize in non-centrosymmetric crystalline structures; therefore efficient SHG process is achieved in these materials. As a result, it has been used to elucidate the information regarding charge transfer within the molecule. The first-order hyperpolarizability (β) of this novel molecular system of LIDNL was calculated using B3LYP with 6-31+G (d, p) basis sets based on the finite field approach. In the presence of an applied electric field, the energy of a system is a function of the electric field. The first order hyperpolarizability is a third-rank tensor that can be described by a 3 ×3 ×3 matrix. The 27 components of the 3D matrix can be reduced to 10 components due to the Kleinman symmetry. Relation connecting nonlinear response, linear polarizability (α_{ij}) and first order hyperpolaraizability (β_{ijk}) can be represented as a Taylor expansion of the total dipole moment as

$$\mu_t = \mu_0 + \alpha_{ij}E_i + \beta_{ijk}E_iE_j + \ldots \quad (1)$$

The components of first order hyperpolarizability can be determined using the relation

$$\beta_{ij} = \beta_{iii} + \frac{1}{3}\sum_{i \neq j}(\beta_{ijj} + \beta_{jij} + \beta_{jji}) \quad (2)$$

Using the x, y and z components the magnitude of first order hyperpolarizability (β_{tot}) tensor can be calculated by the following equation

$$\beta_{tot} = (\beta_x^2 + \beta_y^2 + \beta_z^2)^{1/2} \quad (3)$$

The complete equation for calculating the first order hyperpolarizability from GAUSSIAN 03W output is given as

$$\beta_{tot} = (\beta_{xxx} + \beta_{xyy} + \beta_{xzz})^2 + (\beta_{yyy} + \beta_{yzz} + \beta_{yxx})^2 + (\beta_{zzz} + \beta_{zxx} + \beta_{zyy})^2 \quad (4)$$

The β components of GAUSSIAN 03W output are reported in atomic units and the calculated values have to be converted into electrostatic units (1a.u = 8.3693×10^{-33}esu). The calculated first order hyperpolarizability values for LIDNL molecule are given in Table.4.

3.5. Dipole moment

At molecular level, the response of an isolate molecule to an electric field can be quantified by the dipole moment (μ_i):

$$\mu_i = \mu_i^{(0)} + \Sigma_j \alpha_{ij} E_j + \Sigma_{jk} \beta_{ijk} E_j E_k + \Sigma_{jkl} \gamma_{jkl} E_j E_k E_l + \cdots \quad (5)$$

Where the term $\mu_i^{(0)}$ represents the static dipole moment, α is the polarizability and β is the first hyperpolarizability. Clearly Table.5 shows that LIDNL molecule owns non-zero values of dipole moment which depicts accurately its molecular characteristics.

Table.4. Hyperpolarizability of LIDNL in esu

β_{xxx}	76.3779477
β_{xxy}	-26.3944578
β_{xyy}	-26.8658989
β_{yyy}	-18.5212241
β_{xxz}	76.8848154
β_{xyz}	-19.9037622
β_{yyz}	-62.6059588
β_{xzz}	99.0604543
β_{yzz}	123.1370976
β_{zzz}	807.1457882
β_{tot}	$7.357889277 \times 10^{-30}$

Table.5 Dipole Moment of LIDNL in Debye

μ_X	0.9666
μ_Y	-0.4756
μ_Z	0.1998
μ_{tot}	1.0956

3.6. HOMO-LOMO Analysis

Many organic molecules that containing conjugated π electrons are characterized by hyperpolarizabilities and were analyzed by means of vibrational spectroscopy [5, 6]. The experimental spectroscopic behaviour is well accounted for by ab initio calculations in π conjugated systems that predict exceptionally large infrared intensities for the same normal modes. The analysis of the wave function indicates that the electron absorption corresponds to the transition from the ground to the first excited state and is mainly described by one-electron excitation from the highest occupied molecular orbital (HOMO) to the lowest unoccupied molecular orbital (LUMO). The LUMO is of π nature (i.e. benzene ring) and is delocalized over the whole C–C bond. The atomic orbital compositions of the frontier molecular orbital are sketched in Fig. 5. The HOMO-LUMO energy gap of LIDNL was calculated at the B3LYP/6-3G+ (d, p) level and it reveals that the energy gap reflect the chemical activity of the molecule. LUMO as an electron acceptor represents the ability to obtain an electron. HOMO represents the ability to donate an electron. HOMO energy = 0.1671 a.u LUMO energy = 0.0658 a.u HOMO–LUMO energy gap = 0.1013 a.u. The HOMO and LUMO energy gap explains the eventual charge transfer interactions taking place within the molecule.

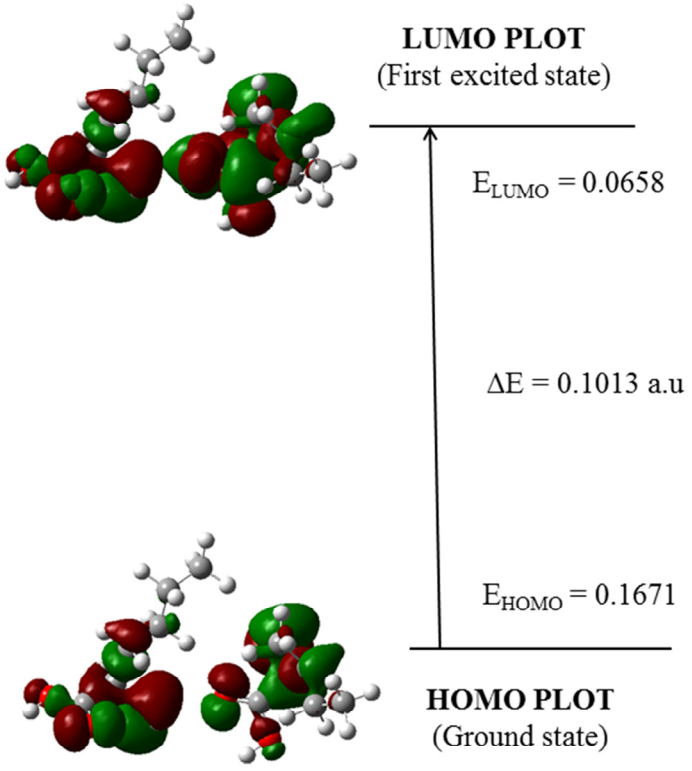

Fig.5. HOMO – LUMO plot of LIDNL molecule

3.7. Vibrational Analysis

The analysis of the vibrational spectra is indeed very helpful not only for the structural characterization of molecular compounds but also because of the detailed information on the electronic response that could be derived from spectroscopic observables. DFT calculations are reported to provide excellent vibrational frequencies of organic compounds if the calculated frequencies are scaled to compensate for the approximate treatment of electron correlation, for basis set deficiencies and for the anharmonicity [7, 8, 9, 10]. The experimental IR spectrum is compared with the results of B3LYP/6-31G+ (d, p) calculation carried out for the studied compound. Some bands in calculated IR spectra were not observed in the experimental spectrum.

FT-IR spectrum of the grown crystal was recorded in the range 400 cm^{-1} to 4000 cm^{-1}, using KBr pellet technique on BRUKKER IFS FT-IR Spectrometer. Recorded FT-IR spectrum and theoretically simulated IR spectrum of the LIDNL molecule are shown in Fig.6 and Fig.7. It is found that LIDNL molecule has 44 atoms and is in stable conformation with C_1 symmetry then exhibits 126 normal modes of vibrations. The normal modes of LIDNL is distributed amongst the symmetry species as

$$\Gamma_{3N-6} = 85A' \text{ (in-plane)} + 41A'' \text{ (out-of-plane) respectively.}$$

All the vibrations are active in Infrared vibrations. The detailed fundamental modes of vibrational assignments with the observed, calculated frequencies, reduced mass and force constants of LIDNL molecule is presented in Table.6

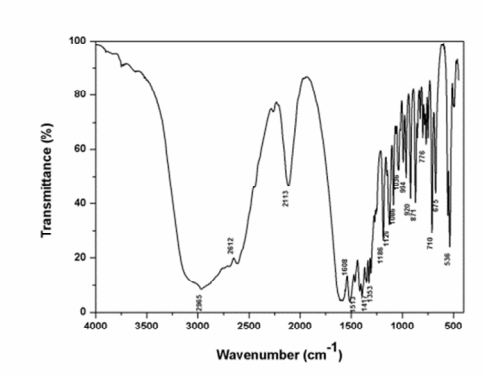

Fig. 6. Experimentally obtained FT-IR spectrum of LIDNL

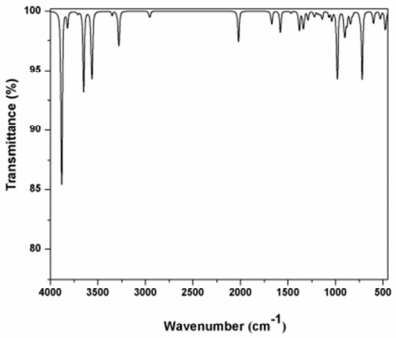

Fig. 7. Theoretically simulated FT-IR spectrum of LIDNL

3.7.1. NH_3^+ group vibration

In zwitterionic molecules, theoretically the NH_3^+ asymmetric and symmetric stretching band appears at the values 3399.2527cm^{-1} and 3085.6288cm^{-1} respectively [11]. The present assignment agrees with the values available in literature [12]. The NH_3^+ symmetric deformation theoretically appears at 1544.3053cm^{-1} [13].

3.7.2 Carboxylate group vibrations

The asymmetric and symmetric stretching modes of carboxylate ion vibrations expected to occur theoretically at 1553.9945 cm^{-1} and around 1439.7305 cm^{-1} respectively [14]. COO^- deformations are usually expected to occur in the region 547.5781 cm^{-1}- 574.7806 cm^{-1} theoretically [15].

3.7.3 C-N vibrations

C-N stretching absorptions are assigned theoretically in the region 1279.7751 cm^{-1}-1367.2456 cm^{-1} for primary aromatic amine with nitrogen directly on the ring. The frequencies are slightly up shifted from the expected value due to the substitution effect [16].

3.7.4. NH_2 vibrations

The NH_2 asymmetric stretching vibrations [17] theoretically gives rise to a strong band at the value 3403.3212 cm^{-1} and the symmetric NH_2 stretching is observed as weak band in the region 3153.0350 cm^{-1} - 3155.9165 cm^{-1} theoretically.

3.7.5. C-H vibrations

Presence of band theoretically occurs in the region 2975.8760 cm^{-1}-2999.2867 cm^{-1} which is the characteristic region for the identification of C-H stretching slightly affected by the nature of the substituent. The C-H bending vibrations from theory are occurred in the region 1405.11 cm^{-1} - 1459.3271 cm^{-1}. The asymmetric and symmetric C-H vibrations for methyl group occurs theoretically in the region 2975.8760 cm^{-1} to 3149.1709 cm^{-1} [18]. Most of the aromatic compounds have nearly four infrared peaks in the region 3016.9684 cm^{-1} -3074.2745 cm^{-1} theoretically due to ring C-H stretching bands.

3.7.6. Vibrations of amine and azane group

The wagging mode of the NH_2 group appears theoretically in the range 655.6477 cm^{-1}-768.4025cm^{-1} [19].

Table.6 Vibrational Assignments of LIDNL Molecule

Wavenumber cm^{-1}		Spectroscopic assignment	Force constant	Reduced mass
B3LYP	Expt.			
547.5781	536	COO^- def	0.2165	1.2254
655.6477	675	NH opd	1.0214	4.0327
730.8063	710	COO^- opd(roc)	2.1400	6.8007
768.4025	776	NH_2 wag	0.3907	1.1232
856.8453	871	CH opb	0.5384	1.2447
921.2398	920	CH st	1.2144	2.4286
998.1486	994	CH opb	0.8361	1.4243
1035.1125	1036	II CH ipd	0.7506	1.1890
1080.4570	1086	NH_2ipd	0.8090	1.1761
1137.0140	1126	CH_3ipb	1.0459	1.3731
1187.9172	1186	II CH ipd	1.2407	1.4922
1356.3534	1353	C-N st(abs)	1.5901	1.4670
1417.1803	1417	C-H b+C=C st	2.3173	1.9583
1544.3053	1513	NH_3^+ sym def	5.1223	3.6454

3.7.7. O-H vibrations

The O-H group gives rise to three vibrations (stretching, in-plane bending and out-of-plane bending vibrations).The O-H group vibrations are likely to be the most sensitive to the environment, so they show pronounced shifts in the spectra of the hydrogen bonded species. The O-H out-of-plane bending mode for the free molecule lies theoretically between 5.2453cm^{-1}-297.2100cm^{-1} and it is beyond the infrared spectral range of the present investigation. However for the associated molecule the O-H out-of-plane bending mode lies theoretically in the region 547.5781cm^{-1}-694.6985cm^{-1} in both intermolecular and intramolecular associations, the frequency is at a higher value than in free O-H [20].

3.7.8. *COOH vibrations*

The carbonyl group is contained in a large number of different classes of compounds, for which a strong absorption band due to C=O stretching vibration that is theoretically observed in the range of 1553.9945cm^{-1}-1726.3655cm^{-1}.

3.7.9. C-C vibrations

The bands between 1405.1143 cm^{-1}-1553.9945 cm^{-1} are due to C-C stretching vibrations from theory in benzene derivations [21, 22]. The carbon-carbon stretching modes of the phenyl group are theoretically expected in the range from 1202.9379 cm^{-1}- 1553.9945 cm^{-1}.The actual position of these modes is determined not so much by the nature of the substituent but by the form of substitution around the ring [23]. In general, the bands of wagging and deformation are of variable intensity and are observed theoretically at 433.6523 cm^{-1}- 487.5575 cm^{-1} and theoretically at the region between 109.8150 cm^{-1} - 297.2100 cm^{-1}.The ring C=C known as semicircle stretching occurs theoretically in the region 1405.1143cm^{-1}-1553.9945cm^{-1} [24].

3.8. Optical absorption spectrum

UV spectral analysis gives useful information about electronic transitions of the compound. Also it would assist to understand the electronic structure and the optical band gap of the crystal to reveal optical properties of L-Isoleucine D-Norleucine single crystal. UV-Vis transmission spectrum was recorded in the range 200-800 nm as shown in Fig.8. The optical cut off wavelength was found to be 240 nm. L-Isoleucine D-Norleucine crystal has low

absorbance in the entire visible region and their optical property enables the material useful for optoelectronic field. Fig.9 shows the band gap energy spectrum. Using linear part of the Tauc's plot hν and $(\alpha h\nu)^2$ values are calculated. From the graph band gap energy of L-Isoleucine D-Norleucine was found to be 4.67eV.

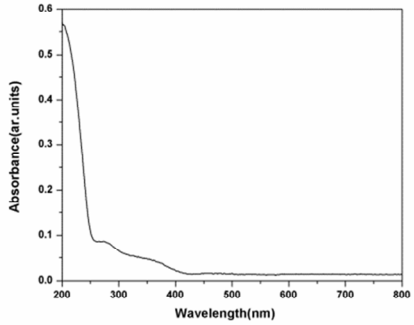

Fig. 8. Optical absorption spectrum of LIDNL crystal

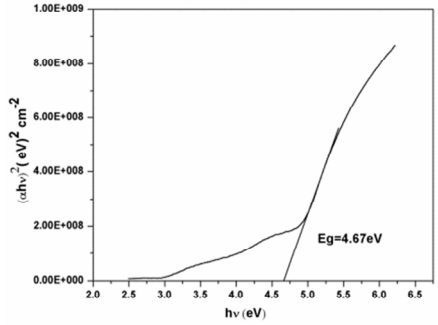

Fig. 9. Optical band gap of LIDNL crystal

3.9. Thermal studies

Thermo Gravimetric Analysis (TGA) and Differential Thermal Analysis (DTA) curves of L-Isoleucine D-Norleucine crystals carried out using Perkin Elmer Thermal analyser with nitrogen atmosphere with temperature range 40°C to 940°C using TGA Q 500 V 20.10 build 36. The resulting TGA and DTA traces are shown in Fig.10. From the thermogram, it is clear that the material is stable up to 175°C. The TGA shows two stages of weight loss. In TGA decomposition takes place after 175°C as the first stage. It goes up to 300°C, resulting in a loss of weight 93.99%. Another weight loss of 5.771% at the second stage, noticed between the temperature ranges 300°C - 450°C, the DTA peaks coincide well with the TGA plot. The sharpness of the peaks shows good degree of crystallinity of the grown crystal.

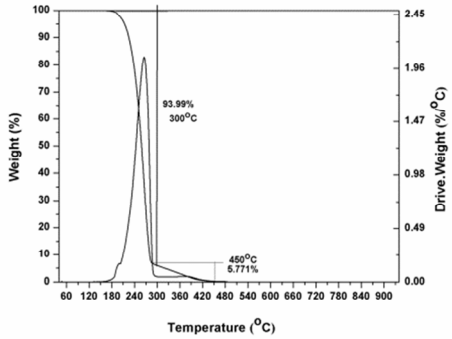

Fig.10. TGA and DTA curves of LIDNL crystal

3.10. NLO studies

The most widely technique for confirming SHG from prospective second order NLO materials is the Kurtz-Perry powder technique. The powder sample was illuminated using a Q-switched mode locked Nd^{3+}: YAG laser of pulse width 8 ns at a wavelength of 1064 nm and 10 Hz fundamental radiation. In the SHG efficiency measurements, microcrystalline material of KDP of the same particle size was used for comparison. A laser input of 0.68 J was passed through L–Isoleucine D-Norleucine and the reference material was KDP. It is found that the efficiency of L-Isoleucine D-Norleucine is three times that of KDP.

4. Conclusion

Good optical quality LIDNL single crystals of dimension up to 21 x 6 x 4 mm^3 have been grown successfully by slow evaporation technique. The solubility curves of LIDNL in different temperatures have been measured gravimetrically. Molecular formula and the structure of the crystal are confirmed by powder X-ray analysis and it is found that the crystal belongs to the monoclinic system with $P2_1$space group. Density functional theory (DFT) computations using (B3LYP) level with 6-31G+(d, p) basis set gives optimized structure parameters of LIDNL molecule. It is understood that hydrogen bonds are prevalent in this material and the optimized C–C bond lengths of LIDNL fall in the range 1.17529–1.75293Å. The theoretically constructed FT-IR spectrum coincides with experimentally observed FT-IR gas phase spectrum. The electric dipole moments and the first hyperpolarizabilities of the compound studied have been calculated by B3LYP method. The results of theoretical calculations are substantiated with powder SHG results. The output of green light confirmed its non-centrosymmetric structure and it exhibits powder SHG efficiencies three times higher than potassium dihydrogen phosphate (KDP). Molecular energy gap of LIDNL was found as 0.10134 au, by HOMO-LUMO analysis. Optical absorption spectrum was recorded for the given crystal in the region 200-800 nm. The optical band gap of the material is found as 4.67 eV.

Acknowledgement

The authors acknowledge University Grants Commission (UGC), India, for funding this research project-F.No.4-4/2015-16 (MRP/UGC-SERO).

References

1. Patil P.S., Dharmaprakash S.M., Hoong-Kun Fun and Karthikeyan M.S., J. Crystal Growth, 297 (2007) 111-116.
2. Pricilla Jeyakumari A., Manivannan .S, Dhanuskodi. S, Spectrochimica Acta Part A, 67 (2004) 83–86.
3. Narayan Bhat., M Dharmaprakash.S.M, Journal of Crystal Growth, 235 (2002) 511–516.
4. Frisch M.J, Trucks G.W, Schlegel H.B, Scuseria G.E, Robb M.A, J.R. Cheeseman J.R, Montgomery Jr J.A, Vreven T, Kudin K.N, Burant J.C, Millam J.M, Iyengar S.S, Tomasi J, Barone V, Mennucci B, Cossi M, Scalmani G,.Rega N, Petersson G.A, Nakatsuji H, Hada M, Ehara M, Toyota K, Fukuda R, Hasegawa J, Ishida M, Nakajima T, Honda Y, Kitao O, Nakai H, Klene M, Li X, Knox J.E, Hratchian H.P, Cross J.B, Adamo C, Jaramillo J, Gomperts R, Stratmann R.E, Yazyev O, Austin A.J, Cammi R, Pomelli C, Ochterski J.W, Ayala P.Y, Morokuma K, Voth G.A, Salvador P, Dannenberg J.J, Zakrzewski V.G, Dapprich S, Daniels A.D, Strain M.C, Farkas O, Malick D.K, Rabuck A.D, Raghavachari K, Foresman J.B, Ortiz J.V, Cui Q, Baboul A.G, Clifford S, Cioslowski J, Stefanov B.B, Liu G, A.Liashenko, Piskorz P, Komaromi I, Martin R.L, Fox D.J, Keith T.,.Al-Laham M.A, Peng C.Y, Nanayakkara A, Challacombe M, Gill P.M.W, Johnson B, Chen W, Wong M.W, Gonzalez C, Pople J.A, Gaussian 03, Revision C.02, Gaussian Inc.,Wallingford, CT, (2004).
5. Ataly Y., Avci D., BaSoglu A., Struct. Chem, 19 (2008) 239
6. Vijayakumar T, I. Hubertjoe, C.P.R. Nair, V.S. Jayakumar, Chem. Phys, 343 (2008) 83.
7. Palafox M.A, Tardajos G., Martines A.G., Rastogi V.K., Mishra D., Ojha S.P.,Kiefer W., Chem. Phys, 340 (2007) 17–31.
8. Stephens P.J., Devlin F.J, Chavalowski C.F., Frisch M.J., J. Phys. Chem, 98 (1994) 11623–11627.
9. Devlin F.J, Finley J.W, Stephens P.J., Frisch M.J., J. Phys. Chem, 99 (1995) 16883–16902.
10. Lee S.Y., Boo B.H., Bull. Korean Chem. Soc, 17 (1996) 754–759.
11. Bellamy L.J., The Infrared Spectra of Compound Molecules, Chapman and Hall, London, (1975).
12. Jesintha John C., Xavier T.S., Lukose G., Hubert Joe I., Spectrochim. Acta, Part A: Molecular and Biomolecular Spectroscopy, 85 (2012) 66–73.
13. Silverstein R, G. C. Bassler, Spectrometric identification of organic compounds, Wiley& sons, New York, (1981).
14. Socrates G., Infrared Characteristic Group Frequencies, John Wiley and Sons, New York, (1981).
15. Dollish F.R., Fateley W.G., Bentley F.F., Characteristic Raman Frequencies of Organic Compounds, John Wiley & Sons, New York, (1997).
16. Marchewka M.K., Pietraszko A., J. Phys. Chem. Solids, 64 (2003) 2169 –2181.
17. Roeges N.G.P., A Guide to the Complete Interpretation of the Infrared Spectra of Organic Structures, Wiley, NY, (1994).
18. Ramalingam S., Periandy S., Narayanan B., Mohan S., Spectrochim. Acta A, 76 (2010) 84–92.
19. Jose P. Abraham, Sajan D., Hubert Joe I., Jayakumar V.S. Spectrochemica Acta Part A, 71 (2008) 355-367.
20. Varsanyi G., Assignments of Vibrational Spectra of Seven Hundred Benzene Derivatives, Adam Hilger, 1–2 (1974).
21. Krishnakumar V, R. John Xavier, Indian J. Pure. Appl. Phys, 41 (2003) 95.
22. Singh N P, R.V. Yadav, Indian J. Phys. B 75 (2001) 347.
23. Bellamy L.J., The Infrared Spectra of Compound Molecules, Chapman and Hall, London, (1975).
24. Altun, Golcuk K, Kumru M, J. Mol. Struct. (Theochem), 155 (2003) 637.

Available online at www.sciencedirect.com

ScienceDirect

Materials Today: Proceedings 8 (2019) 456–463

materialstoday: PROCEEDINGS

www.materialstoday.com/proceedings

ICMEE 2018

Studies on Growth and Characterization of Nonlinear Optical Single Crystal L-Histidine Di Picrate

Subaranjani R[a], Madhavan J[a] Prathap S [a] and Victor Antony Raj M[a,b] *

[a]*Department of Physics, Loyola College, Chennai, India.*

[b]*Loyola Institute of Frontier Energy (LIFE), Loyola College, Chennai, India.*

Abstract

The present article reports the growth of single crystals of a complex L-Histidine with picric acid (LHDP) by solution growth (slow evaporation) method at room temperature. The structure of the grown crystal determined by X-ray diffraction analysis (XRD) reveals that it belongs to the monoclinic system with space group $P_{21,}$ and the cell parameter values. Vibrational patterns and the good crystallinity were indicated by X-ray diffraction method. The structural, thermal, optical and mechanical properties were studied for the grown crystal. The calculated results of first Order hyperpolarizability confirm that these molecules are good non-linear optical materials and can be used for laser device fabrications. From the energy gap of homo lumo, energetic behavior of LHDP was studied. The dielectric tensor, dielectric loss and conductivity over a range of frequencies and temperatures had been presented.

Selection and peer-review under responsibility of the scientific committee of the Materials For Energy and Environment.

Keywords: XRD, NLO, HOMO LUMO, DIELECRIC STUDIES

1. Introduction

Non-linear optical (NLO) compounds have been intensively studied in the last years as a result of their potential application in telecommunications, optical information processes and numerous opto-electronics. Other advantages of organic compounds involve amenability for synthesis, multifunctional substitution, higher resistance to optical damage and maneuverability for device application etc., the growth of good quality and large size NLO crystals with orientation control is needed for application. One of the ways in which an organic molecule can have a large optical non linearity is by possessing a conjugated system of the bonds which gives rise to a strong p-electron

* Corresponding author. Phone: +91-44-28178200; Fax: +91-44-28175566

E-mail address: vicvad2003@yahoo.co.in

Selection and peer-review under responsibility of the scientific committee of the Materials For Energy and Environment.

delocalization. The delocalization of the p-electrons can be further enhanced by the addition of donor and acceptor groups at the opposite ends of the conjugated system. Salts of L-histidine gained the status of promising NLO materials the crystal structures of a large number of picrate salts and picric acid complexes have been studied to understand the conformational features and charge transfer processes [1-6].

2. Synthesis of LHDP

The synthesis of the title compound LHDP was achieved by adding L-histidine and picric acid (E-Merck) in 1:2 stoichiometric proportions in distilled water. The solution was thoroughly mixed to get a clear yellow solution which was filtered and kept aside. The solubility (g LHDP / 100ml H_2O) of LHDP was measured. The seed crystals were hung in the mother solution with proper seasoning and then allowed to grow by using the slow solvent evaporation technique at room temperature. The dimensions of 16 mm x 4 mm x 7 mm were obtained after a period of 45 days. The crystals are highly transparent and free from visible inclusions. Fig.1 shows the photograph of as grown crystal of LHDP.

Fig.1 Photograph of as grown LHDP single crystal

3. RESULT AND DISCUSSION

3.1 X-ray diffraction analysis

The XRD study was carried out to check the correctness of the data and to identify the diffraction pattern of the grown crystal. Experimental XRD pattern is shown in Fig 2. Crystal parameters of LHDP are shown in table 1.

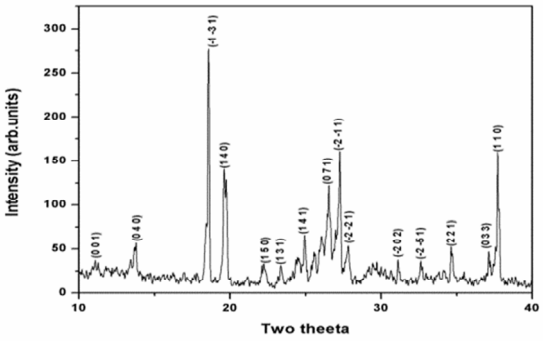

Fig.2 Experimentally obtained XRD pattern of LDHP

Table 1. Crystal parameters of LDHP

Empirical Formula	$C_{18}H_{19}N_9O_{18}$	
Formula weight	255.614 g/mol	
Wave length	0.71073 Å	
Crystal system, Space group	Monoclinic, $P2_1$	
Unit cell dimensions	a = 6.6065(1)Å	α = γ = 90°
	b = 25.7004(2)Å	β =107.536°
	c = 7.9629(2)Å	
Cell volume	1289.20 $Å^3$	
Calculated Density	1.7606 g/cm^3	
Absorption coefficient	0.957 mm^{-1}	
F(000)	264	
Crystal size	.25 x.23 x.19mm^3	
Theta range for data collection	3.93° to 67.92°	
Limiting indices	-13<=h<=0, 0<=k<=6, -13<=l<=13	
Reflections collected/unique	1353/1294 [R(int)=0.0000]	
Completeness to theta = 67.92	100%	
Refinement method	Full matrix least squares on F^2	
Data/restraints/parameters	1353/1/187	
Goodness- of – fit on F^2	1.13	
Final R indices [I>2sigma(I)] 80	R1=0. 028, wR2 =0.0693	
R indices (all data)	R1=0 .030, wR2 =0. 078	

3.2 Vibrational Analysis

Vibrational studies reveal the presence of the possible bonding's that are present in the title compound. The title molecule LDHP has 64 atoms shown in fig 4. It has 186 (3N – 6) normal vibrational modes .The theoretical and experimental wavenumbers are in fair agreement, and assignments of wavenumbers for different functional FT-IR spectrum of the grown crystal was recorded in the range 400 cm^{-1} to 4000 cm^{-1}, using KBr pellet technique on BRUKKER IFS FT-IR Spectrometer. The experimental IR spectrum is compared with the results of B3LYP/6-31 G (d, p) calculation carried out for the title compound the experimental FT-IR spectrum is shown in fig 3.

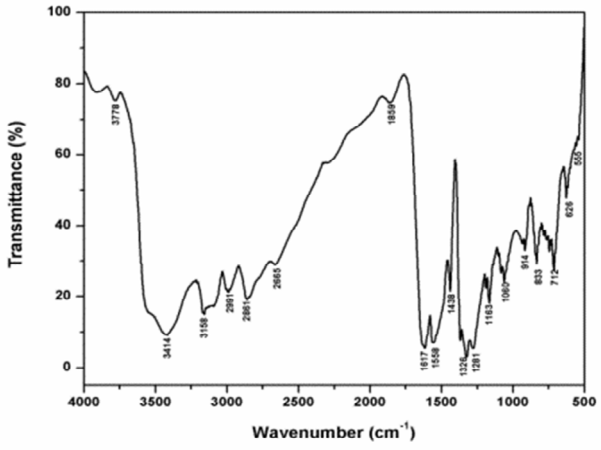

Fig.3. Experimentally obtained FT-IR spectrum of LHDP

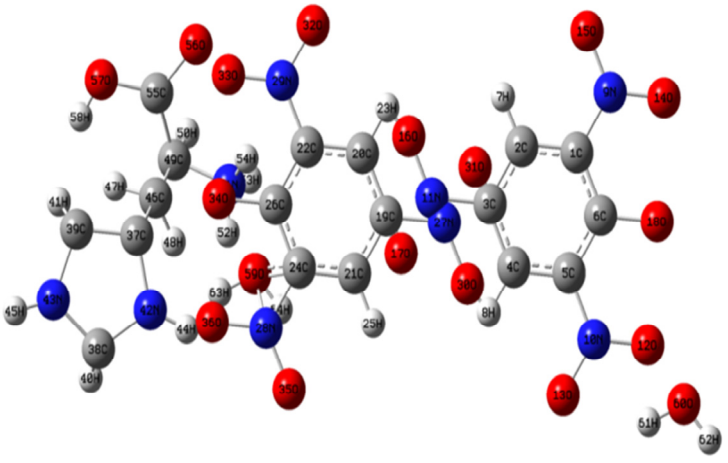

Fig.4 Atomic numbering system adapted for ab initio computations of LHDP molecule

3.3 Hyperpolarizability studies

Molecules with p electron conjugation incorporating electron donor and acceptor groups to influence the asymmetric polarization are the essential candidates for NLO applications such as frequency doubling [7]. A large value of β is the first requirement for high NLO efficiency in a molecular material. The effect of intermolecular hydrogen bonding in the titled crystal would enhance the magnitude of β quantities. The hydrogen bond interactions play an important role in the NLO response the maximum value may be due to electron cloud movement from donor to acceptor which makes the molecule highly polarized and the intermolecular charge transfer possible which was also confirmed by vibrational spectral study. A large value of the first hyperpolarizability is the prerequisite to behave as a good NLO material, and the important parameters influencing β generally are (i) donor–acceptor system, (ii) nature of substituent, (iii) conjugate π system and (iv) the influence of planarity. Selected bond lengths and bond angles of LHDP molecule is shown in table 2 and 3 respectively. The total molecular dipole moment and mean first hyperpolarizability of LHDP is shown in Table 4.

Table 2 Selected bond lengths of LHDP molecule

Atoms	Gaussian(Å)	XRD(Å)
O13-O12	2.35559	2.456
N10-C5	1.47000	1.498
C5-C2	2.78995	2.653
N9-O14	1.36000	1.367
N9-O15	1.36000	1.368
O59-O34	1.98152	1.982
N42-C37	1.52215	1.611
C39-N43	1.52186	1.619
C55-C49	1.54000	1.601
C39-H41	1.11926	1.206
C46-H47	1.07000	1.170
C39-C37	1.52186	1.500
O57-H58	0.96000	1.004

Table 3 Selected bond angles of LHDP molecule

Atoms	Gaussian(˚)	XRD(˚)
O15-N9-O14	120.00000	120.005
N9-C1-C6	120.00430	120.012
O13-N10-O12	120.00002	120.101
H51-C60-H62	109.47124	108.987
C24-C21-C19	120.00471	119.982
C49-C46-H47	89.99985	90.025
C37-C46-H48	89.99894	90.040
C39-N43-H45	126.04304	125.910
C20-C22-N29	119.98081	120.054
N42-C38-N43	107.95915	106.987
H45-N43-C39	126.04304	125.973
O35-N20-C24	119.99996	120.985
C22-C20-H23	119.99718	119.902

Table 4 Hyperpolarizability of LHDP in esu

β_{xxx}	-217.36375
β_{xxy}	-251.23383
β_{xyy}	-189.148803
β_{yyy}	-165.304903
β_{xxz}	103.2400168
β_{xyz}	-114.314853
β_{yyz}	161.5513002
β_{xzz}	-140.921474
β_{yzz}	1.7805245
β_{zzz}	-361.372294
β_{tot}	5.80467×10^{-30}

3.4 HOMO-LUMO Gap

The interaction of two atomic (or) molecule orbital produces two new orbitals. One of the new orbitals is higher in energy than the original ones (the anti-bonding orbital) and one is lower (the lower orbital). When we are dealing with interacting molecular orbitals, the two that interact are generally the highest energy occupied molecular orbital (HOMO) and lowest unoccupied molecular orbital (LUMO) of the compound .The HOMO-LUMO energy gap of LHDP was calculated and found to be -0.183 a. u (4.9796 eV);the orbital picture is shown in Fig 5.

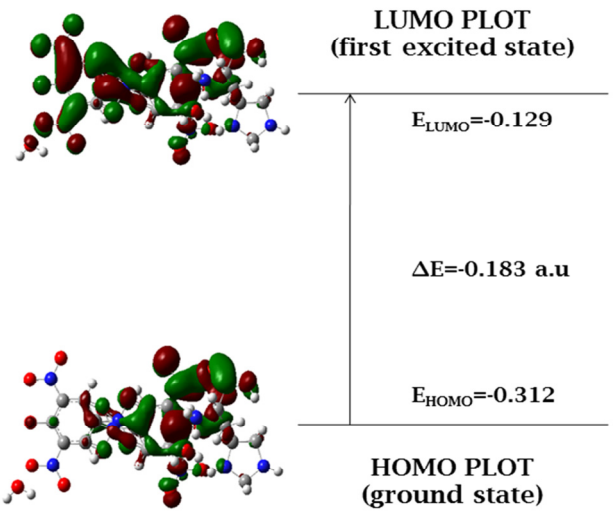

Fig.5 HOMO – LUMO plot of LHDP molecule

3.5 Thermo-dynamical properties

On the basis of vibrational analysis at B3LYP/6-31G(d,p) level, the standard statistical thermodynamic functions, standard heat capacities ($C_P{}^0m$), standard entropies (S^0m), and standard enthalpy changes (ΔH^0m) for the title compound were

obtained from the theoretical harmonic frequencies and listed in Table 5. The correlation equations between heat capacity, entropy, enthalpy changes and temperatures were fitted by quadratic formulas and the corresponding fitting factors (R^2) for these thermodynamic properties are 0.99928, 0.9999 and 0.99932respectively. The corresponding fitting equations are as follows and the correlation graphics of those are shown in Figures 6, 7 and 8 respectively.

Table 5 Thermo-dynamical properties of LHDP

T (K)	S (J/mol.K)	Cp (J/mol.K)	ΔH (kJ/mol)
100	302.47	69.86	4.5
200	370.41	133.36	14.67
298.15	434.9	192.7	30.72
300	436.1	193.75	31.07
400	499.21	245.88	53.14
500	558.78	287.96	79.91
600	614.34	321.15	110.43
700	665.9	347.57	143.92
800	713.76	369.08	179.78
900	758.3	387.03	217.62
1000	799.89	402.3	257.1

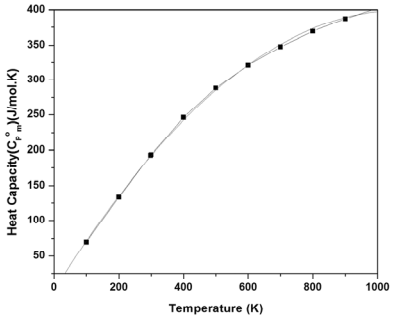

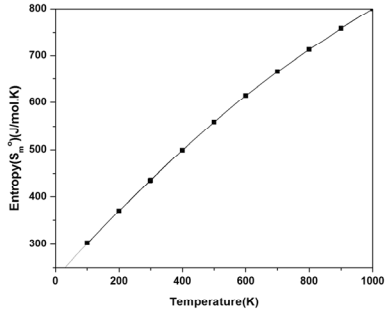

Fig.6 Correlation graph of heat capacity and temperature of LHDP; Fig.7 Correlation graph of entropy and temperature of LHDP

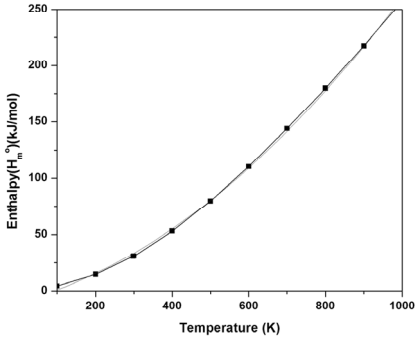

Fig.8 Correlation graph of enthalpy and temperature of LHDP

All thermodynamic calculations were done in gas phase and they could not be used in solution.

$C_P{}^0m = 1.15236 + 0.74016T - 3.43648x\ 10^{-5}\ T^2$ ($R^2 = 0.99928$)

$S^0m = 228.39493 + 0.74782T - 1.76264x\ 10^{-5}\ T^2$ ($R^2 = 0.9999$)

$\Delta H^0m = -10.00441 + 0.09093T + 1.79164x\ 10^{-5}\ T^2$ ($R^2 = 0.99932$)

3.6 Nonlinear optical (NLO) test

A basic motivation for the current research of non-linear optical properties of materials is due to their use in logical operations, switching actions, signal processing, data storage, frequency shifting and optical modulation for the present and nearby future technological advances. To confirm the nonlinear optical property, Kurtz and Perry powder technique was carried out for LHDP crystal [8]. The SHG efficiency of the grown crystal was checked by passing a Q-switched, mode locked Nd:YAG laser of 1064 nm and pulse width of 8 ns (spot radius of 1 mm) on the powder sample of LHDP. For a laser input pulse of 6.9 mJ, the SHG signal (532 nm) of 90 mV and 310 mV were obtained for KDP and LHDP samples respectively. Hence, it is observed that the SHG efficiency of LHDP is 3.44 times higher than KDP

3.7 Dielectric studies

The dielectric properties of the materials are important to know the charge transport phenomena and the lattice dynamics in the crystals. Fig.9.1 shows the plot of dielectric constant (ε_r) versus applied frequency. The dielectric constant has high values in the lower frequency region and then it decreases with the applied frequency. The variation of dielectric loss with frequency is shown in Fig.9.2. The characteristic of low dielectric loss at high frequencies for a given sample suggested that the sample possesses enhanced optical quality with lesser defects [9].

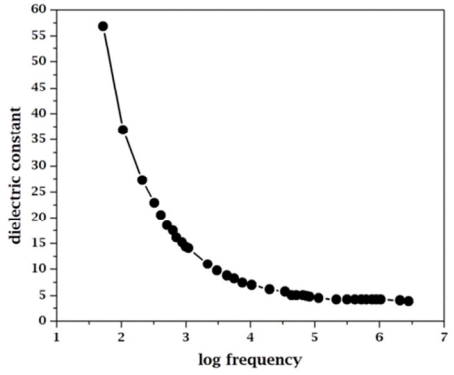

Fig. 9.1 Variation of dielectric constant of LHDP

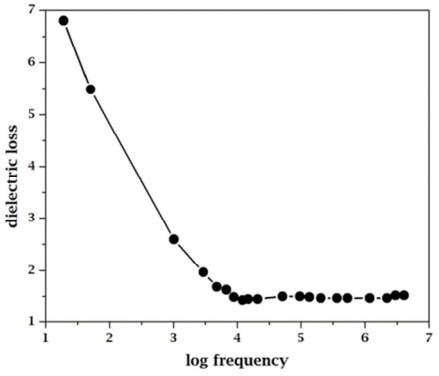

Fig. 9.2 Variation of dielectric loss of LHDP

3.8 Conclusion

The potential organic NLO crystal of L-histidine Di Picrate (LHDP) was grown by slow evaporation method. Well-developed and good optical quality LHDP crystals were obtained. The lattice parameters were confirmed by single crystal X-ray diffraction analysis. The functional groups were ascertained by FT-IR. The magnitude of molecular first order hyperpolarizability for this molecule is 5.80467 x 10^{-30} esu. It is in a suitable range to exhibit NLO behaviour. Molecular energy gap of LHDP was found to be -0.183 a. u (4.9796 eV) by HOMO-LUMO analysis. The dielectric study reveals the low dielectric constant and dielectric loss at high frequency regions.

Acknowledgements

The authors acknowledge University Grants Commission (UGC), India, for funding this research project-F.No.4-4/2015-16 (MRP/UGC-SERO).

References

[1] Amudha M, Madhavan J, Praveen Kumar P, Journal of Optics (India) (2017) "Studies on the growth and characterization of Benzimidazolium Picrtae Single crystals" 46(4) 382-390.
[2] Victor Antony Raj M, Madhavan J, Materials science and Engineering(2015) "Theoretical and Experimental studies on nonlinear optical L-Phenylalanine maleate" IOP Conference Series: 73(1) art.no 012138.
[3] Kumar L B, Murthy K K, Rajeev Y N, Madhavan J, Sagayaraj P, Cole S, Optik(2015) "Influence of rare earth doping on the spectral, thermal, morphological and optical properties of nonlinear optical single crystals of manganese mercury thiocyanate, $MnHg(SCN)_4$" (2015) 126 (24) 4899-4904.
[4] Tamilselvan S, Vimalan M, Vetha Potheher I, Jeyasekaran R, Yogam F, Madhavan J, Optik (2014) "Generation of 532nm laser radiation and phase matching properties of organic nonlinear optical material" 125 (1) 164-169.
[5] Tamilselvan S, Vimalan M, Vetha Potheher I, Rajasekar S, Jeyasekar R, Antony Arockiaraj, Madhavan J, A nonlinear optical single crystal" (2013) "Growth, thermal, dielectric and mechanical properties of L-Phenylalanine-benzoic acid: Spectrochemica Acta-Part:A Molecular and Biomolecular spectroscopy, 114, 19-26.
[6] Senthil S, Pari S, Xavier R, Madhavan J, Optik, (2012) "Linear and nonlinear optical properties of N-(3-nitrophenyl) acetamide single crystals" 123 (2) 104-108.
[7] J. Zyss, J.F. Noud, Curr. Opin. Solid. State, Mater. Sci. 1 (1996)
[8] Kurtz S.K and Perry T.T., J. Appl. Phys., 39 (1968) 3798.
[7] J. Zyss, J.F. Noud, Curr. Opin. Solid. State, Mater. Sci. 1 (1996)
[8] Kurtz S.K and Perry T.T., J. Appl. Phys., 39 (1968) 3798.
[9] Balarew. C, Duhlew. R, (1984) , J. Solid State Chem. Vol. 55. pp. 1–6.

Available online at www.sciencedirect.com

ScienceDirect

Materials Today: Proceedings 8 (2019) 94–98

materialstoday: PROCEEDINGS

www.materialstoday.com/proceedings

ICMEE 2018

Solvothermal Synthesis, Characterization and Photocatalytic activity of ZnO Nanoparticle

A. Anu Ruba, Linu M. Johny, N.S. Nirmala Jothi*, and P. Sagayaraj

Department of Physics, Loyola College, Chennai – 600 034, India

Abstract

A simple and efficient strategy of one–pot synthesis of ZnO photocatalyst was developed using solvothermal synthesis and heat treatment of $ZnCl_2$ with NaOH solutions in polyethylene glycol at a low temperature led to the formation of ZnO nanoparticles consisting of the aggregates of uniform-sized quantum dots. Several analytical techniques including X-ray diffraction (XRD) reveals the hexagonal wurtzite structure of ZnO, FT-IR, and UV-VIS has been used to characterize the resulting ZnO photocatalyst.

Selection and peer-review under responsibility of the scientific committee of the Materials For Energy and Environment.

Keywords: ZnO, Solvothermal, Photocatalyst, PEG.

1. .Introduction

In recent years, water pollution caused due to organic and toxic pollutants has aroused great attention. Photocatalysis, as a "green" technique is used for the degradation of very hard toxic chemicals in water, is of continuing interest. Various nanostructured semiconductor metaloxides, such as TiO_2 and ZnO have been developed as nano photocatalysts for their great ability to produce radicals and decompose most organic pollutants under UV irradiation or sunlight [1, 2]. They are also suggested that ZnO is nontoxic in nature and finds various photocatalytic applications. Various methods are used to synthesize ZnO nanoparticles, few of them are co precipitation method, hydrothermal method, solvothermal method, sol-gel method, electro deposition and solution combustion method. However, ZnO is activated only under UV irradiation because of their large band gap energy, which greatly limits

* Corresponding author Tel.:+91-9444481558; fax: 91-44 28175566.
E-mail address: jmjnirmala@yahoo.co.in

Selection and peer-review under responsibility of the scientific committee of the Materials For Energy and Environment.

their application in environmental decontamination as solar spectra they only contain 5% of UV. Therefore, it is crucial to explore efficient methods to extend their photocatalytic response from UV to visible region. Compared to $TiO_2$and other metaloxides ZnO has a lower cost and a better efficiency in photocatalytic degradation for some organic dyes and ZnO has been extensively investigated and used recently. In the field of photocatalysis, the ZnO is believed to be an efficient Photocatalytic material alternative to TiO_2 because both have similar band gap and photocatalytic mechanism. ZnO is an n-type semiconductor with a direct bandgap of Eg = 3.37eV [3,4]. Various kinds of nanostructured ZnO, such as nanoparticle, nanorods, nanobelt, nanoplate, hollow sphere, and micro/nanostructure, have been used for the photodegradation of dye pollutants.

In the present work an attempt has been made to prepare and characterize ZnO nanoparticles using solvothermal at low temperature.

2. Experimental details

2.1 Materials

The raw materials used were of analytical grade $ZnCl_2$ (98%, Fluka, Sigma-Aldrich Ltd., NSW, Australia), NaOH pellets (97%, Chem-Supply,SA, Australia), and PEG 400 (99%, Sigma-Aldrich Ltd.), all of which were used without further purification.

2.2 Preparation of ZnO

The ZnO nanoparticle is prepared using solvothermal method, 4.0885 g (0.30mol) of $ZnCl_2$ powder was added to 75 ml of poly ethylene glycol (PEG400). Separately, 1.2 grams (0.30 mol) of NaOH pellets was dissolved in 75 ml of PEG. Both the mixture was heated and stirred for a required time separately. Later, the two solutions were mixed together at room temperature and stirred again continuously to get a homogeneous solution. The pH value of the solution was maintained at 8.Next, the mixed solution was cooled at room temperature and poured in a 200ml stainless steel autoclave and sealed .Then, the temperature was raised to140ºC and heated for 10 hours. Finally, the precipitates were separated from PEG and washed with distilled water and ethanol several times using a centrifuge. When the reactions were completed, the synthesized white precipitate was dried at 80ºC in an oven.

2.3 Characterization

The nanopowdered sample of ZnO was characterized by X-ray powder diffraction (XRD) measurement using a X'Pert Pro-PAnalytic X-ray diffractometer equipped with CuKα radiation (λ= 1.540598 Å) to investigate crystal structure, crystallite size, strain and lattice parameters. The morphology and particle size of ZnO Nanocrystals were studied using U V-visible diffuse reflectance spectrum which were recorded using Jasco V-670. Fourier Transform-Infra Red spectroscopy (FT-IR) transmittance was measured using Perkin Elmer spectrometer.

3. Results and Discussion

3.1 XRD Analysis

The crystal structure of the sample was investigated by analyzing the XRD data. The X-ray diffraction patterns of Solvothermal synthesized samples were shown in Fig.1. XRD spectrum. As revealed from the diffraction along the peaks at around 2Θ= 31.7, 34.3, 36.2,47.4, 56.5, 62.9, 66.3, 68.0 and 69.0 are attributed to the(100),(002),(101),(102),(110),(103),(112) and (201) crystal planes, respectively[5,6].The sharpest peak is located at 36.2º. Using the Debye-Scherrer equation the average crystallite size of the sample can be obtained [7,8].

$$D = \frac{k\lambda}{\beta \cos\theta} \quad (1)$$

Where λ is the wavelength of the X-ray radiation,

K is 0.89 as a constant,

β is the line width at half-maximum height and Θ is the diffraction angle (36.2º).The average crystallite size of the sample were calculated to be 25.39nm [9,10].Thus the crystal structure was confirmed to be wurtzite phase corresponding to the standard crystallographic data in the JCPDS-ICDD index card No.36-1451 was observed, indicating that the synthesized powder was a single phase.

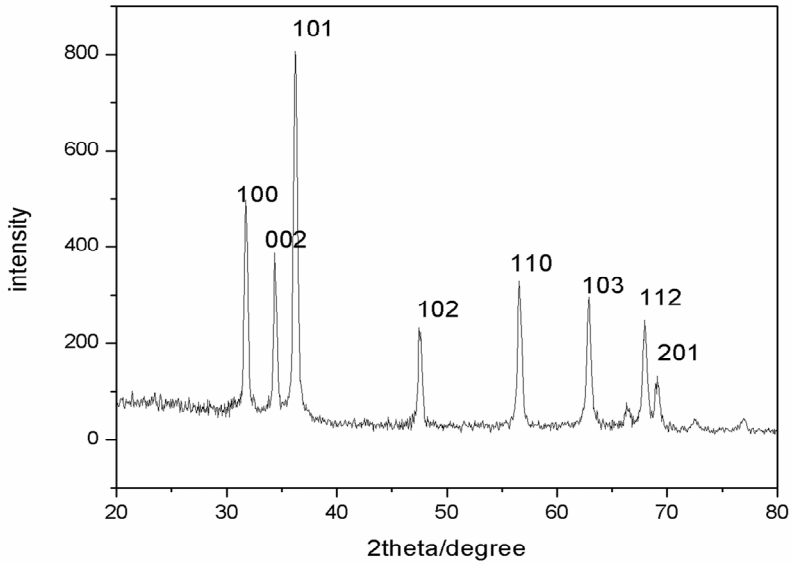

Fig.1.X-ray powder diffraction pattern of ZnO nanoparticles synthesized at 140ºC

3.2 UV-VIS diffuse reflectance spectrum

The absorption spectrum of the synthesized sample was shown in fig.2.acquired using UV-Vis spectrophotometer in the wavelength region of 200-1000 nm. The absorption depends on several factors such as band gap, oxygen deficiency, size and structure of the nanoparticles, surface roughness and impurity centers.[11,12]It is observed from the fig.2.That the peak appearance in the absorption curves positioned at 410nm may be attributed to the fundamental absorption of exciton, which indicates the light response in ultraviolet region. As seen from fig 2.the band gap energy (Eg) of nano-ZnO has been calculated to be 3.03eV using the formula,

Band Gap Energy (E) =h*C/λ
h = Planks constant =$6.626*10^{-34}$ Js
C= Speed of light =$3.0*10^{8}$ ms^{-1}
λ = Cutoff wavelength =$410*10^{-9}$ m

Where

1eV=$1.6*10^{-19}$ J

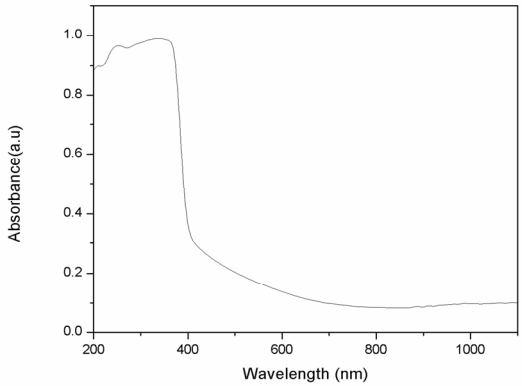

Fig.2.UV-VIS diffuse reflectance spectra of ZnO Nanoparticles

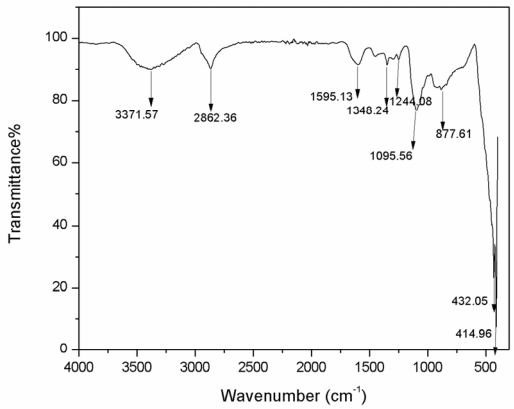

Fig.3. FT-IR spectrum of the ZnO nanoparticle.

3.3 FT-IR Analysis

Figure.3. shows the FT-IR spectrum of pure PEG and ZnO secondary nanoparticles synthesized at 140ºC by solvothermal method, It is well accepted that FTIR spectra can be used as an important analytical tool to identify the functional groups present in materials. The band stretches from acquired range of 500-4000 cm^{-1}.[13, 14]The broad peak at3371.cm^{-1}corresponds to the O–H stretching and bending vibrations, resulting from the presence of water and hydroxyl groups on the particle surface. The stretching mode of vibration corresponding to C=C is obtained at 1095 cm^{-1} and due to the alkyl group is obtained in the range of 2862–1595 cm^{-1}. The vibration due to the carboxyl group is obtained in the range of 1348–1244 cm^{-1}[15,16]. In the spectrum of the ZnO nanoparticles, the strong peak is at 432.05cm^{-1} indicates the appearance of ZnO.

4. Conclusion

We have obtained a low temperature ZnO nano crystals successfully synthesized by solvothermal method by using PEG as solvent. The nanoparticle was synthesized at a low temperature as 140ºC in PEG. Moreover, no surfactant or capping agents were used to limit the size of the particle. The structural and optical properties of ZnO nano crystals were studied. The hexagonal wurtzite structure of ZnO was confirmed from XRD studies. The optical bandgap of the ZnO nanoparticles was found to be 3.02eVfrom UV-vis spectrum. FTIR confirms the band at~ 432 cm^{-1} indicates the presence of Zn-O bond.

References

[1]G Nagaraju, G.C Shivaraju, G Banuprakash, “Photocatalytic Activity of ZnO Nanoparticles: Synthesis via Solution Combustion Method” - Materials Today 2, (2017).
[2]Rongliang He and Takuya Tsuzukiw93 “Low-Temperature Solvothermal Synthesis of ZnO Quantum Dots” 93[8] 2281–2285 (2010).
[3]GN Dar , “Metal oxide nanostructures andtheir applications”1, (2015).
[4]Y Chen, C Zhang, W Huang, Y Situ, H Huang -Multimorphologies nano-ZnO preparing through a simple solvothermal method for Photocatalytic application Materials Letters,14 (2015).
[5]ZhuC, LuB,SuQ,XieE,LanW.Nanoscale2012;4:3060–4.
[6]LvJ,WangF,ZhouZ,LiuC,GongW, FengY,etal.SciAdvMater 2013; 5:617–22.
[7]MclarenAValdes-SolisT,LiG,TsangSCJ.AmChemSoc2009;131:12540–1.
[8]ChengB,SamulskiET.ChemCommun2004;8:986–7.
[9]MilathianakiD,BoutetS,WilliamsG,HigginbothamA,RatnerD,GleasonA, et al.Science2013; 342:220–3.
[10] MannaL,ScherEC,AlivisatosAPJ.AmChemSoc2000;122:12700–6.
[11]U. Koch, A. Fojtik, H. Weller, and A. Henglein, ‘‘Preparation of ExtremelySmall ZnO Particles, Fluorescence Phenomena and Size Quantization Effects,’’Chem. Phys. Lett., 122, 507–10 (1985).
[12] L. Brus, ‘‘Electronic Wave Functions in Semiconductor Clusters: Experimentand Theory,’’ J. Phys. Chem., 90, 2555–60 (1986).
[13]8H. Jiang, J. Hu, F. Gu, and C. Li, ‘‘Large-Scaled, Uniform, MonodispersedZnO Colloidal Microspheres,’’ J. Phys. Chem. C, 112 [32] 12138–41 (2008).
[14]M. Vafaee and M. S. Ghamsari, ‘‘Preparation and Characterization ofZnO Nanoparticles by a Novel Sol–Gel Route,’’ Mater. Lett., 61 [14–15] 3265–8(2007).
[15]S. Suwanboon, “Structural and optical properties of nanocrystalline ZnO powder from sol-gel method,” ScienceAsia, vol. 34, no. 1, pp. 31–34, (2008).
[16]T Thirugnanam - Journal of nanomaterials, “Effect of polymers (PEG and PVP) on sol-gel synthesis of microsized zinc oxide”19(2013)

Available online at www.sciencedirect.com

ScienceDirect

Materials Today: Proceedings 8 (2019) 231–238

materialstoday: PROCEEDINGS

www.materialstoday.com/proceedings

ICMEE 2018

Preparation, Characterization and Magnetic Properties of $BaZrFe_{11}O_{19}$ Nanoparticles via Sol-Gel Auto Combustion Method

S. Anand, N. Vinnarasi, S. Pauline*

Department of Physics, Loyola College (Autonomous), Chennai-600034, India

Abstract

In this study, zirconium (Zr^{4+}) ion substitution on M-type barium hexaferrite ($BaZr_xFe_{12-x}O_{19}$ with x=1) was synthesized via Sol-gel auto combustion technique in the presence of citric acid as fuel. The crystal structure, morphology and magnetic properties of the samples were systematically investigated using X-ray diffraction (XRD), Fourier transform infrared spectroscopy (FT-IR), transmission electron microscopy (TEM), and vibrating sample magnetometer (VSM). The XRD results confirmed the single phase magnetoplumbite type hexagonal structure. Scherrer and Williamson-Hall (W-H) method is applied to determine crystallite size and strain present in the sample. Three vibrational modes were observed in FT-IR spectra which confirm that formation of zirconium substituted barium hexaferrite. Raman spectra showed eight strong and sharp modes, identifies the barium hexaferrite phase. The transmission electron microscopy (TEM) observations revealed that the as-prepared nanoparticles have rods-like shape. The magnetic measurements of the calcined sample were carried out at room temperature with vibrating sample magnetometer.

Selection and peer-review under responsibility of the scientific committee of the Materials For Energy and Environment.

Keywords: $BaZrFe_{11}O_{19}$; Sol-gel auto combustion; W-H method; TEM; VSM

* Corresponding author. Tel.: 9950054040
E-mail address: paulantovero@yahoo.co.in

Selection and peer-review under responsibility of the scientific committee of the Materials For Energy and Environment.

1. Introduction

M-type hexaferrites, $MFe_{12}O_{19}$ (M=Ba, Sr and Pb) have been widely used for microwave devices, high-density recording media and permanent magnet because of their perfect properties such as high saturation magnetization, high Curie temperature, high coercive field, good chemical stability, high uniaxial magnetic anisotropy and corrosion resistance [1,2]. In particular, ultrafine hexagonal barium ferrites ($BaFe_{12}O_{19}$) are widely used in magnetic recording media and microwave devices due to large saturation magnetization (Ms) and high anisotropy field [3]. The crystal structure of $BaFe_{12}O_{19}$ is magnetoplumbite with space group $P6_3/mmc$. The magnetoplumbite unit cell dwells in a total of 10 layers, with hexagonal symmetry of structure.

Different chemical methods, including co-precipitation, sol–gel, glass crystallization, hydrothermal, solvothermal and micro-emulsion were developed for the synthesis of hexaferrites [4−9]. It is good to know that properties of nanostructures depend on their particle size and morphology [10-11]. Therefore, exploring appropriate methods to synthesize ferrites and controlling morphology and size of particles is significant. The sol-gel auto-combustion route is a versatile technique that possesses the advantages of chemical homogeneity, easy components adjustment, high purity of product and low cost [12]. According to the literature, there are very few reports the influence of high doping content of zirconium on structural, morphological and magnetic properties of barium hexaferrite nanoparticles. In this present work, $BaZr_xFe_{12-x}O_{19}$ (x=1) nanoparticles were synthesized by sol-gel auto combustion method and their crystalline structure was confirmed by x-ray diffraction (XRD). Moreover, the synthesized sample was characterized by FTIR spectroscopy for confirmation of vibration bands at the surface of $BaZrFe_{11}O_{19}$ NPs. The morphology and particle size were estimated by TEM analysis. The magnetic properties were measured at room temperature under a magnetic field of +15 KOe by using vibrating sample magnetometer.

2. Experimental

2.1 Materials and method

Zirconium doped barium hexaferrite ($Ba_{1-x}Zr_xFe_{12-x}O_{19}$ with x=1) nanoparticles were synthesized by sol–gel auto-combustion method as follows: The starting precursors $Fe(NO_3)_3 \cdot 9H_2O$, $Ba(NO_3)_2$ and $Zr(NO_3)_4 \cdot 5H_2O$ with a stoichiometric amount of metal nitrates were dissolved in double-distilled water by stirring. The temperature was increased to 70^{o}C and then citric acid was subsequently added to the solution (molar ratio of total metal ions and citric acid in the solution is 1:1) and the resulting mixture was stirred for 30 min. Then, the pH was adjusted to about 7 by adding ammonia solution. Aqueous suspensions were stirred and heated for several hours at 80^{o}C until a highly viscous gel was produced. In the final step of the sol–gel auto combustion process, the obtained gel is allowed to burn via auto-combustion reaction and then was dried at 250^{o}C for 2 h. Finally, the burnt product which has a tree-like structure (Fig. 1) was grounded and annealed at 950^{o}C for 5h in a temperature programmed furnace to convert it into pure hexagonal phase. Eventually, the material was allowed to cool naturally to room temperature.

Fig.1: Tree-like structure (dendritic stucture) of barium hexaferrite after auto-combustion and before any annealing treatment.

2.2 Characterization

X-ray diffraction measurements (XRD) were characterized using Rigaku D/Max—IIIC with Cu Kα radiation in the 2Θ range of 20–70°. Fourier transform infrared (FT-IR, Bruker) spectra were recorded on a spectrometer with a diamond ATR in the range of 400 - 4000 cm^{-1} in order to confirm the formation of M-type hexaferrite metal-oxygen bond. Raman spectra were recorded using a micro-Raman spectrometer (Witech CRM200, the excitation wavelength at 532 nm). The surface morphology of the samples and selected area electron diffraction (SAED) patterns were performed using a transmission electron microscope (TEM, JEOL JSM-6490). Magnetization measurements were performed using a vibrating sample magnetometer (VSM) with a maximum applied magnetic field of 15 kOe.

3. Results and Discussion

3.1 XRD analysis

The XRD patterns of $BaZrFe_{11}O_{19}$ nanoparticles are shown in Figure 2. The main diffraction peaks of barium ferrite were observed at 2θ values of 30.46° (d = 2.84 Å), 32.31° (d = 2.69 Å), 34.25° (d = 2.54 Å), 35.45° (d = 2.54), 37.45° (d = 2.35 Å), 40.45° (d = 2.18 Å), 42.56° (d = 2.07 Å), 55.21° (d = 1.63 Å), 56.64° (d = 1.59 Å) and 63.22° (d = 1.45 Å),67.58° (d = 1.33 Å) and 72.71° (d = 1.26 Å) corresponding to the (110), (107), (114), (200), (203), (205), (206), (217), (2011), (220), (2014) and (317) reflections. The patterns have been indexed to hexagonal crystal system pertaining to the space group P63/mmc (No. 194), which confirms that the phase belongs to the magnetoplumbite crystal structure. The nanoparticle shows all the diffraction peaks that are consistent with the standard patterns (JCPDS no. 39-1433) with no observable secondary phase such as α-Fe_2O_3. The crystallite size can be calculated by using the Debye–Scherrer formula:

$$D = \frac{K\lambda}{\beta \cos\theta} \quad (1)$$

where D is the average crystallite size of nanoparticles, k is the shape factor, λ is the X-ray wavelength, β is the full width at half maximum, θ is the diffraction angle of Bragg and k is often assigned a value of 0.89, which depends on several factors, including the Miller index of the reflecting plane and the shape of the crystal. The (114) reflection of the observed X-ray data was chosen for calculating the crystallite size of $BaZrFe_{11}O_{19}$ nanoparticles. The average size of the $BaZrFe_{11}O_{19}$ nanoparticles was calculated using the above mentioned equation and estimated as 47.67 nm.

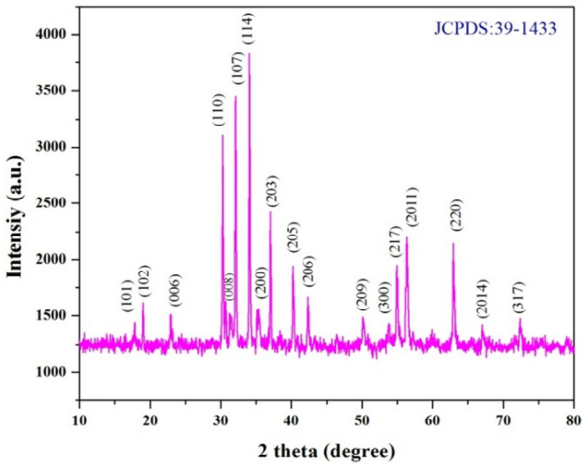

Fig.2: XRD pattern of Zr substituted Barium hexaferrite ($BaZrFe_{11}O_{19}$) nanoparticles

In Williamson-Hall (W-H) relation the strain was assumed to be uniform in all crystallographic direction, β_{hkl} is given by

$$\beta_{hkl} = \left(\frac{K\lambda}{D\cos\theta}\right) + 4\varepsilon\tan\theta \quad (3)$$

Rearranging Eqn. (10) gives

$$\beta_{hkl}\cos\theta = \left(\frac{K\lambda}{D}\right) + 4\varepsilon\sin\theta \quad (4)$$

Here D and ε corresponds to the crystallite size value and dimension value (microstrain) respectively. By plotting $\beta_{hkl}\cos\theta$ as a function of 4sinθ, the average crystallite size and strain can be estimated from the extrapolation and the slop of the fitted line [13]; see fig 3.

The lattice constants, a and c, were calculated using published Miller indices (h, k and l) of the reflections and their measured positions according to the following equation:

$$\frac{1}{d_{hkl}^2} = \frac{4}{3}\left(\frac{h^2+hk+k^2}{a^2}\right) + \frac{l^2}{c^2} \quad (5)$$

The XRD data were used to estimate the unit cell volume (V) and the X- ray density (ρ_x) of the samples. The following relations were used for obtaining the values of the parameters listed in Table 1.

$$V = \frac{\sqrt{3}}{2}a^2c \quad (6)$$

$$\rho_x = \frac{2M}{NV} \quad (7)$$

where M is the molar mass of the sample; N is the Avogadro's number. The lattice constants and cell volume are increasing with Zr^{4+} content. It is known that the ionic radii of Zr^{4+}, Fe^{3+} and Ba^{2+} ions are 0.72 Å, 0.645 Å and 1.49 Å, respectively [14,15]. There is a general agreement that Zr^{4+} ions probably substitute for Fe^{3+} ions in barium ferrites because the radius difference between Zr^{4+} and Fe^{3+} is less than 15%, whereas the difference between Zr^{4+} and Ba^{2+} is a bit larger [14,16]. As a result, the lattice parameters and cell volumes increased due to the substitution of larger Zr^{4+} ions in barium ferrite. It implies that the Zr^{4+} ions substitute for Fe^{3+} ions in the barium ferrites.

.

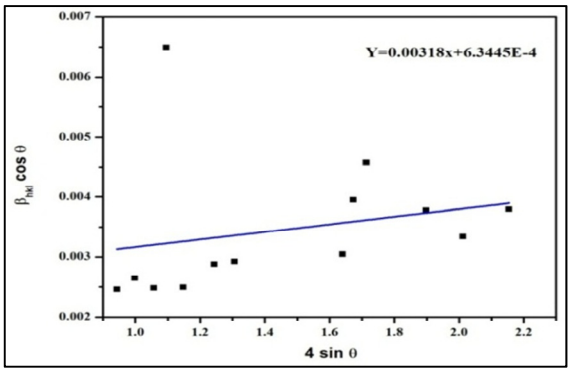

Fig. 3: W-H Plot of $BaZrFe_{11}O_{19}$ nanoparticles

Table 1: Geometric parameters obtained from XRD results

Sample	Crystallite size D (nm)		Strain (ε)	Lattice parameters (Å)		Cell Volume(V) ($Å^3$)	c/a	ρ_x (g/cm^3)
	Scherrer method	W-H method		a	c			
$BaZrFe_{11}O_{19}$	47.67	45.53	0.00036	5.89	23.23	697.71	3.94	5.27

3.2 FT-IR Analysis:

The FTIR spectrum investigation is used to derive information about the nature of bonding in a compound. The peaks are mainly dependent on the structure of the crystal and chemical mixing ratio of the prepared materials. The FT-IR spectra of samples were recorded in the range of 400-4000 cm^{-1} wave numbers. Fig.4 spectrum of the sample indicates the absorption bands at around 561cm^{-1},532cm^{-1} and 424cm^{-1} can be attributed to metal-Oxygen stretching vibration. The pure barium hexaferrite ($BaFe_{12}O_{19}$) with absorption bands at around 566 cm^{-1},537cm^{-1} and 426 cm^{-1} can be attributed to metal-oxygen stretching vibration. From these results, there are lower shifts in wavenumbers for Zr substitution in barium ferrite due to Zr^{4+} ions having higher atomic weight than Fe^{3+} ions. For $BaZrFe_{11}O_{19}$, the transmittance percentage decreases 1.81% from the pure $BaFe_{12}O_{19}$ system. The very weak absorption bands seen at 2975 cm^{-1} region are due to O-H stretching band of H_2O for pure $BaFe_{12}O_{19}$ respectively. In more details the peaks in the range 420-445cm^{-1} illustrate vibrations of octahedral bonds and others two peaks corresponds to tetrahedral bonds [17,18].

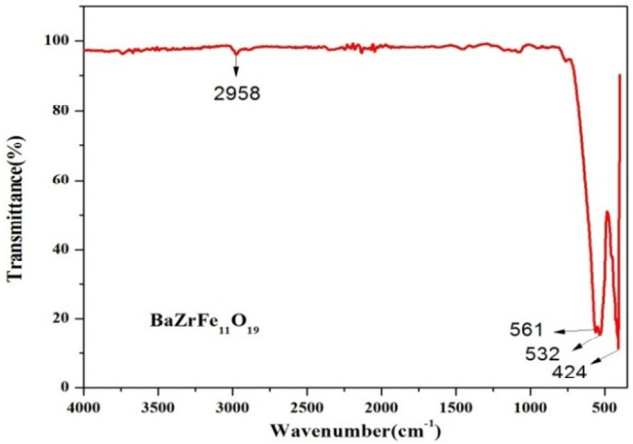

Fig.4: FT-IR spectra of $BaZrFe_{11}O_{19}$ nanoparticles

3.3 Raman spectroscopy Analysis:

Raman spectroscopy has been used to show the nature of bond and bond strength of the Zr substituted $BaFe_{12}O_{19}$ system. From the literature, it is reported that 42 Raman-active modes ($11A_{1g} + 14E_{1g} + 17E_{2g}$) and 30 IR active modes ($13A_{2u} + 17E_{1u}$) are expected for the barium hexaferrite system. All the obtained Raman spectra show a marked polarization effect, which indicates a good orientation and a good crystalline quality of all the prepared compounds. $BaZrFe_{11}O_{19}$ showing sharp intense peaks which reveal defect free environment. The strong peaks observed at about 717, 687, 619, 526, 468, 415, 382,339, 286, 213, 183 and 173 cm^{-1} are in good agreement with the magnetoplumbite structure. The peaks at 717 and 687 cm^{-1} can be assigned to A_{1g} vibrations of Fe-O bonds at the tetrahedral 4f1 and bipyramidal 2b sites, respectively. Other peaks at 619, 526, and 468 cm^{-1} are due to A_{1g} vibrations of Fe-O bonds at the octahedral 4f2, 2a, and 12k sites, whereas peak at 415 cm^{-1} is due to A_{1g} vibration at the octahedral 12k dominated site. The peaks at 286 and 213 cm^{-1} were due to E_{1g} vibrations, while the peak at 339 cm^{-1} was due to E_{2g} vibration. The peak at 184 and 173 cm^{-1} resulted from E_{1g} vibrations of the whole spinel block. Raman spectra for the corresponding lattice symmetries are shown Figure 5.

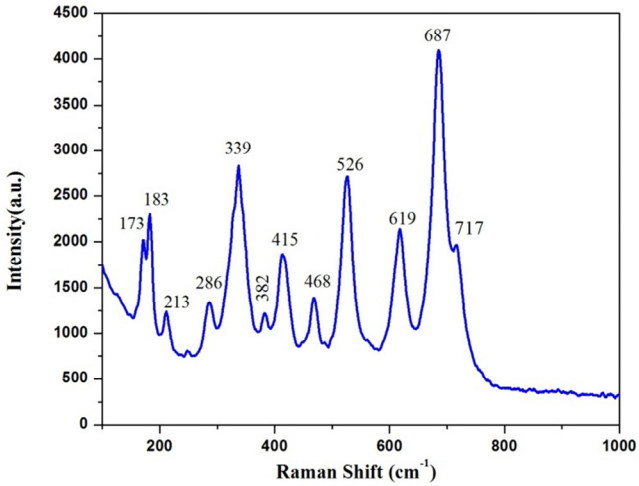

Fig.5: Raman spectra of $BaZrFe_{11}O_{19}$ nanoparticles

3.4 TEM Analysis:

Fig. 6 shows the TEM and HRTEM images of the Zr doped barium hexaferrite ($BaZrFe_{11}O_{19}$) nanostructures. This figure shows formation of $BaZrFe_{11}O_{19}$ with rod-like particles. The selected area electron diffraction (SAED) patterns are corresponding to rod-like nanostructures shown in Fig. 7. It can be well indexed with magnetoplumbite hexagonal structure using the SAED patterns, which is consistent with the results of XRD.

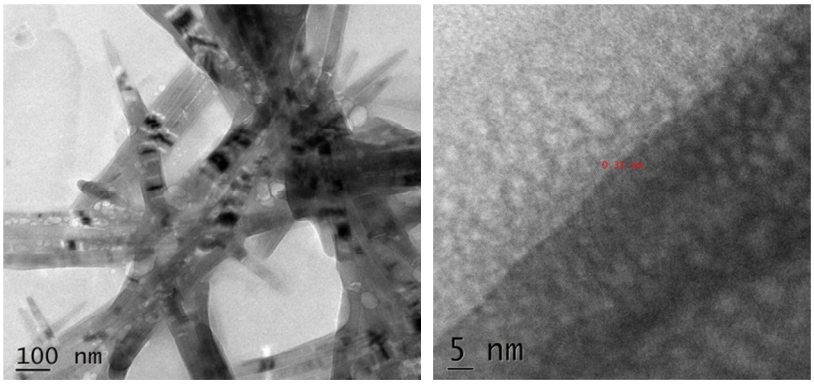

Fig.6: TEM and HRTEM(right) images of $BaZrFe_{11}O_{19}$ rod-like nanoparticles

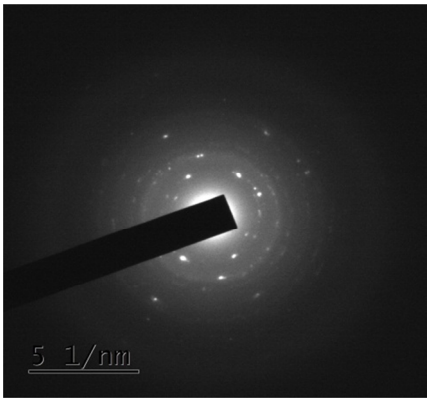

Fig. 7: SAED pattern of $BaZrFe_{11}O_{19}$ nanoparticles

3.4 Vibrating Sample Magnetometer (VSM) analysis:

The magnetic properties were analyzed using VSM at room temperature with an applied magnetic field of 15 kOe. The M-H hysteresis loop of $BaZrFe_{11}O_{19}$ has shown in Fig. 8. Various magnetic parameters, i.e. saturation magnetization (M_s), remanence (M_r), square ratio (M_r/M_s) and coercivity are calculated from the hysteresis loop. It is observed that $BaZrFe_{11}O_{19}$ had a high remanent magnetization (Mr) value of 36.95 emu/g, a high saturation magnetization (Ms) value of 68.48 emu/g and a coercive force (Hc) value of 2.615 kOe.

There are five types of Fe^{3+} ions sites in barium ferrite, which are named as 2a, 2b, 12k, 4f1 and 4f2. The 2a, 12k and 4f2 are octahedral sites, 4f1 is a tetrahedral site and 2b is a bipyramid site (pseudo-tetrahedral site) [19]. It has been confirmed by reported Mossbauer studies that Zr^{4+} prefers to occupy the tetrahedral sites 2b and 4f1, and the distribution of Zr^{4+} at the 2b and 4f1 sites varies with changing Zr^{4+} content [20]. M_s will be influenced by doping Zr^{4+} ions in the ferrites. It is reported that the Fe^{3+} ions at the 2a, 2b and 12k sites are up-spin and the 4f1 and 4f2 sites are down-spin. In this case, the net magnetization of the ferrites is contributed from the excess of up-spin magnetic moments [21]. So that, if Fe^{3+} ions at 12k, 2a, and 2b sites are substituted by non-magnetic Zr^{4+} ions, magnetization will decrease. On the other hand, if Fe^{3+} ions at 4f1 and 4f2 sites are substituted, magnetization will be increase. As we discussed above, Zr^{4+} prefers to occupy 2b and 4f1 sites in barium hexaferrite. In our results M_s increases from 64.85 to 68.48 emu/g in the ferrite with x = 1, which indicates that the preferred occupation of the Zr^{4+} ions is at the 4f1 site.

Table 2: Comparison of various ions doped in barium hexaferrites with their Ms, Mr, and Hc values

Samples	Ionic radii of dopant (Å)	Ms (emu/g)	Mr (emu/g)	Mr/Ms (Oe)	Hc	Ref
$BaFe_{12}O_{19}$	---	61.84	33.95	0.543	2410	25
$BaAlFe_{11}O_{19}$	0.57	56.96	28.26	0.496	7.279	23
$BaCoFe_{11}O_{19}$	0.67	60	26.42	0.440	1.134	24
$BaMnFe_{11}O_{19}$	0.70	51.68	28.45	0.550	4.310	25
$BaBiFe_{11}O_{19}$	0.96	47.72	25.43	0.532	4.810	25
$BaZrFe_{11}O_{19}$	0.72	68.48	36.95	0.539	2.615	(This work)

The squareness ratio (M_r/M_s) is calculated from magnetic data as 0.539. It has been reported that the squareness ratio at or above 0.5 indicates that the material is in single domain and below 0.5 can be indicated to the multi domain structure [22]. In the present study the squareness ratio is found to be 0.539, indicating that the sample is in single magnetic domain.

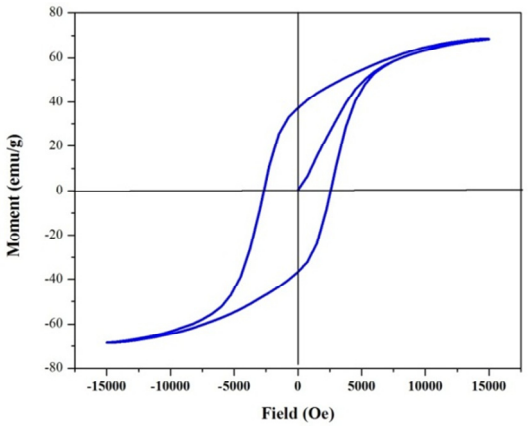

Fig.8: Hysterisis loop of Zr substituted Barium hexaferrite ($BaZrFe_{11}O_{19}$) nanoparticles

4. Conclusion

Nanostructured single phase Zr substituted Barium hexaferrite ($BaZrFe_{11}O_{19}$) nanoparticles have been successfully prepared by simple and economical sol-gel auto combustion method using citric acid as chelating agent. The XRD confirm the single M-type hexaferrite phase for the sample and crystallite size has calculated as 47.67 nm. The FT-IR spectra of calcined samples showed three absorption peaks at bands 424, 532 and 561 cm^{-1} which confirms the presence of metal oxygen stretching bands in ferrites. The rods-like shape revealed for as-prepared nanoparticles by transmission electron microscopy (TEM). The saturation magnetization (Ms), remanent magnetization (Mr) and coercivity (Hc) of the samples were measured at room temperature with 68.48 emu/g, 36.95 emu/g, and 2.615 kOe respectively.

Acknowledgements

The Authors are thankful to STIC, Cochin University for TEM analysis and Department of Chemistry, IITM, Chennai for XRD and VSM analysis.

References

1. I.Auwal, A. Baykal, H. Güngünes, S.E. Shirsath, Ceram. Int. 42 (2016) 3380-3387.
2. I.Auwal, S. Güner, H. Güngünes¸, A. Baykal, Ceram. Int. 42 (2016) 12995-13003.
3. B.Peng, Y. Wang, W. Zhang, W. Zhang and K. Tan, Mod. Phys. Lett. B 26 (2012) 1250168.
4. M.L. Wang, Z.W. Shih, J. Crystal Growth, 114 (1991) 435−445.
5. A.Baykal, J. Supercond. Nov. Magn. 27 (2014) 877−880.
6. H.M. Khan, M.U. Islam, Y. Xu, M. Asif Iqbal, I. Ali, J. Alloys Compd. 589 (2014) 258−262.
7. K. Haneda, C. Miyakawa, H. Kojima, J. Am. Ceram. Soc. 57 (1974) 354−357.
8. H. Sözeri, A. Baykal, B. Ünal, Physica Status Solidi A: Appl. Mater. Sci. 209 (2012) 2002−2013.
9. N.J. Shirtcliffe, S. Thompson, E.S. O'Keefe, S. Appleton, C.C. Perry, Mater. Res Bull. 42 (2007) 281−287.
10. M. Jafari, M. Salavati-Niasari, A. Sobhani, Micro & Nano Lett. 8 (2013) 508−511.
11. A.Sobhani, M. Salavati-Niasari, Superlattices Microstruct. 65 (2014) 79−90.
12. A. Persis Amaliya, S.Anand, S.Pauline, Journal of Magnetism and Magnetic Materials, 467(2018) 14-28.
13. S. Anand, A. Persis Amaliya, M. Asisi Janifer and S. Pauline, Modern Electronic Materials, 3 (2017) 168–173.
14. M. V. Rane, D. Bahadur, S. D. Kulkarni and S. K. Date, J. Magn. Magn. Mater., 1999, 195, 256.
15. C. D. Ling, M. Avdeev, V. V. Kharton, A. A. Yaremchenko, R. B. Macquart and M. Hoelzel, Chem. Mater., 2010, 22, 532.
16. S. Kanagesan, S. Jesurani, R. Velmurugan and T. Kalaivani, J. Mater. Sci.: Mater. Electron., 2012, 23, 952.
17. S.Singhal, T. Namgyal, S. Bansal, K. Chandra, J. Electromagn. Anal. Appl. 2 (2010) 376–381.
18. A.Pradeep, G. Chandrasekaran, Mater. Lett. 60 (2006) 371–374.
19. J. G. Jia, C. Y. Liu, N. Ma, G. R. Han, W. J. Weng and P. Y. Du, Sci. Technol. Adv. Mater., 2013, 14, 045002.
20. M. V. Rane, D. Bahadur, A. K. Nigam and C. M. Srivastava, J. Magn. Magn. Mater., 1999, 192, 288.
21. W. C. Li, X. J. Qiao, M. Y. Li, T. Liu and H. X. Peng, Mater. Res. Bull., 2013, 48, 4449.
22. C. Sudakar, G.N. Subbanna, T.R.N. Kutty, J. Magn. Magn. Mater. 263 (2003) 253–268.
23. Danfeng Wang, Jianzheng Cheng, Chunlong Fei, J Supercond Nov. Magn. 29 (2016) 2327–2331.
24. Isa Araz1, Fazilet Genc, J Supercond. Nov. Magn., DOI 10.1007/s10948-017-4216-0.
25. ayssir Ben Ghzaiel, Wadia Dhaoui, Frédéric Schoenstein, Philippe Talbot, Frédéric Mazaleyrat, Journal of Alloys and Compounds, 692 (2017),774-786.

Available online at www.sciencedirect.com

ScienceDirect

Materials Today: Proceedings 8 (2019) 427–434

materialstoday: PROCEEDINGS

www.materialstoday.com/proceedings

ICMEE 2018

Systematic Investigation and Applications of an Efficient NLO Crystal: Glycine Lithium Sulphate

A Shiny Febena[a], M Victor Antony Raj[a,b], J Madhavan[a,*]

[a]*Department of Physics, Loyola College, Chennai -34. jmadhavang@yahoo.com*
[b]*Loyola Institute of Frontier Energy (LIFE), Loyola College, Chennai-34.*

Abstract

Glycine Lithium Sulphate (GLS), a non-centrosymmetric semi organic NLO single crystals were grown from aqueous solution with dimension of 10 x 11 x 12 mm^3 by slow evaporation technique at room temperature using water as the suitable solvent. Crystalline phase and information on unit cell measurements of the grown Glycine Lithium Sulphate single crystal have been identified by using X-ray powder diffraction (PXRD) study with CuKα radiation. FT-IR spectra of the nonlinear optical material Glycine Lithium Sulphate crystal have been recorded and analyzed. The crystalline perfection has been examined by using High Resolution X-ray diffractometer (HRXRD) technique and found that the specimen quality is good. Optimization of the title compound is done using the Gaussian 09 software with B3LYP using 6-31 G (d, p) as basis set. From the HOMO-LUMO and hyperpolarizability analysis, the stability and the occurrence of strong intermolecular hydrogen bonding in the molecule is confirmed. Nonlinear optical absorption of the title compound has been studied at 633 nm using single laser pulses, using Z-scan technique. It is found that the GLS molecule is a potential candidate for optical limiting applications and optoelectronic device fabrications.

Selection and peer-review under responsibility of the scientific committee of the Materials For Energy and Environment.

Keywords: PXRD; FT-IR; HRXRD; DFT; HOMO-LUMO; Z-Scan

* Corresponding author. Phone: +91-9840479638 ; Fax: +91-44-28175566

E-mail address: jmadhavang@yahoo.com

Selection and peer-review under responsibility of the scientific committee of the Materials For Energy and Environment.

1. Introduction

Materials possessing outstanding nonlinear optical (NLO) properties are necessary in several arenas of photonic device applications such as (i) optical data storage, (ii) optical information processing, (iii) harmonic generators, (iv) optical switching, (v) optical communication, and (vi) optical limiting. These applications require materials with appropriately large and fast second-order NLO responses. Over the past few decades, Amino acids have fascinated increasing attention and it offers the researchers a wide range of structural features to observe and to attempt to rationalize using simple bonding models. Most of the structures have been minimized by using Gaussian software with 6-31G (d, p) as basis set [1–3]. In recent years, organic and inorganic molecules are combined together and significantly their lattice parameters are altered. Semi organic materials of large size possessing second order nonlinearities, short transparency cutoff wavelengths, stable physico-thermal performance, good optical transparency, mechanical properties, large polarizability and wide transmission window are achieved by the hybrid compounds. Amino acids and their complexes are categorized under the family of organic materials that have applications in NLO [4–7].

In our present work, Glycine and Lithium Sulphate components are chosen as starting materials. Glycine Lithium Sulphate amino acid based single crystal has been harvested after a period of 45 days with dimensions 10x11x12 mm^3. Based on various characterization studies the results are reported. Both experimental and theoretical studies have been carried out.

2. Experimental Details

2.1 Material Synthesis

Glycine and Lithium Sulphate was taken in 1:1 molar ratio. The required amount of starting materials for the synthesis was calculated from the following reaction:

$$\mathbf{C_2H_5NO_2 + Li_2SO_4 \longrightarrow (Li_2SO_4)\,(C_2H_5HNO_2)}$$

The evaporation of the solution yielded GLS crystals. The purified GLS was finely powdered and was used for solubility study. The variation of solubility of GLS with temperature in double distilled water is shown in Fig.1. The crystal reached a maximum size of 10 x 11 x 12 mm^3 in 30 days. The as grown crystal of GLS is shown in Fig.2.

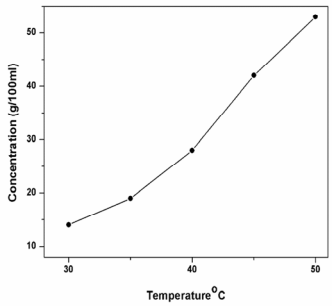

Fig.1. Solubility Curve

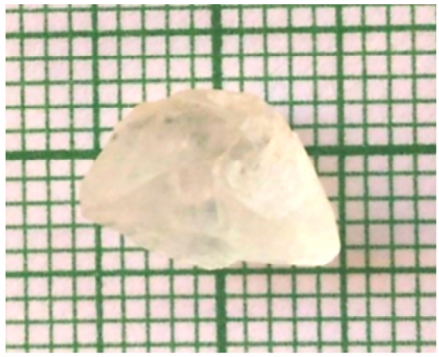

Fig.2. Photograph of as grown crystal

3. Results and Discussion

3.1. *Powder X-Ray Diffraction Analysis*

To test the crystallinity of the sample, Powder X-Ray Diffraction patterns were obtained at room temperature using a Rich-Seifert powder X-ray diffractometer with CuKα radiation (λ = 1.5418 Å) was used at a scan speed of 0.02°/s. The prominent well resolved Bragg's peak at specific 2θ angle reveals the high perfection of the crystals. The recorded powder XRD pattern and the simulated pattern are shown in Fig.3 and Fig.4. The crystal data are given in Table 1. The reflections in the powder XRD patterns were indexed and compared with the theoretically.

3.2. High-Resolution X-Ray Diffraction

High-Resolution X-Ray Diffraction can give the structural information i.e. about the composition, thickness and the super lattice period of the crystal. Fig.5 shows the diffraction curve of the plane (1 1 2) recorded for the grown title compound using HRXRD technique by using the multi crystal X-ray diffractometer with MoKα1 radiation. The grown crystal is inferred to be free from structural grain boundaries by the presence of single sharp peak. The full width at half maximum (FWHM) of the curve is 55 arcs. The low value of half width shows that the crystalline quality of the specimen is quite good. Vacancy and interstitial type of defects are found in the crystal with considerable density is known by the presence of broadness associated with good scattered intensity along the arms of the diffraction curve [8,9].

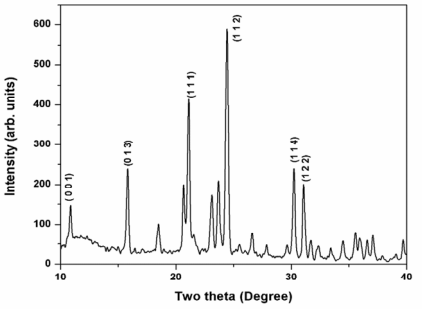

Fig.3. Powder XRD spectrum

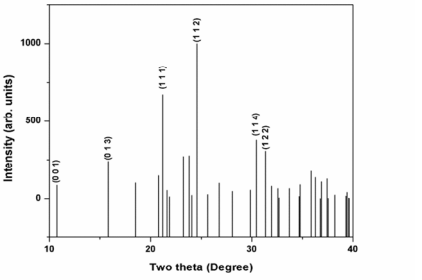

Fig.4. Theoretically simulated powder XRD pattern

Table 1 : Crystal Parameters

Empirical Formula	$C_2 H_5 Li_2 N O_6 S$	
Formula weight	185.01	
Crystal system, Space group	Orthorhombic $Pca2_1$	
Unit cell dimensions	a = 16.443 Å b = 5.105 Å c = 7.753 Å	α= β =γ=90°
Cell volume	650.799 $Å^3$	

3.3. Computational Details

The first assignment of the computational work is to define the optimized geometry. Since the density function results are more reliable than Hatree-Fock calculations, the calculations in the present work are dealt with Quantum chemical density functional theory (DFT) using the Gaussian 09 version [10]. From the calculated vibrational frequencies, the minimum true energy of the title compound was revealed by the deficiency of imaginary values. The above is obtained by allowing all the parameters to relax and hence the calculations converged to an optimized geometry. Finally, the optimizations were carried out at the same level by employing DFT-B3LYP hybrid functional and 6-31G (d, p) basis set.

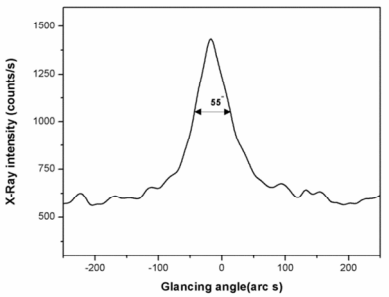

Fig.5. HRXRD spectrum

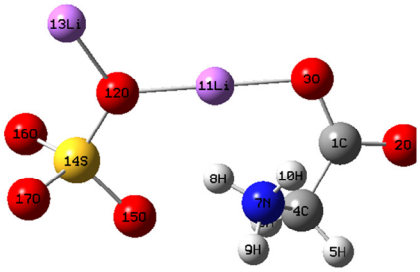

Fig.6. Atomic numbering system of GLS

3.4. Moleculare geometry

The optimized molecular structure of GLS is obtained by using the DFT calculations and the atom numbering scheme is shown in Fig.6. Good approximation results obtained from the optimized geometrical parameters it can be used as a base to calculate other parameters and properties of the grown crystal. Due to the intermolecular interactions in the crystalline state, there are slight deviations in theoretical parameters of optimized geometry from the experimentally obtained values.

3.5. Vibrational Assignments

The vibrational spectral analysis of GLS crystal is performed on the basis of the characteristic vibrations of several functional groups such as nitro group, carbonyl group and imine group vibrations. The observed FT-IR is shown in Fig.7. The GLS molecule has 17 moieties and is in stable conformation.

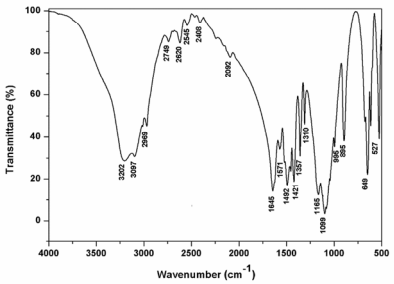

Fig.7. FT-IR Spectrum

3.5.1 Nitrogroup vibrations

The symmetrical and asymmetrical stretching modes of the nitro group absorption result in strong bands in 1370 – 1320 cm-1 and 1570–1485 cm-1 region, respectively [11]. The theoretical asymmetric stretching vibrations occur at 1503 cm-1 and the corresponding experimental peak at 1571 cm-1.

3.5.2 C=O vibrations

In amino acids, the C=O stretching mode of the carboxyl group occurs around 1690±30 cm-1. The C=O in-plane deformation is expected in the region 645±55 cm-1. The C=O out-of-plane deformation is in the range 540±80 cm-1. The theoretical stretching vibration appears at 1679 cm-1 and the in-plane deformation at 653 cm-1 (theoretical) and 649 cm-1 (experimental). The theoretically computed (scaled) frequencies for C=O vibrations by B3LYP/6-31G (d,p) method shows excellent agreement with recorded spectrum.

3.5.3 C=N vibrations

IR spectrum exhibits strong and broad bands due to C=N at 1635 cm-1. In the present work the theoretical and experimental strong and broad bands due to C=N appears at 1626 cm-1 and 1645 cm-1 respectively [12]. The selected vibrational assignments of fundamental modes of GLS by DFT methods are reported in Table 2.

HOMO LUMO Energy Gap

HOMO-LUMO energy gap provides qualitative indication of the molecular excitations and charge transfer interactions that play an essential role in NLO response. Using the DFT method at the B3LYP with 6-31G (d, p) as basis set the HOMO–LUMO energy gap in the crystal was simulated.

Table 2: selected vibrational assignments of fundamental modes of GLS by DFT methods\

No.	Frequency cm^{-1}		Spectroscopic assignment	Force constant	Reduced mass
	B3LYP	Expt.			
1.	520.3388	527	COO^- d	1.8572	11.6421
2.	653.1643	649	COO^- roc ipd	1.7693	7.0388
3.	897.9603	895	CC st	2.4910	5.2433
4.	970.3730	995	CN st	0.9178	1.6543
5.	1050.167	1099	I Ph	2.1834	3.3602
6.	1183.694	1165	CH_2 roc	1.3022	1.5774
7.	1449.395	1492	COO^- sym st	1.4858	1.2004
8.	1503.990	1571	NH_3^+ sym d	1.7639	1.3236
9.	1626.886	1645	NH_3^+ asy d	1.6559	1.0619
10.	1679.372	1675	C=O st	1.9105	1.1498

The calculated energies of HOMO and LUMO are -0.157 a.u and -0.336 a.u respectively and the energy gap of GLS is found to be 0.179 a.u.

HOMO energy (B3LYP) = -0.157 a.u.
LUMO energy (B3LYP) = -0.336 a.u.
HOMO–LUMO energy gap (B3LYP) = 0.179 a.u.

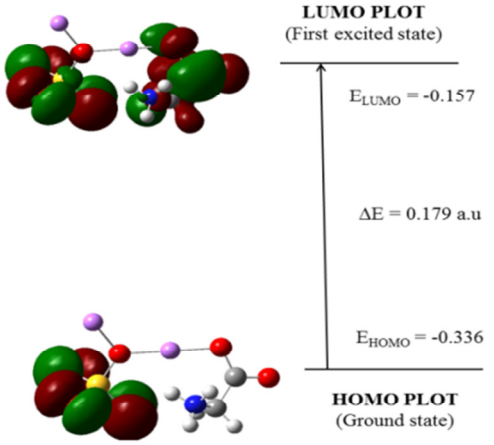

Fig.8. HOMO – LUMO plot of GLS

3.7. Optical absorption spectrum

Fig.9 shows UV–Vis spectrum of GLS crystal of thickness 2 mm. The wavelength increases with a decrease of absorbance at a slow rate till it reaches 260nm after which it gets almost saturated. Thus UV cut off wavelength for the grown crystal is 260 nm. It is clearly indicated that there is no absorbance is due to electronic transitions. Fig.10 shows the calculated band gap energy of GLS that is found to be 4.23 eV.

3.8. Thermogravimetric Analysis

Thermogravimetric analysis (TG–DTA) is a group of technique that measures the changes involved in physical, chemical and structural properties of the compound corresponding to the variations in temperature. The resulting TG–DTA trace of GLS is shown in Fig.11.

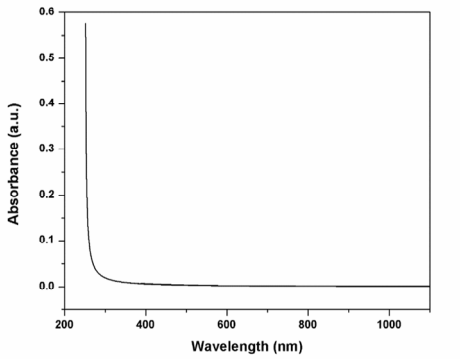

Fig.9. Optical absorption spectrum

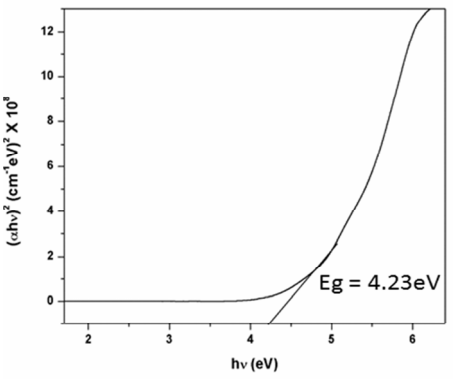

Fig.10. Optical band gap of GLS

The first significant decomposition stage of GLS was observed at 400°C and it was about 40.52% of mass loss of the compound and the next two amounts to 3.3% and 2.7% respectively. Similarly, a sharp endothermic peak observed at 310°C in DTA curve reveals the melting point of GLS. It also indicated the good degree of crystallinity. The residue of GLS left at 860°C was about 53.5%. The observed thermal stability of GLS is most useful for advanced optical applications.

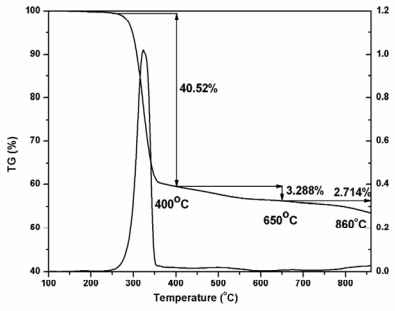

Fig.11. TGA and DTA curve of GLS crystal

3.9. Mechanical property

Materials should not only possess good optical performance but also good mechanical behavior for making them use in various applications. Vickers Hardness number was calculated for the applied loads varying from 5 to 25 g shown in Fig.12. Development of cracks at higher loads made the indentation restricted to a maximum load of 25 g. In order to find the value of 'n' a graph of log P against log d is plotted in Fig.13 which gives a straight line. From the slope of line Meyer's index number 'n' was calculated to be 0.8. The 'n' value calculated in the present studies is 0.8 suggesting that the grown GLS crystal belongs to category of hard material [13].

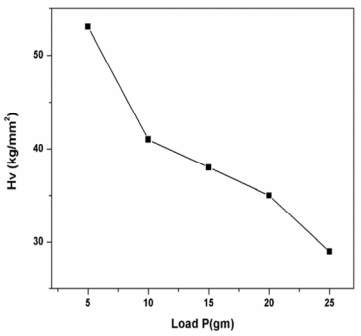

Fig.12. Variation of Vickers hardness number with load

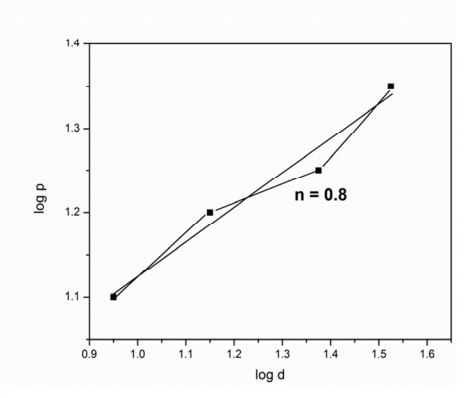

Fig.13. log p Vs log d of GLS single crystal

3.10 Z Scan studies

To determine the sign and magnitude of third-order nonlinear susceptibility of GLS the Z-scan technique was employed. Nonlinear refractive index n is proportional to the real part of third-order nonlinear susceptibility $\chi 3$ and the nonlinear absorption coefficient β relates to the imaginary part of $\chi 3$. Z-scan experiments were performed using

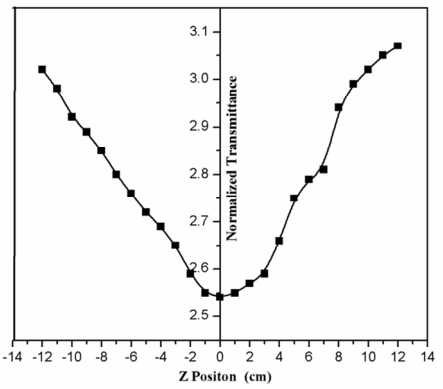

Fig.14. Z Scan of GLS – Open aperture

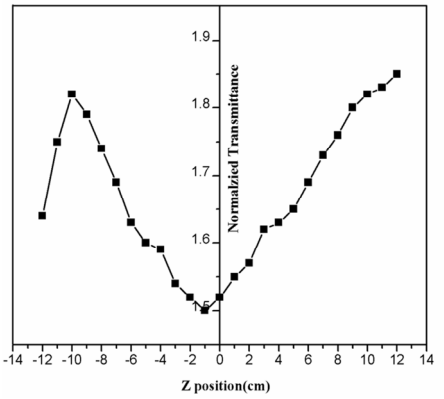

Fig.15. Z Scan of GLS – Closed aperture

He–Ne laser at 633 nm wavelength as an excitation source. The laser beam was focused to a spot size of 10 mm and the Rayleigh length Z of 6.71 mm. A 12 cm focal length lens was used with input power 23 mW and the resultant output power through the samples was recorded using a photo detector. Open aperture and closed aperture measurements were performed in order to determine the nonlinear absorption coefficient β of the GLS. The nonlinear absorption curves obtained for GLS are shown in Fig.14 and Fig.15.

4. Conclusion

Glycine Lithium Sulphate (GLS), noncentrosymmetric semi organic NLO single crystals were grown from aqueous solution, using water as the suitable solvent, by slow evaporation technique. GLS crystallizes in noncentrosymmetric structure. GLS is found to be a very good material for nonlinear optical applications since good optical transparency is observed at the wavelengths of sources that are commonly used in nonlinear optical devices. Optimized structure of the GLS molecule is computed using DFT (B3LYP) level with 6-31G (d, p) basis set. The material grown is found to possess good thermal and mechanical stability. Thus, GLS is a potential material for the fabrication of optoelectronic devices and may be used for the nonlinear optical applications involving frequency-doubling process.

Acknowledgements

The authors acknowledge University Grants Commission (UGC), India, for funding this research project-F.No.4-4/2015-16 (MRP/UGC-SERO).

References

[1] S. Senthil, S. Pari, R.J. Xavier, J. Madhavan, Linear and nonlinear optical properties of N-(3-nitrophenyl) acetamide single crystals, Opt. - Int. J. Light Electron Opt. 123 (2012) 104–108. doi:10.1016/j.ijleo.2011.03.007.

[2] M. Gulam Mohamed, K. Rajarajan, G. Mani, M. Vimalan, K. Prabha, J. Madhavan, P. Sagayaraj, Growth and characterization of 2-amino-5-chlorobenzophenone (2A-5CB) single crystals, J. Cryst. Growth. 300 (2007) 409–414. doi:10.1016/j.jcrysgro.2006.11.341.

[3] K. Ambujam, K. Rajarajan, S. Selvakumar, J. Madhavan, G. Mohamed, P. Sagayaraj, Growth and characterization of gel grown single crystals of bis-glycine hydrogen chloride (BGHC), Opt. Mater. (Amst). 29 (2007) 657–662. doi:10.1016/j.optmat.2005.11.008.

[4] S. Senthil, S. Pari, G.P. Joseph, P. Sagayaraj, J. Madhavan, Thermal, mechanical, electrical, linear and nonlinear optical properties of a nonlinear optical l-ornithine monohydrochloride single crystal, Phys. B Condens. Matter. 404 (2009) 2336–2339. doi:10.1016/j.physb.2009.04.053.

[5] P. Praveen Kumar, V. Manivannan, S. Tamilselvan, S. Senthil, V. Antony Raj, P. Sagayaraj, J. Madhavan, Growth and characterization of a pure and doped nonlinear optical l-histidine acetate single crystals, Opt. Commun. 281 (2008) 2989–2995. doi:10.1016/j.optcom.2008.01.058.

[6] G.P. Joseph, N. Melikechi, Jacob Philip, J. Madhavan, P. Sagayaraj, Studies on the electrical, linear and nonlinear optical properties of Manganese mercury thiocyanate bis-dimethyl sulfoxide, an efficient NLO crystal, Phys. B Condens. Matter. 404 (2009) 295–299. doi:10.1016/j.physb.2008.10.055.

[7] S. Senthil, S. Pari, P. Sagayaraj, J. Madhavan, Studies on the electrical, linear and nonlinear optical properties of Meta nitroaniline, an efficient NLO crystal, Phys. B Condens. Matter. 404 (2009) 1655–1660. doi:10.1016/j.physb.2009.01.042.

[8] V. Vasudevan, R. Ramesh Babu, G. Bhagavannarayana, K. Ramamurthi, Effect of metal and aminoacid dopants on the growth and properties of l-lysine monohydrochloride dihydrate single crystal, Mater. Chem. Phys. 124 (2010) 681–688. doi:10.1016/j.matchemphys.2010.07.033.

[9] P. Anandan, T. Saravanan, G. Parthipan, R.M. Kumar, G. Bhagavannarayana, G. Ravi, R. Jayavel, Crystal growth, structural and thermal studies of amino acids admixtured l-arginine phosphate monohydrate single crystals, Solid State Sci. 13 (2011) 915–922. doi:10.1016/j.solidstatesciences.2011.02.017.

[10] K.M. Al-Ahmary, M.M. Habeeb, A.H. Al-Obidan, Charge transfer complex between 2,3-diaminopyridine with chloranilic acid. Synthesis, characterization and DFT, TD-DFT computational studies, Spectrochim. Acta - Part A Mol. Biomol. Spectrosc. 196 (2018) 247–255. doi:10.1016/j.saa.2018.02.025.

[11] M. Shkir, S. Muhammad, S. AlFaify, A. Irfan, M.A. Khan, A.G. Al-Sehemi, I.S. Yahia, B. Singh, I. Bdikin, A comparative study of key properties of glycine glycinium picrate (GGP) and glycinium picrate (GP): A combined experimental and quantum chemical approach, J. Saudi Chem. Soc. 22 (2015) 352–362. doi:10.1016/j.jscs.2016.05.003.

[12] Ö. Alver, G. Dikmen, Structure analysis and spectroscopic characterization of 2-Fluoro-3-Methylpyridine-5-Boronic Acid with experimental (FT-IR, Raman, NMR and XRD) techniques and quantum chemical calculations, J. Mol. Struct. 1108 (2016) 103–111. doi:10.1016/j.molstruc.2015.11.041.

[13] S.A. Martin Britto Dhas, S. Natarajan, Growth and characterization of a new organic NLO material: Glycine nitrate, Opt. Commun. 278 (2007) 434–438. doi:10.1016/j.optcom.2007.06.052.

Available online at www.sciencedirect.com

ScienceDirect

Materials Today: Proceedings 8 (2019) 310–314

materialstoday: PROCEEDINGS

www.materialstoday.com/proceedings

ICMEE 2018

Enhanced magnetic Properties of $MgFe_2O_4$ nanoparticles

R. C. Sripriya [1, 2], Mahendiran M[1, 2]*, J.Madahavan[1] and M. Victor Antony Raj[1,2]

[1]*Department of Physics, Loyola College, Chennai, India.*
[2]Loyola Institute of Frontier Energy (LIFE), Loyola College, Chennai, India.

Abstract

Recently, magnetic semiconductor nanoparticles have been widely studied in nanoscience and nanotechnology, because of their important applications in magneto-optic materials, photocatalysts, sensors and magnetic drug delivery. From the various magnetic materials, spinel ferrites have become an important material in various interdisciplinary areas. Spinel $MgFe_2O_4$ nanoparticles were synthesized by a simple, economical microwave supported method (MSM) using glycine as the fuel. The structural, vibrational, optical and magnetic properties of the products were determined. The optical band gap (E_g) was measured using Kubelka-Munk model and it shows a value of 1.91 eV. The effect of $MgFe_2O_4$ nanoparticles as photocatalyst on the degradation of methylene blue (MB) was also investigated. It was observed that the sample showed better photo-catalytic degradation efficiency of MB due to the smaller particle size and higher surface area. The above spinel ferrite catalysts are magnetically separable by external magnetic field and can be reusable without change of its activity.

Selection and peer-review under responsibility of the scientific committee of the Materials For Energy and Environment.

Keywords: Nanostructures; Spinel $MgFe_2O_4$; Microwave irradiation

* Corresponding author. Phone: +91-44-28178200 ; Fax: +91-44-28175566
E-mail address: mahe7676@gmail.com

Selection and peer-review under responsibility of the scientific committee of the Materials For Energy and Environment.

1. Introduction

Nanotechnology is the science and engineering of making materials, functional structures and devices in nanometer scale. Nanotechnology has become a very active and vital research topic which is rapidly developing in industrial sectors and spreading to almost every field of science and engineering. Several major research and development programs on nanostructured materials and nanotechnology have been launched by governments worldwide. The field of research has become an area of great scientific and commercial interest because of its rapid expansion to academic institutes, laboratories and industries. Nanomaterials have extremely small size is which having at least one dimensions, two dimensions or three dimensions. They can exist in single, fused, aggregated or agglomerated forms with spherical, tubular, and irregular shapes. Common types of nanomaterials include nanotubes, dendrimers, quantum dots, and fullerenes. Nanomaterials have applications in the field of nanotechnology, and displays different physical and chemical characteristics from normal chemicals. Spinel $MgFe_2O_4$ nanoparticles have been used as a photocatalyst, due to its stability, photochemical stability and also reused several recycles. The photocatalytic action of the ceramic nano materials depends on the surface area and its grain size. Furthermore, spinel $MgFe_2O_4$ nano-catalyst is cost-effectively and eco-friendly viable solid heterogeneous catalyst. The effect of synthesis method on structural, optical, morphological, magnetic property and photocatalytic activity of spinel $MgFe_2O_4$ nano-catalyst were investigated by different characterizations such as powder (XRD), (FT-, UV-Vis specra, FT-IR and dielectric techniques and the obtained results.

2. Experimental Part

All the chemicals used in this study were of analytical grade obtained from Merck, India and were used as received without further purification. Magnesium nitrate ($Mg(NO_3)_2{\cdot}6H_2O$, 98%), ferric nitrate ($Fe(NO_3)_3{\cdot}9H_2O$, 98%) and glycine ($C_2H_5NO_2$) were used as a fuel for this method.

All chemicals such as nitrates of magnesium and iron, and glycine were used as the fuel for this method. The stoichiometry of metal nitrate salts and fuel was calculated based on the total oxidizing and reducing valences related to the oxidant agents and to the fuels. Stoichiometric amounts of metal nitrates and glycine were dissolved separately in a beaker with 20 ml of de-ionized water and stirred for 15 minutes to obtain clear solution. The obtained clear solution was transferred into a silica crucible and it was placed in a domestic microwave-oven (850 W, 2.45 GHz) for 15 minutes. Initially, the precursor solution boiled and underwent dehydration followed by decomposition with the evolution of gases. When the precursor solution reached the point of spontaneous combustion, it was vaporized and instantly became solid powders. The obtained solid powders were washed well with water and ethanol several times and dried at 80 ºC for 1 hour, and labeled as $MgFe_2O_4$-MCM, and then used for further characterizations.

3. Results and discussion

3.1. XRD analysis

The structural and phase purity of the samples were confirmed by analyzing the powder X-ray diffraction (XRD) patterns. Fig. 1 shows the powder XRD patterns of $MgFe_2O_4$- sample. All the observed diffraction peaks could be assigned to cubic spinel lattice indicating their single phase structure with no traces of other impurity phases. The XRD peaks could be indexed and are characteristics of single-phase cubic spinel structure of $MgFe_2O_4$ (JCPDS No. 73-1720) [9]. The results show a significant amount of XRD line broadening, a characteristic of nano-phase materials. The main diffraction XRD peak of cubic spinel ferrite at (311) plane was considered as a measure of its degree of crystallinity. The calculated lattice parameter of the samples is summarized in Table 1.

Table 1. Calculated lattice parameter of $MgFe_2O_4$ sample

Sample	Lattice parameter (Å)	Crystallite size *L* (nm)
		Scherrer formula
$MgFe_2O_4$	8.347	15.42

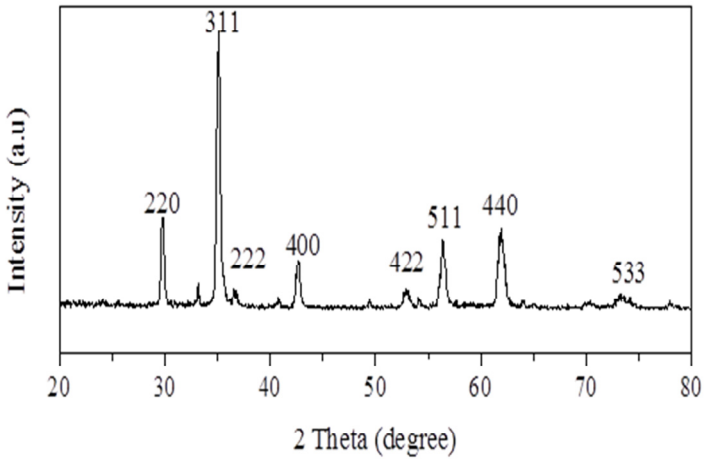

Figure 1 powder X-ray diffraction (XRD) pattern of $MgFe_2O_4$

3.2 UV-Visible diffuse reflectance spectroscopy (DRS) study

The effect of crystallite size on optical property of semiconductor is studied using the UV-Visible diffuse reflectance spectroscopy (DRS) analysis. The UV-Vis DRS has advantages to analyze the optical properties of powdered samples, due to less scattering effects. One can use the DRS data to calculate the direct band gap energy (E_g), as given in the Kubelka-Munk theory [12]. The Kubelka-Munk function *F(R)* was used to calculate the E_g of the sample. Thus the vertical axis is converted into quantity *F(R)* which is equal to the absorption co-efficient. Thus the *'α'* in the Tauc equation is substituted with *F(R*) and hence the relation becomes,

$$\left(F(R)\right) = \alpha = \frac{(1-R)^2}{2R} \qquad \text{---- (3)}$$

where, F(*R*) is Kubelka-Munk function, *'α'* the absorption coefficient, *'R'* the reflectance.
The estimated E_g value of $MgFe_2O_4$ sample is 2.37 eV, respectively.

3.3 Dielectric studies:

The energy storing property of the dielectric material leads to the fabrication of capacitors, which is the most important component in any electrical circuit. The dielectric phenomenon arises from the interaction of electric field with different charged particles such as electrons, ions, protons and electron shells. Fig 2 shows that the

dielectric constant has high values in the low frequency region and thereafter its values decrease with the applied frequency. The high values of (ε_r) at low frequencies may be due to the existence of all the four polarizations, namely orientation, ionic, electronic and space charge polarization. The low values at higher frequencies may be due to the gradual loss of these polarizations. The variation of dielectric loss with frequency is shown in Fig. 3.

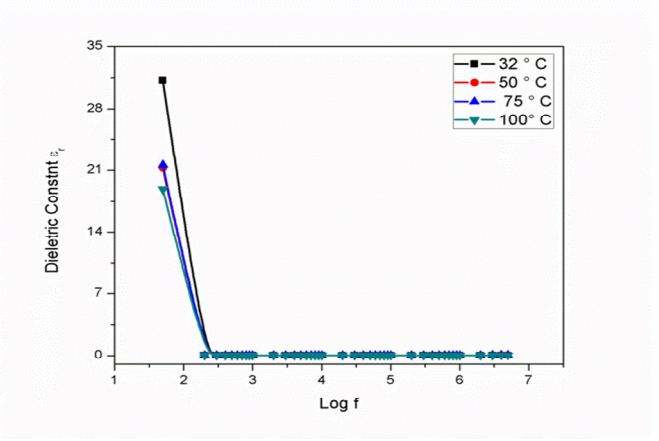

Figure 2: Dielectric Constsnt

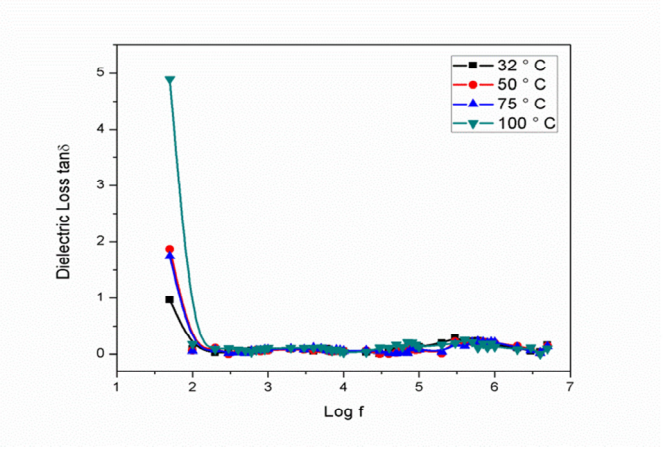

Figure 3: Dielectric Loss

3.4 Photo-catalytic degradation activity

The catalytic performance of $MgFe_2O_4$-MCM sample prepared by MCM method is evaluated in the photocatalytic degradation (PCD) of methylene blue (MB). It is well known that the catalytic activity strongly depends on the particle size and surface area samples. Generally, a high specific surface area has a favourable effect on the activity for heterogeneous photo-catalysis. In this present study, the surface area parameters of the sample is varied according to the preparation methods. In order to have an idea of the adsorbance capability of spinel $MgFe_2O_4$-MCM sample BET surface area was analysed using N_2 adsorption/desorption studies. The surface area of the sample $MgFe_2O_4$-MCM was found to be 71.85 m^2/g and the particle size of $MgFe_2O_4$-MCM is confirmed by powder XRD and HR-TEM analysis. Moreover, it is believed that the high surface area of $MgFe_2O_4$-MCM could enhance the photo-catalytic activity It was found that the sample $MgFe_2O_4$-MCM show higher PCD efficiency (96.48 %). It is mainly due to the uniform distribution with smaller particle size of $MgFe_2O_4$-MCM photo-catalyst. In MCM approach, the final product is formed within few minutes of time with homogeneous and smaller particle

size with higher surface area, which enhance the photocatalytic activity .In addition, when the surface area increases, the amount of the dispersion of particles per volume in the solution will increase, this enhanced the catalytic activity.

3.5 Conclusion

The magnetic $MgFe_2O_4$ nanoparticles were successfully synthesized and characterized. From x-ray diffraction (XRD) particles size is calculated used Scherrer's formula. UV-Visible spectrometer UV helps to find the band gap of the nanoparticles. Dielectric studies like dielectric constant and dielectric loss show the electrical property of the material. The catalytic performance of $MgFe_2O_4$-MCM samples prepared by MCM method is studied. It is well known that the catalytic activity strongly depends on the particle size and surface area samples. The observed photo-catalytic results were summarized.

References

1. Manikandan, M. Durka, S. Arul Antony, J. Supercond. Nov. Magn. 28 (2015) 2047–2058.
2. S. Bhukal, S. Mor, S. Bansal, J. Singh, S. Singhal, J. Mol. Struct. 1071 (2014) 95-102.
3. P. S. Kang, J. H. Seok, Y. H. Kim, J. S. Eun, S. H. Oh, Food Sci. Biotechnol. 16 (2007) 409-414.
4. M. J. Divya, C. Sowmia, K. Joona, K. P. Dhanya, Res. J. Pharm. Bio. Chem. Sci. 4 (2013) 1137-1142.
5. L. Menini, M. C. Pereira, L. A. Parreira, J. D. Fabris, E. V. Gusevskaya, J. Catal. 254 (2008) 355–364.
6. K. Gopinath, K. S. Venkatesh, R. Ilangovan, K. Sankaranarayanan, A. Arumugam, Ind. Crops Products 50 (2013) 737– 742.
7. R. D. Waldron, Phys. Rev. 99 (1955) 1727-1735.
8. F. Gozuak, Y. Koseoglu, A. Baykal, H. Kavas, J. Magn. Magn. Mater. 321 (2009) 2170-2177.
9. A.Manikandan, M. Durka, K. Seevakan, S. Arul Antony, J. Supercond. Nov. Magn. (2015) 28:1405–1416.
10. M. Shahid, L. Jingling, Z. Ali, I. Shakir, M. F. Warsi, R. Parveen, M. Nadeem, Mater. Chem. Phys. 139 (2013) 566-571. M. Sertkol, Y. Koseoglu, A. Baykal, H. Kavasa, A. C. Basaran, J. Magn. Magn. Mater. 321 (2009) 157–162. **DOI**; /10.1016/j.jmmm.2008.08.083.
11. M. Sertkol, Y. Koseoglu, A. Baykal, H. Kavas, A. Bozkurt, M. S. Toprak, J. Alloys Compds 486 (2009) 325–329. **DOI**; 10.1016/j.jallcom.2009.06.128.
12. A. Manikandan, M. Durka, S. Arul Antony, Adv. Sci. Eng. Med. 7 (2015) 33-46. **DOI:** 10.1166/asem.2015.1654.

Available online at www.sciencedirect.com

ScienceDirect

Materials Today: Proceedings 8 (2019) 250–255

materialstoday: PROCEEDINGS

www.materialstoday.com/proceedings

ICMEE 2018

A Correlative Investigation of Photoconductive Behaviour of Bare and Al-Doped ZnO Thin Films

D.J. Sharmila[a], Neena Bachan[a], V. Chandrakala[a], P. Naveen Kumar[a], J. Madhavan[a] and J.Merline Shyla[a]*

[a*]*Department of Physics, Energy Nanotechnology Centre (ENTeC), Loyola Institute of Frontier Energy (LIFE), Loyola College, Chennai 600034, India. e-mail: jmshyla@gmail.com*

Abstract

Zinc Oxide (ZnO) nanoparticles exhibit a wide range of applications owing to their unique properties such as low cost, non-toxicity, abundance in nature and suitability for doping. In the present study, ZnO and Aluminium doped Zinc Oxide (Al-ZnO) nanoparticle thin films were prepared on FTO glass substrate by sol-gel and spin coating methods. The structural and morphological characteristics of the undoped and Al-doped ZnO nanoparticles were examined by X-ray Diffraction (XRD) and High Scanning Electron Microscope (HR-SEM) analysis, respectively. The XRD studies revealed the hexagonal wurtzite structure of the as-synthesized ZnO samples and the crystallite size was estimated using Scherrer's formula to be 28 and 30 nm respectively, in the case of the undoped and doped ZnO nanoparticles. The average particle sizes in nanoscale were analysed using FESEM and found to be 38 nm and 42 nm for the bare and doped samples. The surface area of the as-synthesised particles were correspondingly estimated as 46 m^2/g and 25 m^2/g and their relative pore volume and diameter were determined using BET analysis. The field dependent photoconductivity of Al-ZnO shows a significant increase as against the bare ZnO.

Selection and peer-review under responsibility of the scientific committee of the Materials. For Energy and Environment.

Keywords: Sol-gel; spin coating; thin film; photoconductivity.

* Corresponding author. Phone: +91-9444239551; Fax: +91-44-28175566

E-mail address: jmshyla@gmail.com

Selection and peer-review under responsibility of the scientific committee of the Materials For Energy and Environment.

1. Introduction

ZnO nanoparticles have been widely studied due to their good performance in electronic, optical and photonic devices [1]. ZnO is an n-type semiconductor material that has a wide band gap of 3.37eV [2], high chemical and thermal stability [3]. ZnO in the nano-scale (1–100 nm) can demonstrate the quantum confinement effects, which gives the opportunity to exhibit new physical and chemical properties. This encouraged the researchers to synthesize ZnO as a nanostructure material with various methods and in different shapes such as nanoparticles, nanowires, nanorods, and nanotubes [3-5].

Moreover, ZnO can be used as a pure material in many applications like optical and display devices or it can be doped with elements such as (Al, Ag, or Sn) for high conductance [6] or magnetic elements (Mn, Co, or Ni) to be used as diluted magnetic materials. Recently, doping of ZnO with metals such as Al, Cu, Fe, Se, Ce and Mn widely considered. Aluminum is a suitable impurity for the improvement of photocatalytic activity, which is superabundant, inexpensive and has exclusive physical properties [7].

ZnO thin films can be synthesized by the sol-gel method followed by the spin coating process. Sol–gel spin coating method can be considered as a very simple process for the production of large area of films. ZnO thin films have been widely used as frontal electrode in solar cells, being an alternative to metallic grid contacts that introduce shadows and lower the cell performance [8].

The aim of the present work is to prepare nanocrystalline ZnO semiconducting thin films, which can be used as n-type in thin film solar cells by low cost sol–gel spin coating method (non-vacuum method).

2. Experimental Details

For the synthesis of ZnO nanoparticles and Aluminium doped ZnO nanoparticles, Zinc acetate dehydrate, Aluminium Chloride and Sodium hydroxide were used. All the chemicals were of analytical grade and used without further purification.

2.1 Synthesis of ZnO Nanoparticle

Zinc acetate dehydrate (Zn $(CH3COO)_2 \cdot 2H_2O$) was mixed with 100 ml Ethanol and stirred for 30 minutes. Few grams of sodium hydroxide was mixed with 10 ml distilled water and stirred separately for 15 minutes. After vigorous stirring sodium hydroxide was added in drops to the Zinc acetate dehydrate solution to reach the pH 12 and stirred for 12 hours. After continuous stirring for 12 hours the mixed solution was allowed to settle for sedimentation. FTO glass plate is used as a substrate and cleaned prior with Acetone, Ethanol and Distilled water using an ultrasonicator. Then the precipitate was coated onto the FTO glass plate using Spin Coating method. The coated FTO glass is calcinated at 500 °C for 1 hour. Then the film was subject to various characterisation studies.

2.2 Synthesis of Al-ZnO Nanoparticle

For the synthesis of Aluminium doped Zinc oxide Nanoparticles, Aluminium chloride was mixed with Zinc acetate dehydrate solution and stirred for 30 minutes. Sodium hydroxide was added in drops to the mixed solution to reach the pH 12. Then the mixed solution was stirred continuously for 12 hours and allowed for sedimentation. Then the precipitate is coated on a FTO glass plate using Spin coating method and the coated FTO glass is calcinated at 500 °C for 1 hour.

3. Results and discussion

3.1 X –Ray Diffraction (XRD)

The XRD patterns of ZnO and Al doped ZnO nanoparticles have been recorded by the powder diffraction method using RICH SIEFEST X – RAY DIFFRACTOMETER. Fig. 1(a) and 1(b) shows the XRD pattern of ZnO and Al doped ZnO nanoparticles. The diffraction pattern clearly indicates that, ZnO nanoparticles are highly crystalline and the well-defined peaks are indexed to the hexagonal wurtzite structure of ZnO (JCPDS card no 36-1451). The average crystallite size of ZnO nanoparticle was determined by employing Scherer's equation [9]

$$D = K\lambda/\beta Cos\ \theta$$

where, D is the crystallite size, K constant, λ the wavelength and β the full width at half maximum of the diffraction angle.. The average crystallite size of ZnO Al doped ZnO nanoparticles was found to be 28 nm and 30 nm respectively. The observed lattice planes of (100), (002), (101), (102), (110),(103), and (200) corresponding to the 2θ value of 22.2°, 23.7°, 24.8°, 31.3°, 34.0°, 35.6°, 47.0° and 56.2° of ZnO, indicate that the product is composed of polycrystallites and all the diffraction peaks agreed well with Bragg reflections and no characteristic peaks were observed other than ZnO. Further, doping ZnO with Al reduces the zinc interstitials for charge compensation which results in suppressed ZnO grain growth and deteriorated crystallinity [10]. There is strong orientation of 3 % Al doped in the (0 0 2) plane.

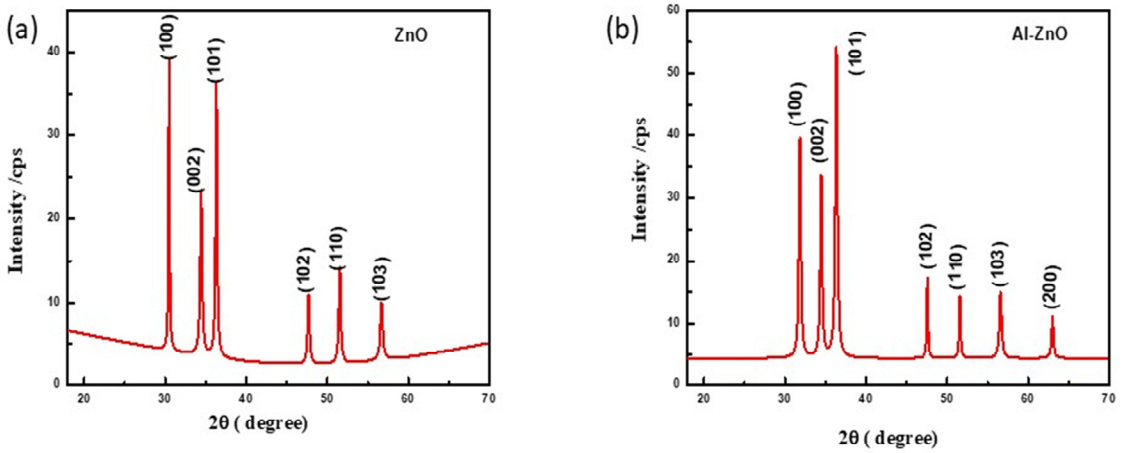

Fig. 1. (a) XRD pattern of ZnO (b) Al doped ZnO.

3.2 HR- Scanning Electron Microscope (HRSEM)

The morphology of ZnO and Al doped ZnO nanoparticles were obtained by High Resolution Scanning Electron Microscope (HR-SEM) and have been recorded using HITACHI S-4800-IIT MADRAS. From the HR-SEM images it is apparent that the nanoparticles are highly dispersed without any aggregation. Fig. 2(a) and 2(b) shows the HRSEM images of ZnO and Al doped ZnO. The particle sizes are in the range of 25 – 50 nm. Increase in the particle size was observed upon Al doping.

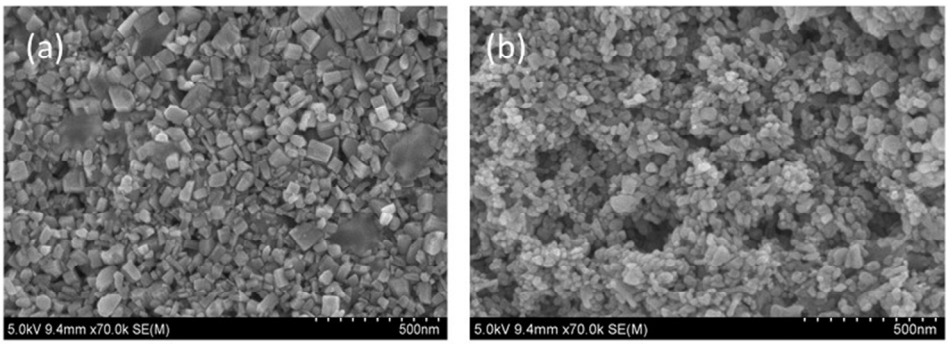

Fig. 2. (a) HRSEM images of ZnO (b) Al doped ZnO

3.3 Specific Surface Area Analysis

The specific surface area analysis of the as-synthesized samples was carried out using Brunauer-Emmett-Teller (BET) studies. Fig. 3(a) and 3(b) shows the adsorption isotherms of the prepared samples. The surface area of the ZnO and Al doped ZnO is found to be 25.29 m^2 /g and 46.25 m^2 /g and the pore diameters were found to be15.544 nm and 15.63 nm. They isotherms are of type IV and hence evidence presence of mesoporous (2-50 nm) materials according to the International Union Pure and Applied Chemistry classification. Doping of Al shows a significant increase in the BET surface area. The augmented surface area on account of Al doping on ZnO would have paved the way for greater photoconduction in doped sample which could be attributed to the presence of more number of surface electrons available for absorbing incoming photons and hence enhanced surface conduction [11].

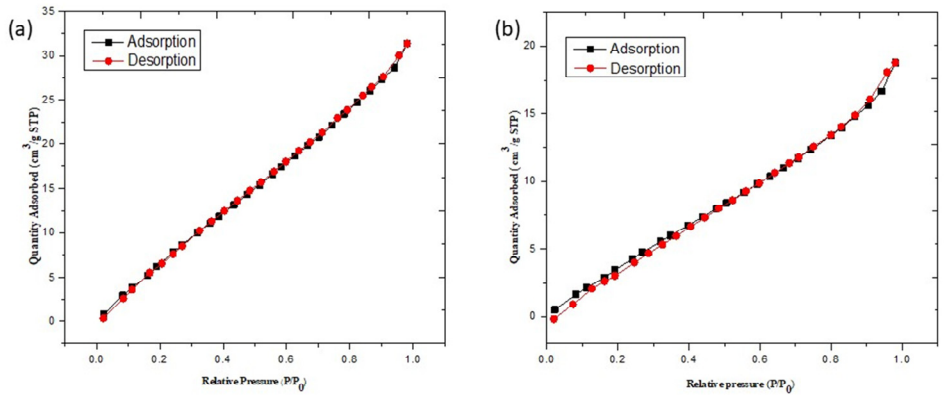

Fig. 3. (a) Adsorbed isotherm of ZnO (b) Al doped ZnO

3.4 Photoconductivity analysis

The field dependent dark and photoconductivity studies were carried out using KEITHLEY PICOAMMETER 6485 for understanding the conducting nature of the as-synthesized samples. Photoconductivity is the tendency of a substance to conduct electricity to an extent that depends on the intensity of light-radiant energy

striking the surface of a sample. All the plots indicate a linear increase of current in the dark and visible light-illuminated samples with increasing applied field depicting the ohmic nature of the contacts [12-13]. Fig. 4(a) and 4(b) shows the field dependent photo and dark current of ZnO and Al doped ZnO. The dark and photocurrents of Al-ZnO showed enchanced values as compared to bare ZnO. For an applied field of 100 V/cm the photo current of ZnO and Al doped ZnO was found to be 2.003 µA and 2.406 µA and the dark current was 1.65 µA and 1.84µA. An increase of about ~ 1.2 folds in photocurrents and ~ 1.1 folds in dark currents was witnessed in the case of doped sample and this significant enhancement could be related to the increased charge carrier concentration which is an effect of enhanced surface area.

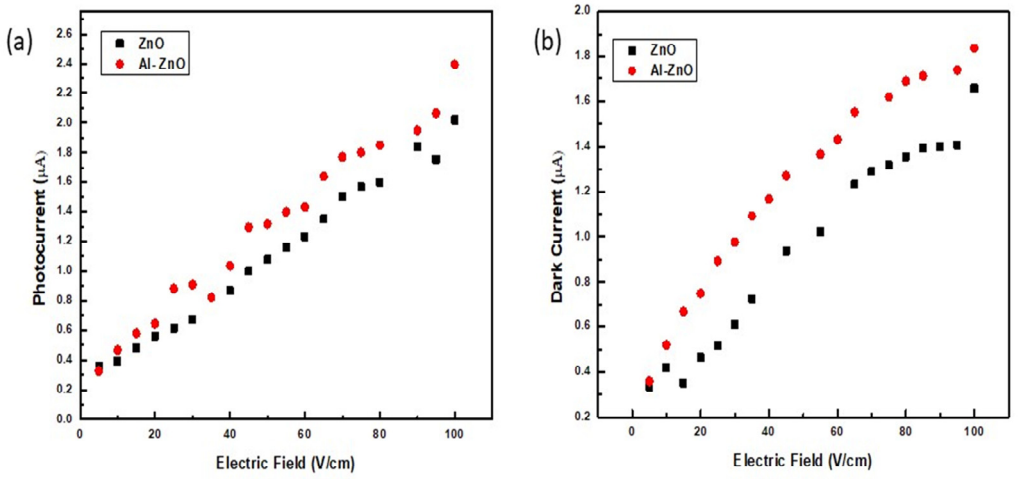

Fig. 4. (a) Field dependent dark and photo current of ZnO (b) Al doped ZnO

4. Conclusions

In this study, ZnO and Al doped ZnO thin films were synthesized using sol –gel spin coating methods. The obtained films are transparent and uniform with good adherence to the substrate. From the XRD the nanocrystalline nature of the sample was confirmed and further its hexagonal wurtzite structure was established. The crystalline size and the particle size increases on doping with Al. The BET analysis shows a rapid increase in the surface area on doping of Al into ZnO and hence witnessing the enhanced surface conduction of electrons on doped candidate. In the photoconductivity analysis there is a linear increase in the dark and the photo current and in addition to that the photoconducting nature of the sample Al- ZnO is greater than the bare ZnO sample. The superior photoconduction in the doped sample exhibited better opto-electrical properties enabling them as a better photo anode for solar cell applications. These films can be used as a window layer for low cost thin film solar cells.Thus it could be concluded that Al doped ZnO would be a promising material for photovoltaic application especially as photoelectrodes in Dye-Sensitized Solar Cells (DSSCs).

Acknowledgement

This research was supported by the Loyola College-Times of India Major Research Grants (6LCTOI14LIF002) and the authors wish to acknowledge the same.

References

[1] Fleischer, K., Arca, E., Smith, C., Shvets, I. 92012. Aluminium doped Zn1-xMgxO-A transparent conducting oxide with tunable optical and electrical properties. Applied Physics Letters 101, 121918.

[2] Samarasekara P, Wijesinghe U, Jayaweera EN (2015) Impedance and electrical properties of Cu doped ZnO thin films. GESJ 1(13):3–9. ISSN 1512-1461.

[3] Chebil W, Fouzri A, Azeza B, Sakly N, Mghaieth R, LussonA,Sallet V (2015) Comparison of ZnO thin films on different substrates obtained by sol–gel process and deposited by spin-coating technique. Indian J Pure Appl. Phys 53(8):521–529.

[4] Abdel-Galil A, Balboul MR, Sharaf A (2015) Synthesis and characterization of Mn-doped ZnO diluted magnetic semiconductors. Phys B 477:20–28.

[5] Khanlary MR, Vahedi V, Reyhani A (2012) Synthesis and characterization of ZnO nanowires by thermal oxidation of Zn thin films at various temperatures. Molecules 17(5):5021–5029.

[6] Lu H, Zhai X, Liu W, Zhang M, GuoM ,Electro depositionof hierarchical ZnO nanorod arrays on flexible stainless steel mesh for dye-sensitized solar cell. Thin Solid Films, 2013 586:46–53.

[7] X. Zhang, Yu Chen, Sh. Zhang, C. Qiu, High photocatalytic performance of high concentration Al-doped ZnO nanoparticles, Sep. Purif. Technol. 172 (2017) 236–241.

[8] Ahmed Abde, GalilFarrag, Mohamed R. Balbou, Nano ZnO thin films synthesis by sol–gel spin coating method as a transparent layer for solar cell applications, DOI 10.1007/s10971-016-4277-8.

[9] DeepshikhaSaini, T. Basu, Synthesis and characterization of nanocomposites based on polyaniline-gold/graphenenanosheets, Applied Nanoscience, 2, 2012, 467–479.

[10] A. Alkahlout, N. Al Dahoudi,I. Grobelsek, M. Jilavi, and P.W. de Oliveiral, (2014) Synthesis and Characterization of Aluminium Doped Zinc Oxide Nanostructures via Hydrothermal Route, Journal of Materials Volume 2014, Article ID 235638

[11] D. Arun Kumar, J. Alex Xavier, J. MerlineShyla, Francis. P. Xavier, Synthesis and structural, optical and electrical properties of TiO2/SiO2 nanocomposites, Journal of Materials Science, 2013, 48, 10, 3700-3707.

[12] YU H., LUI R., WANG X., WANG P., YU J., Investigation of sol-gel processed CuO/SiO_2 nanocomposite as a potential photoanode material, Appl.Catal. B-Environ., 111 32, 2012.

[13] Bojorge, C., Bianchetti, M., Gómez, N., Walsöe de Reca, N., Cánepa, H., Nanocrystalline ZnO photoconductivity measurements. Procedia Materials Science 1, 614-619, 2012.

Available online at www.sciencedirect.com

ScienceDirect

Materials Today: Proceedings 8 (2019) 188–195

materialstoday: PROCEEDINGS

www.materialstoday.com/proceedings

ICMEE 2018

A Relative Investigation of the independent effects of Al-plasmonization and growth procedure on TiO_2/ZnO Photoanodes

Bency .P. Emmanuel[a], W. Jothi Jeyarani[a], Tenzin Tenkyong[a], J. Kethzy Agnes[a], J. Madhavan[a], J. Merline Shyla[a]*

[a*]Department of Physics, Energy Nanotechnology Centre (ENTeC), Loyola Institute of Frontier Energy (LIFE), Loyola College, Chennai 600034, India.

Abstract

Nanoscience and nanotechnology open the door for creation of various nanostructured materials for application in Dye-Sensitized Solar Cells (DSSCs). The aim of the present work is to investigate the as-synthesized TiO_2/ZnO and TiO_2/ZnO encapsulated Al Thin film by doctor blade and spin coating methods and the samples hereby designated as TZ and TAZ and the methods as DB and SC. A detailed investigation into the microstructure, morphology, composition, surface area and optical studies of the as-synthesized samples has been carried out. XRD analysis suggested that the crystallite size of TAZ decreases in comparison with the TZ in both DB and SC. The HRSEM and TEM reports reveal the spherical morphology and reduction in particle size in TAZ which is in good agreement with the XRD results. EDAX analysis confirms the presence of elemental composition of the as-synthesized sample. The presence of the functional groups of the as-synthesized samples was affirmed from FT-IR studies. From the UV-DRS studies a slight modification in band gap was observed possibly due to the lattice disorder arises due to the addition of plasmonic nanoparticles Al. BET analysis confirmed that TAZ shows a significant increase in surface area which would increase the dye absorption, a key factor for enhancing the performance of the DSSCs. Electro-optical studies of TAZ thin film indicated an enhanced photoconductive behavior in the case of hence presenting it as a promising photo anode material for DSSCs.

Selection and peer-review under responsibility of the scientific committee of the Materials for Energy and Environment.

Keywords: DSSCs; Doctor Blade Method; Nano composite thin films;Photoconductivity

* Corresponding author. Phone: +91-9444239551; Fax: +91-44-28175566
E-mail address: jmshyla@gmail.com

Selection and peer-review under responsibility of the scientific committee of the Materials For Energy and Environment.

1. Introduction

Nanotechnology is concerned with the usage of materials on an atomic and molecular scale less than 100 nm which has a great impact on the material's mechanical, electrical characteristics and optical properties [1]. The prospects of nanotechnologies related to solar energy largely depend on improvements in power and efficiency and cost effectiveness [2]. The increasing impact of semiconductor metal oxide nanoparticles in the optic world stimulated the development of new techniques of synthesizing nanoparticles with tailored properties for the photovoltaic applications. Several metal oxides like TiO_2, ZnO, Fe_2O_3, SnO_2 and WO_3 have attracted much interest due to long term stability, high carrier mobility, band gap tunability, thermal and mechanical stability [3]. Among these inorganic materials TiO_2 is the most preferred wide band gap (3.2 eV) semiconductor metal oxide due to its fascinating properties like non toxicity, chemical inertness, stability and its relatively favourable disposition of band edges [4]. Despite the several advantages of TiO_2, the lesser electron transfer and charge separation properties results in low efficiency of DSSCs. Thus ZnO wide band gap (E_g= E_v) semiconductor metal oxide [5] is coupled with TiO_2 as nanocomposite to overcome these limitations. The use of plasmonic effects has been considered as a promising pathway to increase light absorption in active layers of solar cells. Unlike silver and gold, aluminium has material properties that enable strong plasmon resonance scanning much of the visible region of the spectrum and into the ultra-violet [6]. In this work TZ and ATZ were prepared by the simple and versatile sol gel technique and coated on FTO substrate by DB and SC method and the structural and optical properties are deeply investigated.

2. Experimental procedure

First TiO_2 paste was prepared by mixing Degussa powder with polyethylene glycol and acetyl acetone and triton and coated on the FTO substrate by DB and SC methods. ZnO were prepared using zinc acetate dehydrate and anhydrous ethanol by simple sol gel method. Sodium hydroxide (NaOH) was added to adjust the pH value to12. The mixture was allowed to stir continuously for 12 hours. Encapsulation of ZnO of Al was done by dissolving 3% of aluminium nitrate in distilled water. The prepared sol was added drop wise to the ZnO sol and allowed to stir for few minutes. The obtained sol was then deposited over the TiO_2 layer which is coated on the FTO substrate by the spin coating process. The coated TiO_2/Al- ZnO thin film was then calcined at 400°C for 4 hours.

3. Results and Discussion

3.1. Structural analysis

Fig.1. (a) and (b) shows the XRD patterns of TZ and TAZ thin-films coated by DB and SC methods respectively. The intensity and the position of the diffraction peak confirm the anatase phase of TiO_2 and hexagonal wurtzite-type crystalline phase of ZnO with a high degree of crystallinity [7] and matches well with the JCPDS file number[1] of TiO_2 [21-1272] and ZnO [36-1451]. The average crystallite size of TZ and TAZ thin films were calculated using the Scherrer's formula **[8]** and the size of TZ and TAZ obtained by DB method were found to be ~33 nm and ~31 nm and by the SC was found to be ~26 nm and ~22 nm respectively.

From the XRD analysis it is observed that there is a significant decrease in the crystallite size in TAZ thin film in both DB and SC methods. Decrease in crystallite size in TAZ arises due to reduction in the densities of nucleation centers [9], due to the decreased sintering rate that occurred during the sol–gel process[10] and could be due to the replacement of large ionic radii of Zn ion (0.74Å) by the smaller radii of Al (0.53 Å)[11]. From the structural analysis it was observed that the crystallite size of TAZ thin film by SC method is much reduced than the TAZ by DB method.

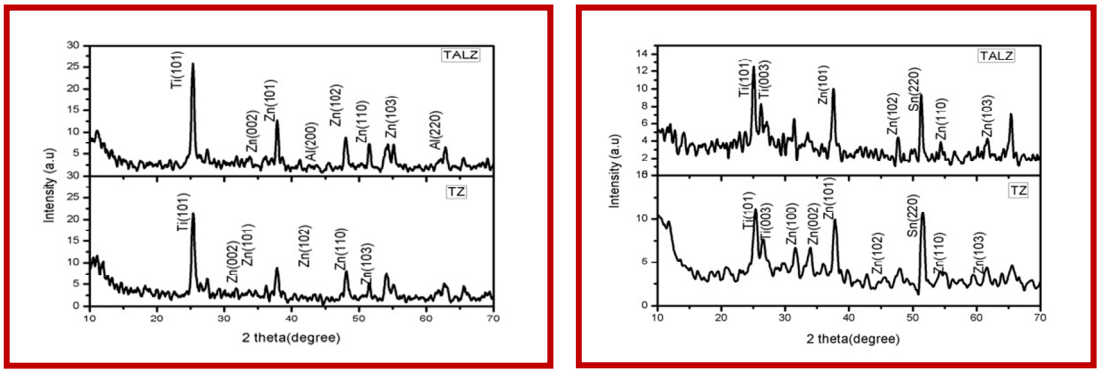

Fig.1. XRD patterns of (a)TZ and TAZ thin film by DB method (b) TZ and TAZ thin film by SC method

3.2 Morphological analysis

In this study, the SEM micrographs of the as-synthesized TZ and TAZ thin films by DB and SC method were shown in the fig.2.

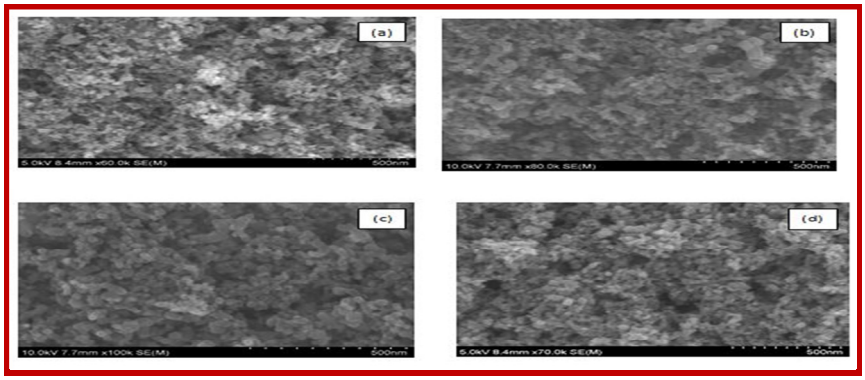

Fig.2. Micrographs of (a) TZ (b) TAZ thin film by DB method (c) TZ (d) TAZ thin film by SC method

From the SEM micrographs it is observed that the as-synthesized TZ and TAZ thin films have well oriented and highly crystalline spherical morphology. The results were found to be in good agreement with the previous literature [12]. From the analysis it is observed that there is decrease in particle size in TAZ thin film than TZ thin film in both DB and SC methods. From the micrographs, the average particle size of TZ and TAZ were found to be ~24nm and ~22nm by DB method and ~23nm and ~20nm by SC method. When Al is added, the grains have a tendency to decrease in size resulting in the reduction of the particle size [13]. Morphological studies show the decreased particle size of TAZ by SC method when compared to the particle size of TAZ by DB method.

3.3 Elemental Analysis

Energy dispersive X-ray spectroscopy (EDAX) is an analytical technique used for the elemental and compositional analysis of the sample. Fig.3. shows the presence of elemental composition of TZ and TAZ thin film by DB and SC method. From the spectrum the presence of Ti, Zn, Al and O in the samples were confirmed which is again in good accordance with XRD data [14].It is also evident that all the samples have high levels of purity.

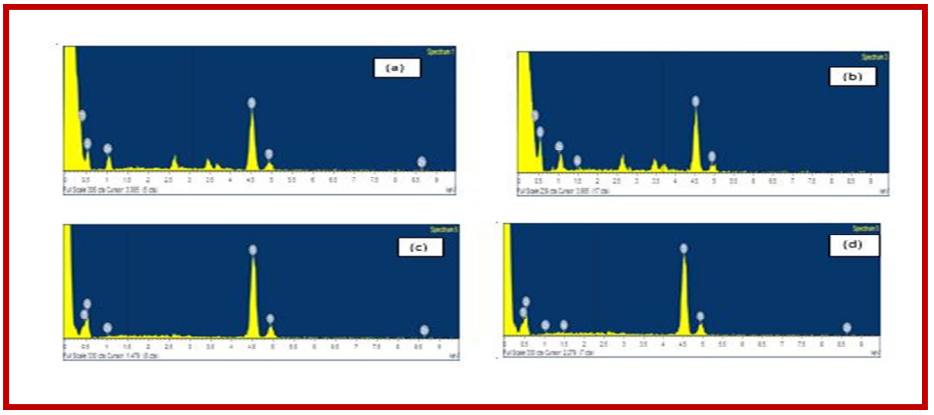

Fig.3. EDAX spectra of (a) TZ (b) TAZ thin film method by DB (c) TZ (d) TAZ thin film by SC method.

3.4 Transmission Electron Microscopy

Fig.4. shows the TEM images of TZ and TAlZ thin films by DB method. The particle size of TZ and TAZ thin films are observed to be ~27nm and ~25nm, which is in good agreement with the SEM results. The anatase phase of TiO_2 and wurtizite phase of ZnO shows a crystalline nature which is in good agreement with the XRD pattern[14]. The lattice spacing of TiO_2 and ZnO was observed as 4.0nm and 2.78nm respectively. From the micrographs it is apparent that the aluminium nanoparticles are homogeneously distributed on the TZ surface. It can be clearly seen that analyzed particle contains differently oriented crystallites.

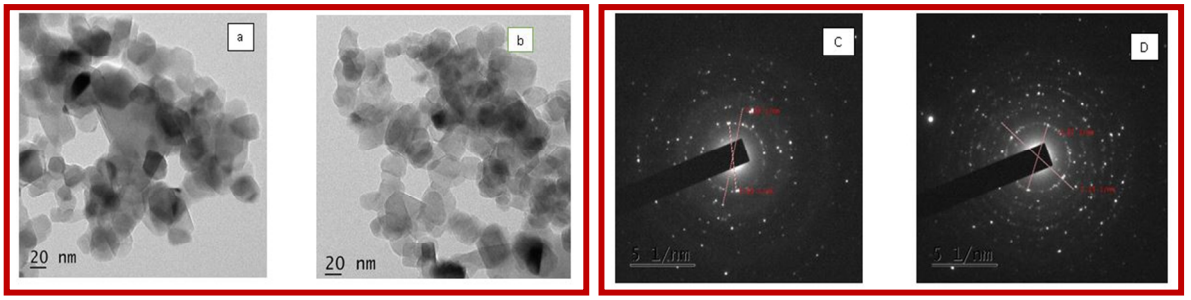

Fig.4. TEM image of (a) TZ (b) TAZ and SAED pattern (c) TZ (d)TAZ thin film by DB method

The particle size of TZ and TAZ thin films are observed to be ~27nm and ~25nm, which is in good agreement with the SEM results. The anatase phase of TiO_2 and wurtizite phase of ZnO shows a crystalline nature which is in good agreement with the XRD pattern[14]. The lattice spacing of TiO_2 and ZnO was observed as 4.0nm and 2.78nm respectively. From the micrographs it is apparent that the aluminium nanoparticles are homogeneously distributed on the TZ surface. It can be clearly seen that analyzed particle contains differently oriented crystallites.

3.5 Optical analysis

The optical absorption spectra of the prepared samples are measured using the UV-Visible Diffuse Reflectance Spectroscopy [15]. Fig.5. shows the optical absorption spectra of TZ and TAZ thin film in the wavelength range 250 to 800 nm. The sample TZ by DB and SC shows strong optical absorption peaks at 318 nm and 358 nm. Moreover, a weak and narrow absorption band was observed in the range 410 nm for TZ in both doctor and spin coated film. The TAZ by DB method shows optical absorption peaks at 282 nm and 313 nm by SC method. This represents that the absorption edge values relate to size and band gap of the nanomaterial. It is observed from the figure that the absorption in the visible regime tends to decrease with the addition of Al in both DB and SC method due to decrease in particle size with increase in band gap.

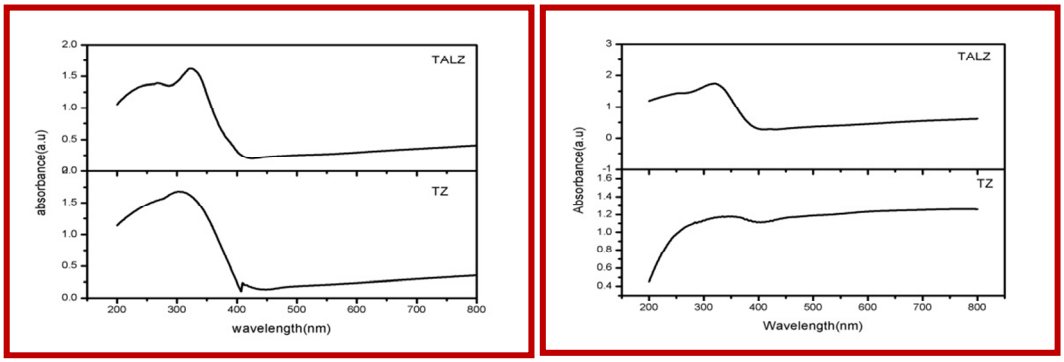

Fig.5. UV-DRS absorption spectra of TZ and TAZ thin film by DB and SC method.

Fig.6. depicits the reflectance spectra of of TZ and TAZ by DB and SC method. The obtained reflectance spectra range from 201 to 429 nm for TZ and 206 to 430nm for TAZ with the strongest peak occuring at 414nm and 418nm for DB method. In the case of SC method the reflectance of TZ ranges from 199 to 416nm and 201 to 447 nm for TAZ and the strongest peak occurs at 411 nm and 432 nm respectively. This confirms that ZnO deposited over TiO_2 contributes to a decrease in the diffuse reflectance, which in turn increases the light harvesting efficiency [15].

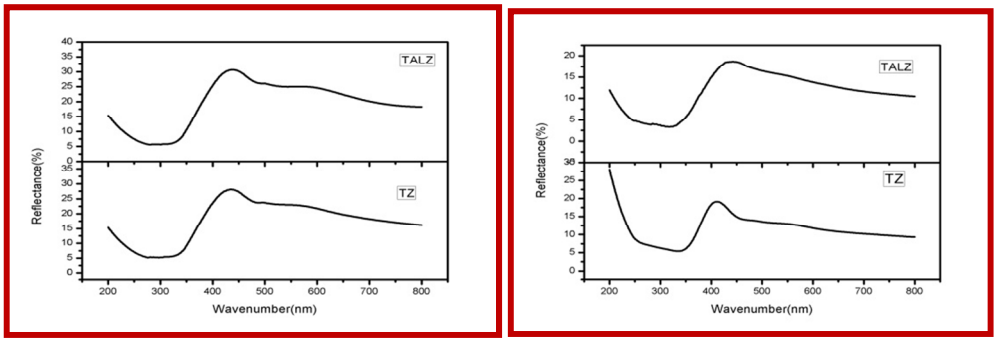

Fig.6. Reflectance spectra of TZ and TAZ thin film by DB and SC method

The optical band gaps were deduced by K-M plot shown in fig.7 and were found to be 2.5eV and 2.0 eV for TZ by DB and SC method and 2.6eV and 2.3eV for TAZ by DB and SC method respectively. It is observed from the graph that there is an increase in the band gap of TAZ, shows possibly due to the addition of small amount of Al causes modification in the band gap. This may be due to the insertion of lattice disorder which occurred due to the addition of Al [16].

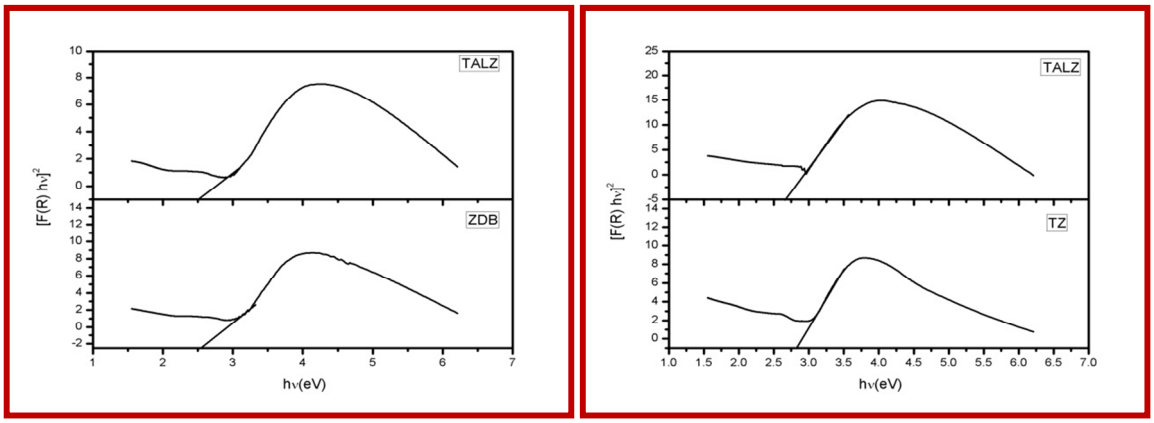

Fig.7. Band gap of TZ and TAZ thin film by DBand SC method

3.6 FTIR Analysis

Fourier Transform Infrared (FTIR) spectroscopy studies are used mainly to confirm the functional groups of the as-synthesized nanocomposite. Fig.8 represents the transmission peaks for TZ and TAZ thin film by DB method. The peaks at 3407.00 cm^{-1} and 3314.7 cm^{-1} show the OH stretching group in TZ thin film and TAZ thin film. The C=N stretching is represented by the peaks at 2177.95 cm^{-1},2178.65 cm^{-1},2113.73 cm^{-1}. The Ti-O stretching vibration is observed in the IR band range of 400cm^{-1} to 900cm^{-1} [17] and that of Zn-O stretching corresponds to the IR range of 1404cm^{-1}[18]. The peak 535cm^{-1} shows the attribution to Zn-O and Ti-O of the TZ thin film.

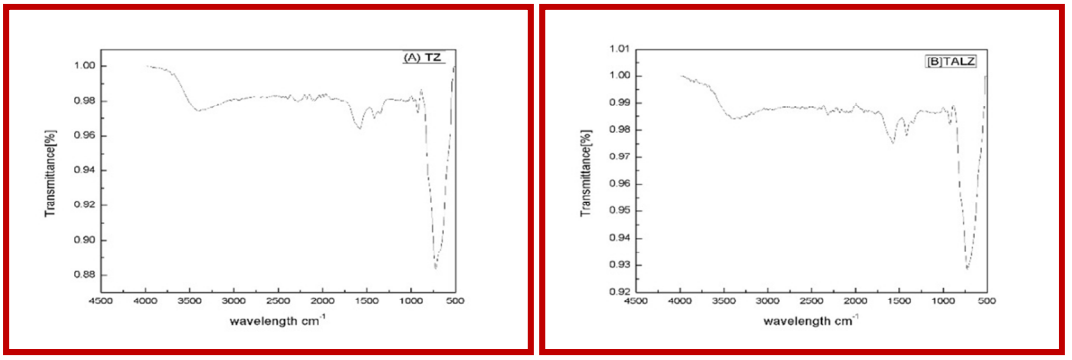

Fig.8. FTIR spectrum of (a) TZ (b) TAZ thin film by DB method

3.7 Specific surface area analysis

Brunauer - Emmett - Teller (BET) analysis is carried out to study the surface area of the as-synthesized samples.The BET surface area of TZ and TAZ thin film by DB method were estimated to be 6.495 m^2/g and 8.188 m^2/g and by SC method the surface area were found to be 3.214 m^2/g, and 9.233 m^2/g respectively. From the analysis it is confirmed that addition of Al shows a significant increase in surface area due to the decrease in the particle size. But when compared to surface area of TAZ thin film by DB method, TAZ thin film by SC method shows increased surface area, which is in good agreement with the SEM and XRD results. Hence the increase in surface area which could in turn increases the dye absorption, a key factor for enhancing the performance of the DSSCs.

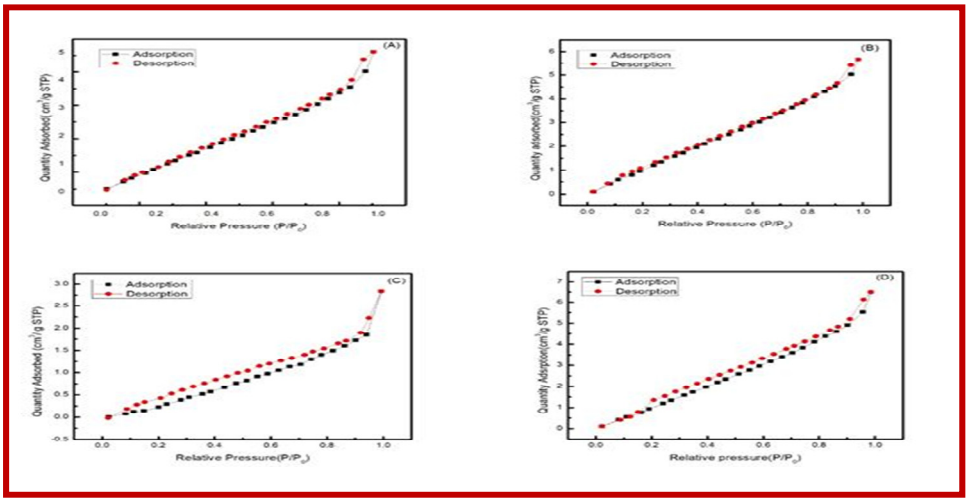

Fig.9. Adsorption isotherms of (a) TZ (b) TAZ thin film by DB method (c) TZ (d) TAZ thin film by SC method

The summary of the analysis have been tabulated in detail in Table 1.

Table1. Crystallite size, Particle size, Surface area and Bandgap of TZ and TAZ thin film.

Method	Samples	Crystallite size (nm)	Average particle size (nm)	S_{BET} (m^2/g)	Band gap(eV)
DB	TZ	~33	~24	6.495	2.5
	TAZ	~31	~22	8.188	2.6
SC	TZ	~26	~23	3.214	2.0
	TAZ	~22	~20	9.233	2.3

3.8 Electro-Optical Analysis

The field dependent dark and photoconductivity studies were carried out by using the Keithley Picoammeter 6485 for better understanding of the surface conductivity of the as- synthesized samples. The plots indicate the linear increase of current in the dark and the visible light illuminated samples with the increase in the applied field depicting the ohmic nature of the contacts fig.10.[19]. From the analysis it is observed that the photo current (Ip) is greater than the dark current (I_D) in both TZ and TAZ thin film by DB and SC methods. But when compared to spin coating method, there is a significant increase in photocurrent for TAZ coated by DB method. Thus, there is an enhanced photocurrent in TAZ by DB method. This could be due to the well-defined thickness of films which facilitates better photoconduction of TAZ, fabricated using the DB method. The enhancement in the photoconduction could also be due to the replacement of Zn^{2+} by Al^{3+} ions which results in the free electron for every zinc atom. This in turn increases the carrier concentration which results in the increase of conductivity of TAZ thin film by DB method [21]. Thus the enhanced photoconductive and interesting behavior of TAZ thin film by DB method elevates it as a promising photo anode material for DSSCs.

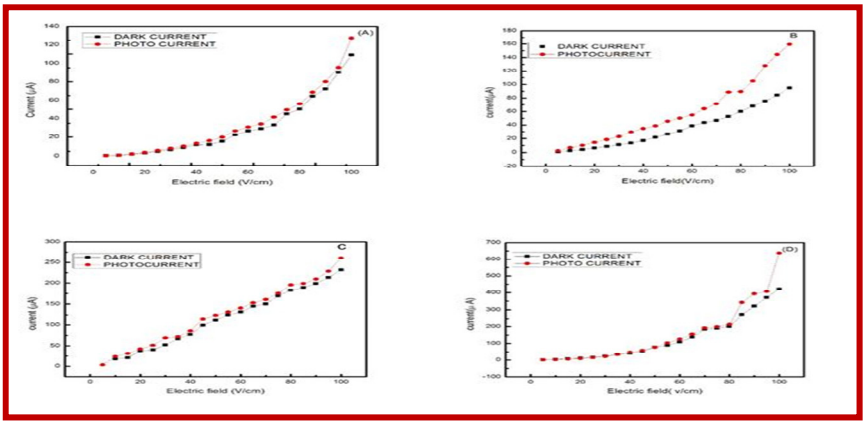

Fig.10. Field dependent conductivity of a) TZ (b) TAZ thin film by DB method (c)TZ (d) TAZ thin film by SC method

4. Conclusions

Highly proficient TZ and TAZ thin films were successfully coated on the FTO substrate by DB and SC methods. The XRD studies confirmed the high crystalline nature of the films and further, a decrease in crystallite size with addition of Al was observed in both the DB and SC samples. This could be due to the reduction in the density of the nucleation centres. The morphology of the as-synthesized samples was characterized and the micrographs showed that the particle size decreases with the addition of Al in both the DB and SC method which is in good agreement with the XRD results. EDAX analysis gave the elemental composition of the sample confirming the presence of Ti, Zn and O in TZ and Al, Ti, Zn and O in TAZ samples. It is also evident from the analysis that all samples have a high level of purity. FTIR helps in confirming the various functional groups present in the as-synthesized sample. TEM reveals the spherical morphology and the diameter is 29nm which is in good agreement with XRD and SEM. UV-DRS studies of the as-synthesized TZ and TAZ thin films revealed that there is a modification in band gap due to the insertion of lattice disorder which occurred due to the addition of Al. From the BET analysis, it is confirmed

that addition of Al shows a significant increase in surface area which would increase the dye adsorption; a key factor for enhancing the performance of the DSSCs. Field dependent photoconductivity studies showed that the photo current I_P in the case of TAZ is found to be significantly greater than the TZ thin film. While comparing the two methods of coating, the samples developed by the DB method, showed enhanced optical and photo conducting property thus indicating their possible improved efficiencies when applied to DSSCs. Thus the enhanced photoconductive and interesting electro-optical behavior of TAZ thin film by DB method promotes it as a promising photo anode material for DSSCs.

Acknowledgement

Authors are grateful for the financial support extended by the Loyola College - Times of India Major Research Grant (6LCTOI14LIF002) toward this work.

References

[1] R. M. Hlihor and M. Gavrilescu, "Book review of nanomaterials: An introduction to synthesis, properties and application by Dieter Vollath," Environmental Engineering and Management Journal, vol. 7, no. 6, pp. 865-870.

[2] Nanotechnology in the sectors of solar energy and energy storage, Ralph Seitz, Björn P. Moller, Axel Thielmann, Andreas Sauer, Michael Meister, Mickael Pero, Oliver Kleine, Clemens Rohde, Antje Bierwisch, Meike de Vries, Victoria Kayser, Technology Report.

[3] A.T. Mane, S.T. Navale, R.C.Pawar, C.S.Lee, V.B.Patil, Microstructural, optical and electrical transport properties of WO_3 nanoparticles coated polypyrrole hybrid nanocomposites, Elsevier

[4] Rimeh Daghrir, Patrick Drogui, and Didier Robert, Modified TiO_2 For Environmental Photocatalytic Applications: A Reviewpubs.acs.org/IECR.

[5] Rajaram S. Mane, Won Joo Lee, Habib M. Pathan, and Sung-Hwan Han, Nanocrystalline TiO2/ZnO Thin Films: Fabrication and Application to Dye-Sensitized Solar Cells**,** J. Phys. Chem. B, 2005, 109 (51), pp 24254–24259, December 6, 2005.

[6] Mark W. Knight, Nicholas S. King, Lifei Liu, Henry O. Everitt, Peter Nordlander, and Naomi J. Halas, Aluminum for Plasmonics , ACS Nano, 2014, 8 (1), pp 834–840DOI: 10.1021/nn405495q

[7] Hafeez ullaha, Amjid Iqbalc, M. Zakriac, Arshad Mahmoodc, Structural and spectroscopic analysis of wurtzite (ZnO)1-x(Sb2O3)x composite semiconductor, Progress in Natural Science: Materials International, 25 ,131–136,2015

[8]Ahmad Monshi, Mohammad Reza Foroughi, Mohammad Reza Monshi, Modified Scherrer Equation to Estimate More Accurately Nano-Crystallite Size Using XRD,World Journal of Nano Science and Engineering, 2, 154-160,2012.

[9] A. S. Riad, S. A. Mahmoud and A. A. Ibrahim, Structural and DC electrical investigations of ZnO thin films prepared by spray pyrolysis technique Physica B 296, 319 (2001).

[10] M. Mazaheri, A. M. Zahedi and S. K. Sadrnezhaad, Two-Step Sintering of Nanocrystalline ZnO Compacts: Effect of Temperature on Densification and Grain Growth, 6 December 2007

[11]Yogeswar kumar, Ahamad Mohiddon,Alok Srivastava, K LYaddav, effect of Ni doping on structural and dielectric properties of BaTiO3, indian journal of engineering and
materials sciences,16,390-394,2009

[12] Pankaj kumar baitha and J.Manam, Luminescence properties of ZnO/TiO_2 nanocomposite activated by Eu3+ and their spectroscopic analysis, Bull. Mater. Sci., Vol. 39, No.5,September 2016,pp.1233–1243,

[13]Daniel H. Herring, Grain Size and Its Influence on Materials Properties, August 2005 – IndustrialHeating.com.630.834.3017

[14]Tenzin Tenkyong, Neena Bachan, J.Raja, P.Naveen Kumar, J.Merline Shyla, Investigation of sol-gel processed CuO/SiO2 nanocomposite as a potential photoanode material

[15]S.S. Kanmani, K. Ramachandran, Synthesis and characterization of TiO2/ZnO core/shell nanomaterials for solar cell applications Renewable Energy, Elsevier, vol. 43(C), pages 149-156.

[16]Majid Jafaria , Sanaz Razavein and Ali Saffar, Synthesis and characterization of TiO2-ZnO-xAl_2O_3 Nano-composite Via Sol-Gel Method.

[17]Manveen kaur, N.K.Verma, $CaCO_3/TiO_2$ nanoparticles based dye senstitized solar cell, J.Mater.Sci.Technol,30,328-334(2014)

[18] Nadia Riaz, Mohamad Azmi Bustam, Fai Kait Chong,Zakaria B. Man, Muhammad Saqib Khan, and Azmi M. Shariff, Photocatalytic Degradation of DIPA Using Bimetallic Cu-Ni/TiO_2 Photocatalyst under visible light irradiation. The Scientific World Journal
Volume 2014 (2014), Article ID 342020, 8 pages http://dx.doi.org/10.1155/2014/342020

[19] Ruh ullah, Joydeep Dutta, Photocatalytic degradation of organic dyes with mganese-doped ZnO nanoparticles, Journal of Hazardous Materials 156 (2008) 194–200

[20] Sabita sharma, Subash Chandra Bhandari, Shankar Prasad Shrestha and Leela Pradhan joshi, Synthesis and study of zinc oxide nanoparticles for dye sensitized solar cells**.** Res. J. Physical Sci., Volume 5, Issue (5), Pages 6-10, June,4 (2017).

[21] T. Ganesh, S. Rajesh and Francis P. Xavier, Photoconducting and photoresponse studies on multilayered thin films of aluminium doped zinc oxide, Indian Journal of Science and Technology, Vol. 5 No. 3 (Mar 2012) ISSN: 0974- 6846.

Available online at www.sciencedirect.com

ScienceDirect

Materials Today: Proceedings 8 (2019) 337–345

materialstoday: PROCEEDINGS

www.materialstoday.com/proceedings

ICMEE 2018

Investigation of Rare Earth Garnet and its Physical Properties Synthesized by Facile Sol-Gel Method

M.Asisi Janifer, S. Anand, V. Maria Vinosel and S. Pauline*

Department of Physics, Loyola College (Autonomous), Chennai -600034, India

Abstract

To meet the demand of electronic devices pure polycrystalline yttrium iron garnet with cubic structure is investigated by sol gel method. The crystalline information and identification of garnet phases is confirmed using X-ray Diffraction. The X-ray diffraction pattern is analyzed by utilizing Rietveld Refinement method using Fullprof Software suite. Well defined domain morphology is observed in the High Resolution Scanning Electron Microscope image (HR-SEM). Pure YIG is inspected by Impedance Spectroscopy (IS) using Cole-Cole plot and Bode plot. It is interpreted using electrical circuit which is the combination of resistors and capacitors. The effect of g value of the sample is measured using Electron Spin Resonance (ESR).

Selection and peer-review under responsibility of the scientific committee of the Materials For Energy and Environment.

Keywords: Garnet, Rietveld refinement analysis, Impedance studies, Electron Spin Resonance (ESR);

1.INTRODUCTION

The continuous development of communication sector has resulted to gain importance of magnetic materials to a great extent. They have become significant due to their interesting wide variation of properties which ultimately makes them suitable for technological applications [1]. Garnets are magnetic materials with general formulae $M_3Fe_5O_{12}$ reside under the category of soft ferrites. They possess high thermal stability, small hysteresis loss, low thermal expansion, better chemical stability and high thermal conductivity.

Yttrium iron garnet also known as YIG or $Y_3Fe_5O_{12}$ belongs to the rare earth iron garnet group. Yttrium iron garnet ($Y_3Fe_5O_{12}$) is a multifaceted ceramic material which has high melting point, large resistivity, better

* Corresponding author. Tel.: +91-9940054040
E-mail address: paulantovero@yahoo.co.in

Selection and peer-review under responsibility of the scientific committee of the Materials For Energy and Environment.

electromagnetic properties and narrow line width [2]. These properties make this material very appropriate for different sectors such as telecommunications, magneto-optical information storage and biomedical application. The oxygen lattice on which the structure is built, is made of closely packed cubic structure with a unit cell containing eight molecules of $Y_3Fe_5O_{12}$. Soft magnetic ferrites are much more advantageous than any other metal counterparts due to their electrical insulation property. This in fact, is the basic property to maintain low eddy current loss and is also used in many areas of applications where magnetic ceramics with low losses are required [3]. The physical properties of garnet ferrites strongly depend on phase formation, microstructure, synthesis techniques and sintering temperature.

In recent years as well in the past, there has been developing interest in the synthesis of YIG by different methods such as solid state reaction, sol-gel, co-precipitation, micro emulsion, hydrothermal methods. As it is important to control the reaction of single phase YIG, a suitable synthesizing method is desired [4]. Solid state method is the customary method used for preparing YIG. This is a very tedious process since additional grinding operation and very high temperature is required whereas at low temperature, impurity phases ($YFeO_3$, Y_2O_3 and Fe_2O_3) are obtained as intermediates [2] while, sol-gel method is an extensive method widely used for necessitating atomic scale mixing with high reaction rate. It also entails well dispersed nanocrystals along with uniform distribution.

2.EXPERIMENTAL PROCEDURE

For the preparation of Yttrium iron garnet, Yttrium nitrate hexa hydrate (Y $(NO_3)_3.6H_2O$, 99.99%) and Iron nitrate nona hydrate (Fe $(NO_3)_3.9H_2O$, 99.99%) are taken as starting materials.

$$3Y_2O_3 + 5Fe_2O_3 \rightarrow 2Y_3Fe_5O_{12}$$

The starting materials were dissolved in an aqueous solution of citric acid ($C_6H_8O_7.H_2O$) which is a chelating agent. The molar ratio of metal nitrates to citric acid was maintained as 1:1. The solution was stirred at 310 rpm for about one hour. The temperature was raised to 80°C with continuous stirring until gel was formed and then dried at 110°C for 20 hours. The dried powder was well ground and finally annealed at 1150°C for 3 hours in air muffle furnace. Green colour powdered YIG sample was obtained.

2.1 Characterization

The phase identification and crystalline information of $Y_3Fe_5O_{12}$ by sol gel method was investigated using X-ray diffractometer (Bruker D8 advance) operated at 40 kV and at 30 mA with CuKα radiation (λ =1.5406 Å). The surface morphology and distribution was studied using FEI Quanta FEG 200-High Resolution Scanning Electron Microscope (HR-SEM). Impedance measurements were carried out with a HP 4192A LF impedance analyzer in the frequency range of 5 Hz to 13MHz. The g-value of the sample is measured using JEOL Model JES FA 200 Electron Spin Resonance (ESR) at room temperature.

3. RESULTS AND DISCUSSION

3.1 Powder XRD analysis

The X-ray diffraction pattern of YIG nanoparticles synthesized by sol–gel method at 1150 °C is shown in Fig.1. It is observed that $Y_3Fe_5O_{12}$ samples exhibits single phase garnet peaks without any impurities at this high temperature exactly matched the standard JCPDS data (75-1852). The average crystallite size of the pure YIG is determined using Scherrer equation,

$$D = \frac{0.9}{\beta \, Cos \, \theta}$$

Where, D is crystallite size in nm, λ the radiation wave length (0.15405 nm for Cu Kα), β is the corrected full width at half maximum and θ is the diffraction angle.

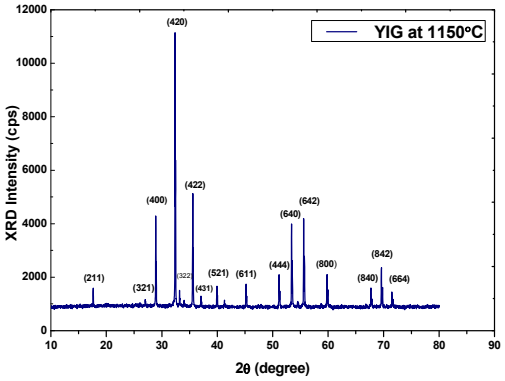

Fig. 1.XRD pattern of pure YIG

3.1.1 Rietveld refinement method

The Rietveld method is used to refine the user-selected parameters to minimize the difference between an experimental pattern (observed data) and instrumental parameters (calculated pattern). The peak profile of the pattern was modelled based on pseudo- Voigt function and with oxygen positions (x=y=z=u) taken as free parameters **[**5**]**. Yttrium iron garnet crystallizes in a cubic structure with space group Ia3d.

In the crystal structure of garnet ferrites two of five Fe atoms in the formula unit occupy octahedral sites (Wyckoff position 16a) while other three atoms occupy tetrahedral sites (Wyckoffposition 24d). The three Y atoms are in dodecahedral sites (Wyckoff position 24c), and twelve O anions are in (Wyckoff positions 96h) [6].

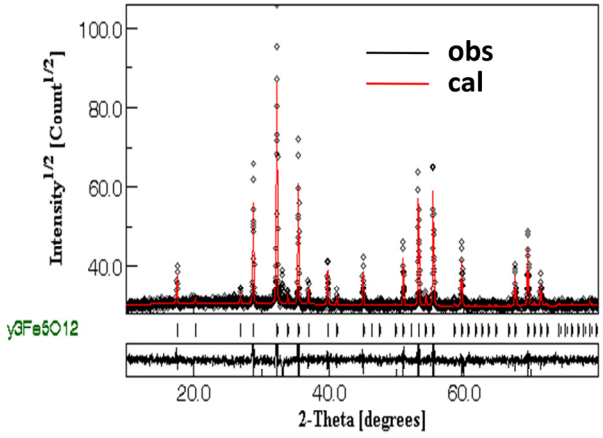

Fig. 2.Rietveld refined XRD pattern of pure YIG

The Rietveld refinement XRD pattern of YIG at room temperature is illustrated in Fig.2. The graph represents the experimental and calculated data and also their difference. The atomic site details from the Rietveld refinement of XRD pattern are represented in Table1. The Rietveld reliability R-factors such as expected Rexp , Bragg RBragg, profile Rp and weighted profile Rwp and goodness of fit is calculated and shown in table4. The calculated and experimental crystalline parameters and the interplanar spacing values are depicted in table 2 and 3 respectively.

Table 1: Atomic site information obtained from the Rietveld refinement of XRD pattern

n	symbol	qauntity	occupancy	x	Y	Z
1.	O1	96	1.0	0.148	-0.029	0.054
2.	Y1	24	1.0	0.125	0	0.25
3.	Fe1	16	1.0	0	0	0
4.	Fe2	24	1.0	0.375	0	0.25

Table 2: Calculated and experimental values of Crystalline parameters

Crystalline parameters	Experimental Rietveld refinement	Calculated
a=b=c(Å)	12.387	12.29
a^3 (Å^3)	1897	1856
density	5.157	5.28
microstrain	8.205201E-5	4.71939E-4

Table 3: The interplanar spacing values from calculated and experimental methods

2θ(degree)	d-spacing	
	Calculated	Experimental
17.62	5.02	5.05
28.87	3.08	3.09
32.4	2.74	2.76
35.5	2.50	2.52
39.9	2.25	2.26
45.2	1.98	2.00
51.2	1.75	1.78
53.4	1.69	1.71
55.5	1.62	1.65
59.8	1.51	1.54
67.7	1.35	1.38
69.6	1.31	1.35

Table 4: Reliability factors calculated from Rietveld refinement method

Reliability factors	
Rb (%)	4.381641
Rwp (%)	7.572881
Rexp (%)	3.224285
χ^2 (%)	2.35

The calculated crystalline parameters of XRD pattern is measured using the formulaes,

The lattice constant (a), $a = \frac{d}{\sqrt{h^2+k^2+l^2}}$

Where, 'a' is lattice constant; 'd' is inter planar distance; h, k, l are the Miller indices of the Crystal planes.

The unit cell volume (V), $V = a^3$

The X-ray density (dx) of the material, $d_x = \frac{8M}{N^3}$

where, 'M' is the atomic wt , 'N' is Avogadro's number (6.022 X 10^{23} mol^{-1}) and a is lattice constant.

The lattice strain was calculated using Williamson-Hall analysis.

3.1.2 Williamson – Hall method

W-H analysis is a simplified integral breadth method that clearly differentiates the size induced and strain induced in the broadening of the peak by considering the peak width as a function of 2θ. In addition to crystallite size XRD pattern is also influenced by lattice strain. Fig.3 depicts W-H analysis of pure YIG. The individual contribution to line broadening of a Bragg reflection can be expressed as:

$\beta_{hkl} = \beta_s + \beta_D$

where, β_{hkl} represents the full width half max of a peak in radian, β_s and β_D are due to size and strain.in W-H realtion the strain was assumed to be uniform in all crystallographic direction , β_{hkl} is given by

$$\beta_{hkl} = \left(\frac{K\lambda}{D\cos\theta}\right) + 4\varepsilon\tan\theta$$

Rearranging this eqn gives

$$\beta_{hkl}\cos\theta = \left(\frac{K\lambda}{D}\right) + 4\varepsilon\sin\theta$$

The crystallite size is calculated as,

$$D = \frac{K\lambda}{Y - intercept}$$

Here D and Ɛ correspond to the crystallite size value and dimension value (micro strain). By plotting β_{hkl} Cosθ as a function of 4 sin θ, the average crystallite size and strain are estimated from the extrapolation and slope of the fitted line **[**6**]**.

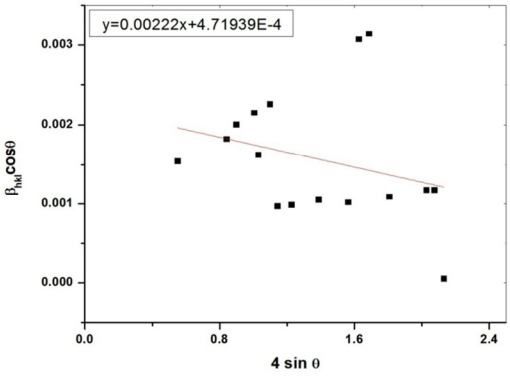

Fig.3.W-H analysis of pure YIG

Table 5: Crystallite size calculated by different methods

Scherrer method	W-H method	Rietveld refined method
65.6nm	65.2nm	65.8nm

The nanoparticle diameter determined by Rietveld refinement Dref is in good agreement with those calculated from Scherrer method and W-H analysis. The quality of fitting from Rietveld is found to be good as χ^2 is less than 1and the wighted difference between measured Rp and calculated value Rwp is less than 10% (Gomes et al). Crystallite size calculated is summarized in table 5.

3.2. Morphology of YIG nanoparticles by HR-SEM

Typical SEM micrograph of yttrium iron garnet samples is represented in fig.4. Well defined grown up particles is obtained. The image eventually imparts the uniformity in the particles [2].

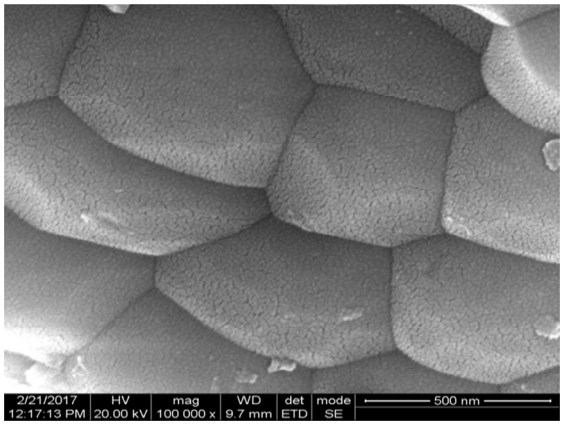

Fig.4. Scanning Electron Micrograph of YIG

3.3 Impedance Spectroscopy

The microstructural effect is the main parameter that influences the impedance properties of ferrites. The resistive (real part) and reactive (imaginary part) components of a material are discussed from the experimental results. The imaginary part of impedance vs. real part (Nyquist plots) over a wide range of frequency and at room temperature is illustrated in figure.

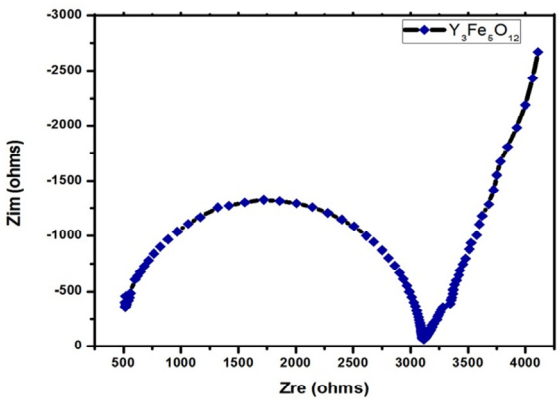

Fig.5. Complex impedance or Nyquist plot of pure YIG

In general, a ferrite material is assumed to consist of crystalline plates that are piled up. From this microstructural point of view, a sample is presumed to be microstructure made up of parallel conducting plates (grains) separated by (grain boundaries) resistive plates [7]. With regard to the impedance plots, the lower frequency dispersion indicates grain boundary and higher frequency dispersion indicates the presence of grain. Fig.5 clearly reveals only one semicircle for the pure YIG sample. This single semi-circle shows the predominant contribution of grain boundary whereas, contribution from grain is not resolved. The occurance of single semi-circle suggests electrical process that obeys single relaxation mechanism [8] or even the additional time constant that may appear outside the measured frequency range as reported by Farea et al for pure sample. Such a model reveals the electrical processes occurring within the sample are correlated with the microstructure of the sample in terms of an electrical equivalent circuit as a combination of resistors and capacitors.

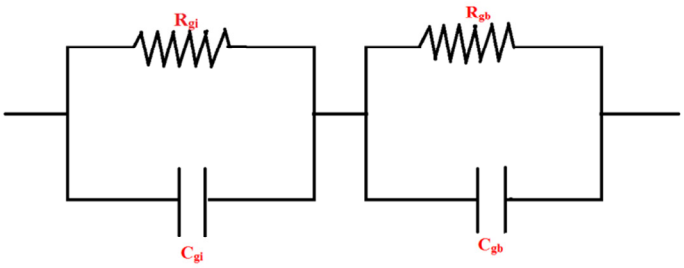

Fig.6. Equivalent circuit for the complex impedance plots

The complex impedance $Z(\omega)$ of a system at an applied frequency (ω) can be written as the sum of real and imaginary part:

$$z(\omega)=z'+jz'' \quad \text{.....(1)}$$

Where Z' and Z'' can be written as,

$$z' = \frac{R_g}{1+\omega_g^2 C_g^2 R_g^2} + \frac{R_{gb}}{1+\omega_{gb}^2 C_{gb}^2 R_{gb}^2} \quad \text{.....(2)}$$

$$z'' = \frac{-R_g^2 \omega_g C_g}{1+\omega_g^2 C_g^2 R_g^2} + \frac{-R_{gb}^2 \omega_{gb} C_{gb}}{1+\omega_{gb}^2 C_{gb}^2 R_{gb}^2} \quad \text{.....(3)}$$

Where, R_g and R_{gb} are the resistances from grain and grain boundary. ω_g and ω_{gb} are frequencies of grain and grain boundary. As at the maximum point in each semicircle z'=z", from this condition and depending on Eqs. (2) and (3) we can get:

$$C_{gb} = \frac{1}{R_{gb}\omega_{gb}} \text{.....(4)}$$

Relaxation time or time constant for grain boundary (τ_{gb}) and grain (τ_g) corresponding to frequencies of grain and grain boundary were calculated using the following equations:

$$\tau_{gb} = \frac{1}{\omega_{gb}} = C_{gb} R_{gb} \quad \text{.....(5)}$$

The resistance from grain boundary (R_{gb}), capacitance from grain boundary (C_{gb}) and relaxation time of grain boundary (τ_{gb}) is calculated and shown in table 6 **[9]**. As suggested by (Farea et al) the air sintered ferrites are characterized by high conductive grains which are separated from high resistive thin layers (grain boundaries). Mostly, the grain boundary regions influences the specimen applied with external electric field. Hence, the properties of grain boundaries control the electric dielectric properties of these materials which is widely suitable for electronic applications.

Fig.7 depicts the bode plot for pure YIG Nanocrystallites. In this plot, frequency is along X-axis and magnitude of impedance (|Z|) is along the Y-axis. Being the useful alternate of Nyquist's plot, Bode plot gives a clear description upon the dependence of impedance with respect to frequency. The frequency values are implicit rather being explicit and also it allows a wide range of frequencies to be plotted on one graph **[10]**. In the entire frequency range from 10Hz to 100 KHz impedance is almost constant.

Table 6: Measured data from impedance analysis

Sample	R_{gb} (kΩ)	C_{gb}(nF)	τ_{gb}(s) ×10^{-05}	Z′(kΩ)
$Y_3Fe_5O_{12}$	3.119	2.424×10^{-11}	7.5624×10^{-4}	73.069

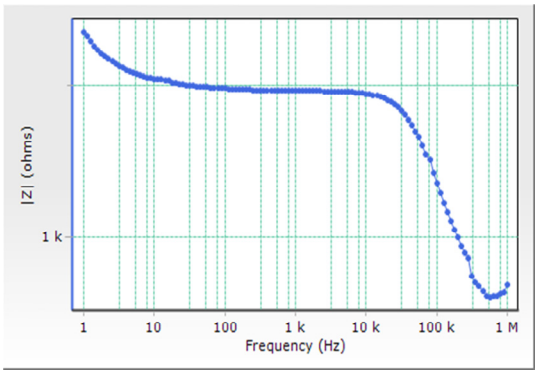

Fig.7. Bode plot of pure YIG

3.4. Electron Spin Resonance (ESR)

Electron spin resonance (ESR) is a powerful tool in the investigation of magnetic properties and spin dynamics in solids. Measurement is made by scanning the magnetic induction (B) at constant microwave frequency (f) in the range of interest. In the present work X-band frequency 9.28 GHz at room temperature is selected. Fig.8 shows the Electron spin resonance of YIG.

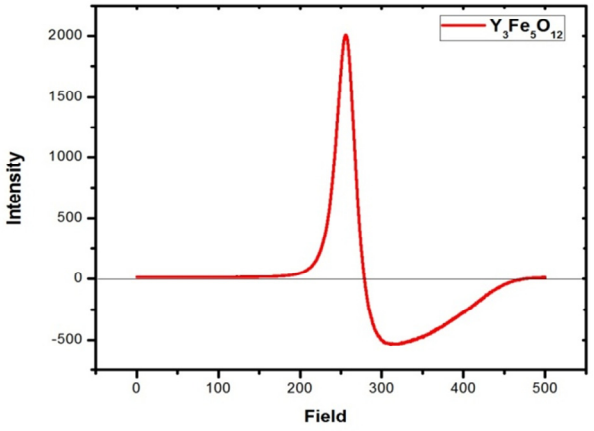

Fig.8. Electron spin resonance of YIG

Usually, the internal magnetic field from magnetic entities is expected to be uniform due to highly ordered magnetic moments at low temperatures; giving rise to narrow ESR line. The parameter g is defined as:

$$g = \frac{h\nu}{\beta B_0}$$

where h is Plank's constant, β is Bohr-magneton, υ is the frequency of operation of the EPR spectrometer and B_0 is the centre of the EPR signal (the resonance magnetic field). The parameter g is found to be 2.6. The interaction of the spins of electrons with adjacent atoms can be related to relaxation time (T) by,

$$\frac{1}{T} = \frac{g\beta\Delta H_{1/2}}{\hbar}$$

where β is Bohr Magneton (9.274 × 10−21 erg G^{-1}), $\Delta H_{1/2}$ is half of peak to peak width [11], the relaxation time (T) is calculated as 1.56E-9. The value of 'g' is mainly contributed by Fe^{3+} ions present at octahedral sites which falls in line with Talwinder et al [11] reported for Barium hexa ferrite. The effective g-value is found to be 2.6 for this sample, which is not in agreement with the g-value of 2.0023 free electrons of typical S state ions. Hence, iron ion in this compound corresponds to high spin ferric (S state) magnetic ion [12].

4. CONCLUSION

Yttrium iron garnet prepared in single phase having cubic structure was confirmed by XRD. From reitveld refinement the difference between the calculated and observed crystalline parameters was minimized and it confirmed the cubic structure with space group Ia-3d. From Impedance Spectroscopy the analysis of Nyquist plots demonstrates the dominant grain boundaries conduction for pure sample and the values of resistance and capacitance from grain boundary is measured. Bode plot depicts the dependence of impedance with respect to frequency. The value of g and narrow linewidth is found from ESR spectra. The properties obtained from impedance and ESR studies enable the prioritization of Yttrium iron garnet for electronic applications.

REFERENCES

1. Wan Fahmin Faiz Wan Ali, Norazharuddin Shah Abdullah, Maslinda Kamarudin, Mohd Fadzil Ain, Zaina Arifin Ahmad, Ceramics International (2016) ,doi.10.1016/j.ceramint.2016.06.004.
2. Majid Niaz Akhtar, Muhammad Azhar Khan,Mukhtar Ahmad, G. Murtaza, R.Raza, S. F. Shaukat, M. H. Asif, Nadeem Nasir, G. Abbas, M. S. Nazir, M. R.Raza, J Magnetism and Magnetic Material, S0304-8853(14)00519-8, doi.10.1016/j.jmmm.2014.06.004.
3. E. J. J.Mallmann, A.S.B.Sombra, J. C. Goes, P. B. A.Fechine, Solid State Phenomena Vol. 202 (2013) pp 65-96, doi:10.4028/SSP.202.65.
4. Wang Minqiang, Zhu Xiangying, Wei Xiaoyong, Zhang Liangying, Yao Xi, Taylor & Francis, ferroelectrics, 5. 2001. Vol. 263. pp. 249-254, doi: 10.1080/00150190108008577.
5. K.Sabri, A.Rais, K.Taibi, M.Moreau, B.Ouddane, A.Addou, Physica B: Physics of Condensed Matter (2016), doi.org/10.1016/j.physb.2016.08.011.
6. S. Anand, A. Persis Amaliya, M. Asisi Janifer, S. Pauline, Modern Electronic Materials(2017),doi.10.1016/j.moem.2017.10.001.
7. Khalid Mujasam Batoo, Physica B 406 (2011) 382–387,doi.10.1016/j.physb.2010.10.075.
8. Dev K. Mahato, Sumit Majumder, S. Banerjee, Applied Surface Science,doi.10.1016/j.apsusc.2017.04.021.
9. A.M.M. Farea, Shalendra Kumar, Khalid Mujasam Batoo, Ali Yousef , Chan Gyu Lee, Alimuddin, Journal of Alloys and Compounds 464 (2008) 361–369, doi:10.1016/j.jallcom.2007.09.126.
10. V. Usha, S. Kalyanaraman, R. Vettumperumal, R. Thangavel, Physica B 504 (2017) 63–68, doi.10.1016/j.physb.2016.10.011.
11. Talwinder Kaur, Jyoti Sharma, Sachin Kumar, and Ajeet K. Srivastava, Cryst. Res. Technol. 2017, 170009, doi: 10.1002/crat.201700098.
12. P.K. Nayak, Materials Chemistry and Physics 112 (2008) 24–26, doi.10.1016/j.matchemphys.2008.05.018.

Available online at www.sciencedirect.com

ScienceDirect

Materials Today: Proceedings 8 (2019) 508–514

materialstoday: PROCEEDINGS

www.materialstoday.com/proceedings

ICMEE 2018

DFT investigations on a Non-Linear Optical crystal L-Valine L-Valinium Perchlorate (LVPCl)

R. Vincent Femilaa[1], M. Victor Antony Raj[1,2] and J. Madhavan[1]*

[1]*Department of Physics, Loyola College, Chennai, India*
[2]*Loyola Institute of Frontier Energy (LIFE), Loyola College, Chennai, India.*

Abstract

Using the density functional theory (DFT), the molecular geometry and vibrational spectrum are predicted with accuracy. Using B3LYP/6-31 (d,p) the vibration frequencies are calculated. Using KBr pellet, the FT-IR spectra of LVPCl is recorded between the range 4000 cm^{-1} to 400 cm^{-1}.The NLO test is performed and a second harmonic efficiency is found to be nearly 2.3 times that of KDP. The single crystals of LVPCl crystal are subjected to thermo gravimetric analysis (TGA) and differential thermal analysis (DTA). To estimate the hardness, Vickers microhardness measurement is carried out on the grown crystal.

Selection and peer-review under responsibility of the scientific committee of the Materials For Energy and Environment.

Keywords: DFT; FT-IR; LVPCl; NLO; TGA; DTA.

1. Introduction

We refer the amino acids to be the building blocks of protein and our genetic information is passed from parent to offspring as the proteins form the structural basis of chromosomes. An essential amino acid is Valine (α-aminoisovalerate) and is derived from alanine by replacing the two methyl groups instead of two H-atoms of the methyl group present on α-carbon atom. An essential amino acid, Valine, is hydrophobic and is generally found in the interior of proteins.

* Corresponding author. Tel.: 9840479638
E-mail address: jmadhavang@yahoo.com

Selection and peer-review under responsibility of the scientific committee of the Materials For Energy and Environment.

By replacing the hydroxyl group with a methyl substituent, the valine differs from the threonine and usually valine is referred as a branched chain amino acid or one of the amino acids with hydrocarbon side chains. To preserve muscle stores of glycogen (a storage form of carbohydrate that can be converted into energy) and to maintain the muscle tissue we require the branched chain amino acids **[1]**. Recently, the interesting materials for NLO applications, complexes of amino acids have been explored. The importance of amino acids in NLO applications is due to the fact of chiral symmetry of all the amino acids and it crystallizes in noncentrosymmetric space groups**.** As the advantages of the organic amino acid and inorganic acid are combined, the optical second harmonic generation (SHG) has got complexes of amino acids with inorganic acids and salts as its promising materials [**2]**. Nonlinear optical materials influence laser technology, optical communication and optical storage technology. New materials exhibiting nonlinear optical (NLO) effects for developing optical devices like optical modulators and frequency-doubling devices have been explored. Attracting attention to the nonlinear optical field, the combination of the high optical nonlinearity and chemical flexibility of organic materials with the good thermal stability and transmittance of inorganic and semiorganic materials has been proposed. Amino acids have the maximum possibility of showing nonlinear optical properties though many materials have nonlinear optical behaviour **[3]**.

2. Experimental Procedure

By slow evaporation method, the material LVPCl is synthesized using stoichiometric ratio of L-Valine and perchloric acid. The solubility data is determined by dissolving the synthesized salt of LVPCl at a constant temperature in 100ml of mixed solvent that contains the double distilled water and acetone. Positive solubility coefficient is exhibited as the solubility of LVPCl increases with the temperature and Fig.1.(a) shows the solubility curve. From the re-crystallization salt, transparent tiny single crystals are obtained. At ambient temperature, seed crystal is placed in its supersaturated solution which is then kept in a bath. In a time of about 50 days, seed crystals are grown to big crystals to a size of about 10 x 7 x 8 mm^3 with good transparency using slow evaporation technique which is clearly shown in Fig.1.(b)

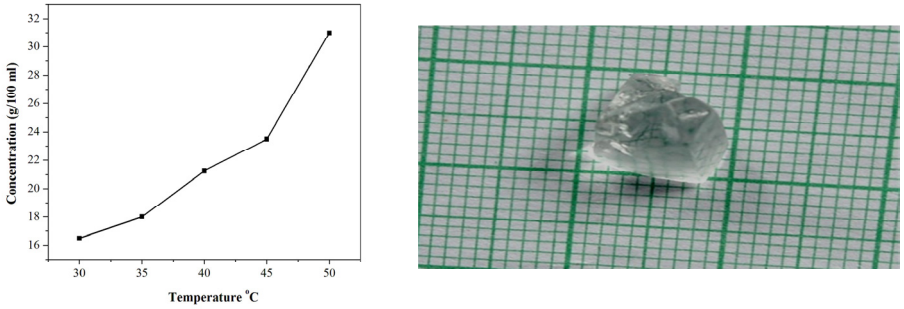

Fig. 1. (a) Solubility curve of LVPCl; (b) Photograph of as grown LVPCl single crystal

3. Characterization

3.1 Computational Details

Using Gaussian'03 program package, the calculations are performed and without constraint the geometries are fully optimized as well. The molecular geometry and vibrational spectrum are predicted with accuracy using the density functional theory (DFT). The lack of imaginary values in the calculated vibration frequencies reveals that the calculations converged to an optimized geometry that corresponds to a true energy minimum after relaxation of

all the parameters. Using B3LYP/6-31 (d,p), the vibration frequencies are calculated. Comparison of vibration mode assignments with the experimental results is performed. Along with the thermodynamic parameters, fundamental vibrational frequencies, the optimized geometrical parameters, IR intensity, reduced mass and force constant are calculated.

3.2 Molecular Geometry

Fig.2. shows the numbering scheme for LVPCl. Table 1 and 2 depicts the calculated optimized structural parameters.

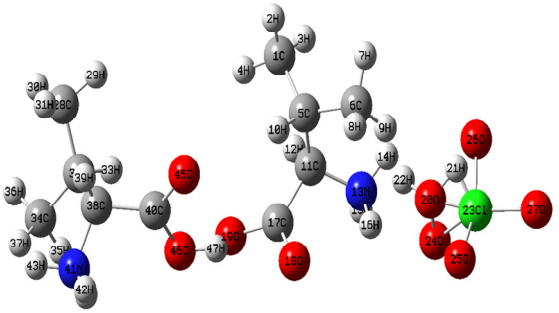

Fig. 2. Atomic numbering system adapted for ab initio computations of LVPCl molecule

Table 1 Selected bond lengths of LVPCl molecule

Atoms	Gaussian(Å)	XRD(Å)
C1-C5	1.54000	1.498
C11-N13	1.47000	1.483
N13-H14	1.00000	1.001
Cl23-O26	1.65000	1.592
C17-O18	1.43000	1.429
C40-O46	1.43000	1.428
O46-H47	0.96000	1.001
Cl23-H21	1.01814	1.015
C28-H31	1.07000	1.091

Table 2 Selected bond angles of LVPCl molecule

Atoms	Gaussian(˚)	XRD(˚)
C1-C5-C6	120.00010	122.025
C5-C11-N13	119.99999	121.256
C17-C11-N13	107.18775	106.189
O26-Cl23-O27	94.46460	94.501
C28-C32-C38	107.18770	107.191
C28-H29-H31	120.0120	119.875
C40-O45-O46	88.1254	87.235
C5-H10-C6	128.2678	127.346

3.3 Vibrational assignments

Using KBr pellet, the FT-IR spectra of LVPCl is recorded on BRUKER IFS 66V FT-IR SPECTROMETER between the range 4000 cm^{-1} to 400 cm^{-1}. Fig.3. shows the observed FT-IR. Table 3 shows the detailed vibrational assignments of fundamental modes of LVPCl along with the FT-IR experimental frequencies, spectral assignments, reduced mass and force constant. LVPCl has got 47 atoms and 135 normal vibrational modes where 91 of these modes are in-plane symmetric (A′) and 44 out-of-plane symmetric (A″) with respect to the reflection on the symmetry plane.

$$\Gamma_{78} = 91\ A'\ (\text{in-plane}) + 44\ A''\ (\text{out-of-plane})\ \text{respectively}$$

On further, we discuss the assignments of wave numbers for different functional groups where the theoretical and experimental wave numbers are in fair agreement.

3.3.1 C – C Vibrations

The region 1625–1400 cm^{-1} and 1380–1280 cm^{-1} has got a semicircle stretching which depicts the ring C=C and C-C stretching vibrations. At 1508 cm^{-1} occurs the C=C stretching vibrations for LVPCl (title molecule). Due to C=C stretching vibrations, the experimental spectrum shows a peak at 1505.1341 cm^{-1}. By the form of substitution around the ring, the actual positions of C-C stretching modes are determined.

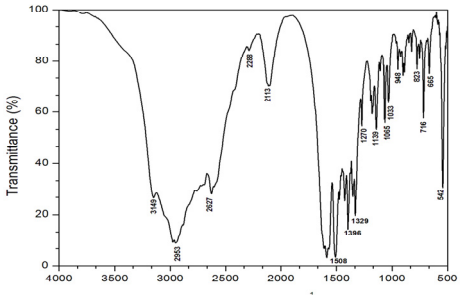

Fig. 3. Experimentally obtained FT-IR spectrum of LVPCl

3.3.2 Nitrogroup vibrations

At 1570–1485 cm^{-1} and 1370–1320 cm^{-1} strong absorptions are found at aromatic nitro compounds due to asymmetric and symmetric stretching vibrations of the nitro group respectively. By B3LYP method, the symmetric NO_2 stretching is observed in IR at the value 1336.8213 cm^{-1} as a medium band and the experimental values with the computed values are found to be good in agreement.

Table 3 Selected Vibrational Assignments of LVPCl molecule

No	FT-IR B3LYP cm^{-1}	Experimental FT-IR cm^{-1}	Reduced mass	Force constant	Assignments
135	3752.0585		1.0660	8.8423	OH st
130	3273.3514	3149	1.1017	6.9552	CH_2 asy st

122	2923.4370	2953	1.0610	5.3425	CH st
109	2681.9047	2627	1.1242	4.7642	CH st
98	2137.2235	2288	1.0554	2.8404	CN st
83	1847.0101	2113	1.1703	2.3522	NH_2 sci
59	1505.1341	1508	1.1811	1.5765	C=C st
51	1386.6427	1396	2.3404	2.6513	CH opb
49	1336.8213	1329	1.9227	2.0245	CO st
45	1267.5543	1270	1.1110	1.0517	OH ipb
43	1139.2063	1139	1.0891	0.8328	CH opb
38	1040.0327	1065	1.2239	0.7800	OH ipb
35	827.5760	823	3.7957	1.5317	CH opb
29	726.2427	716	1.6119	0.5009	CH opb
26	656.8500	665	2.6728	0.6794	NH b
22	557.7985	542	1.4038	0.2573	H_2O
1	60.4825		0.0136	33.5042	NH_2 tor

st-stretching; **asy st**- asymmetry stretching; **sci-** scissoring; **ipb**-in-plane bending; **opb**- out-of-plane bending; **b-** bending; **tor** – torsional.

3.4 Nonlinear optical (NLO) test

Using a Q-switched mode locked Nd: YAG laser of 1064 nm and pulse width 8 ns, the nonlinear optical property of the grown crystal is tested. Through an IR reflector, the input laser beam is passed which is then directed on the microcrystalline powdered sample. The light emitted by the sample is detected using photodiode detector and oscilloscope assembly. The microcrystalline powder KDP is taken as the reference material which evaluates the SHG efficiency of the LVPCl crystal. For KDP and LVPCl samples the SHG signals of 90 mV and 210 mV are obtained respectively for a laser input pulse of 5.6 mJ/pulse. Thus it is concluded that the SHG efficiency of LVPCl is nearly 2.3 times more than that of KDP.

3.5 Thermal analysis

Using STA 409C instrument, the single crystals of LVPCl crystal are subjected to thermo gravimetric analysis (TGA) at a heating rate of 10 K/min (in the nitrogen atmosphere) and differential thermal analysis (DTA) simultaneously. The resulting TGA and DTA trace is shown clearly in Fig. 4. Around 179 °C, a sharp weight loss of the material starts as the material is thermally stable up to 179°C. A sharp endotherm matching with the decomposition of LVPCl is clearly shown in the DTA trace. The quality of the grown crystal is determined from the single stage weight loss of about 94.15%.

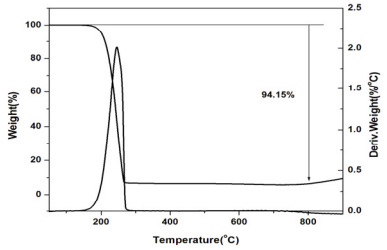

Fig. 4. TG - DTA curves of LVPCl single crystal

3.6 Microhardness test

To estimate the hardness, Vickers microhardness measurement is carried out on the grown crystal. Hardness is a mechanical parameter which relates the structure strongly and composition of solids. It is defined as the motion of dislocations that was against resistance, deformation or damage under an applied stress **[4].** By fitting Vickers microhardness tester with a diamond pyramidal indenter, the microhardness study is performed. At room temperature, the static indentation tests are made on the crystal. For a constant indentation period of 10s, the applied load is varied from 10 to 50 gm. Fig. 5.(a) shows the variation of Hv with the applied load. The graph pointed that the increasing load will have a decrease in the microhardness number to be 2.31. For hard materials n should lies between 1 and 1.6 and for soft materials it should be more than 1.6 according to Onitsch **[5]**. From the plot of log P versus log d by the least square fit method, the value of the 'n' is estimated which is nothing but the work hardening coefficient and is clearly shown is Fig.5.(b). 1.566 is determined to be the value of 'n' and thus it is concluded saying that the grown crystal belongs to the category of hard materials.

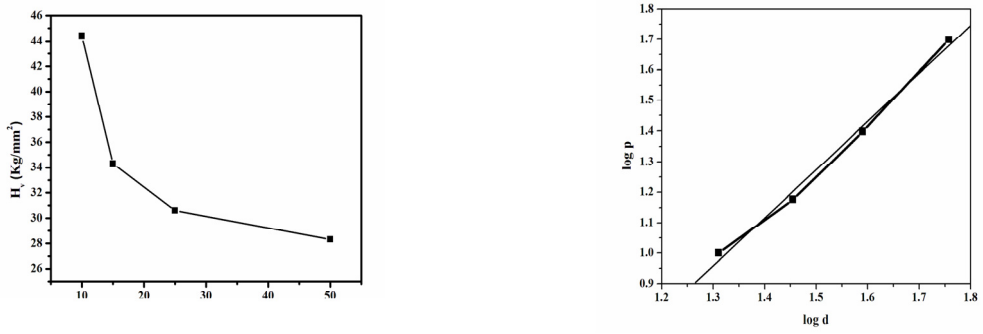

Fig. 5. (a) Vickers hardness number Vs applied load of LVPCl single crystal; (b) log p Vs log d of LVPCl single crystal

4. Conclusion

Using B3LYP/6-31 (d,p) the vibration frequencies are calculated. Comparison of vibration mode assignments with the experimental results is performed. Along with the thermodynamic parameters - the optimized geometrical parameters, fundamental vibrational frequencies, IR intensity, reduced mass and force constant are calculated. By a Q-switched mode locked Nd: YAG laser of 1064 nm and pulse width 8 ns, the nonlinear optical property of the grown crystal is tested. It is concluded that the SHG efficiency of LVPCl is nearly 2.3 times more than that of KDP. From thermal analysis study the quality of the grown crystal is determined from the single stage weight loss of about 94.15%. To estimate the hardness, Vickers microhardness measurement is carried out on the grown crystal. 1.566 is determined to be the value of 'n' and thus it is concluded saying that the grown crystal belongs to the category of hard materials.

Acknowledgements

The authors acknowledge University Grants Commission (UGC), India, for funding this research project-F.No.4-4/2015-16 (MRP/UGC-SERO).

References

[1] S. Pandiarajan, M. Umadevi, R.K. Rajaram, V. Ramakrishnan, Spectrochimica Acta Part A, 62 (2005) 630–636
[2] V.Siva Shankar, R.Siddheswaran, R.Sankar, R.Jayavel, P.Murugakoothan, Materials Letters, 63 (2009) 363–365.
[3] R.Surekha, R.Gunaseelan, P.Sagayaraj and K.Ambujam, Cryst Eng Comm, 16 (2014) 7979–7989.
[4] G. Pasupathi, P. Philominathan, Journal of Minerals and Materials Characterization and Engineering, 11 (2012) 904-907
[5] S. Nalini Jayanthi, A.R. Prabakaran, D. Subashini, K.Thamizharasan, Materials Today: Proceedings, 2 (2015) 1356 – 1363

Available online at www.sciencedirect.com

ScienceDirect

Materials Today: Proceedings 8 (2019) 108–116

materialstoday: PROCEEDINGS

www.materialstoday.com/proceedings

ICMEE 2018

Density Functional Theoretical and Experimental investigation on L - Asparaginium Picrate-a nonlinear optical material

Subaranjani R[a], Madhavan J[a] and Victor Antony Raj M[a,b] *

[a]*Department of Physics, Loyola College, Chennai, India.*
[b]*Loyola Institute of Frontier Energy (LIFE), Loyola College, Chennai, India.*

Abstract

An organic nonlinear optical material, L-Asperginium picrate has been successfully synthesized and by slow evaporation method, good quality single crystal was grown. The structure of LAsP was elucidated using single crystal X-ray diffraction data. For synthesized compound, the functional group was confirmed by FTIR spectral analysis. The thermal stability of the crystal was revealed by Thermogravimetric and differential thermal analyses. Density functional theory(DFT) calculations with B3LYP/6-31G(d, p) basis sets was used to determine ground state molecular geometries, vibrational frequencies The optical properties such as optical band gap and cut off wavelength of the title material were obtained from the UV–visible spectrum, the band gap (E_g) is found to be 4.5eV.

Selection and peer-review under responsibility of the scientific committee of the Materials For Energy and Environment.

Keywords: XRD;FT-IR;DFT;UV-visible

1. INTRODUCTION

Recent advances in organic nonlinear optical (NLO) materials have invoked a large revival of interest in this area of research on account of their widespread industrial potential applications. Purely inorganic nonlinear optical (NLO) materials typically have excellent mechanical and thermal properties, but possess relatively modest optical nonlinearity because of the lack of extended p-electron delocalization [1,2].Picric acid (PA), as an electron acceptor form charge transfer molecular complexes with a number of electron donor compounds such as amines [3–6] through electrostatic or hydrogen bonding interactions.L-Asparaginium picrate LAsP is one such π donor

* Corresponding author. Phone: +91-44-28178200 ; Fax: +91-44-28175566
E-mail address: vicvad2003@yahoo.co.in

Selection and peer-review under responsibility of the scientific committee of the Materials For Energy and Environment.

acceptor molecular compounds in which L-Asperginium acts as donor and picric acid act as an electron acceptor. Both picric acid [7] and L-Asparagine belong to non-centric space groups and possess NLO property. However, the SHG efficiency is low. It was thought that a complex of the above two materials might have a higher SHG efficiency, due to the presence of aromatic ring in the picric acid and the protonated carboxyl group in the amino acid. It was identified as an NLO material and reported recently [8]. The synthesis, elucidation of structure, details of the hydrogen bonding, possible structural features leading to the SHG efficiency, FTIR and UV–vis–NIR studies of the title compound are discussed in this paper.

2. EXPERIMENTAL PROCEDURE

All the starting materials for synthesis of LAsP are purchased as AR grade (purity ≥ 99 %). Equimolar ratio of L-asparagine and picric acid is dissolved in deionized water (1:1). Synthesized salt of LAsP was obtained from the solution by evaporating the solvent and collecting the precipitate formed at the bottom of the container having the solution. Solubility corresponds to saturation i.e. to equilibrium between a solid and its solution at a given temperature and pressure. Thermodynamically, this means that the chemical potential of the pure solid is equal to the chemical potential of the same solute in the saturated solution. The growth rate of a crystal depends on its solubility and temperature. Solubility data of a material govern the amount of material, which is available for the growth and hence, defines the total size limit. Solvent and solubility factors define super saturation, which is the driving force for the rate of crystal growth. Hence, for a material to grow as a crystal, determination of its solubility in a particular solvent is an essential criterion.The synthesized salt of LAsP was further purified by repeated crystallization process. A 250 ml glass beaker containing 100 ml of deionized water was placed in the temperature bath. The initial temperature of the bath was set at 30°C. The beaker was closed with an acrylic sheet containing a hole at the center through which a spindle from an electric motor, placed on the top of the sheet was introduced into the solution. A Teflon paddle was attached at the end of the rod for stirring the solution. The synthesized salt was added in small amounts and stirring of the solution by a motorized stirrer was continued till the formation of precipitate, which confirmed the saturation of the solution. After attaining saturation, the equilibrium concentration of the solution was analyzed gravimetrically. A 20 ml of the clear supernatant liquid was withdrawn by means of a warmed pipette and the same was poured into a clean, dry and weighed empty petri dish. The solution was then kept for slow evaporation in a heating mantle till the solvent was completely evaporated. The mass of LAsP in 20 ml of solution was determined by weighing the petri dish with salt and hence the amount of LAsP salt (in gram) dissolved in 100 ml of water was determined. The same procedure was repeated for various temperatures 30, 35, 40, 45 and 50°C and the solubility of LAsP was estimated. Fig 1(a) shows the solubility curve of LAsP. By seeding the supersaturated solution and evaporating the solvent, good optical quality crystal of dimesion upto 12 X 4 x 5 mm^3 were harvested after the period of 35 to 40 days. The photograph of as grown crystal LAsP shown in fig 1 (b).

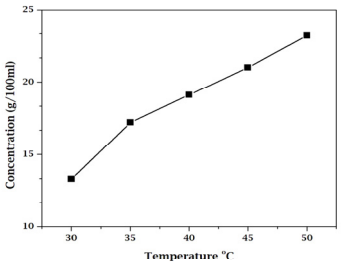

Fig. 1.(a) Solubility curve of LAsP

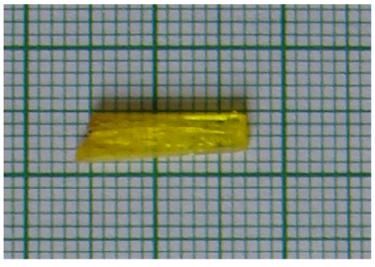

Fig.1 (b) Photograph of as grown LAsP single crystal

3. RESULT AND DISCUSSION

3.1 X-ray diffraction analysis

X-ray diffraction analysis was carried out for the identification of the synthesized crystal using an X-ray diffractometer, MODEL RICHSEIFERT, XRD 3000P with monochromatic nickel filtered Cu K_α (λ = 0.15406 nm) radiation. The sample was scanned over the range 10 - 40° at the rate of one degree/minute. Experimentally recorded XRD pattern of LAsP single crystal is given in Fig 2 (a).Theoretically Simulated XRD pattern of LAsP single crystal is given in Fig 2.(b). The crystal data and structural refinement data are given in Table 1.

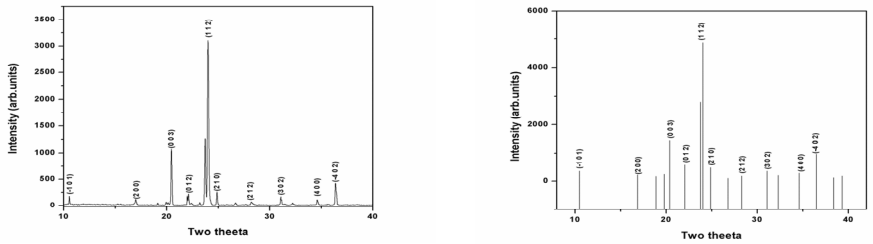

Fig 2.(a) Experimentally obtained XRD pattern of LAsP and Fig 2(b) Theoretically simulated XRD pattern of LAsP

Table 1 crystal parameters of LAsP

Embrical Formula	$C_{10}H_{11}N_5O_{10}1$	
Formula Weight	361.21	
Wave length	0.71073Å	
Crystal system ,space group	Monoclinic P_{21}	
Unit cell dimensions	A=10.365Å	$\alpha = \gamma = 90^\circ$
	B=5.1618Å	$\beta = 93.24^\circ$
	C=13.122Å	
Cell volume	702.05399Å^3	

3.2 Computational details

Density Functional Theory with Beckee-3-Lee-Yag-Parr (B3LYP) combined with 631G(d, p) basis set is used to find the parameters. The fundamental vibrational frequencies, IR intensity and force constants were calculated using the Gaussian 03 package [10]. The first task of the computational work was to determine the optimized geometry. All the parameters are allowed to relax and all the calculations converged to an optimized geometry which corresponds to a true energy minimum as revealed by the lack of imaginary values in the calculated vibrational frequencies. The defined coordinates form complete set and matches quite well with the motions observed using GAUSSVIEW program.

3.3 Molecular geometry and Vibrational analysis

The molecular structure along with numbering of atoms of LAsP is as shown in Fig.3(a). The vibrational spectral analysis of LAsP crystal is performed on the basis of the characteristic vibrations of several functional groups such as amino group, carbonyl group modes. The calculated vibrational wavenumbers and the atomic displacement corresponding to the different normal modes are used for identifying the vibrational modes unambiguously The present work describes the vibrational spectral studies of LAsP molecule. In order to qualitatively analyse the presence of functional groups in LAsP, FT-IR spectrum of the grown crystal was recorded in the range 500 cm^{-1} to 4000 cm^{-1}, using KBr pellet technique on BRUKER IFS FT-IR Spectrometer. Recorded FT-IR spectrum of the LAsP molecule is shown in Fig 3(b). Selected vibrational assignments of LAsP for the experimental FT-IR frequencies along with the calculated frequencies are tabulated in Table 2.

.

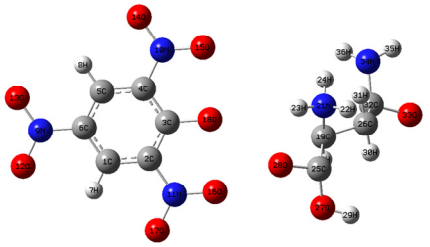

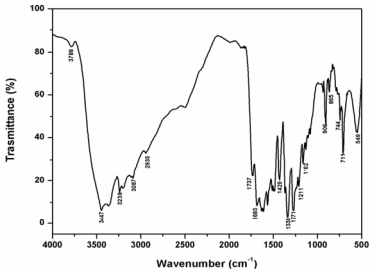

Fig .3 (a)Atomic numbering system adapted for ab initio computations of LAsP molecule and Fig .3 (b) Experimentally obtained FT-IR spectrum of LAsP

3.3.1 C-H Vibrations

Presence of band in the region 2700–3000cm^{-1} is the characteristic region for the identification of C–H stretching vibrations [11]. The C-H vibrations are around 2800cm^{-1} for LAsP molecule. The experimental C–H vibrations are in good agreement with theoretical vibrations For LAsP molecule prominent number of CH in plane bending vibrations are obtained at frequencies 1429,1271 and 1162cm^{-1}. The absorption bands arising from C–H out-of-plane bending vibrations are usually observed in the region at 1000–675 cm^{-1} [12]. The C–H out-of-plane bending vibrations for LAsP are observed as medium bands in FTIR spectrum at 906, 865, 744 and 711 cm^{-1}.

3.3.2 C-C Vibrations

The carbon–carbon stretching modes of the phenyl group are expected in the range from 1650 to 1200 cm^{-1}. The actual position of these modes is determined not so much by the nature of the substituents but by the form of substitution around the ring [13]. In general, the bands are of variable intensity and are observed at 2240–2030, 1765–1625, 1460–1310 $cm^{-1}$for LAsP molecule. The in-plane deformations are at higher frequencies than the out-of-plane vibrations. For this title molecule C-C in plane bending vibrations is plane bending vibrations is observed at 549cm^{-1}.

Table. 2. Selected Vibrational Assignments of LAsP molecule

No	Frequency cm^{-1}		Spectroscopic assignment	Force constant	Reduced mass
	B3LYP	Experimental			
102	4304.8635	-	CC st	11.029	1.0101
99	3790.6997	3788	NH_2symst	9.2935	1.0977
94	3489.8461	3447	NH_2symst	7.3726	1.0890
86	3255.1609	3239	CH_2asyst	6.7871	1.0871
84	3084.9343	3087	CH st	6.2451	1.0924
81	2947.1815	2935	CH st in CH_3	5.6849	1.1109
62	1749.9298	1737	C =O st	2.2562	1.2505
59	1474.7202	1429	CH ipb	2.4421	1.9059
55	1339.1812	1338	CH_3 sym de	1.8852	1.7068
42	1271.3736	1271	CH ipb	1.0695	1.1230
35	1232.5695	1211	CH ipb+NH_2 roc	1.4962	1.6715
26	1176.8658	1162	CH ipb	1.5071	1.8469
23	986.0382	906	CH opb	1.2132	2.1178
20	863.1166	865	CHopb	0.5498	1.2527
17	737.0078	744	CH opb	0.5468	1.7086
15	713.2664	711	CH opb	1.3051	4.3542
11	557.6624	549	C-C ipb	0.5823	3.1780
1	51.9664	-	CH_3 tor	0.0088	5.5569

3.4*Hyperpolarizability studies*

Theoretical determination of hyperpolarizability provides a guideline to experimentalists for the design and synthesis of organic NLO materials. Nonlinearity in organic chromophores can be synthetically modulated by varying the composition or length of conjugated p-systems, and by evaluating the effects of various electron-donor and electron-acceptor groups. First order hyperpolarizability values of LAsP are given in table 3

Table. 3. Hyperpolarasibility of LAsP in esu

Hyperpolarasibility in esu	
β_{XXX}	312.8102596
β_{XXY}	239.1859887
β_{XYY}	140.4088875
β_{YYY}	30.8112495
β_{XXZ}	614.0092547
β_{XYZ}	271.2546683
β_{YYZ}	175.2584435
β_{XZZ}	719.6000286
β_{YZZ}	315.7385443
β_{ZZZ}	499.6161224
β_{tot}	$15.3863^{x}10^{-30}$

3.5 Homo-lumo gap

In order to evaluate the energetic behavior of LAsP, the energies of HOMO and LUMO their orbital energy gaps using B3LYP/ 6-31 G (d, p) and shown in Fig 4. The electronic absorption corresponds to the transition from the ground to the first excited state and is mainly described by one electron excitation from the highest occupied molecular orbital (HOMO) to the lowest unoccupied molecular orbital (LUMO). The energy gap is found to be -0.192 a.u (5.225 eV). The analysis of the wave function indicates that the electronic absorption corresponds to the transition from the ground to the first excited state and it is mainly described by one-electron excitation from the HOMO to the LUMO.

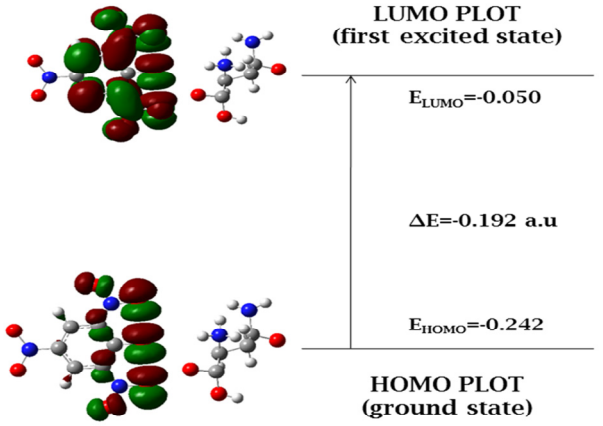

Fig 4 HOMO–LUMO plot of LAsP molecule

3.6 Theoretical Thermo-dynamical properties

The standard statistical thermodynamic functions at B3LYP/631G (d, p) level such as heat capacity $C_P{}^0m$, entropy S^0m and enthalpy changesΔH^0m for the title compound are obtained from the theoretical wavenumbers This shows that these thermodynamic functions are increasing with temperature ranging from 100 to 1000 K due to the fact that the vibrational band intensities increases with temperature [14].

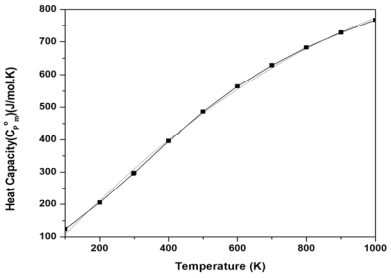

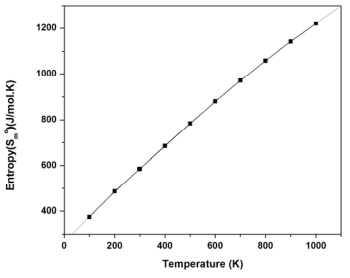

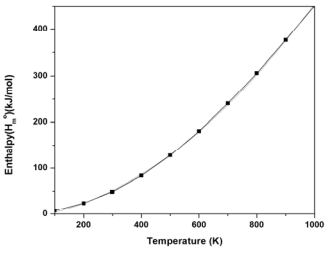

Fig 5 (a) Correlation graph of heat capacity and temperature of LAsP ; Fig 5 (b) Correlation graph of entropy and temperature of LAsP ; Fig 5 (c) Correlation graph of enthalpy and temperature of LAsP

3.7 Uv-vis study

The optical absorption spectrum of the grown crystal LAsP was recorded using VARIAN CARY 5E model spectrophotometer. in the wavelength range from200 and 1100nm. The recorded spectrum is shown in Fig.6(a) . The spectrum exhibits the strong absorption peak at 240nm. The cut-off wavelength as observed from the absorption spectrum is 240 nm. Interestingly, in the entire visible region the crystal has almost less than 0.2 unit of absorption. Using Tauc relation a graph was plotted to estimate the band gap values Fig 6 (b). From this graph, the band gap (E_g)of LAsP is found to be 4.5 eV.

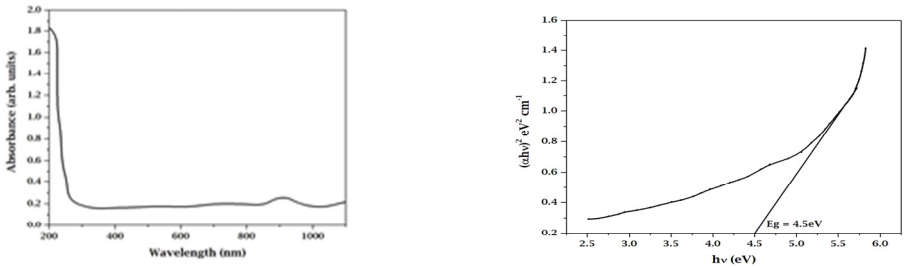

Fig .6.(a)Optical Absorption spectrum of LAsP and Fig.6 (b). Energy band gap of LAsP

3.8 Nonlinear optical (NLO) test

The NLO property of grown crystals **LAsP** was studied by Kurtz and Perry [15]. by passing the output of first harmonic generation laser beam of wavelength 1064 nm The powder sample, with an average particle Size of 100-150 μm was illuminated using a Q-switched mode-locked Nd^{3+}:YAG laser of pulse width 8ns and a wavelength of 1064 nm and 10 Hz When a laser input of 6mJ was passed through LAsP, second harmonic signal of 3.6 V is produced and the experiment confirms a second harmonic efficiency of nearly 65.4 times that of KDP (55 mV). Thus SHG efficiency of LAsP sample is comparable with other promising amino acid based NLO crystals.

3.9. *Experimental Thermal Analysis*

Before using any crystal for device fabrication we should know about the thermal stability of that crystal. Thermo dynamical properties of a material helps device manufacturer to understand the suitability of the material for the required device. Molecular motion in the synthesized material alters and controls the thermo dynamical parameters. The interaction among atoms in the molecule and bonding scenario with in the molecule is also a deciding factor of the thermal properties of the material. So it is very important to check the thermal stability of the grown crystals from the various application points of view. The thermal expansion, specific heat and thermal conductivity are the main properties for lasers and high power systems therefore many researcher and scientists tried to grow the single crystal of various materials with high thermal stability and still searching good one The TGA and DTA thermo gram of LAsP crystal is shown in Fig 7. From the TGA curve it is clear that the material is stable up to 175°C. In TGA, decomposition takes place at175°C as the first stage. It goes up to 320°C which may be due to the loss of C_2H_4 and $2CO_2$, resulting in a loss of weight of 55.26%. Another weight loss of 18.93% at the second stage, noticed between the temperatures 320–500°C. The next stage of decomposition results in a loss of 25.49% between the temperature range 500-840°C is due to the release of CO_2. The residue that remains after 900 °C is 0.32% and it is negligible. The sharp DTA peaks are attributed to the decomposition of the material, which match well with the first and second stage of decomposition in the TGA curve respectively.

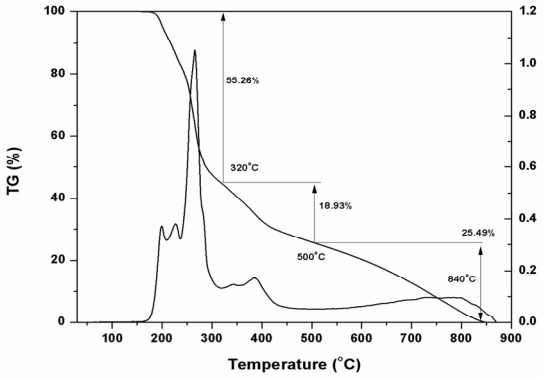

Fig. 7: TG-DTA curves of LAsP single crystal

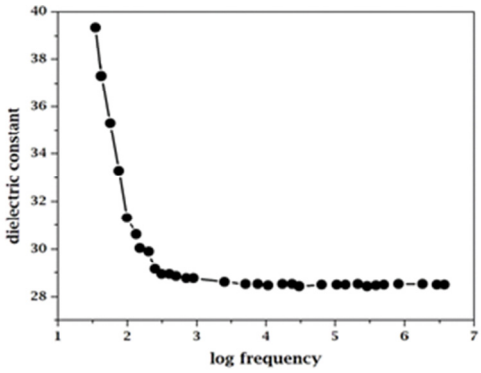

Fig. 8.(a) Variation of dielectric constant of LAsP

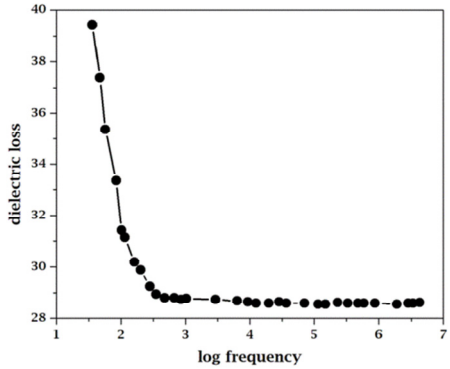

Fig. (b) Variation of dielectric loss of LAsP

The space charge, ionic, orientation and atomic polarizations are all active at low frequency. With increasing frequency, the dielectric loss and dielectric permittivity values decrease which depend on the excitation of bound electrons, lattice vibrations, dipole orientations and space charge polarizations. The contribution of space charge depends upon the purity and perfection of the crystal. Most of the solid electrolytes have high dielectric constant [19]. The dielectric constant and dielectric loss are calculated using the equations, $\varepsilon_r = Cd/\varepsilon_o A$, where A is the area of the sample and d is the thickness of the sample. The relative permittivity (ε_r) is usually known as permittivity. The frequency dependence of the dielectric constant is shown in Fig 8(a), Fig 8 (b) shows the exponential decrease of dielectric loss of LAsP as a function of frequency along (001) orientation. The low value of dielectric loss indicates that the grown crystals are good in quality .

4. CONCLUSION

Good quality single crystals of L-Asperginium picrate (LAsP) were grown by the slow evaporation solution growth technique. The lattice parameters were confirmed using powder crystal X-ray diffraction analysis. Optimized structure of the isolated LAsP molecule obtained by DFT calculations give the minimum energy state. First order hyperpolarizability of LAsP is calculated as 15.3863×10^{-30} esu,it is due to the π electron cloud movement from donor to acceptor which makes the molecule highly polarized and the intermolecular charge transfer interaction which is justified by the FTIR spectrum. Frontier molecular orbital analysis gives the HOMO-LUMO energy gap value as 5.225 eV. The optical studies reveal that the crystal has very low absorption in the entire visible and infrared region, with the lower UV cut off around 240 nm, which is an essential consideration for NLO crystals. The optical band gap of the material is found as 4.5 eV. The Kurtz SHG test shows that the grown crystal has its SHG efficiency 65.4 times that of KDP. The frequency dependence of the dielectric constant and dielectric loss of LAsP are investigated.

References

[1] M.H. Jiang, Q. Fang, Adv. Mater. 11 (1999) 1147.
[2] M.D. Aggarwal, J. Choi, W.S. Wang, K. Bhat, R.B. Lal, A.D. Shields, B.G. Penn, D.V. Frazier, J. Cryst. Growth 179 (1999) 2004.
[3] C.Muthamizhchelvan,K.Saminathan,J.Fraanje,R.Peschar,K.Sivakumar,XrayStruct.Anal.Online21(2005) x61–x62
[4] K.Saminathan,J.Fraanje,R.Peschar,K.Sivakumar, , Acta Cryst.E61(2005)o1153–o1155.
[5] C.Muthamizhchelvan, K.Saminathan, K.SethuSankar, K.Sivakumar, ActaCryst.E61 (2005)o3605–o3607.
[6] K.Muthu,SubbiahMeenakshisundaram, ,J.Cryst.Growth352(2012)163–166
[7] P. Srinivasan, T. Gunasekaran, T. Kanagasekaran, R. Gopalakrishnan,P. Ramasamy, J. Cryst. Growth 289 (2006) 639.
[8] P. Srinivasan, T. Kanagasekaran, R. Gopalakrishnan, G. Bhavannarayana,P. Ramasamy, Cryst. Growth Des. 6 (2006) 1663.
[9] K. Anitha,S.Athimoolam,R.K.Rajaram ,ActaCrystal- logr.E61(2005)o1463–o1465,ISSN1600-5368.
[10] Frisch M.J, Trucks G.W et al, Gaussian 03, Revision C.02, Gaussian Inc.,Wallingford, CT, 2004.
[11] Shanmugam, Sathyanarayana.,Spectrochim. Acta., 40A (1984) 757.
[12] Colthup N.B, L.H. Daly, S.E. Wiberley.,., Academic Press, New York, 1990.
[13] Bellamy. L. J et al Bellamy L.J., The IR spectra of Complex Molecules., John Wiley and Sons, NY, 1975.
[14] Ott J.B.,Goates J.B., Chemical Thermodynamics: Principles and Applications, Academic Press, San Diego, 2000
[15] Kurtz SK, Perry TT. J Appl Phys 1968;39:3798.
[16] Li Keyan, Wang Xingtao, Zhang Fangfang, Xue Dongfeng. Phys Rev Lett 2008; 100:235504.
[17] Bent Charles J, Gnanm FD. J Mater Sci Lett 1990;9:165.
[18] Onitsch E.M., 'The present status of testing the hardness of materials'., Mikroskopie, 95(1956) 12
[19] Madhavan J, Aruna S, Thomas P C, Vimalan M, Rajasekar S. A, Sagayaraj P., *Cryst. Res Tech* 42(2007), 59-64.

Available online at www.sciencedirect.com

ScienceDirect

Materials Today: Proceedings 8 (2019) 239–244

materialstoday: PROCEEDINGS

www.materialstoday.com/proceedings

ICMEE 2018

Plasmon (Al) Impregnated Sno_2/Tio_2 and Zno/Tio_2 Nanocomposites as Efficient Photoelectrodes for Dsscs – a Relative Analysis

B. Praveen[a], K. Pugazhendhi[a], J. Sahaya Selva Mary[a], S. Padmaja[a], E. Merlin Arnold[a], J. Madhavan[a] and J. Merline Shyla[a]*

[a*]*Department of Physics, Energy Nanotechnology Centre (ENTeC), Loyola Institute of Frontier Energy (LIFE), Loyola College, Chennai 600034, India.*

Abstract

We report herein a relative analysis of plasmon (Al) impregnated SnO_2/TiO_2 and ZnO/TiO_2 nanocomposite systems synthesized using sol-gel method. The properties of the Al-SnO_2/TiO_2 and Al-ZnO/TiO_2 have been studied using various characterisation techniques such as XRD, EDAX, FESEM, UV-DRS, and Photoconductivity techniques. The elemental composition and phase structures of the as-synthesized Al-SnO_2/TiO_2 and Al-ZnO/TiO_2 nanocomposites were investigated using Energy Dispersive X-Ray (EDAX) and X-Ray Diffraction (XRD), which showed high degree of purity and crystallinity respectively. The crystallite sizes estimated with Scherrer's formula were about 24 and 22 nm respectively. The FESEM images revealed that, both the samples were mesoporous in nature. The optical properties of both Al-SnO_2/TiO_2 and Al-ZnO/TiO_2 samples exhibited strong absorption and diffused reflectance which suggested the possibility of the samples being used as photoelectrodes and the band gap value was found to be 3.38 eV and 3.07 eV using Kubelka-Munk plot. The photoconductivity studies suggested that Al-SnO_2/TiO_2 showed higher photo current values in reference to the Al-ZnO/TiO_2 nanocomposite. Upon overall comparison, it is concluded that the Al doped SnO_2/TiO_2 exhibited enhanced characteristics over that of Al-ZnO/TiO_2 nanocomposite and hence could be applied as efficient photoelectrodes for DSSCs.

Selection and peer-review under responsibility of the scientific committee of the Materials For Energy and Environment.

Keywords: Plasmon impregnation, Sol-gel, UV-DRS, Photoconductivity, photoelectrodes.

* Corresponding author. Phone: +91- 94442 39551; Fax: +91- 44-28175566
E-mail address: jmshyla@gmail.com

Selection and peer-review under responsibility of the scientific committee of the Materials For Energy and Environment.

1. Introduction

Recent works have been focused on nanoparticles which find various technological applications in areas such as ceramics, semiconductors, electronic, magnetic and optical properties compared with bulk materials [1]. Among various semiconductors, Zinc Oxide, Tin Oxide and Titanium dioxide have aroused considerable attention due to their potential applications such as catalysis, drug delivery, gas sensing, and lithium-ion batteries. Modification of optical properties of SnO_2/TiO_2 and ZnO/TiO_2 nanocomposites has proven to be an effective way to improve the photocatalytic activity as it contributes for the decrease in recombination (hole-electron pair formation) rate of photogenerated charge carriers. Localized Surface Plasmon Resonance (LSPR) can occur in properly designed nanostructures in which confined free electrons oscillate with the same frequency as the incident radiation and eventually enter resonance, giving rise to intense, highly localized electromagnetic fields [2]. In this regard, Aluminium is capable of being an alternative plasmonic material compared to conventional gold and silver nanostructures offering new approaches, such as access to high energy regions of the spectrum, low-cost and sustainable material. In the present work, Al-SnO_2/TiO_2 and Al-ZnO/TiO_2 nanocomposites were successfully synthesized via a facile sol-gel route and a detailed investigation of the changes arising in the structural, morphological and opto-electrical properties of the former upon plasmon (Al) impregnation is performed with a view to estimate its performance as an efficient photoanode in DSSCs.

2. Experimental Setup

2.1 Synthesis procedure of Al doped SnO_2/TiO_2 nanocomposite

For the formation of SnO_2/TiO_2 nanocomposite, an amount of $SnCl_2.2H_2O$ (Stannous Chloride) precursor was added along with oxalic acid (1.2607g), deionised water (10 ml) and iso-propyl alcohol (10 ml) and stirred for 30 minutes. The impregnation is achieved by adding 0.024 g of Al (1%) with 10 ml of distilled water, stirring for 15 minutes and mixing with the SnO_2 precursor solution. Later, 10 ml of ammonia is added dropwise to the above solution to tune the pH of the solution. Then commercially available TiO_2 (Degussa P25) powder was mixed with 10 ml of deionised water in a mild stirring process. The resultant solution was ultrasonicated for 30 minutes. Further the solution was stirred for 24 hours and later washed several times with distilled water and then filtered using filter paper. The obtained powder was loaded in the furnace and calcinated at 400^{o}C for 4 hrs to obtain of Al-SnO_2/TiO_2 nanocomposite [3].

2.2 Synthesis procedure of Al doped ZnO/TiO_2 nanocomposite

For the synthesis of Al-ZnO/TiO_2 nanocomposite, 2.195g of Zinc Acetate dehydrate is added to 10mL of ethanol. 0.072g of Al (3%) is added with 10mL of distilled water and stirred for 0.25h before being added to the prepared Zinc Acetate Dehydrate solution. Few grams of TiO_2 (Degussa P25) is added to 10mL of de-ionized water and then added to the Zinc Acetate dehydrate solution prepared earlier. The pH value of the mixture solution is tuned to 8.0 using NaOH solution. Before being mixed together, the precursors with respective solvents are stirred for 0.5h. The solution is stirred continuously for 12h and then left undisturbed for 7h. The sediment is carefully isolated and washed with 20mL of ethanol and the process is repeated several times. Subsequent to this process it is filtered and kept in furnace at 120^{o}C for 12h to obtain nanocomposite powder. The powder is calcined at 500^{o}C for 1h to obtain the final product.

3. Results and Discussion

3.1 XRD Analysis

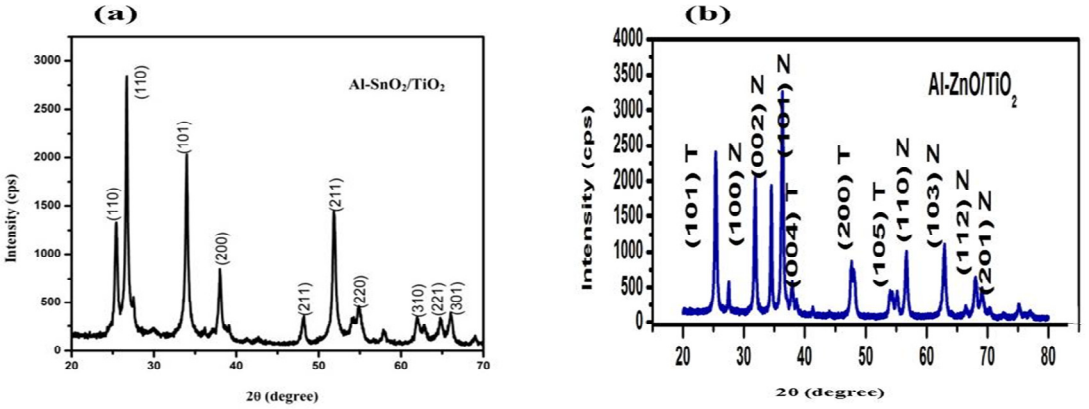

Fig. 1 XRD patterns of (a) Al-SnO_2/TiO_2 and (b) Al-ZnO/TiO_2 nanocomposites

Fig 1(a) shows the XRD pattern of Al-SnO_2/TiO_2 and it can be clearly observed that the major peaks with 2θ values of 27.46^0 34.14^0, 38.22^0, 48.77^0 and 51.57^0 corresponding to (h k l) planes (110), (101), (200), (211) and (211) which are consistent with rutile and anatase phases of the TiO_2 (JCPDS #88-1175) [4] and the observed peaks at 55.650^0, 63.140^0, 65.290^0 and 67.140^0 correspond to (h k l) planes (220), (310), (221) and (301) which are consistent with the JCPDSvalue (78-1063) [5] of the SnO_2 with tetragonal phase respectively.

From the XRD pattern of the Al-ZnO/TiO_2 nanocomposite shown in Fig 1(b), it is found that the characteristic diffraction peaks corresponding to the crystallographic planes (denoted as Z) are consistent with standard hexagonal wurtzite ZnO patterns of JCPDS card no. 36-1451[6], while the peaks corresponding to the crystallographic planes (denoted as T) matched well with the standard anatase TiO_2 patterns of JCPDS card no. 84-1286[7]. In both the cases the XRD pattern of Al impregnation is absent, probably due to the lower concentration of Al in the nanocomposite.

3.2 FESEM Analysis

Morphologies of the as-synthesized nanoparticles were observed using FEI quanta 200 FEG Field Emission Scanning Electron Microscopy (FESEM). FESEM images of the Al doped SnO_2/TiO_2 nanocomposite samples are as shown in the Fig 2. From the FESEM images it is clearly observed that there is formation of cluster like spherical shape and also that the particles tend to agglomerate which could be due to the combination of SnO_2/TiO_2 nanoparticles in the samples [8]. The average particle size was found to be ~ 18 nm for Al-SnO_2/TiO_2 nanocomposite.

Fig. 3 shows the FESEM micrographs of Al-ZnO/TiO_2 nanocomposite particles with uniform size distribution and the average particle size of ~25nm, which also revealed the mesoporous nature of the nanocomposites.

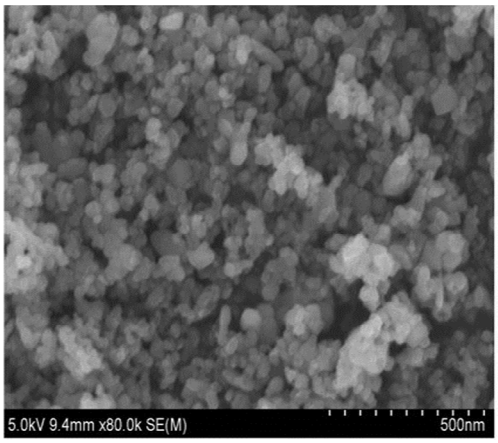

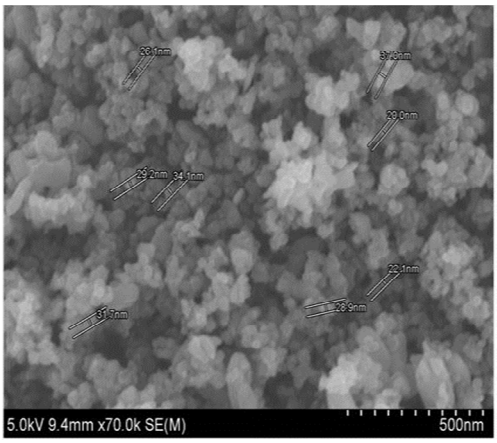

Fig. 2 FESEM images of Al doped SnO_2/TiO_2 nanocomposite Fig. 3 FESEM images of Al doped ZnO/TiO_2 nanocomposite

3.3 Ultraviolet Visible Diffuse Reflectance Spectroscopy (UV- DRS) Studies

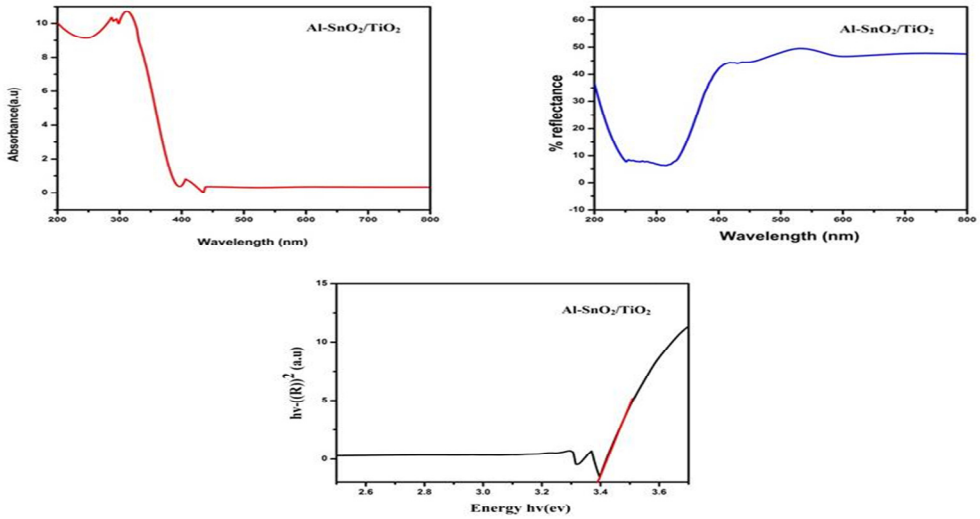

Fig. 4 UV-Vis (a) Absorption spectrum (b) Diffuse Reflectance Spectrum and (c) Kubelka-Munk transformed reflectance spectrum of Al-SnO_2/TiO_2 nanocomposite

The absorption spectrum, diffused reflectance spectrum and Kubelka-Munk plot of the Al doped SnO_2/TiO_2 nanocomposites are presented in Fig 4. Here the reflectance maximum was observed around 335 nm and also the occurrence of multiple peaks centered at 600 and 450 nm was noticed. The band gap value for this sample estimated using K-M plot was about 3.38 eV. [9]. The absorption spectrum reveals the maximum absorption around 345 nm possibly due to the surface plasmon resonance of the sample owing to the featured presence of metal nanoparticles in the sample.

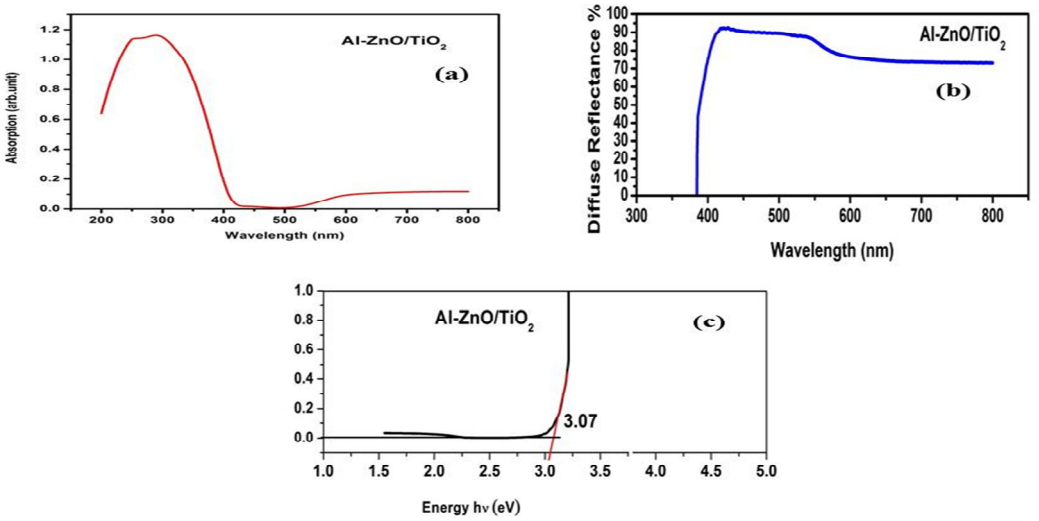

Fig. 5 UV-Vis (a) Absorption spectrum (b) Diffuse reflectance spectrum and (c) Kubelka-Munk transformed reflectance spectrum of Al-ZnO/TiO_2 nanocomposite

Fig 5 shows the absorption spectrum, diffused reflectance spectrum and Kubelka-Munk plot of the Al doped ZnO/TiO_2 nanocomposite. Here the reflectance maximum was observed around 485 nm and also the occurrence of multiple peaks centered at 550 and 400 nm was noticed. The absorption spectrum reveals the maximum absorption around 315 nm. The optical band gaps of the samples were calculated by plotting Kubelka-Munk function $[F(R)\ h\nu]^2$ versus incident photon energy ($h\nu$). The bandgap was found to be 3.07eV for Al-ZnO/TiO_2 nanocomposite. The lower bandgap of Al-ZnO/TiO_2 nanocomposite compared to the Al-SnO_2/TiO_2 is due to the extended absorption resulting from the occurrence of red shift [10] which is an essential condition for high light absorbing and improve the power conversion efficiency (PCE). The maximum of absorption recorded in Al-SnO_2/TiO_2 nanocomposite qualifies it as an efficient photoanode for DSSCs.

3.4 Field dependent photoconductivity analysis

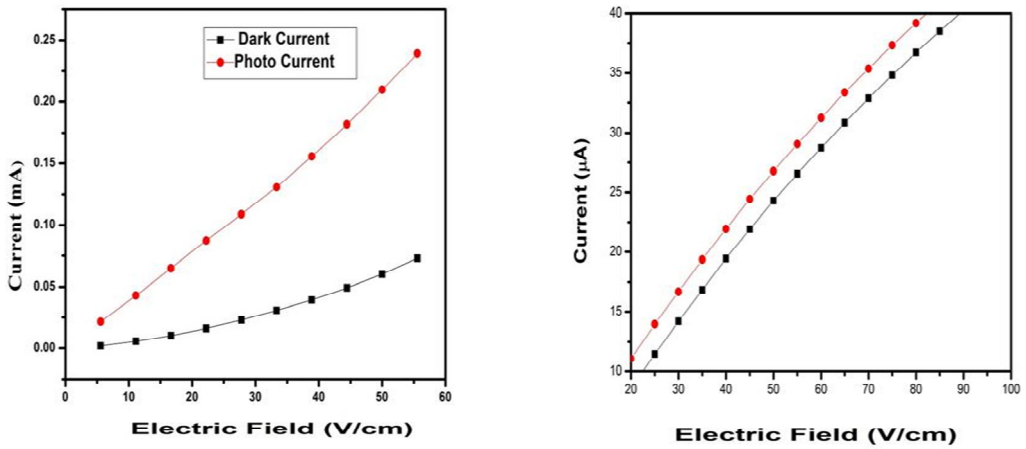

Fig. 6 Field dependent dark and photoconductivity of Al-SnO_2/TiO_2 and (b) Al-ZnO/TiO_2 nanocomposites

The field dependent dark and photoconductivity studies are carried out using 2450 SOURCE METER for understanding the photoconduction behaviour of the as-synthesized samples. The variation of dark and photoconductivity of Al-SnO_2/TiO_2 and Al-ZnO/TiO_2 nanocomposites with applied field is shown in Fig 6. Both the plots indicate linear increase of current in the dark and visible light illuminated samples with increasing applied field depicting the ohmic nature of the contacts.

The samples recorded very high values of dark and photocurrent in the order of mA for Al-SnO_2/TiO_2 and μA for Al-ZnO/TiO_2 respectively, depicting the superior photoconducting capability of the samples which is highly desirable for DSSC applications [11]. In comparison to the Al-ZnO/TiO_2 nanocomposite, the Al-SnO_2/TiO_2 composite exhibits significantly enhanced photoconductivity which could have boosted the light scattering ability of the sample and thereby the photocurrent. This is attributed to the fact that Al plasmons exhibit optimistic behaviours such as improved photoconductivity and plasmonic enhancement [12]. For a fixed field of 50 V/cm, Al-SnO_2/TiO_2 showed photo currents of 2 folds higher magnitude than Al-ZnO/TiO_2 nanocomposite.

4. Conclusions

Al-SnO_2/TiO_2 and Al-ZnO//TiO_2 nanocomposites were successfully synthesized via a facile sol-gel route. The XRD patterns of the composites depicted the characteristic peaks of ZnO, SnO_2 and TiO_2 in both the cases. The average crystallite size of the samples estimated using Scherrer's formula is about 24 and 22 nm, respectively. Surface morphology of the samples studied with FESEM suggested formation of cluster like spherical nanoparticles. The particle size calculated from FESEM images indicates a decrement in Al-SnO_2/TiO_2 nanocomposite making it superior in optical and surface properties. UV-Visible DRS studies revealed the enhanced optical properties of the samples. The band gap of the samples found from K-M plots describe that the Al-SnO_2/TiO_2 nanocomposite possessed higher value anticipated from FESEM results. The field dependent dark and photo conductivity studies portrayed the ohmic nature of the samples in the present study. The Al-SnO_2/TiO_2 sample showed better photo current, manifested by an increase of 2 folds than the Al-ZnO/TiO_2 nanocomposite. The studies strongly suggest that the Al impregnated SnO_2/TiO_2 nanocomposites are highly potential photoanode materials for DSSCs.

Acknowledgements

This work was funded by the Loyola College-Times of India Major Research Grants (6LCTOI14LIF002) and the authors would like to acknowledge the same.

References

[1] N. Sriharan and D. Sridhar, International Journal of Science and Research (IJSR), 2319-7064, 3.358 (2012)
[2] Zhaoyang Liu and Darren Delai Sun, Nano Lett, 7, 4 (2007)
[3] Lin-Rui Hou et al, Journal of Hazardous Materials (2007)
[4] V. Chandrakala and J. Merline Shyla, International Journal of Latest Research in Engineering and Technology, 2454-5031, 32-35 (2016)
[5] M. Marikkannan and V. Vishnukanthan, AIP Advances, 5, 027122 (2015)
[6] Vanaja, G. V Ramaraju, K.S. Rao, Mech. Mater. Sci. Eng. 9 (2016) 1–6.
[7] K. Thamaphat, P. Limsuwan, B. Ngotawornchai, Nat. Sci. 42 (2008) 357–361.
[8] Hye Moon Lee n and Yong-Jin Kim, Solar Energy Materials & Solar Cells 95, 3352–3358 (2011)
[9] M. Mansoob Khan and Moo Hwan Cho, Nanoscale, 5, 4427–4435 (2013)
[10] H. Lin, C.P. Huang, W. Li, C. Ni, S.I. Shah, Y.H. Tseng, Appl. Catal. B Environ. 68 (2006) 1–11.
[11] J. Annai Joseph Steffy and J. Merline Shyla, Surface and Coatings Technology, 310,113-121 (2017)
[12] Merline Shyla J and Francis P Xavier, Int. J. Microstructure and Materials Properties, 8, 6, 462-477 (2013)

Available online at www.sciencedirect.com

ScienceDirect

Materials Today: Proceedings 8 (2019) 28–36

materialstoday: PROCEEDINGS

www.materialstoday.com/proceedings

ICMEE 2018

Synthesis, Growth and Characterization of $[DAMS]_2[CdI_4]$ single crystal [DAMS =4-N, N-dimethylamino-N-methyl-stilbazolium iodide]

A. Karolin Martina, J.Arul Martin Mani, J.Reena Priya, N.S. Nirmala Jothi*, and P. Sagayaraj

Department of Physics, Loyola College, Chennai – 600 034, India.

Abstract

The hybrid complex of inorganic-organic $[DAMS]_2[CdI_4]$ [[DAMS =4-N, N-dimethylamino-N-methyl-stilbazolium iodide] was synthesized by metathesization of the 4-N,N-dimethylamino -N-methyl stilbazolium iodide [DAMS.I^-] salt with cadmium acetate. The $[DAMS]_2[CdI_4]$ single crystals were grown by slow evaporation method using methanol as solvent. The single crystal X-ray diffraction analysis was carried out and the cell parameters a = 11.0569(3) Å, b = 12.8526(3) Å, c = 14.1427(4) Å, α = 73.7240(10)°, β = 73.9810(10)°, γ = 83.6640(10)° and Volume1853.17 (9) $Å^3$ were determined. The presence of functional groups and their corresponding vibrational modes are evaluated by FT-IR spectrum. The linear optical properties are investigated by UV-vis absorption. The melting point and thermal behavior of $[DAMS]_2[CdI_4]$ were investigated by Thermogravimetric / Differential Thermal Analysis [TG/DTA].

Selection and peer-review under responsibility of the scientific committee of the Materials For Energy and Environment.

Keywords: Single crystal XRD; Slow evaporation method; Thermal stability.

* Corresponding author. Tel.:+91-9444481558; fax: 91-44 28175566.
E-mail address: jmjnirmala@yahoo.co.in

Selection and peer-review under responsibility of the scientific committee of the Materials For Energy and Environment.

1. Introduction

The ability to combine the organic and inorganic compound with in one single molecule scale, have made the preparation of inorganic-organic hybrid compounds a focus area of chemistry and materials science. Second order nonlinear optical (NLO) response, magnetism, luminescence are some special properties exhibited by these crystals with interesting structure. [1-3]. Amoung the organic crystals, the organic stilbazolium salt 4-N, N – dimethylamino -4'-N'-methyl stillbozolium toysylate (DAST) is well known and potential material for electro optic application. This ionic organic material DAST has been investigated by many researchers for their use in optical applications. [4-5]. It has the advantages that the alignment of ionic chromophore can be controlled in a polar structure by changing the counter ion. Also it is an interesting material for phase-matched parametric interactions such as frequency doubling and optic parametric oscillations in the near infrared. [6] By changing the counter anion in the DAST structure, many derivatives has been developed and investigated. Here the hybrid organic-inorganic structure has been synthesized which has, organic cationic chromophore and inorganic anion. [7-8]. In this article we report synthesis, structural, optical and thermal properties of the grown crystal, which has potential application in the field of optics. [9] 4-dimthylamino benzaldehyde is a well-known chromophore exhibiting a large molecular hyperpolarizability (β) and large conjugation system, which will be beneficial to the exhibition on second order NLO property and luminescence [10-12]. As the effectiveness in solubility control is an important features of anion, an appropriate solubility of the crystal is required for the crystal growth from the solution. The properties will be varied according to the anion exchange and the new compounds with large NLO properties and with easy crystalline ability formed, is an interesting investigation. [13,14].

This crystal has been grown by slow evaporation method using methanol as solvent .In this present study cadmium atom was bonded to 4 iodine atoms to form a distorted tetrahedron, which was surrounded by DAMS cations. There is interaction between the 2 adjacent antiparallelly arrayed DAMS cations. The grown crystal has been subjected to single crystal XRD, FTIR, UV and thermal analysis.

2. Materials and method

In this work, slow evaporation method is used for synthesis and cell parameters values are found to be slightly different from that synthesized by solvothermal method [15]. ($[DAMS]_2[CdI_4]$) was prepared by metathesization reaction of the DAMS [4-N, N-dimethylamino-N-methyl-stilbazolium iodide] with Cadmium acetate. DAMS was synthesized by the condensation of 1,4-dimethyl pyridinium iodide (2.35g/10ml), methanol(30ml) and dimethylamino benzaldhyde (1.46g/12ml) in the presence of piperidine (0.2ml). The above mixture was refluxed for nearly a day and then cooled to room temperature. The product was filtered and recrystallized from methanol for about 6 times and stirred for 24 hours. The product appeared as a white precipitate which was later dried in an oven at 100^0 C for 8 hours.

Fig. 1. Photograph of as grown crystal $[DAMS]_2[CdI_4]$

During the next stage, the metathesization reaction was carried out by the following procedure. DAMS as synthesized is dissolved in Millipore water and simultaneously Cadmium acetate was dissolved in Millipore water by heating at 70 °C. These two hot solutions were mixed and heated for 30 min at 70 °C and then allowed to cool naturally to room temperature. A red precipitate was obtained as a result of exchange reaction between anion and

cation. The purity of $[DAMS]_2[CdI_4]$ was further improved by successive re-crystallization from methanol. $[DAMS]_2$ $[CdI_4]$ crystals with size up to 4 x 4 x 3 mm^3 are grown within a period of 4-5 weeks. The photograph of as grown crystal is shown in Fig. 1

3. Result and discussion

3.1. Single crystal x-ray diffraction analysis

The structural analysis of $[DAMS]_2[CdI_4]$ single crystal was carried out using Bruker APEX-II CCD' single crystal X-ray diffractometer. The XRD data was monitored at 293(2) K. The structural elucidation of precursors and refinements were performed using the SHELXL program. The Semi-empirical from equivalents influences the absorption correction and the structure was solved by Full-matrix least-squares and the refinements by using F2 taking all the unique refinements. The experimental conditions supporting the data and refinement for the $[DAMS]_2[CdI_4]$ is given in the table:1 This crystal $[DAMS]_2[CdI_4]$ belongs to the triclinic family with space group P-1 Centro symmetric and the cell parameters are very similar to that of DAST reported by Marder et all.[4]. The hydrogen atoms causing the H-bonds were located from the different Fourier and refined with isotropic thermal parameters while the non-hydrogen atoms were refined with anisotropic thermal parameters. The atomic co-ordinates and equivalent isotropic displacement parameters, bond length and bond angles, anisotropic displacement parameters, the hydrogen co-ordinates and isotropic displacement parameters of the$[DAMS]_2[CdI_4]$ are listed in table 2 -3respectively.

Fig: 2 shows the molecular structure of the hybrid compound. Fig: 3 show the crystal packing along *c* direction. It is clear that the cadmium atom is bonded to four iodine atoms in a distorted tetrahedron geometry, which is surrounded by DAMS cations. The DAMS cations can be divided into two groups between which the molecular planes are perpendicular to each other. It is interesting to note that the dipole directions of two adjacent DAMS cations are contrary to each other, that is, they are antiparallelly arrayed. [16,17]

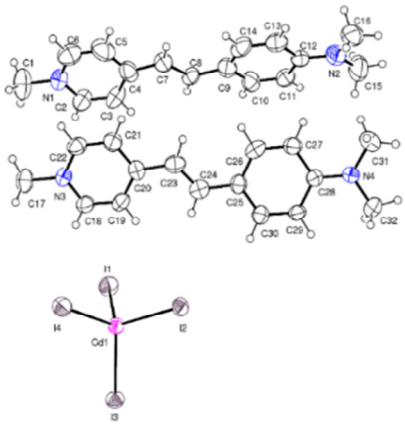

Fig.2 ORTEP diagram of $[DAMS]_2[CdI_4]$ crystal

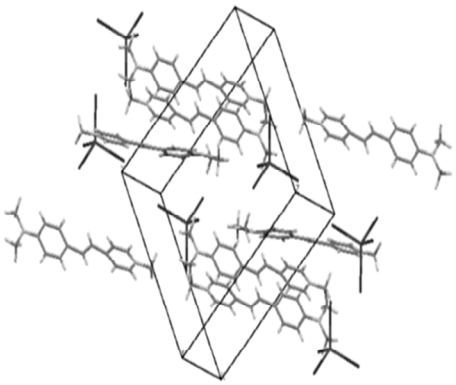

Fig.3 The crystal packing diagram of $[DAMS]_2[CdI_4]$

Table 1. Crystal data and structure refinement for $[DAMS]_2[CdI_4]$

Identification code	$[DAMS]_2[CdI_4]$	
Empirical formula	$C_{32}\ H_{38}\ Cd\ I_4\ N_4$	
Formula weight	1098.66	
Temperature	293(2) K	
Wavelength	0.71073 Å	
Crystal system	Triclinic	
Space group	P-1	
Unit cell dimensions	a = 11.0569(3) Å	α= 73.7240(10)°
	b = 12.8526(3) Å	β= 73.9810(10)°.
	c = 14.1427(4) Å	γ = 83.6640(10)°.
Volume	1853.17(9) $Å^3$	
Z	2	
Density (calculated)	1.969 Mg/m^3	
Absorption coefficient	3.947 mm^{-1}	
F(000)	1036	
Crystal size	0.150 x 0.100 x 0.100 mm^3	
Theta range for data collection	2.391 to 25.000°.	
Index ranges	-13<=h<=13, -15<=k<=15, -16<=l<=16	
Reflections collected	35805	
Independent reflections	6508 [R (int) = 0.0350]	
Completeness to theta = 25.000°	99.9 %	
Absorption correction	Semi-empirical from equivalents	
Max. and min. transmission	0.7456 and 0.6212	
Refinement method	Full-matrix least-squares on F^2	
Data / restraints / parameters	6508 / 70 / 389	
Goodness-of-fit on F^2	1.068	
Final R indices [I>2sigma(I)]	R1 = 0.0313, wR2 = 0.0509	
R indices (all data)	R1 = 0.0558, wR2 = 0.0622	
Extinction coefficient	n/a	
Largest diff. peak and hole	1.019 and -1.003 e.$Å^{-3}$	

For the same crystal grown by solvothermal method, the cell parameters are parameters a = 12.9849(19) Å, b = 13.1935(13) Å, c = 13.8792(10) Å, α= 106.798(10)°, β= 109.827(6)°, γ = 108.206(9)° and Volume 1906.0 (4) $Å^3$ [15]. The cell parameter values and bond angles for the same crystal are completely different when grown by slow evaporation method.

Table 2. Anisotropic displacement parameters ($Å^2 x\ 10^3$) for $[DAMS]_2[CdI_4]$. The anisotropic displacement factor exponent takes the form: $-2\pi^2[\ h^2\ a^{*2}U^{11} + ...\ + 2\ h\ k\ a^*\ b^*\ U^{12}\ ]$

	U^{11}	U^{22}	U^{33}	U^{23}	U^{13}	U^{12}
C(1)	153(8)	91(6)	107(7)	-46(5)	-80(6)	37(6)
C(2)	74(5)	53(4)	107(6)	-22(4)	-37(5)	-1(4)
C(3)	60(5)	85(5)	107(6)	-46(5)	-40(4)	15(4)
C(4)	80(5)	78(5)	57(4)	-12(4)	-6(4)	15(4)
C(5)	111(7)	60(5)	104(7)	1(5)	-15(6)	-21(5)
C(6)	82(6)	81(6)	114(7)	-36(5)	-25(5)	-22(5)
C(9)	65(5)	89(5)	51(4)	-19(4)	-6(3)	8(4)
C(10)	76(5)	59(4)	70(5)	-15(4)	-15(4)	6(4)
C(11)	58(4)	64(4)	71(4)	-26(4)	-18(4)	-3(3)
C(12)	48(4)	58(4)	54(4)	-17(3)	-5(3)	-4(3)
C(13)	63(4)	74(5)	74(5)	-29(4)	-9(4)	-15(4)
C(14)	56(4)	125(7)	65(5)	-42(5)	-19(4)	-7(4)
C(15)	120(8)	111(7)	128(8)	4(6)	-73(7)	-19(6)
C(16)	81(6)	67(5)	128(7)	4(5)	-9(5)	-1(4)
C(17)	85(5)	57(4)	81(5)	-18(4)	-40(4)	13(4)
C(18)	50(4)	57(4)	65(4)	-9(3)	-13(3)	-8(3)
C(19)	46(4)	74(4)	71(4)	-21(4)	-22(3)	-2(3)
C(20)	67(4)	46(3)	48(4)	-17(3)	-18(3)	6(3)
C(21)	61(4)	46(3)	66(4)	-11(3)	-17(3)	-9(3)
C(22)	50(4)	54(4)	73(4)	-15(3)	-14(3)	-10(3)
C(23)	58(4)	62(4)	71(5)	-22(3)	-9(4)	-13(3)
C(24)	61(4)	59(4)	64(4)	-29(3)	-13(3)	-3(3)
C(25)	59(4)	54(4)	53(4)	-18(3)	-20(3)	3(3)
C(26)	41(4)	74(4)	74(5)	-34(4)	-10(3)	-1(3)
C(27)	51(4)	57(4)	61(4)	-10(3)	-7(3)	-7(3)
C(28)	48(4)	39(3)	53(4)	-16(3)	-12(3)	0(3)
C(29)	39(3)	54(4)	59(4)	-12(3)	-7(3)	-7(3)
C(30)	57(4)	49(3)	59(4)	-16(3)	-17(3)	2(3)
C(31)	81(5)	87(5)	76(5)	13(4)	-12(4)	-18(4)
C(32)	57(4)	86(5)	84(5)	-9(4)	-30(4)	-3(4)
N(1)	69(4)	63(4)	68(4)	-30(3)	-28(3)	12(3)
N(2)	79(4)	66(4)	82(4)	-8(3)	-21(3)	-13(3)
N(3)	49(3)	51(3)	56(3)	-19(2)	-20(2)	5(2)
N(4)	48(3)	56(3)	57(3)	-3(3)	-9(3)	-5(2)
Cd(1)	48(1)	42(1)	50(1)	-9(1)	-15(1)	-5(1)
I(1)	70(1)	76(1)	73(1)	-28(1)	-12(1)	19(1)
I(2)	58(1)	41(1)	66(1)	-1(1)	-21(1)	-6(1)
I(3)	52(1)	51(1)	67(1)	-11(1)	-12(1)	-13(1)
I(4)	71(1)	78(1)	62(1)	-14(1)	-23(1)	-29(1)
C(7)	75(6)	60(6)	65(6)	-17(5)	-26(5)	-16(5)
C(8)	52(6)	67(7)	58(6)	-25(5)	-19(4)	-5(5)
C(7')	62(9)	67(9)	61(9)	-28(8)	-29(8)	-2(8)
C(8')	62(10)	82(10)	58(9)	-18(9)	-25(8)	-3(9)

Table 3. Hydrogen coordinates (x 10^4) and isotropic displacement parameters ($Å^2$x 10^3) for $[DAMS]_2[CdI_4]$

	x	y	z	U(eq)
H(1A)	4824	4107	998	160
H(1B)	4462	3220	567	160
H(1C)	3518	3562	1490	160
H(2)	6188	3541	1947	90
H(3)	7089	2289	3030	93
H(5)	4705	153	3106	117
H(6)	3856	1452	2039	106
H(10)	8581	107	5538	84
H(11)	9445	-1172	6640	75
H(13)	7816	-3478	6051	83
H(14)	6958	-2173	4963	93
H(15A)	10319	-3604	8135	176
H(15B)	10696	-2528	7281	176
H(15C)	9462	-2551	8159	176
H(16A)	9595	-4818	7759	153
H(16B)	8265	-4554	7538	153
H(16C)	9465	-4589	6643	153
H(17A)	6839	2668	-1092	108
H(17B)	7559	3603	-998	108
H(17C)	8181	2960	-1813	108
H(18)	9781	2915	-760	70
H(19)	10722	1732	382	74
H(21)	7692	-94	1324	69
H(22)	6847	1100	158	71
H(23)	9269	-664	2250	77
H(24)	11501	334	1391	71
H(26)	9942	-1771	3540	73
H(27)	10846	-2919	4738	70
H(29)	14200	-1627	3160	62
H(30)	13266	-493	2002	65
H(31A)	13070	-4332	6017	133
H(31B)	11750	-3787	5935	133
H(31C)	12466	-4480	5184	133
H(32A)	14704	-3467	5345	114
H(32B)	14973	-3151	4153	114
H(32C)	14665	-2244	4739	114
H(7)	6131	-626	3927	76
H(8)	7536	792	4334	67
H(7')	7324	1033	4171	70
H(8')	6397	-806	4163	79

3.1 FT-IR analysis

Vibrational spectroscopy has been extensively used to understand the factors contributing to the linear electro-optic effect from the vibrational modes in organic materials and to provide deeper knowledge regarding the intermolecular interaction nonlinear response and the hyper polarizability, molecular architecture and their relationship could also be studied. [14] The stilbazolium cation group comprise the vinyl group vibrations, phenyl ring vibrations and methyl group vibrations while the tosylate anion group encompass the sulfonate group and skeletal vibrations. The FTIR spectrum recorded using BRUKER IFS 66V FT-IR spectrometer. The measurement was done with KBr method for the wavelength range 400-4000 cm^{-1} and shown in figure: 4. The peak seen around 3036cm^{-1} C-H stretching vibrations of stilbene derivative, 2904 cm^{-1} derivative, alkyl C-H stretch, 1591 cm^{-1} trans stilbene C=C stretching, 821 cm^{-1}1,4distribution aromatic vibration, 962 cm^{-1}1,2 substituted pyridinium ring and 530 cm^{-1} is due to the phenyl ring C-H out of plane bending. The peak at 1160 cm^{-1} S=O Stretch of sulfonate group. [6].Various atomic molecular vibration are listed in Table 4.

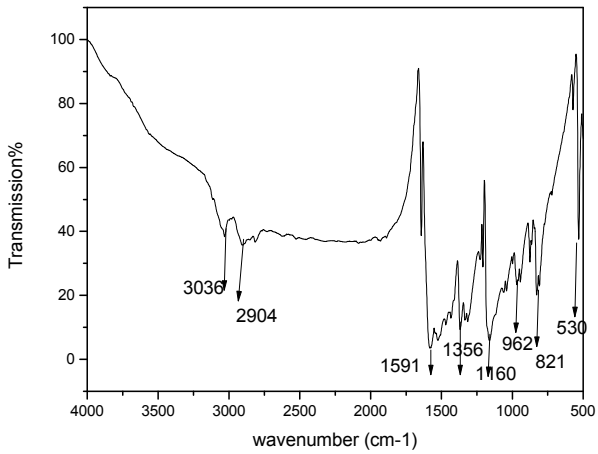

Fig.4. FT-IR spectrum of for $[DAMS]_2[CdI_4]$ crystal

Table 4. FTIR wavenumber assignment for $[DAMS]_2[CdI_4]$

S.No	Wavenumber cm^{-1}	Assignment
1	3036	C-H stretching vibrations of stilbene derivative
2	1160	S=O Stretch of sulfonate group
3	2904	alkyl C-H stretch
4	1591	stibence C=C stretching
5	962	1,2 substituted pyridinium ring
6	821	1,4 distribution aromatic vibration
7	530	phenyl ring C-H out of plane bending

3.3 *UV-Vis absorption analysis*

Figure. 5 shows the absorption spectrum of $[DAMS]_2[CdI_4]$ in solid phase using KAPPA APEX-II spectrophotometer recording in a wavelength region 200-1100 nm. The optical absorption spectrum of $[DAMS]_2[CdI_4]$ dissolved in methanol it is well known that when the DAST and its derivatives are dissolved in methanol, it leads to dissociated state generating free cations and anions. [19] The UV cut – off wavelength is found to be 450 nm. It is very useful to identify the optical absorption or transmission window and cut-off wavelength of the crystal. Also it is useful to understand its electronic states, when interacting with linear light. Absence of absorption in the region is between 545 and 1093 nm.

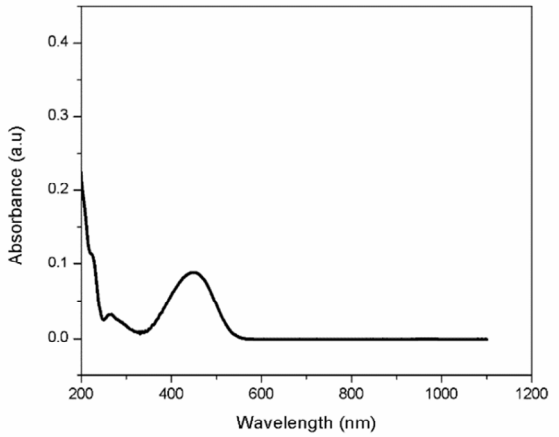

Fig.5 optical absorption spectrum of $[DAMS]_2[CdI_4]$

3.4 Thermal analysis

The thermal behavior of $[DAMS]_2[CdI_4]$ grown crystal was investigated by Thermogravimetric / Differential Thermal Analysis [TG/DTA] using carried between 28°C and 1000 °C at a heating rate of 15°C min^{-1} using the instrument Perkin-Elmer TGA-7 spectrometer. From the TG/DTA thermogram figure: 6. The TGA curve reveals the three distinct weight loss stages occurred on sample: the first one at 319.34°C connected with 3% mass loss was due to the removal of moisture absorbed by the compound. The 74% mass loss 433.83°C is indicative for the decomposition of pyridine moiety. DTA curve shows one main endothermic at 269.81◦C which corresponds to melting point and three exothermic peaks at 319.34, 395.51 and 498.30 °C indicating the major decomposition of materials.

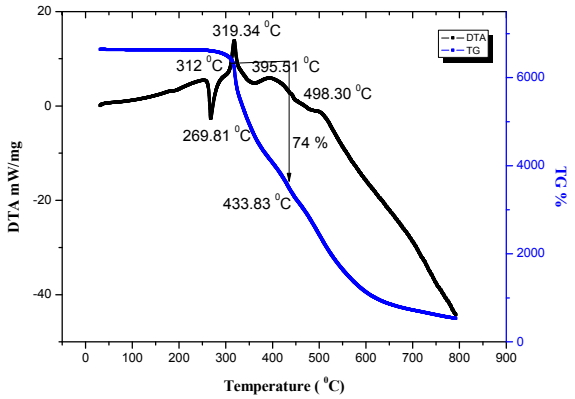

Fig.6. TG/DTA thermogram of $[DAMS]_2[CdI_4]$

4. Conclusion

The growth of the single crystal $[DAMS]_2[CdI_4]$ was achieved by slow evaporation method. The present study demonstrates the enhancement in the size of the crystal achieved through proper choice of solvent and growth conditions. The cell parameters of the grown crystals are determined using single crystal X-ray diffraction analysis. The presence of functional groups in the sample is verified using FT-IR analysis. The UV cut – off wavelength is found to be 450 nm. It is very useful to identify the optical absorption or transmission window and cut-off wavelength of the crystal. Thermal studies indicate that the sample was thermally more stable than DAST and a few other DAST derivatives.

References

[1] Mitzi, D.B. J. C. S., Dalton Trans. 2001, 1.
[2] Mitzi, D.B. Prog. Inorg. Chem. 1999, 48, 1.
[3] Qin, J.; Dai, C.; Liu, D.; Chen, C.; Wu, B.; Yang, C.; Zhan, C.Co ord. Chem. Rev. 1999, 188, 23.
[4] S. R. Marder, J. W. Perry, and W. P. Schaefer, "Synthesis of organic salts with large second-order optical nonlinearities," Science 245, 626–628 (1989).
[5] F. Pan, G. Knopfle, Ch. Bosshard, S. Follonier, R. Spreiter, M.S. Wong, P.Gunter,¨Appl. Phys. Lett. 69 [1996] 13.
[6] Y. Mori, Y. Takahashi, T. Iwai, M. Yoshimura, Y.K. Yap, T. Sasaki, Jpn. J. Appl. Phys. 39 [2000] L1006.
[7] Y.Li, J.Zhang, G.Zhang, L.Wu.Fu, Y.Wu, J.Cryst.Growth 327 [2011]127-132.
[8] Qin, J.; Dai, C.; Liu, D.; Chen, C.; Wu, B.; Yang, C.; Zhan, C. Coord. Chem. Rev. 1999,188, 23.
[9] Jiang, M.; Fang, Q. Adv. Mater. 1999, 11, 1147.
[10] S.R.Marder, J.W.Perry, W.P Schaefer, Science 245 (1989) 626.
[11] V.Alan, M.Blanchard-Desce, I.Ledoux-Rak, J.Zyss, Journal Chemical Society, Chemical communications 353 (2000).
[12] J.Ogawa,S.Okada,Z.Glavcheva,H.Nakanishi, Journal of Crystal Growth 310 (2008) 836.
[13] Ogawa, M.; Kuroda, K. Chem. Rev. 1995, 95, 399.
[14] P´ecaut, J.; Le Fur, Y.; Levy, J.; Masse, P.R. J. Mater. Chem 1993, 3, 333.
[15] Peng Ren,Jingui Qin,Chuangtian Chen,Deqing Zhang and Huanming Hu Journal of Chemical Crystallography, Vol.34.No,4. April (2004).
[16] Lacroix, P.G. Chem. Mater. 2001, 13, 3495.
[17] Lacroix, P.G.; Clement, R.; Nakatani, K.; Delaire, J. A.; Zyss,J.; Ledoux, I. Science 1994, 263, 658.
[18] C.Bosshard, R.Spreiter,I.Degiorgi and P.Gunter,Phys.Rev.B,66(2002) 205107.
[19] R.Macchi, E.Cariati, D.Marinotto, D.Roberto, E.Tordin, R.Ugo, R.Bozio. M,Cozzuol, D.Pedron, G.Mattei, J.Mater, Chem. 20 (2010) 1885-1890.

Available online at www.sciencedirect.com

ScienceDirect

Materials Today: Proceedings 8 (2019) 476–483

materialstoday: PROCEEDINGS

www.materialstoday.com/proceedings

ICMEE 2018

Structural Rietveld Refinement and Vibrational Study of M-Type $BaFe_{12}O_{19}$ Nanoparticles

S. Anand, S. Pauline*, V. Maria Vinosel, M. Asisi Janifer

Department of Physics, Loyola College (Autonomous), Chennai-600034, India

Abstract

M-type barium hexaferrites with the general formula $BaFe_{12}O_{19}$ was synthesized by the sol-gel auto combustion method and characterized by X-ray diffraction. The XRD diffraction patterns confirmed that the ferrite samples are in the hexagonal structure with space group $P6_3/mmc$ which is further validated by Rietveld refinement. The crystal structure and cell parameters were refined by Rietveld analysis. The vibrational spectrum obtained using Fourier Transform-Infrared (FT-IR) and Raman spectroscopy was reported. Three vibrational modes were observed in FT-IR spectra of the samples, which indicated the presence of metal-oxygen stretching bands in hexaferrite structure. A Raman spectrum shows eight strong and sharp modes, identifying the presence of barium hexaferrite phase.

Selection and peer-review under responsibility of the scientific committee of the Materials For Energy and Environment.

Keywords: $BaFe_{12}O_{19}$; XRD; Rietveld refinement; FT-IR; Raman studies.

1. Introduction

M-type barium hexaferrite $BaFe_{12}O_{19}$ (BaM) has been widely applied for permanent magnets, magnetic recording media, and microwave absorbers, due to its high stability, excellent high-frequency response, large magneto-crystalline anisotropy, and large magnetization as well [1]. According to the planar anisotropy picture, the planar anisotropy BaM should exhibit the large permeability in microwave frequency. However, the BaM has disadvantages such as high density, narrow absorption bandwidth and unstable in harsh environments, thus limiting the overall performances [2]. Barium hexaferrite ($BaFe_{12}O_{19}$) is one of the most versatile hard magnetic materials. It is not only a magnetic medium but also a dielectric medium and exhibits good magnetic loss and dielectric loss. In

* Corresponding author. Tel.:9940054040
E-mail address: paulantovero@yahoo.co.in

Selection and peer-review under responsibility of the scientific committee of the Materials For Energy and Environment.

addition, it has attractive magnetic properties, high Curie temperature, excellent chemical stability and low cost and has been widely used in the field of EM wave absorption.

The basis for multiphase profile analysis of powder diffraction patterns was firstly introduced completely by Rietveld in 1969. Rietveld showed the possibility of replicating the results of diffraction pattern measurements with pattern calculation. The advantage of such pattern calculation is when there is an occurrence of an error that is caused by an intensity deviation in an imperfect model structure; it will tend to leave the remaining intensity, both negative and positive. The basic principle of Rietveld analysis is to match (fitting) the peak profile of the calculation with the peak profile of the observation. The profile matching (fitting) is carried out by applying the procedure of a nonlinear least square calculation. FT-IR and Raman spectroscopies are mutually complementary parts of molecular vibrational spectroscopy [3,4]. Their molecular physics is essentially the same since both are concerned with the observation of the excitation of molecular vibrational energy states associated with the electronic ground state. In FT-IR spectroscopy, vibrational excitations occur upon the absorption of electromagnetic radiation. In Raman measurements the excitation is a consequence of inelastic light scattering by molecule [5-7].

In this work, $BaFe_{12}O_{19}$ nanoparticles were prepared through simple sol–gel auto-combustion method. Powder X-ray diffraction, Fourier transforms infrared spectroscopy and micro Raman spectroscopy, room temperature magnetization measurements by vibrating sample magnetometer were carried out for their characterization. The results observed from the above mentioned studies are briefly discussed below.

2. Experimental

2.1 Materials

Barium nitrate ($Ba(NO_3)_2$), ferric nitrate $Fe(NO_3)_3$), zirconium nitrate ($Zr(NO_3)_4$), citric acid and ammonium hydroxide solution were purchased from Merck (India) were used as received without further purification.

2.2 Method

$BaFe_{12}O_{19}$ nanoparticles were synthesized by sol–gel auto-combustion method. The starting precursors ($Fe(NO_3)_3 \cdot 9H_2O$, $Ba(NO_3)_2$; Ba/Fe = 1:12) with a stoichiometric amount of metal nitrates were dissolved in double-distilled water by stirring. The temperature was increased to 70^{o}C and then citric acid was subsequently added to solution (molar ratio of total metal ions and citric acid in the solution is 1:1) and the resulting mixture was stirred for 30 min. Then, the pH was adjusted to about 7 by adding ammonia solution. Aqueous suspensions were stirred and heated for several hours at 80^{o}C until a highly viscous gel was produced. In the final step of the sol–gel auto-combustion process, the obtained gel is allowed to burn via auto-combustion reaction and then was dried at 250^{o}C for 2 h. Finally, the burnt product was grounded and annealed at 950^{o}C for 5h.

2.3 Characterization

X-ray diffraction data of annealed powder samples were recorded for identification of phase and structure with X-ray diffractometer (X'pert-Philips). The refinement of diffraction data has been performed through Rietveld refinement technique using MAUD software. FTIR spectra were obtained in transmission mode by FTIR spectrometer (Perkin Elmer, 1600) in order to identify functional groups of the nanoparticles. Raman spectra were recorded using a micro-Raman spectrometer (Witech CRM200, the excitation wavelength at 532 nm).

3. Results and Discussion

3.1 XRD Analysis

Fig. 1 shows the XRD pattern of $BaFe_{12}O_{19}$, The major diffraction peaks of barium ferrite were observed at 2θ values of 30.35^o, 32.34^o, 34.29^o, 35.42^o, 37.49^o, 40.42^o, 42.52^o, 55.23^o, 56.69^o and 63.18^o, 67.51 and 72.67^o corresponding due to the (110), (107), (114), (200), (203), (205), (206), (217), (2011), (220), (2014) and (317) reflections. The patterns have been indexed to hexagonal crystal system pertaining to the space group P63/mmc (No. 194), which confirms that the phase belongs to the magnetoplumbite crystal structure. The synthesized nanoparticle shows all the diffraction peaks are very well consistent with the standard ICDD patterns (JCPDS no. 43-0002) with no observable secondary phase such as α-Fe_2O_3.

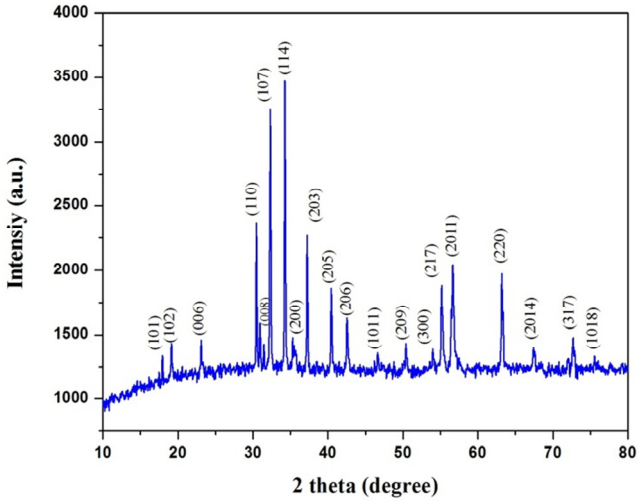

Fig.1: Powder XRD pattern of $BaFe_{12}O_{19}$ Nanoparticles

The crystallite size of $BaFe_{12}O_{19}$ nanoparticles can be calculated by using the Debye–Scherrer formula:

$$D = \frac{K\lambda}{\beta \cos\theta} \quad (1)$$

where D is the average crystallite size of nanoparticles, k is the shape factor, λ is the X-ray wavelength, β is the full width at half maximum, θ is the diffraction angle of Bragg and k is often assigned a value of 0.89, which depends on several factors, including the Miller index of the reflecting plane and the shape of the crystal. The (114) reflection of the observed X-ray data was chosen for calculating the crystallite size of $BaFe_{12}O_{19}$ nanoparticles. The average size of the $BaFe_{12}O_{19}$ nanoparticles was calculated using the above mentioned equation and estimated as 44.54 nm.

3.2 Williamson-Hall analysis:

The individual contribution to the line broadening of a Bragg reflection can be expressed as:

$$\beta_{hkl} = \beta_s + \beta_D \quad (2)$$

Where β_{hkl} represents the full width at half maximum (FWHM) of a peak in radian, β_s and β_D are the breadth due to size and strain, respectively. In W-H relation the strain was assumed to be uniform in all crystallographic direction, β_{hkl} is given by

$$\beta_{hkl} = \left(\frac{K\lambda}{D\cos\theta}\right) + 4\varepsilon \tan\theta \quad (3)$$

Rearranging Eqn. (10) gives

$$\beta_{hkl}\cos\theta = \left(\frac{K\lambda}{D}\right) + 4\varepsilon \sin\theta \quad (4)$$

Here D and ε corresponds to the crystallite size value and dimension value (microstrain) respectively. By plotting $\beta_{hkl}\cos\theta$ as a function of 4sinθ, the average crystallite size and strain can be estimated from the extrapolation and the slop of the fitted line [8]; see fig 2.

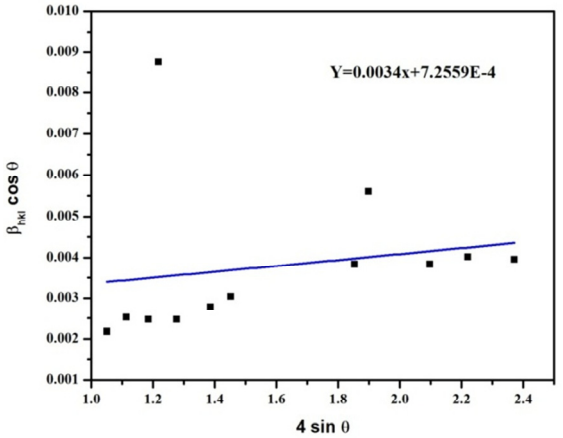

Fig.2: Williamson –Hall plot of $BaFe_{12}O_{19}$ Nanoparticles

3.3 Rietveld crystal structure refinement

The XRD patterns of the sample were analyzed by employing the Rietveld refinement method with the help of MAUD software program. A typical XRD along with theoretical data with Rietveld analysis is shown in the fig. 3. Vertical lines are allowed Bragg's positions for $P6_3/mmc$ space group. One can observe that all the observed peaks are allowed Bragg's position only, which is consistent with the analysis carried out by using ICDD data base. During the refinement, atomic fraction positions have been kept as fixed parameters and other parameters such as, lattice constants, isothermal parameters, shape and scale parameters have been taken as free parameters. Various structural parameters R_p (profile fitting of R-Value), R_{wp} (weighted profile of R-Value) and χ^2 (goodness of fit factor) obtained from the Rietveld refinement are presented in the Table 1. The low values of χ^2 and profile parameters (R_p, R_{wp}) suggest that the derived samples are better quality and refinements of samples are effective. The structural parameters: lattice constants ('a', 'c') and volume (V) are also given in Table 1. Comparison between calculated and observed inter-planner spacing (d-values) of hkl Bragg planes for $BaFe_{12}O_{19}$ after Rietveld refinement are tabulated in Table 2.

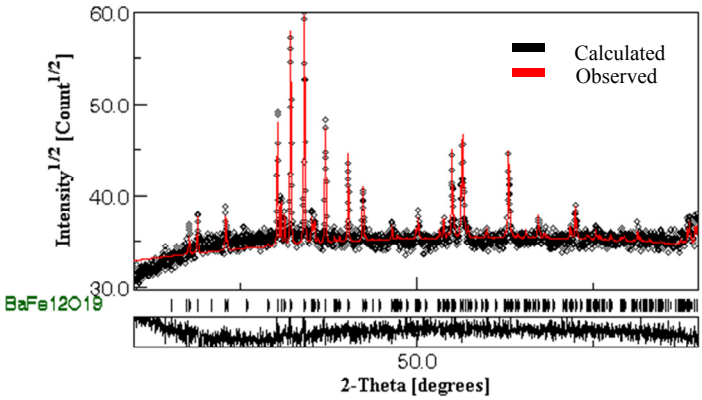

Fig.3: Rietveld analysis of $BaFe_{12}O_{19}$ Nanoparticles

Table 1: Refined structural parameters obtained from Rietveld analysis

Sample	Space group	R_p	R_{wp}	χ^2	a (Å)	c (Å)	c/a	V (Å^3)
$BaFe_{12}O_{19}$	$P6_3/mmc$	3.081	3.984	2.823	5.89	23.23	3.94	697.92

Table 2: Comparison between some of the calculated and observed inter-planner spacing (d-values) of hkl Bragg planes for $BaFe_{12}O_{19}$ after Rietveld refinement.

hkl	Inter planer spacing (d-spacing)	
	Calculated Values	Observed Values
101	4.961	4.987
102	4.649	4.674
006	3.849	3.872
110	2.932	2.948
107	2.767	2.783
114	2.614	2.629
200	2.539	2.553
203	2.412	2.424
205	2.225	2.237
206	2.120	2.131
209	1.805	1.815
300	1.694	1.703
217	1.659	1.668
2011	1.618	1.627
220	1.467	1.474
2014	1.383	1.392
317	1.296	1.303

3.4 FT-IR Analysis:

The FTIR spectrum investigation is used to find the information of bonding in a compound. The peaks are mainly dependent on the structure of the crystal and chemical mixing ratio of the prepared materials. The FT-IR spectra of pure and substituted barium hexaferrite samples are recorded in the range of 400-4000 cm^{-1} wave numbers as shown in fig 4. FT-IR spectrum of the sample indicates the formation barium hexaferrite ($BaFe_{12}O_{19}$) with absorption bands at around 567 cm^{-1},537cm^{-1} and 426 cm^{-1} can be attributed to metal-Oxygen stretching vibration in hexaferrite structure. The very weak absorption bands seen at 2975 cm^{-1} region is due to O-H stretching band of H_2O for $BaFe_{12}O_{19}$. In more details the peaks in the range 420-445cm^{-1} illustrate vibrations of octahedral bonds and others two peaks indicate tetrahedral [9,10].

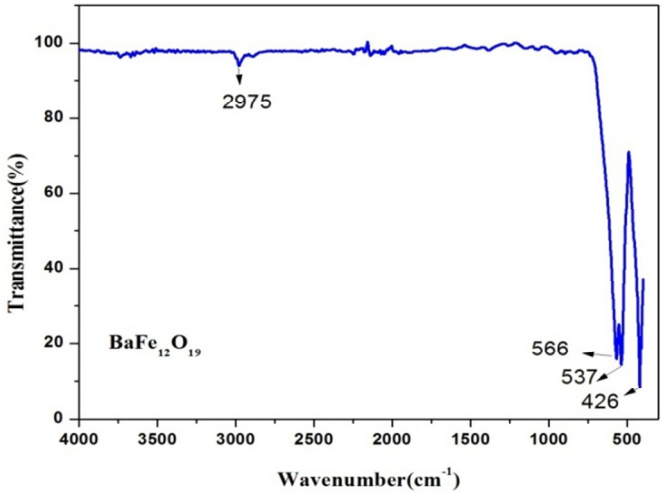

Fig. 4: FT-IR spectra of barium hexagonal ferrite

3.5 Raman spectroscopy Analysis:

Raman spectroscopy involves molecular and crystal lattice vibrations and is therefore sensitive to the composition, bonding, chemical environment, phase and crystalline structure of the sample material in any physical form. In the present work, Raman spectroscopy has been used to show the phase composition and homogeneity of the $BaFe_{12}O_{19}$ system by comparing the observed results with the selection rules and mode assignments discussed by Kreisel et al.(1998) [11]. From the literature, it is reported that 42 Raman-active modes ($11A_{1g} + 14E_{1g} + 17E_{2g}$) and 30 IR active modes ($13A_{2u} + 17E_{1u}$) are expected for the barium hexaferrite system ($BaFe_{12}O_{19}$). Raman spectra of all the prepared compounds were recorded and normalized with respect to the most intense band at room temperature. In order to analyze the polarization dependence of the Raman signals, the Raman bands were fitted with the Lorentzian line shape and the results are shown in Fig. 5. The observed Raman spectra have been indexed and the comparative statement of vibrational modes observed was listed in the Table 3.

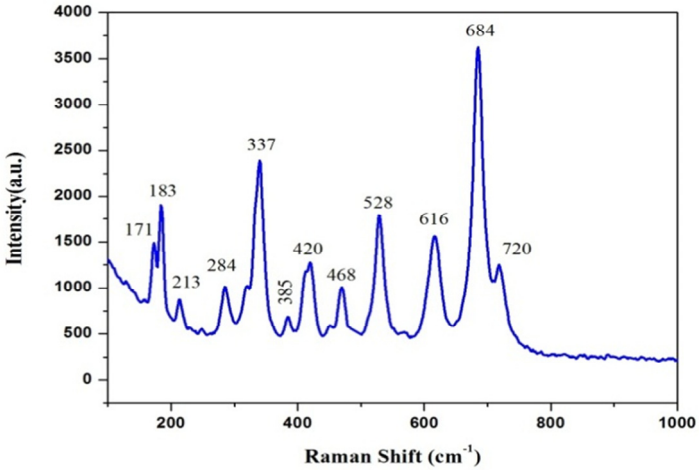

Fig. 5: Raman spectra of barium hexagonal ferrite

The major peaks observed at about 720, 684, 528, 468, 420, 385, 337, 284, 213, 183 and 171 cm^{-1} are in good agreement with the magnetoplumbite structure. The peaks at 720 and 684 cm^{-1} can be assigned to A_{1g} vibrations of Fe-O bonds at the tetrahedral 4f1 and bipyramidal 2b sites, respectively. Other peaks at 616, 528, and 468 cm^{-1} are due to A_{1g} vibrations of Fe-O bonds at the octahedral 4f2, 2a, and 12k sites, whereas peak at 420 cm^{-1} is due to A_{1g} vibration at the octahedral 12k dominated site. The peaks at 284 and 213 cm^{-1} were due to E_{1g} vibrations, while the peak at 337 cm^{-1} was due to E_{2g} vibration. The peak at 183 and 171 cm^{-1} resulted from E_{1g} vibrations of the whole spinel block.

Table 3: Assignment of the main Raman- active modes observed in $BaFe_{12}O_{19}$

Wave number (cm^{-1})		Symmetry	Assignment
$BaFe_{12}O_{19}$	Kreisel et al.(1999)		
173	173	E_{1g}	Whole spinel block
183	184	E_{1g}	Whole spinel block
337	335	A_{1g}	Octahetra (mixed)
411	409	A_{1g}	$Fe^{(5)}$ O_6 octahetra dominated
468	467	A_{1g}	Octahetra $Fe^{(1)}$ O_6 and $Fe^{(5)}$ O_6
616	614	A_{1g}	Octahetra $Fe^{(4)}$ O_6
684	684	A_{1g}	Bi pyramid $Fe^{(2)}$ O_5
720	719	A_{1g}	Tetrahetra $Fe^{(3)}$ O_4

4. Conclusion:

The single phase nanocrystalline barium hexaferrite ($BaFe_{12}O_{19}$) has been prepared by sol-gel auto combustion method. The hexagonal magnetoplumbite crystal structure with space group $P6_3/mmc$ was exhibited in powder X-ray diffraction analysis and Rietveld analysis. The lower values of profile parameters such as R_p, R_{wp}, χ^2 and inter planer spacing indicated that the calculated diffraction pattern is in fair agreement with observed pattern. The crystallite size and lattice strain in sample was investigated by Williamson-Hall (W-H) method. $BaFe_{12}O_{19}$ compounds exhibit intense Raman resonance peaks which reveal the formation of well crystalline hexaferrite system.

Acknowledgements

The Authors are thankful to Department of Chemistry, IITM, Chennai for XRD analysis.

References:

1. C.L. Yuan, Y.S. Hong, J. Mater. Sci. 45 (2010) 3470-3476.
2. X.G. Liu,, C. Feng, N.N. Bi, Y.P. Sun, J.C. Fan, Y.H. Lv, C.G. Jin, Y.R. Wang, C.T. Li, Ceram. Int. 40 (2014) 9917-9922.
3. R.D. Waldron, Infrared spectral studies in spinnel structure ferrites, Phys. Rev. 99 (1955) 1727.
4. W.B.White, B.A.DeAngelis, , Spectrochim.Acta A, 23 (1967) 985-990.
5. R.Gupta, A.K.Sood, P.Metcalf, J.M.Honig, Phys.Rev.B65 (2002) 104430.
6. P.R.Grave, C.Johnston, J.J.Campaniello, , Mater.Res.Bull.23 (1988) 1650–1660.
7. A.Kumar,P.Sharma,D.Varshney, Ceram.Int.40 (2014) 12855–12860.

8. S. Anand, A. Persis Amaliya, M. Asisi Janifer and S. Pauline, Modern Electronic Materials, 3 (2017) 168–173.

9. S.Singhal, T. Namgyal, S. Bansal, K. Chandra, J. Electromagn. Anal. Appl. 2 (2010) 376–381.

10. A.Pradeep, G. Chandrasekaran, Mater. Lett. 60 (2006) 371–374.

11. J. Kreisel, G. Lucazeau, and H. Vincent, J. Solid State Chem. 137, (1998) 127-137.

Available online at www.sciencedirect.com

ScienceDirect

Materials Today: Proceedings 8 (2019) 476–483

materialstoday: PROCEEDINGS

www.materialstoday.com/proceedings

ICMEE 2018

Structural Rietveld Refinement and Vibrational Study of M-Type $BaFe_{12}O_{19}$ Nanoparticles

S. Anand, S. Pauline*, V. Maria Vinosel, M. Asisi Janifer

Department of Physics, Loyola College (Autonomous), Chennai-600034, India

Abstract

M-type barium hexaferrites with the general formula $BaFe_{12}O_{19}$ was synthesized by the sol-gel auto combustion method and characterized by X-ray diffraction. The XRD diffraction patterns confirmed that the ferrite samples are in the hexagonal structure with space group $P6_3/mmc$ which is further validated by Rietveld refinement. The crystal structure and cell parameters were refined by Rietveld analysis. The vibrational spectrum obtained using Fourier Transform-Infrared (FT-IR) and Raman spectroscopy was reported. Three vibrational modes were observed in FT-IR spectra of the samples, which indicated the presence of metal-oxygen stretching bands in hexaferrite structure. A Raman spectrum shows eight strong and sharp modes, identifying the presence of barium hexaferrite phase.

Selection and peer-review under responsibility of the scientific committee of the Materials For Energy and Environment.

Keywords: $BaFe_{12}O_{19}$; XRD; Rietveld refinement; FT-IR; Raman studies.

1. Introduction

M-type barium hexaferrite $BaFe_{12}O_{19}$ (BaM) has been widely applied for permanent magnets, magnetic recording media, and microwave absorbers, due to its high stability, excellent high-frequency response, large magneto-crystalline anisotropy, and large magnetization as well [1]. According to the planar anisotropy picture, the planar anisotropy BaM should exhibit the large permeability in microwave frequency. However, the BaM has disadvantages such as high density, narrow absorption bandwidth and unstable in harsh environments, thus limiting the overall performances [2]. Barium hexaferrite ($BaFe_{12}O_{19}$) is one of the most versatile hard magnetic materials. It is not only a magnetic medium but also a dielectric medium and exhibits good magnetic loss and dielectric loss. In

* Corresponding author. Tel.:9940054040
E-mail address: paulantovero@yahoo.co.in

Selection and peer-review under responsibility of the scientific committee of the Materials For Energy and Environment.

addition, it has attractive magnetic properties, high Curie temperature, excellent chemical stability and low cost and has been widely used in the field of EM wave absorption.

The basis for multiphase profile analysis of powder diffraction patterns was firstly introduced completely by Rietveld in 1969. Rietveld showed the possibility of replicating the results of diffraction pattern measurements with pattern calculation. The advantage of such pattern calculation is when there is an occurrence of an error that is caused by an intensity deviation in an imperfect model structure; it will tend to leave the remaining intensity, both negative and positive. The basic principle of Rietveld analysis is to match (fitting) the peak profile of the calculation with the peak profile of the observation. The profile matching (fitting) is carried out by applying the procedure of a nonlinear least square calculation. FT-IR and Raman spectroscopies are mutually complementary parts of molecular vibrational spectroscopy [3,4]. Their molecular physics is essentially the same since both are concerned with the observation of the excitation of molecular vibrational energy states associated with the electronic ground state. In FT-IR spectroscopy, vibrational excitations occur upon the absorption of electromagnetic radiation. In Raman measurements the excitation is a consequence of inelastic light scattering by molecule [5-7].

In this work, $BaFe_{12}O_{19}$ nanoparticles were prepared through simple sol–gel auto-combustion method. Powder X-ray diffraction, Fourier transforms infrared spectroscopy and micro Raman spectroscopy, room temperature magnetization measurements by vibrating sample magnetometer were carried out for their characterization. The results observed from the above mentioned studies are briefly discussed below.

2. Experimental

2.1 Materials

Barium nitrate ($Ba(NO_3)_2$), ferric nitrate $Fe(NO_3)_3$), zirconium nitrate ($Zr(NO_3)_4$), citric acid and ammonium hydroxide solution were purchased from Merck (India) were used as received without further purification.

2.2 Method

$BaFe_{12}O_{19}$ nanoparticles were synthesized by sol–gel auto-combustion method. The starting precursors ($Fe(NO_3)_3 \cdot 9H_2O$, $Ba(NO_3)_2$; Ba/Fe = 1:12) with a stoichiometric amount of metal nitrates were dissolved in double-distilled water by stirring. The temperature was increased to 70^{o}C and then citric acid was subsequently added to solution (molar ratio of total metal ions and citric acid in the solution is 1:1) and the resulting mixture was stirred for 30 min. Then, the pH was adjusted to about 7 by adding ammonia solution. Aqueous suspensions were stirred and heated for several hours at 80^{o}C until a highly viscous gel was produced. In the final step of the sol–gel auto-combustion process, the obtained gel is allowed to burn via auto-combustion reaction and then was dried at 250^{o}C for 2 h. Finally, the burnt product was grounded and annealed at 950^{o}C for 5h.

2.3 Characterization

X-ray diffraction data of annealed powder samples were recorded for identification of phase and structure with X-ray diffractometer (X'pert-Philips). The refinement of diffraction data has been performed through Rietveld refinement technique using MAUD software. FTIR spectra were obtained in transmission mode by FTIR spectrometer (Perkin Elmer, 1600) in order to identify functional groups of the nanoparticles. Raman spectra were recorded using a micro-Raman spectrometer (Witech CRM200, the excitation wavelength at 532 nm).

3. Results and Discussion

3.1 XRD Analysis

Fig. 1 shows the XRD pattern of $BaFe_{12}O_{19}$, The major diffraction peaks of barium ferrite were observed at 2θ values of 30.35^o, 32.34^o, 34.29^o, 35.42^o, 37.49^o, 40.42^o, 42.52^o, 55.23^o, 56.69^o and 63.18^o, 67.51 and 72.67^o corresponding due to the (110), (107), (114), (200), (203), (205), (206), (217), (2011), (220), (2014) and (317) reflections. The patterns have been indexed to hexagonal crystal system pertaining to the space group P63/mmc (No. 194), which confirms that the phase belongs to the magnetoplumbite crystal structure. The synthesized nanoparticle shows all the diffraction peaks are very well consistent with the standard ICDD patterns (JCPDS no. 43-0002) with no observable secondary phase such as α-Fe_2O_3.

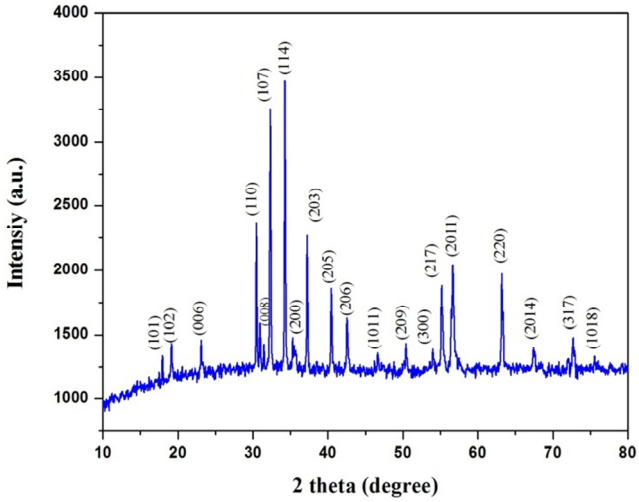

Fig.1: Powder XRD pattern of $BaFe_{12}O_{19}$ Nanoparticles

The crystallite size of $BaFe_{12}O_{19}$ nanoparticles can be calculated by using the Debye–Scherrer formula:

$$D = \frac{K\lambda}{\beta \cos\theta} \quad (1)$$

where D is the average crystallite size of nanoparticles, k is the shape factor, λ is the X-ray wavelength, β is the full width at half maximum, θ is the diffraction angle of Bragg and k is often assigned a value of 0.89, which depends on several factors, including the Miller index of the reflecting plane and the shape of the crystal. The (114) reflection of the observed X-ray data was chosen for calculating the crystallite size of $BaFe_{12}O_{19}$ nanoparticles. The average size of the $BaFe_{12}O_{19}$ nanoparticles was calculated using the above mentioned equation and estimated as 44.54 nm.

3.2 Williamson-Hall analysis:

The individual contribution to the line broadening of a Bragg reflection can be expressed as:

$$\beta_{hkl} = \beta_s + \beta_D \quad (2)$$

Where β_{hkl} represents the full width at half maximum (FWHM) of a peak in radian, β_s and β_D are the breadth due to size and strain, respectively. In W-H relation the strain was assumed to be uniform in all crystallographic direction, β_{hkl} is given by

$$\beta_{hkl} = \left(\frac{K\lambda}{D\cos\theta}\right) + 4\varepsilon \tan\theta \quad (3)$$

Rearranging Eqn. (10) gives

$$\beta_{hkl}\cos\theta = \left(\frac{K\lambda}{D}\right) + 4\varepsilon \sin\theta \quad (4)$$

Here D and ε corresponds to the crystallite size value and dimension value (microstrain) respectively. By plotting $\beta_{hkl}\cos\theta$ as a function of 4sinθ, the average crystallite size and strain can be estimated from the extrapolation and the slop of the fitted line [8]; see fig 2.

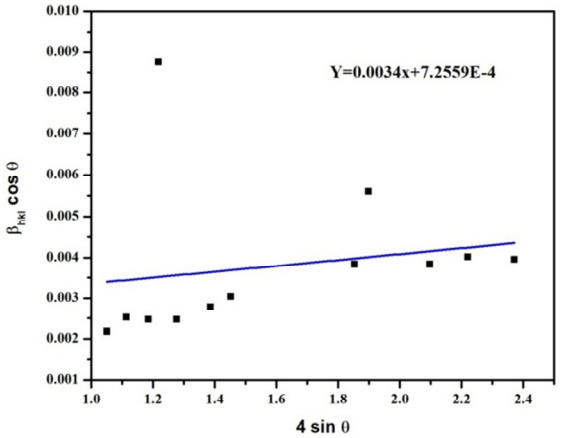

Fig.2: Williamson –Hall plot of $BaFe_{12}O_{19}$ Nanoparticles

3.3 Rietveld crystal structure refinement

The XRD patterns of the sample were analyzed by employing the Rietveld refinement method with the help of MAUD software program. A typical XRD along with theoretical data with Rietveld analysis is shown in the fig. 3. Vertical lines are allowed Bragg's positions for $P6_3/mmc$ space group. One can observe that all the observed peaks are allowed Bragg's position only, which is consistent with the analysis carried out by using ICDD data base. During the refinement, atomic fraction positions have been kept as fixed parameters and other parameters such as, lattice constants, isothermal parameters, shape and scale parameters have been taken as free parameters. Various structural parameters R_p (profile fitting of R-Value), R_{wp} (weighted profile of R-Value) and χ^2 (goodness of fit factor) obtained from the Rietveld refinement are presented in the Table 1. The low values of χ^2 and profile parameters (R_p, R_{wp}) suggest that the derived samples are better quality and refinements of samples are effective. The structural parameters: lattice constants ('a', 'c') and volume (V) are also given in Table 1. Comparison between calculated and observed inter-planner spacing (d-values) of hkl Bragg planes for $BaFe_{12}O_{19}$ after Rietveld refinement are tabulated in Table 2.

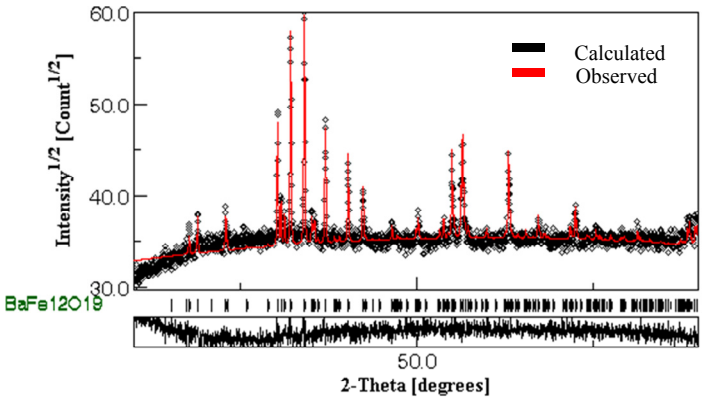

Fig.3: Rietveld analysis of $BaFe_{12}O_{19}$ Nanoparticles

Table 1: Refined structural parameters obtained from Rietveld analysis

Sample	Space group	R_p	R_{wp}	χ^2	a (Å)	c (Å)	c/a	V (Å^3)
$BaFe_{12}O_{19}$	$P6_3/mmc$	3.081	3.984	2.823	5.89	23.23	3.94	697.92

Table 2: Comparison between some of the calculated and observed inter-planner spacing (d-values) of hkl Bragg planes for $BaFe_{12}O_{19}$ after Rietveld refinement.

hkl	Inter planer spacing (d-spacing)	
	Calculated Values	Observed Values
101	4.961	4.987
102	4.649	4.674
006	3.849	3.872
110	2.932	2.948
107	2.767	2.783
114	2.614	2.629
200	2.539	2.553
203	2.412	2.424
205	2.225	2.237
206	2.120	2.131
209	1.805	1.815
300	1.694	1.703
217	1.659	1.668
2011	1.618	1.627
220	1.467	1.474
2014	1.383	1.392
317	1.296	1.303

3.4 FT-IR Analysis:

The FTIR spectrum investigation is used to find the information of bonding in a compound. The peaks are mainly dependent on the structure of the crystal and chemical mixing ratio of the prepared materials. The FT-IR spectra of pure and substituted barium hexaferrite samples are recorded in the range of 400-4000 cm^{-1} wave numbers as shown in fig 4. FT-IR spectrum of the sample indicates the formation barium hexaferrite ($BaFe_{12}O_{19}$) with absorption bands at around 567 cm^{-1},537cm^{-1} and 426 cm^{-1} can be attributed to metal-Oxygen stretching vibration in hexaferrite structure. The very weak absorption bands seen at 2975 cm^{-1} region is due to O-H stretching band of H_2O for $BaFe_{12}O_{19}$. In more details the peaks in the range 420-445cm^{-1} illustrate vibrations of octahedral bonds and others two peaks indicate tetrahedral [9,10].

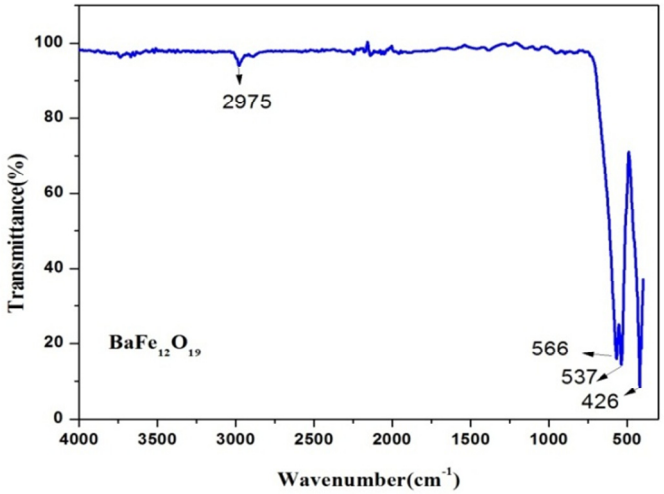

Fig. 4: FT-IR spectra of barium hexagonal ferrite

3.5 Raman spectroscopy Analysis:

Raman spectroscopy involves molecular and crystal lattice vibrations and is therefore sensitive to the composition, bonding, chemical environment, phase and crystalline structure of the sample material in any physical form. In the present work, Raman spectroscopy has been used to show the phase composition and homogeneity of the $BaFe_{12}O_{19}$ system by comparing the observed results with the selection rules and mode assignments discussed by Kreisel et al.(1998) [11]. From the literature, it is reported that 42 Raman-active modes ($11A_{1g} + 14E_{1g} + 17E_{2g}$) and 30 IR active modes ($13A_{2u} + 17E_{1u}$) are expected for the barium hexaferrite system ($BaFe_{12}O_{19}$). Raman spectra of all the prepared compounds were recorded and normalized with respect to the most intense band at room temperature. In order to analyze the polarization dependence of the Raman signals, the Raman bands were fitted with the Lorentzian line shape and the results are shown in Fig. 5. The observed Raman spectra have been indexed and the comparative statement of vibrational modes observed was listed in the Table 3.

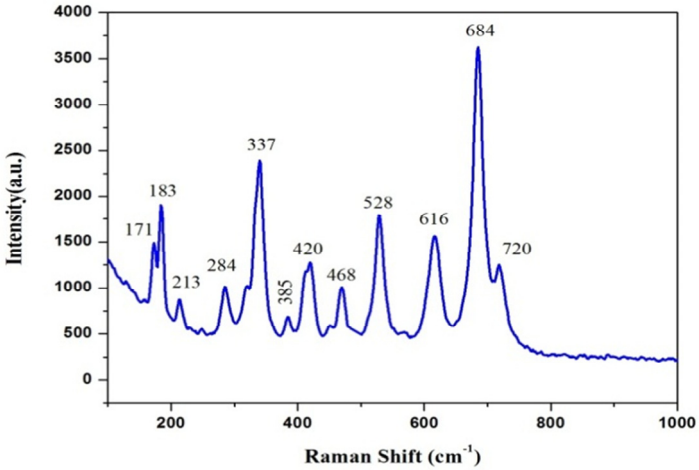

Fig. 5: Raman spectra of barium hexagonal ferrite

The major peaks observed at about 720, 684, 528, 468, 420, 385, 337, 284, 213, 183 and 171 cm^{-1} are in good agreement with the magnetoplumbite structure. The peaks at 720 and 684 cm^{-1} can be assigned to A_{1g} vibrations of Fe-O bonds at the tetrahedral 4f1 and bipyramidal 2b sites, respectively. Other peaks at 616, 528, and 468 cm^{-1} are due to A_{1g} vibrations of Fe-O bonds at the octahedral 4f2, 2a, and 12k sites, whereas peak at 420 cm^{-1} is due to A_{1g} vibration at the octahedral 12k dominated site. The peaks at 284 and 213 cm^{-1} were due to E_{1g} vibrations, while the peak at 337 cm^{-1} was due to E_{2g} vibration. The peak at 183 and 171 cm^{-1} resulted from E_{1g} vibrations of the whole spinel block.

Table 3: Assignment of the main Raman- active modes observed in $BaFe_{12}O_{19}$

Wave number (cm^{-1})		Symmetry	Assignment
$BaFe_{12}O_{19}$	Kreisel et al.(1999)		
173	173	E_{1g}	Whole spinel block
183	184	E_{1g}	Whole spinel block
337	335	A_{1g}	Octahetra (mixed)
411	409	A_{1g}	$Fe^{(5)}$ O_6 octahetra dominated
468	467	A_{1g}	Octahetra $Fe^{(1)}$ O_6 and $Fe^{(5)}$ O_6
616	614	A_{1g}	Octahetra $Fe^{(4)}$ O_6
684	684	A_{1g}	Bi pyramid $Fe^{(2)}$ O_5
720	719	A_{1g}	Tetrahetra $Fe^{(3)}$ O_4

4. Conclusion:

The single phase nanocrystalline barium hexaferrite ($BaFe_{12}O_{19}$) has been prepared by sol-gel auto combustion method. The hexagonal magnetoplumbite crystal structure with space group $P6_3/mmc$ was exhibited in powder X-ray diffraction analysis and Rietveld analysis. The lower values of profile parameters such as R_p, R_{wp}, χ^2 and inter planer spacing indicated that the calculated diffraction pattern is in fair agreement with observed pattern. The crystallite size and lattice strain in sample was investigated by Williamson-Hall (W-H) method. $BaFe_{12}O_{19}$ compounds exhibit intense Raman resonance peaks which reveal the formation of well crystalline hexaferrite system.

Acknowledgements

The Authors are thankful to Department of Chemistry, IITM, Chennai for XRD analysis.

References:

1. C.L. Yuan, Y.S. Hong, J. Mater. Sci. 45 (2010) 3470-3476.
2. X.G. Liu,, C. Feng, N.N. Bi, Y.P. Sun, J.C. Fan, Y.H. Lv, C.G. Jin, Y.R. Wang, C.T. Li, Ceram. Int. 40 (2014) 9917-9922.
3. R.D. Waldron, Infrared spectral studies in spinnel structure ferrites, Phys. Rev. 99 (1955) 1727.
4. W.B.White, B.A.DeAngelis, , Spectrochim.Acta A, 23 (1967) 985-990.
5. R.Gupta, A.K.Sood, P.Metcalf, J.M.Honig, Phys.Rev.B65 (2002) 104430.
6. P.R.Grave, C.Johnston, J.J.Campaniello, , Mater.Res.Bull.23 (1988) 1650–1660.
7. A.Kumar,P.Sharma,D.Varshney, Ceram.Int.40 (2014) 12855–12860.

8. S. Anand, A. Persis Amaliya, M. Asisi Janifer and S. Pauline, Modern Electronic Materials, 3 (2017) 168–173.

9. S.Singhal, T. Namgyal, S. Bansal, K. Chandra, J. Electromagn. Anal. Appl. 2 (2010) 376–381.

10. A.Pradeep, G. Chandrasekaran, Mater. Lett. 60 (2006) 371–374.

11. J. Kreisel, G. Lucazeau, and H. Vincent, J. Solid State Chem. 137, (1998) 127-137.

Available online at www.sciencedirect.com

ScienceDirect

Materials Today: Proceedings 8 (2019) 117–122

materialstoday: PROCEEDINGS

www.materialstoday.com/proceedings

ICMEE 2018

Growth, Spectral, Linear and Nonlinear Optical Characteristics of A Novel Organic L-Proline Adipate Single Crystals

N. Indumathi[a], K. Deepa[b], E. Chinnasamy[a], D. Suresh Kumar[c], J. Madhavan[b] and S. Senthil[a, *]

[a]*Department of Physics, Government Arts College for Men, Nandanam, Chennai, India.*

[b]*Department of Physics, Loyola College, Chennai, India.*

[c]*Department of Chemistry, Loyola College, Chennai, India.*

Abstract

The growth and characterization of the L-Proline Adipate (LPA) nonlinear optical single crystals have been grown by slow evaporation technique at room temperature. The single crystal XRD illustrates the LPA corresponds to monoclinic system. The discrete functional groups exist in LPA were calculated by FTIR spectral investigation. The UV-VIS-NIR emits the optical properties for the grown LPA crystals. Several optical properties specifically Extinction coefficient, Reflectance, Linear refractive index were also determined. The calculated dielectric property of LPA was investigated by employing the dielectric studies. The Thermal behaviour of the LPA crystal has been found out by Thermal Gravimetric Analysis and Differential thermal Analysis. The SHG was characterized by utilizing the Kurtz Perry technique.

Selection and peer-review under responsibility of the scientific committee of the Materials For Energy and Environment.

Keywords: Single crystal XRD; FTIR; UV-VIS-NIR; Thermal studies.

* Corresponding author. Tel.: +91-9840074456

E-mail address: ssatoms@yahoo.co.in

Selection and peer-review under responsibility of the scientific committee of the Materials For Energy and Environment.

1. Introduction

To make practical and effective use of crystal engineering approaches for the production of new novel materials exhibit the nonlinear optical (NLO) properties [1], which is very effective and efficient in the field of organic compounds based on hydrogen bonding materials are derived from co-crystals of compatible polarizing organic molecules.

The crystal structure of those compounds are formed by choosing the organic cations molecule, which are initially credible for the observed NLO properties and the anion molecules are interconnected through the system of H-bonds. The formed H- bond structure exhibit good use of physical and chemical properties. Examples of NLO properties, which is used for the attractive technical applications i.e. new tuning laser frequencies, optical power limiting, all-optical switching, Data storage and image manipulation of these compounds [2,3]. The recent applications of Hydrogen bonded salts of organic molecules was based on stimulated Raman scattering [4,5]. Many physical properties of solid state materials are closely related to the structures of crystal symmetry (the absence of centre of symmetry which is vital for the second order NLO phenomena). The selection of the title compound L-Proline Adipate (LPA) was grown for the efforts in the field of Crystal Engineering of novel new NLO materials [6]. Adipic acid forms crystalline Adipate salts with various organic molecules are reported as NLO materials such as Piperazinium Adipate [7], L-arginine adipate [8]. The main goal of this paper is the preparation and gives detailed characterization of novel NLO organic materials of LPA.

2. Experimental Details

The LPA single crystal was prepared by combining the commercially available salts of L-Proline and Adipic acid was taken in a stoichiometric ratio of 1:2 with the deionised water as the solvent. The prepared solution was stirred vigorously for 4 hours. The synthesized purified salt was achieved by the process of successive re-crystallization. The saturated LPA mixture was filtered using Whatman filter paper and the clean solution was poured into the Petri dish and kept in a dust free environment for slow evaporation. After the period of 50 days, the water solvent was evaporated and good transparent LPA single crystal of 12x5x4 mm^3 was harvested. The photograph of LPA single crystal was shown in Fig. 1.

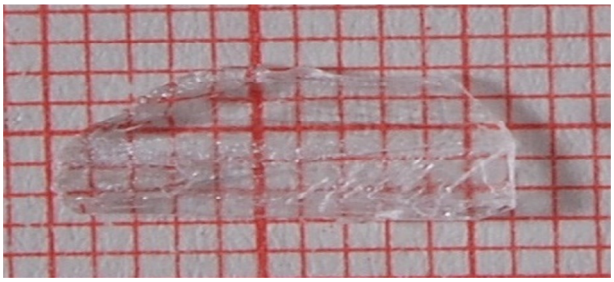

Fig. 1. Photograph of LPA Single crystal

3. Result and Discussion

3.1. Single crystal X-ray diffraction analysis

The XRD data of LPA single crystal was carried using ENRAF NONIUS CAD4 X-ray diffractometer. The cell parameters of LPA single crystal have been crystallised at monoclinic symmetry of a = 9.875 Å, b = 8.155 Å, c = 10.006 Å, $\alpha = \gamma = 90^{\circ}$, $\beta = 110.038^{\circ}$, and volume = 856.1$Å^3$ with the non centrosymmetric space group of P21/n. The

cell parameters are deviated from the L-Proline and Adipic acid cell parameters [9,10], which confirms the obtained LPA crystal is a newly obtained.

3.2. Fourier Transform Infrared (FT-IR) Spectroscopic Studies

Fig. 2 shows the FTIR spectrum of LPA single crystal. The different vibrational frequencies of amino acid molecular groups were identified in the FTIR spectral regions. The 3097 cm^{-1} peak corresponds to N-H lower frequency region of L-Proline. The peak at 1693 cm^{-1} is indicate the presence of NH_2^+ group in LPA crystal, which confirms the protonation of NH group with the COOH group of Adipic acid. The symmetric and asymmetric stretching vibrations are observed at 1041 and 1267 cm^{-1} respectively. The band at 1182 cm^{-1} is due to the C-O stretching vibration. The peak at 1420 and 913 cm^{-1} are due to O-H in plane and out of plane bending vibrations respectively. The C-C stretching and bending vibrations are observed at 729 and 502 cm^{-1} respectively.

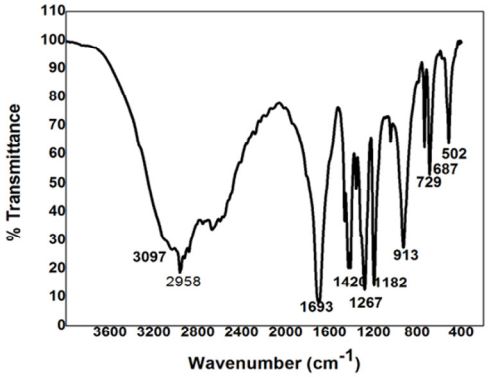

Fig. 2. FTIR Spectrum of LPA Single crystal

3.3. Optical Absorption Studies

The absorption spectrum of LPA was recorded by using UV-VIS-NIR spectrophotometer in the range of 200-1100 nm by using UV 2450 spectrophotometer. Fig. 3(a) shows the absorption spectrum of LPA crystal. The lower cut off wavelength for LPA crystal is 240 nm, which is closer to other L-Proline/Adipate derivatives. The high transparency and low absorption in the entire visible region suggests that the LPA crystal is suitable for SHG and it can be used for the NLO applications. The plot of $(\alpha h\gamma)^2$ Vs $h\gamma$ was evaluated the band gap (Eg) of LPA crystal is 5.2eV which is shown in Fig. 3(b). The wide band gap confirms which is used for UV tunable lasers [11].

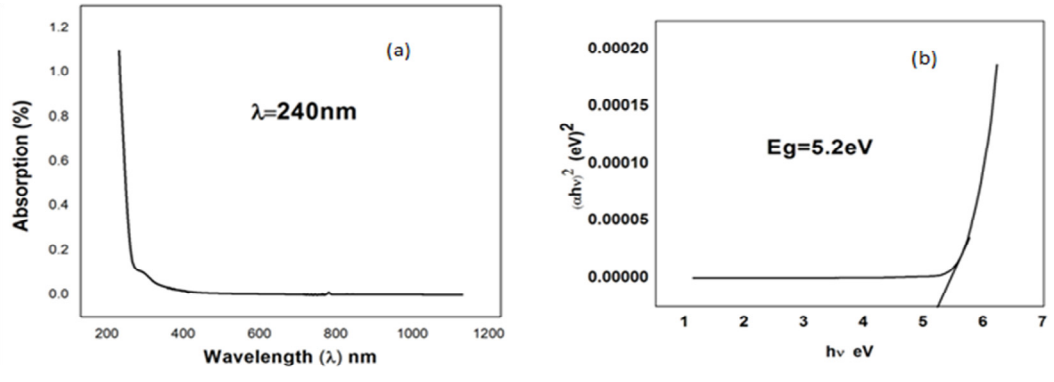

Fig. 3(a) *UV-VIS-NIR Spectrum; (b) Energy band gap of LPA single crystal.*

3.3.1 Determination of optical constants.

The optical behaviours of the crystal is significant to evaluate its usage in optoelectronics devices. The following relations was used to determine the absorption coefficient

$$\alpha = \frac{2.303\, log(1/T)}{d} \tag{1}$$

Where T is the Transmittance and d is the thickness of the LPA crystal

The reflectance in the terms of α is calculated by using the relation

$$R = 1 \pm \frac{\sqrt{1 - \exp(-\alpha t) + \exp(\alpha t)}}{1 + \exp(-\alpha t)} \tag{2}$$

$$n = \frac{-(R+1) \pm \sqrt{-3R^2 + 10R - 3}}{2(R-1)} \tag{3}$$

The Extinction coefficient (k) was obtained from the relation of wavelength (λ) and absorption coefficient (α)

$$k = \frac{\lambda \alpha}{4\pi} \tag{4}$$

Where λ is the wavelength of uv radiation.

The variation of reflectance (R) with wavelength and the variation of refractive index (n), extinction coefficient (K) with photon energy were shown in Figs 3(c), 3(d), 3(e).

The calculated linear refractive index (n) for LPA single crystal is 2.98 at 241 nm. The high transparency and low refractive index for LPA crystal makes the crystal is prominently suitable for antireflection coating in solar thermal devices and NLO application [12].

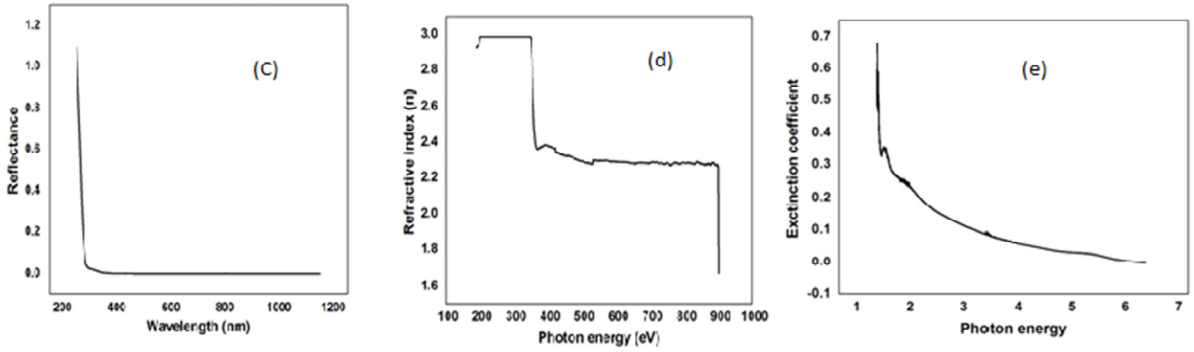

Fig. 3(c) reflectance Vs wavelength*; (d)* refractive index Vs Photon energy; (e) extinction coefficient Vs photon energy

3.4 Dielectric studies

The dielectric measurements for the LPA single crystals are used to study the basic electrical properties of solids [13]. The study of dielectric constant and dielectric loss of a material gives the detail about the nature of

atoms in the solids, ionic nature and corresponding molecular bonding in the crystals. The dielectric constant (ε_r) and dielectric loss (tanδ) values obtained for LPA crystal are shown in Fig. 4(a) and Fig. 4(b) respectively. The increase in dielectric constant at lower frequency may contributed to the electric, ionic, orientation and space charge polarization and it decrease at higher frequency are due to the loss of consequence of these polarization gradually [14]. It found that the ε_r and tanδ values are decrease with the increase in frequency. This is the common dielectric behaviour and it refers that it used for NLO applications.

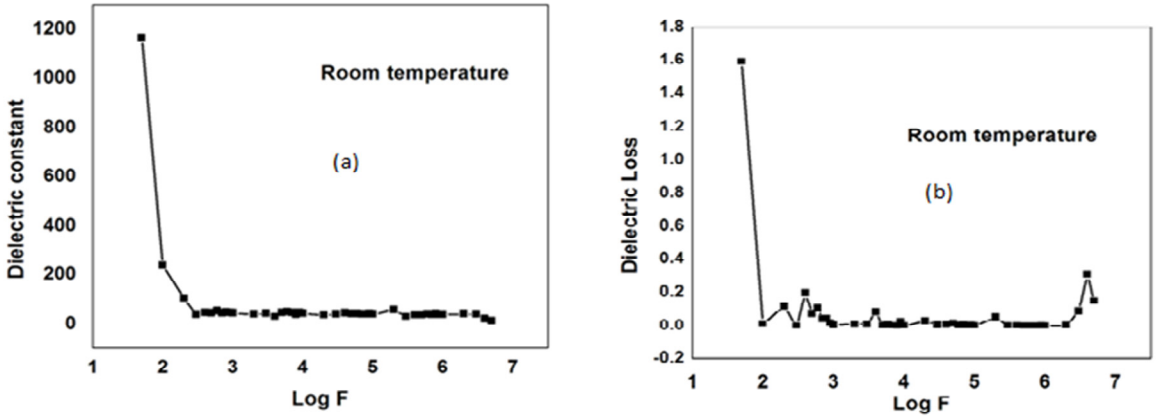

Fig. 4(a) *Dielectric Constant (b) Dielectric Loss of LPA Single crystal*

3.5. Thermal analysis

The TG/DTA of grown LPA crystal was recorded in an nitrogen atmosphere with heating rate of 20°C/min at temperature range 30–600°C by using CNST thermal analyzer. Fig. 5 shows the recorded TG/DTA spectrum. From the TG curve, the material is stable up to 157 ºC, it indicate the crystal exclude the water solvent during crystallization, and on further heating the material suffers one stage weight loss pattern. The maximum decomposition occurs in between the temperature range of 200ºC - 300ºC. From DTA curve, the endothermic peak observed at 154 °C is assigned the LPA melting point. Hence, material is stable upto 157 °C and it suitable for the device fabrications.

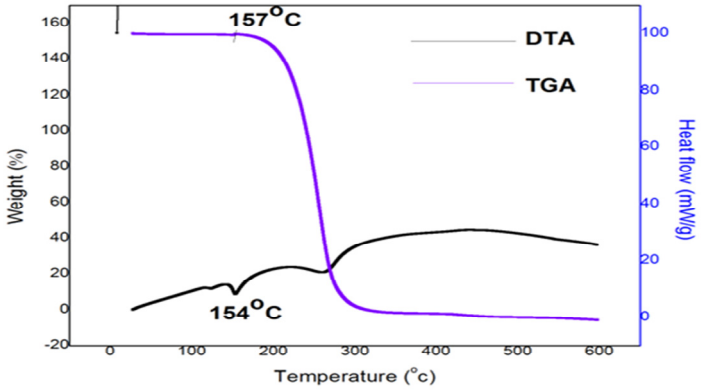

Fig. 5. TGA/DTA curve of LPA Single crystal

3.6. NLO Studies

The wavelength 1064 nm from a Q-switched Nd: YAG laser with a pulse energy 2.8mJ/pulse, pulse width 8 ns, and repetition rate of 10 Hz was used. The collected green emission from the LPA sample, the output confirms the nonlinear behaviour of LPA crystal. The output signal of 9.93 mJ was obtained for LPA single crystal compared to input signal of reference KDP is 8.91 mJ. Thus, the measured SHG efficiency was found that the grown LPA crystal has nearly 1.12 times higher NLO efficiency than KDP.

4. Conclusion

The L-Proline Adipate single crystals (LPA) were grown by SEST method. The different vibrational frequencies were studied by FTIR spectrum. The LPA single crystal XRD determines the monoclinic symmetry with P21/n space group of LPA crystals. The high transparency and lower cut-off wavelength (240 nm) of LPA crystal indicates the crystal has the potential for device fabrications. The dielectric property was studied. The characteristics of low dielectric loss with high frequency for LPA crystal indicates that the crystal possesses high optical quality with lesser defects and this parameter is vital for various applications of NLO materials. TG/DTA analysis show thermal stability of the materials up to 157°C which is ambient temperature for NLO application. The existence of second harmonic generation (SHG) signal was observed.

Acknowledgement

The corresponding author gratefully acknowledges the support from the Department of Science and Technology (DST), Government of India, for the Research project (SB/EMEQ-248/2014).

References

[1] Senthil S, Pari S, Xavier R, Madhavan J, “Linear and nonlinear optical properties of N-(3-nitrophenyl) acetamide single crystals” (2012) Optik, 123 (2) 104-108.
[2] Tamilselvan S, Vimalan M, Vetha Potheher I, Rajasekar S, Jeyasekar R, Antony Arockiaraj, Madhavan J, A nonlinear optical single crystal” Spectrochemica Acta-Part:A Molecular and Biomolecular spectroscopy, 114, (2013) 19-26.
[3] Victor Antony Raj M, Madhavan J, Materials science and Engineering 73(1) art.no 012138.
[4] Amudha M, Madhavan J, Praveen Kumar P, Journal of Optics (India) 46(4) (2017) 382-390.
[5] Sharad Kumar Panday, Tetrahedron Asymmetry, 22 (2011) 1817-1847.
[6] N. Indumathi, K. Deepa, J. Madhavan, S. Senthil, Mechanics, Materials Science & Engineering, 9 (2017) 2412-5954.
[7] B. Dhanalakshmi, S. Ponnusamy, C. Muthamizhchelvan, V. Subhashini, J. Cryst Growth, 127 (2016) 2495-2499.
[8] K. Ramya, N.T. Saraswathi, C. Ramachandra Raja, Optik, 426 (2015) 103-109.
[9] J. Janczak, P. Luger, Acta Crystallogr, Sect C:Cryst Struct Commun., 53 (1997) 1954.
[10] S.Bhattacharya, V.G.Saraswatula, B.K.Saha, Cryst.Growth Des., 13 (2013) 3651.
[11] R.Robert, G. Justin Raj, S. Krishnan, S. Jerome Das, Physica B, 405 (2010) 20-24.
[12] V. Sangeetha, K. Gayathri, P. Krishnan, N. Sivakumar, N. Kanagathara, G. Anbalagan, J. Crys. Growth, 389 (2014) 30-38.
[13] P. Kalaiselvi, S. Alfred Cecil Raj, K. Jagannathan, N. Vijayan, G. Bhagavannarayana, S. Kalainathan Spectrochim Acta A Mol and Biomol Spectrosc, 132 (2014) 726-732.
[14] N. Renuka, R. Ramesh Babu, N. Vijayan, G. Vasanthakumar, A. Krishna, K. Ramamurthi, 137 (2014) 601-606.

Available online at www.sciencedirect.com

ScienceDirect

Materials Today: Proceedings 8 (2019) 99–107

materialstoday: PROCEEDINGS

www.materialstoday.com/proceedings

ICMEE 2018

Growth and Optical, Mechanical, Electrical Behaviour of Zinc Formate Dihydrate Single Crystal: A Third Order Nonlinear Optical Material

E. Chinnasamy[a], N. Indumathi[a], K. Deepa[b], J. Madhavan[b] and S. Senthil[a, *]

[a]*Department of Physics, Government Arts College for Men, Nandanam, Chennai, India.*

[b]*Department of Physics, Loyola College, Chennai, India.*

Abstract

Optically good quality single crystals of Zinc Formate Dihydrate (ZFD) were grown by slow evaporation technique. The grown crystals were characterized by various characterization techniques such as single crystal XRD, FT-IR, UV-Vis, dielectric, microhardness and Z-scan studies. The monoclinic crystal system of the grown crystal was confirmed by Single crystal X-ray Diffraction analysis. The functional groups present in the crystal were identified by FT-IR analysis. The transparency of the crystal was identified using UV-Vis spectral studies. Dielectric studies were measured for the crystal from 50 Hz to 5 MHz at room temperature. Mechanical behaviour of the crystal was measured using Vickers microhardness tester and this study confirms that the grown crystal belongs to soft material category. The nonlinear absorption coefficient (β), nonlinear refractive index (n_2) and third harmonic generation studies were also carried out for the title crystal.

Selection and peer-review under responsibility of the scientific committee of the Materials For Energy and Environment.

Keywords: Zinc Formate dihydrate; Single crystal XRD; Dielectric study; Microhardness; Z-scan study.

1. Introduction

Non-linear optics is the main focus of many researches going on around the world. It is most attracting due to their potential applications in the field of optical processing, optical computing, optical data storage and sensor application [1,2].

* Corresponding author. Tel.: +91-9840074456
E-mail address: ssatoms@yahoo.co.in

Selection and peer-review under responsibility of the scientific committee of the Materials For Energy and Environment.

In this regard many organic and inorganic materials have been investigated and are found to exhibit very good NLO efficiency. The inorganic materials are known for their stability where as the organic crystals are known for their higher non-linear response. Thus attempt to combine the advantages of the both the inorganic and organic materials has resulted in the metal organic complexes [3-5]. Among the metal organic complexes, the Zinc acetate complexes play a vital role because of their high non-linear efficiency, transparency over the entire range of UV-vis region, good thermal and mechanical stability [6,7]. The metal coordination complexes of highly polarizable organic molecules together with the hydrogen bonds increase the thermal and mechanical stabilities of the crystal [8,9]. In the present context, the researchers are focusing on the third order materials due to their requirements in photonic fields. Especially, the third order nonlinear optical materials are investigated for their efficient optical switching behavior. Organic NLO materials, which may be critical with centrosymmetric space group plays a major role in third-harmonic generation (THG) finds a wide range of application in optical power limiting for sensor production, optical signal processing, optical communication networks and integrate optics [10]. The growth of single crystals and their characterization towards device fabrication have assumed great impetus due to their significance in both academic research and applied research. This is also one of the reasons behind the aim to design a molecule with higher order nonlinearity and also it may incorporate them with devices for optical signal processing application [11]. In the present investigation, the non-linear optical crystal Zinc Formate Dihydrate (ZFD) were grown by slow evaporation solution growth technique and the grown crystals were characterized by single crystal X-ray diffraction (XRD), Fourier Transform Infrared (FT-IR) analysis and Optical absorption studies. Dielectric studies were measured for the crystal from 50 Hz to 5 MHz at room temperature. A mechanical behavior of the crystal was measured using Vickers microhardness tester and third orders nonlinear optical (Z-scan) studies.

2. Experimental Details

The commercially available of Zinc acetate dihydrate ($C_4H_6O_4Zn.2H_2O$) (AR Grade (99.5%) M.wt:219.50 g/mol) and Formic acid (CH_2O_2) (Sigma-Aldrich AR (90%) M.wt:46.03 g/mol), complex material were taken is an equimolar ratio and dissolved in deionised water at room temperature. The resulting solution was stirred well for about 4 hours using a magnetic stirrer to attain a homogeneous mixture. The expected reaction mechanism for this title compound is

$$Zn\,(CH_3\,COO)_2.\,2H_2O + 2HCOOH \longrightarrow Zn\,(HCOO)_2\,.2H_2O$$

Suspended impurities from the solution were removed using high quality Whatmann filter paper. Then the solution was allowed to evaporate very slowly at room temperature. The slow evaporation of the solvent is yielded good transparent crystals over a time span of 25 days. The size of the grown crystal is 10 x 9 x 5 mm^3 was successfully grown and is shown in Fig. 1.

Fig. 1. Photograph of single crystal of ZFD.

3. Result and Discussion

3.1. Single crystal X-ray diffraction analysis

The lattice parameters of the grown crystal are confirmed using the Bruker AXS kappa APEXII diffractometer with MoKα radiation (λ=0.71073 Å) single crystal XRD instrument. From the single crystal X-ray diffraction analysis the lattice parameters are observed as a=8.71 Å, b=7.17 Å, c=9.34 Å, and α=90°, β=90.53°, γ=90°, V= 578 $Å^3$ and it is belongs to monoclinic crystal system with centrosymmetric space group $P2_1/C$.

3.2. Fourier Transform Infrared (FT-IR) Spectroscopic Studies

Fourier transform infra-red (FT-IR) spectrometer is an important tool for analysis to find the functional groups of the grown crystal. The spectrum of grown crystals was recorded by KBr pellet technique using a Perkin Elmer FT-IR spectrometer in the range 4000-500 cm^{-1}. The recorded FT-IR spectrum is shown in the Fig. 2. The peak appearing at 3078 cm^{-1} is due to the O-H stretching vibrations [12].Two principal absorption peaks at 1438 and 1580 cm^{-1} correspond to the symmetric and asymmetric stretching of COO vibrations. The mild peak observed at 1390 cm^{-1} corresponds to C-O-H in plane bending vibrations. The peaks observed at 1017 cm^{-1} are assigned to CH_3 rocking and bending vibration respectively. The other peaks at 952 cm^{-1} and 690 cm^{-1} are due to the out of plane bending of OH and C-H group vibration.

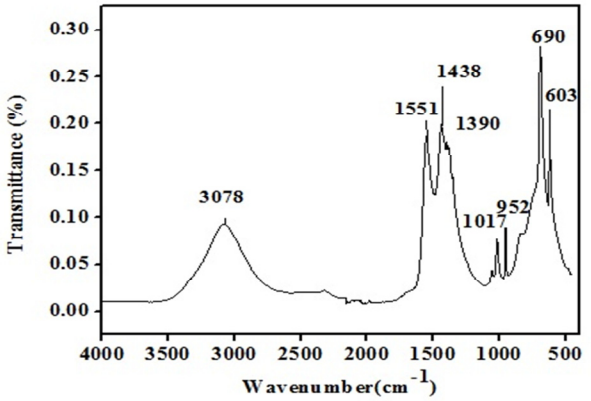

Fig. 2. FTIR Spectrum of ZFD Single crystal.

3.3. Optical Absorption Studies

The optical absorption was recorded in the wavelength range of 200-1200 nm using a Perkin Elmer lambda 35 UV-Vis spectrometer at room temperature. The recorded absorption spectrum of ZFD crystal is shown in Fig. 3(a). The lower cut off wavelength of grown single crystal is 245 nm. The entire visible region is free from absorption. The band gap of the material Eg sets the limiting cut-off wavelength λc define by λc =hc/Eg, where h is the Planck's constant and c is the velocity of the light. Eg is calculated from the plot $(\alpha h\upsilon)^n$ versus hυ. α is the absorption coefficient, n=2 for direct transition α was determined from the Transmittance using the relation shown in Eq. (1) as

$$\alpha = \frac{2.3026\, log(1/T)}{t} \quad (1)$$

Where, t is the sample thickness and T is the Transmittance. The optical band gap Eg from Tauc's expression is shown in Eq.(2) as

$$h\upsilon\alpha = A(h\upsilon - E_g)^2 \quad (2)$$

Where, the parameter A is a constant. From the graph as shown in (Fig. 3(b)), the intersection of the extrapolated spectrum with abscissa gives the direct optical band gap energy (Eg). The optical energy gap was found to be 5.0 eV and this shows the suitability of ZFD crystal for optical application.

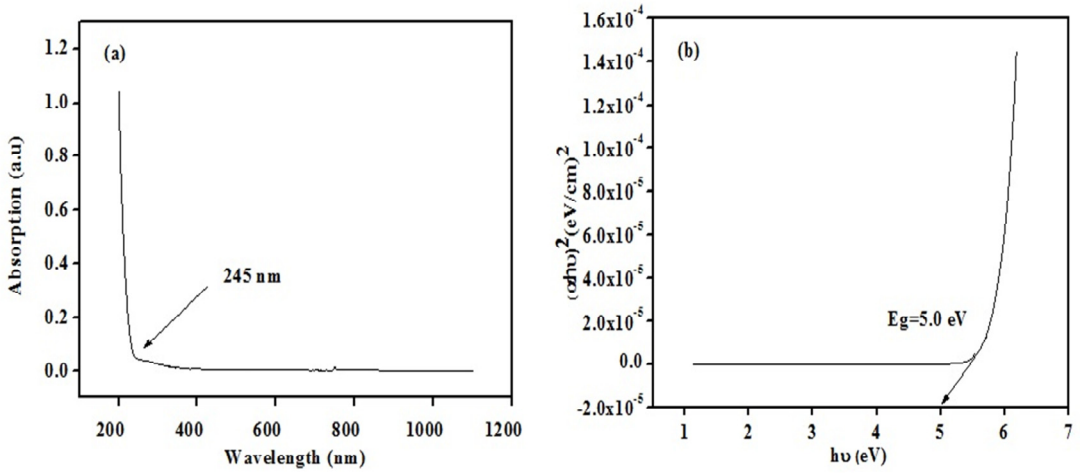

Fig. 3(a). UV-Vis absorption of ZFD crystal; 3(b) Tauc's plot for optical band gap.

3.4.Dielectric studies

The study of dielectric parameters such as dielectric constant, dielectric loss and ac conductivity as a function of frequency reveals various polarization mechanism and electrical processes that are taking place in materials. Hence, the grown crystal was subjected to dielectric studies using HIOKI 3532-50 LCR HITESTER instrument in the frequency range 50 Hz to 5 KHz at room temperature. The variation of dielectric constant (ε_r), dielectric loss (tanδ) and ac conductivity were measured as a function of frequency at room temperature. Dielectric constant and Dielectric loss were calculated using then (3) and (4) respectively

$$\varepsilon_r = \frac{Cd}{\varepsilon_o A} \tag{3}$$

$$tan\delta = \varepsilon_r D \tag{4}$$

where C is the capacitance, d is the thickness of the sample, $\varepsilon_o = 8.854\times10^{-12}$ F/m^{-1} is the permittivity of free space, A is the area of cross section and D is the dissipation factor. Figs. 4(a) and 4(b) shows the frequency dependency plot of dielectric constant and dielectric loss at room temperature. It was found that the values of dielectric constant and dielectric loss decrease with the increase of frequency. The very high values of ε_r and tanδ at low frequencies are due to the presence of all the four polarizations namely, space charge, orientation, ionic and electronic polarizations. As the frequency increases, the space charge cannot sustain and comply with the external field and hence the polarization decreases [13]. It is observed from the Fig.4(a). that there are some peak at certain lower temperature. The reason for this is that at certain critical frequencies of the applied field, standing waves are established in the crystal through the inverse piezoelectric effect. The resonances of this stationary wave with the applied electric field at selected frequencies lead to the observed peak. These critical frequencies are dependent on the dimension of the sample studies. According to Miller rule, the low value of dielectric loss at high frequencies revealed the high optical quality of the crystal with less electrically active defect is a desirable property for NLO application [14].

The AC conductivity is calculated using the Equation (5)

$$\sigma_{ac} = \omega\, \varepsilon_o \varepsilon_r \tan\delta \quad (5)$$

Where ω=2πf, f is the frequency of the applied electric field. The observed variation is shown in the Fig. 4(c). It is seen that the conductivity increases with increase in the frequency. This nature is attributed to the reduction in the interfacial polarization at higher frequencies. It is also observed that at low temperature the conductivity is less due to trapping of charge carrier at defect sites. As temperature increases, more defects are created by thermal activation and the conductivity increases. The higher value of conductivity at higher frequencies for all the measured temperature indicates the dielectric breakdown of the material.

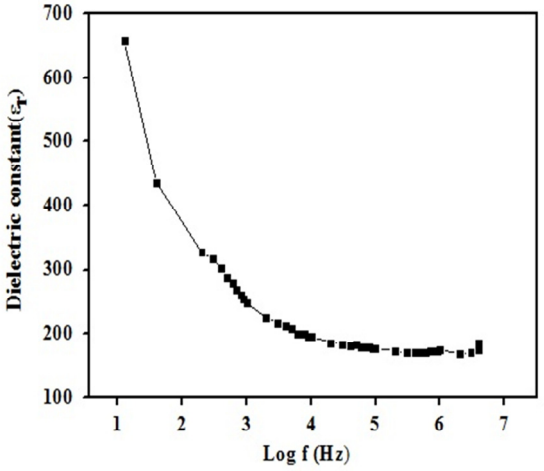

Fig.4(a).Dielectric constant Vs Log f.

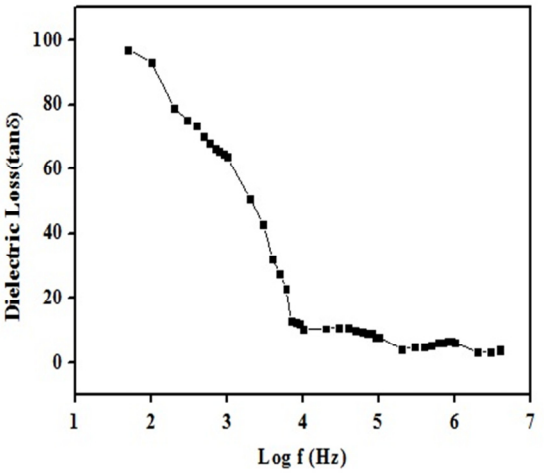

Fig.4(b). Dielectric loss Vs Log f.

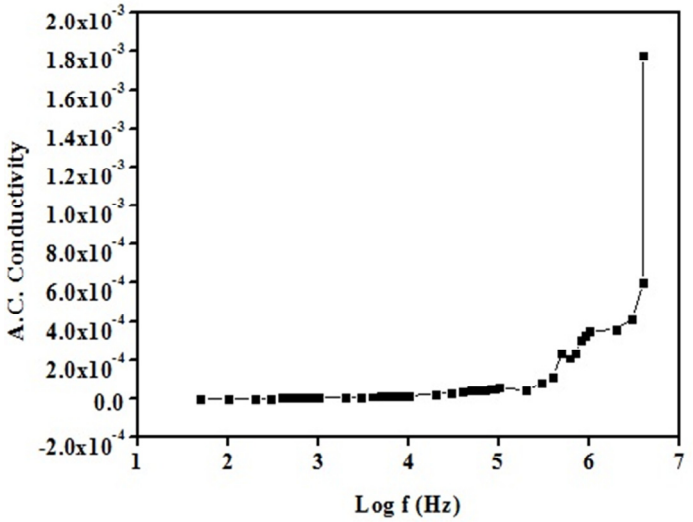

Fig. (4c). Frequency dependence of AC conductivity

3.5. Microhardness Measurements

Single crystals with good mechanical strength are very necessary for the device fabrication. At room temperature, the Vickers microhardness measurement were carried out for grown ZFD single crystals using an FM-800 Type-E Vicker's hardness tester fitted with a pyramid indenter. By applying load, the indentation marks were made on the polished crack free surface of the grown crystal. By keeping the indentation time of 7 seconds, the loads were applied on the sample crystal ranging from 10, 25, 50 and 100 g. Fig. 5. Show the plot of Load P vs. Hardness number (H_v) for the ZFD crystal. From that graph, it is noticed that the hardness number increases when load increases. The hardness values (H_v) were calculated from the Equation (6)

$$H_v=1.854\ (P/d^2) \qquad kg/mm^2 \tag{6}$$

Where P is the applied load in Kg and d is the diagonal length of the indentation impression in millimetre. The hardness increases gradually with the increase of load. The relation between load and size of the indentation is given by well known Meyer's law $P=ad_n$. Here 'a' and 'n' are constants depending upon the material [15]. The value of the work hardening coefficient n was found to be 2.47 from the Fig. 6. According to Onitsch. $1.0 \leq n \geq 1.6$ for hard materials and $n > 1.6$ soft materials [16]. Hence, it is concluded that ZFD belongs to the soft category materials.

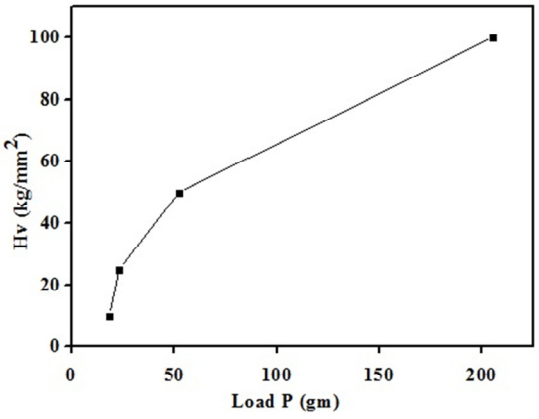

Fig.5. plot of Load versus Hv for ZFD crystal

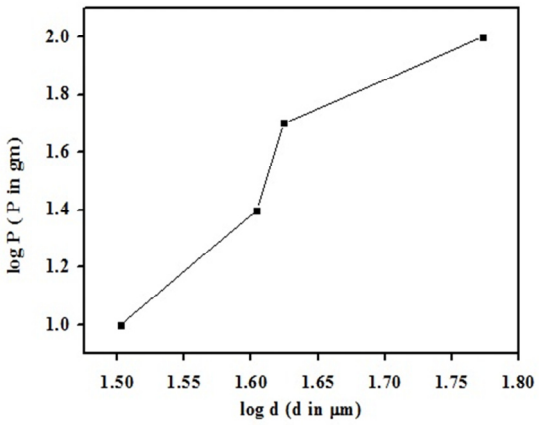

Fig. 6. plot of Log d versus Log P for ZFD crystal

3.6. Z-Scan Studies

The third harmonic generations of ZFD crystals were analyzed by calculating the nonlinear refractive index (n_2), nonlinear absorption coefficient (β) and third order nonlinear optical susceptibility (χ^3) through closed aperture and open aperture Z-scan measurements. In this Z-scan experiment He-Ne laser of wave length 632.8 nm with beam diameter 1 cm is to scan the sample. In this work third order non-linear refractive index (n_2) non linear absorption coefficient (β) and susceptibility of aqueous solution of grown crystal were evaluated by measurement of Z-scan. Fig. 7(a) and (b).Shows the closed and open aperture of Z-scan data for the sample. The special distribution for the temperature in a crystal surface produced due to localized absorption of a tightly focused beam propagating through the absorbing sample. The calculation details as follows. The position of the peak and valley, relative to the Z- axis, depends on sign of the non linear phase shift Δφ. The calculation details are as follows. The on-axis phase shift at the focus, $|\Delta\phi 0|$ is related to the difference in the peak and valley. Transmission ΔT_{p-v} in closed aperture Z-scan trance as,

$$\Delta T_{p-v} = 0.406(1-S)^{0.25} \left| \Delta\phi_0 \right| \quad (7)$$

Where ΔT_{p-v} is the difference between the normalized peak and valley transmittance, $\Delta\phi_0$ is the one axis phase shift at the focus; S is the linear transmittance aperture and is calculated using the relation [17].

$$S = 1-exp\ (-2r_a^2/\omega_a^2) \quad (8)$$

Where r_a is the radius of the aperture and ω_a is the beam radius at the aperture, the non-linear refractive index is given by the relation [18].

$$n_2 = \Delta\phi_0/KL_0L_{eff} \quad (9)$$

Where, $K=2\pi/\lambda$ (where λ is the laser wavelength) I_0 is the input intensity, Z=0, $L_{eff} = [1-exp(-\alpha L)] / \alpha$ is the effective thickness of the sample α is the linear absorption co-efficient of the inosine crystal. From the open aperture Z-scan data, the non–linear absorption co-efficient is estimated as

$$\beta = 2\sqrt{2}\Delta T/I_0Leff \quad (10)$$

Where, ΔT is the one valley at the open aperture Z-scan cure. The value of β will be negative for saturable absorption and positive for two photon absorption. The real and imaginary parts of the third order non -linear optical susceptibility χ^3 are defined as equation.

$$Re\ \chi^3(\ esu\ ) = 10^{-4}\ \mathcal{E}_0c^2n_0^2n_2)/\pi \qquad (cm^2/w) \quad (11)$$

$$Im\ \chi^3(\ esu\ ) = 10^{-2}\ (\mathcal{E}_0c^2n_0^2\lambda\beta)/4\pi^2 \qquad (cm^2/w) \quad (12)$$

Where $\mathcal{E}_0$ is the vacuum permittivity, c is the velocity of light in vacuum, n_o is the linear refractive index of the sample, and λ is the wavelength of laser beam. The third order nonlinear optical susceptibility was calculated using the relation.

$$\chi^{(3)} = [\ (Re\chi^{(3)})^2 + (Im\ \chi^{(3)})^2\ ]^{1/2} \quad (13)$$

The calculated value of the nonlinear refractive index (n_2) and the nonlinear absorption coefficient (β) are $4.24 \pm 0.21\times10^{-4}$ cm^2/W respectively. The real and imaginary parts of $\chi^{(3)}$ have been measured at 632.8 nm and were found to be $3.18 \pm 0.15 \times10^{-10}$ esu and $1.26 \pm 0.06\times10^{-7}$ esu respectively. Also, the absolute value of the third order non-linear optical susceptibility $\chi^{(3)}$ of ZFD crystal is $3.5 \pm 0.17\times10^{-4}$ esu. The results of the Z-scan technique for ZFD crystal are tabulated in Table. 1. The ZFD crystal possesses a high third order nonlinear susceptibility and the value $\chi^{(3)}$ is found to be larger due to the π-electron cloud movement from donor to acceptor which makes the molecule highly polarized.The closed and open aperture measurement using Z-scan technique shows the ZFD crystal possesses the negative nonlinear refraction and two photon absorption respectively. The measured third order nonlinear properties confirm that the ZFD crystal is a suitable material for optical limiting, switching and nonlinear optical applications.

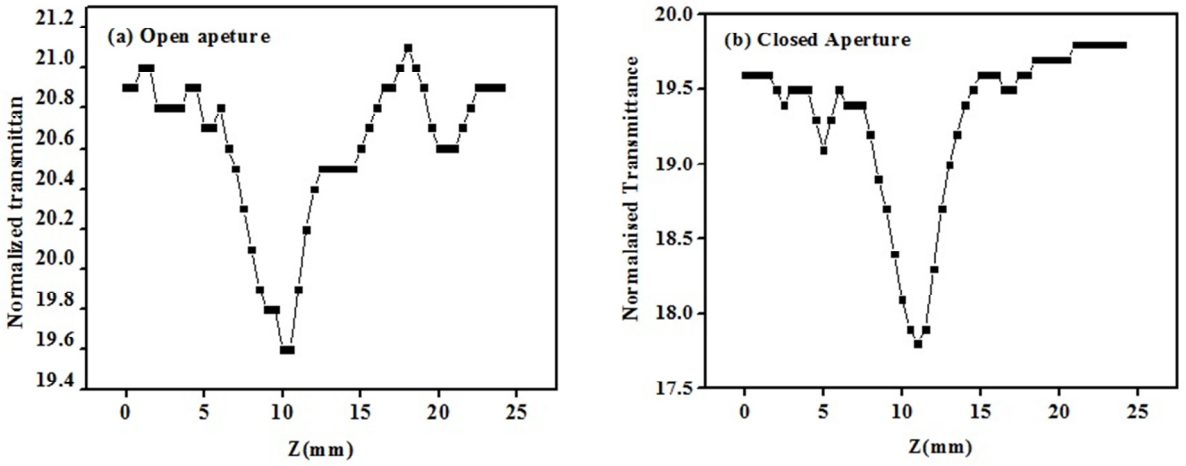

Fig.7 (a). Open aperture curve of ZFD crystal; 7(b) Closed aperture curve of ZFD crystal.

Table 1. Evaluated third order nonlinear properties of ZFD crystal.

Third order nonlinear properties of ZFD crystal	Values
Laser beam wavelength (λ)	632.8 nm
Lens focal length (f)	18.5 cm 8.5cm
Optical path distance (Z)	115 cm
Spot-size diameter in front of the aperture (ωa)	1 cm
Aperture radius (ra)	2 mm
Incident intensity at the focus (Z=0)	3.13 MW/CM^2
Effective thickness Leff	2.09 mm
Linear absorption coefficient	0.0118
Nonlinear refractive index (n2)cm2/W	$5.36 \pm 0.26 \times 10^{-12}$
Nonlinear absorption coefficient (β)	$4.24 \pm 0.21 \times 10^{-4}$ cm/W
Real part of the third-order susceptibility [Re(χ3)]	$3.18 \pm 0.15 \times 10^{-10}$ esu
Imaginary part of the third-order susceptibility [Im(χ3)]	$1.26 \pm 0.06 \times 10^{-7}$ esu
Third-order nonlinear optical susceptibility (χ3)	$3.5 \pm 0.17 \times 10^{-4}$ esu

4. Conclusion

Optically transparent single crystals of Zinc Formate Dihydrate (ZFD) have synthesized and good quality single crystal has been grown by slow solvent evaporation technique at room temperature. Crystal of size 10 x 9 x 5 mm^3 was obtained in a period of 25 days. The single crystal X-ray diffraction confirms that the grown crystal belongs to the monoclinic crystal system with the space group of $P2_1/C$. FT-IR spectrum reveals the presence of functional

various groups of the material. UV-Vis study showed the less absorption in the visible region. The lower cut-off wavelength and band gap energy found to be 245 nm and 5.0 eV respectively. The dielectric studies revealed the presence of interface polarization and dipole relaxation in the sample. The low value of dielectric loss indicated the good quality of crystal which is suitable for nonlinear optical application and the AC conductivity was increased with increase in frequency. Mechanical studies for ZFD sample were done using Vickers diamond pyramid indenter. The Vickers microhardness test clearly revealed that the grown crystal belonged to soft material category and obeyed the reverse indentation size effect for the applied loads. From the Z-scan study, the value of refractive index (n_2), the absorption coefficient (β) and the susceptibility value (χ^3) have been measured. Thus, with attaching linear and nonlinear optical properties, it is concluded that the synthesized Zinc Formate Dihydrate is a suitable candidate for optoelectronic application.

Acknowledgement

The corresponding author gratefully acknowledges the support from the Department of Science and Technology (DST), Government of India, for the Research project (SB/EMEQ-248/2014).

References

[1] X. Zhu, X. You, M. Ren, W.L. Tan, S.S. Sundara Raj, H. Fun, Chem. Lett. (2000) 473.
[2] D. Wang, G.Zhou, X.Xu, X. Wang, H. Liu, Y.Ren, Z. Shao and M. Jiang, Opt. Laser Technol, 32(2002) 343-346.
[3] M.Somac, A. Somac, B.L. Davies, M.G. Humphery, M.S. Wong, Third-order optical nonlinearities of oligomers, dendrimers and polymers derived from solution Z-scan studies, Opt.Mater.,21(2003) 485-488.
[4] D.S.Chemla, J. Zyss (Eds.), Nonlinear Optical Properties of Organic Molecules and Crystals. Academic Press, New York, 1997.
[5] P.Tansuri, K. Tansuree, B.Gabriele,R.Lara, Cryst. Growth Des. 4(2004)743-747.
[6] H.O. Marey, L.F. Warren, M.S. Webb, C.A.Ebbers, S.P.Velsko, G.C.Kennedy, G.C.Catella, Applied Opts. 31(1992) 5051.
[7] R.Mohankumar, D. Rajan Banu, G. Ravi, R. Jayavel, J. Cryst. Growth 250 (2003)113.
[8] R.Hanumantha rao, S.Kalainathan, Spectro. Chim.Acta A 86 (2012) 80-84.
[9] P.R. Newman, L.F.Warren, P.Cunningham, T.Y. Chang, D.E. Cooper, G.L. Burdge, P.Polok-Dingels, C.K. Lowe-Ma, Mater.Mater. Res. Soc. Proc. 173 (1990) 557.
[10] V. Vekataraman, G. DHanraj, V.K. Wadhawan, J.N. Sherwood, H.L. Bhat,J. Cryst. Growth 154 (1995) 92.
[11] J. Ramajothi, S. Dhanushodi, K.Nagarajan. Crystal Research and Technology.39 (2004) 414.
[12] M.I.Kay,I.Almodovar and S.F.Kaplan,Acta Cryst.24(1968)1312.
[13] S.A. Martin BrittoDhas, G. Bhagavannarayana, S.Natatajan, Open Crystallogr.1(2008) 42-45.
[14] R.Uthrakumar, C. Vesta, G.Bhagavannarayana, R. Robert,S. Jerome, Das.J.Alloys Compd.509 (2011) 2343.
[15] K.Sangwal, B.Surowska,P.Blaziak, Mat. Chem. Phys., 80 (2003) 428-437.
[16] E.M.Onitsch, Mikroscopia 2 (1947) 131.
[17] M.Shakir, V. Ganesh, B. Riscob, K. Maurya, M.Wahab, G.Bhagavannarayana, K. Kishan Rao, Physica B.Condensed Matter, 406 (2011) 3392-3397.
[18] T .C. Sabrigirisun, S.Dhanuskodi, Cryst. Res. Tech. 44(2009) 1297-1302.

Available online at www.sciencedirect.com

ScienceDirect

Materials Today: Proceedings 8 (2019) 130–135

materialstoday: PROCEEDINGS

www.materialstoday.com/proceedings

ICMEE 2018

Performance of TiO_2 Based Dye-Sensitized Solar Cells Fabricated Using Coomassie Brilliant Blue in Acetonitrile Solution

P. Sanjay[a], K .Deepa[b], J. Merline Shyla[b], J. Madhavan[b] and S. Senthil[a, *]

[a] *Department of Physics, Government Arts College for Men, Nandanam, Chennai, India.*

[b] *Department of Physics, Loyola College, Chennai, India.*

Abstract

The synthetic dye sensitizer based solar cells were successfully fabricated and photovoltaic performance was measured. Titanium dioxide (TiO_2) nanoparticles were synthesized using sol–gel technique. The XRD and HRTEM analysis were carried out to determine the structural and morphological property of TiO_2 nanoparticles. The crystalline sizes of the TiO_2 particles were determined by XRD and were confirmed by TEM. The synthetic Coomassie Brilliant Blue (CBB) dissolved in acetonitrile was used as a dye in the nanocrystalline Tio_2 solar cell. TiO_2 films on FTO glass substrate were prepared by simple doctor blade technique. The dye was characterized by UV-Vis absorption spectroscopic analysis. The strong absorption of the CBB dye enhanced the DSSC property. The results showed that TiO_2 as photoanode and CBB as a sensitizers showed good conversion efficiency.

Selection and peer-review under responsibility of the scientific committee of the Materials For Energy and Environment.

Keywords: Titanium dioxide, DSSC, CBB, TEM, XRD, etc.

1. Introduction

Dye-sensitized mesoporous nanocrystalline TiO_2 solar cells have received considerable attention as a potential, cost-effective alternative to silicon solar cells [1]. In the DSSC structure, the counter electrode acts as a catalyst to

* Corresponding author. Tel.: 9840074456.
E-mail address: ssatoms@yahoo.co.in

Selection and peer-review under responsibility of the scientific committee of the Materials For Energy and Environment.

reduce the oxidized species of the redox couples. Platinum (Pt) is the most commonly used material for the DSSCs. The most extensively applied and successful material for the photoelectrode, is the high band gap semiconductor TiO_2, sensitized by a molecular antenna. The key points to be observed are high efficiency, efficient light harvesting, high injection yield of the electrons from the excited dye to the semiconductor and fast electron transport combined with low recombination [2-5].These parameters depend largely on the surface properties, morphology and structure of TiO_2. DSSCs have attracted considerable attention because of their low costs and facile fabrication procedures. It is well known that various morphologies including nanorods or nanowires offers direct electrical pathways for photogenerated electrons and could increase the electron transport rate, which in turn may improve the performance of photovoltaic devices such as DSSCs [6–10]. DSSCs, there are a few studies made on utilization of water as solvent for electrolyte preparation. Photovoltaic performance durability of DSSCs is one of the most important parameters that should be considered for commercial application purposes [11].

In the present work, to improve the efficiency, the photo anode material for the fabrication of DSSC was prepared using sol–gel process, which leads to uniform adsorption of synthetic dye on the TiO_2 nanoparticles. The efficiency of DSSCs increased due to improved structural, optical and morphological properties of TiO_2 nanoparticles. The synthetic dye CBB was dissolved in solvent like acetonitrile and the UV-Vis responses of CBB dye were also characterized. Photovoltaic parameters including open-circuit voltage short-circuit current density, fill factor, and efficiency was determined by the help of a sun-simulator to evaluate overall cells performance.

2. Experimental methods

2.1 Synthesis of TiO_2 Nanoparticles

The Titanium dioxide nanoparticles were prepared using sol - gel method by taking titanium isopropoxide as titanium precursor and an alcohol with distilled water as hydrolysis medium. The solution was prepared to the overall volume ratio of Ti $[OCH(CH_3)_2]_4$: C_3H_8O: CH_3COOH: Distilled H_2O = 5:30:4.4:30. The isopropyl alcohol was mixed thoroughly with distilled water and this solution was stirred vigorously. About 5ml of titanium isopropoxide solution was added drop wise to result a white precipitation. The pH of sol was adjusted to 2-3 by adding 1 or 2 drops of ammonia with stirring at room temperature for 12h. This yields a high viscous white suspension which is washed in distilled water and then in ethanol to remove the impurities. After hydrolysis process, the turbid solution containing TiO_2 precipitation was heated up to 100°C for 1h. The prepared white precipitate powder was calcined at 400°C for 4h to obtain fine particles of undoped anatase phase TiO_2.

2.2 Preparation of Dye (CBB R-250)

The dye was prepared by dissolving 25mg of CBB in 50ml of acetonitrile solution a bluish green coloured dye was obtained. The dye solution was filtered using a whatman filter paper and stored in brown bottle. The colour of dye in acetonitrile solvent is shown in (Fig. 1a). The structure of CBB dye is given in (Fig. 1b).

2.2 Fabrication of DSSC

The FTO glass (Fluorine doped tin oxide) (sheet resistance 7.5kΩ/cm^2) was used as the current collector. The FTO plate was first cleaned using an ultrasonic bath with acetone, ethanol, and water for about 15 min respectively. FTO glasses were rinsed well with distilled water and air dried which are used as anode and cathode in DSSC. Scotch tape was used as a spacer to control the film thickness and to provide non-coated areas for electrical contact. The prepared TiO_2 nanoparticles were made as paste by mixing with polyethylene glycol binder and coated on FTO by doctor blade technique to prepare DSSC photoanode. The prepared TiO_2 film was air dried at 70 °C for 30 min and the films were annealed at 450 °C for 1h to eliminate the polymer binder. The coated glasses were soaked in Coomassie Brilliant Blue (CBB) dye solution for 12h. After the dye-sensitization process, the photoanode was washed with ethanol to remove the unanchored dye molecules and air dried. A platinum coated FTO glass plate was used as the counter electrode. The dye-covered TiO_2 electrode and Pt counter electrode were assembled as a sandwich-type cell. The electrolyte solution was prepared by dissolving 0.3 M of Lithium Iodide (LiI) and 0.03 M of Iodine (I_2) in tert-butyl alcohol and acetonitrile in 1:1 volume ratio, which can be used as charge transport mediator between photoanode and counter electrode in DSSC.

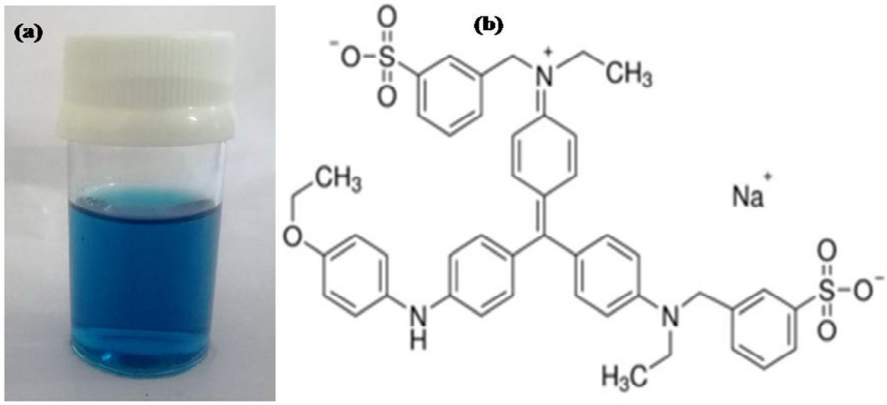

Fig.1. (a) CBB dissolved in acetonitrile. (b) Structure of CBB

3. Results and discussion

3.1 Powder XRD analysis

Figure 2 shows the Powder X-ray diffraction pattern of prepared TiO_2 nanopowder and it confirms the structure and crystalline size of TiO_2 nanoparticles. The smaller size of the TiO_2 nanoparticles was indicated by the broadened characteristic diffraction peaks. The particle size was obtained by Scherrer's equation, $D = K\lambda/(\beta\cos\theta)$, where, 'D' is the particle size, 'K' is shape factor a dimensionless constant (0.94 in case of spherical shaped particles) and 'β' is the full width at half-maximum height (FWHM) of the respective diffraction peaks. The average particle size of the TiO_2 nanoparticles in anatase phase is 20nm.

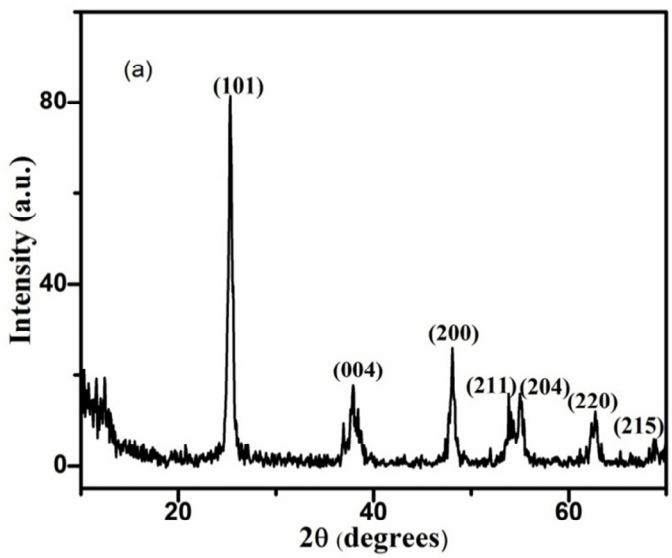

Fig.2. Powder X-ray diffraction analysis of TiO_2 nanoparticles

3.2 Transmission Electron Microscopy (TEM) Analysis

The morphology of the material in powder form was observed by Transmission electron microscopy. TEM images (Fig. 3) shows that the particles consisting of interconnected TiO_2 nanoparticles formed during the deposition process. The particles are spherical with rough surface, indicating that the homogeneity both in size and

shape is achieved by the synthesis method. The spherical particles have average small nanoparticles with diameters in the range of 20nm. During the sol-gel process, nanoparticles are combined into larger agglomerates as a result of coagulation and thus form large particles. Double layer compression mechanism is the most likely process for the formation of such morphology.

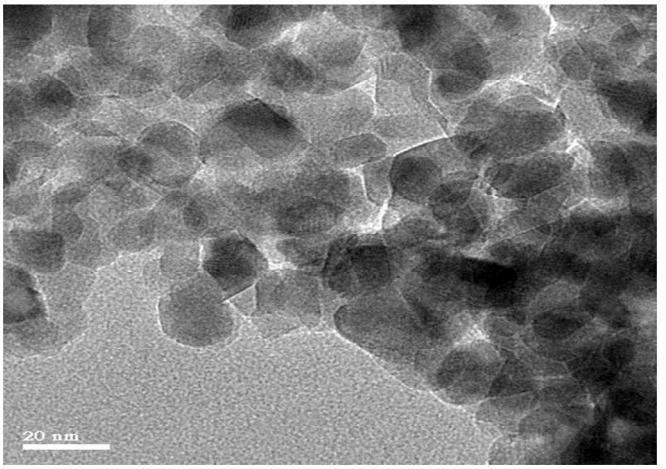

Fig.3. Transmission Electron Microscopy (TEM) Analysis

3.3 Optical studies

UV-Vis spectrophotometer was used to calculate the energy band gaps and to investigate the optical properties of the TiO_2 nanoparticles. In order to measure the band gap energies of the synthesized nano powders a UV-Vis absorption was measured in the wavelength range of 180-1200nm. The cut off wavelength for TiO_2 nanoparticles was found to occur at 362nm as shown in Figure.4a. The band gap energy of the synthesized TiO_2 powder was calculated with using the following relation

$$\alpha = \frac{(h\nu - E_g)^{1/2}}{h\nu}$$

The optical band gap (E_g) of TiO_2 nanoparticles were obtained by extrapolating the linear part of the plots of $(\alpha h\nu)^2$ versus ($h\nu$). The band gap value is obtained as 3.31eV as shown in Figure.4b. As the band gap value of the TiO_2 is decreased it increases the conducting property of the material which is more suitable for DSSC fabrication.

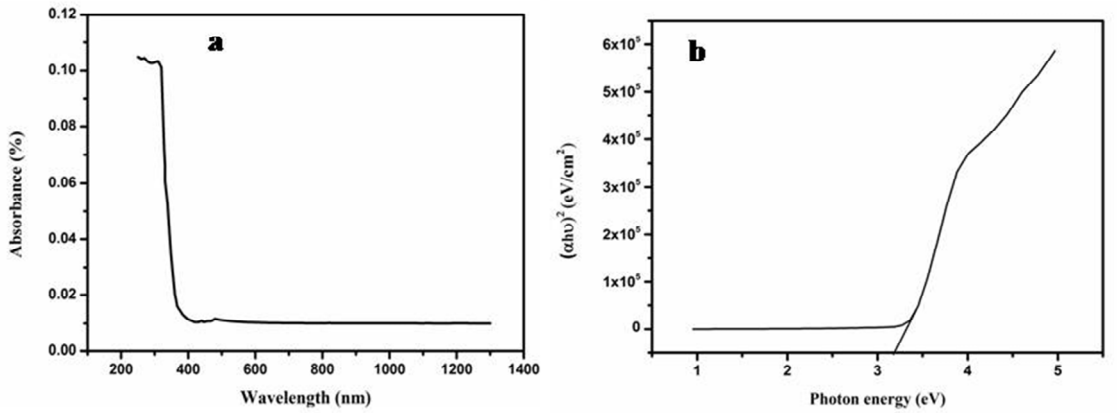

Fig. 4.(a) UV-Vis absorption spectra of TiO_2 nanoparticles; 4(b) Band gap value of TiO_2 nanoparticles.

3.4 Optical property of Coomassie Brilliant Blue

The optical property is the most crucial one for deciding the ability of the compound to act as photosensitizer. The absorption spectrum of CBB with acetonitrile solvent is shown in (Fig. 5). The absorption spectrum of CBB dye in acetonitrile solution indicates absorption in the range of 335 – 680 nm with a sharp peak at 550 nm. The onset of absorption, which occurs at around 700 nm is extended up to 340nm, covering a large fraction of the visible region of the solar radiation. With reference to its absorption range it is possible to use as a sensitizer for extending the spectral response of TiO_2 to visible range of solar radiation.

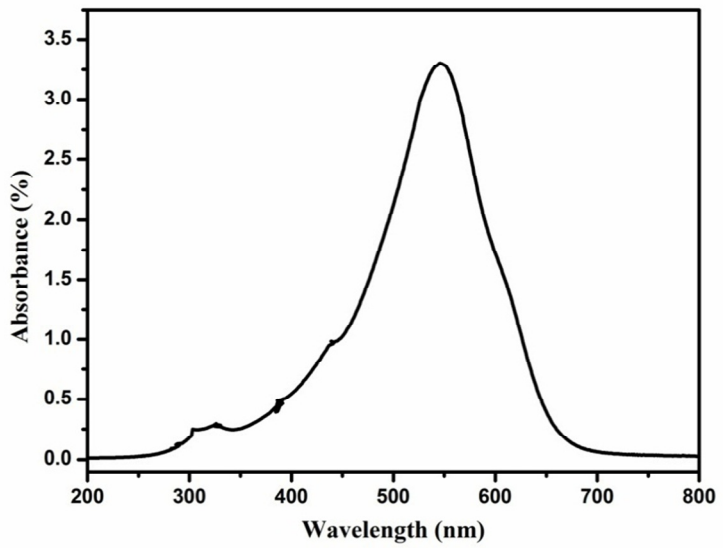

Fig. 5. UV-Vis absorption spectrum of the CBB

3.5 Characteristics of Dye sensitized solar cell (DSSCs)

Figure 6 shows the J - V characteristics of TiO_2 based solar cells which were sensitized using synthetic dye CBB in acetonitrile. The photo electrochemical activity is dependent on the morphology of the photo anode, therefore morphology of TiO_2 is supposed to be an effective way to improve the DSSCs performance. The sensitization was performed using standard solar simulator at 1Sun intensity (AM 1.5 G). The overall efficiency (η) was calculated from the current density–voltage (J–V) curves using the following equation,

$$\textit{Power conversion efficiency } (\eta) = \frac{J_{sc} \cdot V_{oc} \cdot FF}{P_{in}} \times 100\%$$

where P_{input} is the radiation power incident on the cell, J_{sc} is short circuit current density generated under illumination, and V_{oc} is the open-circuit voltage. FF is the fill factor calculated from the following equation,

$$FF = \frac{I_{max} \cdot V_{max}}{J_{sc} \cdot V_{oc}}$$

The solar cell fabricated using TiO_2 nanoparticles sensitized with the Coomassie Brilliant Blue dye dissolved in acetonitrile exhibited a power conversion efficiency of 2.264% with a short circuit current density (Jsc) of 2.70mA/cm^2, open circuit voltage (Voc) of 0.750 V and fill factor (FF) of 55.919%.

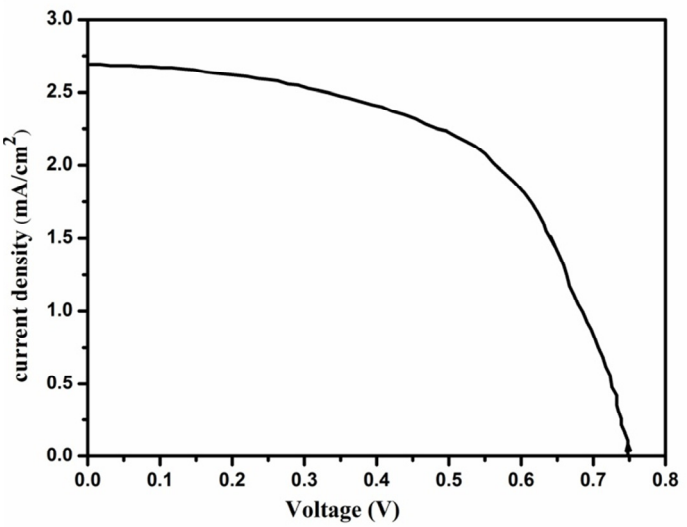

Fig.6. J-V characteristics of TiO_2 based solar cells sensitized by using synthetic dye CBB

4. CONCLUSION

The TiO_2 nanoparticles were synthesized by sol-gel method. The structural, morphology and optical properties of the TiO2 were investigated via X-ray diffraction analysis, transmission electron microscopy, UV-vis spectroscopy. XRD pattern shows the formation of anatase phase of TiO_2 nanoparticles. From the UV–vis absorption spectrum the band gap energy was calculated as 3.31eV. The optical studies suggested the suitability of material for optoelectronics applications. The fabricated DSSC showed an enhanced solar-to-electrical energy conversion. The DSSC sensitized by CBB in acetonitrile offered good conversion efficiency of 2.264 %. Through this investigation it is clearly been demonstrated that the dye can perform better function in sensitization. Further improvements can possibly be accomplished by optimizing the system.

References

[1] O. Regan, B. Gra¨tzel, M. Nature.353 (1991) *737*–740.
[2] Jobin Job Mathen, Madhavan J, Thomas A, Edakkara A J, Sebastin J, Ginson P joseph, Journal of Materials Science: Materials in Electronics, 28(10) 7190-7203.
[3] EzhilArasi S , Victor Antony Raj M , Madhavan J, Journal of Materials Science: Materials in Electronics, 29 (4), (2018) , 3170-3177.
[4]Jobin Job Mathen, Thomas, Edakkara A J, Sebastin J, Madhavan J, Ginson P Joesph, Journal of Materials Science: Materials in Electronics, 28(11), (2017), 7544-7557.
[5] S. Ngamsinlapasathian, S. Pavasupree, Y. Suzuki, S. Yoshikawa, Sol. Energy Mater. Sol. Cells 90 (2006) *3187*-3192.
[6]Y.J. Kim, M.H. Lee, H.J. Kim, G. Lim, Y.S. Choi, N.G. Park, K. Kim, W.I. Lee, Adv. Mater. 21 (2009) *3668*-3673.
[7] Sanjay P, Deepa K, Madhavan J, Senthil S, Materials Letters 219 (2018) 158–162..
[8]B. Liu, E.S. Aydil, J. Am. Chem. Soc. 131 (2009) *3985*–3990.
[9]J.H. Bang, P.V. Kamat, Adv. Funct. Mater. 20 (2010) 1970-1976.
[10]L. Vayssieres, M. Graetzel, Angew. Chem. Int. Ed. 43 (2004) *3666*–3670.
[11] K .Zhu, S .Jang, J .Arthur, A.J. Frank ,Energy Environ Sci. 5(2012) 9492–9495

Available online at www.sciencedirect.com

ScienceDirect

Materials Today: Proceedings 8 (2019) 214–222

materialstoday: PROCEEDINGS

www.materialstoday.com/proceedings

ICMEE 2018

Camellia Sinensis Leaf Extract Mediated Synthesis of Copper Oxide Nanostructures for Potential Biomedical Applications

J. Emima Jeronsia[1], L. Allwin Joseph[2], P. Annie Vinosha[2], A. Jerline Mary[2], S. Jerome Das[2,*]

[1]*Department of Physics, Holy Cross College, Trichy, India-620002*

[2] *Department of Physics, Loyola College, Chennai, India-600034*

Abstract

Despite the great progress in nanotechnologies, to date, there is still a lack of definite knowledge on the effects of CuO nanoparticles on cancer cell lines. In this present work, CuO nanoparticles were synthesized using Tea (Camellia sinensis) leaf extract. The devised method provides a simple, cost-effective aqueous means of producing spherical copper oxide nanoparticles. Preliminary characterization of green synthesized CuO NPs was carried out using UV-Vis spectroscopy, XRD, FT-IR, Zeta Potential, TEM and SAED analysis. The average crystallite size of the CuO nanoparticles is estimated to be 22.44 nm and the band gap for CuO nanoparticles was found to be 1.54 eV which are higher than bulk CuO. TEM images of CuO NPs shows a spherical morphology with moderate size distribution of larger nanoparticles due to agglomeration. The average particle size obtained from TEM is in the range of 25-32 nm which agrees well with the crystallite size calculated from XRD. CuO NPs has negative zeta potential of -70.2 mV which could keep it suspension stability for longer period of time. The antibacterial activity test results revealed a highest inhibition zone of 21 mm for gram positive *S.aureus.* Gram positive *Staphylococcus aureus* and gram negative *Klebsiella pneumonia* depicted highest sensitivity to nanoparticles compared to other strains and was more adversely affected by the copper oxide nanoparticles. CuO NPs have been tested for their potent cytotoxic activity against MCF-7 (breast cancer cells) using MTT assay. CuO NPs at the concentration of 50 µg/ml decreased the viability of MCF-7 cells by 50%.The quantification of cellular CuO NPs uptake using the imaging revealed a clear dose dependent toxic activity

Selection and peer-review under responsibility of the scientific committee of the Materials For Energy and Environment.

Keywords: Green synthesis, Camellia sinensis leaf extract, CuO NPs, Anticancer activity, Antibacterial efficacy

* Corresponding author. +91-9381190314

E-mail address: jeromedas.s@gmail.com

Selection and peer-review under responsibility of the scientific committee of the Materials For Energy and Environment.

1. Introduction

Over the last few decades " wonder nanoparticles" have played a crucial role in adding novel armamentarium in the field of medicine and pharmaceutics. Precious metal nanoparticles such as Ag and Au have been used for medical purposes for many years [1-3]. New nanoparticles are constantly being screened for their potential biological properties. In recent years, we found a plethora of literature explaining the biological activity of metal oxide nanoparticles such CuO which has the potential to deliver paradigm-shifting solution to global health problems [4].

CuO nanoparticles has been subjected to extensive investigations for its prospective applications in various fields such as gas sensors, catalysis, batteries, high temperature superconductors, solar energy conversion, photovoltaic devices and field emission emitters [5-9]. Apart from this CuO nanoparticles show exclusive antimicrobial efficacy which makes them a promising candidate for biomedical applications. Various physical and chemical methods such as hydrothermal [10], sonochemical [11], sol gel [12], thermal decomposition [13], colloidal thermal synthesis [14], microwave irradiation [15], thermal decomposition [16], solution method [17] and quick precipitation method [18-20] are currently used for the preparation of CuO nanoparticles with preffered size and morphologies. In general these method has its own drawbacks, which includes toxicity, expensiveness, hazardous materials, chemical reagents and labour-intensiveness. There has usually been a demand for green and bio based strategic approach for the synthesis of CuO nanoparticles due to its sustainability, realiability and low toxicity. Furthermore, biological synthesis CuO nanoparticles of different size and shape using Aloe Vera [21], Acalypha indica [22], Phyllanthus Amarus Leaf [23], T. Arjuna bark extract [24], Calotropis gigantean leaf extract [25], Malva sylvestris Leaf Extract [26], aqueous extract of the flowers of Cassia alata [27], Ocimum Sanctum Leaf Extract [28], Gloriosa superba L. [29], Carica papaya [30] has been reported.

In the present study, Camellia sinensis popularly known as green tea leaf extracts were used as reducing and capping agent for the synthesis of CuO nanoparticles. The most important bioactive compounds present in Camellia sinensis leaves are alkaloid, flavonoids, steroids and terpenoids which replaces the chemical reagents [31]. UV-Visible spectrometry, Fourier transform infrared spectroscopy (FTIR), transmission electron microscope (TEM), X-ray diffraction (XRD), Zeta potential measurement were applied for nanoparticle characterisation. As synthesised CuO nanoparticles were tested for its antibacterial efficacy against various pathogens and also its anticancer activity was tested in human breast cancer cell line (MCF-7) revealing conclusive evidence of the cytotoxic effect of CuO nanoparticles.

2. Materials and Methods

2.1 Materials

The starting materials used in this work were cupric acetate (monohydrate) ($CuAc_2.2H_2O$) obtained from Merck, India. All chemicals were of analytical grade reagents commercially available and used without further purification. Double distilled water was used for the preparation of all aqueous solutions.

2.2 Preparation Of Leaf Extract

The weighed amount of 5 g of Camellia sinensis leaf was boiled with 100 ml of double distilled water for 2 h at 60ºC. During the procedure of boiling, a light brown colored solution was formed and was cooled at room temperature. After that, the brown colored extract was filtered with filter paper (Whatman No.1) and stored in refrigerator for further use.

2.3 Preparation Of CuO Nanoparticles

The nanoparticles of copper oxide were synthesized by the facile green method using Camellia sinensis leaf extract. In the typical procedure, 2.7951g of cupric acetate (monohydrate) ($CuAc_2.2H_2O$) is dissolved in 70 ml of double distilled water using magnetic stirrer and stirred for a few minutes. Now 20 ml of Camellia sinensis leaf aqueous extract was taken from the stock solution (stored in refrigerator) and added. Then the mixture was stirred for 30 min. The prepared solution was centrifuged to remove impurities and dried in oven at 60 °C overnight. The

dried powder was transferred to a ceramic crucible cup and heated in a furnace at 300 °C for 2 h. Finally, obtained pale black colored CuO nanopowder product (CuO NPs) was used for the further studies.

3. Results and Discussion

3.1 X-ray diffraction analysis

The XRD patterns of green synthesized CuO nanoparticles are depicted in Fig.3.1. The diffraction peaks of the samples were indexed and it is found that the samples belong to the monoclinic crystal system. The patterns explain a high purity of the samples since no additional peaks were present. The result matches well with the standard diffraction patterns (JCPDS Card No. 652309), no characteristic peaks corresponding to the impurities, such as $Cu(OH)_2$ or Cu_2O are detected, which further confirms the growth of CuO NPs. Furthermore, the intensity of the diffraction peaks indicates good crystallization of CuO NPs. The average size of the CuO nanoparticles is estimated to be 22.44 nm according to the Scherrer equation. The particle sizes were estimated from Scherrer formula

$$D = 0.9\lambda/\beta cos\theta$$

Where D is the average grain size, λ is wavelength of X-ray, θ and β are the diffraction angle and FWHM (full width at half maximum) of the corresponding peaks. The diffraction peaks of the nanoparticles were significantly broadened owing to the finite nanoparticles size.

3.2 Optical Properties

The UV–Vis diffuse reflectance spectrum of green synthesized CuO nanoparticles is shown in Fig.3.2 The UV–vis absorption spectra of the samples were recorded in the wavelength range of 200 to 800 nm in diffuse reflectance mode. The absorption band gap Eg, can be determined by the equation

$$(\alpha h\nu)\, n = \beta(h\nu - Eg)$$

Where, hν is the photo energy, α is the absorption coefficient, β is a constant relative to the material and n is either 2 for a direct transition or 1/2 for an indirect transition. The graph is plotted against $(\alpha h\nu)^2$ and hν curves in order to determine the band gap. According to Fig.3.2.(inset), the band gap for CuO nanoparticles was found to be 1.54 eV which are higher than bulk CuO (Eg=1.4 eV) [31]. The observed differences between the calculated band gap and the reported values in the literatures arise from the size and density of CuO nanoparticles. The blue shift behavior of the peak position is observed for the samples formed with Camellia sinensis leaf extract due to their changing morphologies, particle size and surface structure.

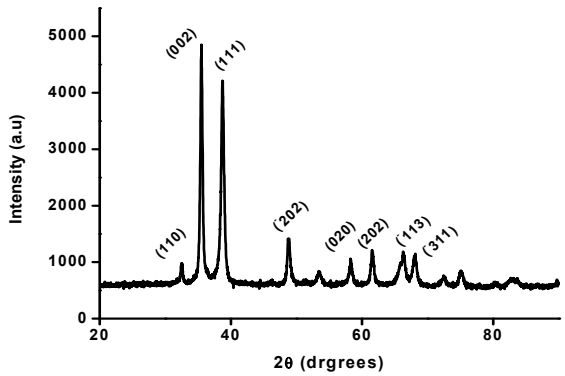

Fig.3.1 X-ray diffraction pattern of CuO NPs synthesized using *Camellia sinensis* leaf extract.

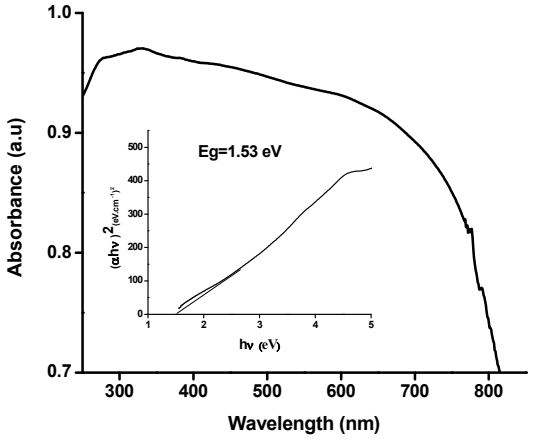

Fig.3.2 The UV-Vis diffuse reflectance spectrum with inset showing the plot $(\alpha h\nu)^2$ versus hν plot for CuO nanoparticles

3.3 FT-IR analysis

FT-IR analysis was performed to characterize the surface nature of the resulting CuO nanoparticles, depicted as wave number vs. transmittance in Fig.3.3. A strong absorption band at 532 cm^{-1} related to the vibrations of the Cu–O functional group. This confirmed the presence of nano-sized CuO particles.An intense and broadband contour which appears in the range of 3200–3550 cm^{-1} corresponds to the stretching mode of the hydroxyls of adsorbed water. Peaks appeared at 1410 and 1564 cm^{-1} corresponding to the C O stretching of carboxylate ion bond to the CuO nanoparticles as bidentate ligand. The peak at 1564 cm^{-1} also represented the formation of a covalent bond between the –OH on the surface of CuO. A Similar behavior was also observed by A. El-Trass et al., 2012.

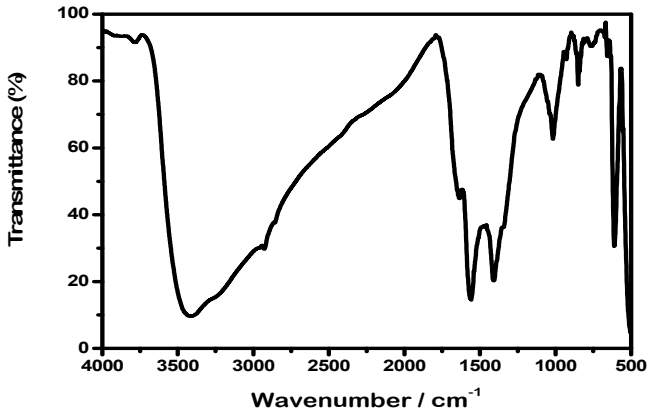

Fig.3.3. FT-IR Spectrum of *Camellia sinensis* leaf extract mediated CuO nanoparticles

3.4 Morphological and SAED pattern analysis

TEM studies were performed to reveal the morphology and size of the green synthesized nanoparticles. Fig.3.4. (a, b and c) shows the TEM images of CuO NPs having a spherical morphology with moderate size distribution of larger nanoparticles due to agglomeration. The average particle size obtained from TEM is in the range of 25-32 nm which agrees well with the crystallite size calculated from XRD. Fig.3.4. (d) shows the selected area diffraction pattern of as synthesized CuO NPs. The presence of diffraction rings suggests the formation of spherical shaped

nanoparticles. The diffraction rings match with the XRD diffraction planes which proves the monoclinic structure of CuO NPs. The presence of dark and light spots in the diffraction pattern indicates the formation of small nanoparticles.

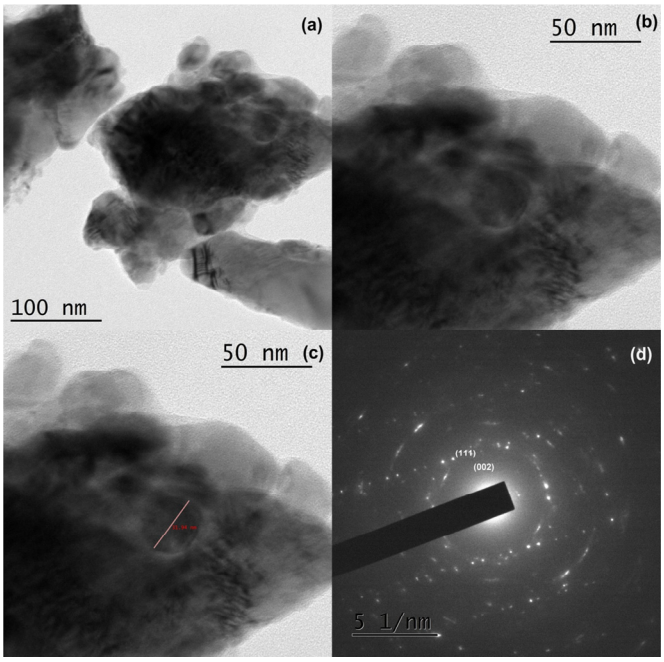

Fig.3.4. TEM images of CuO NPs synthesized via *Camellia sinensis* leaf extract (a) 100 nm (b) 50 nm (c) 50 nm (d) SAED pattern

3.5 Zeta potential analysis

The study of the electrophoretic behavior through measurement of the zeta potential becomes important for understanding dispersion behaviour of CuO nanoparticles in the dispersion medium. It is known from the literature that when the Zeta potential of a fluid is greater than 30 mV, the nanofluid can maintain its suspension stability. The nanoparticles in a fluid achieve a stable situation through the electrostatic repulsion force. From Fig.3.5 the CuO nanoparticles prepared using Camellia sinensis leaf extract has negative zeta potential of -70.2 mV which could keep it suspension stability for longer period of time.

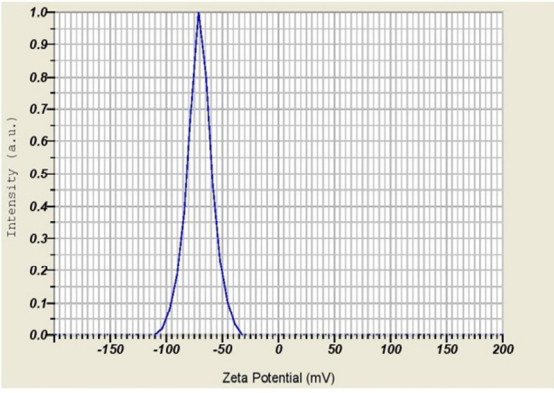

Fig.3.5. Zeta Potential Measurement of CuO NPs

3.6 Antibacterial performance of CuO NPs

Table.1.1. Antibacterial efficacy of synthesized CuO NPs against human pathogenic bacteria (NZ- No Zone)

S.No	Concentration (µg/ml)	Zone of inhibition (mm)			
		Staphylococcus aureus	Bacillus subtilis	Escherichia coli	Klebsiella pneumonia
1	Control (30)	10	10	10	15
2	250	NZ	NZ	NZ	11
3	500	NZ	NZ	NZ	12
4	750	18	10	10	13
5	1000	21	11	10	13

The antibacterial activity test results of green synthesized CuO nanoparticles against different gram positive (*Staphylococcus aureus, Bacillus subtilis*) and gram negative (*Klebsiella pneumonia, Escherichia coli*) bacterial strains are shown in table 1.1. In the current study, CuO nanoparticles with average size of 25-32 nm displayed antibacterial activity against tested strains. A higher inhibition zone of 21 mm was observed in the gram positive *S.aureus* compared to other gram-negative strains employed in this antibacterial susceptibility assay. For all bacterial strains, the highest activity was observed for 1000 µg/ml. Gram positive Staphylococcus aureus and gram negative *Klebsiella pneumonia* depicted highest sensitivity to nanoparticles compared to other strains and was more adversely affected by the copper oxide nanoparticles between the zones of inhibition observed in well diffusion method.

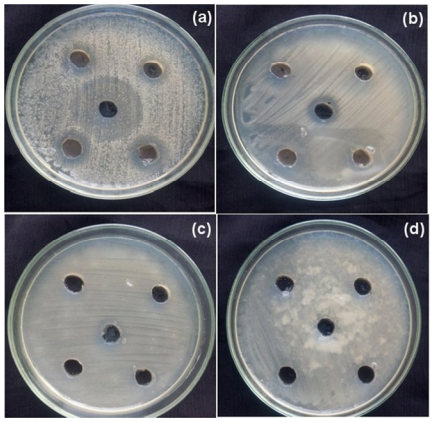

Fig.3.6. Antibacterial activity of CuO NPs synthesized using *Camellia sinensis* leaf extract (a) *Staphylococcus aureus* (b) *Bacillus subtilis* (c) *Klebsiella pneumonia* (d) *Escherichia coli*

Based on these results, it can be concluded that the green synthesized CuO nanoparticles had significant antibacterial action on both the gram classes of bacteria. The bactericidal effects observed in this study might have been influenced by the release of Cu^{2+} ions in solution. Copper ions released by the nanoparticles may attach to the negatively charged cell wall and rupture it, thereby leading to cell death. Fig.3.6 shown below represents the antibacterial activities of CuO nanoparticles in pathogenic bacterial strains. It is observed that the gram positive bacterial strains have higher sensitivity than gram negative since the zone of inhibition is large in the former compared with the later.

3.7 Cytotoxic activities of synthesized CuO NPs against MCF 7 cells

The green synthesized CuO NPs have been tested for their potent cytotoxic activity against MCF-7 (breast cancer cells) using MTT assay. It is a sensitive colorimetric assay for the determination of the number of viable cells

in cell proliferation and cytotoxicity assays. Fig.3.7. shows the proliferation rate, relative to non-exposed control cells, evaluated after 24 h exposure to CuO NPs of various concentrations ranging from (1, 2, 4, 6, 12, 25, 50 and 100 µg/ml). The result shows a decrease in proliferation rate with an increase in concentration of CuO NPs. The half maximal Inhibitory Concentration (IC50) was calculated as the concentration required to inhibit the growth of tumor cells in culture by 50% compared to the untreated cells. CuO NPs at the concentration of 50 µg/ml decreased the viability of MCF-7 cells by 50%.

The metabolic activity of MCF-7 cells presented a dose-dependent characteristic, which decreased with the decreasing of the dose of CuO NPs incubated with the MCF-7cells. After 24h of exposure, cell viability decreases as a result of mitochondrial dysfunction and the results suggest that CuO NPs were able to reduce the cell viability of MCF-7 cells in a dose dependent mode. Fig.3.8. illustrates the images of MCF-7 cells exposed to CuO NPs. The quantification of cellular CuO NPs uptake using the imaging revealed a clear dose dependent toxic activity.

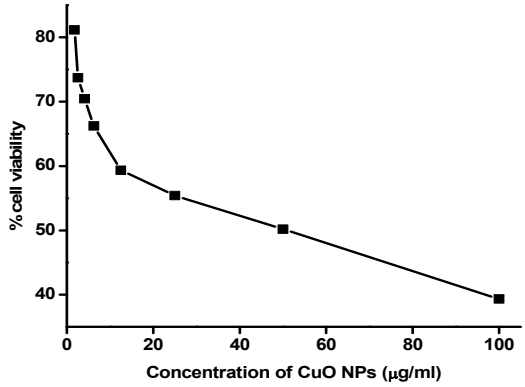

Fig 3.7 Percentage of viability on MCF-7 cell line

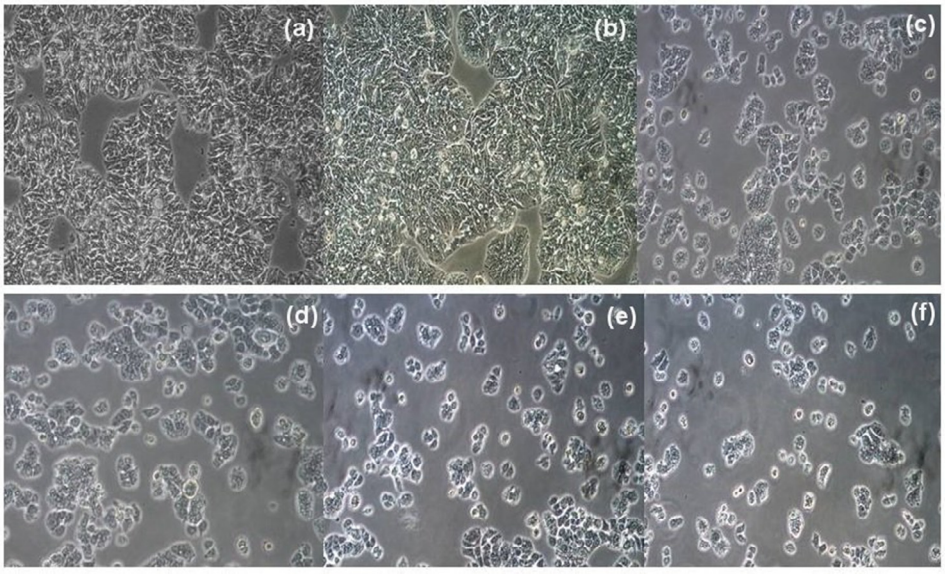

Fig.3.8 Images of green synthesized CuO NPs using *Camellia sinensis* leaf extract in MCF-7 cell line at different concentration (a) Untreated cells (b) 2 µg/ml (c) 12 µg/ml (d) 25 µg/ml (e) 50 µg/ml (f) 100 µg/ml

4. Conclusions

In summary, CuO nanoparticles were proven to be a promising anticancer and antibacterial agent. It was confirmed that the survivability of bacteria decreases with the appending of proficient CuO nanoparticles. Thus the as synthesized CuO NPs proved the outstanding antibacterial efficacy and it was well established by the clear zone of inhibitions against bacterial strains. To this end, the cytotoxic effect of copper oxide nanoparticles against human breast cancer cell line (MCF-7) was remarkable with 50% mortality at 50 µg/ml. Therefore the green synthesized CuO nanoparticles can be promising candidate for pharmaceutical, biomedical and environmental applications

5. References

1. Allardyce, C. S and Dyson, P.J (2016) Metal- based drugs that break the rules. Dalton Trans., 45, 3201-3209.
2. Abadeer, N.S and Murphy, C. J (2016) Recent progress in cancer thermal therapy using gold nanoparticles, J.Phys,chem C, 120 (9), 4691-4716.
3. Eckhardt, S., Brunetto, P.S, Gagnon, J., Priebe, M., Giese.B., and Fromm, K.M (2013) Nanobio Silver: It's interaction with peptides and bacteria, and its uses in medicine. Chem. Rev., 113(7), 4708-4754.
4. Santini, C., Pellei, M., Gandlin, V., Porchia, M., Tisato, F., and Marzano, C (2014) Advances in copper complexes as anticancer agent. Chem. Rev., 114 (1) 815-862.
5. Minjie Gao, Lei Sun, Zhiqiang Wang, Yanbao Zhao, Synthesis of Ag nanoparticles with different morphologies and their antibacterial properties. Materials Science and Engineering C, 33, 397–404 (2013).
6. Sathish Reddy, B.E. Kumara Swamy, H. Jayadevappa. CuO nanoparticle sensor for the electrochemical determination of dopamine Electrochimica Acta, 61,78– 86 (2012).
7. Nikhil V. Suramwar, Sanjay R. Thakare, Nandkishor N. Karade, Niren T. Khatya. Green synthesis of predominant (1 1 1) facet CuO nanoparticles: Heterogeneous and recyclable catalyst for N-arylation of indoles. Journal of Molecular Catalysis A: Chemical, 359, 28– 34 (2010).
8. S.L. Wang , P.G. Li , H.W. Zhu , W.H. Tang. Controllable synthesis and photocatalytic property of uniform CuO/Cu2O composite hollow microspheres, Powder Technology, 230, 48–53 (2012).
9. Nezar G. Elfadill , M.R. Hashim, Khaled M. Chahrour, M.A. Qaeed, M. Bououdina, The influence of Cu_2O crystal structure on the Cu_2O/ZnO heterojunction photovoltaic performance, Superlattices and Microstructures, 85, 908–917 (2015).
10. Tingting Jiang, Yongqian Wang, Dawei Meng , Meihua Yu, Facile synthesis and photocatalytic performance of self-assembly CuO microspheres, Superlattices and Microstructures, 85, 1–6 (2015). 17.
11. Fei Tenga,Wenqing Yao, Youfei Zhenga, Yutao Mac, Yang Teng, Tongguang Xu, Shuhui Liang, Yongfa Zhu. Synthesis of flower-like CuO nanostructures as a sensitive sensor for catalysis. Sensors and Actuators B, 134, 761–768 (2008).
12. Sambandam Anandan , Gang-Juan Lee, Jerry J. Wu. Sonochemical synthesis of CuO nanostructures with different morphology, Ultrasonics Sonochemistry, 19, 682–686 (2012).
13. K.Karthik,N.VictorJaya,M.Kanagaraj,S.Arumugam, Temperature- dependent magnetic anomalies of CuO nanoparticles. Solid State Communications, 151: 564–568 (2011).
14. Mei Kong, Weixin Zhang, Zeheng Yang, Shaoying Weng, Zhangxian Chen, Facile synthesis of CuO hollow nanospheres assembled by nanoparticles and their electrochemical performance.Applied Surface Science, 258, 1317– 1321 (2011).
15. Dong Ick Son,Chan Ho You,Tae Whan Kim, Structural, optical, and electronic properties of colloidal CuO nanoparticles formed by using a colloid-thermal synthesis process. Applied Surface Science, 255, 8794– 8797 (2009).
16. Leilei Guo, Fang Tong, Haowen Liu, Hanmin Yan , Jinlin Li, Shape-controlled synthesis of self-assembly cubic CuO nanostructures by microwave. Materials Letters, 71, 32–35 (2012).
17. Nasser Mohammed Hosny,Mohamed Shafick Zoromba, Polymethacrylic acid as a new precursor of CuO nanoparticles. Journal of Molecular Structure, 1027, 128–132 (2012).
18. Xueqin Liu, Zhen Li, Qiang Zhang, Fei Li,Tao Kong, CuO nanowires prepared via a facile solution route and their photocatalytic property. Materials Letters, 72, 49–52 (2012).
19. Rujun Wua, Zhenye Maa, Zhenggui Gua, Yan Yanga, Preparation and characterization of CuO nanoparticles with different morphology through a simple quick-precipitation method in DMAC–water mixed solvent. Journal of Alloys and Compounds, 504, 45–49 (2010).
20. Junwu Zhu, Dan Li, Haiqun Chen, Xujie Yang, Lude Lu, Xin Wang, Highly dispersed CuO nanoparticles prepared by a novel quick-precipitation method. Materials Letters, 58, 3324– 3327 (2004).
21. P. P. N. Vijay Kumar, U. Shameem, Pratap Koll, R. L. Kalyan, S. V. N. Pam, Green synthesis of copper oxide nanoparticles using Aloe vera leaf extract and its antibacterial activity against fish bacterial pathogens, BioNanoScience, 5, 135-139 (2015).
22. Rajeshwari Sivaraj., Pattanathu K.S.M. Rahman., P. Rajiv., S. Narendhran., R. Venckatesh. Biosynthesis and characterization of Acalypha indica mediated copper oxide nanoparticles and evaluation of its antimicrobial and anticancer activity Molecular and Biomolecular Spectroscopy, 129, 255–258 (2014).

23. N. P. S. Acharyulu., R. S. Dubey., V. Swaminadham., R. L. Kalyani Pratap Kollu., S. V. N. Pammi, Green sunthesis of CuO nanoparticles using Phyllanthus Amarus leaf extract and their antibacterial activity against multidrug resistant bacteria. International Journal of Engineering Research & Technology 3, (2014).
24. S. Yallappa., J. Manjanna., M.A. Sindhe., N.D. Satyanarayan., S.N. Pramod., K. Nagaraja, Microwave assisted rapid synthesis and biological evaluation of stable copper nanoparticles using T. arjuna bark extract, Spectrochimica Acta Part A: Molecular and Biomolecular Spectroscopy 110, 108–115 (2013).
25. Jitendra Kumar Sharma., M. Shaheer Akhtar., S. Ameen., Pratibha Srivastava., Gurdip Singh, "Green synthesis of CuO nanoparticles with leaf extract of Calotropis gigantea and its dye-sensitized solar cells applications." Journal of Alloys and Compounds, 632, 321–325 (2015).
26. Awwad, A.M., Albiss, B.A, Salem N.M. Antibacterial Activity of synthesized Copper Oxide Nanoparticles using Malva sylvestris Leaf Extract. SMU Medical Journal, 2, (2015).
27. Jayalakshmi A., Yogamoorthi, International, Green synthesis of copper oxide nanoparticles using aqueous extract of flowers of Cassia alata and particles characterisation. Journal of Nanomaterials and Biostructures , 4, 66-71(2014).
28. Vasudev D. Kulkarni., Pramod S. Kulkarni, Green Synthesis of Copper Nanoparticles Using Ocimum Sanctum Leaf Extract, International Journal of Chemical Studies. 1, 3 (2013).
29. H. Raja Naika., K. Lingaraju., K. Manjunath., Danith Kumar., G. Nagaraju., D. Suresh., H.Nagabhushana, Green synthesis of CuO nanoparticles using *Gloriosa superba* L. extract and their antibacterial activity. Journal of Taibah University for Science, 9, 7–12 (2015).
30. Renu Sankar., Perumal Manikandan., Viswanathan Malarvizhi., Tajudeennasrin Fathima., Kanchi Subramanian Shivashangari., Vilwanathan Ravikumar, Green synthesis of colloidal copper oxide nanoparticles using Carica papaya and its application in photocatalytic dye degradation. Spectrochimica Acta Part A: Molecular and Biomolecular Spectroscopy, 121, 746– 750 (2014).
31. Lister E and Wilson, P. Antioxidant activity and total phenolic content of selected Jordanian plant species. Crop Research Institute. (2001)

Available online at www.sciencedirect.com

ScienceDirect

Materials Today: Proceedings 8 (2019) 264–270

materialstoday: PROCEEDINGS

www.materialstoday.com/proceedings

ICMEE 2018

Growth, Spectral, Optical, Studies of A Zinc Picolinate Dihydrate NLO Single Crystal

E. Chinnasamy[a], S. Arulmani[a], K. Deepa[b], D. Suresh Kumar[c], J.Madhavan[b] and S. Senthil[a,]*

[a]*Department of Physics, Government Arts College for Men, Nandanam, Chennai, India.*
[b]*Department of Physics, Loyola College, Chennai, India.*
[c]*Department of Chemistry, Loyola College, Chennai, India.*

Abstract

Nonlinear optical material Zinc Picolinate dihydrate (ZPD) was synthesized by slow evaporation solution growth technique. The grown crystals were characterised by Single crystal X-ray diffraction analysis. The presence of functional groups in the grown crystal was analyzed using FT-IR spectrum. The UV-vis spectrum shows a low absorption in the entire visible region. Optical band gap of the grown crystal was found to be 3.98 eV.The evaluation of optical constants by employing UV-visible absorbance data such as, reflectance, extinction coefficient, refractive index, are supportive towards good performance as NLO devices. The nonlinear optical behaviour from the non-centrosymmetric crystal was observed by the generation of frequency doubled (2ω) optical radiation when subjected to pulsed Nd:YAG laser (1064 nm,10 ns,10 Hz) using Kurtz-Perry method.

Keywords: Zinc Picolinate dihydrate, Single crystal XRD, FT-IR, UV-Vis, NLO etc.,

1. Introduction

The searching, designing and development of new nonlinear optical (NLO) materials have become very important during recent years since the development of new optical devices used as optical data storage, optical information processing, optical limiting optical bistability, optical switches and computing devices depend on the design of efficient NLO materials [1-3]. The modern crystal science and technology, in recent years, the design and synthesis

* Corresponding authorTel.: +91-9840074456
*E-mail address:*ssatoms@yahoo.co.in

Selection and peer-review under responsibility of the scientific committee of the Materials For Energy and Environment.

of metal-organic coordination frame works have gathered great attention due to their potential applications in the molecular adsorption, gas storage, magnetism, molecular recognition, nonlinear optic and other fields [4].
Zinc acetate dihydrate, a chemical compound with wide applications in many industries, as one of the important fertilizers for plants and well known in chemical industries, has been used as a raw material for manufacturing various chemicals. Compounds containing carboxyl group [5] have important position among organic reagents as potential donor ligands for the transition metal ions. The carboxylate compounds including transition metals have a number of coordination modes due to both versatile bonding capability of carboxylate group and different oxidation levels of transition metals [6]. On the other hand, nitrogen containing ligands have been also used in coordination chemistry in order to obtain complexes that are able to the mimic structural, spectroscopic and catalytic features of active sites of metallo-enzymes [7-9].Therefore α-picolinic acid has attracted significant attention owing to its excellent coordination flexibility and versatility. Complexes of α-picolinic acid with different metal ions have been potentially used in various types of materials for human consumption such as pills and sports drinks. α-Picolinic acid complexes have been also used as pharmaceuticals for the prevention and treatment of arteriosclerosis and liver disorders [10-12].

In the present work, Zinc Picolinate dihydrate (ZPD), a desirable semi organic nonlinear optical crystal, has been grown from aqueous solution using slow evaporation technique. The grown crystals were subjected to various characterizations such as single crystal X-ray diffraction analysis, Fourier Transform Infrared (FT-IR) analysis, UV-Vis study and nonlinear optical studies are reported for the grown compound.

2. Experimental Process

2.1 Material synthesis

The commercially available of Zinc acetate dihydrate ($C_4H_6O_4Zn.2H_2O$) and α-Picolinic acid (C_5H_4NCOOH), complex material were taken in a stoichiometric ratio 1:1 and dissolved using deionised water at room temperature. The resulting solution was stirred well for about 5 hours using a magnetic stirrer to attain a homogeneous mixture. Suspended impurities from the solution were removed using high quality Whatmann filter paper. Then the solution was allowed to evaporate very slowly at room temperature without disturbance. The slow evaporation of the solvent yielded good transparent crystals over a time span of 45 days. The reaction scheme is illustrated in Fig. 1. A crystal of size 13 x 3 x 2 mm^3 was successfully grown as shown in Fig. 2.

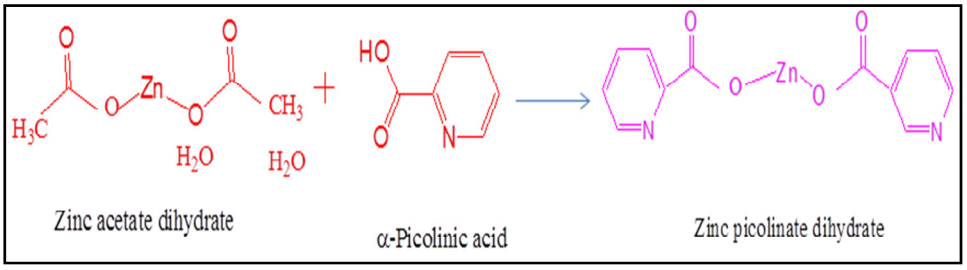

Fig. 1. Reaction scheme of the ZPD crystal.

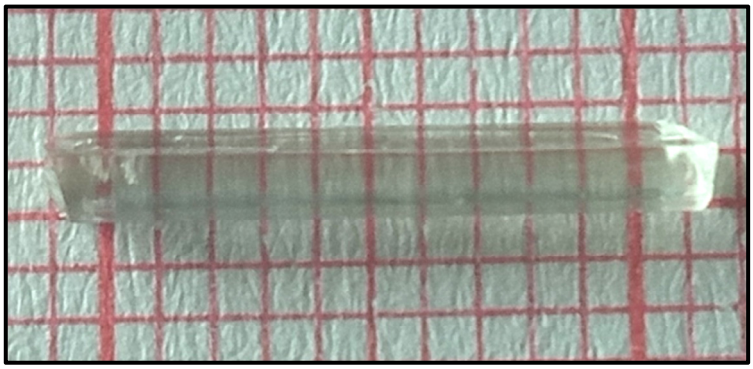

Fig 2.Photo of the grown ZPD crystal

2.2 Characterization techniques

The good quality harvested crystals were analyzed by single crystal X-ray diffraction study using Bruker AXS KAPPA APEX2 CCD X-ray diffractometer employing MoKα (λ= 0.7170 Å). The FTIR vibrational spectrum was recorded using Perkin Elmer Fourier transform infrared spectrometer in the range 4000-500 cm^{-1} by KBr pellet technique at room temperature. Optical studies were carried out using VARIN CARY 5E UV-Vis spectrophotometer. The NLO property of the material was assessed by Q switched high energy Nd:YAG laser Quanta Ray Model Lab-170-10.

3. Result and Discussion

3.1. Single crystal X-ray diffraction analysis

The single crystals were subjected to single crystal X-ray diffraction analysis using Bruker AXS KAPPA APEX2 CCD X-ray diffractometer employing MoKα (λ= 0.7170 Å) to determine the cell parameters and it reveals that the ZPD crystal crystallizes in Orthorhombic system having non-centrosymmetric space group $P2_12_12_1$. The lattice parameters were found to be a=5.23Å, b=9.81 Å, c=14.60Å, α = 90˚, β= 90˚, γ =90˚ and V=921$Å^3$.

3.2. Fourier Transform Infrared (FT-IR) Spectroscopic Studies

The FTIR spectrum of grown crystal was recorded using Perkin Elmer Fourier transform infrared spectrometer in the range 4000-500 cm^{-1} by KBr pellet technique at room temperature shown in Fig. 3. The vibrations of various functional groups present in the molecule are analyzed through absorption peaks. The approximate position of O–H bond will depend on the strength of hydrogen bond. The peaks positioned at 3217 cm^{-1} and 3099 cm^{-1} are due to NH_3^+ stretching vibration. The sharp intense peak that exists at 2122 cm^{-1} is due to N–H stretching vibration. Two sharp peaks that occur at 1624 cm^{-1} and 1445 cm^{-1} are due to COO^- bending vibration. Aromatic amines display strong C-N stretching absorption appears in the 1372-1299 cm^{-1} region. The other peaks at 694 cm^{-1} and 981 cm^{-1} are due to the out of plane bending of C-H and OH group vibrations.

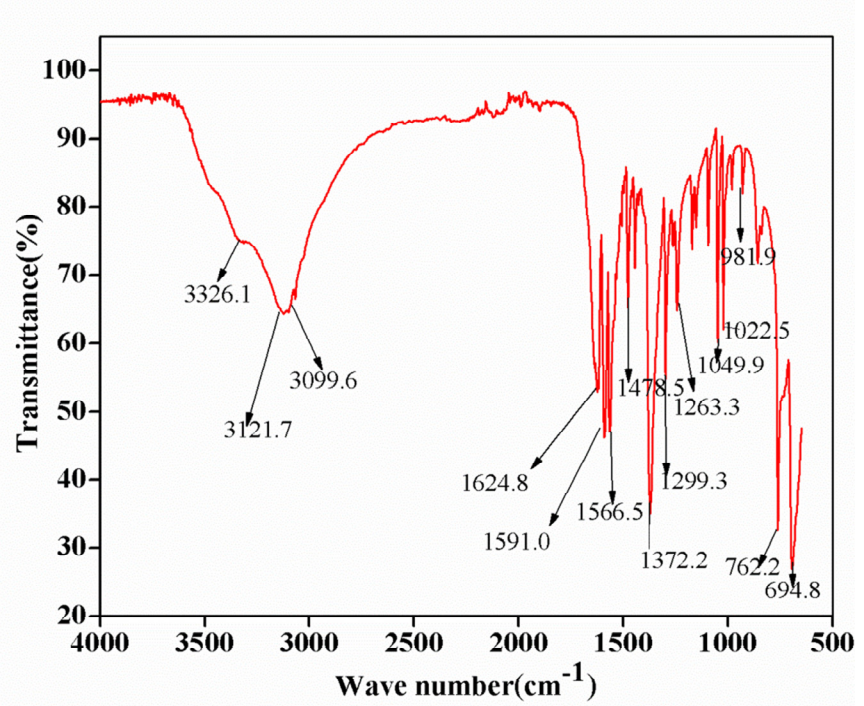

Fig.3. FTIR spectrum of ZPA single crystal

3.3. Optical studies

The Ultra Violet visible absorbance study of ZPD crystal exemplifies the linear optical properties. The optical absorption spectrum recorded in the region 200-800 nm is shown in Fig. 4(a). Ultra Violet visible spectral analysis gives information about electronic transitions of the compound [13]. Also it would help to understand the electronic structure and the optical band gap of the crystal. The lower optical cut-off wavelength of the ZPD crystal was found to be 286 nm, which is in the UV- region confirms the π-π* electronic transition occurrence at this region [14]. Hence this optical absorption spectrum reveals the usefulness of ZPD crystal suitability in optoelectronic applications.

The optical electronic band gap (E_g) of the material is very closely related to the atomic and electronic band structures [15]. The optical absorption coefficient (α) was computed using the formula,

$$\alpha = \frac{2.3026\ log\ \left(\frac{1}{T}\right)}{t} \quad (1)$$

where T,t denotes the transmittance, thickness of the crystal. The absorption coefficient (α) was computed using the formula, In this equation A is a constant, E_g is electronic band gap energy, h is plank's constant, υ is frequency of the incident photon. The electronic band gap energy of Zinc Picolinate dihydrate (ZPD) single crystal was evaluated from linear part of the tauc's plot by plotting $(h\upsilon\alpha)^2$ versus hυ shown in Fig. 4(b). The figure clearly shows the realization of direct allowed transition for ZPD crystal over the range 3.98 eV. The extrapolation of the straight line

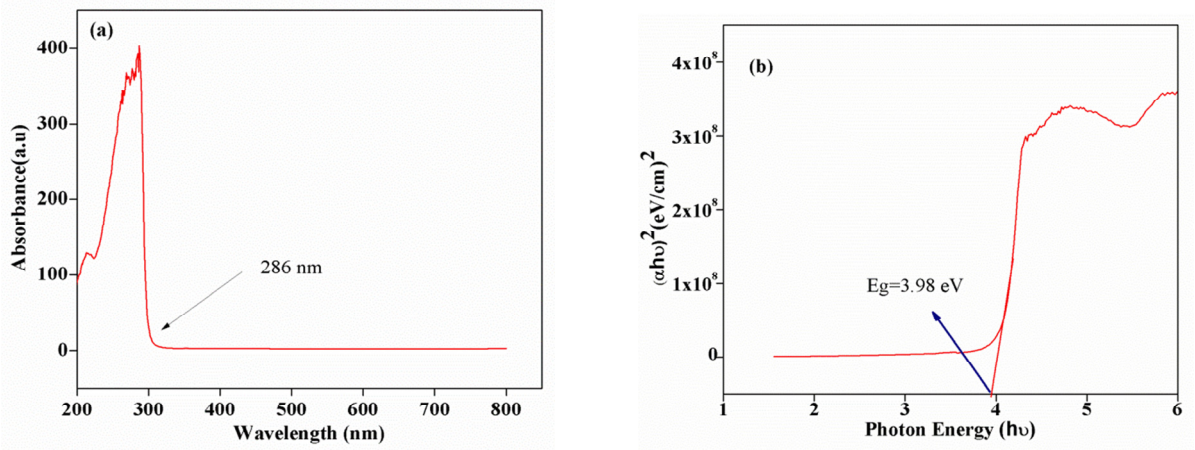

Fig 4. (a) UV-visible profile and (b) Tauc's plot of ZPD.

3.3.1. Determination of Optical Constant

The optical characteristics are vital to find out materials usability in the fabrication of optoelectronic devices. The information about the optical constants is very necessary to analyze the potentiality of materials in the applications of optoelectronics [16]. The refractive index (n) and extinction coefficient (k) are estimated by,

$$T = \frac{(1-R)^2\, exp\ (-\alpha t)}{1-R^2\, exp(-2\alpha t)} \tag{2}$$

Where, t denotes the thickness.

The extinction coefficient (k) is obtained using the relation,

$$K = \frac{\alpha\lambda}{4\pi} \tag{3}$$

The reflectance (R) can be written as,

$$R = 1 \pm \frac{\sqrt{1-exp(-\alpha t)+exp(\alpha t)}}{1+exp(-\alpha t)} \tag{4}$$

And using the reflectance (R), the refractive index (n) can be determined as,

$$N = -\left\{\frac{(R+1)\pm\sqrt{3R^2+10R-3}}{2(R-1)}\right\} \tag{5}$$

The variation of reflectance, extinction coefficient and refractive index with Wavelength are shown in Figs. 5(a), 5(b) and 5(c). The calculated refractive index is 2.72 for ZPD crystal. The extinction coefficient, reflectance and the internal efficiency of the material depends upon the absorption coefficient (α). By tailoring the optical parameters, the material can be made suitable for device fabrication.

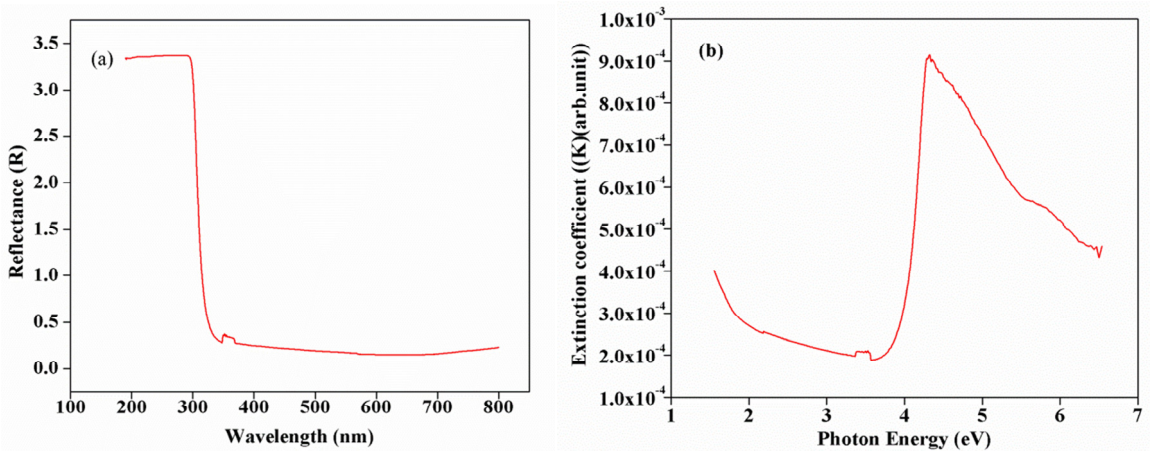

Fig. 5 (a) Variation of reflectance with Wavelength Fig. 5 (b) Variation of extinction coefficient with photon energy

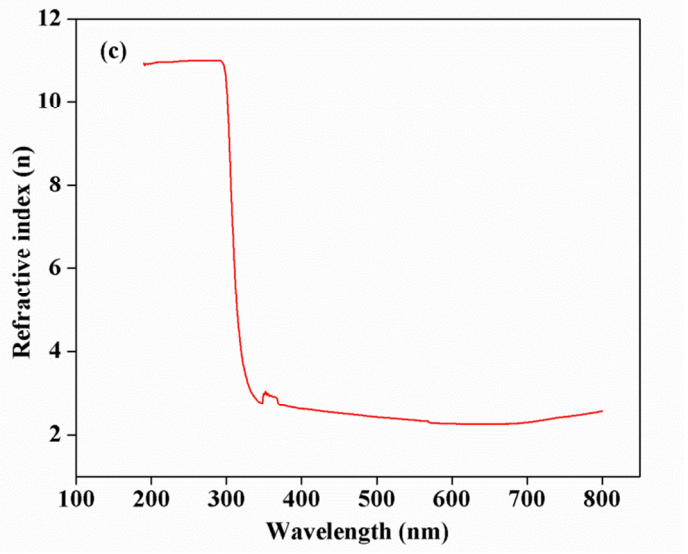

Fig. 5 (c) Variation of refractive index with wavelength

3.4 SHG studies

Kurtz powder SHG test confirmed the nonlinear property of ZPD crystal. A fundamental beam of 1064 nm with pulse energy of 6mJ/s and pulse width of 10 ns and repetition rate of 10 Hz was employed. Powdered samples of standard KDP and title compound ZPD with the same particle size were considered for powder SHG measurement. The fundamental beam was filtered by using an IR filter. A photomultiplier tube was used as detector. For the input energy of 0.70 J/pulse, the output from the sample was measured to be 2.97 times of standard KDP. The SHG measurement on the crystal proves it to be a potential candidate for frequency doubling process.

4. Conclusion

In the present study efficient semi organic single crystals of Zinc Picolinate Dihydrate (ZPD) have synthesized and good quality single crystal has been grown by slow solvent evaporation technique at room temperature. Crystal of size 13 x 3 x 2mm^3 was obtained in a period of 45 days. The single crystal X-ray diffraction confirms that the grown crystal belongs to the orthorhombic crystal system with the space group of $P2_12_12_1$. FT-IR spectrum reveals the presence of various functional groups of the material. UV-Vis study showed the absorption in visible region.

The lower cut-off wavelength and band gap energy found to be 286 nm and 3.98 eV respectively. The SHG response of ZPD crystal revealed that the efficiency is 2.97 times greater than KDP which ensures the crystal can be suitable for NLO applications.

Acknowledgement

The corresponding author gratefully acknowledges the support from the Department of Science and Technology (DST), Government of India, for the Research project (SB/EMEQ-248/2014).

References

[1] S .Senthil, S .Pari, R .Xavier, J .Madhavan, Optik, 123 (2) (2012) 104-108.
[2] E.Chinnasamy, and S.Senthil, American Institute of Physics 1832 (2017) 100019
[3]P .Prabakaran, M .Victor Antony Raj, S.Jobin Job Mathen, Prathap, J .Madhavan, Springer proceedings in Physics, 189, (2017) 255-262.
[4] S. Anie Roshan, Joseph Cyriac, M.A. Ittyachen, Mater. Lett. 49 (2001) 299.
[5] J .Jobin Job Mathen, Madhavan, A .Thomas, E.dakkara J, Sebastin J, Ginson P joseph, Journal of Materials Science: Materials in Electronics, 28(10) 7190-7203.
[6] Yanjing Hu, Hanbin Hu, Yingying Li, Ruixin Chen, Yu Yang, Leiwang, J. Mol. Struct.1122 (2016) 256-267.
[7] Z. Latajka, G. Gajewski, A.J. Barnes, D Xue, H. Ratajczak, J. Mol. Struct. 928 (2009) 124.
[8] A. Wójcik, M. Godlewski1, E. Guziewicz, R. Minikayev, W. Paszkowicz, J. Crystal Growth. 310(2008) 284–289 .
[9] J. Ramajothi, S. Dhanuskodi, K. Nagarajan, Cryst. Res. Technol. 39 (2004) 414.
[10] Z.J.Li, Y.Abramov, J.Bordner, J.Leonard, A.Medek, A.V.Trask J.Am.Chem.Soc.128(2006)8199-8210.
[11] P.V. Dhanraj, N.P. Rajesh, J. Cryst. Growth 318 (2011) 974–978.
[12] N.N.Daneshwar, S.S.Tavale and L.L.MPant, Acta Crystallogr. Sec.B 34 (1978).
[13] R. Surekha, R. Gunaseelan, P. Sagayaraj, K. Ambujam, Cryst. Eng. Comm. 16 (2014) 7979–7989.
[14] K. Nivetha, S. Kalainathan, M. Yamada, Y. Kondo, F. Hamada, RSC Adv. 6 (2016) 35977-35990.
[15] Amit Kumar Chawla, Davinder Kaur, Ramesh Chandra, OpticalMaterials 29 (2007) 95.
[16] P.Jayaprakash,M.PeerMohamed,P.Krishnan,M.Nageshwari,G.Mani,M.LydiaCaroline, Physica B 503 (2016) 25-31.

Available online at www.sciencedirect.com

ScienceDirect

Materials Today: Proceedings 8 (2019) 123–129

materialstoday: PROCEEDINGS

www.materialstoday.com/proceedings

ICMEE 2018

Dye-Sensitized Solar Cells Using Natural Dye as Light-Harvesting Material Extracted From the Leaves of *Peltophoroum Pterocarpum*

P Sanjay[a], K. Deepa[b], M. Victor Antony Raj[b], J. Madhavan[b] and S Senthil[a,]*

[a]*Department of Physics, Government Arts College for Men, Nandanam, Chennai, India.*
[b]*Department of Physics, Loyola College, Chennai, India.*

Abstract

The Dye Sensitized Solar Cell (DSSC) was fabricated using the dye extracted from the leaves of *Peltophorum pterocarpum*. The dye was extracted using cold extraction with ethanol and water. The absorption nature of the extracted dye was analyzed using UV-Vis spectrometer. The structural property of the pure titanium dioxide (TiO_2) nanoparticles was analyzed using powder X-ray diffraction (PXRD). The Surface morphology of the synthesized pure TiO_2 nanoparticles was identified with high resolution scanning electron microscopy (HRSEM) analysis. The TiO_2 films were coated on Fluorine doped Tin Oxide (FTO) using doctor blade method. The current - voltage character of the prepared DSSC are measured. From the J-V characteristic curves of cells, the parameters related to the solar cell performance were calculated. Natural dye is biodegradable and non-toxic having most of the extraction process harmless to environment. In addition, natural dye has the promising future as it is abundant.

Selection and peer-review under responsibility of the scientific committee of the Materials For Energy and Environment.

Keywords: Titanium dioxide, DSSC, Natural dye, *Peltophorum pterocarpum*, HRSEM.

1. Introduction

Performance of dye-sensitized solar cells (DSSCs) is influenced by semiconductors, electrolytes, transparent conductive oxide substrates, counter electrode, and dye sensitizers [1-3]. Dye plays an important role in the performance of DSSCs. When synthetic dye such as ruthenium complex is used as a sensitizer in a wide-

* Corresponding author. Tel.: 9840074456.
*E-mail address:*ssatoms@yahoo.co.in

Selection and peer-review under responsibility of the scientific committee of the Materials For Energy and Environment.

bandgap semiconductor, the DSSC efficiency becomes over 10% [4]. Recently, considerable efforts have focused on improving the energy conversion efficiency and long-term stability of the dye, electrolyte, and working electrode because of high costs, presence of heavy metals, and complex synthesis processes of synthetic dyes, natural dyes obtained from leaves, fruits, and plants are a cheaper option and they are nontoxic and completely biodegradable also [5-6]. The sensitizers in DSSCs are adsorbed to a nanostructured wide band gap semiconductor. When the dye absorbs light, the excited electron will be transferred to the conduction band of the semiconductor. A redox couple in electrolyte, comprised of I-/I_{3-}, then reduces the oxidized dye back to the ground state and transports the positive charge to the counter electrode. in order to get a high solar conversion efficiency in DSSCs, a high surface area for the porous TiO2 films for efficient absorption of the sensitizer and good networking between the particle to particle or particle to FTO substrate are very important. So many researches, in order to increase the solar conversion efficiency in DSSCs, have been studied about photoelectrodes such as synthesis of the wide bandgap of TiO2, the small particle size of 10 to approximately 20 nm, the wide surface area of TiO_2, and the porosity. As stated above, these can increase the adsorption of dye, and by extension, the solar conversion efficiency could be increased [7-12]. In the present work, we report the synthesis of photoanode material (TiO_2) using sol-gel process for the fabrication of DSSC. The natural dye extracted from *P. pterocarpum* leaves using water and ethanol is reported. The performance of the DSSCs fabricated using TiO_2 nanoparticles as photoanode and extracted natural dye as sensitizer were investigated. The J-V characterization was also done for the fabricated Dye sensitized solar cells.

1. Experimental methods

2.1 Synthesis of TiO_2 Nanoparticles

Titanium dioxide nanoparticles were prepared using sol - gel method by taking titanium isopropoxide as titanium precursor and an alcohol with distilled water as hydrolysis medium. The solution was prepared to the overall volume ratio of Ti [OCH $(CH_3)_2]_4$: C_3H_8O: CH_3COOH: Distilled H_2O = 5:30:4.4:30. The isopropyl alcohol was mixed thoroughly with distilled water and this solution was stirred vigorously. About 5 ml of titanium isopropoxide solution was added drop wise to result a white precipitation. The pH of solution was adjusted to 2-3 by adding 1 or 2 drops of ammonia with stirring at room temperature for 12h. This yields a high viscous white suspension which is washed in distilled water and then in ethanol to remove the impurities. After hydrolysis process, the turbid solution containing TiO_2 precipitation was heated up to 100°C for 1h. The prepared white precipitate powder was calcined at 400°C for 4h to obtain fine particles of anatase phase TiO_2.

2.2 Preparation of natural dye

The leaves of *Peltophoroum pterocarpum* were collected and the samples were washed thoroughly with running tap water to get rid of the dust particles. After washing, the samples were shade dried for four weeks at room temperature. The samples were then crushed with mortar and pestle to coarse powder. Cold maceration is done at room temperature by mixing the plant with the solvent and leaving the mixture for two days with occasional shaking. Here we used distilled water and ethanol as solvents. About 25 g of coarse powdered leaves of *P.pterocarpum* leaves were dissolved in 100 ml of solvents such as water and ethanol and kept for 48h with occasional stirring. After 48h the extracts were filtered by decantation followed by filtration using whatman filter paper to obtain clear solutions (Fig. 1). To prevent the dye from light exposure, the extracted dyes were covered with aluminum foil.

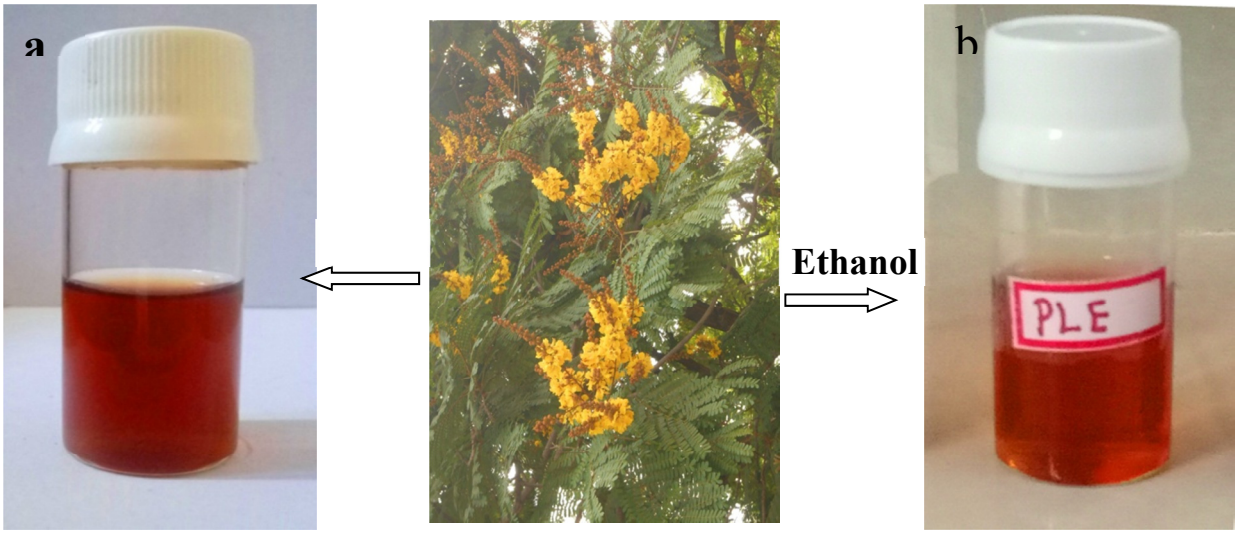

Fig. 1. Peltophorum pterocarpum plant with dye extracts of (a)water and (b)ethanol

2.3 Fabrication of dye-sensitized solar cells

The FTO glass was used as substrate after careful cleaning with acetone, ethanol, and water for about 15 min respectively. The FTO glasses were rinsed well with distilled water. The TiO2 paste was coated onto FTO substrate using a doctor-blade method. The prepared TiO_2 film was air dried at 70 °C for 30 min and the films were annealed at 450°C for 1h to eliminate the polymer binder. The coated glasses were dipped into dye extracts for 12h and the excessive dye was washed away by using ethanol, followed by drying at 60°C. The platinum-coated FTO was used as the counter electrode. A drop of electrolyte solution was injected into the photoelectrode and then the counter was clamped onto the photoelectrode; the electrolyte solution is prepared by dissolving of 0.3 M of Lithium Iodide (LiI) and 0.03 M of Iodine (I_2) in tert-butyl alcohol and acetonitrile in the ratio of 1:1 which is used as charge transport mediator between photoanode and counter electrode in DSSC.

3. Results and discussion

3.1 UV-Vis analysis of Dye

The overall performance of DSSC is dependent on the light absorption capacity of the dye sensitizer and the diffusion of the ejected electron through the mesoporous TiO2 film. The UV-vis spectra of the *P.pterocarpum* dye extract (ethanol and water) show a series of bands between 400 to 600 nm as shown in Fig. 3. This intense absorption in the visible region corresponds to that of carotene and anthocyanin are shown in Fig. 2a&b. The structure of the pigment Plant parts containing anthocyanins have been widely investigated to use as photosensitizers in the fabrication of DSSC. Since anthocyanin molecule has colour from red to blue in visible light, it can be considered as a suitable sensitizer material for wide band gap semiconductors. Moreover, these anthocyanin molecules have carbonyl and hydroxyl group which can bind to TiO_2 film, resulting in better electron transfer from dye molecule to conduction band of TiO_2 layer.

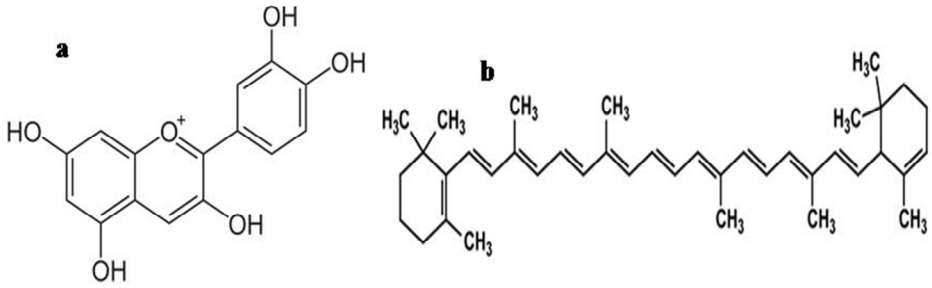

Fig.2. Structure of (a) anthocyanin and (b) carotene

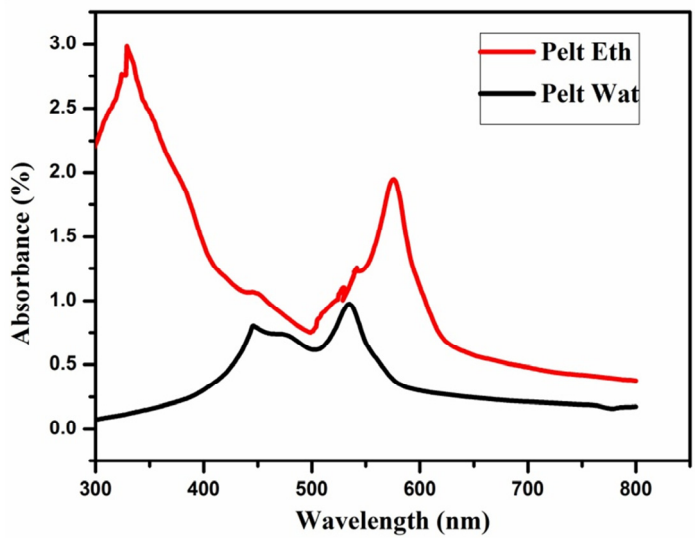

Fig.3. UV- Vis spectrum of P. pterocarpum extracts

3.2 Powder XRD and HRSEM analysis

The crystalline phase of TiO_2 nanoparticles were analyzed by The X-ray diffraction analysis was carried out at room temperature by using Siemens X-ray diffraction D500 with CuKα. The crystalline phase of TiO_2 nanoparticles was analyzed. Figure 4 shows the powder XRD pattern of as-prepared TiO_2 nano particles and the presence of sharp diffraction peak in the XRD confirm that products are highly crystalline. The diffraction peaks corresponding to 2θ value are identified ass (101), (004),(200),(211),(204),(220) and (215) and it matches well with the titania peaks (JCPDS 73-1764). The crystalline size was calculated by the debye scherrer formula $D = 0.89\lambda/\beta \cos\theta$, where D is the crystalline size, λ is the wavelength of X-ray radiation (0.154 nm), 'β' is the full width half maximum and θ is the diffraction angle. It was found that the average crystalline size of Tio2 surface were 20 nm. HRSEM analysis is carried out to view the surface morphology of nanoparticles. The surface morphology of synthesized TiO_2 nano powders was investigated and shown in Fig.5. The TiO_2 nanoparticles have agglomerated together to form lot of nanoclusters. This behavior is affected by the photo material for DSSCs.

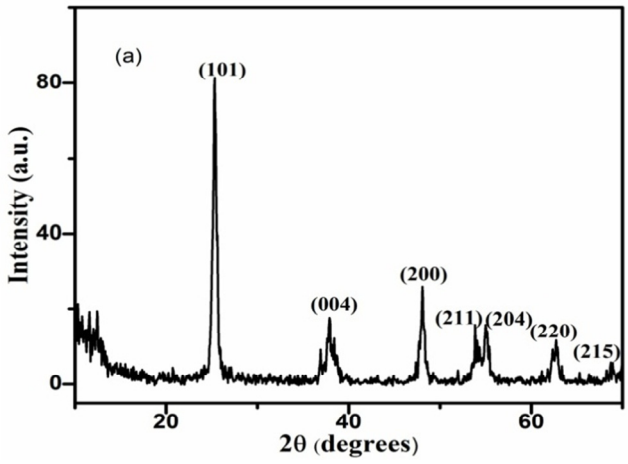

Fig.4. Powder X-ray diffraction analysis of TiO_2nanoparticles

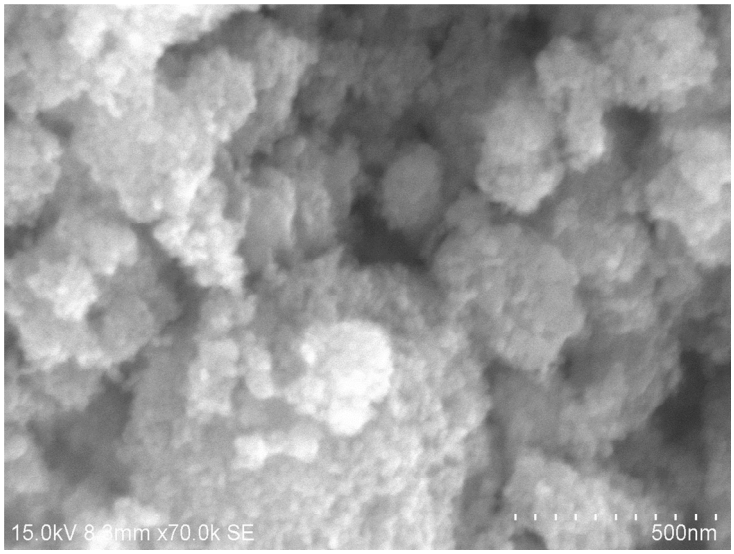

Fig.5. HRSEM image of TiO_2 nanoparticles

3.3 J-V characteristics of Dye sensitized solar cell (DSSCs)

The morphology of the TiO_2 photo anode plays a vital role in determining the photo electrochemical activity. The photocurrent density-voltage (J-V curve) measurement of the DSSCs is based on TiO_2 nanoparticles. The sensitization was performed using standard solar simulator at 1Sun intensity (AM 1.5 G). The overall efficiency (η) was calculated from the current density–voltage (J–V) curves using the following equation,

$$\text{Power conversion efficiency } (\eta) = \frac{P_{max}}{P_{input}}$$

$$\eta = \frac{J_{sc} \cdot V_{oc} \cdot FF}{P_{in}} \times 100\%$$

where the P_{max} is the maximum power output point in the J–V curve yielding maximum product of current and voltage, P_{input} is the radiation power incident on the cell, J_{sc} is short circuit current density generated under illumination, and V_{oc} is the open-circuit voltage. FF is the fill factor calculated from the following equation

$$FF = \frac{I_{max} \cdot V_{max}}{J_{sc} \cdot V_{oc}}$$

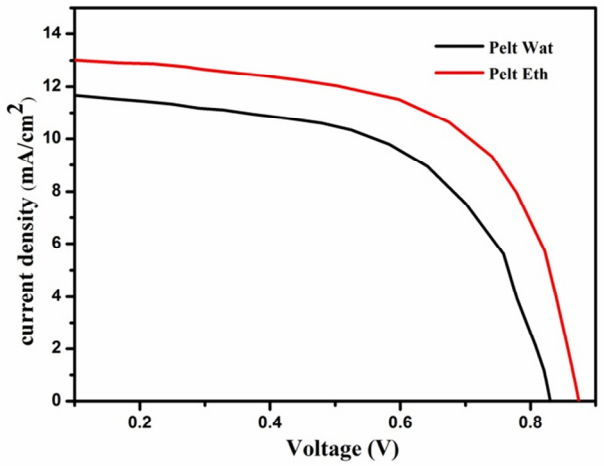

Figure .6.J-V characteristics of TiO_2 based solar cells sensitized by using natural

The photocurrent density-voltage (*J-V*) characteristics of the DSSCs based on TiO_2 film photoelectrodes using *P. pterocarpum* leaves ethanol and water extract is shown in Fig. 6. The best photovoltaic performance was obtained from *P. pterocarpum* ethanolic dye extract which showed energy conversion efficiency (η) of 7.17% with a short circuit current density (Jsc) of 13.22 mA/ cm^2, open circuit voltage (Voc) of 0.871 V and fill factor (FF) of 62%. The power conversion efficiency exhibited by the solar cell fabricated using TiO_2 sensitized by leaves of P. pterocarpum water extract exhibited a power conversion efficiency of 5.75% with a short circuit current density (Jsc) of 11.89 mA/ cm^2, open circuit voltage (Voc) of 0.830 V and fill factor (FF) of 58%.

4. Conclusion

In this study, *P. pterocarpum* dyes were used as sensitizer. The spectral response of TiO_2 nanoparticles to visible light was successfully accomplished using natural sensitizers. By increasing the optical absorption of natural dyes, the performance of DSSCs will be improved. This is due to better charge transfer between the dye molecules and the TiO_2 surface, which is related to the sensitizer structure. The TiO_2 solar cell fabricated using P. pterocarpum ethanolic dye extract exhibited a power conversion efficiency of 7.17% with a short circuit current density (Jsc) of 13.22 mA/ cm^2, open circuit voltage (Voc) of 0.871 V and fill factor (FF) of 62%. The power conversion efficiency exhibited by the solar cell fabricated using TiO_2 sensitized by leaves of *P. pterocarpum* water extract exhibited a power conversion efficiency of 5.75% with a short circuit current density (Jsc) of 11.89 mA/ cm^2, open circuit voltage (Voc) of 0.830 V and fill factor (FF) of 58%. Use of natural sensitizers, such as anthocyanins, carotenes can be an alternative source of energy, being environmentally friendly for producing economical DSSCs. The performance of DSSCs using natural sensitizers is low. However, this investigation showed a great potential for natural sensitizers in improving the DSSCs performance.

References

[1] Y. Ooyama and Y. Harima, ChemPhysChem. 13(2012) 4032–4080.
[2] Suyitno, A. Zainal, A. S. Ahmad, T. S. Argatya, and Ubaidillah, Applied Mechanics and Materials.575 (2014) 689–695.
[3] J. Hu, J.Cheng, S.Tong, Y. Yang,M.Chen, and S.Hu, International Journal of Photoenergy 2016 (2016) 9.
[4] Sanjay P, Deepa K, Madhavan J, Senthil S, Materials Letters 219 (2018) 158–162..
[5] I.N.Obotowo, I. B.Obot, andU. J. Ekpe, Journal of Molecular Structure. 1122 (2016) 80–87.
[6] R. Syafinar,N.Gomesh, M. Irwanto, M. Fareq, andY.M. Irwan, Energy Procedia. 79 (2015) 896–902.
[7] S. Suyitno, T. J. Saputra, A. Supriyanto, and Z. Arifin, Spectrochimica Acta -Part A: Molecular and Biomolecular Spectroscopy. 148 (2015) 99–104.
[8] Tang Y-B, Lee C-S, Xu J, Liu Z-T, Chen Z-H, He Z, Cao Y-L, Yuan G, Song H, Chen L, Luo L, Cheng H-M, Zhang W-J, Bello I, Lee, Am Chem Soc. 4 (2010) 3482-3488.
[9] Jobin Job Mathen, Madhavan J, Thomas A, Edakkara A J, Sebastin J, Ginson P joseph, Journal of Materials Science: Materials in Electronics, 28(10) 7190-7203.
[10] EzhilArasi S , Victor Antony Raj M , Madhavan J, Journal of Materials Science: Materials in Electronics, 29 (4), (2018) , 3170-3177.
[11]. Jobin Job Mathen, Thomas, Edakkara A J, Sebastin J, Madhavan J, Ginson P Joesph, Journal of Materials Science: Materials in Electronics, 28(11), (2017), 7544-7557.
[12] Nair AS, Jose R, Yang S, Ramasrishna, J Colloid Interface Sci. 353 (2011) 39-45.

Available online at www.sciencedirect.com

ScienceDirect

Materials Today: Proceedings 8 (2019) 301–309

materialstoday: PROCEEDINGS

www.materialstoday.com/proceedings

ICMEE 2018

Photocatalytic and Antibacterial Applications of Magnetic Fe_3O_4–CuO Nanocomposite

V. Maria Vinosel, S. Anand, M. Asisi Janifer, S. Pauline*

Department of Physics, Loyola College, University of Madras, Chennai – 34, India

Abstract

Fe_3O_4–CuO nanocomposite was prepared by hydrothermal method, which is simple and cost effective. The prepared nanocomposite was characterized for XRD that confirms the presence of crystalline peaks corresponding to both Fe_3O_4 and CuO. The morphology and phase composition were characterized by High resolution scanning electron microscope (HRSEM) and Energy dispersive X-ray analysis (EDAX). The Fourier transforms infrared (FTIR) spectra reveals information about metal oxygen bands in the composite. UV-visible spectroscopy was used to study their optical properties. The photocatalytic degradation of organic dye crystal violet using the composite as catalyst under visible light illumination was studied. The antibacterial activity of the sample was also examined.

Selection and peer-review under responsibility of the scientific committee of the Materials For Energy and Environment.

Keywords: UV-visible spectra; Antibacterial studies; Photocatalytic activity; Nanocomposite.

1. Introduction

A magnetite nanoparticle has given a new impetus in their use of ferro fluids, anti-cancer agents, biological imaging and therapies. Magnetic iron oxides (Fe_3O_4) with oxygen forming cubic inverse spinel structure, the interstitial tetrahedral and octahedral sites are occupied by iron (Fe) cations. At the room temperature Fe^{+2} and Fe^{+3} ions flip among themselves in the octahedral sites giving rise to a class called half-metallic materials [1,2]. CuO is an important *p*-type material which has a narrow bandgap, non-toxic and readily available semiconductor. The intrinsic properties of copper oxide are stable, robust and have a longer shelf life compared to organic antibacterial

* Corresponding author. Tel.: 9940054040
E-mail address: paulantovero@yahoo.co.in

Selection and peer-review under responsibility of the scientific committee of the Materials For Energy and Environment.

agents, low toxicity, low price, good environmental acceptability, make it a potential candidate for antibacterial applications [3].

Microbial contamination always creates health hazards to mankind. Different kinds of bacteria can result in different types of serious illness and sometimes leading to death. Therefore it is significant and necessary to develop effective, low cost and environmentally benign biocides. Heterogeneous photocatalysis has become an important advanced oxidation process for environmental clean-up. Magnetic nanoparticles are a kind of environmentally benign support material for the immobilization of active nanocatalysts, and their magnetic response provides an efficient separation and recovery strategy for composite catalysts. Zhao et al [4] reported that the urchin-like Fe_3O_4@TiO_2@Ag core-shell nanocomposites could display enhanced photocatalytic and recycling properties for the degradation of Ampicillin. In the case of wastewaters containing highly concentrated dyes, photocatalytic treatment suffers from a high tendency of catalyst binding. The greatly reduced transparency also lowers the efficiency of UV and visible light utilization. Recently, ultrasound (US) irradiation in the presence of a catalyst (sonocatalytic degradation) has been proposed as an environment friendly technique to eliminate dyes in wastewater [5].

Furthermore Wang et al [6] prepared and developed an antibacterial and high light transmittance bulk material to incorporate the hydrophobic and hydrophilic antibiotics. In another work Yadav et al [7] synthesized nickel-doped TiO_2 nanoparticles that show visible light photocatalytic antibacterial activity against Gram-positive and Gram- negative bacteria. The nanomaterials, including silver, copper and some other metal or metal based materials are also efficient bacteriostatic agents. Khashan et al. [8] reported the antibacterial effect of CuO NPs against *E. coli*, *P. aeruginosa*, *P. vulgaris,* and *S. aureus*

Inorder to completely utilize the superior magnetic property of Fe_3O_4 and the outstanding solar absorbency power of CuO, it is feasible to coat the Fe_3O_4 nanoparticles with CuO nanoparticles. Fe_3O_4–CuO coupled nanometal oxides have been prepared using various methods such as coprecipitation, thermal decomposition, sol–gel, hydrothermal, Microwave and photodeposition methods. These magnetic catalysts, not only show high efficiency and selectivity towards the antibacterial activity, but also can be separated and recovered efficiently from the reaction solution by simply applying external magnetic fields [9].

In the present work, we have developed a simple hydrothermal route for the preparation of Fe_3O_4/CuO nanocomposite. The structure, morphology and optical properties of Fe_3O_4/CuO nanocomposite were studied by X-ray diffraction (XRD), High resolution scanning electron microscopy (HR-SEM), Energy dispersive X-ray analyzer (EDAX), Fourier Transform Infrared (FTIR) and UV-Visible spectroscopy techniques. The micro structural analysis was carried out using XRD peak broadening analysis. We have calculated crystallite size and lattice strain for the composite using Scherrer equation and Williamson-Hall analysis.

2. Experimental

2.1 Preparation of Fe_3O_4 nanoparticles

In the present work, Fe_3O_4 NPs were synthesized by hydrothermal method. 5g of $Fecl_2$ and 3.1g of NaOH were dissolved in 40ml of DI water under magnetic stirring. The solution was transferred into a Teflon-lined stainless steel autoclave temperature maintained at 180°C for 12 h. The resulting precipitate was separated by centrifugation, washed several times with water and ethanol and finally dried at 50°C for 12 h.

2.2 Preparation of Fe_3O_4/CuO nanocomposite

In a typical procedure, 0.92g of as-prepared Fe_3O_4 NPs was dispersed in 20ml of DI water by ultrasonication. Then, 3.9g of $CuSO_4.5H_2O$ and 1.5g of NaOH were dissolved in 40ml of DI water under magnetic stirring. Fe_3O_4 NPs were then dissolved into the above solution under ultrasonication. The mixture solution was then transferred into the Teflon-lined autoclave and then hydrothermally heated at 180°C for 12 h. The precipitate was centrifuged and washed several times with water and ethanol. The final product was dried at 250°C for 4 h. Fe_3O_4 NPs and $CuSO_4$ were synthesized in 1:4 molar ratio and the sample is used for further characterization.

2.3 Antibacterial performance

30 mg of the Fe_3O_4–CuO nanocomposite was suspended in 3.0 ml of Milli Q water to get a stock suspension of 10 mg/mL. From this stock suspension six different working suspensions of the concentrations 100, 200,300, 400, 500 and 600 µg were prepared with sterile deionized water in sterile test tubes. Using sterile cotton swab, the subculture of Staphylococcus aureus was made as a suspension in sterile Tryptone Soya broth. Using sterile micro tip7shallow wells were punched in the culture media with a gap of 1 cm between each well. The wells were marked at the base of the plate as 1,2,3,4,5,6 and control. With sterile micro tip 100 µL of each one of the 6 working Fe_3O_4–CuO nanocomposite suspension was added to the duly marked wells. The bacterium was also exposed to an antibiotic disc containing 5µg of Ciprofloxacin, as an antibiotic control. The culture plate was incubated in the bacteriological incubator [Equitron] at 37°C for 24 h. After the incubation period the plate was examined for zone of inhibition.

2.4 Photocatalytic performance

The photocatalytic activity was estimated by measuring the decomposition rate of CV aqueous solutions in visible light irradiation. The visible light irradiation was carried out using a projection lamp (7748XHP 250 W, Philips, 532 nm) in a photoreactor. Reaction suspensions were prepared by adding the 500 mg of catalyst in 500 mL of aqueous CV solution taken with an initial concentration of 2×10^{-5} mol/L. The aqueous suspension containing CV and the photocatalyst was irradiated while being continuously stirred. The analytical samples from the suspension were collected at regular intervals of time, centrifuged and filtered. The concentration of CV in each sample was analysed using UV–visible spectrophotometer at a wavelength of 588 nm. The photocatalytic efficiency was calculated using the expression

$$\eta = (1\text{-}C/C_0)*100$$

Where C_0 is the concentration of CV before illumination and C is the concentration after irradiation time.

2.5 Material characterization

The structure and crystallinity of the as-prepared samples were investigated by a X-ray diffraction system (XRD 3003 TT) using monochromatic nickel filtered Cu K_α (λ = 1.5406 Å) radiation. The morphology of the sample were investigated by High resolution scanning electron microscopy (HRSEM , Quanta 200 FEG) and it has an energy dispersive X-ray analyzer (EDAX) for performing the elemental analysis. The FTIR analyses were recorded by using Perkin-Elmer system 2000 FT-IR spectrometer. Varian Cary 5000 UV-Visible spectrophotometer is used to optically probe the synthesized sample.

3. Results and discussion

3.1 X-ray diffraction analysis

The structure and crystallinity of the prepared sample were investigated by powder XRD. Fig 1 shows the XRD pattern of Fe_3O_4/CuO nanocomposite. For Fe_3O_4, the diffraction peaks are located at 2Θ = 35.53°, 30.20°, 43.05°, 57.48°, 62.69° which are associated with [220], [311], [400], [511], [440] planes respectively. This pattern corresponds to the cubic phase of Fe_3O_4 with lattice parameters a=b=c= 8.381 Å matching well with the JCPDS file no 85-1436. The additional diffraction peaks at 32.5°, 35.5°, 38.9°, 48.7°, 55.2°, 58.5°are associated with [110], [-111], [200], [-202], [021], [202] planes respectively. This pattern can be indexed to the reflection of monoclinic phase of CuO with lattice constants a= 4.683 Å, b= 3.421 Å, c= 5.129 Å that match well with the JCPDS file no 80-1268. For the coupled metal oxides two sets of diffraction peaks are observed, these are ascribed to cubic Fe_3O_4 and monoclinic CuO. No characteristic peaks from other crystalline impurities were detected, thus suggesting the purity of the sample. The crystallite size of the sample was calculated by Debye Scherrer formula.

$$d = \frac{K\lambda}{\beta cos\Theta}$$

Where d is the average crystallite size (nm), K is the grain shape factor (0.9), λ is the X-ray wavelength (nm), β is the full width at half maximum in radians, and Θ is the Bragg diffraction angle of the 2Θ peak. The average crystalline size was estimated to be 43 nm.

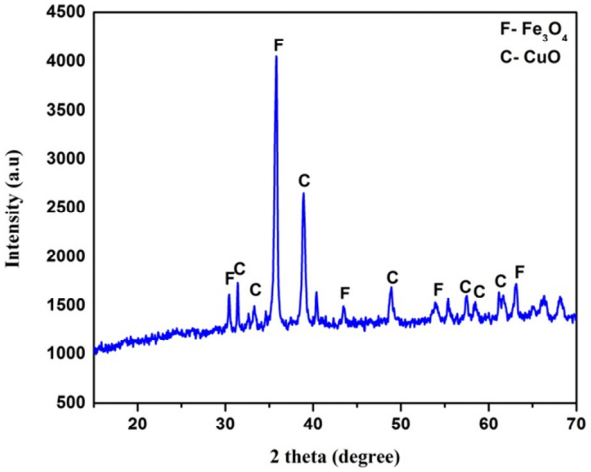

Fig.1: XRD pattern of Fe_3O_4/CuO nanocomposite

3.2 Williamson-Hall analysis

W–H analysis is a simplified integral breadth approach that clearly differentiates size induced and strain induced peak broadening by considering the peak width as a function of 2θ. The W-H method does not follow a *1/cos*θ dependency as in the Scherrer method, but instead varies with *tan*θ. This basic difference allows for a separation of broadening when both small crystallite size and micro-strain occur together. The above difference in approaches presented in the following assumes that size and strain broadening are additive components of the total integral breadth of Bragg peak. Strain induced broadening arising from crystal imperfection and distortion is given by

$$\varepsilon = \frac{\beta}{4\ tan\Theta}$$

It is confirmed that the peak width from crystallite size varies as 1/cosθ whereas strain varies as tanθ. The W–H analysis is suitable for calculating the strain and the crystalline size. So, the strain induced line broadening β_s is given by the relation

$$\beta_s = 4\varepsilon tan\theta$$

$$\beta_{hkl} = \beta_D + \beta_s$$

therefore

$$\beta_{hkl} = \frac{K\lambda}{\beta cos\theta} + 4\varepsilon tan\theta$$

The above equation can be rearranged into

$$\beta_{hkl}\ cos\theta = \frac{K\lambda}{D} + 4\ \varepsilon sin\theta$$

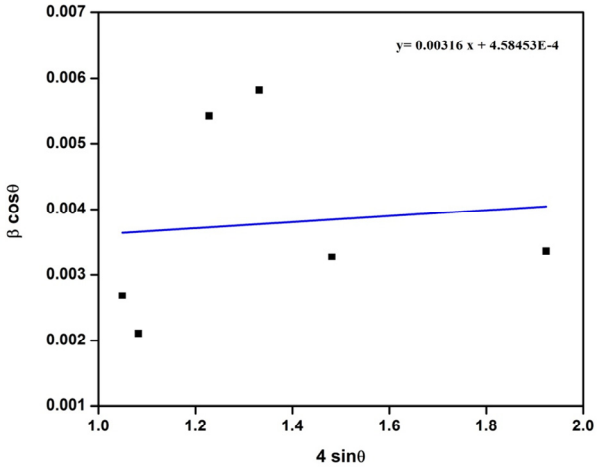

Fig. 2**:** Willamson-Hall plot of Fe_3O_4/CuO nanocomposite

Fig. 2 depicts the W-H Plot drawn between 4 sinθ and β cosθ. From the figure using slope and the intercept both strain ε and the crystallite size were obtained [10–13]. The above equation assuming a uniform strain in all crystallographic directions, suggesting the isotropic nature of the crystal in which its properties are independent of the direction along which they are measured. The lattice strain (ε) and the crystallite size were evaluated as $0.4585x10^{-3}$ and 45 nm respectively.

3.3 Scanning electron microscopy

The surface morphology and elemental composition of the coupled metal oxides were investigated in detail using HRSEM and EDX. The morphology of Fe_3O_4/CuO nanocomposite for different magnification is depicted in Fig.3. In the coupled metal oxide Fe_3O_4 nano-spheres are embedded on the matrix of the CuO nanoparticles. The Fe_3O_4/CuO nanocomposite consists of both spherical and plate - like particle with some agglomeration. The elemental analysis of the sample was performed by energy dispersive X-ray spectroscopy (EDS). The EDX spectrum of Fe_3O_4/CuO nanocomposite (Fig.4) confirms the presence of Fe, Cu and O elements in the sample and thereby signifying the formation of Fe_3O_4/CuO nanocomposite.

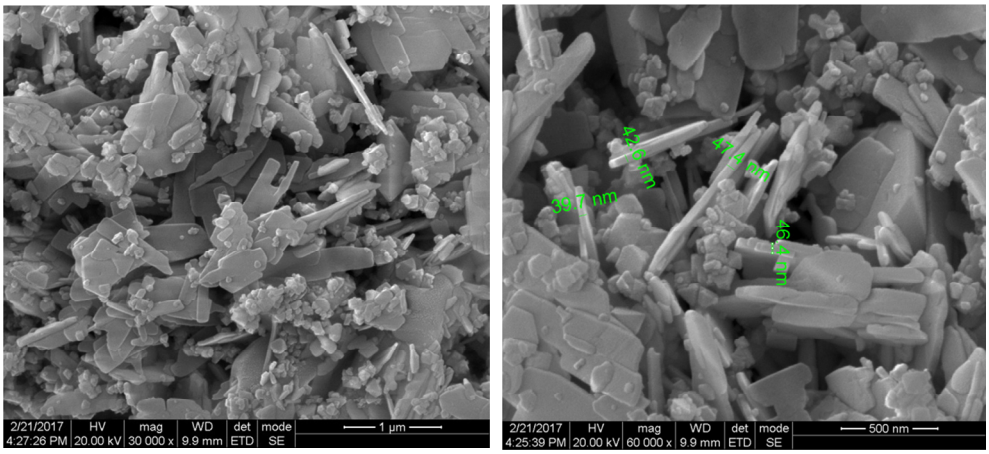

Fig.3**:** SEM micrograph of Fe_3O_4/CuO nanocomposite

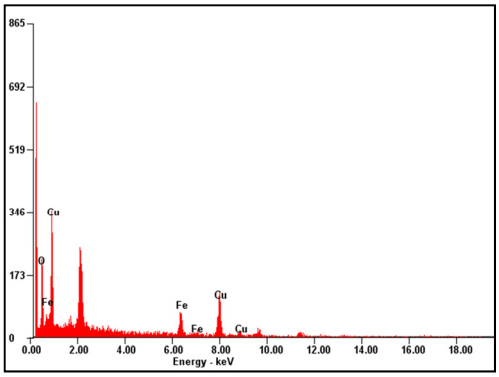

Fig.4**:** EDX analysis of Fe_3O_4/CuO nanocomposite

3.4 Fourier Transform Infrared Spectroscopy

Fourier transform infrared spectroscopy was recorded to investigate the formation of composite with Fe_3O_4 and CuO. Fig.5 shows the FT-IR spectra of the prepared sample. The bands at 494 and 562 cm^{-1} were assigned to be Fe-O and Cu-O stretching vibrations of Fe_3O_4 and CuO. The peak observed at 868 cm^{-1} was assigned to Fe-O-H bending vibrations. The absorption peak observed at 3425 cm^{-1} in the sample could be assigned to O-H stretching due to adsorbed hydroxyl group. The FT-IR study therefore endorses the successful formation of Fe_3O_4/CuO nanocomposite.

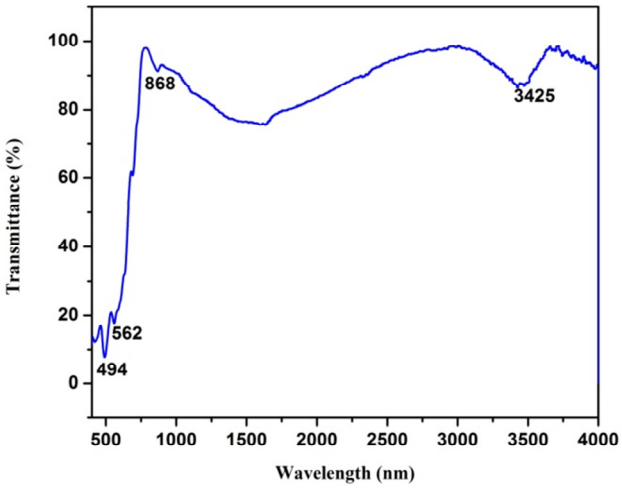

Fig.5**:** FTIR spectrum of Fe_3O_4/CuO nanocomposite

3.5 UV-Visible spectra

Optical characterization was performed by observing the diffuse reflectance spectra at room temperature in the range of 200-800 nm. Diffuse reflectance spectroscopy is a powerful tool for measuring the optical absorption and energy band gap. The absorbance spectra are shown in Fig.6 (a). The optical band-gap energy (E_g) of the semiconductor is given by an equation

$$(\alpha h\nu)^2 = A\,(h\nu - E_g)$$

Where, α is an absorption coefficient, h is Planck constant, ν is the frequency and hν is the incident photon energy. Fig.6 (b) shows the Kubelka Munk plot is plotted between $(\alpha h\nu)^2$ vs hν. The band gap energy E_g was estimated from the intercept of the tangents to the plots of $(\alpha h\nu)^2$ vs hν (photon energy). The calculated band gap energy of Fe_3O_4/CuO nanocomposite is around 1.7 eV. This indicates that Fe_3O_4/CuO nanocomposite could sufficiently absorb visible light and acquire constructive photocatalytic properties under visible light irradiation.

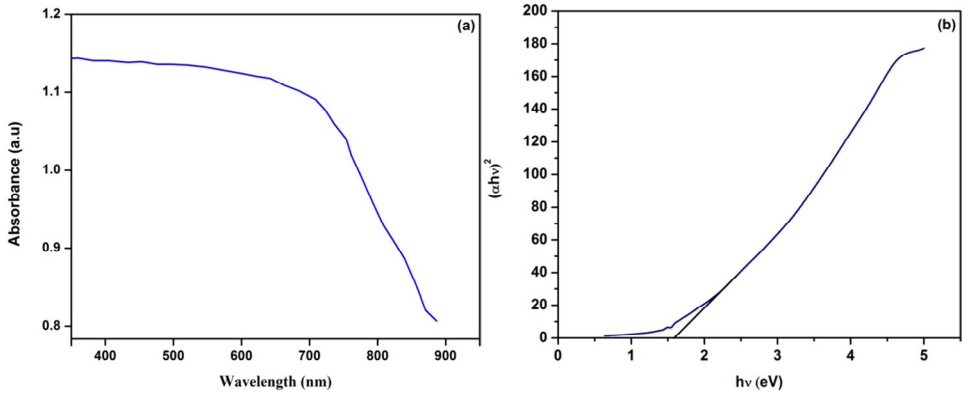

Fig.6: (a) UV-Vis absorption spectrum and **(b)** Tauc's plot

3.6 Antibacterial activity

In this study, the relative antibacterial activity of Fe_3O_4/CuO nanocomposite was quantitatively investigated. Fig.7 shows the four different concentration of Fe_3O_4/CuO nanocomposite suspension tested against gram positive (*Staphylococcus aureus*) bacteria with respect to the positive control. Based on the observations from fig.7 the presence of an inhibition zone clearly indicates the biocidal action of the sample. The size of the inhibition zone increases significantly with the increasing concentration of nanocomposite. Moderate antibacterial activity against gram positive bacteria was observed. The toxicity of Fe_3O_4/CuO nanocomposite depends on their concentration and these nanoparticles are mildly toxic at low concentrations. The nanoparticle toxicity depends on composition, size, surface modification, intrinsic properties and bacterial species. The possible mechanism of action is that the metal nanoparticles are carrying the positive charges and the microbes are having the negative charges which create the electromagnetic attraction between the nanoparticles and the microbes. Nanoparticles attach to the bacterial cell membrane by electrostatic interaction and disrupt the integrity of bacterial cell, which in turn increases its permeability leading to cell death. Generally, the nanomaterials release ions, which react with the thiol groups (–SH) of the proteins present on the bacterial cell surface which leads to cell lysis. The toxicity induced due to dissolved Fe ions and Cu ions from Fe_3O_4/CuO nanocomposite is negligible and the toxicity strength of nanoparticles depends on intrinsic toxic properties of heavy metals.

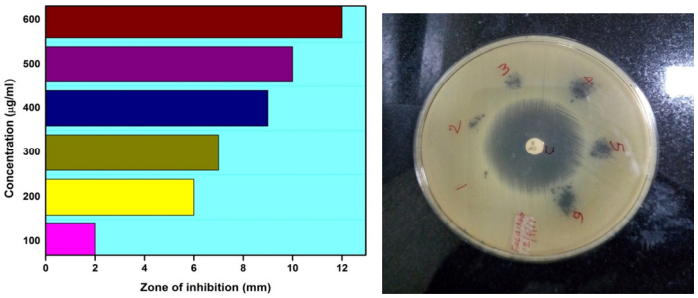

Fig.7: Antibacterial efficacy of Fe_3O_4/CuO nanocomposite against gram positive (Staphylococcus aureus) bacteria.

3.7 Photocatalytic degradation of Crystal Violet dye

The main objective of the present study is to degrade the organic pollutants. For this purpose, crystal violet is used as model organic pollutants. The photocatalytic activity of Fe_3O_4/CuO nanocomposite was tested in the degradation of crystal violet (CV). The required amount of the catalyst that was mixed with CV aqueous solution was irradiated by visible light for various time intervals under constant stirring. The resulting irradiated samples were filtered and the absorbance measurements were carried out using UV–vis spectrophotometer. The degradation results of crystal violet were shown in fig. 8. In fig. 8, the disappearance of the band at 588 nm indicates that most of the CV has been degraded by Fe_3O_4/CuO sample under visible light irradiation within 3h. The degradation efficiency of the catalyst was calculated using the formula,

$$D\% = \frac{Co-Ct}{Co} * 100$$

The degradation efficiency of Fe_3O_4/CuO nanocomposite is 40%. The efficiency of the sample were shown in fig.9. When the energy of UV light in terms of photon is equal to or greater than the bandgap, the electrons receive energy and transfer of electrons takes place from the valence band (VB) to the conduction band (CB) which result in the formation of a hole (h^+) in the VB and an electron (e−) in the CB. The holes react with water and generate OH radicals, which can oxidize the organic pollutants. The conduction band electron reacts with oxygen in the reduction process and produces OH radicals. These radicals reduce the organic pollutants. These oxidation and reduction processes were capable of degrading the organic pollutants under visible light irradiation. The decrease in the crystallite size increases the surface area. Thus the surface area depends mainly on the size of the particle. It is known that the photocatalytic redox reaction mainly takes place on the surface of the photocatalysts and so the surface properties significantly influence the efficiency of catalyst.

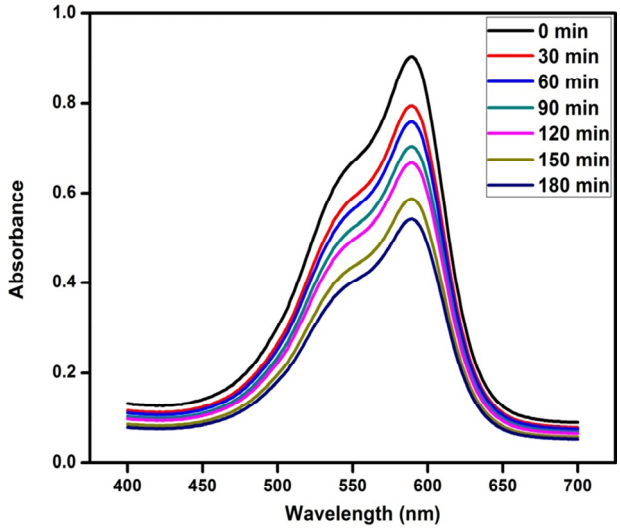

Fig.8: Photocatalytic degradation of Crystal violet under visible light irradiation of Fe_3O_4/CuO nanocomposite

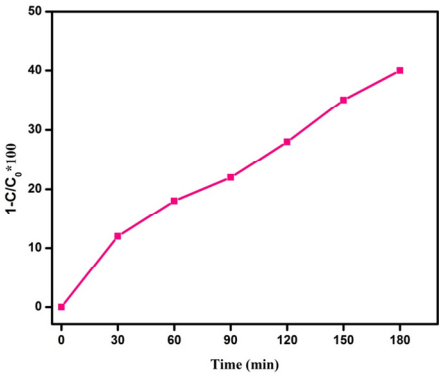

Fig.9: Degradation efficiency of Crystal violet dye under visible light irradiation of Fe_3O_4/CuO nanocomposite

3.8 Conclusion

The crystalline Fe_3O_4/CuO nanocomposite was successfully synthesized by hydrothermal method. The prepared nanocomposite was characterized by different studies. Based on the results, we conclude that Fe_3O_4/CuO nanocomposite exhibits efficient antibacterial activity, which makes them an aspirant for biomedical applications. Fe_3O_4/CuO nanocomposite was used as a catalyst to degrade crystal violet dye under visible light irradiation. The photocatalytic activity indicates a connection between shape, size and surface area of the material. These magnetic nanocomposites can be reused because of their magnetic property. These results suggest that the nanocomposite we used may serve as an effective, sustainable and recyclable antibacterial agent.

References

1. H.T.Jeng, G.Y.Guo, D.J.Huang, Phys.Rev.Lett.93 (2004)156403.
2. D.J.Craik, Magnetic Oxides Q3 , A Wiley-Intersience Publication (JohnWileyand Sons), 1975.
3. O. Akhavan, M. Abdolahad, R. Asadi, J. Phys. D Appl. Phys. 42 (2009) 135416.
4. Y. Zhao, C. Tao, G. Xiao, G. Wei, L. Li, C. Liu, H. Su, Nanoscale 8 (2016) 5313-5326.
5. L. Song, Y. Li, P. He, S. Zhang, X. Wu, S. Fang, J. Shan, D. Sun, Ultrason. Sonochem. 21 (2014) 1318–1324
6. Wang B, Liu H, Zhang B, Han Y, Shen C, Lin Q and Chen H (2016) Colloids Surf. B Biointerface 141- 483
7. Yadav H M, Otari S V, Bohara R A, Mali S S, Pawar S H and Delekar S D (2014) J. Photochem. Photobiol. A Chem. 294 130
8. Khawla S. Khashan, Ghassan M. Sulaiman, Farah A. Abdulameer, Arabian Journal for Science and Engineering, 41 (2016) 301–310.
9. S.K. Rajabi, Sh. Sohrabnezhad, S. Ghafourian 244(2016) journal of solid state chemistry 160-163
10. S. Anand, A. Persis Amaliya, M. Asisi Janifer and S. Pauline, Modern Electronic Materials, 3 (2017) 168–173.

Available online at www.sciencedirect.com

ScienceDirect

Materials Today: Proceedings 8 (2019) 142–147

materialstoday: PROCEEDINGS

www.materialstoday.com/proceedings

ICMEE 2018

Synthesis,Crystal Growth Spectral and Optical Studies on Amino Acid Based New Novel NLO Single Crystal: L-Isoleucinium Phthalate (LIP)

A.Hemalatha[a,b], S.Arulmani[b], K.Deepa[c], D. Suresh Kumar[d], J. Madavan[c], S.Senthil[b,*]

[a]*Department of Physics,Quaid-E-Millath Government College for Women, Chennai-600 002, India.*
[b] *Department of Physics,Government College for Men, Chennai-600 035, India.*
[c] *Department of Physics, Loyola College, Chennai-600 000, India.*
[d]*Department of Chemistry,Government College for Men, Chennai-600 035, India.*

Abstract

Good quality colourless transparent nonlinear optical single crystals of L-Isoluecinium phthalate (LIP) was grown successfully by slow evaporation solution growth method from aqua solution at room temperature. Single crystals of LIP of dimensions 15mm x 8mm x 5mm were harvested after 50 days. The lattice parameter of grown crystal was studied by single crystal X- ray diffraction analysis and it was confirmed that the grown crystals belong to monoclinic crystal system with noncentrosymmetric space group of C_2. Fourier transform infrared spectroscopic (FT-IR) studies was carried out using Jasco FT/IR 6300 Fourier transform infrared spectrometer by ATR method in the range of 400 – 4000 $cm^{-1}$and it has been used to confirm the vibrational frequencies of various functional groups present in the crystal. Laser induced damage threshold study was carried using Q-Switced Nd: YAG laser and the laser power with the threshold value of 0.323 GW/cm^2 also calculated. The UV-Vis-NIR spectroscopic study confirms that the crystal has good optical transparency and the cut off wavelength was found to be 300 nm. The band gap of the grown crystal was determined from the Tauc plot. The nonlinear optical property was confirmed by Kurtz Perry powder technique and it was compared with the standard pure potassium dihydrogen phosphate (KDP) crystals. In addition, a photoluminescence analysis was carried out for LIP crystal.

*Keywords:*Single crystal,FT-IR, UV-Vis-NIR,Nd:YAG, Photoluminescence

* Corresponding author. Tel.:9840074456.
E-mail address:ssatoms@yahoo.co.in (S. Senthil)

Selection and peer-review under responsibility of the scientific committee of the Materials For Energy and Environment.

1. Introduction

Nonlinear optical materials are reputed candidate due to its interesting and variety of application of device fabrication for good mechanical strength, better nonlinearity high thermal stability and large laser damage threshold. In the beginning of research work, the researchers have concentrated on inorganic materials compared to the organic materials. Currently organic materials attracted more attention over inorganic materials due to the conjugated π electron system as well as the presence of the asymmetric charge transfer which have a high order of nonlinearity. So the considerable effort to develop new organic materials with large second-order nonlinear optical susceptibilities with reasonable thermal stability and good transparency would be the choice of optoelectronic applications [1]. Among the organic materials amino acids are more potential material for NLO applications because they have donor carboxylic (COOH) group and the proton acceptor amino (NH_2) group with them called as zwitterions which produces hydrogen bonds [2]. L-Isoleucine is one of the aliphatic amino acid with hydrophobic side chain which is promising candidate for NLO applications. [3]. L-Isoleucine is one of the essential organic amino acid in nature. Phthalic acid is an important organic NLO material for electro optic processor. Phthalate crystals have high piezoelectric coefficients with acousto-optical interaction and also identified by the application in the long wave X-ray spectrometers and its optical, piezoelectric, NLO and elastic properties. [4]. Ammonium phthalate crystals have large NLO property compared to the other phthalate crystal literature. In this paper, an organic NLO material of L-Isoleucinium Phthalate (LIP) has been synthesized by combining L-Isoleucine with Phthalic acid. After a detailed literature survey shows that there are no other reported papers available on this LIP crystal. So, we report for first time, synthesis, crystal growth, spectral and optical studies on amino acid based new novel nonlinear optical L-Isoleucinium Phthalate single crystal.

2. Experimental details

2.1. Synthesis and Growth of LIP

L-Isoleucinium Phthalate (LIP) crystal was synthesized by reacting equimolar ratio of (AR grade 99% purity) L-Isoleucine and phthalic acid. The saturated solution was prepared by dissolving L-Isoluecine in deionised water and phthalic acid was added to the same solution. To get a homogenous solution the saturated solution was stirred well for 6 hrs using magnetic stirrer at room temperature. The solution was then filtered using whatman filter paper to remove suspended impurities and kept aside without any mechanical disturbance for the growth of crystals by slow evaporation solution method at room temperature. Colourless and transparent crystal of dimensions 9x15x7 mm^3 was collected after 50 days and is shown in fig.1.

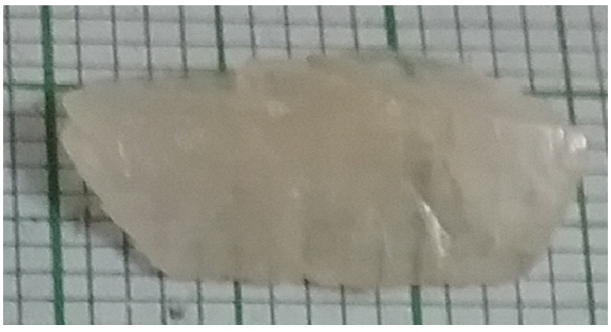

Fig.1 photograph of as grown crystal of LIP

2.2. X-ray diffraction studies:

The grown LIP single crystal was subjected to single crystal X-ray diffraction studies using ENRAF NONIUS CAD- 4 x ray diffractometer with MoKα (λ=0.1770 Å) radiation. The single crystal XRD confirms the crystallinity and enumerated that the crystal belongs to the monoclinic system with the space group C_2 and the lattice parameters are a=5.05 Å, b=14.26 Å, c=9.61 Å, α=β=90°, γ=93° and the volume V=691 A^3. The obtained single crystal XRD values are well matched with following reported phthalate literature mentioned in table 1[5-7].

Table 1. . Lattice Parameter of LIP and other phthalate crystals

Crystal Name	Crystal System	a A	b Å	cÅ	V(A^3)	Ref
LIP	Monoclinic	5.05	14.26	9.61	691	Present work
LiBP [6]	Monoclinic	5.02	14.29	9.59	687	[5]
LTP	Monoclinic	5.09	14.40	9.67	709	[6]
PT	Monoclinic	5.058	14.287	9.609	693	[7]

2.3. FTIR Studies:

Fourier transform infrared (FTIR) spectra of LIP were recorded in the wavelength range between 4000- 400 cm^{-1} by ATR crystal method with a JASCO FT/IR-6300 Fourier Transform Infrared Spectrometer at room temperature and the FTIR spectra of LIP crystal is shown in fig.2. The broad peak observed in the high frequency range attributed to the combination of COOH, NH and OH stretching vibration of LIP crystal. A peak at 3078 cm^{-1} was due to the C-H stretching vibrations [5]. The absorption bands assigned at 2646 cm^{-1} and 2526 cm^{-1} were due to the combination of NH_3^+ bending vibration [6]. The peak observed at 1582 cm^{-1} was due to the asymmetric NH_3^+ deformation vibration and the peak at 1508 cm^{-1} was due to the symmetric NH_3^+ deformation vibration [5].

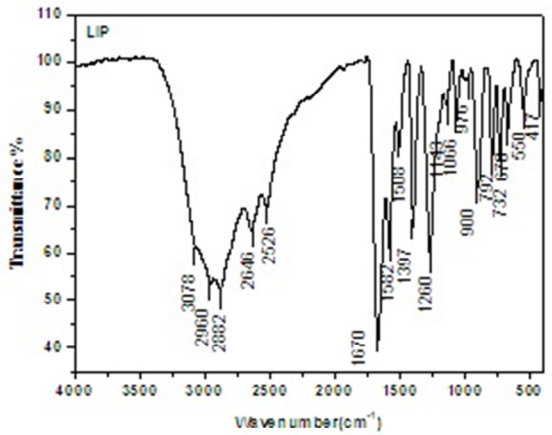

Fig. 2. FT-IR spectrum of LIP crystal

The medium peak 1397 cm^{-1} was observed due to the symmetric stretching of the COO^- in amino acid [6] The strong peak observed at 1260 cm^{-1} was due to the C=O stretching and the medium peak at 1066 cm^{-1} due to the OH bending confirmed the carboxylic group in phthalic acid C-N stretching vibration is confirmed by the absorption

peak 1143 cm^{-1}[8]. The strong peak at 900 cm^{-1} was due to out of plan OH....O hydrogen deformation confirmed the presence of carboxylic acid. The absorption peaks at 670 cm^{-1} and 550 cm^{-1} confirm the symmetric bending and rocking vibration of COO^{-1} respectively [5]. The peaks at 792 cm^{-1} and 732 cm^{-1} correspond to the twisting and wagging of NH. The peak observed at 976 cm^{-1} and 417 cm^{-1} indicate the C-C-C breathing and C-C plane bending of ring, confirmed the presence of aromatic ring. All the functional group present in the FTIR spectra confirm the formation of new LIP crystals.

2.4. UV-Vis-NIR studies:

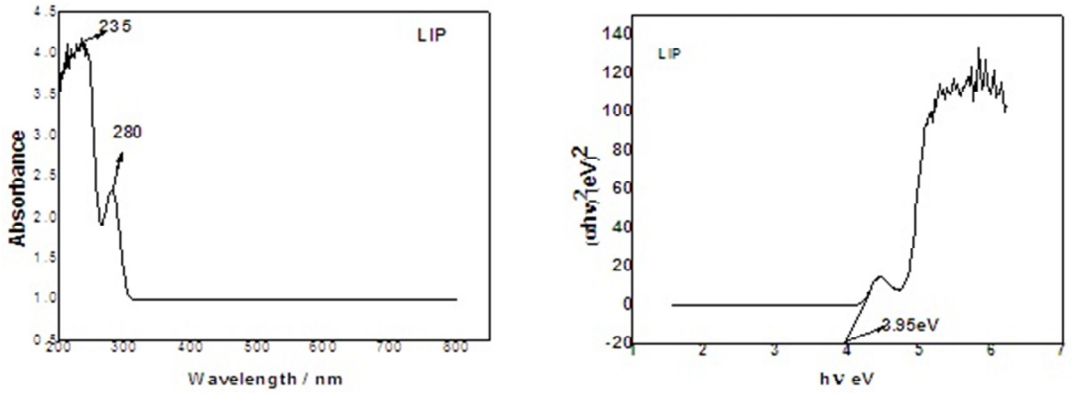

Fig. 3. (a) UV-Vis Absorption spectrum of LIP crystal; (b) Plot of $(\alpha h\upsilon)^2$ verses$h\upsilon$ of LIP crystal

To study the optical character of any materials the linear optical spectra are very important. The UV-Vis-NIR spectra is depends upon the crystal transparency and it is the most powerful tool to check whether the crystal is optically active or not. The UV-Vis-NIR absorption spectrum was recorded in the range 200-850 nm using Perkin Elmer Lambda-35 spectrometer is shown in fig.3(a). Single crystal of optically good quality, transparent and thickness 0.5 mm was used for UV-Vis-NIR study. From the recorded absorption spectrum, the lower cut-off wavelength value was found to be 300 nm. The spectrum gives two peaks, one lower intensity peak at 234 nm and the high intensity peak at 280 nm. The peak at 234 nm is corresponding to n-π^* transition and the peak at 280 corresponding to $\pi - \pi^*$ transition [8]. The maximum intensity peak at 280 nm is due the protonation of amino group to the carboxyl group and the minimum intensity peak at 234 nm due to the deprotonation of carboxyl group. These transitions are expected from OH and carbonyl groups, that may be one electron acceptor carbonyl group C=O and the other being electron donor group of OH. The above $\pi - \pi^*$ and n-π^* transitions are the agreement for the two peaks present in the UV-Vis-NIR spectra. The transparency is increased and also there is no absorption from 300 nm to 850 nm confirmed that the LIP crystal could be exploited for optoelectronic device applications. These are the required property for NLO crystals. Energy band gap value also calculated using tauq plot is as shown fig 3(b). and the band gap value is found to be 3.95 eV.

2.5. Photoluminescence studies:

Photoluminescence spectroscopy (PL) is the method to detecting the defects, vacancies, imperfection. Also used for the contactless non-destructive technique of probing the electronic structure of the material. Fluorescence behaviour present in a materials that are having aromatic and conjugated double bond with a high degree of

resonance stability. Photoluminescence study is also more important to learn the application of photo chemistry, electroluminescent display and chemical sensors. The PL spectra of the powdered crystals were recorded using a carry Eclipse luminescence spectrometer in the wavelength range 275 – 625 nm at room temperature with excitation wavelength of 280 nm [9]. In the excitation wavelength, a broad emission spectra of LIP was recorded between 320 -420 nm [9] as shown in fig.4. In the broad band, there are three very small tiny peaks were observed at 345 nm [9,10], 356 nm and 382 nm. The band gaps of the peaks were calculated using the formula Eg= (hc/ λ) eV [10], where h is the Planck's constant, c is the velocity of the light and λ is the wavelength of the peaks, the band gap values are 3.6eV, 3.5 eV, 3.2 eV [10] which is nearly equal to the UV energy band gap value. The broad spectrum around 320-420 nm confirming the violet-blue emission and their after no other visible emission was observed. From the above discussion the LIP material emits violet blue colour radiation and it is suitable for making new violet-blue light emitting materials.

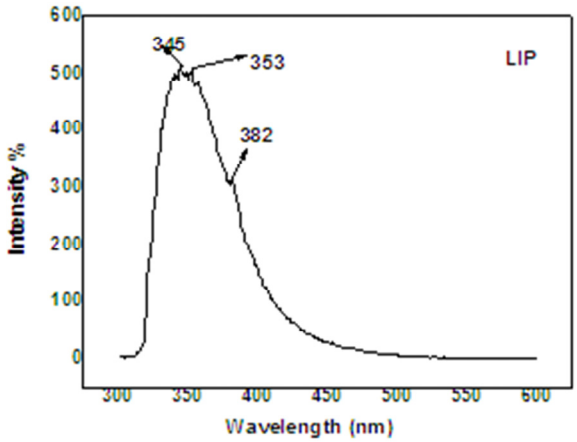

Fig. 4.PL Emission spectrum of LIP crystals with exited at 280 nm

2.6. Laser threshold damage studies

Laser damage threshold (LDT) plays an important role in NLO materials to show the ability on surface to withstand from high power laser intensities. But bulk crystals have higher ability when compared with the surfaces. The LDT studies have been carried out for LIP single crystals. The LDT value was measured by using Q-switched high energy Nd:YAG laser (QUANTARAY MODEL) system at 1064 nm in the repetition rate of 10 HZ with laser input pulse width of 6 ns. The laser beam diameter setting was adjusted for 1mm with the help of the Biconvex Lens of focal length (f) 15 cm and it was focused onto the polished surface of the LIP to irradiate laser damage threshold measurement. Pulse energy of the input laser beam was measured by a power and energy meter of EPM 2000 and the energy range from 1.5 mJ to 3 mJ and the input energy of the crystal was 69.5 mJ. The surface laser damage threshold of LIP crystal was calculated using the relation of power density , $P_d = E/\tau A$ [11], where E is the intensity of the incident laser beam (mJ), τ is the pulse width (ns) and A is the area of the circular spot size (cm^2). The laser damage threshold value of LIP crystal was found to be 0.323 GW/cm^2 [14] which is greater than KDP crystal of value 0.20 GW/cm^2 [11,12]. The laser damage threshold value is also nearly equal to the p-TTS, 2A4PTS, and GT crystals of energy values are 0.30 GW/cm^2,0.36 GW/cm^2 and 0.344 GW/cm^2[12] respectively.

2.7. Kurrtz and Perry powder studies

The second harmonic generation property of the grown single crystals was determined using a Q-switched high energy Nd: YAG laser QUANTARAY MODEL employing Kurtz and Perry powder technique [13]. The fundamental beam of Nd: YAG laser with 1064 nm wavelength, pulse duration of 6 ns and 10 Hz repetition rate is focused on to the powder sample of LIP crystal. A green light of wave length 532 nm with radiation energy 4.84 mW was obtained as the output from the grown crystal where as the output radiation emitted from the KDP reference sample was 8.94mw. Thus the efficiency of the as grown LIP single crystal was found to be nearly 0.54 times that of the standard KDP.

3. Conclusion

Optically transparent organic LIP crystals have been grown by slow evaporation solution growth technique at room temperature. The single crystal X-ray diffraction analysis reveals that grown crystal belongs to monoclinic system with the space group C_2. The lattice parameters of grown LIP crystals are a=5.05 Å, b=14.26 Å, c=9.61 Å and γ=93˚.The functional group present in LIP crystals are confirmed by FTIR spectroscopic studies. UV-Vis-NIR studies reveal that the LIP crystal is visible and there is no considerable absorption in the entire visible region. The lower cutoff wavelength occurs at 300 nm and the band gap value is found to be 3.95 eV and hence the crystals are suitable for optoelectronic device applications. The PL study shows the emission spectrum of LIP crystal between 320 -420 nm with the exited wavelength 280 nm and it indicates that the crystal emits violet-blue emission. The Laser threshold damage value was found to be 0.323 GW/cm^2 which is greater than that of the reported KDP value. NLO studies confirm that the second harmonic generation efficiency of the crystal is 4.84 mW which is 0.54 times that of the KDP crystals. All the above characteristic studies confirm that the LIP crystals are potential material for optoelectronic applications.

Acknowledgement

The corresponding author S. Senthil gratefully acknowledges the support from the Department of Science and Technology (DST), Government of India, for the Research project (SB/EMEQ-248/2014).

References

[1] J, Balaji, S. Prabu, D.Sajan, P. Srinivasan, J. Molecular Structure 1137 (2017) 142-149.
[2] Prince Thoomas, R. Santhosh Kumar, G. Sreekanth, Bitto John, Ganesh Sanjeev, Ginson.P.Joseph, J. Nuclear Instruments and Methods in Physics Research B 410 (2017) 68-77.
[3] Senthil S, Pari S, Xavier R, Madhavan J, Optik, 123 (2), (2012)104-108.
[4]Amudha M, Madhavan J, Praveen Kumar P, Journal of Optics (India) 46(4), (2017) 382-390.
[5] K.Mohanraj, D. Balasubramanian, N. Jhansi, J, Optics and Laser Technology, 96 (2017) 318-322.
[6] Tamilselvan S, Vimalan M, VethaPotheher I, Rajasekar S, Jeyasekar R, Antony Arockiaraj, Madhavan J, SpectrochemicaActa-Part:A Molecular and Biomolecular spectroscopy, 114, (2013) 19-26.
[7] Tamilselvan S, Vimalan M, VethaPotheher I, Jeyasekaran R, Yogam F, Madhavan J, Optik 125 (1) (2014)164-169.
[8] M. Suresh Kumar, S. Krishnan, S. Jerome Das, Optick,127,5 (2015) 2509-2511
[9] G. Senthil Murugan, P. Ramawamy, J. Phisica B, 406 (2011) 1169-1172.
[10] Kiran T. Ratyhod, B. Patel, C.F. Desai, Y.H. Gandhi, International J. Luminescence and Applications, 05,(2015) 86-88.
[11] T. Balakrishnan, S. Sathiskumar, K. Ramamurthi, Sthamotharan, J. Materials Chemistry and Physics, 186 (2017),115 -123
[12] Paavai Era, Ro. Mu. Jauhar, G. Vinitha, P. Murugakoothan, J. Optics and Laser Technology, 101, (2018) 127-137.
[13] SK. Kurtz, T.T. Perry, J. Appl. Phys 39 (1968) 3798-3813.

Available online at www.sciencedirect.com

ScienceDirect

Materials Today: Proceedings 8 (2019) 279–283

materialstoday: PROCEEDINGS

www.materialstoday.com/proceedings

ICMEE 2018

Studies on Growth,Thermal, Vibrational And Optical Characterization of a Novel Nonlinear Organic Single Crystal of L-Isoleucinium Hydrogen Maleate Hemihydrates(LIM)

A. Hemalatha[a,b], K. Deepa[c], A. Venkatesan[d], D. Suresh Kumar[e], J, Madavan[c], S. Senthil[b,] *

[a]*Department of Physics,Quaid-E-Millath Government College for Women,Chennai-600 002,TamilNadu, India*
[b]*Department of Physics,Government Arts College(Men), Nandanam, Chennai – 600 035,TamilNadu, India*
[c]*Department of Physics, Loyola College, Chennai – 600 034, TamilNadu, India*[d]*Department of Physics,Aringnar Anna Government Arts College, Villupuram – 605 602, Tamil Nadu, India*
[d]*Department of Chemistry, Loyola College, Chennai – 600 034, TamilNadu, India*

Abstract

L-Isoleucinium Hydrogen Maleate Hemihydrate (LIM) nonlinear optical single crystal was grown by the slow evaporation solution growth method using water as solvent at room temperature. The grown crystals were analyzed by the single crystal X ray diffraction analysis which proved that the grown LIM crystals belongs to monoclinic system with the space group $P2_1$. FT-IR spectroscopy studies were carried out to understand the presence of various functional groups in the LIM Crystal and it was confirmed by FT-RAMAN spectroscopy. The second harmonic generation (SHG) efficiency measurement of LIM crystals were confirmed by Kurtz and Perry powder technique. Thermo-gravimetric and differential thermo gravimetric studies reveal good thermal stability of the material. The optical transparency has been studied using UV-vis-NIR spectroscopy and the band gap energy was found out from the absorption studies. The laser damage threshold of the crystal was found to be 0.15 GW/cm^2. Photoluminescence spectrum shows emission peak around 415-435 nm and it is suitable for fabricating blue light emitting diodes..

Selection and peer-review under responsibility of the scientific committee of the Materials For Energy and Environment.

*Keywords:*Single crystal,FT-IR ;FT-RAMAN ;UV-Vis-NIR ;Nd:YAG ;TGA/DTA ;Laser Threshold Damage ;Photoluminescence ;

*Corresponding Author: Tel.: 9840074456
*E-mail address:*ssatom@yahoo.com

Selection and peer-review under responsibility of the scientific committee of the Materials For Energy and Environment.

1. Introduction

Nonlinear optical materials have received enormous attention due to their attractive interest such as frequency conversion, light modulation, optical switching, etc., In addition to this organic crystalline material have a large nonlinear coefficient compared to inorganic materials. Among organic NLO materials amino acids play a dominating role in growing nonlinear optical crystals. Most of the amino acids exhibit nonlinear properties because they have chiral carbon atom, a proton donor carboxylic acid (-COOH) and the proton acceptor amino (NH_2)group present in the amino acids [1]. Due to this reason all amino acids are crystallized in non-centrosymmetric space group which is the necessary quality for nonlinear optical materials. L-Isoleucine is one of the organic amino acid and arethe potential material with excellent optical, thermal and mechanical properties. L-Isoleucine is one of the amino acid with hydrocarbon side chain and it is a natural amino acid that is more important for human body. L-Isoleucine is a potential candidate for NLO application and is reported in the literature [2]. L-Maleic acids also one of the organic acid with large π – conjugation which has attracted great deal of attention [3]. Maleic acid is basically dicarboxylic acid and it has very strong intermolecular hydrogen bond. It forms crystalline maleate of vaoius organic moleclules by hydrogen bonding and π– π interaction. In the present work L-isoluecinium hydrogen maleate hemihydrates (LIM) was grown from aqueous solution by slow evaporation method. The material was characterised by powder XRD analysis, UV-Vis-Nir spectroscopic studies, FT-IR and FT-RAMAN studies, TGA/DTA analysis and Nonlinear optical Studies Photolluminescencence and Laser Threshold damage were discussed.

2. Experimental proceedure

2.1. Synthesis and Crystal growth

Single crystals of LIM was synthesized by dissolving stoichiometric amount of L-Isoleucine (99% pure AR grade) and L-Maleic acid (99% pure AR grade) in deionized water and stirred well for about six hours using a magnetic stirrer to obtain a homogeneous mixture. Then the saturated solution was filtered to remove suspended impurities and tranfered to a beaker for crystallization by slow evaporation method at room temperature. LIM crystal was obtained in a period of 40 days by slow evaporation solution growth method.

3. Results and discussion

3.1 Single Crystal x-ray diffraction analysis

Single crystal x-ray diffraction study was caarried out on the LIM crystal with ENRAF NONIUS CAD4 x-ray diffractrometer with MoKα radiation (λ=o.1770Å). The Single crystal XRD study enumerates that the LIM crystal belong to the monoclinic crystal system with space group $P2_1$[4,5] and the lattice parameters were found to be a=11.745 Å, b=6.1011 Å,c=19.2198 Å, α=γ=90°,β=96.7329°. The obtained single crystal XRD datas are in good agreement with the reported literature value [4].

3.2. Vibrational Analysis

The FTIR spectrum of LIM crystal was recorded using the Brukers IFS66 spectrometer in the range 4000 – 400 cm^{-1} by KBr pellet to identify the functional group present in the crystal and the FTIR spectra of the grown LIM single crystal were observed on the powder samples is as shown in Fig. 1. Raman spectra of LIM crystals recorded in the range of 0 – 4000 cm^{-1} at room temperature using Bruker IFS27 Raman spectrograph is shown in Fig. 2. From 3600 cm^{-1}-2400 cm^{-1} there is a broad band observed in the high energy region which is assigned for O-H stretching vibration of carboxlic group. The peaks observed at 1472 cm^{-1} and 1395 cm^{-1} are assigned to COO^{-1} symmetric

stretching vibration of –COOH group and the corresponding band is also observed at 1453 cm^{-1} in the Raman spectrum. The CN vibration is assigned at 1347 cm^{-1} and 1004 cm^{-1} and the corresponding peak is observed at 1005 cm^{-1} in the Raman spectrum. The peak observed at 1308 cm^{-1} is due to CH_2 wagging vibration and the corresponding peak is also observed at 1302 cm^{-1} in the Raman spectrum. The peak at 1174 cm^{-1} indicates NH_3 rocking vibration. . The band observed at 2964 cm^{-1} is due to the CH_3 assymetric stretching vibration.NH_3 assymetric stretching vibration is observed at 2946 cm^{-1} which is also over lap on the OH stretching vibration and the corresponding band in the Raman spectrum is observed at 2942 cm^{-1}. The peak at 926 cm^{-1} representsC-CN symetric stretching vibtation. Very strong band observed at 871 cm^{-1} due to the C-C stretching vibration. The peak observed at 3346 cm^{-1} corresponding to NH assymetric stretching vibration due to the primary amines of NH_2Strong band observed at 1739 cm^{-1} due to the C=O symetric vibration of –COOH group. The peak against 1578 cm^{-1} indicates NH_3 deformation. The peaks at 578 cm^{-1} and 483 cm^{-1} are attributed toCOO^{-1} wagging and rocking vibrations and the corresponding bands are observed at 540 cm^{-1} and 479 cm^{-1} in the Raman spectrum. Hence the vibrational study confirms the presence of COOH and NH_2 group in the FTIR spectrum and it is confirmed by RT-RAMAN spectrum in the LIM crystal.

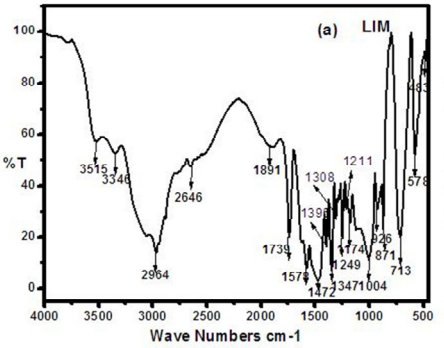

Fig.1 FT-IR spectrum of the grown LIM crystal

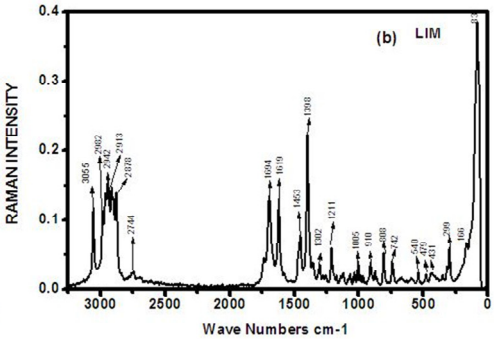

Fig. 2. FT-RAMAN spectrum of the grown LIM crystal

3.3. UV-Vis-NIR Studies

The LIM crystal was dissolved in 2D water at room temperatur and the UV-Vis-NIR absorption spectrum was recorded in the range between 200-700 nm using Perkin Elmer Lambda-35 spectromenter is shown in Fig 3. The lower cutoff wave length was found to be 215 nm above that there is no significant absorption in the entire visible region. It confirm that the crystal is highly transparent in the entire visible region which is useful for nonlinear device application and the second harmonic generation (frequency conversion) application. Optical band gap value is calculated from the UV-Vis-NIR absorption data and the value is plotted between hυ and $\alpha h\upsilon^2$ as shown in the Fig.4. The optical band gap is found to be 4.75 eV and the large band gap confirms that the defeect concentrantion in the LIM crystals is very low [6]

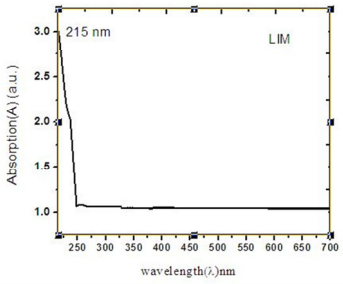

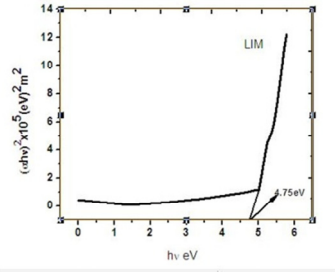

Fig.3 UV-Visabsorption Spectrumof LIM crystal Fig.4 Plot of $(\alpha h\upsilon)^2$versushυ of LIM crystals.

3.4. Second harmonic generation efficiency (SHG) studies

The powder SHG efficiency of LIM crystal was determined using Kurtz and Perry powder technique [7]. A Q-Switched ND:YAG laser (Quanta Ray model Lab 170-10) emitting fundamental wavelength of 1064 nm and 8 ns width with an input repetition rate of 10 Hz and 0.7mj/pulse energy was used. The SHG efficiency was confirmed by emitting green light radiation of wavelength 532 nm from the crystalline powder and the doubling frequency of LIM crystals was found to be 4.48 mW. From the obtained data, it is found that the SHG Efficiency of LIM crystals are 0.9 times that of the standard KDP crystals.

3.5Photoluminescence (PL) Studies

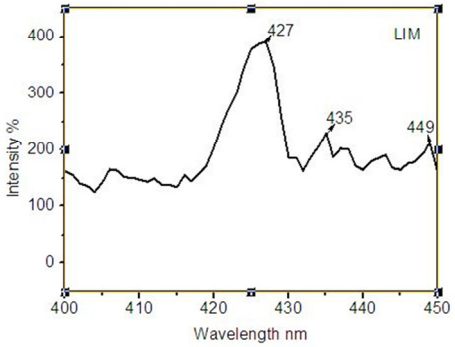

Fig 5.PL Emission spectrum of LIM crystal

Photoluminescence study has enormous importance due to its applications in photo chemistry, chemical sensors and electroluminescent display. Photoluminescence study is also used to investigate direct knowledge regarding material's physical properties at molecular level, i.e. defects in the deep and shallow level mechanism and energy gap states. The PL spectra of the powdered crystals were recorded using a carry Eclipse luminescence spectrometer in the wavelength range 275 – 625 nm at room temperature with excitation wavelength of 215 nmas shown in Fig.5. The PL emission peaks at 435nm, 449 nm and also observed between 415-435nm which gives rise to blue light emission. From the above discussion the LIM material emits blue colour radiation and it is suitable for making blue light emitting diodes.

3.5 Laser damage threshold (LDT) Studies

Laser damage threshold (LDT) is plays a virtual role in NLO materials to device fabrication such as THz wave generation, electro-optic modulation, etc. LDT is also one of the important parameter because NLO materials have to withstand the high power intensities. When NLO materials exposed to laser radiation, LDT helps to detect and estimate permanent defects or damage caused by the melting,ablation, cracking, Plasma formation etc. The laser damage threshold (LDT) has been carried out using a Q-switched high energy Nd : YAG laser (QUANTARAY MODEL) system with a source at 1064 nm in the repetition rate of 10 HZ with laser input pulse width of 6 ns. The cut ad polished sample was place the focus of Biconvex Lens of focallength 15 cm and laser beam of diameter 1 mm was focused on the LIM crystal. The pulse energy of the input laser beam was measured by a power meter (EPM 2000) with the energy range between 1.5 mJ to 3mJ. The surface laser damage threshold was calculated using the relation $P_d=E/\tau A$,[8] Where E is the intensity of the incident laser beam (mJ), τ is the pulse width (ns) and A is the area of the circular spot size (cm^2). The laser damage threshold value of LIM crystal is found to be 0.15GW/cm^2.

3.6 TGA/DTA analysis

The thermo gravimetric(TGA) analysis and differential thermal (DTA) analysis was carried out between room temperature and 700°C in a heating rate of 10°C/min in the nitrogen gas atmosphere and the TGA/DTA curves present in Fig.6.There is a major weight loss starting between 144°C to 570°C due to the elimination of molecule such as CO_2, H, O and major weight loss occur due to decomposition of the crystal. The remaining weight loss occurs due to the complete decomposition of the crystal sample. DTA shows the same changes in the TGA curves. DTA curve shows three endothermic peak and two exothermic peaks at 82°C,128°C,144°C, 489°C and 540°C respectively. The endothermic peak at 87°C shows the weight loss due to the liberation of water molecules present in the crystal itself. The first exothermic peak absorbed at 144°C indicates the melting point of the material and it is the decomposition point of the TGA curve. The second exothermic peak observed at 489°C which is also matched with the TGA curve. From the DTA and TGA Study, it is observed that the material has water molecules in its crystal lattice and it has thermal stability till its 144°C. Thus from themal analysis, it is seen that the crystal can be utilized for device applications in the field of optoelectronics up to 144°C.

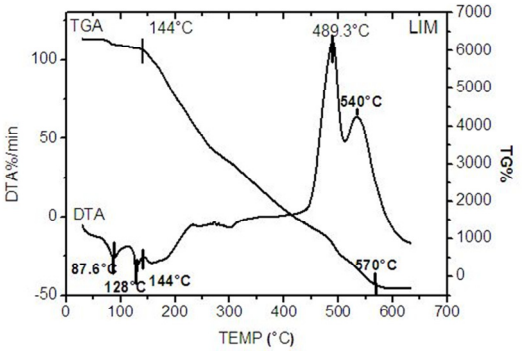

Fig.6 TG/DTA curve for LIM crystal

4. Conclusion

Single crystals of LIM were grown by slow evaporation solution growth method at room temperature. Single x-ray diffraction analysis was carried out and the LIM crystal belong to monoclinc structure with the space group P_{21}. The lattice parameters were calculated and the values are good in agreement with the reported values. UV-Vis-NIR study shows that the crystals are transperant in entire visible region and have minimum cut off wavelength of 215nm. The band gap value is found to be 4.75 eV. PL study indicates that the LIM crystal can be used as blue light emmitting diodes. The value of Laser damege Threshold (LDT) of the title compound is found to be 0.15GW/cm^2 Thermal analysis was carried out and it confirms the crystal is stable upto 144°C. Its Second Harmonic Generation efficiency was found to be 0.9 times that of standard KDP value. The functional groups present in the LIM crystal is identified by FTIR analysis and it is confirmed by the FT-RAMAN. Hence LIM single crystals are suitable material for nonlinear optical device fabrication.

References

[1] Tamilselvan S, Vimalan M, VethaPotheher I, Rajasekar S, Jeyasekar R, Antony Arockiaraj, Madhavan J, SpectrochemicaActa-Part:A Molecular and Biomolecular spectroscopy, 114, (2013)19-26.

[2] Senthil S, Pari S, Xavier R, Madhavan J, Optik, 123 (2) (2012) 104-108.

[3] Victor Antony Raj M, Madhavan J, Materials science and Engineering 73(1) art.no 012138.

[4] Sergey G. Arkhipov, Denis A. Rvchkov, Alexey M. Pugachev and Elena V. Boldyrevaa, J. Acta Crystal C, C17 (2015) 1-9.

[5] G. Ramasamy, SubbiahMeenakchisundaram, J. Optic Communication, 125 (2014) 4422-4426.

[6] Mohdshkir, Haider Abbas, J. SpectrochemicaActa Part A, 118 (2014) 172-176.

[7] Kurtz.SK. Perry.T.T, J. Applied Physics, 39 (1968) 3798 – 3813.

[8] T. Balakrishnam, S. Sathishkumar, K. Rmamurthi, S. Thamotharan, J. Materials Chemistry and Physics, 186 (2017) 115-123.

Available online at www.sciencedirect.com

ScienceDirect

Materials Today: Proceedings 8 (2019) 310–314

materialstoday: PROCEEDINGS

www.materialstoday.com/proceedings

ICMEE 2018

Enhanced magnetic Properties of $MgFe_2O_4$ nanoparticles

R. C. Sripriya [1, 2], Mahendiran M[1, 2]*, J.Madahavan[1] and M. Victor Antony Raj[1,2]

[1]*Department of Physics, Loyola College, Chennai, India.*
[2]Loyola Institute of Frontier Energy (LIFE), Loyola College, Chennai, India.

Abstract

Recently, magnetic semiconductor nanoparticles have been widely studied in nanoscience and nanotechnology, because of their important applications in magneto-optic materials, photocatalysts, sensors and magnetic drug delivery. From the various magnetic materials, spinel ferrites have become an important material in various interdisciplinary areas. Spinel $MgFe_2O_4$ nanoparticles were synthesized by a simple, economical microwave supported method (MSM) using glycine as the fuel. The structural, vibrational, optical and magnetic properties of the products were determined. The optical band gap (E_g) was measured using Kubelka-Munk model and it shows a value of 1.91 eV. The effect of $MgFe_2O_4$ nanoparticles as photocatalyst on the degradation of methylene blue (MB) was also investigated. It was observed that the sample showed better photo-catalytic degradation efficiency of MB due to the smaller particle size and higher surface area. The above spinel ferrite catalysts are magnetically separable by external magnetic field and can be reusable without change of its activity.

Selection and peer-review under responsibility of the scientific committee of the Materials For Energy and Environment.

Keywords: Nanostructures; Spinel $MgFe_2O_4$; Microwave irradiation

* Corresponding author. Phone: +91-44-28178200 ; Fax: +91-44-28175566
E-mail address: mahe7676@gmail.com

Selection and peer-review under responsibility of the scientific committee of the Materials For Energy and Environment.

1. Introduction

Nanotechnology is the science and engineering of making materials, functional structures and devices in nanometer scale. Nanotechnology has become a very active and vital research topic which is rapidly developing in industrial sectors and spreading to almost every field of science and engineering. Several major research and development programs on nanostructured materials and nanotechnology have been launched by governments worldwide. The field of research has become an area of great scientific and commercial interest because of its rapid expansion to academic institutes, laboratories and industries. Nanomaterials have extremely small size is which having at least one dimensions, two dimensions or three dimensions. They can exist in single, fused, aggregated or agglomerated forms with spherical, tubular, and irregular shapes. Common types of nanomaterials include nanotubes, dendrimers, quantum dots, and fullerenes. Nanomaterials have applications in the field of nanotechnology, and displays different physical and chemical characteristics from normal chemicals. Spinel $MgFe_2O_4$ nanoparticles have been used as a photocatalyst, due to its stability, photochemical stability and also reused several recycles. The photocatalytic action of the ceramic nano materials depends on the surface area and its grain size. Furthermore, spinel $MgFe_2O_4$ nano-catalyst is cost-effectively and eco-friendly viable solid heterogeneous catalyst. The effect of synthesis method on structural, optical, morphological, magnetic property and photocatalytic activity of spinel $MgFe_2O_4$ nano-catalyst were investigated by different characterizations such as powder (XRD), (FT-, UV-Vis specra, FT-IR and dielectric techniques and the obtained results.

2. Experimental Part

All the chemicals used in this study were of analytical grade obtained from Merck, India and were used as received without further purification. Magnesium nitrate ($Mg(NO_3)_2{\cdot}6H_2O$, 98%), ferric nitrate ($Fe(NO_3)_3{\cdot}9H_2O$, 98%) and glycine ($C_2H_5NO_2$) were used as a fuel for this method.

All chemicals such as nitrates of magnesium and iron, and glycine were used as the fuel for this method. The stoichiometry of metal nitrate salts and fuel was calculated based on the total oxidizing and reducing valences related to the oxidant agents and to the fuels. Stoichiometric amounts of metal nitrates and glycine were dissolved separately in a beaker with 20 ml of de-ionized water and stirred for 15 minutes to obtain clear solution. The obtained clear solution was transferred into a silica crucible and it was placed in a domestic microwave-oven (850 W, 2.45 GHz) for 15 minutes. Initially, the precursor solution boiled and underwent dehydration followed by decomposition with the evolution of gases. When the precursor solution reached the point of spontaneous combustion, it was vaporized and instantly became solid powders. The obtained solid powders were washed well with water and ethanol several times and dried at 80 ºC for 1 hour, and labeled as $MgFe_2O_4$-MCM, and then used for further characterizations.

3. Results and discussion

3.1. XRD analysis

The structural and phase purity of the samples were confirmed by analyzing the powder X-ray diffraction (XRD) patterns. Fig. 1 shows the powder XRD patterns of $MgFe_2O_4$- sample. All the observed diffraction peaks could be assigned to cubic spinel lattice indicating their single phase structure with no traces of other impurity phases. The XRD peaks could be indexed and are characteristics of single-phase cubic spinel structure of $MgFe_2O_4$ (JCPDS No. 73-1720) [9]. The results show a significant amount of XRD line broadening, a characteristic of nano-phase materials. The main diffraction XRD peak of cubic spinel ferrite at (311) plane was considered as a measure of its degree of crystallinity. The calculated lattice parameter of the samples is summarized in Table 1.

Table 1. Calculated lattice parameter of $MgFe_2O_4$ sample

Sample	Lattice parameter (Å)	Crystallite size *L* (nm)
		Scherrer formula
$MgFe_2O_4$	8.347	15.42

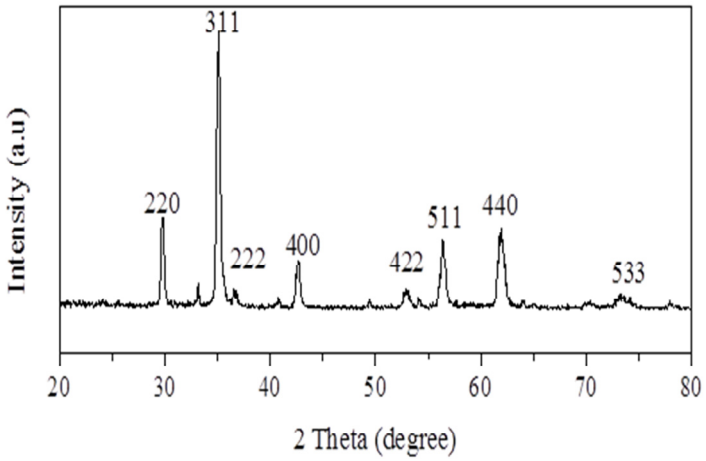

Figure 1 powder X-ray diffraction (XRD) pattern of $MgFe_2O_4$

3.2 UV-Visible diffuse reflectance spectroscopy (DRS) study

The effect of crystallite size on optical property of semiconductor is studied using the UV-Visible diffuse reflectance spectroscopy (DRS) analysis. The UV-Vis DRS has advantages to analyze the optical properties of powdered samples, due to less scattering effects. One can use the DRS data to calculate the direct band gap energy (E_g), as given in the Kubelka-Munk theory [12]. The Kubelka-Munk function *F(R)* was used to calculate the E_g of the sample. Thus the vertical axis is converted into quantity *F(R)* which is equal to the absorption co-efficient. Thus the *'α'* in the Tauc equation is substituted with *F(R*) and hence the relation becomes,

$$\left(F(R)\right) = \alpha = \frac{(1-R)^2}{2R} \qquad \text{---- (3)}$$

where, F(*R*) is Kubelka-Munk function, *'α'* the absorption coefficient, *'R'* the reflectance.
The estimated E_g value of $MgFe_2O_4$ sample is 2.37 eV, respectively.

3.3 Dielectric studies:

The energy storing property of the dielectric material leads to the fabrication of capacitors, which is the most important component in any electrical circuit. The dielectric phenomenon arises from the interaction of electric field with different charged particles such as electrons, ions, protons and electron shells. Fig 2 shows that the

dielectric constant has high values in the low frequency region and thereafter its values decrease with the applied frequency. The high values of (ε_r) at low frequencies may be due to the existence of all the four polarizations, namely orientation, ionic, electronic and space charge polarization. The low values at higher frequencies may be due to the gradual loss of these polarizations. The variation of dielectric loss with frequency is shown in Fig. 3.

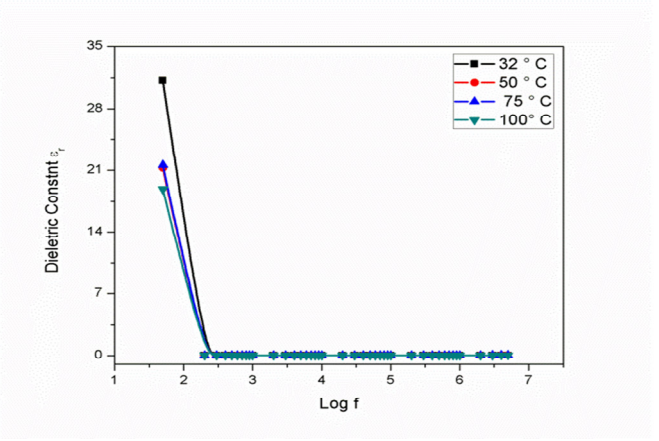

Figure 2: Dielectric Constsnt

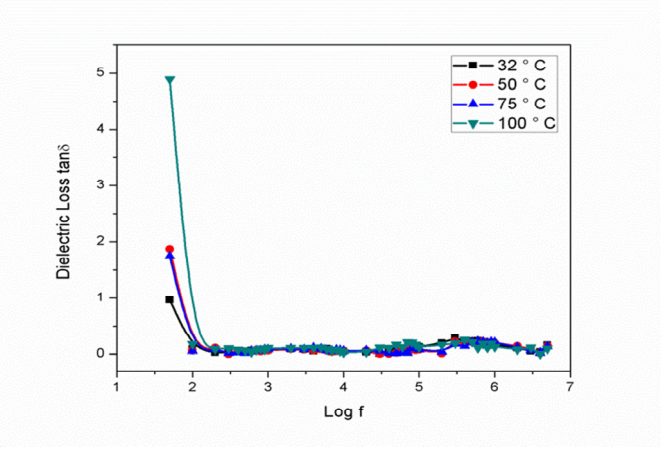

Figure 3: Dielectric Loss

3.4 Photo-catalytic degradation activity

The catalytic performance of $MgFe_2O_4$-MCM sample prepared by MCM method is evaluated in the photocatalytic degradation (PCD) of methylene blue (MB). It is well known that the catalytic activity strongly depends on the particle size and surface area samples. Generally, a high specific surface area has a favourable effect on the activity for heterogeneous photo-catalysis. In this present study, the surface area parameters of the sample is varied according to the preparation methods. In order to have an idea of the adsorbance capability of spinel $MgFe_2O_4$-MCM sample BET surface area was analysed using N_2 adsorption/desorption studies. The surface area of the sample $MgFe_2O_4$-MCM was found to be 71.85 m^2/g and the particle size of $MgFe_2O_4$-MCM is confirmed by powder XRD and HR-TEM analysis. Moreover, it is believed that the high surface area of $MgFe_2O_4$-MCM could enhance the photo-catalytic activity It was found that the sample $MgFe_2O_4$-MCM show higher PCD efficiency (96.48 %). It is mainly due to the uniform distribution with smaller particle size of $MgFe_2O_4$-MCM photo-catalyst. In MCM approach, the final product is formed within few minutes of time with homogeneous and smaller particle

size with higher surface area, which enhance the photocatalytic activity .In addition, when the surface area increases, the amount of the dispersion of particles per volume in the solution will increase, this enhanced the catalytic activity.

3.5 Conclusion

The magnetic $MgFe_2O_4$ nanoparticles were successfully synthesized and characterized. From x-ray diffraction (XRD) particles size is calculated used Scherrer's formula. UV-Visible spectrometer UV helps to find the band gap of the nanoparticles. Dielectric studies like dielectric constant and dielectric loss show the electrical property of the material. The catalytic performance of $MgFe_2O_4$-MCM samples prepared by MCM method is studied. It is well known that the catalytic activity strongly depends on the particle size and surface area samples. The observed photo-catalytic results were summarized.

References

1. Manikandan, M. Durka, S. Arul Antony, J. Supercond. Nov. Magn. 28 (2015) 2047–2058.
2. S. Bhukal, S. Mor, S. Bansal, J. Singh, S. Singhal, J. Mol. Struct. 1071 (2014) 95-102.
3. P. S. Kang, J. H. Seok, Y. H. Kim, J. S. Eun, S. H. Oh, Food Sci. Biotechnol. 16 (2007) 409-414.
4. M. J. Divya, C. Sowmia, K. Joona, K. P. Dhanya, Res. J. Pharm. Bio. Chem. Sci. 4 (2013) 1137-1142.
5. L. Menini, M. C. Pereira, L. A. Parreira, J. D. Fabris, E. V. Gusevskaya, J. Catal. 254 (2008) 355–364.
6. K. Gopinath, K. S. Venkatesh, R. Ilangovan, K. Sankaranarayanan, A. Arumugam, Ind. Crops Products 50 (2013) 737– 742.
7. R. D. Waldron, Phys. Rev. 99 (1955) 1727-1735.
8. F. Gozuak, Y. Koseoglu, A. Baykal, H. Kavas, J. Magn. Magn. Mater. 321 (2009) 2170-2177.
9. A.Manikandan, M. Durka, K. Seevakan, S. Arul Antony, J. Supercond. Nov. Magn. (2015) 28:1405–1416.
10. M. Shahid, L. Jingling, Z. Ali, I. Shakir, M. F. Warsi, R. Parveen, M. Nadeem, Mater. Chem. Phys. 139 (2013) 566-571. M. Sertkol, Y. Koseoglu, A. Baykal, H. Kavasa, A. C. Basaran, J. Magn. Magn. Mater. 321 (2009) 157–162. **DOI**; /10.1016/j.jmmm.2008.08.083.
11. M. Sertkol, Y. Koseoglu, A. Baykal, H. Kavas, A. Bozkurt, M. S. Toprak, J. Alloys Compds 486 (2009) 325–329. **DOI**; 10.1016/j.jallcom.2009.06.128.
12. A. Manikandan, M. Durka, S. Arul Antony, Adv. Sci. Eng. Med. 7 (2015) 33-46. **DOI:** 10.1166/asem.2015.1654.

Available online at www.sciencedirect.com

ScienceDirect

Materials Today: Proceedings 8 (2019) 250–255

materialstoday: PROCEEDINGS

www.materialstoday.com/proceedings

ICMEE 2018

A Correlative Investigation of Photoconductive Behaviour of Bare and Al-Doped ZnO Thin Films

D.J. Sharmila[a], Neena Bachan[a], V. Chandrakala[a], P. Naveen Kumar[a], J. Madhavan[a] and J.Merline Shyla[a]*

[a*]*Department of Physics, Energy Nanotechnology Centre (ENTeC), Loyola Institute of Frontier Energy (LIFE), Loyola College, Chennai 600034, India. e-mail: jmshyla@gmail.com*

Abstract

Zinc Oxide (ZnO) nanoparticles exhibit a wide range of applications owing to their unique properties such as low cost, non-toxicity, abundance in nature and suitability for doping. In the present study, ZnO and Aluminium doped Zinc Oxide (Al-ZnO) nanoparticle thin films were prepared on FTO glass substrate by sol-gel and spin coating methods. The structural and morphological characteristics of the undoped and Al-doped ZnO nanoparticles were examined by X-ray Diffraction (XRD) and High Scanning Electron Microscope (HR-SEM) analysis, respectively. The XRD studies revealed the hexagonal wurtzite structure of the as-synthesized ZnO samples and the crystallite size was estimated using Scherrer's formula to be 28 and 30 nm respectively, in the case of the undoped and doped ZnO nanoparticles. The average particle sizes in nanoscale were analysed using FESEM and found to be 38 nm and 42 nm for the bare and doped samples. The surface area of the as-synthesised particles were correspondingly estimated as 46 m^2/g and 25 m^2/g and their relative pore volume and diameter were determined using BET analysis. The field dependent photoconductivity of Al-ZnO shows a significant increase as against the bare ZnO.

Selection and peer-review under responsibility of the scientific committee of the Materials. For Energy and Environment.

Keywords: Sol-gel; spin coating; thin film; photoconductivity.

* Corresponding author. Phone: +91-9444239551; Fax: +91-44-28175566

E-mail address: jmshyla@gmail.com

Selection and peer-review under responsibility of the scientific committee of the Materials For Energy and Environment.

1. Introduction

ZnO nanoparticles have been widely studied due to their good performance in electronic, optical and photonic devices [1]. ZnO is an n-type semiconductor material that has a wide band gap of 3.37eV [2], high chemical and thermal stability [3]. ZnO in the nano-scale (1–100 nm) can demonstrate the quantum confinement effects, which gives the opportunity to exhibit new physical and chemical properties. This encouraged the researchers to synthesize ZnO as a nanostructure material with various methods and in different shapes such as nanoparticles, nanowires, nanorods, and nanotubes [3-5].

Moreover, ZnO can be used as a pure material in many applications like optical and display devices or it can be doped with elements such as (Al, Ag, or Sn) for high conductance [6] or magnetic elements (Mn, Co, or Ni) to be used as diluted magnetic materials. Recently, doping of ZnO with metals such as Al, Cu, Fe, Se, Ce and Mn widely considered. Aluminum is a suitable impurity for the improvement of photocatalytic activity, which is superabundant, inexpensive and has exclusive physical properties [7].

ZnO thin films can be synthesized by the sol-gel method followed by the spin coating process. Sol–gel spin coating method can be considered as a very simple process for the production of large area of films. ZnO thin films have been widely used as frontal electrode in solar cells, being an alternative to metallic grid contacts that introduce shadows and lower the cell performance [8].

The aim of the present work is to prepare nanocrystalline ZnO semiconducting thin films, which can be used as n-type in thin film solar cells by low cost sol–gel spin coating method (non-vacuum method).

2. Experimental Details

For the synthesis of ZnO nanoparticles and Aluminium doped ZnO nanoparticles, Zinc acetate dehydrate, Aluminium Chloride and Sodium hydroxide were used. All the chemicals were of analytical grade and used without further purification.

2.1 Synthesis of ZnO Nanoparticle

Zinc acetate dehydrate (Zn $(CH3COO)_2 \cdot 2H_2O$) was mixed with 100 ml Ethanol and stirred for 30 minutes. Few grams of sodium hydroxide was mixed with 10 ml distilled water and stirred separately for 15 minutes. After vigorous stirring sodium hydroxide was added in drops to the Zinc acetate dehydrate solution to reach the pH 12 and stirred for 12 hours. After continuous stirring for 12 hours the mixed solution was allowed to settle for sedimentation. FTO glass plate is used as a substrate and cleaned prior with Acetone, Ethanol and Distilled water using an ultrasonicator. Then the precipitate was coated onto the FTO glass plate using Spin Coating method. The coated FTO glass is calcinated at 500 °C for 1 hour. Then the film was subject to various characterisation studies.

2.2 Synthesis of Al-ZnO Nanoparticle

For the synthesis of Aluminium doped Zinc oxide Nanoparticles, Aluminium chloride was mixed with Zinc acetate dehydrate solution and stirred for 30 minutes. Sodium hydroxide was added in drops to the mixed solution to reach the pH 12. Then the mixed solution was stirred continuously for 12 hours and allowed for sedimentation. Then the precipitate is coated on a FTO glass plate using Spin coating method and the coated FTO glass is calcinated at 500 °C for 1 hour.

3. Results and discussion

3.1 X –Ray Diffraction (XRD)

The XRD patterns of ZnO and Al doped ZnO nanoparticles have been recorded by the powder diffraction method using RICH SIEFEST X – RAY DIFFRACTOMETER. Fig. 1(a) and 1(b) shows the XRD pattern of ZnO and Al doped ZnO nanoparticles. The diffraction pattern clearly indicates that, ZnO nanoparticles are highly crystalline and the well-defined peaks are indexed to the hexagonal wurtzite structure of ZnO (JCPDS card no 36-1451). The average crystallite size of ZnO nanoparticle was determined by employing Scherer's equation [9]

$$D = K\lambda/\beta Cos\ \theta$$

where, D is the crystallite size, K constant, λ the wavelength and β the full width at half maximum of the diffraction angle.. The average crystallite size of ZnO Al doped ZnO nanoparticles was found to be 28 nm and 30 nm respectively. The observed lattice planes of (100), (002), (101), (102), (110),(103), and (200) corresponding to the 2θ value of 22.2°, 23.7°, 24.8°, 31.3°, 34.0°, 35.6°, 47.0° and 56.2° of ZnO, indicate that the product is composed of polycrystallites and all the diffraction peaks agreed well with Bragg reflections and no characteristic peaks were observed other than ZnO. Further, doping ZnO with Al reduces the zinc interstitials for charge compensation which results in suppressed ZnO grain growth and deteriorated crystallinity [10]. There is strong orientation of 3 % Al doped in the (0 0 2) plane.

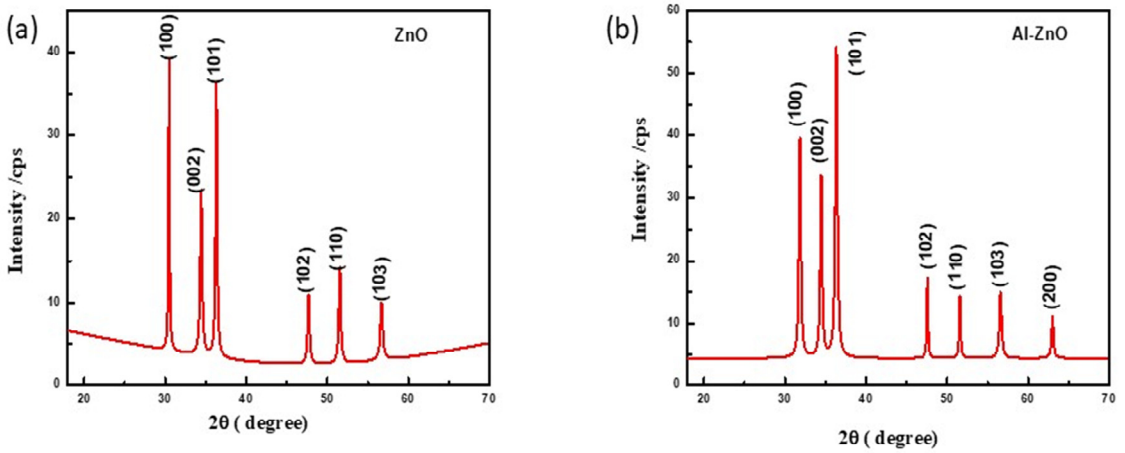

Fig. 1. (a) XRD pattern of ZnO (b) Al doped ZnO.

3.2 HR- Scanning Electron Microscope (HRSEM)

The morphology of ZnO and Al doped ZnO nanoparticles were obtained by High Resolution Scanning Electron Microscope (HR-SEM) and have been recorded using HITACHI S-4800-IIT MADRAS. From the HR-SEM images it is apparent that the nanoparticles are highly dispersed without any aggregation. Fig. 2(a) and 2(b) shows the HRSEM images of ZnO and Al doped ZnO. The particle sizes are in the range of 25 – 50 nm. Increase in the particle size was observed upon Al doping.

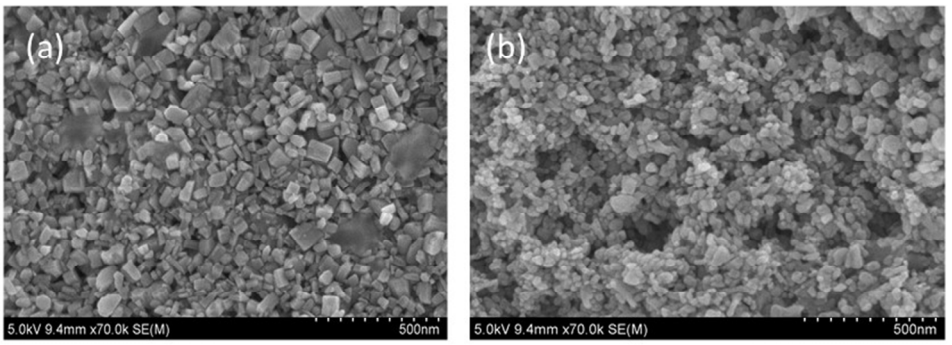

Fig. 2. (a) HRSEM images of ZnO (b) Al doped ZnO

3.3 Specific Surface Area Analysis

The specific surface area analysis of the as-synthesized samples was carried out using Brunauer-Emmett-Teller (BET) studies. Fig. 3(a) and 3(b) shows the adsorption isotherms of the prepared samples. The surface area of the ZnO and Al doped ZnO is found to be 25.29 m^2 /g and 46.25 m^2 /g and the pore diameters were found to be15.544 nm and 15.63 nm. They isotherms are of type IV and hence evidence presence of mesoporous (2-50 nm) materials according to the International Union Pure and Applied Chemistry classification. Doping of Al shows a significant increase in the BET surface area. The augmented surface area on account of Al doping on ZnO would have paved the way for greater photoconduction in doped sample which could be attributed to the presence of more number of surface electrons available for absorbing incoming photons and hence enhanced surface conduction [11].

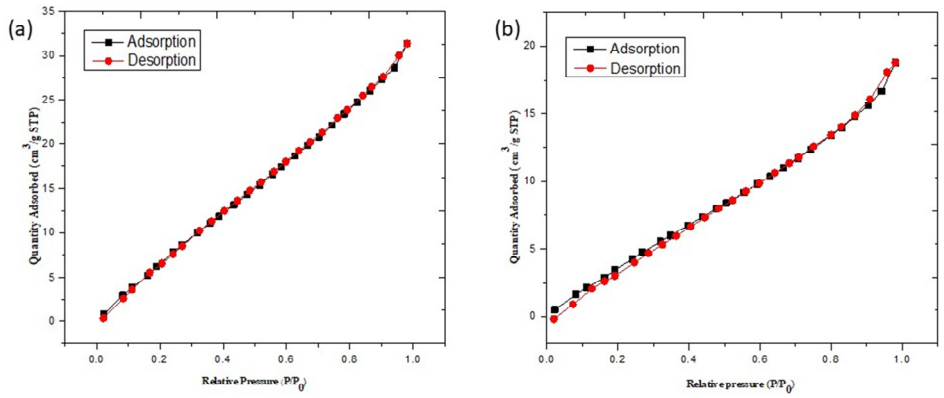

Fig. 3. (a) Adsorbed isotherm of ZnO (b) Al doped ZnO

3.4 Photoconductivity analysis

The field dependent dark and photoconductivity studies were carried out using KEITHLEY PICOAMMETER 6485 for understanding the conducting nature of the as-synthesized samples. Photoconductivity is the tendency of a substance to conduct electricity to an extent that depends on the intensity of light-radiant energy

striking the surface of a sample. All the plots indicate a linear increase of current in the dark and visible light-illuminated samples with increasing applied field depicting the ohmic nature of the contacts [12-13]. Fig. 4(a) and 4(b) shows the field dependent photo and dark current of ZnO and Al doped ZnO. The dark and photocurrents of Al-ZnO showed enchanced values as compared to bare ZnO. For an applied field of 100 V/cm the photo current of ZnO and Al doped ZnO was found to be 2.003 µA and 2.406 µA and the dark current was 1.65 µA and 1.84µA. An increase of about ~ 1.2 folds in photocurrents and ~ 1.1 folds in dark currents was witnessed in the case of doped sample and this significant enhancement could be related to the increased charge carrier concentration which is an effect of enhanced surface area.

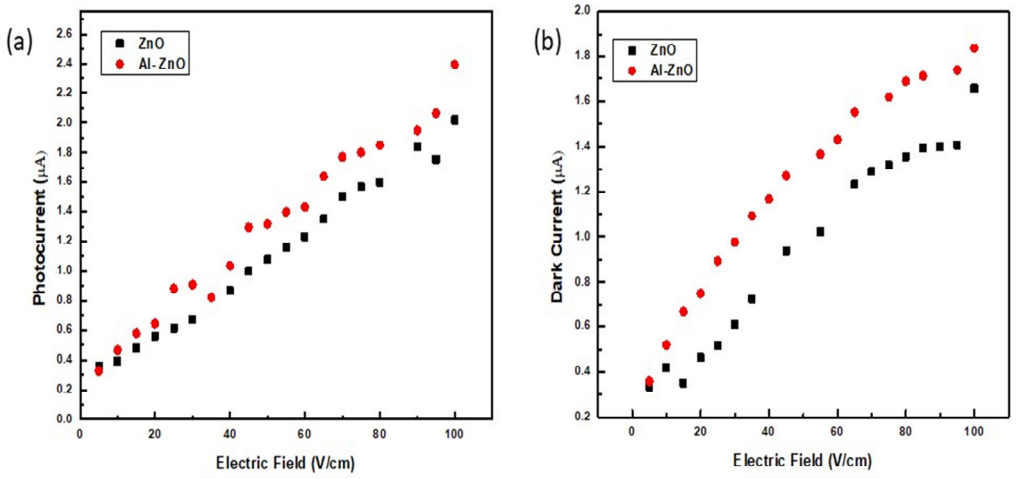

Fig. 4. (a) Field dependent dark and photo current of ZnO (b) Al doped ZnO

4. Conclusions

In this study, ZnO and Al doped ZnO thin films were synthesized using sol –gel spin coating methods. The obtained films are transparent and uniform with good adherence to the substrate. From the XRD the nanocrystalline nature of the sample was confirmed and further its hexagonal wurtzite structure was established. The crystalline size and the particle size increases on doping with Al. The BET analysis shows a rapid increase in the surface area on doping of Al into ZnO and hence witnessing the enhanced surface conduction of electrons on doped candidate. In the photoconductivity analysis there is a linear increase in the dark and the photo current and in addition to that the photoconducting nature of the sample Al- ZnO is greater than the bare ZnO sample. The superior photoconduction in the doped sample exhibited better opto-electrical properties enabling them as a better photo anode for solar cell applications. These films can be used as a window layer for low cost thin film solar cells.Thus it could be concluded that Al doped ZnO would be a promising material for photovoltaic application especially as photoelectrodes in Dye-Sensitized Solar Cells (DSSCs).

Acknowledgement

This research was supported by the Loyola College-Times of India Major Research Grants (6LCTOI14LIF002) and the authors wish to acknowledge the same.

References

[1] Fleischer, K., Arca, E., Smith, C., Shvets, I. 92012. Aluminium doped Zn1-xMgxO-A transparent conducting oxide with tunable optical and electrical properties. Applied Physics Letters 101, 121918.

[2] Samarasekara P, Wijesinghe U, Jayaweera EN (2015) Impedance and electrical properties of Cu doped ZnO thin films. GESJ 1(13):3–9. ISSN 1512-1461.

[3] Chebil W, Fouzri A, Azeza B, Sakly N, Mghaieth R, LussonA,Sallet V (2015) Comparison of ZnO thin films on different substrates obtained by sol–gel process and deposited by spin-coating technique. Indian J Pure Appl. Phys 53(8):521–529.

[4] Abdel-Galil A, Balboul MR, Sharaf A (2015) Synthesis and characterization of Mn-doped ZnO diluted magnetic semiconductors. Phys B 477:20–28.

[5] Khanlary MR, Vahedi V, Reyhani A (2012) Synthesis and characterization of ZnO nanowires by thermal oxidation of Zn thin films at various temperatures. Molecules 17(5):5021–5029.

[6] Lu H, Zhai X, Liu W, Zhang M, GuoM ,Electro depositionof hierarchical ZnO nanorod arrays on flexible stainless steel mesh for dye-sensitized solar cell. Thin Solid Films, 2013 586:46–53.

[7] X. Zhang, Yu Chen, Sh. Zhang, C. Qiu, High photocatalytic performance of high concentration Al-doped ZnO nanoparticles, Sep. Purif. Technol. 172 (2017) 236–241.

[8] Ahmed Abde, GalilFarrag, Mohamed R. Balbou, Nano ZnO thin films synthesis by sol–gel spin coating method as a transparent layer for solar cell applications, DOI 10.1007/s10971-016-4277-8.

[9] DeepshikhaSaini, T. Basu, Synthesis and characterization of nanocomposites based on polyaniline-gold/graphenenanosheets, Applied Nanoscience, 2, 2012, 467–479.

[10] A. Alkahlout, N. Al Dahoudi,I. Grobelsek, M. Jilavi, and P.W. de Oliveiral, (2014) Synthesis and Characterization of Aluminium Doped Zinc Oxide Nanostructures via Hydrothermal Route, Journal of Materials Volume 2014, Article ID 235638

[11] D. Arun Kumar, J. Alex Xavier, J. MerlineShyla, Francis. P. Xavier, Synthesis and structural, optical and electrical properties of TiO2/SiO2 nanocomposites, Journal of Materials Science, 2013, 48, 10, 3700-3707.

[12] YU H., LUI R., WANG X., WANG P., YU J., Investigation of sol-gel processed CuO/SiO_2 nanocomposite as a potential photoanode material, Appl.Catal. B-Environ., 111 32, 2012.

[13] Bojorge, C., Bianchetti, M., Gómez, N., Walsöe de Reca, N., Cánepa, H., Nanocrystalline ZnO photoconductivity measurements. Procedia Materials Science 1, 614-619, 2012.

Published Online: 10 April 2018

In-situ microwave irradiation synthesis of ZnO-graphene nanocomposite for high-performance supercapacitor applications

AIP Conference Proceedings **1942**, 140077 (2018);
https://doi.org/10.1063/1.5029208

R. Gunaseelan[1,*], V. Venkatachalam[2], *and* A. Antony Raj[3]

Hide Affiliations

[1]Department of Physics, Pachaiyappa's College for men, Kanchipuram-631 503, India
[2]Centre for Nanoscience and Technology, Anna University, Chennai-25, India
[3]Department of Physics, Loyola College, Chennai-34, India
[*]Corresponding author Email:krgunal84@gmail.com





Topics

ABSTRACT

In this paper, the ZnO/G nanocomposite was synthesized by facile in-situ microwave irradiation method. The as-prepared ZnO/G composite has been characterized with X-ray powder diffraction. The electrochemical properties of the obtained composite electrode for supercapacitor have been studied by cyclic voltammetry and electrochemical impedance spectra analyses. The ZnO/G nanocomposites showed a good capacitive behavior with a higher specific


PDF

1M KOH electrolyte. Based on the electrochemical results revealed that the composite electrode is a suitable candidate for supercapacitor applications.

REFERENCES

1.

X. Xiao, B. Han, G. Chen, L. Wang and Yude Wang, *Sci. Rep.* **7**, 40167–7 (2017). https://doi.org/10.1038/srep40167, Google Scholar, Crossref

---

2.

Y. Haldorai, W. Voitb and J.J. Shima, *Electrochim. Acta*, **120**, 65–72 (2014) https://doi.org/10.1016/j.electacta.2013.12.063, Google Scholar, Crossref

---

3.

Z. Zhang, L. Ren, W. Han, L. Meng, X. Wei, X. Qi, J. Zhong *Ceram. Int.* **41**, 4374–4380 (2015) https://doi.org/10.1016/j.ceramint.2014.11.127, Google Scholar, Crossref

4.

Z. Zhang, X. Liu, X. Qi, Z. Huang, L. Ren and J. Zhong, *RSC Adv.* **4**, 37278–37283 (2014) https://doi.org/10.1039/C4RA05078A, Google Scholar, Crossref

5.

Z. Zhang, X. Liu, X. Qi, Z. Huang, L. Ren and J. Zhong, *RSC Adv.* **4**, 37278–37283 (2014) https://doi.org/10.1039/C4RA05078A, Google Scholar, Crossref

6.

T. Lu, Y. Zhang, H. Li, L. Pan, Y. Li and Z. Sun, *Electrochim. Acta*, **55**, 4170–4173 (2010) https://doi.org/10.1016/j.electacta.2010.02.095, Google Scholar, Crossref

7.

W.T. Song, J. Xie, S.Y. Liu, Y.X. Zheng, G.S. Cao, T.J. Zhu and

Google Scholar

8.

H. Zeng, Y. Cao, J. Yang, Z. Tang, X. Wang and L. Sun, *Nanoscale Res. Lett.* **8**, 133–139 (2013) https://doi.org/10.1186/1556-276X-8-133, Google Scholar, Crossref

9.

A. Prakash and D. Bahadur, *ACS Appl. Mater. Interfaces*, **6**, 1394–1405 (2014) https://doi.org/10.1021/am405031y, Google Scholar, Crossref

10.

V. Venkatachalam, A. Alsalme, A. Alghamdi and R. Jayavel, *J. Electroanal. Chem*, **756**, 94–100 (2015) https://doi.org/10.1016/j.jelechem.2015.08.019, Google Scholar, Crossref

11.

J. Zhang, L.B. Kong, J.J. Cai, Y.C. Luo and L. Kang, *J. Solid*

https://doi.org/10.1007/s10008-010-1035-7, Google Scholar , Crossref

Published by AIP Publishing.

Available online at www.sciencedirect.com

ScienceDirect

Materials Today: Proceedings 5 (2018) 8662–8671

materialstoday: PROCEEDINGS

www.materialstoday.com/proceedings

ICRAMC_2017

Investigation on the role of pH for the structural, optical and magnetic properties of cobalt ferrite nanoparticles and its effect on the photo-fenton activity

P. Annie Vinosha [1] and S. Jerome Das [1,*]

[1 *] *Department of Physics, Loyola College, Chennai, 600 034, India.*

Abstract

Inverse spinel cobalt ferrite ($CoFe_2O_4$) nanoparticle has ensnared colossal consideration owing to its implausible and incredible properties, predominantly its optical and magnetic properties. These enhanced properties make $CoFe_2O_4$ a fitting candidate in the waste water treatment. A facile and economically viable low temperature co-precipitation route was used to synthesize $CoFe_2O_4$ nanoparticles, the samples were synthesized at different pH conditions ranging from 9 to 12. The structural and crystallite size of the synthesized sample was characterized by Powder X-Ray Diffraction and found that on raising the pH crystallite size and lattice constant decreases. In Fourier Transform Infrared spectrum two absorption bands were observed at ~500 (v_1) and ~400 cm^{-1}(v_2). Using High Resolution Transmission Electron Microscopy the particle size was found to be varying from that of XRD calculated crystallite size, the pH variation had no noticeable sway on the morphology, but it has significant influence on the particle size. By UV-visible and Photoluminescence studies reveals the significant optical properties and their bandgap was calculated using Kubelka-Munk plot, bandgap was found to be decreasing on raising the pH. The synthesized cobalt ferrite nanocatalyst was premeditated for its photo-degradation application of Methylene blue (MB) dye, which is a very important organic dye used in textile industries and the results point out that the catalyst can be reused without any significant loss, which makes it an competent candid in industries for distillation of water.

Selection and/or Peer-review under responsibility of International Conference On Recent Advances In Material Chemistry.

Keywords: Cobalt ferrite; inverse spinel; co-precipitation; photo-fenton.

* Corresponding author. Tel: +91-93811 90314
E-mail address: annieakash@gmail.com, jeromedas.s@gmail.com

Selection and/or Peer-review under responsibility of International Conference On Recent Advances In Material Chemistry.

1. Introduction

The amputation of perilous dyes in water is one of the main exertions of developing countries. Some of these dyes, due to their synthetic origin and multifaceted aromatic structure are thorny to degrade, in addition they produce carcinogenic or noxious by-products by numerous reactions such as oxidation and hydrolysis in aqueous medium, thus they should be degraded duly for public health [1–6]. Heterogeneous (e.g. Fenton reaction) or homogeneous catalysts can be used to produce hydroxyl radicals from H_2O_2 [7]. Advanced oxidation processes (AOPs) are used to degrade organic pollutants in aqueous medium by strapping oxidants such as hydroxyl radicals (HO_). An emerging field in AOPs is the application of magnetic catalysts to degrade pollutants [8-11]. The ascendancy of photocatalytic modus operandi in waste water treatment is due to some of its rewards over the conventional techniques, such as oxidation of pollutants in the ppb range, quick oxidation, non formation of polycyclic products, etc. [12]. Dyes, the foremost pollutants from diverse industries such as leather, paper, plastics, textile, cosmetics, etc, used for colouring, turn out to be dangerous and noxious to numerous living organisms. Therefore effectual removal of organic dyes from waste water remains a massive challenge currently. Inverse spinel ferrites are emerging as a focal area for research community due to their excellent catalytic recital reactions such as methane oxidative, CO_2 reduction, conversion, water gas shift reaction, adsorbent for amputation of toxic substances etc. The nano ferrites are been likely honoured for its photocatalytic activity, hence these ferrites have a relevant band gap which smear in the visible band region. These properties allow ferrites to be imaginatively utilized in the visible region of the planetary spectrum for photocatalytic reactions such as degradation of different organic pollutants using decomposition of H_2O_2 and oxidative dehydrogenation of hydrocarbons. In adding up, ferrites can be used as an alarming photo catalyst as they augment oxidizing power of Fenton type reactions [13]. It was reported that the magnetic catalyst are removable and reused even after seven cycles. As a proficient member of inverse spinel ferrites, cobalt ferrite ($CoFe_2O_4$) nanoparticles show elite properties such as large magneto- crystalline and the magneto - optical coefficient at low temperature, these properties along with immense chemical and physical fidelity formulate $CoFe_2O_4$ as an apt material for photocatalysts and electronic applications [14, 15]. $CoFe_2O_4$ is an n-type semiconductor material that worn photo-fenton application in visible light region due to its smaller bandgap of 1.92 eV. The magnetic behaviour of cobalt ferrite nanoparticles depends on dimension, structure and also purity of the material. Because of these magnetic properties, $CoFe_2O_4$ nanoparticles have impending applications in photocatalytic activity, antenna rods, high density storage devices, transformers, ferrofluids, audio and videotapes, microwave devices, humidity sensors, electrochemical sensing, photo-detectors [16-18]. In this paper, $CoFe_2O_4$ nanoparticle was synthesized by an economically viable low temperature co-precipitation technique, due to its plentiful rewards such as homogeneity, control over the particle size and free from impurities [19]. The synthesized nanomaterials were characterized to study their physical and chemical properties. Methylene blue (MB) dye which is an important organic dye used in textile industry was tested with the synthesized nanocatalyst for its photocatalytic application.

2. Synthesis of $CoFe_2O_4$ nanostructures

All the chemicals used in the experiment were used without any further refinement. Nanosized $CoFe_2O_4$ particles have been synthesized by chemical precipitation method. The essential mass of ferric nitrate (Fe $(NO_3)_3$) and cobalt nitrate (Co $(NO_3)_2$) was biased in a stoichiometric ratio of 2:1. The solution was then magnetically stirred in order to have an eloquent and homogeneous solution. Then, 1M of NaOH aqueous solution was added as a mineralizer in order to adjust the pH (9-12), then it was kept at an ambient temperature of 80 °C for 3 hours to obtain a thick precipitate, which was then magnetically centrifuged using double distilled water and ethanol alternately. The product obtained was then dried in a hot air oven at 80 °C for 24 h. The dried product was powdered well by a mortar and calcinated at 500 °C for 3 h in a furnace as the result $CoFe_2O_4$ nanoparticles were obtained and characterized [20].

3. Results and discussion

3.1 Structural analysis of $CoFe_2O_4$ nanoparticles

The synthesized nano samples was subjected to Powder X-ray Diffraction analysis using BRUKER DRX500 X-ray with CuKα radiation of wavelength 1.5406 Å through the angular range 20-70° by scanning at the step of 0.01°

per minute to analyze the structure of $CoFe_2O_4$ nanoparticles. The X-ray diffraction pattern (Fig.1) confirms the presence of $CoFe_2O_4$ nanoparticle with cubic spinel structure. The diffraction peaks were indexed by the crystal planes (220), (311), (400), (422), (511) and (440). The prominent peaks matches well with the JCPDS file number 22-1086. Besides the cubic phase of $CoFe_2O_4$, an extra secondary phase of Fe_2O_3 (JCPDS, 86-0550) was also observed in the XRD pattern which is indicated by star symbol. The particle size sturdily depends on pH of the media and molarity of the precursor in the co-precipitation technique. As the pH rises, molarity of the solution increases, which in turn corresponds to the diminution of the crystallite size. The crystalline size was determined by the Scherrer formula were K instrumental constant '*D*' is the crystalline size, 'λ' is the wavelength, 'θ' is the Braggs angle, 'β' is the Half Width Full Maxima, thus the crystallite size was measured.

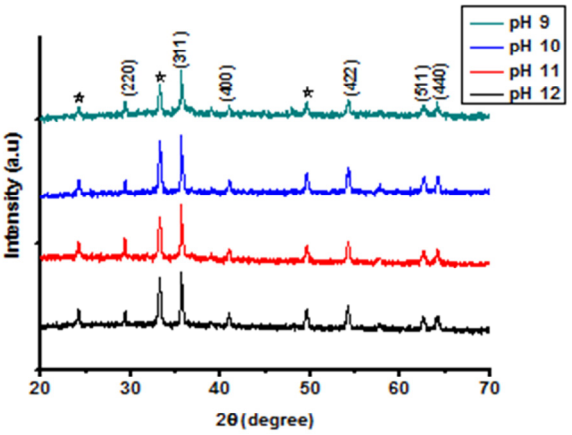

Fig.1 X-Ray Diffraction pattern of $CoFe_2O_4$ nanoparticles

$$D = \frac{k\lambda}{\beta \cos\theta} \tag{1}$$

Lattice strain (ε) has been calculated using the relation,

$$\varepsilon = \frac{1}{d^2} \tag{2}$$

By using the crystallite size (D) and lattice strain (ε) we calculate dislocation density (δ) by the relation,

$$\delta = \frac{15\,\varepsilon}{aD} \tag{3}$$

In Eq.4 lattice parameters is calculated were h, k, l is the Miller indices and d is the interlinear distance, the crystallite size and the lattice constant increases as the pH concentration increases shown in Fig.2, In Eq.5 and 6 unit cell volume (V) and X-ray density (d_x) is calculated were M, a and N represents molecular weight, lattice constant and Avogadro number of $CoFe_2O_4$, In Eq.7 porosity (P) is calculated were d_x is the X-ray density, whereas d is the bulk density is given by,

$$a = d(h^2 + k^2 + l^2)^{\frac{1}{2}} \tag{4}$$

$$V = a^3 \tag{5}$$

$$d_x = \frac{8M}{Na^3} \tag{6}$$

$$P = 1 - \frac{d_x}{d} \tag{7}$$

Table 1 Calculated parameters from the XRD pattern of $CoFe_2O_4$ nanoparticles

Parameters	**pH concentration**			
$CoFe_2O_4$	9	10	11	12
Crystallite size (D) (nm)	13.41	16.77	24.22	29.06
Interplanar distance (d)	2.524	2.516	2.512	2.511
Lattice constant (a) (Å)	8.371	8.344	8.332	8.321
Volume ($Å^3$)	586.5	580.9	578	575.9
Bulk density (d) (gm/cm^3)	4.11	4.12	4.14	4.15
Lattice strain (ε)	0.156	0.157	0.158	0.159
dislocation density (δ)	0.0208	0.0167	0.0117	0.0098
X-ray density ($d_{x)}$ (gm/cm^3)	5.302	5.296	5.284	5.278
Plasma energy (eV)	18.92	18.88	18.82	18.76
Fermi energy (eV)	14.94	14.86	14.78	14.73
Penn gap (eV)	18.91	18.89	18.81	18.75
Porosity (P) (%)	22.88	21.56	21.28	20.82

The non-hygroscopic nature of the nanoparticles and the valence plasma energy ($\hbar\omega_p$) is obtained by using the relation,

$$\hbar\omega_p = \left(\frac{Zp}{M}\right)^{\frac{1}{2}} 28.8 \tag{8}$$

The Penn gap (E_P) and Fermi energy (E_F) is dependent on the plasma energy, which is given by,

$$E_P = \frac{\hbar\omega_P}{(\varepsilon_\infty - 1)^{\frac{1}{2}}} \tag{9}$$

$$E_F = 0.2948(\hbar\omega_P)^{4/3} \tag{10}$$

All these calculated parameters are given in table 1.

3.2 FTIR analysis

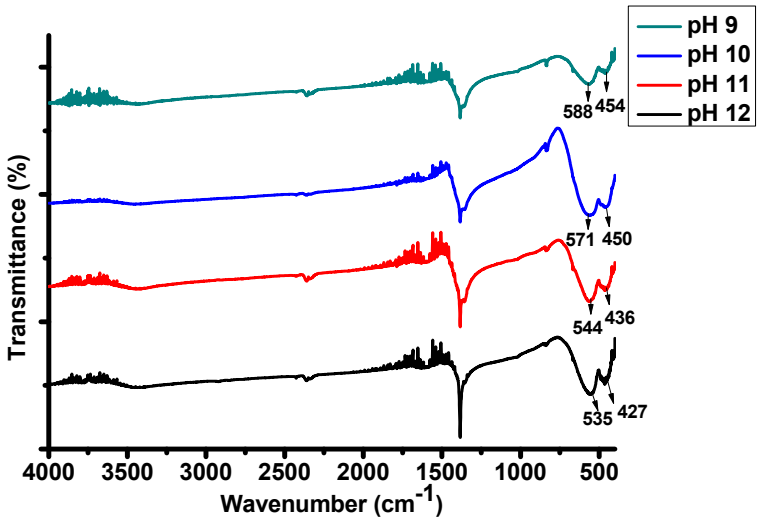

Fig.2 FTIR spectra of $CoFe_2O_4$

Table.2 FTIR Interatomic force constant (k)

pH	$\nu_1 \times_{10}{}^{-2} m^{-1}$	$\nu_2 \times_{10}{}^{-2} m^{-1}$	$k_t \times_{10}{}^{2} (Nm^{-1})$
9	588	454	1.479
10	571	450	1.345
11	544	436	1.265
12	535	427	1.223

The FTIR absorption spectrums are recorded in the range of 400- 4000 cm^{-1} is depicted in Fig.2. The bonding between both metal and oxygen ions at octahedral (ν_2) and tetrahedral (ν_1) sites are bands around 400 and 600 cm^{-1} [21]. The IR spectrum was used to assess the purity of the compounds and to know their structure. The force constant, the indicator of the Interatomic bonding strength is of the form shown in Table. 2,

$$k_t = 7.62 \times M_w \times \nu_1^2 \times 10^{-7} \quad (11)$$

where, ν_1^2 is the vibrational frequency, M_w the molecular weight of the tetrahedral cation. The broadened band observed at 3777 cm^{-1} indicates the presence of O-H bonding, whereas, the wave number at 1570 cm^{-1} is attributed to H-O-H absorption. The vibrational frequencies depend on the cation mass, cation oxygen distance and bonding force. The difference in frequency between the characteristic vibrations ν_1 and ν_2 may be attributed to the long bond length of oxygen - metal ions in the tetrahedral sites. The tetrahedral peaks are shifted to lower frequencies pH concentration increases due to the perturbation of Fe-O bands is revealed.

3.3 Optical analysis

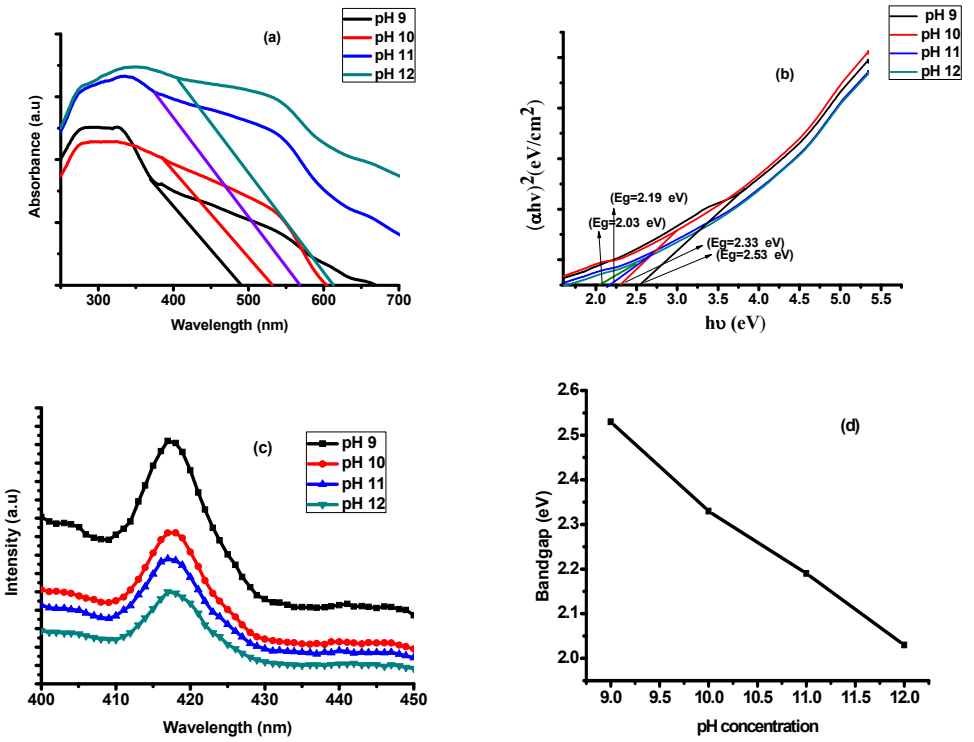

Fig. 4 (a), (b), (c) and (d) UV-vis, band gap energy plot, PL spectrum and variation in band gap of $CoFe_2O_4$ nanoparticles

$CoFe_2O_4$ nanoparticles were analyzed using Diffused Uv-Visible reflectance spectroscopy to study their optical properties shown in Fig.4 (a). The absorbance study demonstrated that Cobalt ferrite nanoparticles had momentous absorbance in the range of 400-700 nm that is in the visible region which is significant pro photo- Fenton application. Absorption edge was found for $CoFe_2O_4$ nanoparticles was 489, 530, 566 and 612 nm for pH= 9, 10, 11 and 12 respectively. Photolumininescence spectra present information about impurity level, deficiency states and band gap. The electrons carry radiative energy when it moves to the ground state, in this state the sample becomes optically exited and further emission process takes place [22]. The band gap was calculated using Kubelka-Munk plot of $(\alpha h\upsilon)^2$ vs photon energy ($h\upsilon$) as shown in Fig. 4 (b). The absorption near the band edge was calculated using the equation,

$$\alpha h\upsilon = A(h\upsilon - Eg)^{1/2} \quad (12)$$

Where A, Eg, h, α and υ are the proportionality constant, band gap, Planck constant, absorption coefficient and light frequency. The band gap decreases from 2.53 to 2.03 eV with respect to increasing pH concentration shown in Fig. 4 (d). In Photoluminescence spectrum a slight peak shift to higher level was observed as pH concentration increased shown in Fig. 4 (c). The band gap is influenced by diverse factors such as particle size, morphological parameters and presence of impurities. The worth mentioning attribute is the relation between bandgap and the particle size.

3.4 HR-TEM analysis

The morphology of the powder was investigated by High Resolution Transmission Electron microscope (HR-TEM) model Joel/JEM 2100. The pH had no palpable influence on the structural property, but it affects the speck size, which demonstrates that the cobalt ferrite nanoparticles were cubically spherical shape and monodisperse with average grain size of around 12-26 nm, which is lesser than that of XRD calculation deliberated in Fig.5.

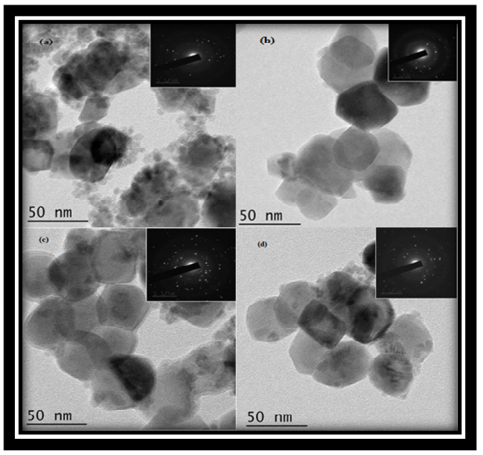

Fig. 5 (a), (b), (c), (d) HR-TEM at 50 nm with inset of SAED pattern of $CoFe_2O_4$ (pH=9, 10,11,12) nanoparticles.

3.5 Dielectric Analysis

The dielectric properties of the synthesized $CoFe_2O_4$ samples were studied using HIOKI 1352 LCR Hi TESTER in the frequency range of 50 Hz and 5 MHz. The imaginary and real parts of the dielectric permittivity

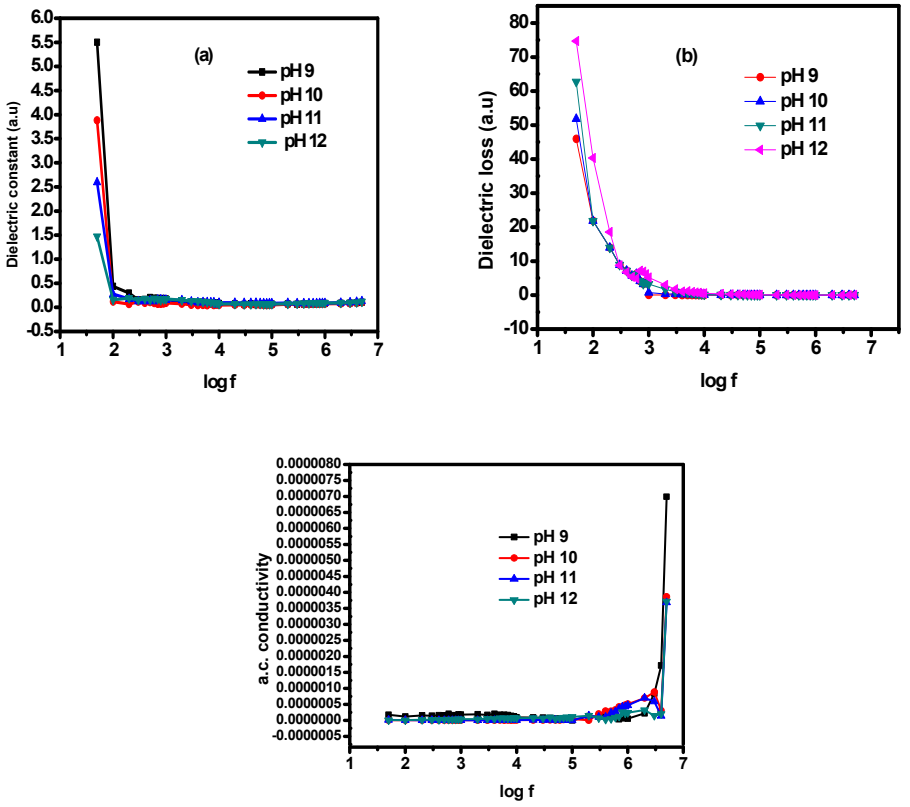

Fig.6 (a), (b) and (c) Variation of dielectric constant (ε'), dielectric loss and a.c conductivity with log f of $CoFe_2O_4$ nanoparticles

($\varepsilon^* = \varepsilon' - J\varepsilon''$) where obtained for the studied cell which is equivalent to a circuit consisting of a pure (ohmic) R_p with a ideal capacitance (C_P) in parallel. The capacitance of a capacitor for the real case, when the losses are,

$$C = \varepsilon^* C_0 = \frac{\varepsilon_0 (\varepsilon' - J\varepsilon'')\mathrm{A}}{d} \quad (13)$$

where ε' dielectric permittivity, ε'' is the imaginary part of the permittivity , ε_0 is the absolute permittivity, A is the area of the plate, d is the distance between the plate and C_0 is the capacitance of the empty cell,

$$C_0 = \varepsilon_0 A/d \quad (14)$$

The imaginary part of the complex permittivity is calculated by the relation,

$$\varepsilon'' = \frac{1}{C_0 R_p 2\pi f} \quad (15)$$

The dielectric loss for the capacitance is,

$$\tan\delta = \frac{G}{2\pi f C_P} = \frac{1}{2\pi f C_P R_P} \quad (16)$$

where G is the electrical capacitance. The a.c. conductivity $\sigma_{a.c.}$ for an ionic electrolyte sample is calculated from the dielectric loss by the relation,

$$\sigma_{a.c.} = \varepsilon_0 \varepsilon'' 2\pi f \quad (17)$$

It can be observed that the dielectric permittivity decreases with frequency and thus we can understand that permittivity is a frequency dependent parameter shown in Fig.6 (a), (b) and (c).

3.7 Photocatalytic activity

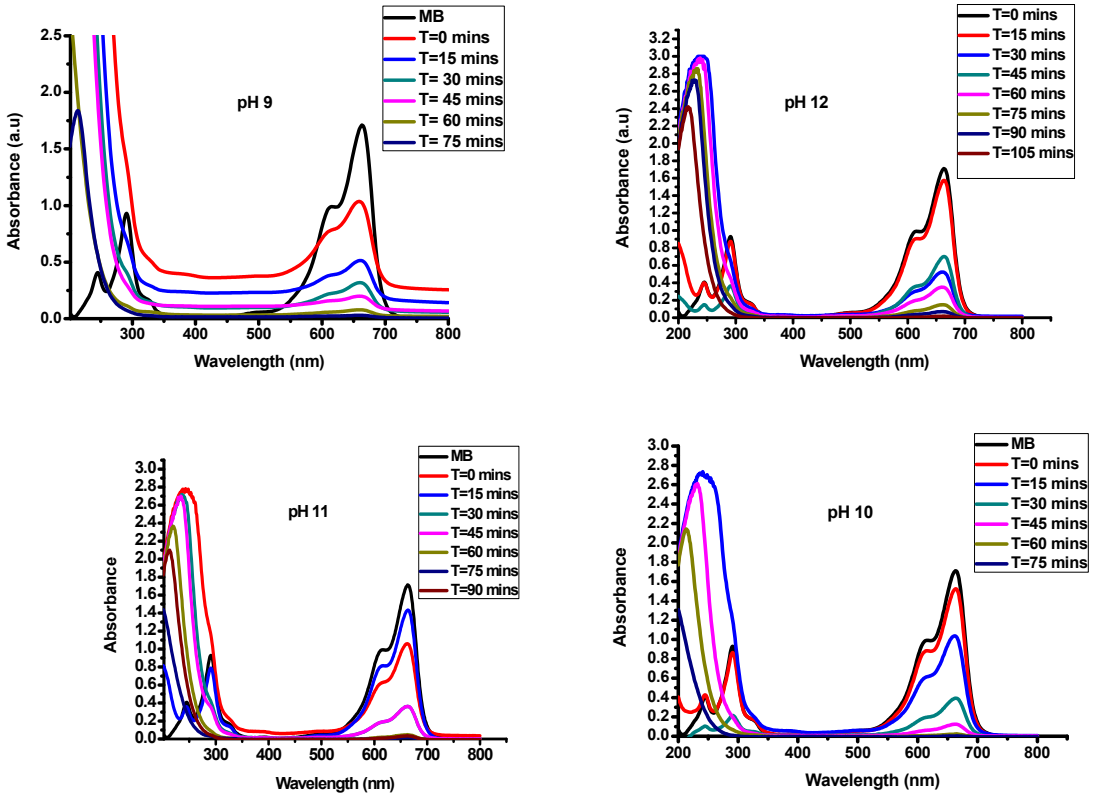

Fig.7 Change in spectra of MB with time in the presence of $CoFe_2O_4$ nanocatalyst

Table.3 Degradation of crystallite size and degradation rate constant

pH	D (nm)	Degradation (%)	Rate constant
9	13.41	99.3	0.002
10	16.77	99	0.007
11	24.22	98.7	0.008
12	29.06	98.6	0.019

Photo-Feton activity of $CoFe_2O_4$ nanoparticles was examined by evaluating the degradation of organic Methylene blue dye in the presence of aqueous solution under irradiation of visible light with a 125 W mercury source. In this experiment 100 mg of photo-catalyst was dispersed in 100 ml of 20 mg/l of MB solution. Prior to irradiating, the solution was magnetically stirred in dark for 20 minutes to make certain desorption-adsorption equilibrium of MB aqueous solution with the nanocatalyst. Then the aqueous solution with the catalyst was exposed to light after addition of 3 ml of 30% H_2O_2. At given time intervals, 3 ml of aliquots were centrifuged to remove ferrite nanoparticles. The concentration of MB was observed with the UV-vis spectrophotometer is observed in Fig.7. The percentage of degradation of Methylene blue is listed in Table. 3.

3.7.1 Recyclability

Solidity and Recyclability of the catalyst is of prime significance for industrial applications in long term progression to degrade the organic pollutants present in water. Ferrites own first-rate photo-Fenton activity, hence can be effortlessly separated using magnetic field. After degradation of MB, the nanocatalyst was centrifuged twice with distilled water followed by drying at 75 °C for 24 hours in a hot air oven. The ferrite nanoparticles had no vital loss even after five cycles hence confirms their applications in treating waste water. The typical degradation percentage of organic dye in the presence of nanocatalyst for 5 successive cycles is shown in Fig. 8.

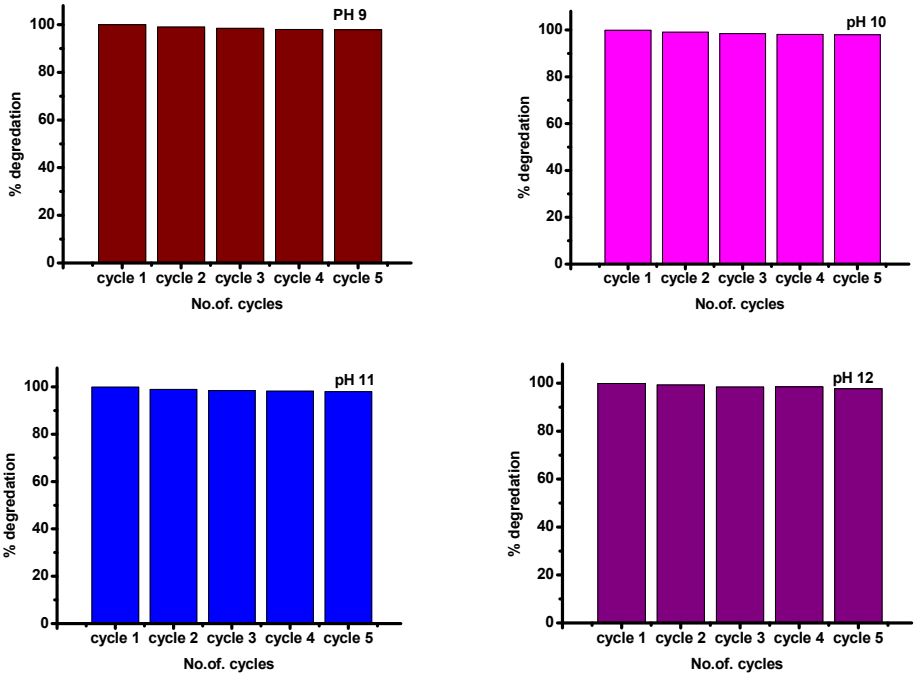

Fig.8 Recyclability of $CoFe_2O_4$ for 5 consecutive cycles

4 Conclusions

The inverse spinel $CoFe_2O_4$ nanoparticles were effectively synthesized by co-precipitation technique. The average crystallite size and various parameters were calculated from the XRD pattern. From UV-vis and Photoluminescence spectra optical properties were studied. The functional groups present in the synthesized sample were examined by FT-IR, which confirmed the attribute bands of $CoFe_2O_4$. The photo-fenton activity revealed the efficiency of $CoFe_2O_4$ in the degradation (~ 99.3 % in 75 minutes) of Methylene blue dye. Investigation on degradation kinetics exposed that the photo-fenton follows pseudo first order. The synthesized catalyst possessed exceptional magnetic and optical properties. In addition, the recyclability result indicated that the catalyst could be reused which helps in long term application in pollution control and waste water treatment.

References

[1] Z .Zainal,, L. K . Hui,., M. Z . Hussein,., &A. H . Abdullah,. J Hazard *Mater* 2009; 164 : 138-145.

[2] M . Uğurlu,. Microporous MesoporousMater 2009; 119: 276-283.

[3] A . Özcan,., &A. S . Özcan,. J Hazard *Mater* 2005; 125: 252-259.

[4] H. J . Fan, H. Y. Shu,., &K. J . Tajima, Hazard *Mater* 2006; 128: 192-200.

[5] V. P .Santos, M. F .Pereira,. , P. C. C .Faria., &J. J . Órfão,. J Hazard *Mater* 2009; 162 :736-742.

[6] N. M . Mahmoodi. J. Chem. Eng. Data 2011; 56: 2802-2811.

[7] T. A . Kurniawan,., &W. H . Lo, Water Res 2009; 43: 4079-4091.

[8] E . Casbeer,., V. K . Sharma,., &X. Z . Li,. Sep. Purif. Technol 2012; 87: 1-14.

[9] S . Xu,., D . Feng,., &W . Shangguan,. J. Phys. Chem. C 2009; 113: 2463-2467.

[10] C. H . Chen, Y. H . Liang,., &W. D. Zhang,. J Alloys Compd 2010; *501*: 168-172.

[11] J .Qiu, C . Wang & Gu, Mat Sci Eng B-Solid 2004*;* 112: 1-4.

[12] O .Legrini,., E . Oliveros,., &A. M. Braun, Chem. Rev. 1993; *93*: 671-698.

[13] Y. Sun, W. Wang , L .Zhang,, S .Sun,., & E. Gao. Mater. Lett 2013; *98*:124-127.

[14] J .Wang,, J . Zhang,, A. K . Sundramoorthy,., P . Chen,., &M. B . Chan-Park, , Nanoscale 2014;6: 4560-4565.

[15] M. Houshiar, F . Zebhi, Z. J. Razi,, A .Alidoust,., &Z . Askari,. J. Magn. Magn. Mater. 2014; 371: 43-48.

[16] O . Sadak,., A. K . Sundramoorthy, &S . Gunasekaran,. Biosens. Bioelectron 2017; *89*: 430-436.

[17] G. C. Lavorato., E . Lima,., H. E . Troiani,., R. D . Zysler,., &E. L . Winkler,. J Alloys Compd. 2015; 633: 333-337.

[18] K. S . Rao., G. S. V. R. K .Choudary, K. H . Rao,., &C. Sujatha, Procedia Materials Science 2015; 10: 19-27

[19] M .Ebrahimi., R. R . Shahraki,., S. S., . Ebrahimi, &S. M . Masoudpanah,. J Supercond Nov Magn , 2014; 27: 1587-1592.

[20] R. R . Shahraki, M. Ebrahimi, S. S . Ebrahimi,., &S. M . Masoudpanah,. J. Magn. Magn. Mater. 2012; 324: 3762-3765.

[21] W. B . White,&B. A . DeAngelis,. Spectrochim. Acta Mol. mol. Spectrosc 1967; 23: 985-995.

[22] G . Pandey &S. J. Dixit,. Phys. Chem. C. 2011; 115: 17633-17642.

Vibrational, Spectral Investigation of Nonlinear Optical L-Isocleucine D-Alanine: Experimental and Theoretical Confirmation

IOP Conf. Series: Materials Science and Engineering **360** (2018) 012046 doi:10.1088/1757-899X/360/1/012046

Vibrational, Spectral Investigation of Nonlinear Optical L-Isocleucine D-Alanine: Experimental and Theoretical Confirmation

R Vincent Femilaa[1], P Geetha[1,2] and J Madhavan[1]*

[1]*Department of Physics, Loyola College, Chennai, Tamilnadu, India*
[2]*Department of Physics, Quaid-E-Millath Government College for Women, Chennai, TamilNadu, India.*

*E-mail: jmadhavang@yahoo.com

Abstract. Optically transparent amino acid based nonlinear crystal of L-Isoleucine D-Alanine (LIDA) was grown from its aqueous solution by slow solvent evaporation technique. The material was studied in-depth by using vibrational spectrum and density functional theory (DFT). The Fourier transform infrared (FT-IR) spectrum was recorded in the range 4000 cm^{-1} – 450 cm^{-1}. Meanwhile, the DFT computations are performed at B3LYP/6-31G+ (d, p) level to obtain equilibrium geometry, vibrational wave numbers and first hyperpolarizability. The scaled theoretical wave numbers are also shown to be in good agreement with experimental data. From the UV-Vis spectrum the transmittance abilities of the crystal were studied. The band gap of the material was determined from the Tauc plot.

1. INTRODUCTION

In the modern world, the development of science in many areas has been achieved through the growth of single crystals. Crystal growth of organic materials has been recently attracting scientific attention in the search of new nonlinear optical materials. Many organic materials have been found to have greatly nonlinear or optoelectrical properties than inorganic substances [1]. Some organic compounds exhibit large NLO response, in many cases, order of magnitude larger than widely known inorganic materials. They also offer the flexibility of molecular design and the promise of virtually an unlimited number of crystalline structures. Amino acids are the famous organic materials which can play a role in nonlinear optics as they contain proton carboxylic acid (COOH) group and the proton acceptor amino (NH_2) group. Considerable efforts have been made on the amino acid mixed complex crystals in order to make them suitable for device fabrications. L-Isoleucine is one of the protein genic amino acids that aids in the production of protein. It is a branched chain amino acid (BCAA) that is classified as a hydrophobic amino acid. One of its main benefits is increased strength and rapid muscle repair when combined with other amino acids. It is also beneficial for children and teens that are in their growing years because it is vital for healthy growth. Alanine is an efficient organic NLO compound under the amino acid category. It is the simplest amino acids with an asymmetric carbon atom. Alanine and DL-Alanine are the usually available forms of alanine. In this chapter, we tried to report the growth and characterization of L-Isoleucine D-Alanine (LIDA) single crystal.

2. EXPERIMENTAL DETAILS

The LIDA compound was synthesized by the direct combination of L-Isoleucine and D-Alanine in distilled water at room temperature. The synthesized compound was further purified by repeated recrystallization. Purified salt of LIDA were collected and further used for bulk single crystal growth. The grown crystal is shown in the figure.1 of size measuring 8 x 5 x 7 mm^3. Finely crushed powder of LIDA crystal was subjected to powder X-ray diffraction analysis using CuK_α (λ = 1.5418 Å) radiation. LIDA crystal has a monoclinic structure and the lattice parameters are tabulated in Table.1.

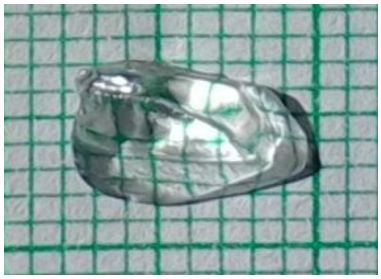

Figure.1 Photograph of as grown LIDA single crystal

Table 1. Crystal data

Crystal data	
Empirical formula	$C_9H_{20}N_2O_4$
Crystal System	Monoclinic
Space Group	$P2_1$
a(Å)	9.8944
b(Å)	4.7425
c(Å)	12.9045
β(°)	93.374

3. RESULTS AND DISCUSSION

3.1 Vibrational Spectral Analysis

The main objective of the vibrational analysis is to find vibrational modes connected with specific molecular structures of the compound. The best possible fitting was done between the calculated and experimental vibrational wavenumbers. The title molecule consists of 35 atoms, hence undergoes 99 normal modes of vibrations. These normal modes of vibrations are further classified into 67 in-plane vibrations and 32 out plane vibrations. The experimental FT-IR spectrum is as shown in Figure.2.

NH_3^+ group vibration

In zwitterionic molecules, theoretically the NH_3^+ symmetric stretching band appears at the value 3085.4737 cm^{-1} and experimentally appears at the value 3088 cm^{-1} respectively [2]. The NH_3^+ symmetric deformation theoretically appears at 1537.3389 cm^{-1}[3].

Carboxylate group vibration

The asymmetric and symmetric stretching modes of carboxylate ion vibrations theoretically occur at 1557.9300 cm^{-1} and 1451.4792 cm^{-1} respectively [4]. COO^- deformations theoretically occurs in the region 528.6117 cm^{-1}-582.6304 cm^{-1} and experimentally present at the value 539 cm^{-1}[5]. The COO^- deformation coupled with rocking mode appears theoretically at the value 675.0159 cm^{-1}- 740.3881 cm^{-1} in IR as a very strong band.

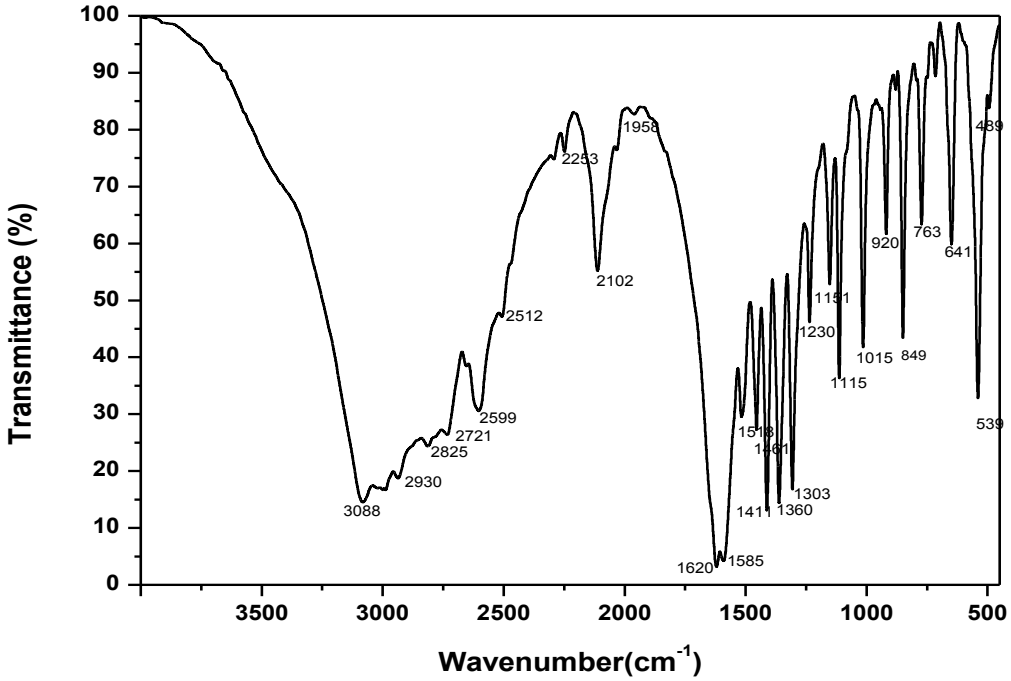

Figure 2. Experimentally obtained FT-IR spectrum of LIDA

C-N vibrations

C-N stretching absorptions are assigned theoretically in the region 1271.3646 cm^{-1} -1383.5730 cm^{-1} and experimentally at 1303 cm^{-1}, 1360 cm^{-1} for primary aromatic amine with nitrogen directly on the ring.

NH_2 vibrations

The NH_2 asymmetric stretching vibrations theoretically give rise to a strong band in the region 3404.9086 cm^{-1} - 3429.2699 cm^{-1} and the symmetric NH_2 stretching is observed as weak band in the region 3152.8348 cm^{-1} - 3160.8503 cm^{-1} theoretically.

O-H vibrations

The O-H out-of-plane bending mode for the free molecule lies in the region 5.0714 cm^{-1} - 289.9627cm^{-1} theoretically and it is beyond the infrared spectral range of the present investigation. However, for the associated molecule the O-H out-of-plane bending mode lies theoretically in the

region 528.6117 cm^{-1} - 675.0159 cm^{-1} and experimentally at 539 cm^{-1} in both intramolecular and intermolecular associations, the frequency is at a higher value than in free O-H.

COOH vibrations

The carbonyl group is contained in many different classes of compounds, for which a strong absorption band due to C=O stretching vibration is observed theoretically in the range of 1557.9300 cm^{-1} - 2086.7851 cm^{-1}. The vibrational assignments are presented in Table.2.

Table 2. Vibrational Assignments of LIDA Molecule

No	Wavenumber (cm^{-1})		Spectroscopic assignment	Force constant	Reduced mass
	B3LYP	Expt.			
1.	528.6117	539	COO^- def	0.3631	2.2058
2.	843.3942	849	C-N abs	0.5149	1.2286
3.	932.3841	920	NH_3 roc	1.0113	1.9744
4.	1024.5942	1015	NH_2 t	0.7400	1.1965
5.	1109.4946	1115	OH ipb	1.1096	1.5299
6.	1138.4561	1151	CH_2 roc	1.4700	1.9250
7.	1233.3331	1230	COO^- st &b	1.3043	1.4553
8.	1309.8000	1303	COO^- st & b	1.6224	1.6051
9.	1362.7537	1360	COO^- st & b	1.8737	1.7125
10.	1421.2563	1411	C-H b+ C=C st	2.1903	1.8403
11.	1460.9092	1461	C-H b+ C=C st	4.0324	3.2067
12.	2929.0913	2930	CH_2 st+ C-H st	5.3970	1.0677
13.	3085.4737	3088	NH_3^+ sym st	5.9061	1.0529

def- deformation, st- stretching, abs- absorption, st &b-stretching &bending, t- twisting, sym st- symmetric stretching.

3.2 Molecular Geometry and Hyperpolarizability

Computational chemistry is an important tool to design and modeling the NLO materials. The geometry of the investigated compound was treated as an isolated gas molecule. Becke-Lee-Yang-Parr hybrid exchange correlation three parameter (B3LYP) level at 6-31G basis set is used to derive the optimized structure in Gaussian 03W software package. Optimized structure was confirmed to minimum energy conformations. The optimized molecular structure of the isolated LIDA is shown in Figure.3. The second-order polarizability or first hyperpolarizability was calculated by B3LYP using 6-31G (d, p) basis set on the basis of the finite-field approach. Theoretical calculations on molecular hyperpolarizability become one of the key factors in the second-order NLO materials design. Theoretical determination of hyperpolarizability provides a guideline to experimentalists for the design and synthesis of organic NLO materials. Nonlinearity in organic chromophores can be synthetically modulated by varying the composition or length of conjugated p-systems, and by evaluating the effects of various electron-donor and electron-acceptor groups. They determine not only the strength of molecular interactions (long-range interaction, dispersion force, etc.) and the cross

sections of different scattering and collision process but also the NLO properties of the system. The hyperpolarizability values are listed in Table.3.

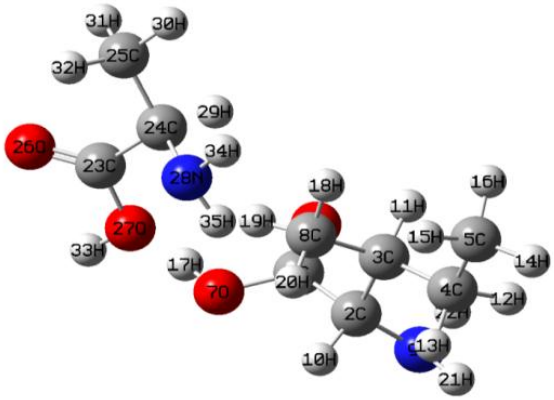

Figure 3. Atomic numbering for ab initio computations of LIDA molecule

Table 3. Hyperpolarizability of LIDA in esu

β_{xxx}	-275.705
β_{xxy}	-109.758
β_{xyy}	-187.947
β_{yyy}	-9.47754
β_{xxz}	-0.0259567
β_{xyz}	-0.00107375
β_{yyz}	-0.0120082
β_{xzz}	6.55646
β_{yzz}	-30.2164
β_{zzz}	0.0216665

3.3 Optical Absorption Spectrum

In order to determine the optical transmission characteristics of the grown crystal UV-Vis spectrum was recorded on the cut and polished grown sample. The UV-Vis spectral absorption was studied using a Varian Cary 5E UV-Vis-NIR spectrophotometer with a single crystal of 6mm thickness in the range of 200–800nm. The recorded spectrum is shown in Figure. 4 and 5. The crystal has sufficient transmission in the entire visible and IR region. The lower cut off wavelength is around 240 nm. From the absorbance energy band gap was evaluated. The E_g could be estimated from the plots of hν versus $(\alpha\ h\nu)^2$.

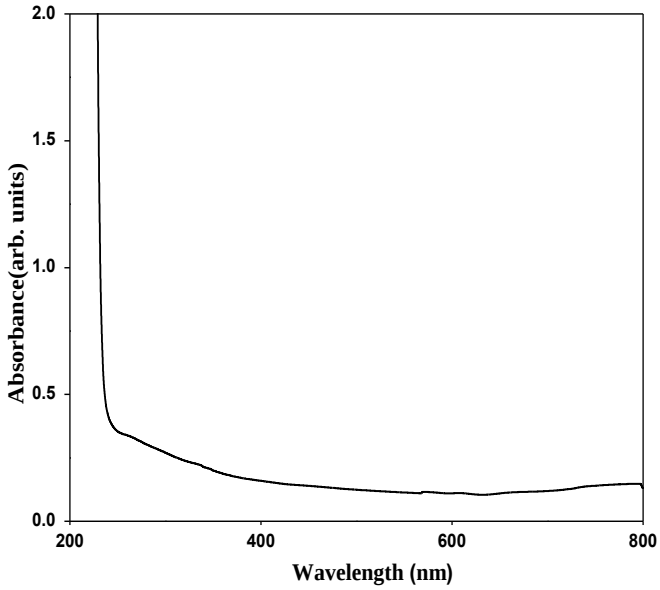

Figure 4. Optical absorption spectrum of LIDA crystal

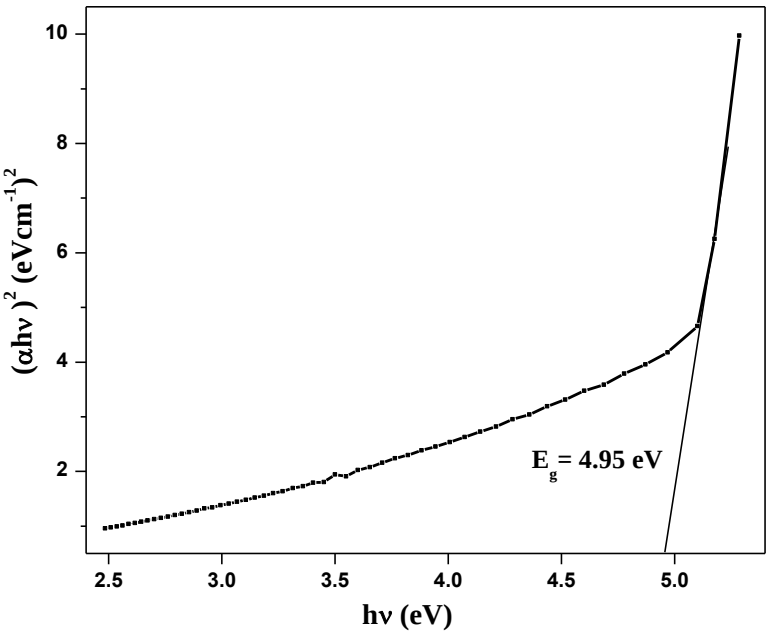

Figure 5. Optical band gap of LIDA crystal

4. Conclusion

Single crystal of L-Isoleucine D-Alanine (LIDA) was grown successfully by slow evaporation technique. Optimized structure of the isolated LIDA molecule obtained by DFT calculations give the minimum energy state. Existence of strong hydrogen bond in the donor accepter coupling was understood from bond lengths. First order hyperpolarizability of LIDA is calculated as $4.024860812 \times 10^{-30}$ esu and found useful in molecular designing. Theoretical and experimental spectroscopic studies exemplify the presence of various functional groups in the molecule. The UV-Vis spectrum reveals minimum absorption in the entire visible region.

Acknowledgment

The authors acknowledge University Grants Commission (UGC), India, for funding this research project-F.No.4-4/2015-16(MRP/UGC-SERO) - 2914.

REFERENCES

[1] Badan.J, Hierie.R, Perigaud.A, Zyes.J, Symp.A.C.S.ser 233 (1983) 81.
[2] Bellamy.L.J*, the infrared and Raman Spectra of Poly atomic molecules Wiley*: New York (1975).
[3] Silverstein R. M, Webster. F. X., *Spectrometric Identification of Organic Compounds*. John Wiley and sons, New York (2003).
[4] Socrates G., *Infrared and Raman Characteristic Group Frequency, third ed*., Wiley, New York (2001).
[5] Dollish F.R., Fateley W.G., Bentley F.F., *Characteristic Raman Frequencies of Organic Compounds*, John Wiley & Sons, New York (1997).

Synthesis, Structural, Morphological and Optical Characterization of TiO_2 and Nd^{3+} Doped TiO_2 Nanoparticles by Sol Gel Method: A Comparative Study for Photovoltaic Application

IOP Conf. Series: Materials Science and Engineering **360** (2018) 012011 doi:10.1088/1757-899X/360/1/012011

Synthesis, Structural, Morphological and Optical Characterization of TiO_2 and Nd^{3+} Doped TiO_2 Nanoparticles by Sol Gel Method: A Comparative Study for Photovoltaic Application

P Sanjay[1], E Chinnasamy[1], K Deepa[2], J Madhavan[2] and S Senthil[1,]

[1] Department of Physics, Government Arts College for Men (Autonomous), Nandanam, Chennai - 35, Tamil Nadu, India.
[2] Department of Physics, Loyola College, Chennai – 34, Tamil Nadu, India.
Email: ssatoms@yahoo.co.in

Abstract. Nano structured materials are currently receiving wide attention due their optical, electronic, magnetic, chemical, physical and mechanical properties. Semiconductor nano crystals have been widely studied for their fundamental properties. Pure and Nd^{3+} doped titanium dioxide nano powder was successfully synthesized by sol-gel method. The morphological and structural properties of as-prepared samples were characterized by X-ray diffraction (XRD), High resolution scanning electron microscope (HRSEM). The HRSEM analysis shows the partial crystalline nature of undoped, and doped TiO_2 nanoparticles and it was performed to obtain the particles size. The energy dispersive X - ray (EDAX) technique was used to determine their elemental compositions. The optical properties of doped and undoped TiO_2 nano particles were investigated by UV-Vis spectroscopy and Photoluminescence (PL). The band gap of the doped TiO_2 nanoparticles was found to be less than un-doped TiO_2 nanoparticles.

1. Introduction

Titanium dioxide (TiO_2) has been extensively studied oxide as a pigment and in sunscreens, paints, ointments and toothpaste and as a photocatalytic material for self cleaning coatings. Environmental purifiers, antifogging mirrors and in many other applications. Semiconductor nano crystals have been widely studied for their fundamental properties especially titanium dioxide (TiO_2). Nano sized titanium dioxide materials have been the focus of great interest because they exhibit modified physical-chemical properties in comparison with its bulk. Inexpensiveness, excellent chemical stability, non toxicity, high photo-catalytic property, a wide band gap and high refractive index of TiO_2 make it attractive for practical applications [1]. The use and performance for a given application are strongly influenced by the crystalline structure, the morphology and the size of the particles. The use of TiO_2 nano particles is in great demand because of its properties and application in various fields such as photocatalysis , solar energy conversion and electronic

devices. The photocatalytic performance of TiO_2 based devices is largely influenced by the particle size, apparently at the nanometer scale. Following the literature the photocatalytic activity of TiO_2 has been improved by optimizing the nanostructure size using various synthetic methods such as sol-gel, hydrothermal, solvothermal, co-precipitation etc. Furthermore, doping with alkali metals, transition metal ions or rare earth metal ions (lanthanides) or non metal ions has been considered as a promising way for improving the photocatalytic efficiency of nano sized TiO_2.

The optical and electronic properties of nano structured TiO_2 can be tailored by a variety measures including thermal treatments, supported film growth, and metal-ion doping [2]. In particular, doping with lanthanide metal ions has been shown to increase the photocatalytic efficiency for selected reaction. It is critical to assess the effects of lanthanide-ion doping on the structure of titania which will allow greater control over the desired properties. Doping of TiO_2 with neodymium ion would introduce a distortion in TiO_2 lattice [3]. The interstitial neodymium does not affect the charge balance in the anatase lattice, as a substitutional neodymium does.

Sol-gel process is one of the most successful techniques for preparing nanocrystalline metallic oxide materials due to low cost and easy for fabrication. Generally in a typical sol-gel process a colloidal suspension or a sol is formed due to the hydrolysis and polymerization reaction of the precursors, which on complete polymerization and less of solvent leads to the transition from the liquid sol into a solid gel phase, the wet gel can be converted into nano crystals with further drying and hydrothermal treatments. In this paper, we report synthesis and characterization of Nd^{3+} doped TiO_2 nanoparticles obtained by sol-gel method. The prepared samples were characterized by X-ray diffraction (XRD), High resolution scanning electron microscope (HRSEM), the energy dispersive (EDAX) studies, ultraviolet - visible spectroscopy (UV-Vis) and photoluminescence (PL) studies.

2. Experimental Details

Pure titanium dioxide nanocrystals were prepared using the sol-gel method. Titanium isopropoxide (TIP) was used as the precursor for titania sol preparation. The sol corresponds to the overall volume ratio of Ti $[OCH(CH_3)_2]_4$: C_3H_8O: CH_3COOH: Distilled H_2O = 5:30:4.4:30. Ti $[OCH(CH_3)_2]_4$ was first dissolved in isopropanol and distilled water to form titania sol and then stirred for 1h at room temperature. The pH of sol was adjusted to 2-3 by adding 1-2 drops of ammonia with stirring in room temperature for 12h. The prepared sol was left to stand for the formation of gel and dried at 100°C for an hour in a furnace to remove the solvents. The obtained gel was milled into powder and calcined at 400°C for 4h to keep anatase phase. The neodymium (Nd^{3+}) doped TiO_2 was synthesized using the same procedure as the reference sample. The doping rate with $Nd^{3+}$is equal to 0.5% wt. The prepared sample was characterized by X-ray diffraction [XRD] measurements which were carried out at room temperature by using Siemens X-ray diffraction D500 with CuKα. Scanning electron micrograph images were taken with a JEOL (JSM-840 A), High resolution scanning electron microscope (HRSEM) equipped with an EDAX spectrometer. The absorption spectrum of the sample was measured on a UV-3101 Shimadzu visible spectrometer. Photoluminescence (PL) study was carried out on a Perkin-Elmer LS-55 luminescence spectrometer using a Xe-lamp at room temperature.

3. Results and Discussion

3.1. XRD analysis

The crystalline phase of undoped and doped TiO_2 nanoparticles was analyzed by X-ray diffraction [XRD]. Figure 1a and 1b shows the powder XRD pattern of as-prepared pure and Nd^{3+} doped TiO_2 nano particles. The presence of sharp diffraction peaks in the XRD confirm that products are highly crystalline and the crystalline size was calculated by the Debye Scherrer formula $D = 0.89\lambda/\beta \cos\theta$, where D is the crystalline size, λ is the wavelength of X-ray radiation (0.154 nm), 'β' is the full width half maximum and θ is the diffraction angle [4,5]. It was found that the

average crystalline size of pure and Nd^{3+} doped TiO_2 surface were 18 and 20 nm respectively.

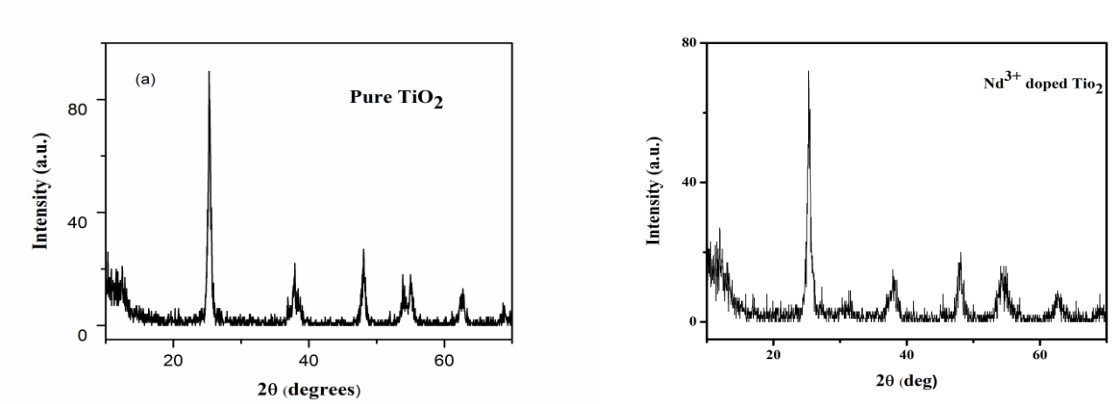

Figure 1. Powder X-ray diffraction analysis of (a) Pure TiO_2 nanoparticles (b) Nd^{3+} doped TiO_2 nanoparticles.

3.2. UV-Vis Absorption spectroscopy

Optical properties were observed by UV–Vis spectroscopy. Figure 2a and 2b demonstrates the optical absorption spectra of undoped and Nd^{3+} doped TiO_2 nano particles. The absorption edge of TiO_2 nano particles at 374 nm moved to a longer wavelength after doping with Nd^{3+} (0.5%) showing the absorption edge at 386 nm. After doping with Nd^{3+} the response of TiO_2 nanoparticles to visible light was increased and showed blue shift (towards increased wavelength). The blue shift of the absorption curve results in a reduction of the band gap energy. The band gap energy of the materials were calculated using the formula, $E_g = h\frac{C}{\lambda} \times 6.2415 \times 10^{18}$ eV. Where, h is Planks constant (6.626 × 10−34J s), C is Speed of light (3.0×10^8m/s) and λ is Cut-off wavelength and its value is 372×10^{-9}m. The calculated band gap energy of pure TiO_2 is 3.3eV and the Nd^{3+} doped TiO_2 is 3.02 eV. The optical band gap energy decrease with the Nd^{3+} doped TiO_2 nanoparticles.

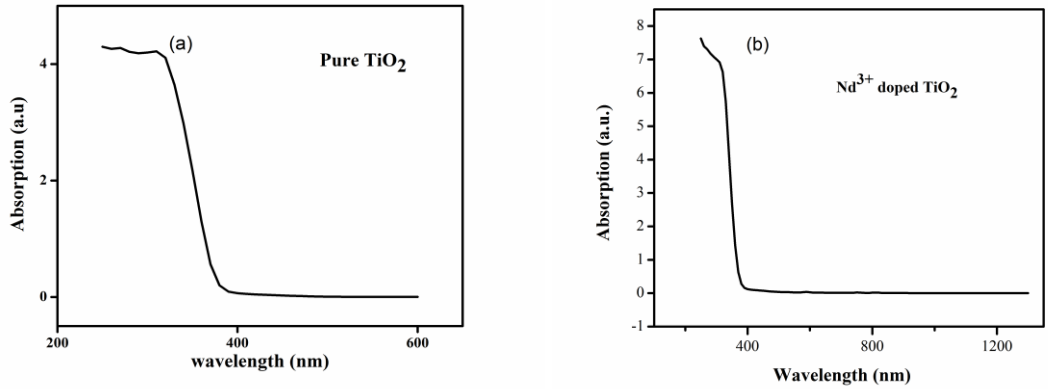

Figure 2 UV-Vis absorption spectra of (a) Pure TiO_2 nanoparticles (b) Nd^{3+} doped TiO_2 nanoparticles.

3.3. Photoluminescence spectroscopy

Photoluminescence spectroscopy (PL) is a practical method for probing the electronic structure of nano materials [6], the PL emission spectra of the TiO_2 and Nd^{3+} doped TiO_2 excited at a wavelength of 285 nm at room temperature is shown in figure 3. The TiO_2 nano particles showed the emission peak in a range of 350-400 nm and another one in range of 400-430 nm, there after doping with Nd^{3+} one peak at 350-390 nm and another one in the range of 420-430 nm corresponds to the radioactive transition of the excited electron from fermi level. The PL intensities of Nd^{3+} doped TiO_2 (0.5%) were

lower in comparison to those of the TiO_2 nanoparticles because the neodymium cause some changes in the electronic structure of the doped TiO_2 nanoparticles. The PL emission is directly related to the recombination of excited electrons and holes, so the lower PL intensity indicates a delay in recombination rate.

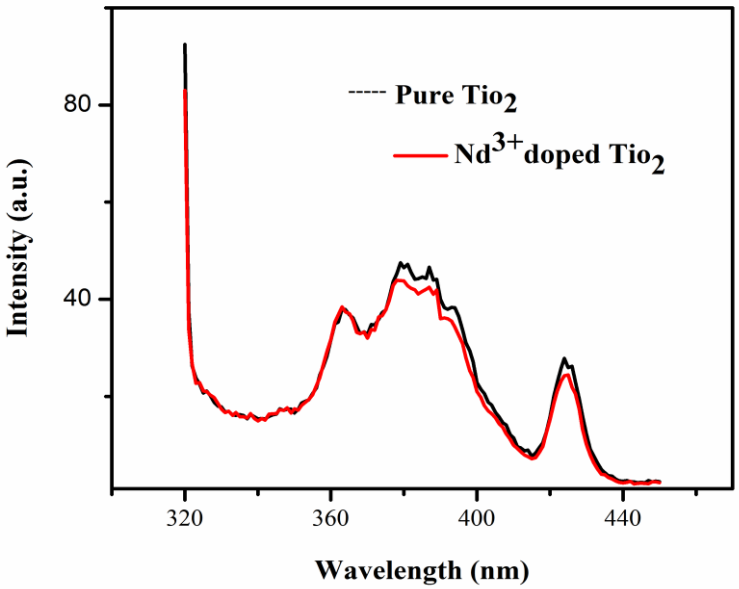

Figure 3. Photoluminescence spectra of (a) Pure TiO_2 nanoparticles (b) Nd^{3+} doped TiO_2 nanoparticles.

3.4. High Resolution Scanning Electron Microscopy (HRSEM)

High resolution scanning electron microscope (HRSEM) was used to examine the surface morphology of prepared samples. Figure 4a and 4b shows HRSEM im ages of the undoped and Nd^{3+} doped TiO_2. The HRSEM investigation of the synthesized samples reveals that the crystallites are of nanometer size and all samples show uniform morphology in the form of TiO_2 nano clusters.

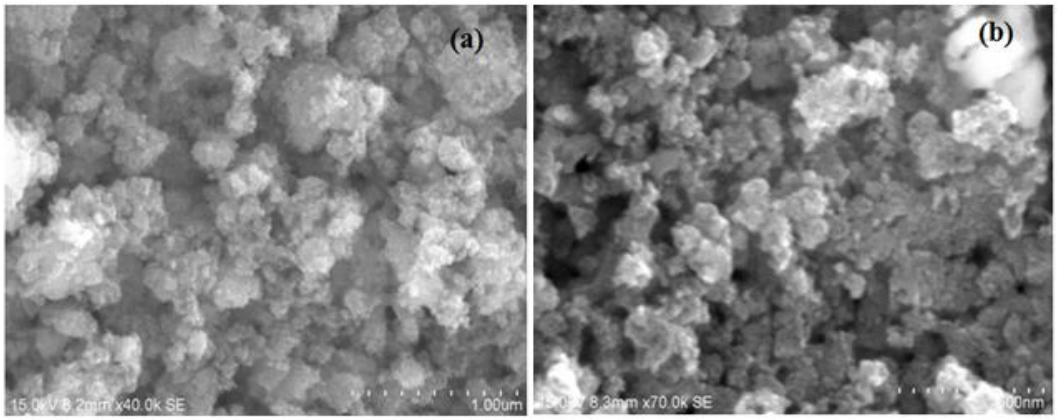

Figure 4. HRSEM image of (a) Pure Tio_2 nanoparticles (b) Nd^{3+} doped Tio_2 nanoparticles.

3.5. Energy Dispersive X-Ray (EDAX) analysis

To identify the type of elements present in the sample, Energy dispersive X-ray spectroscopy (EDAX) was used. The EDAX spectra of the undoped and Nd^{3+} doped TiO_2 nano particles were recorded and they are shown in figure 5a and 5b. From the results, it is confirmed that Ti, O and Nd^{3+} ions are present in the sample, the presence of Nd^{3+} is confirmed which indicates the doping has entered into the sample.

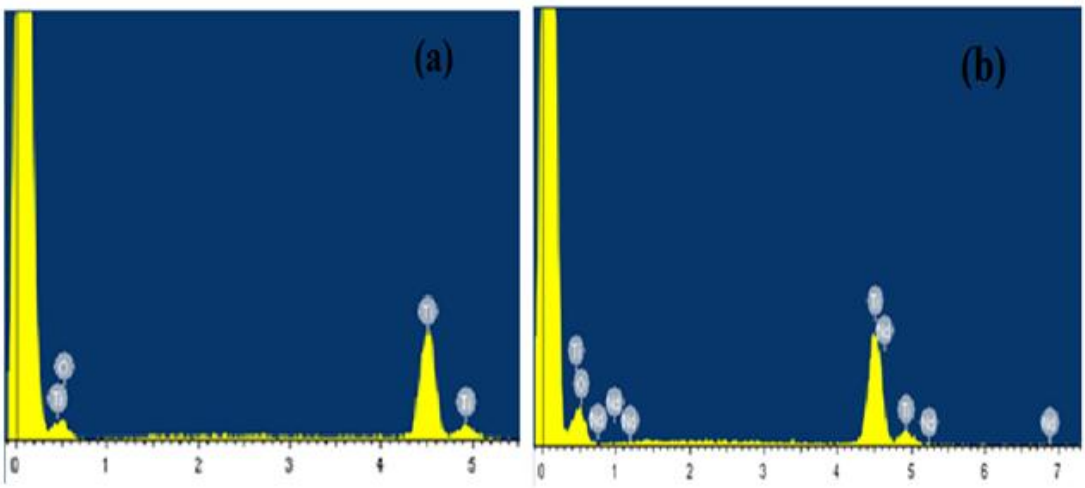

Figure 5. EDAX spectra: (a) Pure Tio_2 nanoparticles. (b) Nd^{3+} doped Tio_2 nanoparticles.

4. Conclusion

The pure and Nd^{3+} doped TiO_2 nanoparticles were synthesized by sol-gel technique. The powder X-ray diffraction analysis confirmed the crystalline phase of the synthesized TiO_2 nanoparticles. From the optical absorption spectra, a blue shift has been observed as compared to the bulk excitonic peak, which clearly shows the effect of quantum confinement and the presence of strong PL intensity which is due to both high crystalline and good surface states of the synthesized nanoparticles. The HRSEM and EDAX studies confirmed the morphological features of the nanoparticles and the composition of the undoped and Nd^{3+} doped TiO_2 nanoparticles.

References

[1] Xue-wei W U, Dajian W U and Xiao L I U, 2009 silver- doping induced lattice distortion in Tio_2 nanoparticles *Chinese Physics. Letters.***26** 7

[2] Li W, Wang Y, Lin H, Shah S I, Huang C P, Doren D J, Rykov S A, Chen J G and Barteau M A, 2003 Band gap tailoring of Nd^3-doped TiO_2 nanoparticles *Appl Phys Lett*. **83** 4143-4145

[3] Xu J, Ao Y, Fu D and Yuan C, 2008 A simple route forth preparation of Eu, N-codoped Tio_2 nanoparticles with enhanced visible light- induced photo catalytic activity *Journal of Colloid and Interfacial Science*. **328** 447–451

[4] Chi C, Choi J, Jeong Y, Lee O Y and Oh H J 2011 Nitrogen and europium doped TiO_2 anodized films with application sin photo- catalysis *Thin Solid Films.* **519** 4676–4680

[5] Ramya S, George R P, Subba Rao R.V, Dayal R K 2010 Effect of biofouling on anodized and sol–gel treated titanium surfaces: a comparative study *Biofouling.* **26** 883–891

[6] Hu S, Wang A, Li X, Wang Y and Lowe H, 2010 Hydrothermal Synthesis of Ionic Liquid [Bmim]OH-Modified TiO2 Nanoparticles with Enhanced Photocatalytic Activity under Visible Light, *Chem. Asian J.* **5** 1171–1177

Vibrational and Homo-Lumo Analysis of L - Asparginium Tartrate by Density Functional Theory

Vibrational and Homo-Lumo Analysis of L - Asparginium Tartrate by Density Functional Theory

E Kavitha[1], A Shiny Febena[2], R Subaranjani[2] and J Madhavan[2*]

[1]Department of Physics, Dr. M. G. R University, Chennai – 95

[2]Department of Physics, Loyola College, Chennai – 34

[*]**Corresponding Author: jmadhavang@yahoo.com**

Abstract. L - Asparginium Tartrate (LAsT), a semi organic nonlinear optical material was synthesized by slow solvent evaporation technique. Fourier transform infrared (FT-IR) spectroscopic studies were performed for identifying different functional groups present in the compound and was compared with the theoretical data obtained from DFT studies. Non-linear optical (NLO) behavior of the LAsT was investigated by the determination of the dipole moment μ and the hyper polarizability β obtained by B3LYP/6-31G (d, p) method. The calculated highest occupied molecular orbital (HOMO) and lowest unoccupied molecular orbital (LUMO) with frontier orbital gap were presented.

1. INTRODUCTION

Nonlinear optical (NLO) crystals with high conversion efficiencies for second harmonic generation (SHG) and transparent in visible and ultraviolet ranges are required for numerous device applications. In the last few years, much progress has been made in the development of nonlinear optical (NLO) organic materials for second harmonic generation (SHG). However, most of the or Nonlinear optical (NLO) crystals with high conversion efficiencies for second harmonic generation (SHG) and transparent in visible and ultraviolet ranges are required for numerous device applications. In the last few years, much progress has been made in the development of nonlinear optical (NLO) organic materials for second harmonic generation (SHG). However, most of the organic NLO crystals are constituted by weak van der Waals and hydrogen bonds with conjugated π electrons [1]. In this respect, amino acids are interesting materials for NLO applications [2-3]. To the best of our knowledge, no density functional theory DFT wavenumber and structural parameters calculations of LAsT has been reported so far. The present work deals with the growth and characterization along with the detailed vibrational spectral investigation of LAsT.

2. EXPERIMENTAL PROCEDURE

L-Asparagine–L-tartaric acid (LAsT) was synthesized by dissolving one mole of L- Asparagine (Merck 99%) in double distilled water containing one mole of L-tartaric acid. The reaction is as follows

$$C_4H_8N_2O_3 + C_4H_6O_6 \longrightarrow C_8H_{14}N_2O_9$$

The synthesized salt was further purified by repeating the crystallization process at least thrice. The solubility of LAsT in deionized water (solvent) was determined by adding a solute in solvent till it is completely dissolved. The temperature dependence of solubility of LAsT is shown in Figure 1. Figure 2 shows the photograph of as grown crystal of LAsT.

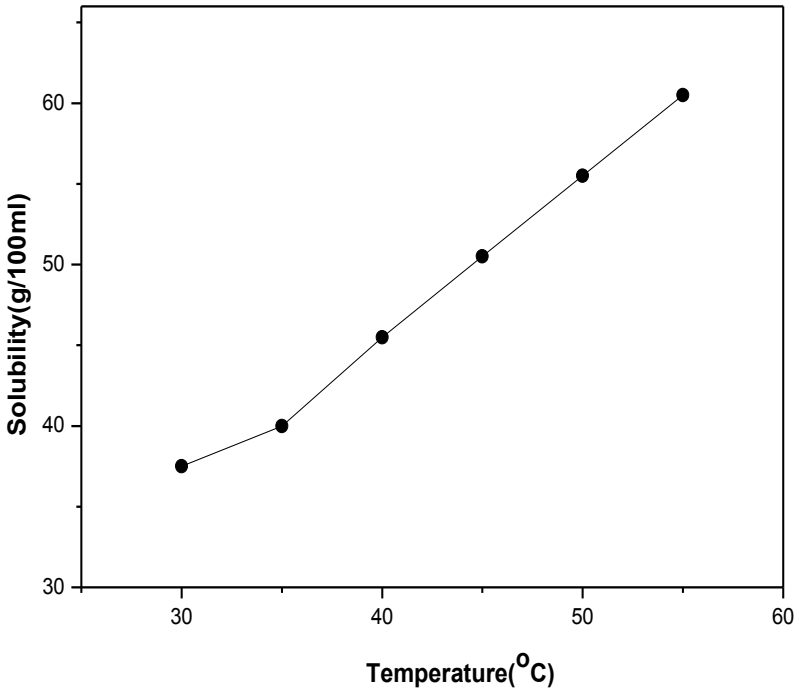

Figure 1.The solubility curve of LAsT crystal

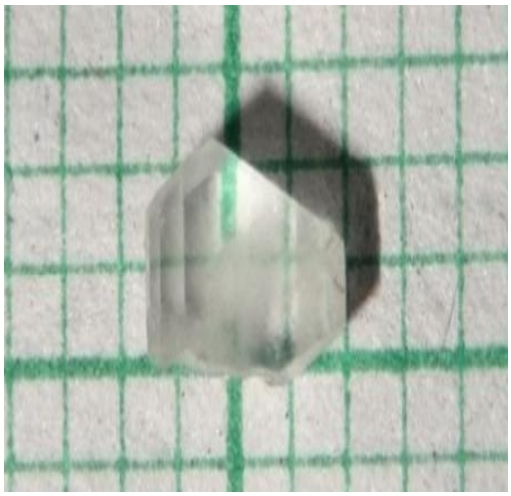

Figure 2.The grown LAsT crystal

3. RESULTS AND DISCUSSION

3.1 X-ray diffraction analysis

The selected well shaped, transparent, single crystal of LAsT was mounted on a BRUKER NONIUS CAD4/MAC4 X-ray diffractometer. Reflection data were measured at 20˚C using graphite monochromated Mo-Kα radiation and a ω-2θ scan mode. The structure was solved by direct methods and refined by full-matrix least-squares method using the SHELXS-97 software package [4]. From the single crystal analysis, it was observed that the crystal belongs to monoclinic crystal system having non-centrosymmetry with $P2_1$ space group. A summary of the key crystallographic information is given in Table 1.

Table 1. Crystal parameters of LAsT single crystal

Crystal data	
Emprical formula	$C_8H_{14}N_2O_9$
Crystal System	Monoclinic
Space Group	$P2_1$
a(Å)	5.086 Å
b(Å)	9.672 Å
c(Å)	11.834 Å
β(°)	95.31°

3.2 COMPUTATIONAL DETAILS

Quantum chemical density functional theory calculations were carried out with the 2003 version of the Gaussian program package using B3LYP functions [5] combined with the 6-31+G(d, p) basis set. The optimized geometrical parameters, fundamental vibrational frequencies, IR intensity, the atomic small charges, dipole moment, reduced mass and force constant were calculated.

VIBRATIONAL ASSIGNMENTS

The title molecule LAsT has 33 atoms. It has 93 (3N – 6) normal vibrational modes. The 93 normal modes of LAsT are distributed amongst the symmetry species as

$$\Gamma_{vib} = 63\ A' \text{ (in-plane)} + 30\ A'' \text{ (out-of-plane)}.$$

3.3 FT-IR ANALYSIS

FT-IR spectrum of the grown crystal was recorded in the range 500 cm^{-1} to 4000 cm^{-1}, using KBr pellet technique on BRUKKER IFS FT-IR Spectrometer. The experimental IR spectrum is compared with the results of B3LYP/6-31+ G (d, p) calculation carried out for the title compound. The experimental FT-IR is shown in the Figure. 3.

C-H Vibrations

Presence of band in the region 2700–3000cm^{-1} is the characteristic region for the identification of C–H stretching vibrations [6]. In this region the bands are slightly affected by the nature of the substituent. The IR vibrations are around 2900cm^{-1}. The experimental C–H vibrations are in good agreement with theoretical vibrations. For LAsT molecule prominent numbers of CH symmetric vibrations are obtained at frequencies 3092, 2977 and 2960cm^{-1}.

NH_2 Vibrations

The NH_2 asymmetric stretching vibrations [7] give rise to a strong band in the region 3390±60cm^{-1} and the symmetric NH_2 stretching is observed as weak band in the region 3210±60cm^{-1}. In our title molecule the theoretically computed NH_2 asymmetric and symmetric stretching vibration by B3LYP/6-311(d,p) method is at 3369 and 3344 cm^{-1}. But the recorded spectrum does not show any kind of peak in this region. In the present work, NH_2 symmetric stretching is assigned at 3320 cm^{-1} in IR region and also in 3280 cm^{-1}. The experimental values are well coincides with DFT values.

COO^- Vibration

Carboxyl group vibrations give rise to intense characteristic bands due to conjugation or formation of hydrogen bonds. These stretching and bending vibrations of acid group are generally expected in the region 1400–1200 cm^{-1} In the present work COO symmetric stretching is at 1420 cm^{-1} and 1553 cm^{-1} have asymmetric stretching in IR region.

O–H Vibrations

The O–H group gives rise to three vibrations (stretching, in-plane bending and out-of-plane bending vibrations). The O–H group vibrations are likely to be the most sensitive to the environment, so they show pronounced shifts in the spectra of the hydrogen bonded species. The hydroxyl stretching vibrations are generally observed in the region around 3500cm^{-1}[8] . In the title compound the O-H vibrations is present at 3450 cm^{-1} in IR region. The detailed vibrational assignments of LAsT for the experimental FT-IR along with the calculated frequencies for different basis sets are tabulated in Table 2.

Table 2. Vibrational Assignments of LAsT molecule

S.NO	FT-IR frequency		Vibrational Assignments
	Experimental	B3LYP	
1	3320	3327	υOH
2	3280	3308	υasym NH_3^+
3	1673	1678	βNH_2
4	1310	1307	βCH, υCC
5	1065	1048	γCO
6	690	689	Sym ring breath
7	510	510	φNCN

υ-stretching; **β**-bending; **δ**-in-planebending; **γ**-out-of-plane bending;

ω- wagging; φ-rocking;**τ**-torsion

3.4 Hyperpolarizability

The non-linear optical properties play an important role for the design of materials in modern communication technology, signal processing, optical switches and optical memory devices [9]. The non-linear optical properties of the organic molecules arise from delocalized π electrons that move along molecule. The increase of the conjugation on molecule leads to an increase in its nonlinear optical properties. One another way to increase non-linear optical properties is to add donor and acceptor groups. Acceptor group is opposite of donor group in the organic molecules containing donor and acceptor groups and π electron cloud moves from donor group to acceptor group. If the donor and acceptor groups are powerful, delocalization of π electron cloud on organic molecules increases and as a result of this the polarizability and first hyperpolarizability of organic molecules

increase [10]. First-order molecular hyperpolarizability is a third rank tensor that can be described by 3 × 3 × 3 matrix. The 27 components of the 3D matrix can be reduced to 10 components due to the Kleinman symmetry . The calculated polarizability α and first hyperpolarizability β of LAsT is 1.765808 x 10^{-30} esu that is greater than that of urea (0.37289×10^{-30} esu), respectively.

3.5 HOMO-LUMO energy gap

Both the highest occupied molecular orbital (HOMO) and the lowest unoccupied molecular orbital (LUMO) are the main orbital take part in chemical stability. The HOMO represents the ability to donate an electron, LUMO as an electron acceptor represents the ability to obtain an electron. The HOMO and LUMO energy calculated by B3LYP/6-31G (d,p) method as shown in figure 4.

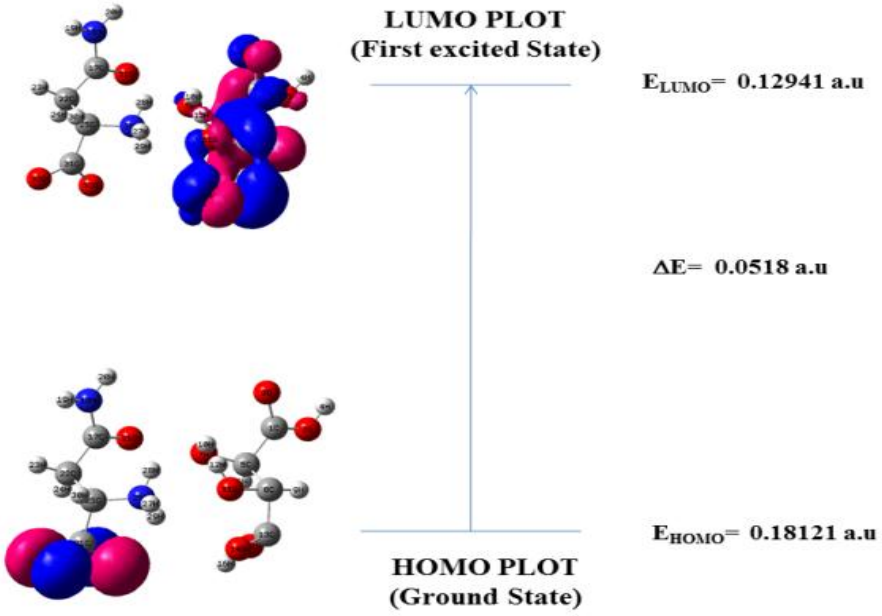

Figure 3. HOMO – LUMO plot of LAsT at B3LYP/6-31 G (d, p)

3.6 SHG efficiency studies

The second harmonic generation efficiency of the powdered material is measured using Kurtz and Perry method. A second harmonic signal of 161 mV is obtained for LAsT with reference to KDP (53 mV). Thus the SHG efficiency of LAsT is 3 times that of KDP.

Acknowledgment

The authors acknowledge University Grants Commission (UGC), India, for funding this research project-F.No.4-4/2015-16(MRP/UGC-SERO) - 2914.

4. CONCLUSION

Single Crystals of L-Asparagine–L-tartaric acid (LAsT) of dimension 5 x 3 x 8 mm^3 are conveniently grown by slow evaporation technique at room temperature. The XRD analysis proves that LAsT crystal belongs to monoclinic in structure with a non centrosymmetric space group $P2_1$. Fourier transform infrared (FT-IR) spectroscopic studies were performed for identifying different functional groups present in the compound. Non-linear optical (NLO) behavior of the LAsT was investigated by the determination of the dipole moment μ and the hyperpolarizability β obtained by B3LYP/6-31G (d, p) method. The calculated highest occupied molecular orbital (HOMO) and lowest unoccupied molecular orbital (LUMO) with frontier orbital gap were presented.

REFERENCES

[1] Xu D., Jiang M. and Tan Z. (1983), 'A new phase matchable nonlinear optical crystal L-arginine phosphate monohydrate', Acta Chem. Sinica, Vol. 41, pp. 570-573.
[2] Tapati Mallik and Tanusree Kar, (2005), 'Optical, thermal and structural characterization of an NLO crystal: L-arginine perchlorate', *Journal of Crystal Growth*, Vol. 274, pp.251-
[3] Tapati Mallik and Tanusree Kar, (2005) 'Growth and characterization of nonlinear optical L-arginine dihydrate single crystals', *J. Crystal growth*, Vol. 285, pp. 178-182.
[4] Kechen, Wu, Jaap, G, Snijders, & Chensheng, L 2002 'Theoretical studies of Nonlinear optical crystals in metal cluster compounds', *J. Phys. Chem B*, vol.106, pp.8954-8958.
[5] Becke, AD 1993 'Density functional thermochemistry. III. The role of exact exchange', *J. Chem. Phys*, vol. 98, pp. 5648–5652.
[6] Shanmugam, Sathyanarayana,1984 'Raman & polarized infrared spectra of pyridine-2- thione', *Spectrochimica Acta*, vol. 40A, no.8, pp. 757-761
[7] Roeges, NGP, 1994 '*A Guide to the Complete Interpretation of the Infrared Spectra of Organic Structures*', Wiley, NewYork
[8] Sajan, D, Hubert Joe,I, Jayakumar, VS, Zaleski, J 2006, 'Structural & electronic contributions to hyperpolarizability in methyl p-hydroxy benzoate' *J. Mol. Struct*.,vol. 785, pp. 43-53
[9] Thanthiriwatte K.S., Nalin de Silva K.M., Non-linear optical properties of novel fluorenyl derivatives—ab initio quantum chemical calculations *J. Mol. Struct*. (Theochem) 617 (2002)169–175.
[10]Gunasekaran, S, Balaji, RA, Kumeresan, S, Anand ,G, Srinivasan, S 2008 'Experimental & theoretical investigations of spectroscopic properties of N- acetyl-5- methoxytryptamine', Can. *J. Anal. Sci. Spectrosc* ,vol.53, pp.149-160

A Report on Growth And Spectroscopic Studies on The L-Tartaric Acid Doped Potassium Dihydrogen Phosphate Non-Linear Optical Single Crystals

IOP Conf. Series: Materials Science and Engineering **360** (2018) 012043 doi:10.1088/1757-899X/360/1/012043

A Report on Growth And Spectroscopic Studies on The L-Tartaric Acid Doped Potassium Dihydrogen Phosphate Non-Linear Optical Single Crystals

S Arulmani[1], P Sanjay[1], E Chinnasamy[1], K Deepa[2], J Madhavan[2] and S Senthil[1]

[1]Department of Physics, Government Arts College for Men (Autonomous), Nandanam, Chennai - 600035

[2]Department of Physics, Loyola College, Chennai -600034

Email: ssatoms@yahoo.co.in

Abstract. In recent years study of non-linear optical (NLO) materials is gaining rapid momentum due to their needs in several device applications. Potassium Dihydrogen Phosphate (KDP) is a well-known NLO material, whose non-linearity is enhanced by doping with amino acids. In this present study, single crystal ofL- Tartaric acid doped potassium Dihydrogen phosphate (LTKDP) have been grown by slow evaporation method at room temperature. Good quality transparent crystals were obtained with 27-30 days. The crystallinity and cell parameters were characterized by X-ray diffraction analysis (XRD), the shifts in frequency assignments of various functional groups of KDP due to the addition of L-Tartaric acid was analysed by Fourier transform infrared (FTIR) and Fourier transform Raman spectroscopic studies. The dielectric constant and the dielectric loss of the single crystals were studied as a function of frequency. Kurtz- Perry power technique was employed to determine the Second Harmonic Generation (SHG) efficiency of LTKDP single crystal.

1. INTRODUCTION

The rapid development in the field of science and technology necessitates searching for newer and efficient non–linear optical materials. Potassium dihydrogen phosphate (KDP) crystals have created interest because of its Piezo-electric, electro-optic, non-linear optical properties and its extensive application in x-ray monochromators [1, 2].The electro-optic effect in KDP is used to obtain phase and amplitude modulations[3]. KDP crystal based world's largest laser to generate UV beams has been demonstrated [4]. In order to get good quality crystals, many techniques have been introduced by several workers. The modern world is witnessing revolutionary advancements in the various aspects of science and technology. Organic non-linear materials are attracting a great deal of attention as they have large optical susceptibilities inherent ultra-fast response times and high optical thresholds for laser power as compared with inorganic materials [5]. A number of such materials have been reported in Literature for this potential application [6]. Among organic class of NLO materials, amino acids exhibits some specific features such as molecular chirality weak vanderwaals hydrogen bonds, absence of strongly conjugated bonds wide transparency range in the visible and ultraviolet regions, amenability for synthesis multi-functional substitution, higher resistance to optical damage and manoeuvrability for device application etc [7,8]. Among amino acids molecular are usually linked

through the hydrogen bond. The aim of the present study is to investigate the effect of L-Tartaric acid in KDP crystal by slow evaporation method at room temperature. The doping of L-Tartaric acid into KDP was achieved by adding 0.4wt %, this solution was prepared in double distilled water, and the solution was stirred for 3-4 hours to achieve homogenization. The solution was filtered and sealed with porous lid and placed in a dust free atmosphere for slow evaporation. The optically good quality and transparent crystals were harvested in 27-30 days. The crystals were characterized using powder x-ray diffraction studies, Fourier transform infrared (FT-IR) and FT- RAMAN analysis, Second harmonic generation (SHG), Dielectric studies etc.

2. EXPREMENTALMETHODS

2.1. Crystal Growth

Single crystal of L-Tartaric acid doped KDP was grown by slow evaporation technique at room temperature. Higher grade KDP salt was dissolved in double distilled water and and 0.4% of L-Tartaric Acid was doped with KDP, the saturated solution of LTKDP was prepared in accordance with the solubility data. The solution was thoroughly stirred for homogenization and then filtered into a Borosil beaker using whatmann filter paper. The pH of the solution was noted. The saturated solution was closed with perforated cover and kept in a dust free atmosphere to allow slow evaporation of the solvent. Transparent and good quality LTKDP crystals were harvested. The photograph of as grown doped LTKDP crystal is shown in figure.1.

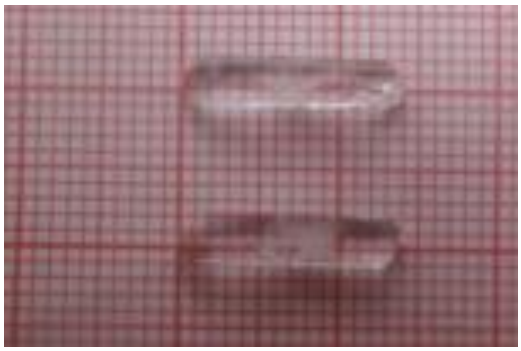

Figure 1. Photograph of as grown LTKDP crystal

3. RESULT AND DISCUSSION

3.1. Powder X-Ray Diffraction Studies (XRD)

The powder X-ray diffraction studies have been carried out to confirm the crystallinity and to determine the lattice parameter of the grown crystals. The powder x-ray diffraction (PXRD) analysis was carried out using XPERT–PRO Diffractometer with CuKα radiation of wavelength 1.5406 Å with the scanning rate 2degree per minute over the range of 10 - 70°. The PXRD studies for the grown crystal show the appearance of sharp and strong peaks which confirms the good crystallinity of the grown crystals, there are no other phases emerging besides the tetragonal system. The cell parameter value of the grown crystal is a = b = 7.433Å, **c** = 6.932Å with the angles $\alpha = \beta = \gamma = 90^{\circ}$ having space group 1.42 d and the calculated lattice parameter values are in agreement with the reported values. Powder x-ray diffraction pattern for LTKDP crystal is shown in figure (1).

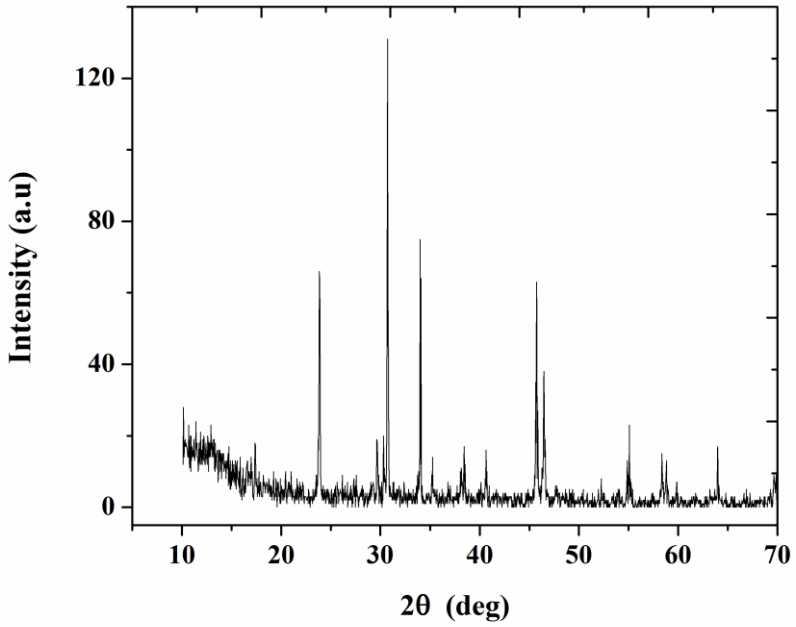

Figure 2. Powder XRD pattern of LTKDP

3.2.FT-IR and FT- RAMAN spectral analysis

FT-IR and FT-RAMAN studies are very useful techniques for qualitative analysis and identification of compounds. The recorded FT-IR and FT-RAMAN spectra of LTKDP are depicted in Figure 3 and Figure 4. The spectral bands are interpreted and compared with the standard spectra of the functional groups[9]. The bands which appear in the spectral region 450-4000 cm^{-1}arise from the internal vibration of LTA , and water molecules , the vibration of O-H and O=H types of hydrogen bonds. In the high frequency region of IR spectra, the sharp peaks observed at 536cm^{-1} are ascribed to PO_4 stretching vibration in the crystal. Their Raman equivalents are observed in the region of 514 cm^{-1}. In the IR spectra the peak will be observed at 3223 cm^{-1} are in O-H stretching hydrogen bonded of KDP. Their Raman equivalents are not observed due to insufficient detector sensitivity in the region above 3091 cm^{1}. An intensive IR bands assigned to the in -plane band vibration is observed at 1096 cm^{-1} with equivalent Raman band at 1295cm^{-1}. It is observed that some of the bands originate from both LT and KDP simultaneously. The IR bands at 2738 cm^{-1} is assigned to P-O-H asymmetric stretching vibration. In Raman it cannot be observed at this region. In IR bands the frequency of 2376cm^{-1} in the doped crystal corresponds to P-O=H stretching [10]. The broad absorption peak at 1694 cm^{-1} is due to O=P-OH bending vibration. The O-H deformation and P=O stretching will be observed in the frequency of 1297 cm^{-1}. In IR the absorption band at 912 cm^{-1} is due to P-O-H bending vibration in the doped LTKDP. In Raman the sharp peak will be observed at 1079 cm^{-1} are ascribed to P-O-H stretching molecule in the doped LTKDP crystal. In Raman spectra, the peaks will be observed at 681 cm^{-1} for O-H bending (out of plane). In the IR band 550 cm^{-1} and in Raman 514 cm^{-1} frequencies will be observed due to the P=O symmetric bending. The frequencies of 481 cm^{-1} in IR band and 402 cm^{-1} in Raman band.

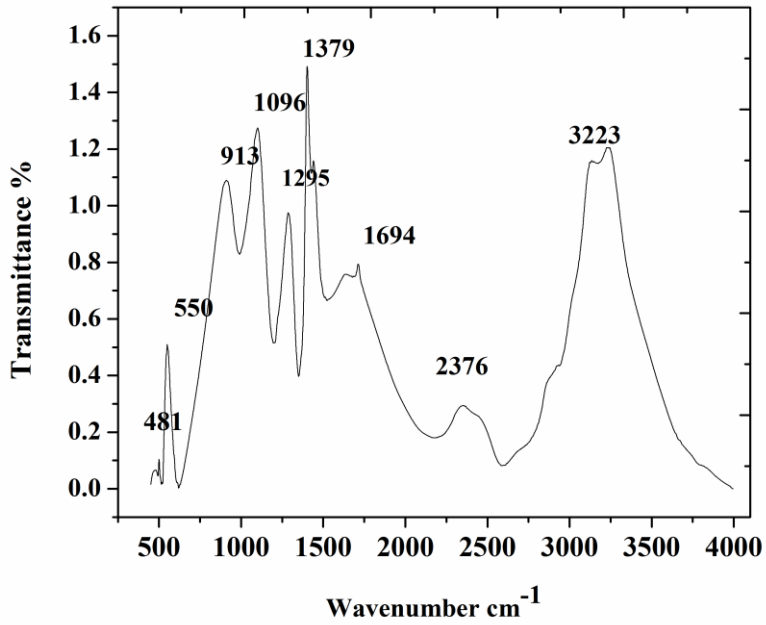

Figure 3.FT-IR Spectrum of LTKDP

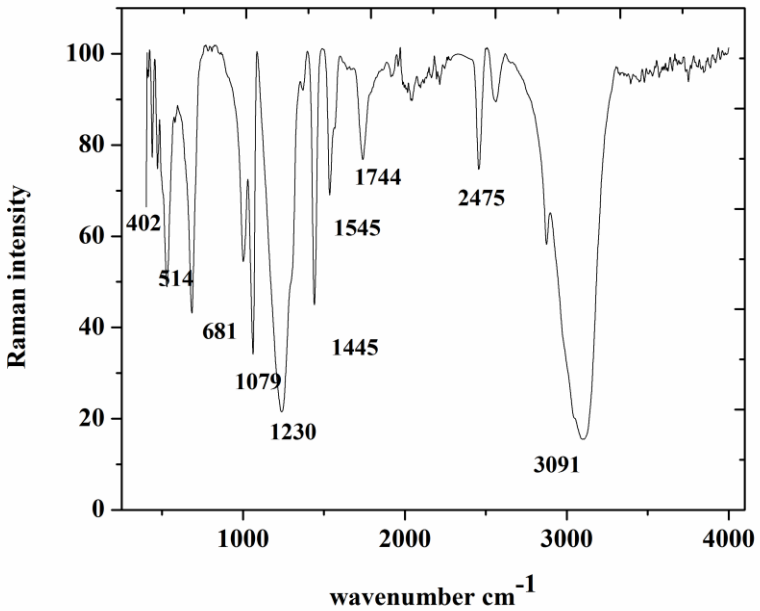

Figure 4.FT-Raman spectrum of LTKDP

3.3. Second Harmonic Generation efficiency studies

Kurtz and Perry second harmonic generation efficiency test (SHG) is performed for the comprehensive analysis of second order nonlinearity. Nonlinear optic measurements were carried out

by using Kurtz powder technique. A Q-switched Nd: YAG laser beam of 1064nm wavelength with 1.9 mj/ pulse input power, 8ns pulse width and repetition rate 10Hz was used to estimate SHG efficiency of the grown crystals. The grown crystals of LTKDP were grounded into a fine powder and then packed in a micro-capillary of uniform bore and exposed to laser radiation. The fundamental input radiation (1064nm) was separated or filtered by a monochromator and the output was measured. Second harmonic radiation generated by the randomly oriented micro- crystals was focused by a lens and detected by a photo multiplier tube. SHG was confirmed by the emission of green light. Using the pure potassium dihydrogen phosphate (KDP) crystalline powder as reference material, the output of SHG range was compared and found the SHG conversion efficiency of LTKDP is 1.09 times greater than that of reference KDP.

3.4. Dielectric Studies

Every material has a unique set of electrical characteristics that are dependent on its dielectric properties. The variation of dielectric constant of the sample with frequency is studied at room temperature using H10K1 3532 LCR HITESTER in the frequency range 300HZ to 3MHZ and is shown in figure 5. The high value of dielectric constant at high frequency may be due to the presence of all the four polarizations namely space charge, orientation, electronic and ionic. The dielectric characteristic of a crystal is determined by the dielectric constant. The dielectric constant determines the share of the electric stress which is absorbed by the material. It is the ratio between the permittivity of the medium and the permittivity of free space. If E_0 is the applied electric field, Ep is the electric field produced due to polarization of the material, then the dielectric, $\dot{\varepsilon} = \frac{E0}{E0-Ep}$. The dielectric constant ἐ has no units and it is a measure of the polarization in the dielectric material. Any small change in dielectric constant with respect to temperature can be attributed to the transition of the material. When the temperature raises, the orientation of the dipoles is increased and this increases the dielectric constant ἐ. Potassium dihydrogen phosphate (KH_2PO_4) has very good photorefractive performance and electro-optic properties due to its high dielectric constant. Figure 6 shows the variation of dielectric loss with frequency. The crystal possesses enhanced optical quality with lesser defects and this parameter play a vital role for the fabrication of nonlinear optical device because of low dielectric loss with high frequency for the samples.

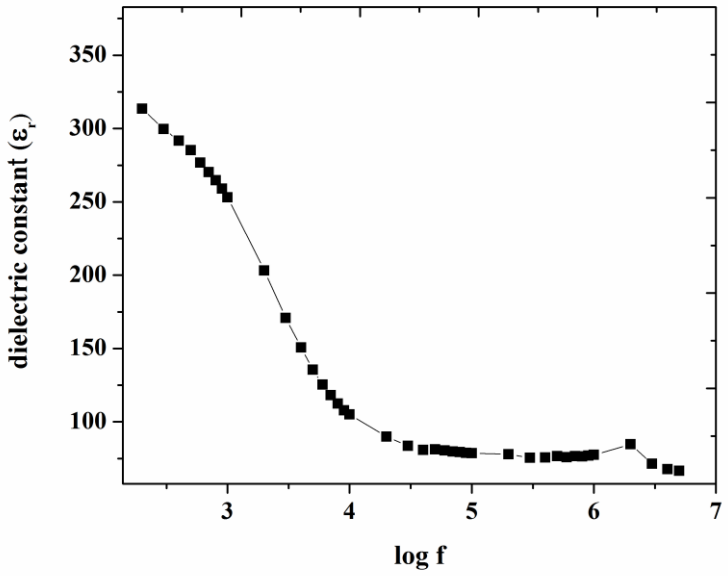

Figure 5. Variation of dielectric constant of LTKDP

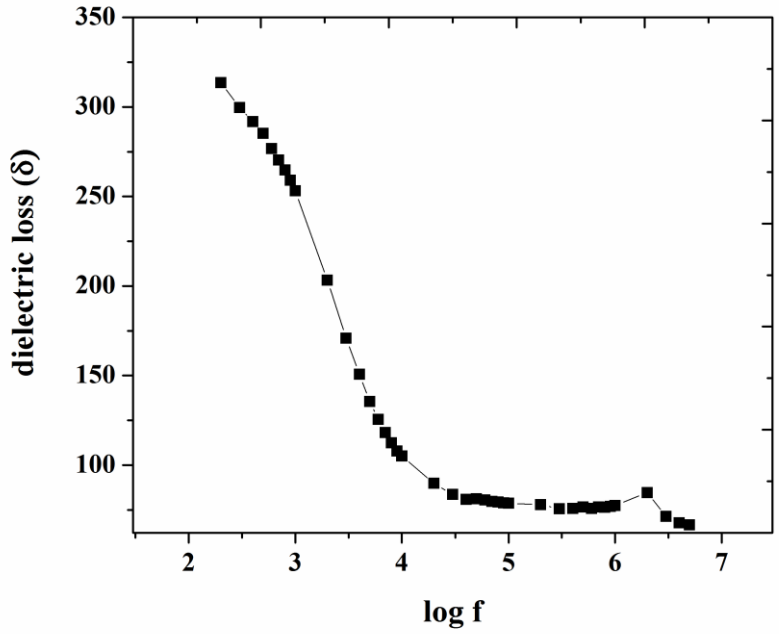

Figure6. Dielectric constant of LTKDP

4. Conclusions

High quality and transparent LTKDP single crystal has been grown by slow evaporation method at room temperature. Powder XRD studies shows that the grown crystals are tetragonal in structure. The transmission spectrum reveals that the crystal has sufficient transmission in the entire visible and IR region. The vibrational frequencies were assigned from FT-IR and FT-RAMAN spectral analysis which confirms the presence of functional groups. The SHG efficiency of the grown crystal was measured by Kurtz and Perry power method and its efficiency was found to be 1.09 times that of the pure KDP crystal. All the above results strongly attributes LTKDP is a novel material for non-linear optical applications.

Acknowledgment

The authors acknowledge University Grand Commission (UGC), India for funding this research project- F.No.4-4/2015-16 (MRP/UGC-SERO) – 2914.

References

[1] Dhumane N R, Hussaini S SDongre V G, Ghughare P, Shirsat M D, 2009Growth and characterization of glycine doped bis thiourea cadmium chloride single crystal Research *and Technology* **44**269–27

[2] Suresh Kumar B, .RajendraBabu K,2008 Effects of L-Arginine, L-Histidine and Glycine on the growth of KDP single crystal and their characterization *Indian Journal of Pure & Applied Physics, (IJRST)*.**46**123-12**6.**

[3] Parikh K D, Parekh B B, .Dave D J, Joshi M J, 2007 Thermal, FT-IR AND SHG efficiency studies of L-Argine doped KDP Crystals *Bulletin of Materials science* **30** 105-112

[4] Ferdousi Akhtar and Jiban Podder, 2011A Study on Structural, Optical, Electrical and Etching Characteristics of Pure and L-Alanine Doped Potassium Dihydrogen Phosphate Crystals *Journal of Crystallization Process and Technology*. **1** 55-62 .
[5] Jagadish P and Rajesh N P, 2011J.Effect of L-proline on the growth and NLO properties of KDP crystal*Journal Of Optoelectronics And Advanced Materials*. **13** 962.
[6] Muley G G, 2012 , Study on Growth Habit, SHG and Thermal properties of urea Phosphate Doped KDP Crystal *Journal of Science and Technology*.**2**109-113
[7] Dhumane N R, Hussaini S S, Dongre V G, Ghugare P, Shirsat M D 2009 Growth and Characterisation of L-Alanine doped Zinc Thiourea Chloride Single Crystal (ZTC) *Applied Physica A* **95** 727-732.
[8] Dave d J, Parikh K D, Parekh B B,JoshiM J, 2009Growth and spectroscopic, thermal, dielectric and SHG studies of L- threonine doped KDP crystals *Journal Of Optoelectronics And Advanced Materials*,**11**602 – 609.
[9] Dhanaraj P V, Rajesh N P, Mahadevan C K and G. Bhagavannarayana, 2009Growth and Characterization of Non Linear Optical Crystal: L-Alanine Doped KDP *Physica B.* **40** 404.
[10] KumeresanP, MoorthyBabu S, Anbarasan P M, *2008* Thermal, dielectric studies on pure and amino acid L-glutamic acid,L-histidine, L-valine doped KDP single crystals *Journal of. Crystal. Growth.***30** 1361–1368.

Crystal Structure, Vibrational Spectra and Theoretical Studies on Glycine Lithium Sulphate

Crystal Structure, Vibrational Spectra and Theoretical Studies on Glycine Lithium Sulphate

A Shiny Febena[2], A Chitra[1,2], R Subaranjani[2] and J Madhavan[2]*
[1]Department of Physics, S.I.V.E.T College,Gowrivakkam,Chennai-73,Tamilnadu,India

[2]Department of Physics, Loyola College, Chennai -34,Tamilnadu, India.

[*]**Corresponding Author: jmadhavang@yahoo.com**

Abstract. In this work we present structural and FT-IR studies on the nonlinear semi organic molecular crystal Glycine Lithium Sulphate (GLS). Vibrational spectral measurements were made for GLS. Optimized geometrical structure and harmonic vibrational frequencies were computed by DFT (B3LYP) method using 6-31++G (d, p) basis set. Complete assignments of the observed spectra were proposed. To investigate microscopic second order nonlinear optical behavior of the examined complex the electric dipole, the polarizability and the first order Hyper polarizability were computed.

1. INTRODUCTION

Recently several studies dealing with organic, inorganic and semi organic materials possessing nonlinear properties are being reported due to the increasing need for photonic applications [1]. In this work, the growth and characterization of Glycine Lithium Sulphate by slow evaporation method from aqua solution are reported. Also Literature survey shows that computation studies have not been done so far on the title compound. The aim of this study is to give a complete description of the molecular geometry and molecular vibrations of the GLS.

2. EXPERIMENTAL DETAILS

Glycine Lithium Sulphate crystal were synthesized by taking Analytical grade of Glycine and Lithium Sulphate in the molar ratio and dissolved in double distilled water.

$$C_2H_5NO_2 + Li_2(SO_4) \longrightarrow Li_2(SO_4)(C_2H_5NO_2)$$

Based on the solubility data as shown in Figure.1 supersaturated solution of GLS was prepared and stirred well for 3 hours. The beaker containing solution was kept in the constant temperature bath and tiny crystals of GLS were observed at the bottom of the beaker. The transparent tiny crystals were chosen as the seeds for growing bulk crystals. Crystals of size 10 x 11 x 12 mm^3 were harvested and is as shown in Figure.2. The grown sample was subjected to powder XRD analysis and its lattice parameters were calculated.

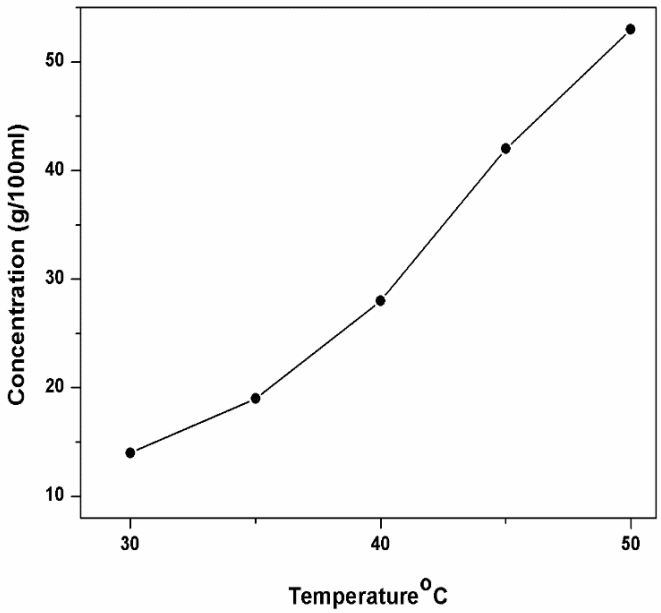

Figure 1.The solubility curve of GLS crystal

Figure 2.The grown GLS crystal

3. RESULTS AND DISCUSSION

3.1 X-ray diffraction analysis

From the powder x-ray diffraction analysis, it was observed that the crystal belongs to orthorhombic crystal system having non-centro symmetric with $Pna2_1$ space group. The crystal data are given in Table 1. The recorded powder XRD pattern is given in Figure 3.

3.2 Computational Details

All calculations are performed using Gaussian03 program package. Vibration frequencies are calculated using B3LYP/631(d,p) [2,3]. Vibration mode assignments were also compared with the

experimental results. The optimized geometrical parameters, fundamental vibrational frequencies, IR intensity, reduced mass, and force constant were calculated.

Table 1. Crystal parameters of GLS

Crystal Data	
Empirical formula	$C_2 H_5 Li_2 N O_6 S$
Crystal System	Orthorhombic
Space Group	$Pna2_1$
a(Å)	16.423
b(Å)	5.0050
c(Å)	7.654
β(°)	629.1

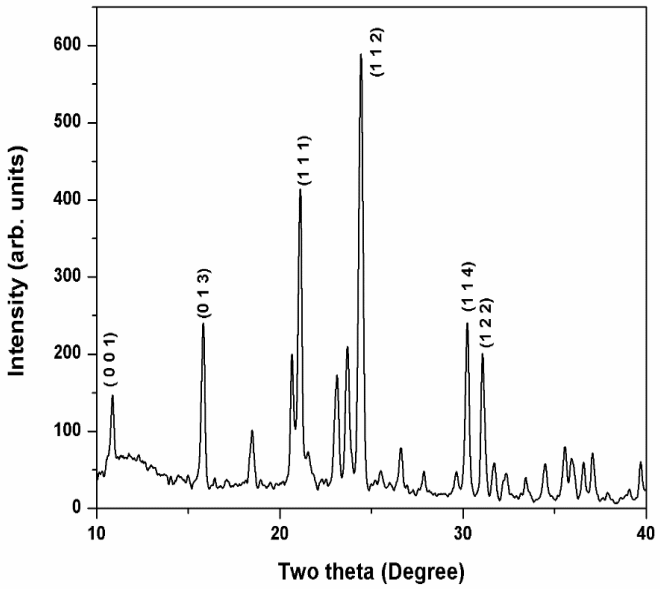

Figure 3. Powder XRD spectrum of GLS crystal

3.3 Molecular Geometry

The atomic numbering scheme for GLS is shown in Figure 4.. The most optimized geometric parameters (bond length and bond angles) were calculated and were depicted in Table 2. From the theoretical values, the most optimized bond lengths are slightly shorter as well as longer than the experimental values. Many researchers explained the changes in bond length of the C-H bond on substitution due to a change in the charge distribution on the carbon atom of the benzene ring [5]. The experimental values of C_4-H_5 bond length is longer than the theoretical values. A notable difference among the methods occurs in the computed N_7-H_9, H_{10}-Li_{11}, N_7-Li_{11} and O_{15}-O_{17}bond lengths. The DFT gives bond angle O_2-C_1-O_3 = 120°, H_8-N_7-H_9=109.47 and N_7-O_{12}-Li_{11}=135.2 whereas the

corresponding XRD values are 124.267,108.58 and 134.645 respectively. The comparison of Table 2. reveals the DFT calculation describes the geometry of the crystal with good quality.

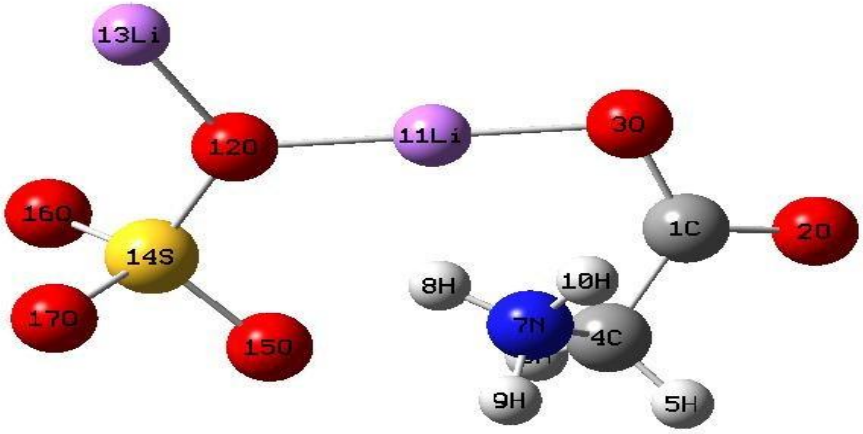

Figure 4. Atomic numbering system adapted for *ab* initio computations of GLS molecule

Table 2. Selected bond lengths and bond angles of GLS molecule

S.No	Molecule	Bond length (Å)	Molecule	Bond angles (°)
1	**C_1-O_2**	1.430000	O_2-C_1-O_3	120
2.	**O_2-O_3**	2.476833	C_1-C_4-H_6	109.4712
3.	**O_3-Li_{11}**	1.89	H_9-N_7-O_{12}	118.5122
4.	**C_4-H_5**	1.07	H_8-N_7-H_9	109.4712
5.	**H_5-N_7**	2.086720	O_3-C_1-C_4	120

3.4 Vibrational Assignments

The Fourier Transform Infra Red spectra of GLS was recorded on IFS 66V FT-IR SPECTROMETER using KBr pellet in the range 4000 cm^{-1} to 500 cm^{-1}. The observed FT-IR is shown in Figure 5. The GLS molecule has 17 moieties and is in stable conformation with C_1 symmetry then exhibits 45 normal modes of vibrations. The normal modes of GLS is distributed amongst the symmetry species as

$$\Gamma_{3N-6} = 31A' \text{ (in-plane)} + 14A'' \text{ (out-of-plane) respectively}$$

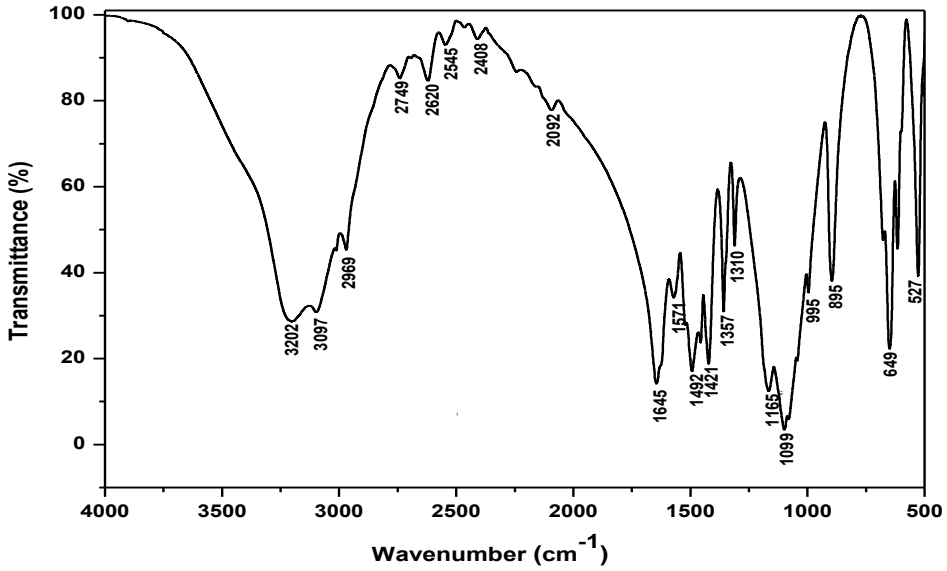

Figure 5. Experimental FT-IR Spectrum of GLS

Nitrogroup vibrations

Aromatic nitro compounds have strong absorptions due to asymmetric and symmetric vibrations of the nitro group at 1570-1485 cm^{-1} and 1370-1320 cm^{-1} [4,5]. The theoretical asymmetric stretching vibrations occur at 1503 cm^{-1} and the corresponding experimental peak at 1571 cm^{-1}.

C=O vibrations

The stretching vibration C=O is commonly expected in the region1690±30 cm^{-1}. The C=O in-plane deformation is expected in the region 645±55 cm^{-1}. The C=O out-of-plane deformation is in the range 540±80 cm^{-1}. The theoretical stretching vibration appears at 1679 cm^{-1} and the in-plane deformation at 653 cm^{-1}(theoretical) and 649 cm^{-1} (experimental).

C=N vibrations

According to Henry et al (2008), IR spectrum exhibits strong and broad bands due to C=N at 1635 cm^{-1}. In the present work the theoretical and experimental strong and broad bands due to C=N appears at 1626 cm^{-1} and 1645 cm^{-1} respectively.

The selected vibrational assignments of fundamental modes of GLS by DFT methods are reported in Table 3.

Table 3. Vibrational frequencies of GLS

No.	Wavenumber cm^{-1}		Spectroscopic assignment	Force constant	Reduced mass
	B3LYP	Expt.			
1.	457.3058	457	COO^- opd	1.7983	14.5946
2.	520.3388	527	COO^- d	1.8572	11.6421
3.	653.1643	649	COO^- roc ipd	1.7693	7.0388
4.	897.9603	895	CC st	2.4910	5.2433

5.	970.3730	995	CN st	0.9178	1.6543
6.	1050.167	1099	I Ph	2.1834	3.3602
7.	1183.694	1165	CH_2 roc	1.3022	1.5774
8.	1449.395	1492	COO^- symst	1.4858	1.2004
9.	1503.990	1571	NH_3^+ sym d	1.7639	1.3236
10.	1626.886	1645	NH_3^+ asy d	1.6559	1.0619

Symst-symmetric stretching, asyst-asymmetric stretching, st(ph)-stretching of phenyl, roc-rocking, opb-out of plane bending, opd-out of plane deformation, wag-wagging, ipd-in plane deformation, d-deformation

3.5 Hyperpolarizability

First hyperpolarizability is a third rank tensor that can be described by a 3x3x3 matrix. The 27 components of this 3D matrix can be reduced to 10 components due to Kleinman symmetry [6]. In the presence of applied electric field, the energy of a system is a function of electric field. The components of β are defined as the coefficients in the Taylor series expansion of the energy in the external electric field[7]. The first static hyperpolarizability (β_0) and its related properties have been calculated using B3LYP/6-31G level based on finite field approach. The calculated dipole moment(μ), polarizability(α) and first order hyperpolarizability values for GLS molecule are given in Table 4.

Table 4. Dipole moment, Polarizability and Hyperpolarzability

Dipole Moment in Debye		Polarizability in esu		Hyperpolarizability in esu	
μ_x	1.7681	α_{xx}	67.4945318	β_{xxx}	339.8812369
μ_y	4.2611	α_{xy}	0.9920316	β_{xxy}	68.9682643
μ_z	13.2300	α_{yy}	58.9864308	β_{xyy}	130.2321786
μ_{tot}	14.0113	α_{xz}	-4.5362599	β_{yyy}	268.4342981
		α_{yz}	6.6848818	β_{xxz}	-78.79471
		α_{zz}	85.163995	β_{xyz}	-16.2330359
		α_o	5.9043×10^{-31}	β_{yyz}	5.503936
				β_{xzz}	140.9210373
				β_{yzz}	151.7801336
				β_{zzz}	-114.5418743
				β_{tot}	$6.7368\ 10^{-30}$

3.6 Hyperpolarizability

First hyperpolarizability is a third rank tensor that can be described by a 3x3x3 matrix. The 27 components of this 3D matrix can be reduced to 10 components due to Kleinman symmetry [6]. In the

presence of applied electric field, the energy of a system is a function of electric field. The components of β are defined as the coefficients in the Taylor series expansion of the energy in the external electric field[7]. The first static hyperpolarizability (β_0) and its related properties have been calculated using B3LYP/6-31G level based on finite field approach. The calculated dipole moment(μ), polarizability(α) and first order hyperpolarizability values for GLS molecule are given in Table 4.

3.7 HOMO-LUMO energy gap

HOMO and LUMO analysis have been used to elucidate the information regarding charge transfer within the molecule. The intermolecular charge transfer from the donor to acceptor group through a single-double bond conjugated path can induce large variations of both the molecular dipole moment and the molecular polarizability. The HOMO and LUMO energy calculated by B3LYP/6-31G (d,p) method as shown in Figure 5.

HOMO energy (B3LYP) = -0.336 a.u.
LUMO energy (B3LYP) = -0.157 a.u.
HOMO–LUMO energy gap (B3LYP) = 0.179 a.u.

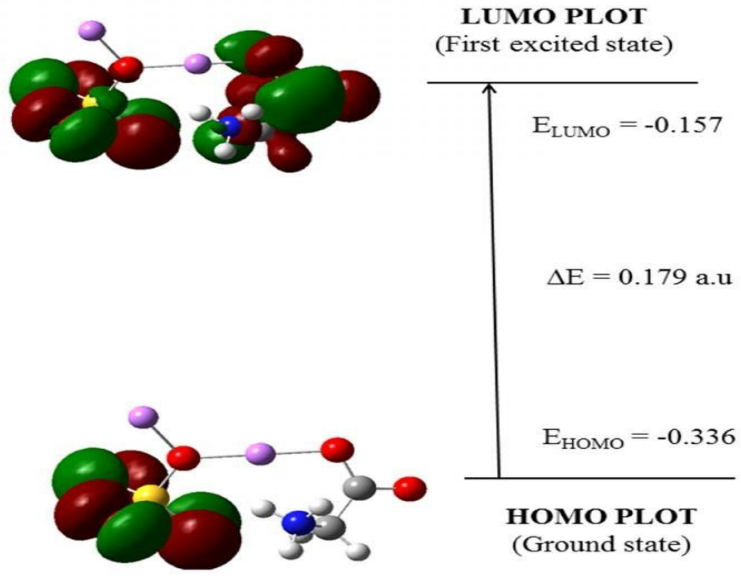

Figure 6. HOMO – LUMO plot of GLS at B3LYP/6-31 G (d, p)

4. CONCLUSION

Good optical quality bulk single crystal of GLS has been grown successfully by slow evaporation growth technique. The single crystal analysis shows that the crystal belongs to orthorhombic crystal system with $Pna2_1$ space group. DFT computations of GLS molecule calculated by DFT (B3LYP) level with 6-31G (d,p) basis set gives the optimized structure. Experimentally obtained bond lengths and bond angles are compared with theoretically calculated one. Theoretical and experimental IR spectroscopic analysis was carried out and the presence of functional groups in GLS molecule was qualitatively analyzed. Nonlinear optical NLO behaviour of the examined sample was investigated by the determination of the electric dipole moment μ, the polarizability α and the hyperpolarizability β using DFT method. HOMO-LUMO analysis reveals the molecular energy gap.

Acknowledgment
The authors acknowledge University Grants Commission (UGC), India, for funding this research project-F.No.4-4/2015-16(MRP/UGC-SERO) - 2914.

REFERENCES

[1] Sankar D, Vinay Raj Menon, Sagayaraj P and Madhavan *J.,Physica B*., 405 (2010) 192.
[2] Borisenko, C.W. Boch, I.J. Hargittai, *J. Phys. Chem*. 98 (1994) 1442
[3] Frisch M.J, Trucks G.W Pope J.A, Gaussian 03, Revision C.02,Gaussian Inc. Wallingford, CT, 2004
[4] N.Sundaragganesan,G.Elango.S.Sebastian&P.Subramani,*Indian Journal of Pure& Applied Physics*,Vol.47,2009,pp.481-490
[5] Vijayakumar T, I. Hubertjoe, C.P.R. Nair, V.S. Jayakumar, *Chem. Phys*. 343 (2008) 83.
[6] Wojtkowaik.B, Chabanel.M, Spectrochimie Molecular Technique Documentn.Paris(1977)265.
[7] Henry, Lagrenee, Abraham, Inorg. *Chem. Commun*, 4 (2008) 1071
[8] Kleinman A, *J. Phys.* Rev. 126 (1962) 1977.
[9] Anoop M R,Binil P S, Suma S, Sudarsanakumar M R, Sheena Mary Y, Hema Tresa Varghese, YohannanPanicker C, *J.Mole.Structure* 969 (2010) 48-54.

Crystal Growth and Characterization of a Novel Non Linear Optical Single Crystal of Urea Phthalic Acid

IOP Conf. Series: Materials Science and Engineering **360** (2018) 012032 doi:10.1088/1757-899X/360/1/012032

Crystal Growth and Characterization of a Novel Non Linear Optical Single Crystal of Urea Phthalic Acid

N Indumathi[1], P Sanjay[1], K Deepa[2], J Madhavan[2] and S Senthil[1]

[1] Department of physics, Government Arts College For Men (Autonomous), Nandanam, Chennai – 35, Tamil Nadu, India.
[2] Department of Physics, Loyola College, Chennai – 34, Tamil Nadu, India.
Email: ssatoms@yahoo.co.in

Abstract. The Nonlinear optical (NLO) material of Urea Phthalic acid (UPA) was grown by slow evaporation method. The unit cell parameters were determined by single crystal XRD. The fundamental frequency vibrations of UPA were identified by FTIR analysis. The optical properties of UPA were determined by UV-Vis spectral studies. The Laser damage threshold value of UPA single crystal was found to be 5.3 GW/Cm^2. Z-scan techniques with He–Ne laser has measured the optical nonlinearity of UPA crystal.

1. Introduction

Developments of novel nonlinear optical (NLO) materials and crystal design technique for assembling the materials are used for many device applications in the domain of opto-electronics and photonics [1]. In particular, Organic NLO crystals are attracting a great deal of attention due to their high NLO coefficient, high damage threshold, high thermal stability and mechanical strength. The crystal engineering technology of the nonlinear optical material is based on the anchorage of organic molecules exhibiting a large NLO efficiency on the amino acid groups [2]. The unique optoelectronic properties of organics are due to the formation of weak Vander waals and hydrogen bonds hence, it shows high degree of localization. Urea is one of such organic NLO materials which have been explored as a first for NLO device for second to fifth harmonic generation [3]. In addition to this, the potentiality of urea as a first organic parametric oscillator is having extended transparency in the UV region, large birefringence and high optical damage threshold. The significant efforts were being made by many researchers to explore the potentialities of urea mixed systems and its derivatives through molecular engineering procedure. Such attempts involve the doping of other organic and inorganic NLO materials with urea. Many such efforts have become successful [4,5].With this reported background, we have ventured into growth and characterization of Urea Phthalic acid (UPA) single crystal and it is expected that this would be a non-centrosymmetric complex, but to our surprise it has been formed as a centrosymmetric structure in which third order nonlinearity which is more favourable and prominent. Similar results of third order nonlinear optical properties have been reported earlier [6]. In the present paper, the synthesis, crystal growth and characterizations by Single

crystal XRD, FTIR, UV-Visible, LDT and Z-Scan of Urea Phthalic Acid (UPA) single crystal are reported in detail.

2. Experimental Details

The UPA crystal was synthesized by taking Urea and Phthalic acid in a 1:1 stiochiometric ratio in methanol and stirred separately for about half an hour using a magnetic stirrer. After that these solutions were mixed together and stirred well for about 1h and filtered. The filtered solution was allowed to dry at room temperature and the crystals were obtained by slow evaporation technique. The purity of the synthesized crystal was improved by successive recrystallization process thereby good optical quality colorless single crystals were obtained in 30 days which is shown in Figure 1.

Figure 1. Photograph of as grown UPA single crystal

3. Results and Discussion

3.1. XRD analysis

The single crystal X-ray diffraction analysis for the grown UPA crystal has been carried out to identify the cell parameters using an ENRAF NONIUS CAD4 automatic X-ray diffractometer. The UPA crystal retained its triclinic structure with lattice parameters of a=7.402 Å, b=7.654 Å, c=10.052 Å and α=85.92°, β=81.94°, γ=65.20° and the volume of the crystal V=511.9 $Å^3$ with Centro symmetric group P1. The lattice parameters are in good agreement with the reported values [7].

3.2. UV-Vis Absorption spectroscopy

The UV-Vis spectral analysis of UPA was carried out using Varian Cary 5E spectrophotometer in the wavelength range 200 to 900 nm. The resulting spectrum is shown in figure. 2. The cut off wavelength as observed from the spectrum for UPA is 258 nm. It is due to the direct transition of an electron from a non - bonding 'n' orbital to an anti bonding 'π*' orbital (n →π*). It is important that for efficient NLO crystal, lower cut-off wavelength should be in the range of 200 to 400 nm. The steep decrease in the absorption of the compound around 276 nm may be assigned to the electronic excitation in coo^- group. As there is no appreciable change in the transmittance in the entire visible region upto 900 nm, the material can be useful as optical windows in the spectral instruments in the wavelength studied. The material is found to be transparent to all radiation in the wavelength range of 300-900 nm. The wide optical transmission window is an encouraging optical property seen in UPA and is of vital importance for NLO materials.

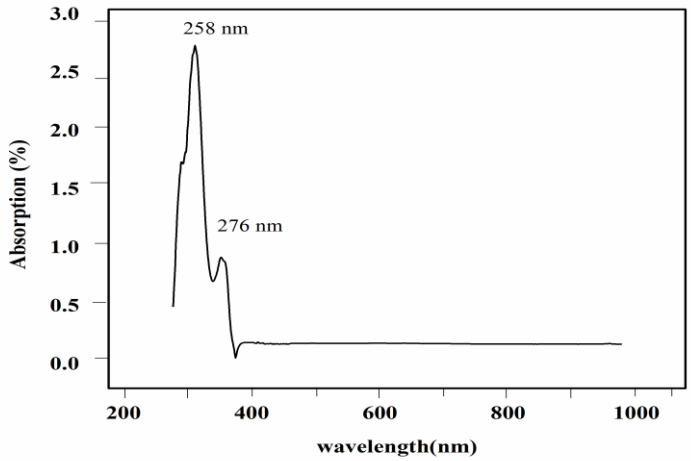

Figure 2. Absorption spectrum for UPA crystal

3.3. FT-IR analysis

The FTIR spectra of the grown UPA single crystal were observed on the powder sample is shown in Figure. 3. The spectrum of UPA crystal was recorded using the Brukers IFS66 spectrometer in the range 4000 – 400 cm^{-1} by KBr pellet to identify the functional group present in the crystal. In the high energy region the broad band in the range 3458 cm^{-1} is due to N-H stretching vibrations. The symmetric and asymmetric stretching vibrations of NH_2 are observed in range of 3233 cm^{-1} and 3337 cm^{-1} respectively. The absorption peaks at 3136 cm^{-1} and 1687 cm^{-1} are due to the symmetric and asymmetric stretching vibrations of C=O carboxylic group. The absorption peak at 1441 cm^{-1} is assigned for NH_2 bending which shows the presence of urea. The peaks observed at 1372 and 1014 cm^{-1} are corresponding to N-C-N stretching vibrations. The peak at 922 cm^{-1} is due to O-H out of plane bending vibration. All these observations clearly show the formation of the urea phthalic acid crystal.

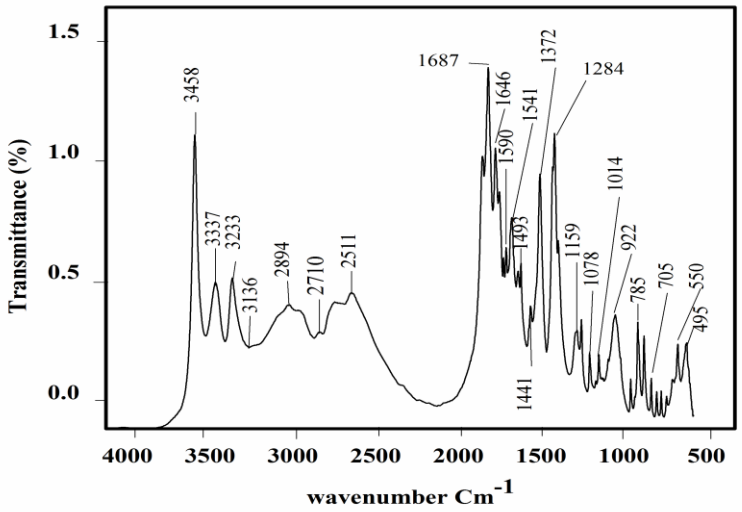

Figure 3. FT-IR vibrational spectrum of UPA crystal.

3.4. *Laser Damage Threshold Studies*

To measure laser-damage threshold for our UPA crystals, we used the laser with the pulse width 10 ns, the repetition rate 10 Hz and the fundamental wavelength 1064 nm. The laser beam with the diameter of 1 mm was focused on the sample. The sample was placed at the focus of a planoconvex lens (the focal length 30 cm). The energy of laser pulses was varied using attenuator that included a polarizer and a half-wave plate. The pulse energy of each laser shot was measured with a combination of a phototube and an oscilloscope. Finally, the surface damage threshold was calculated using the following relation for the power density (P_d), $P_d = E/\tau\pi r^2$. Here E is the input energy in mJ, τ the pulse width in ns and r the radius of the spot in mm. As a result, the laser damage threshold for the UPA crystals is found to be 5.3 GW/Cm^2, which is higher than that of Urea tartaric acid (4.6 GW/ Cm^2) [8].

3.5. Z-Scan analysis

The Z-scan method has gained rapid acceptance by the NLO community as a standard technique for determining the nonlinear changes in refractive index and nonlinear optical absorption. The nonlinear absorption and refractive index of UPA crystals were estimated using the single beam Z-scan method with laser beam intensity of 60mW and the wavelength of source used for the measurement was 632.8 nm. The study of nonlinear refraction by the Z-scan method depends on the position (Z) of the thin samples under the investigation along a focused Gaussian laser beam. The sample causes an additional focusing or defocusing, depending on whether nonlinear refraction is positive or negative. Such a scheme, referred to as an "Open aperture" Z-scan and it is suited for measuring nonlinear absorption in the UPA crystal. Results obtained from a typical closed aperture and open aperture of Z-scan study for the grown UPA crystals are represented by Figure. 4a and b. The nonlinear refractive index (n_2) of the crystal was calculated using the standard relations $\Delta Tp\text{-}v = 0.406(1- S)\ 0.25/\Delta\phi_o$. Where $S= 1- \exp(-ra^2/\omega a^2)$ is the aperture linear transmittance, $\Delta\phi_o$ is the on-axis phase shift. The on-axis phase shift is related to the third-order nonlinear refractive index by $|\Delta\phi_o| = kn_2L_{eff}\ I_o$ Where $k = 2\pi/\lambda$, $L_{eff} = [1-\exp(-\alpha L)]/\alpha$ is the effective thickness of the sample, α is the linear absorption coefficient, L the thickness of the sample, I_o is the on-axis irradiance at focus and n_2 is the third-order nonlinear refractive index. The calculated values of third order nonlinear refractive index (n_2) is 2.24 x 10^{-11} cm^2/w , nonlinear absorption coefficient (β) = 3.481 x 10^{-6} cm/w. the positive value of nonlinear refraction reveals the self-focusing nature and nonlinear absorption co-efficient (β) exhibits the two-photon absorption process. Real and imaginary value of third order susceptibility of UPA is 9.98 x 10^{-8} esu and 7.887 x 10^{-6} esu respectively. The third order susceptibility ($\chi^{(3)}$) is 7.88 x 10^{-6} esu and it is due to the π-electron cloud movement from the donor to acceptor which makes the molecule highly polarised.

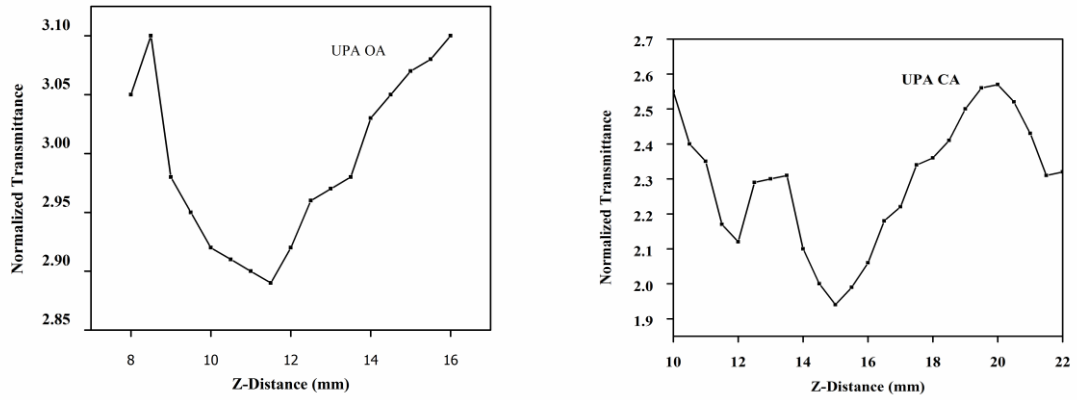

Figure 4. Z-scan spectrum of UPA (a) Open aperture (b) Closed aperture.

4. Conclusion

The novel single crystal of Urea Phthalic acid (UPA) was successfully grown from the methanol solvent by slow evaporation technique. The crystal structure has been confirmed and the lattice parameters have been calculated by single crystal X-ray diffraction studies. The absence of significant absorption in the entire visible region and lower cut-off wavelength indicates the suitability of UPA for optical applications. The vibration spectral analyses confirm the different functional groups in UPA. The laser damage threshold value for the grown crystal is 5.4 GW/cm^2. The third order nonlinear refractive index, absorption coefficient and optical susceptibility was calculated by the Z-scan techniques and it reveals that the UPA crystal possess self-focusing and two-photon absorption process.

Acknowledgments

The corresponding author gratefully acknowledges the support from the Department of Science and Technology (DST), Government of India for the research project (SB/EMEQ/248/2014).

References

[1] Fleck M, Petrosyan A M, 2010 Difficulties in the growth and characterization of nonlinear optical materials a case study of salts of amino acids *J. Cryst. Growth* .**312 (15),** 2284-2290
[2] Cyrac Peter A, Vimalan M, sagayaraj P, Madhavan J, 2010 Thermal, optical, mechanical, and electrical properties of a novel NLO active L-Phenylalanine phenylalaninium perchlorate single crystals *Physica B* **405,** 65-71
[3] Kato K, 1980 High efficiency, high power difference frequency generation at 2-4 μm in $LiNbO_3$ *J. Quant.Elect.* **16**, 810
[4] Chithambaram V, Jerome Das S, Arivudai Nambi R, Krishnan S, 2012 Synthesis growth and Characterization of nonlinear optical urea-ammonium chloride *Solid State Sci.* **14**, 216-218
[5] Selvarajan P, Glorium Arul Raj J, Perumal S, 2009 Characterization of Pure and urea doped γ-Glycine Single Crystals Grown by Solution Method *J. Cryst. Growth.* **311**, 15
[6] Shanthi A, Krishnan C, Selvarajan P, 2014, Growth and characterization of a single crystal of Urea adipic acid *Spectrochimica Acta A.* **122**, 521
[7] Videnova V, Adrabinska, 1996 The hydrogen bond as a design element in crystal engineering. Two- and three-dimensional building blocks of crystal architecture *J. Mol. Struct.* **374**, 199
[8] Vinothkumar P, Rajeswari K, Mohan Kumar R, Bhaskaran A, 2015 Structural, optical, thermal and mechanical properties of Urea tartaric acid single crystals, *Spectrochimica Acta Part A.* 1386

Synthesis and Spectroscopic Characterization of Cdse Nanoparticles for Photovoltaic Applications

IOP Conf. Series: Materials Science and Engineering **360** (2018) 012010 doi:10.1088/1757-899X/360/1/012010

Synthesis and Spectroscopic Characterization of Cdse Nanoparticles for Photovoltaic Applications

P Sanjay[1], K Deepa[2], J Madhavan[2] and S Senthil[1]
[1]Department of Physics, Government Arts College For Men (Autonomous), Nandanam, Chennai - 35,Tamil Nadu, India.
[2]Department of Physics, Loyola College, Chennai - 34, Tamil Nadu, India.
Email: ssatoms@yahoo.co.in

Abstract. Cadmium selenide nanoparticle [CdSe] is an important chemical substance gaining great importance and widely used as an additive in the production of various, industrial products like rubber, cosmetics, catalyst, optical materials solar cells etc. CdSe being a wide band gap material and with better lattice matching properties made it suitable option for solar cell applications, the CdSe nano rods are synthesized by a simple solvothermal method at the morphology, phase and the optical properties of Cdse nano particles are studied using powder X-ray diffraction [XRD], High resolution transmission electron microscope [HRTEM], UV-visible absorption spectroscopy, and Photoluminescence [PL] Spectroscopy, the HRTEM images confirm the formation of CdSe nano rods. The presence of elements was confirmed by Fourier transform infrared spectroscopy [FTIR], energy dispersive X-ray spectroscopy [EDAX], SEM images showed the morphology of the samples.

1. Introduction

Nowadays nano structured material research is a rapidly growing field of science, where the efforts of chemists, physicists, materials scientists and recently biologist and engineers have merged. Inorganic semiconductor nano crystals have exhibited interesting and novel size – dependent physical properties, which greatly differ from those of the corresponding bulk materials. For example, semiconductor nano crystals show blue shifts in both optical absorption and emission spectra with the decrease of nano crystal size due to quantum confinement effect [1]. The size and shape of inorganic nano materials are well known to have an important influence on their widely varying electrical and optical properties [2], which are important in various applications such as catalysis, optoelectronics, luminescent materials, lossing materials, solar cells, light emitting diodes and biomedical imaging. As one of the most important II – VI group semiconductors and nanocrystalline wurtzite structured Cadmium selenide (Eg = 1.74 eV) has attracted great interest in their various promising optoelectronic application owing to its excellent optical conductivity, such as photoelectron – chemical cells, photoconductors. One dimensional semiconductor nanocrystals having unique structural, optical and electrical properties have been considered as structural

unit for modern electronic devices sensors, photonics materials. Several synthesis routes have been employed for production nanorods and nanowires [3-4].

This include template directed method, vapor phase approach, vapor liquid solid growth, sol-gel technique, solvothermal synthesis, solution phase growth based on capping agents. Sonochemical, radiolytic method among others reported. Therefore, the need to develop different methodologies for synthesis of nano materials is inevitable in synthetic chemistry. Among the II – VI semiconducting nano materials, Cds and CdSe are widely synthesized, because of their high crystallites size dependent features of photoluminescence and absorption [5] and great deal of work has been done to characterize Cds and CdSe nano crystals. In the ongoing research on "bottom – up" approach to produce nano particles, the hydrothermal method is turning out to be the most feasible as well as versatile approach. From the environmental perspective, solvothermal method are more environmentally benign them many other synthesis method [6]. The investigation on the role of hydrazine hydrates as the reducing agent proves that it not only controls the morphology of the nano particles but also provides stability to the CdSe nano rods by preventing the oxidation of nano particles due to its reducing capacity [7], the as - prepared nano particles have characterized structurally and optically using powder X -ray diffraction, UV-visible spectroscopy, photoluminescence, Fourier transform infrared spectroscopy (FTIR), High resolution transmission electron microscopy (HRTEM), etc. studies.

2. Experimental Procedure

All the chemicals used were of analytical grade and were of highest purity, Cadmium nitrate ($Cd(NO_3)_2$ $4H_2O$, Merck 99%) and Sodium selenite (Na_2SeO_3, Merck 90%), no need to undergo any post treatment after the reactions with excess of ($N_2H_4H_2O$) and ammonia (NH_3 H_2O).During the synthesis, the molar ratio of $Cd(NO_3)_2$ $4H_2O$ and Na_2SeO_3 was kept 2:1. Cadmium nitrate $Cd(NO_3)_2$ $4H_2O$ (0.01 mol) was dissolved in 10 ml of Milli Q – water and then NH_3H_2O was slowly added into the solution, which initially led to the formation of white precipitate, however, with further addition of ammonia, a clear solution was formed. This indicates the conversion of Cd^{2+} into Cd $(NH_3)_4^{2+}$. The Se source, Na_2SeO_3 (0.005 mol) was stirred for 5 mins with 15 ml of hydrazine hydrate ($N_2H_4H_2O$) and it was mixed with the previously prepared solution (Cd source), this resulted in colorless and transparent solution. The final solution was transferred into Teflon – coated autoclave and then filled with Milli Q – water up to 70% of filling. The pH of the solution was found to be 11 before heating. The autoclave was selected and heated at 180°C for a reaction time of 4 hr. After the completion of the reaction, the autoclave was allowed to return to room temperature. Finally, the deep dark red product was collected, washed repeatedly with Milli Q – water, ethanol and then dried at 80°C.

The prepared CdSe nanopowder was characterized by X – ray diffraction (XRD). Measurements were carried out at room temperature by using Siemens X – ray diffraction D500 with CuK_α. The UV – visible absorption spectrum of the sample was recorded in the range 190 – 1200 nm, Photoluminescence (PL), Scanning Electron Microscope (SEM) was used to examine the surface morphology of samples. The energy dispersive - ray (EDAX) technique was used to determine their elemental compositions. The FTIR spectroscopic measurement is carried out to study the chemical groups present in the sample. The high resolution transmission electron microscopy was done with a JEOL JEM 3010 microscopy. The sample for HRTEM analysis was prepared by dissolving the cdse nanoparticles with few drops of dilute methanol.

3. Results and Discussion

3.1. XRD analysis

The powder XRD result for cdse nanoparticle is shown in figure 1. All the reflection peaks can be indexed to wurizite phase of CdSe. From the XRD pattern, it is clear from the broadening of diffraction peaks of that the particles crystallize at nano scale region. The intensity of the peaks indicates that the CdSe nano particles are of high crystalline and there is no trace of cubic phase. The products are pure in phases with the calculated lattice constant, a = 4.218 A°, b = 4.218 A° , c = 6.887 A°, which are in good agreement with the values given in literature (JCPDS 77 – 2307). The average grain size (D) of CdSe is calculated by the Debye – Scherrer formula, $D = 0.89\lambda/\beta \cos\theta$, where, λ is the wavelength of CuK_{α} line, β is full width at half maximum and θ is the diffraction angle. From the XRD analysis the average particle size of the nano rods was estimated at 35nm.

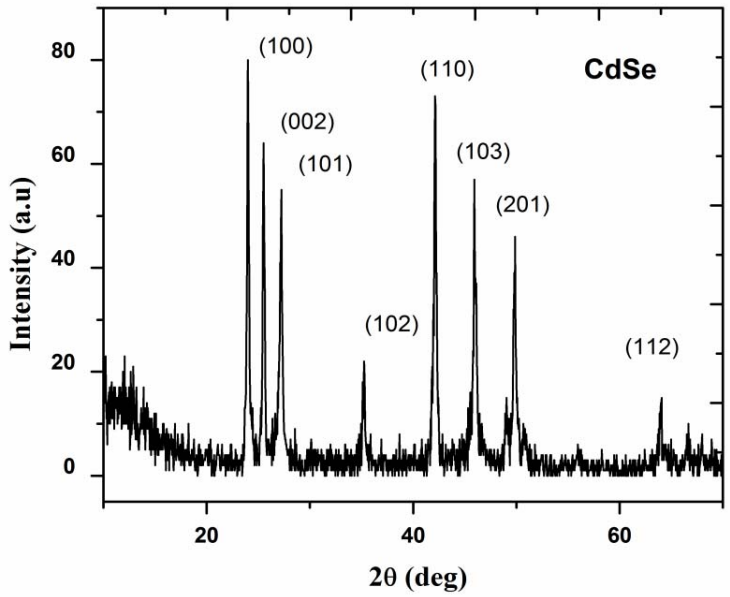

Figure 1. XRD pattern of CdSe nanoparticles.

3.2. UV – Vis Spectroscopy

The optical properties were observed by UV – Vis spectroscopy. The UV – Vis absorption spectroscopy of CdSe nano structural material was measured and shown in figure 2, in the wavelength range 200 – 1200 nm the absorption was measured at room temperature. The absorption edge of CdSe narrowed at 244 nm to be blue shifted the blue shift of the absorption curve results in a reduction of the band gap energy.

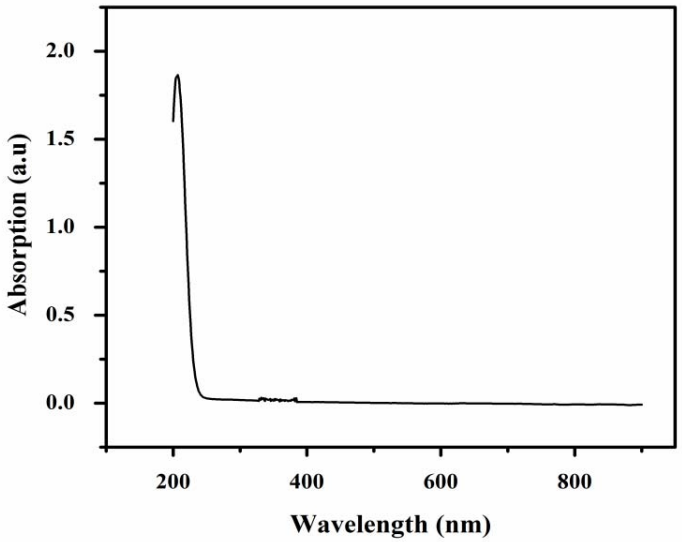

Figure 2. UV-Vis absorption spectra of CdSe nano particles.

3.3. Photoluminescence Spectroscopy (PL)

Figure 3 shows the photoluminescence spectra of the prepared CdSe nano rods. The influence of the width of the CdSe nano rods/nano shows on the shifting behavior in the photoluminescence spectrum has been reported by few researchers [8,9]. The photoluminescence emission spectra of the CdSe nano rods excited at a wavelength of 600 – 720 nm. The sharp peak observed at 642 nm confirms a blue shift compared with bulk wurtzite CdSe which may result which may result from the quantum size effect. The strong PL intensity attains good crystalline quality of the synthesize nano rods.

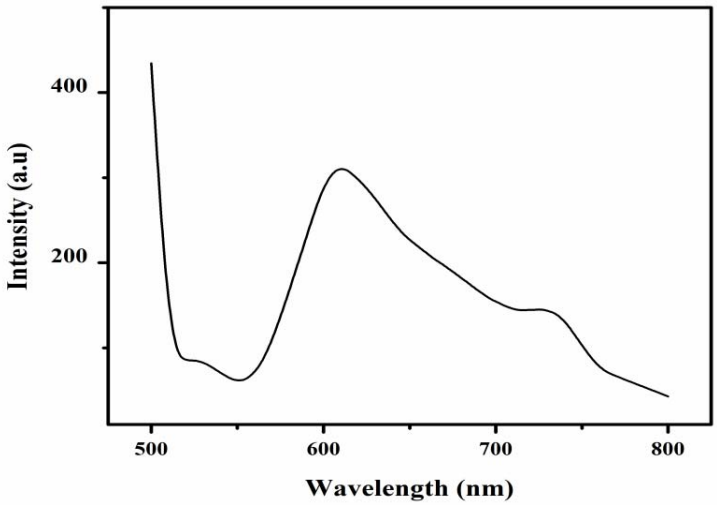

Figure 3. Photoluminescence spectra of CdSe nanoparticles.

3.4. SEM analysis

The surface morphology of the prepared CdSe sample was studied using Scanning Electron Microscope. The SEM micrographs of the CdSe with different magnification at room temperature are shown in Figure 4. The CdSe nano rods were observed at different magnification level at 50 nm. The solvents hydrazine and ammonia ($NH_3.H_2O$) play an important role in the growth of as – formed cadmium selenide nano rods. When the loss of hydrazine is faster, selenide molecules will agglomerate together and condense as rod shaped crystals. The SEM investigation of all the nano CdSe samples reveals that the crystallites are nanometer in size.

Figure 4. SEM image of the CdSe nanoparticles.

3.5. EDAX analysis

To identify the type of element in the samples Energy Dispersive X- ray Spectroscopy (EDAX) was used. The EDAX spectrum was taken using Jeol 6390LV model Scanning Electron Microscope. The EDAX spectra of the synthesized CdSe nano particles were recorded and they are displayed in figure 5. From the results it is confirmed that the elements such as Cd and Se are present in the samples.

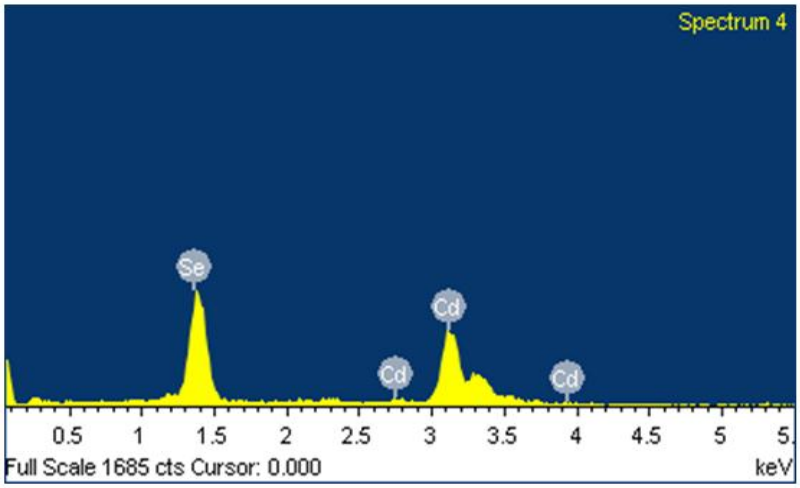

Figure 5. EDAX spectra of the CdSe nanoparticles.

3.6. High Resolution Transmission Electron Microscope (HRTEM)

High – resolution Transmission Electron Microscope is an important research tool for the study of the structure of individual CdSe nano rods. The formation of individual nano rods of CdSe with narrow size distribution is evident from the HRTEM images. Figure 6 shows the HRTEM images of the CdSe nano rods it confirms the uniform size and shape distribution with CdSe nano rods. The influence of hydrazine hydrate to control the morphology of CdSe nano rods has been reported by few research groups. In the present study we used an increased quantity of hydrazine hydrate and still managed to get CdSe nano rods of good crystalline nature. The average particle size of the nano rod is estimated as 35 nm.

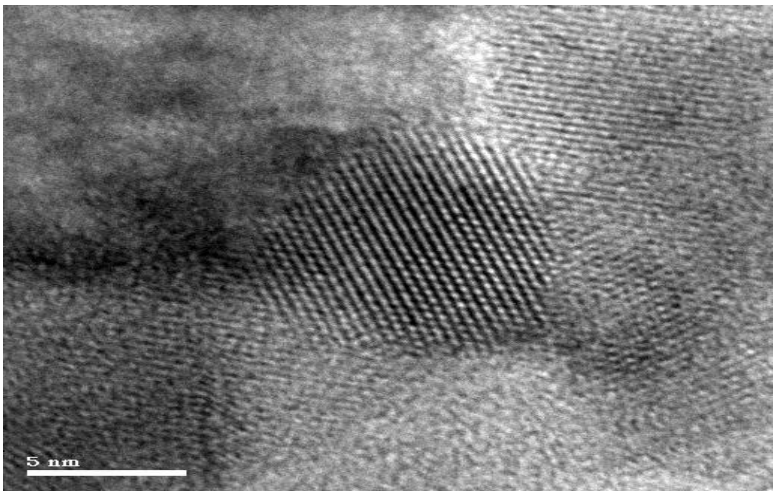

Figure 6. HRTEM image of the CdSe nanoparticles.

3.7. FTIR analysis

FTIR spectroscopy is used to identify and characterize the organic species present in the CdSe nonstructural material. The FTIR spectrum was recorded in the range 400 – 4000 cm^{-1} employing Brukker model IFS 66V FTIR spectrometer. The FTIR spectrum of CdSe nano particles is shown in Fig. 7. The FTIR spectrum of the compound shows two prominent peaks at the weak band at 3730 cm^{-1} and 2926 cm^{-1} arise from C – CH_3 asymmetric stretching. 2510 cm^{-1} and 2614 cm^{-1} are assigned to asymmetric and symmetric stretching vibration of C – CH_2 from the methylene chain respectively. A peak at 738 cm^{-1} is due to Cd - Se band stretching. The absorption band found between 500 cm^{-1} and 700 cm^{-1} are due to the metal oxygen bonding vibrations. Thus the FTIR spectra confirm the presence of functional group and their mode of vibrations.

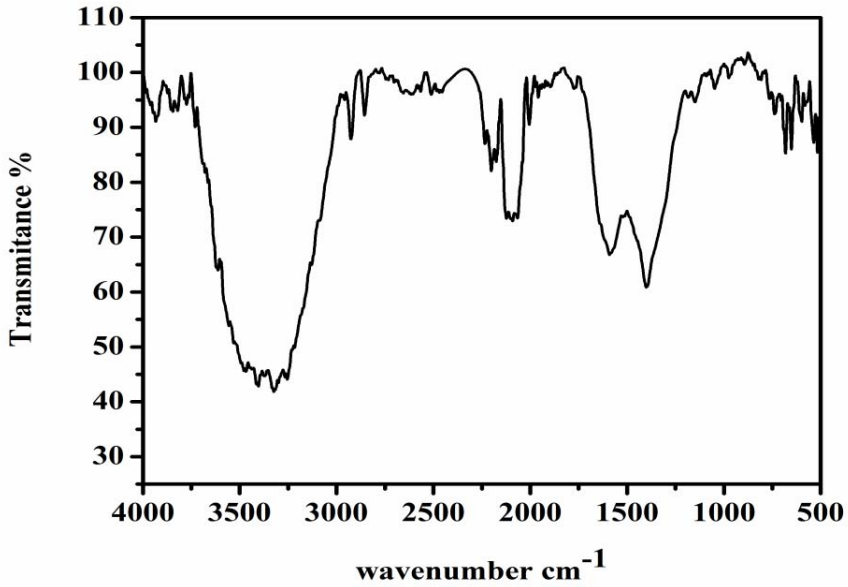

Figure 7. FTIR spectrum of the CdSe nano particles.

4. Conclusion

A CdSe nano rod was successfully synthesized by a simple hydrothermal method and easy process and with better control over the morphology and crystalline quality. The particle size and morphology are verified by powder XRD and HRTEM. The blue shift in the photoluminescence spectrum of CdSe nano rods has been confirmed by the absorption spectrum. UV- Vis spectrum shows blue shift as compared to bulk materials. FTIR analysis shows the presence of surfactant in the final product. This study opens up new avenues for research to find suitable experimental conditions and the possibilities of using different reaction mechanisms to bring out better control over the size/morphology of the semi conducting nano particles.

References

[1] Wang Q, Pan D, Jiang S, Ji X, An L and Jiang B 2006 A solvothermal route to size- and shape controlled CdSe and CdTe nanocrystals *J. Cryst. Growth.* **286** 84-90.

[2] Ma C, Moore D F, Ding Y, Li J and Wang Z L, 2004 Nanobelt and nano saw structures of II-VI semiconductors *Int. J. Nanotechnol.* **1(4)** 431**.**

[3] Duan X F, Huang Y, Cui Y, Wang J F and Lieber C M **2001** Indium phosphide nanowires as building blocks for nanoscale electronic and optoelectronic devices *Nature.* 409**.**

[4] Gates B, Wu Y, Yin Y, Yang P and Xia Y, 2001 Single-crystalline nanowires of Ag2Se can be synthesized by templating against nanowires of trigonal Se *Journal of the American Chemical Society.* **123** 11500-11501.

[5] Ramalingam G and Madhavan J, 2011 Investigation on the structural and morphological behaviour of CdSe nanoparticles by hydrothermal method*Archives of Applied Science Research,* **3 (3)** 217-224.

[6] Ramalingam G, Melikechi N, Dennis Christy P, Selvakumar S and Sagayaraj P 2009 Structural and optical property studies of CdSe crystalline nanorods synthesized by a solvothermal method. *Journal of Crystal Growth* **311** 3138-3142.

[7] Riman R E, Suchanek W L and Lencka M M 2002 hydrothermal crystallization of ceramics Cristallisation hydrothermale de ceramiques. Annales de Chimie Science des Matériaux **27** 15-36.

[8] Yang J, Zeng J H, Yu S H, Yang L, Zhang Y H and Qian Y T, Formation process of CdS nanorods via solvothermal route Chemistry of materials. **12** 3259-3263.

[9] Peng Q, Dong Y, Deng Z and Li Y 2001 Low-Temperature Elemental-Direct-Reaction Route to II−VI Semiconductor Nanocrystalline ZnSe and CdSe *Inorg. Chem.* **40 (16)**, pp 3840–3841.

Reliability analysis of a standby system with two stage Erlangian repair

Venkata S.S. Yadavalli
Department of Industrial & Systems Engineering, University of Pretoria, 0002, Pretoria, South Africa
Sarma.yadavalli@up.ac.za

Shagufta Abbas
Department of Industrial & Systems Engineering, University of Pretoria, 0002, Pretoria, South Africa
Abbas.mujahid@gmail.com

V.S. Vaidyanathan
Department of Statistics, Pondicherry University,
Puducherry – 605 014, India
Vaidya.stats@gmail.com

P. Chandrasekhar
Department of Statistics, Loyola College,
Chennai – 600 034, India.
drchandrasekharin@yahoo.co.in

Abstract

By making a detailed study of a two unit cold standby system with constant failure rate and two stage Erlangian repair time distribution, measures of system performance and its statistical inferential aspects are discussed through classical and Bayesian approaches.

Keywords

Bayes estimator, confidence limits, Slustky theorem, standby system, steady state availability.

1. Introduction

Reliability theory is concerned with statistical description of a system and has been studied in detail using the failure time and repair time density functions. The failures and repairs in any system are influenced by several factors such as system configuration, the environmental conditions under which the system operates and the varying failures (minor and major) and so on, which cannot be controlled or assessed well in advance. For a detailed study of systems operating in random environments, see Chandrasekhar and Natarjan (2001) and Chandrasekhar et al. (2005). In real life situations with problems involving system configurations, it is essential to carry out an analysis of measures of system performance. These problems often require the applications of statistical tools such as point estimation, interval estimation, hypotheses testing and Bayesian inference. Most of the times, it is possible that some statistical information pertaining to the parameters of both lifetime and repair time distributions is available. In such a scenario, Bayesian approach provides statistical methodology to incorporate the prior information with the data at hand. Analysis of systems using the above mentioned statistical tools is scarce in literature.

In recent times, there has been great interest in analyzing the system from a Bayesian perspective. However, all the Bayesian research work till date has been on constant failure and service rates. In this paper, we study in detail a two unit cold standby system with constant failure rate λ and constant repair rate μ (both unknown) and two repair stages. Several authors have studied extensively two unit standby redundant systems in the past. Osaki and Nakagawa (1976) give a bibliography of the work on two unit systems. Our interest in this paper is on statistical inference procedures of a standby system with two stage Erlangian repair. The choice of the Erlangian distribution is motivated by the fact that an Erlangian variate with shape parameter k is the sum of k independent and identically distributed (iid) exponential variates. Hence, an Erlangian repair model can be thought of as a model with repair in k exponential phases, where repair at each phase is exponential with rate μ.

In our model, we perform a simple experiment by observing m lifetimes and n repair times. Given this experiment, the likelihood is of the form

$$L(\text{parameters}|\text{data})=\lambda^{m}e^{-\lambda u}\left(\frac{\mu^{2n}}{\Gamma(2)^{n}}e^{-\mu v}\prod_{j=1}^{n}y_j\right)$$

$$=\mu^{2n}e^{-(\lambda u+\mu v)}\lambda^{m}\prod_{j=1}^{n}y_j \qquad (1.1)$$

where u and v are the sums of m observed lifetimes and n repair times respectively. For the system under consideration, in the subsequent sections, we have described maximum likelihood and Bayesian procedures. Flexible priors for lifetime and repair time parameters are introduced under the assumption that priors for life time and repair time parameters are independent. By using these conjugate prior distributions, we evaluate the posterior distributions along with Bayes estimators. The model and the assumptions, expressions for system reliability, MTBF, availability and associated statistical inference together with numerical illustration are discussed in detail in the following sections.

2. Model (Two unit cold standby system with a single repair facility)

2.1 Assumptions

The assumptions of the model are as follows:

(i) The system has two statistically independent and identical units each with constant failure rate say λ and one perfect repair facility.

(ii) A standby unit will not fail.

(iii) The repair time distribution is a two stage Erlangian with probability density function (pdf) given by

$$g(t)=\mu^{2}e^{-\mu t}t,\ 0<t<\infty;\mu>0 \qquad (2.1)$$

(iv) Once a unit is repaired, it is as good as new.

(v) There is a perfect switch with negligible switchover time.

2.2 Analysis of the system

The state of the system is described by discrete valued stochastic process $\{X(t),\ t\in[0,\infty)\}$, where $X(t)$ denotes the number of units failed at time t. It may be noted that the stochastic process $\{X(t)\}$ is a Markov Process (since a two stage Erlangian variate is the sum of two iid exponential variates and exponential distribution satisfies lack of memory property) on $\{0,1,2\}$. We note that at any given instant of time t, the system is found in any of the following mutually exclusive and exhaustive states S_i, $i=0,1,\ldots,4$. Here S_0 corresponds to the situation, wherein both the units are operable but only one unit is operating online and the other unit is kept in cold standby. S_1 (S_2) represents the state of the system in which one unit is operating online and the other unit is in the first (second) stage of repair. It is clear that the states S_0, S_1 and S_2 are the system upstates. Similarly, S_3 (S_4) denotes the situation that one unit is in the first (second) stage of repair and the other unit is waiting for repair and are the system downstates. Clearly the Markov process $\{X(t)\}$ has the infinitesimal generator given by

$$Q = \begin{array}{c} \\ 0 \\ 1 \\ 2 \\ 3 \\ 4 \end{array} \begin{array}{c} \begin{array}{ccccc} 0 & 1 & 2 & 3 & 4 \end{array} \\ \begin{pmatrix} -\lambda & \lambda & 0 & 0 & 0 \\ 0 & -(\lambda+\mu) & \mu & \lambda & 0 \\ \mu & 0 & -(\lambda+\mu) & 0 & \lambda \\ 0 & 0 & 0 & -\mu & \mu \\ 0 & \mu & 0 & 0 & -\mu \end{pmatrix} \end{array} \quad (2.2)$$

Let $p_i(t)$ be the probability that the system is in state S_i, $i=0,1,\ldots,4$ at time t with the initial condition $p_0(0)=1$. Initially, we assume that both the units are operable and obtain the system performance measures.

2.2.1 System reliability

The system reliability $R(t)$ is the probability that the system does not fail upto time t. To derive an expression for system reliability, it is necessary to study the transitions of the Markov process $\{X(t)\}$ into the states S_0, S_1 and S_2 without passing through S_3 and S_4. The differential – difference equations corresponding to these upstates are given below which are obtained using the infinitesimal generator of the process given in (2.2).

$$\frac{dp_0(t)}{dt} = -\lambda p_0(t) + \mu p_2(t) \quad (2.3)$$

$$\frac{dp_1(t)}{dt} = \lambda p_0(t) - (\lambda+\mu) p_1(t) \quad (2.4)$$

$$\frac{dp_2(t)}{dt} = \mu p_1(t) - (\lambda+\mu) p_2(t) \quad (2.5)$$

The equations (2.3) – (2.5) are solved by using Laplace transformation. Suppose $L_i(s)$ represents the Laplace transform of $p_i(t)$, $i=0,1,2$. Taking Laplace transform, solving and inverting, we get the solution for $p_i(t)$, $i=0,1,2$ as follows:

$$p_0(t) = \sum_{i=1}^{3} \frac{(\alpha_i+\lambda+\mu)^2}{\prod_{j=1, j\neq i}^{3} (\alpha_i-\alpha_j)} e^{\alpha_i t} \quad (2.6)$$

$$p_1(t) = \lambda \sum_{i=1}^{3} \frac{(\alpha_i+\lambda+\mu)}{\prod_{j=1, j\neq i}^{3} (\alpha_i-\alpha_j)} e^{\alpha_i t} \quad (2.7)$$

$$p_2(t) = \lambda\mu \sum_{i=1}^{3} \frac{1}{\prod_{j=1, j\neq i}^{3} (\alpha_i-\alpha_j)} e^{\alpha_i t} \quad (2.8)$$

Adding (2.6), (2.7) and (2.8), we obtain the system reliability as

$$R(t) = \sum_{i=1}^{3} \frac{[(\alpha_i+\lambda+\mu)^2 + \lambda(\alpha_i+\lambda+2\mu)]}{\prod_{j=1, j\neq i}^{3} (\alpha_i-\alpha_j)} e^{\alpha_i t} \quad (2.9)$$

where $\alpha_i, i=1,2,3$ are the roots of the equation
$s^3+(3\lambda+2\mu)s^2+(3\lambda^2+4\lambda\mu+\mu^2)s+\lambda^2(\lambda+2\mu)=0$.

2.2.2 Mean time before failure

The system MTBF is the expected or average time to failure and is given by

$$MTBF = L_0(0)+L_1(0)+L_2(0) = \frac{(2\lambda^2+4\lambda\mu+\mu^2)}{\lambda^2(\lambda+2\mu)} \quad (2.10)$$

2.2.3 System availability

The system availability $A(t)$ is the probability that the system is in operable condition at any arbitrary point of time t. To obtain the availability function, we have to study the transitions of the Markov process $\{X(t)\}$ into the states S_i, $i=0,1,\ldots,4$. Using the infinitesimal generator given in (2.2), we get the following system of differential – difference equations.

$$\frac{dp_0(t)}{dt} = -\lambda p_0(t) + \mu p_2(t) \quad (2.11)$$

$$\frac{dp_1(t)}{dt} = \lambda p_0(t) - (\lambda+\mu) p_1(t) + \mu p_4(t) \quad (2.12)$$

$$\frac{dp_2(t)}{dt} = \mu p_1(t) - (\lambda+\mu) p_2(t) \quad (2.13)$$

$$\frac{dp_3(t)}{dt} = \lambda p_1(t) - \mu p_3(t) \quad (2.14)$$

$$\frac{dp_4(t)}{dt} = \lambda p_2(t) + \mu p_3(t) - \mu p_4(t) \quad (2.15)$$

Solving (2.11) – (2.15) with the condition $\sum_{i=0}^{4} p_i(t) = 1$, we obtain the solution as follows.

$$p_0(t) = \frac{\mu^4}{\prod_{i=1}^{4}\alpha_i} + \lambda\mu^2 \sum_{i=1}^{4} \frac{(\alpha_i+\mu)^2}{\alpha_i(\alpha_i+\lambda)\prod_{j=1,j\neq i}^{4}(\alpha_i-\alpha_j)} e^{\alpha_i t} \quad (2.16)$$

$$p_1(t) = \frac{\lambda\mu^2(\lambda+\mu)}{\prod_{i=1}^{4}\alpha_i} + \lambda \sum_{i=1}^{4} \frac{(\alpha_i+\mu)^2(\alpha_i+\lambda+\mu)}{\alpha_i \prod_{j=1,j\neq i}^{4}(\alpha_i-\alpha_j)} e^{\alpha_i t} \quad (2.17)$$

$$p_2(t) = \frac{\lambda\mu^3}{\prod_{i=1}^{4}\alpha_i} + \lambda\mu \sum_{i=1}^{4} \frac{(\alpha_i+\mu)^2}{\alpha_i \prod_{j=1,j\neq i}^{4}(\alpha_i-\alpha_j)} e^{\alpha_i t} \quad (2.18)$$

$$p_3(t) = \frac{\lambda^2\mu(\lambda+\mu)}{\prod_{i=1}^{4}\alpha_i} + \lambda^2 \sum_{i=1}^{4} \frac{(\alpha_i+\mu)(\alpha_i+\lambda+\mu)}{\alpha_i \prod_{j=1,j\neq i}^{4}(\alpha_i-\alpha_j)} e^{\alpha_i t} \quad (2.19)$$

$$p_4(t) = \frac{\lambda^2\mu(\lambda+2\mu)}{\prod_{i=1}^{4}\alpha_i} + \lambda^2\mu \sum_{i=1}^{4} \frac{[\lambda+2(\alpha_i+\mu)]}{\prod_{j=1,j\neq i}^{4}(\alpha_i-\alpha_j)} e^{\alpha_i t} \quad (2.20)$$

where α_i, $i=1,2,3,4$ are the roots of the equation
$s^4+(3\lambda+4\mu)s^3+(3\lambda^2+10\lambda\mu+6\mu^2)s^2+(\lambda^3+8\lambda^2\mu+9\lambda\mu^2+4\mu^3)s+\mu(2\lambda^3+4\lambda^2\mu+2\lambda\mu^2+\mu^3)=0.$
Hence, the system availability is obtained by adding (2.16), (2.17) and (2.18) and is given by

$$A(t) = \frac{\mu^2(\lambda+\mu)^2}{\prod_{i=1}^{4}\alpha_i} + \lambda\mu^2 \sum_{i=1}^{4} \frac{(\alpha_i+\mu)^2}{\alpha_i(\alpha_i+\lambda)\prod_{j=1,j\neq i}^{4}(\alpha_i-\alpha_j)} e^{\alpha_i t} + \lambda \sum_{i=1}^{4} \frac{(\alpha_i+\mu)^2(\alpha_i+\lambda+\mu)}{\alpha_i \prod_{j=1,j\neq i}^{4}(\alpha_i-\alpha_j)} e^{\alpha_i t}$$

$$+ \lambda\mu \sum_{i=1}^{4} \frac{(\alpha_i+\mu)^2}{\alpha_i \prod_{j=1,j\neq i}^{4}(\alpha_i-\alpha_j)} e^{\alpha_i t} \quad (2.21)$$

Allowing $t\to\infty$ on both the sides of (2.21), the system steady state availability is obtained as

$$A_\infty = \frac{\mu(\lambda+\mu)^2}{(2\lambda^3+4\lambda^2\mu+2\lambda\mu^2+\mu^3)}, \quad (2.22)$$

which is in agreement with Chandrasekhar and Natarajan (1994).

2.3 ML estimator of system reliability

Let $X_1, X_2, \ldots, X_n$ and $Y_1, Y_2, \ldots, Y_n$ be random observations on exponential failure times and Erlangian repair times with the pdf given by (2.1). It is well known that $\overline{X}$ and $\frac{\overline{Y}}{2}$ are the ML estimators of $\frac{1}{\lambda}$ and $\frac{1}{\mu}$ respectively, where $\overline{X}$ and $\overline{Y}$ are the corresponding sample means. Thus, the ML estimator of $R(t)$ is given by

$$\hat{R}(t) = \sum_{i=1}^{3} \frac{[(2\overline{X}+\overline{Y}+\hat{\alpha}_i\overline{X}\overline{Y})^2+\overline{Y}(4\overline{X}+\overline{Y}+\hat{\alpha}_i\overline{X}\overline{Y})]}{(\overline{X}\overline{Y})^2 \prod_{j=1,j\neq i}^{3}(\alpha_i-\alpha_j)} e^{\hat{\alpha}_i t} \quad (2.23)$$

where $\hat{\alpha}_i$, i=1,2,3 are the roots of the cubic equation

$$\overline{X}^3\overline{Y}^2s^3+\overline{X}^2\overline{Y}(4\overline{X}+3\overline{Y})s^2+\overline{X}(2\overline{X}+\overline{Y})(2\overline{X}+3\overline{Y})s+\overline{Y}(4\overline{X}+\overline{Y})=0 \quad (2.24)$$

2.4 Confidence limits for A_∞

In section 2.3, we have seen that $\overline{X}$ and $\frac{\overline{Y}}{2}$ are the ML estimators of $\frac{1}{\lambda}$ and $\frac{1}{\mu}$ respectively. Let $\theta_1=\frac{1}{\lambda}$ and $\theta_2=\frac{1}{\mu}$. Clearly, A_∞ given in (2.22) is simplified to

$$A_\infty=\frac{\theta_1(\theta_1+\theta_2)^2}{(\theta_1^3+2\theta_1^2\theta_2+4\theta_1\theta_2^2+2\theta_2^3)} \quad (2.25)$$

and hence ML estimator of A_∞ is given by

$$\widehat{A}_\infty=\frac{\overline{X}(2\overline{X}+\overline{Y})^2}{(4\overline{X}^3+4\overline{X}^2\overline{Y}+4\overline{X}\overline{Y}^2+\overline{Y}^3)} \quad (2.26)$$

By the asymptotic property of ML estimators, it is clear that

$\sqrt{n}[\widehat{A}_\infty-A_\infty]\xrightarrow{d}N(0,\sigma^2(\boldsymbol{\theta}))$ as $n\to\infty$,

where $\boldsymbol{\theta}=(\theta_1,\theta_2)$ and

$$\sigma^2(\boldsymbol{\theta})=\theta_1^2\left(\frac{\partial A_\infty}{\partial\theta_1}\right)^2+\frac{\theta_2^2}{2}\left(\frac{\partial A_\infty}{\partial\theta_2}\right)^2 \quad (2.27)$$

The partial derivatives $\left(\frac{\partial A_\infty}{\partial\theta_i}\right)$, i=1,2 are given by

$$\left(\frac{\partial A_\infty}{\partial\theta_1}\right)=\frac{2\theta_2^2(3\theta_1^3+6\theta_1^2\theta_2+4\theta_1\theta_2^2+\theta_2^3)}{(\theta_1^3+2\theta_1^2\theta_2+4\theta_1\theta_2^2+2\theta_2^3)^2} \quad (2.28)$$

$$\left(\frac{\partial A_\infty}{\partial\theta_2}\right)=\frac{-2\theta_1\theta_2(3\theta_1^3+6\theta_1^2\theta_2+4\theta_1\theta_2^2+\theta_2^3)}{(\theta_1^3+2\theta_1^2\theta_2+4\theta_1\theta_2^2+2\theta_2^3)^2} \quad (2.29)$$

Substituting (2.28) and (2.29) in (2.27) and simplifying, we get

$$\sigma^2(\theta)=\frac{6\theta_1^2\theta_2^4(3\theta_1^3+6\theta_1^2\theta_2+4\theta_1\theta_2^2+\theta_2^3)^2}{(\theta_1^3+2\theta_1^2\theta_2+4\theta_1\theta_2^2+2\theta_2^3)^4} \quad (2.30)$$

Thus, $\widehat{A}_\infty$ is a CAN estimator of A_∞. One can also use the method of moments to generate CAN estimator of A_∞, see Sinha (1986).

Using Slutsky theorem and a property of consistent estimator, it can be shown that the confidence limits for the steady state availability of the system are given by $\hat{A}_\infty\pm k_{\frac{\alpha}{2}}\frac{\hat{\sigma}}{\sqrt{n}}$, where $k_{\frac{\alpha}{2}}$ is the upper $100\left(1-\frac{\alpha}{2}\right)\%$ quantile of standard normal distribution and $\hat{\sigma}$ is obtained from (2.30) and is given by

$$\hat{\sigma}=\sqrt{\frac{3\overline{X}^2\overline{Y}^4(24\overline{X}^3+24\overline{X}^2\overline{Y}+8\overline{X}\overline{Y}^2+\overline{Y}^3)^2}{2(4\overline{X}^3+4\overline{X}^2\overline{Y}+4\overline{X}\overline{Y}^2+\overline{Y}^3)^4}} \quad (2.31)$$

In the next section, Bayes estimator of MTBF under squared error loss function is obtained.

3. Bayes estimation of MTBF in a two unit cold standby system

In this section, we derive the Bayes estimator of MTBF by considering Gamma distributions with parameters (α,β) and (δ,ω) as natural conjugate priors for the lifetimes and repair times respectively. In other words, λ and μ have the following prior distributions with the probability density functions as follows.

$$\tau_1(\lambda|\alpha,\beta)=\frac{\alpha^\beta}{\Gamma(\beta)}e^{-\alpha\lambda}\lambda^{\beta-1},\ 0<\lambda<\infty;\ \alpha,\beta>0 \quad (3.1)$$

$$\tau_2(\mu|\delta,\omega)=\frac{\delta^\omega}{\Gamma(\omega)}e^{-\delta\mu}\mu^{\omega-1},\ 0<\mu<\infty;\ \delta,\omega>0 \quad (3.2)$$

It can be shown that the posterior distributions of λ and μ given the sample observations $X_1, X_2,...,X_m$ and $Y_1, Y_2,...,Y_n$ are respectively given by

$$q_1(\lambda|x_1,x_2,\ldots,x_m) = \frac{(\alpha+u)^{m+\beta}}{\Gamma(m+\beta)} e^{-\lambda(\alpha+u)} \lambda^{(m+\beta)-1},\ 0<\lambda<\infty;\ \alpha,u,m,\beta>0 \qquad (3.3)$$

$$q_2(\mu|y_1,y_2,\ldots,y_n) = \frac{(\delta+v)^{2n+\omega}}{\Gamma(2n+\omega)} e^{-\mu(\delta+v)} \mu^{(2n+\omega)-1},\ 0<\mu<\infty;\ \delta,v,n,\omega>0 \qquad (3.4)$$

In other words, λ and μ are distributed as Gamma with parameters $(\alpha+u,\ m+\beta)$ and $(\delta+v,\ 2n+\omega)$ respectively.

Bayes estimator of MTBF say MTBF*, given the sample observations is defined as

MTBF* = E[MTBF | sample observations]

$$= \int_0^\infty \int_0^\infty \frac{(2\lambda^2+4\lambda\mu+\mu^2)}{\lambda^2(\lambda+2\mu)}\ q_1(\lambda|x_1,x_2,\ldots,x_m) q_2(\mu|y_1,y_2,\ldots,y_n)\ d\lambda\ d\mu \qquad (3.5)$$

$$= \int_0^\infty \int_0^\infty \left(\frac{1}{\mu}+\frac{2}{\lambda}+\frac{\mu}{2\lambda^2}\right) \sum_{j=0}^\infty \frac{(-1)^j}{2^j} \left(\frac{\lambda}{\mu}\right)^j q_1(\lambda|x_1,x_2,\ldots,x_m) q_2(\mu|y_1,y_2,\ldots,y_n)\ d\lambda\ d\mu,\ \lambda<\mu$$

$$= \frac{1}{\Gamma(m+\beta)\Gamma(2n+\omega)} \left[\sum_{j=0}^\infty \frac{(-1)^j}{2^j} \frac{(\delta+v)^{j+1}}{(\alpha+u)^j} \Gamma(m+\beta+j)\Gamma(2n+\omega-j-1) + 2\sum_{j=0}^\infty \frac{(-1)^j}{2^j} \frac{(\delta+v)^j}{(\alpha+u)^{j-1}} \Gamma(m+\beta+j-1)\Gamma(2n+\omega-j) + \frac{1}{2}\sum_{j=0}^\infty \frac{(-1)^j}{2^j} \frac{(\delta+v)^{j-1}}{(\alpha+u)^{j-2}} \Gamma(m+\beta+j-2)\Gamma(2n+\omega-j+1) \right] \qquad (3.6)$$

4. Numerical Illustration

The performance of the Bayes estimate of MTBF i.e., MTBF* is illustrated in this section through simulated data. The estimates are obtained using (3.5). Monte Carlo integration method is used to evaluate the integrals in (3.5) in two steps. First, the inner integral is evaluated by generating random observations using the posterior density of λ treating μ as unknown. The outer integral is then evaluated using random observations generated from the posterior density of μ. The values of hyper parameters in the posterior density functions are fixed as $m=n=50$; $\alpha=2.5$; $\beta=3.0$; $\delta=0.75$; $\omega=1.5$. u and v are determined by taking the sums of iid samples of sizes m and n generated respectively from exponential distribution and Erlangian distribution with pdf given in (2.1). For generating samples, the following choices of λ and μ namely, $\lambda=3, 6, 9, 12$ and $\mu=2, 4, 6, 8$ are used. The results of the simulation based on 10,000 Monte Carlo runs are presented below.

Table 1: Bayes estimate of MTBF

μ \ λ	3.0	6.0	9.0	12.0
2.0	0.01662	0.03390	0.07491	0.11261
4.0	0.02634	0.05689	0.14142	0.15921
6.0	0.02723	0.11658	0.16159	0.26393
8.0	0.03311	0.14515	0.26254	0.39131

From the above table, it can be observed that for fixed repair rate (μ), the Bayes estimate of MTBF increases as the failure rate (λ) increases. Similarly, for fixed λ, the Bayes estimate of MTBF increases as μ increases. In other words, whenever the two unit cold standby system with single repair facility under consideration exhibits high failure and repair rates, the estimated mean time before failure is also high.

5. Conclusion

An attempt is made in this paper to study in detail a two unit cold standby system with a single repair facility. Mathematical expressions for $R(t)$, MTBF, $A(t)$ and A_∞ are obtained. Further, asymptotic confidence limits for A_∞, ML estimator of $R(t)$ and Bayes estimator of MTBF are obtained. Also the performance of the Bayes estimator of MTBF is illustrated through simulation study.

6. References

Chandrasekhar, P. and Natarajan, R. Confidence limits for steady state availability of a two unit standby system, *Microelectronics and Reliability*, Vol. 34, No. 7, pp. 1249 – 1251,1994

Chandrasekhar, P. and Natarajan, R. A system operating in a random environment, *Statistical Methods*, Vol.3, No. 2, pp. 98 – 107, 2001

Chandrasekhar, P., Natarajan, R., Yadavalli, V.S.S. and Malada, A. An n unit system operating in a random environment, *OPSEARCH*, Vol. 42, No.3, pp. 280 – 287, 2005

Osaki, S. and Nakagawa, T. Bibliography for reliability and availability of stochastic systems, *IEEE Trans. on Reliability.*, Vol.R-25, pp. 284 – 287, 1976

Sinha, S.K. , Reliability and Life testing, *Wiley Eastern Pvt. Ltd*., New Delhi, 1976.

Biography

Dr VSS Yadavalli is a Professor and Head of Department of Industrial & Systems Engineering, University of Pretoria. Professor Yadavalli has published over 150 research paper mainly in the areas of Reliability and inventory modeling in various international journals like, International Journal of Production Economics, International Journal of Production Research, International Journal of Systems Science, IEEE Transactions on Reliability, Stochastic Analysis & Applications, Applied Mathematics & Computation, Annals of Operations Research, Computers & Industrial Engineering etc. Prof Yadavalli is an NRF (South Africa) rated scientist and attracted several research projects. Professor Yadavalli was the past President of the Operations Research Society of South Africa. He is a `Fellow' of the South African Statistical Association. He received a `Distinguished Educator Award 'from Industrial Engineering and Operations Management Society in 2015.

Dr Shagufta Abbas is currently working as an assistant professor in department of Mathematics in Govt Degree College for Women, Lahore. She completed her PhD in 2016 from Department of Industrial and Systems Engineering , University of Pretoria, South Africa. Her areas of interest include distribution theory, reliability theory and mathematical analysis.

V.S.Vaidyanathan obtained M.Sc. degree in Statistics in the year 1995 and M.Phil. degree in Statistics in the year 1999 from University of Madras, India. He was awarded Ph.D. degree in Statistics in the year 2011 from University of Madras, India for his thesis "Contributions to Clustering and Classification algorithms". He joined the Department of Statistics, Loyola College, Chennai, India in the year 2000 as Lecturer in Statistics and later got appointed in Pondicherry University, India in the year 2010. Currently, he serves as Assistant Professor in the Department of Statistics, Pondicherry University, India. His research interests include Statistical Inference for queueing and stochastic models, mixture models and distribution theory

Dr. P. Chandrasekhar has obtained his M. Sc (Statistics) and M. Phil (Statistics) degrees from the University of Madras in 1974 and 1984 respectively. Further, he has received his Ph. D degree in 1996 from the same University. His doctoral thesis is entitled "Stochastic models of redundant systems operating in random environments". His biographical profile was included in Marquis who's who in the world in 16th edition. He was the faculty member in the department of Statistics, Loyola College, Chennai, India from 1978 to 2010. He was the University Grants Commission - Emeritus Fellow from 2011 to 2013. He has nearly 50 research publications - both National and International. His areas of research are stochastic modelling in Reliability Theory and Statistical Inference for Queueing Models.

Growth and Characterization of L-Leucenium Hydrogen Maleate Single Crystals for Nonlinear Optical Applications

IOP Conf. Series: Materials Science and Engineering **360** (2018) 012044 doi:10.1088/1757-899X/360/1/012044

Growth and Characterization of L-Leucenium Hydrogen Maleate Single Crystals for Nonlinear Optical Applications

A Hemalatha[1,2], S Arulmani[2],P Sanjay[2], K Deepa[3], J Madhavan[3] and S Senthil[2]

[1]Department of Physics, Quaid-E-Millath Government College for Women, Anna salai, Chennai – 02,Tamil Nadu, India.
[2]Department of Physics ,Government Arts College For Men (Autonomous), Nandanam, Chennai – 35, Tamil Nadu, India.
[3]Department of Physics, Loyola College, Chennai – 34, Tamil Nadu, India.
E mail – ssatoms@yahoo.co.in

Abstract. Good quality single crystals of amino acid based L-Leucenium maleate (LLM) has been grown from aqueous solution by slow evaporation method at room temperature. The crystalline nature of the crystal has been confirmed by the X-ray diffraction analysis Using Cuk_{α} radiation of wavelength of 1.54 A°. The presence of various functional groups in the LLM is confirmed by FT-IR using the Bruker IFS66 spectrometer. The functional groups present in the sample were also confirmed by FT-RAMAN spectral analysis. The thermal stability of LLM crystal has been analyzed by TGA and DTA studies. Second harmonic generation test was done on the LLM sample using Kurtz and Perry technique. The NLO efficiency of the grown crystal is nearly 0.6 times that of the standard KDP crystal. The transparent nature of the sample has been conformed from the UV-Vis-NIR spectrum and optical band gap of the LLM crystal also calculated.

1. Introduction

Nonlinear optical materials have been extensively studied in the recent years due to their potential applications in various fields like optical data storage, optical switching images, processing and manipulation. Therefore, there is a need to produce high efficiency NLO materials. Among the class of NLO materials, organic NLO materials are generally preferred to be more efficient than the inorganic counterpart due to their favorable nonlinear responds [1]. Amino acid crystals have subjected to extensive investigation by several researchers for their excellent characteristics. Amino acids are interesting useful organic materials for NLO applications as they contain a proton donor carboxyl acid (-COOH) group and proton acceptor amino (NH_2) group in them, known as zwitterions which produce hydrogen bonds. Due to this dipolar nature, amino acids have physical properties which make them ideal candidates for application [2]. Among the various amino acids, L-Leucine has

formed several complexes, which are promising materials for second harmonic generation. Maleic acid, basically dicarboxylic acid with large π conjugation has attracted a great deal of attention [3]. The intermolecular hydrogen bond in maleic acid is very strong. Maleic acid forms crystalline maleate of various organic molecules through hydrogen bonding and π -π interaction [4]. On the basis of earlier reports on L-Leucine salt [5], we have successfully grown a good quality crystal of L-Leucinium hydrogen maleate, a new organic compound. In this paper, the crystal growth and its characterization by powder XRD, FT-IR, FT-RAMAN, UV-Vis-NIR, NLO and Thermal analysis are reported for the grown compound.

2. ExperimentalProcedure

L-Leucinium hydrogen maleate (LLM) crystal was synthesized from highly pure L-Leucine and L-Maleic acid and they were taken in the equimolar ratio of 1:1. The required quantity of L-Leucine and L-Maleic acid was thoroughly dissolved by adding double distilled water according to their solubility data and stirred well for about five hours using a magnetic stirrer to obtain a homogenous mixture. The solution was filtered to remove insoluble impurities using Whatman filter paper of pore size ten micrometers. Then, saturated solution was taken in a beaker and tightly covered with a polythene paper of perforated sheet in order to control the evaporation rate and kept undisturbed at room temperature for crystallization. Finally, a well-defined single crystal was obtained after 35 days by slow evaporation method. The photo graph of the as grown crystal of LLM is shown in Figure. 1.

Figure1. Photograph of as grown single crystal of LLM

3.Results and Discussion

3.1. .X-ray diffraction analysis

The crystalline nature of the grown crystal was checked by taking the X-ray diffraction pattern of powder samples of L-Leucinium hydrogen maleate (LLM) with Cuk_{α} (λ = 1.5406 A˚) radiation. The sample was scanned over a 2θ in the range of 10 -30˚ at the rate of 2˚per min. From this measurement we found the lattice dimensions as a=21.132 A˚, b=5.226 A˚, c=31.452 A˚, β=98.439° having the space group C2, it is crystallize in monoclinic system and is well matched with the reported literature [5]. The presence of a sharp and well defined peak confirms the good crystalline nature of the L-Leucinium hydrogen maleate (LLM) crystal. The differences in the peak amplitude can be attributed to the different sizes and orientation of the powdered grains. The recorded powder XRD pattern is shown in Figure 2.

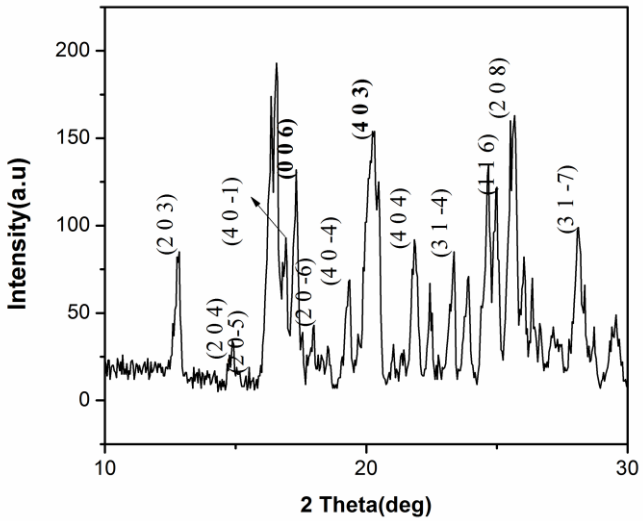

Figure 2. Powder X-ray diffraction pattern of the LLM crystals

3.2. UV-Vis Absorption spectroscopy

The optical absorption study is an important tool in identifying the usefulness of a NLO material in the visible regions. The UV-Visible absorption spectrum was recorded for the grown compound in wavelength range of 200 - 900nm using Varian carry 5E model UV-Vis spectrometer. There is no appreciable absorption of light in the entire visible range as in the case for all amino acids [6]. No absorption was found in the entire visible region of the UV-Vis-NIR spectra. UV-Vis-NIR studies also give important structural information because absorption of UV and visible light involves promotion of the electron in π and n orbital from the ground state to higher energy state [7]. The optical absorption spectrum of LLM is shown in Figure. 3a. The lower cut of wave length is around 212nm. There is no sufficient absorption from 200nm to 900nm. This is an advantage of the use of grown crystal, where the absence of strongly conjugated bonds leads to wide transparency ranges in the visible and UV spectral regions. The optical absorption coefficient of photon energy helps to study the band structure and explains the type of transition of electrons.

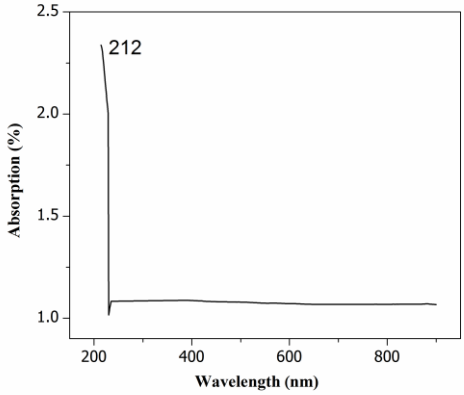

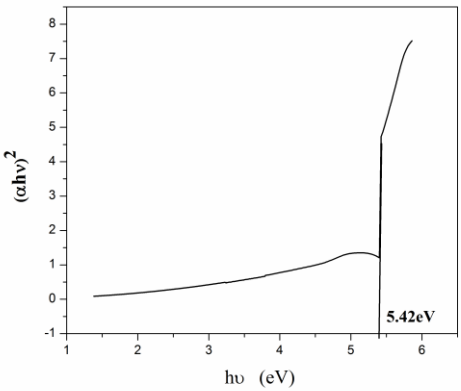

Figure 3.(a) UV-Vis absorption spectrum of LLM **Figure 3. (b)** Plot of $(\alpha h\nu)^2$ versus hν of LLM

The optical absorption coefficient α is calculated using the following relation α = Abs/t where Abs is the absorbance and t is the thickness of the crystal [8]. The optical energy band gap of the crystal is determined from the transmittance spectra using the relation $\alpha h\nu = A(h\nu - E_g)^{1/2}$ where A is a constant which varies with transitions, h is the Plank's constant, ν is the frequency of the photon, Eg is the band gap of the material. The band gap of LLM crystal was estimated by plotting $(\alpha h\nu)^2$ versus hν as shown in Figure. 3b. As per Tauc's idea, the optical band gap has been calculated from the extrapolation of linear part at absorption edge. The value of band gap was found to be 5.42 eV. As a consequence of wide band gap, the grown crystal has large absorption in the visible region.

3.3. FT-IR analysis

The FTIR spectra of the grown LLM single crystal were observed on the powder sample is shown in Figure. 4. The FTIR spectrum of LLM crystal was recorded using the Brukers IFS66 spectrometer in the range 4000 – 400 cm^{-1} by KBr pellet to identify the functional group present in the crystal. The medium intensity band at 3131 cm^{-1} appearing in IR spectrum is due to the NH_3^+ asymmetric stretching mode [9]. The stretching vibrations of the CH_2 group have been observed in the region 2960–2840 cm^{-1}. The position and intensity of the peaks are at 2959 cm^{-1} [10,11] and 2873 cm^{-1} is due to the asymmetric and symmetric stretching of CH_2 group of LLM [4,9]. The combination and overtone vibrations overlap in the range 2653 – 1880 cm^{-1} [4]. The strong carboxyl absorption at 1730 cm^{-1} is assigned to C=O stretching confirms the –COOH and $COO^{-1}$of compound [1,2]. The presence of N-H bending observed at 1572 cm^{-1} confirms presence of amino acid in the crystal lattice [9]. The absorption at 1390 cm^{-1} is due to the COO- ions. CH_2 wagging vibration is absorbed due to the peak at 1321 cm^{-1}[8,12]. The symmetric C-O stretching frequency is observed at 1241 cm^{-1} in the spectrum[13,4]. The broad band of CH_2 wagging vibration absorbed at 1035 cm^{-1} and CH_2 rocking vibration between 839 – 894 cm^{-1}. The strong band of the C-C stretching is observed at 867 cm^{-1} [3,4]. The COO^{-1} bending, scissoring, wagging vibrations observed at 749, 662, 589 cm^{-1}. The vibrational study confirms the LLM exists as zwitterions in which the carboxyl group is present as COO^- Carboxylate ion and the amino group exists as NH_3^+ ammonium ion.

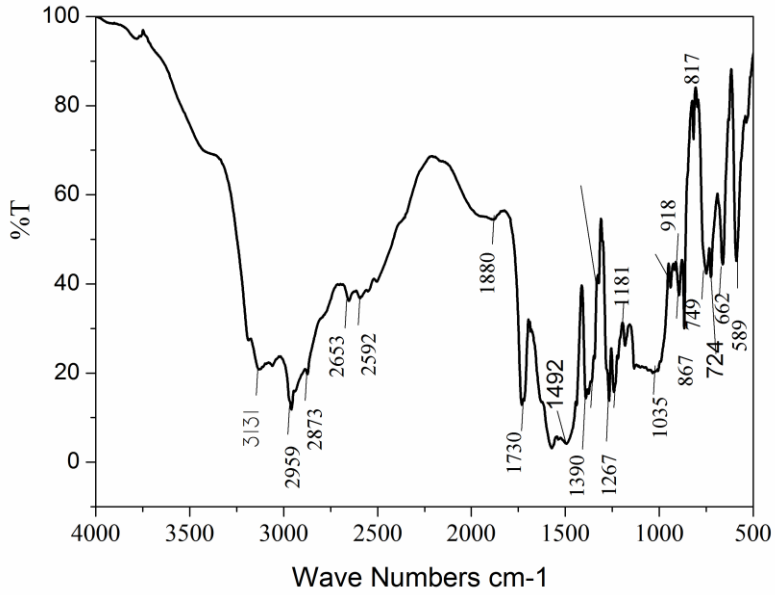

.

Figure 4 FT-IR spectrum of the grown LLM crystal

3.4. FT-RAMAN analysis

Figure 5 shows the Raman spectra of LLM crystals recorded in the range of 500 – 3500cm^{-1} at room temperature using Bruker IFS27 Raman spectrograph. The peaks at 3058.47 cm^{-1} confirm NH_3^+ stretching of amino group. The strong band at 1695 cm^{-1} and a shoulder at 1623 cm^{-1} are attributed to NH_3^+ asymmetric deformation mode. The peak against 2961 cm^{-1} and 2936 cm^{-1} are corresponding to the CH_2 asymmetric stretching vibrations. NH_3^+ rocking is observed at 1179 cm^{-1}. Symmetric stretching of CH band in the Raman spectrum is at 2871 cm^{-1}. C-C stretching revealed due to the peak at 1460 cm^{-1} 897 cm^{-1}. The corresponding COO^{-1} symmetric and COO^- wagging are confirmed due to the peaks at 1390 cm^{-1} in FT Raman spectrum. NH_3^+ rocking is observed at 1179 cm^{-1} and 962 cm^{-1}. Therefore the functional groups identified by FT-IR spectrum are also confirmed by FT-RAMAN spectrum.

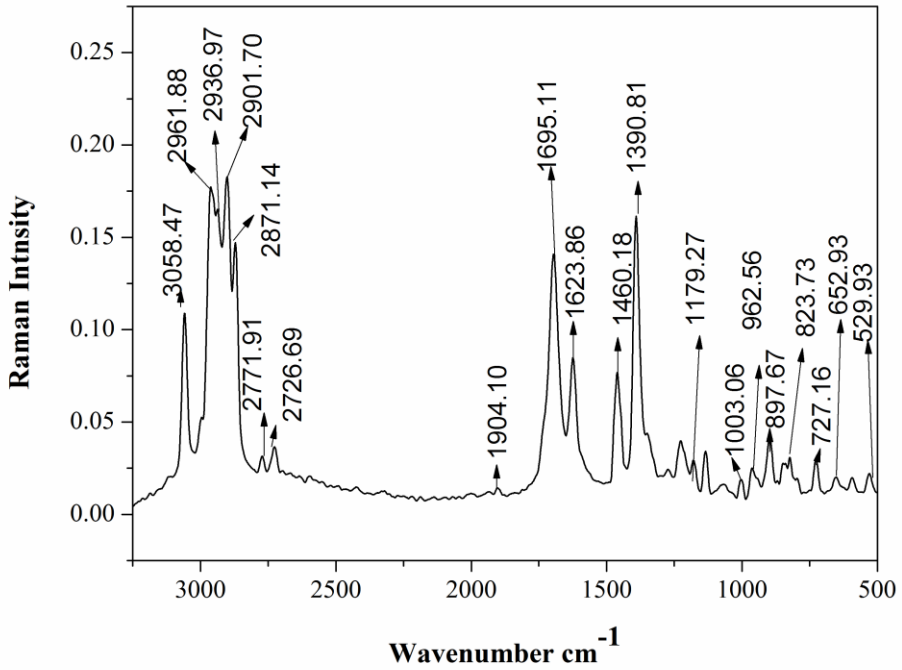

Figure 5. FT –Raman spectrum of the grown LLM crystal.

3.5. Thermal analysis

Thermo gravimetric and Differential thermal analysis gives information regarding phase transition, water of crystallization and different stages of decomposition of the crystal. The Thermo gravimetric analysis (TGA) and Differential Thermal analysis (DTA) of the crystal were carried out between 25˚C to 650˚C at a heating rate of 10K/min in the nitrogen atmosphere. The resulting spectrum is shown in Figure 6. There was no weight loss up to 140˚C, hence the material is free of any solvent entrapped in the crystal lattice. The TGA curve shows a weight loss in one stage and the same near 150˚C .is assigned to loss of water. The weight loss due to water is also associated with melting of the sample, which is clearly observed in the DTA curve as an endothermic transition occurred at 142˚C. At this temperature, LLM and water molecule were dissociated from the compound and the LLM started to melt as its melting point is nearly 150˚C, an exothermic transition as observed at 478˚C and 554˚C in the DTA curve. From the results of DTA it is established that no

transformation in structure was observed before melting. Hence the material can be exploited for any suitable application up to its melting.

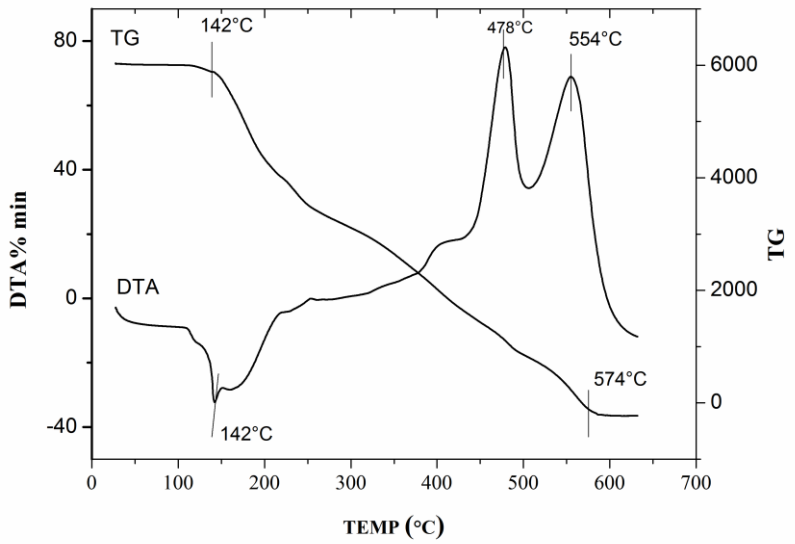

Figure 6.TG/DTA curve for LLM crystal

3.6. Nonlinear optical studies

Second harmonic generation efficiency of the grown crystal was confirmed using Kurtz and Perry powder technique [14]. A Q-switched Nd: YAG laser emitting a fundamental wavelength of 1064nm and a pulse width of 8ns with a repetition rate of 10 Hz was used. The incident input energy of 0.7J/s was incident on the crystalline powder packed between two transparent glass slides. The emission of green light from the sample confirmed the frequency doubling of LLM crystal. The second harmonic generation output signal of 2.98mW obtained for LLM crystal whereas the standard KDP crystal gave an SHG signal of 5.03mW for the same input energy. Hence, SHG efficiency of LLM crystal was 0.6 times that of potassium dehydrogenate phosphate (KDP) crystal.

4. Conclusion

Single crystals of L-Leucenium maleate (LLM) were successfully grown by slow evaporation technique at room temperature. Powder X-ray diffraction analysis reveals the monoclinic crystalline nature of the LLM crystal. The UV-Vis-NIR studies shows that these crystals are transparent in the entire visible region with a lower cut-off wavelength 212 nm and band gap value were calculated for LLM crystal. The presence of various functional groups was identified by FT-IR analysis and is confirmed by FT-Raman. The TG/DTA studies established that the compound undergoes no phase transition and is stable up to 150°C. The SHG efficiency studies show the suitability of the crystals for NLO application.

Acknowledgments

The corresponding author gratefully acknowledges the support from the Department of Science and Technology (DST), Government of India for the research project (SB/EMEQ/248/2014).

References

[1] Victor Antony Raj M and Madhavan J, 2011 Linear and nonlinear optical properties of pure and doped L-alaninium maleate single crystals *J. Archives of Physics Research (Scholars Research Library)* **2(1)** 160-168.
[2] Fuchs B A,Chaisyn K, StephanVelsko P,1989 Electrical Studies on Organic Nonlinear Optical Single Crystal: L-leucine Nitrate *J. Appl Opt* **28** 113-119.
[3] Natarajan S, Brito S A M, and Ramachandiran E S, 2006 Growth Thermal Spectroscopic and optical Studies of L-Alaninium Maleate a New Organic Nonlinear Optical Material Optical Material *J. Crystal Growth and design* **6** 137-140.
[4] Baraniraj.T., PhilominathanP.2010, Growth and Characterization of NLO based L-arginine maleate dihydrate single crystal *J. Spectrochem Acta.***75A** 74-76.
[5] Sergey G Arkhipov, Denis A Rychkov, Alexey M Pugachev and Elena V Boldyreva, 2015 New hydrophobic L-amino acid salts: maleates of L-Leucine L-Isoleucine and L- Norvaline *J. Acta Crystal Structural Chemistry* **C17** 1-9**.**
[6] Rodrigues Jr J J, Misoguti L, Nunes F D, Mendonca C R, Zilio S C, 2003 Optical properties of L-threonine crystals, *J. Opt Mater* **22** 235-240.
[7] Prakash.M,.Geetha D, Lydia Caroline M, 2011 Crystal growth and characterization of L-phenylalaninium trichloroacetate-A new organic nonlinear optical material, *J.Physica B.* **406(13)** 2621-25.
[8] MohdShkir, Haider Abbas, 2014 Physico chemical properties of L-asparagine L-tartaric acid single crystals: A new nonlinear optical material *J. Spectrochemica Acta Part A:Molecular and biomolecular.Spectroscopy* **118** 172-176.
[9] Soma Adhikari, TanusreeKar, 2012 Bulk single crystals growth and characterization of L-Luecine- A nonlinear optical material ,*J. Material Chemistry and physics* **133** 1055-1059.
[10] Bhagavananarayan G, Riscop B, Mohemed Shakir, 2011 Growth and characterization of L-Luecine L-Leucinium picrate single crystal: A new nonlinear optical material, *J. Materials Chemistry and Physics* **126** 20-23.
[11] Madhavan J, Aruna S, Anuradha A, Premanand D,VethaPotheher I,Thamizharasan K, Sagayaraj P, 2007 Growth and characterization of a new nonlinear optical L-histedine acetate single crystal *J. Optical Materials* **29** 1211-16.
[12] Brigt Mary.M,Sasirekha.V,Ramakrishnan.V,2006,Vibrational spectral analysis of DL-valine DL-valinium and DL-methionine DL-methioninium picrates *J. Spectrochemica Acta Part A* **65** 955-963.
[13] Praveen Kumar P, Manivannan V, Tamilselvan S, Senthil S, Victor Antony Raj, Sagayaraj P Madhavan J, 2008 Growth and characterization of a pure and doped nonlinear optical L-histidine acetate single crystals *Optics Communications* **281** 2989-95.
[14] Kurtz S K. Perry T T, 1968 A Powder Technique for the Evaluation of Nonlinear Optical Materials *J. Appl. Phys.* **39** 3798-13**.**

Kohonen SOM Deployment in Android App-based Cognitive Behavioral Therapy for Personality Disorders

Chris M Jayachandran, Asst. Professor
Dept. of Computer Apps (MCA), Loyola College
Chennai – 600 034 /
Ph.D (Part-time) Research Scholar,
University of Madras, Chennai – 600 005
Tamil Nadu, INDIA.

Dr. K. Shyamala, Associate Professor & Research Guide, PG and Research Dept. of Computer Science
Dr. Ambedkar Govt. Arts College (Autonomous)
University of Madras
Chennai – 600 005
Tamil Nadu, INDIA.

***Abstract*— Deployment of Kohonen's SOM Algorithm in Smartphone App-based Cognitive Behavioral Therapy for Personality Disorders is one of its kinds Research Work. The crux of the research paper is to highlight the scope of Android App-based Cognitive Behavioral Therapy in coping up with, and conquering various forms of Personality Disorders, by empowering the Android App to Self-learn. Such prowess on the part of the envisioned Android App will be harnessed through Kohonen's SOM Algorithm. This paper also explores the confinements of the research pursuit jointly embarked by the scientists at the universities of Liverpool and Manchester, UK; christened 'Catch It' which is an iOS-based smartphone App using the basic principles of CBT in treating depression and anxiety. Furthermore, this research paper establishes that the aforementioned 'Catch It' app lacks the axioms and evidently amplifies as to how the proposed research work will be a systemic advancement, being more scientific and having more scope to yielding measurable results over the 'Catch It' App.**

***Keywords*— *Personality disorders; Cognitive Behavioral Therapy (CBT), Kohonen SOM; Winner take-all strategy*.**

I. INTRODUCTION

It is estimated that during 2016, the global Behavioral Therapy Industry will reach a whopping market capitalization of $8 billion.[1] According to the National Institute of Mental Health, more than a quarter of American adults experience depression, anxiety or another mental disorder in any given year.[2] In India, a country with a population of 1.2 billion, as many as 65 million are suffering from mental diseases. As many as 20% of teenagers in India reported a lifetime prevalence of depression.[3] There are around 14 000 healthcare smartphone apps available, of which around 6% are devoted to mental health. 'Catch It' is an innovative iOS App which uses the basic principles of CBT and has been developed jointly by the universities of Liverpool and Manchester, UK.[4] However, such app does not offer cost-affordability or comprehensive applicability to the slew of personality disorders, on the premises of any ANN algorithm that empowers the app to self-learn. Deployment of Kohonen SOM Algorithm in Cognitive Behavioral Therapy for Personality Disorders, a pioneering effort is the amalgamation of the fields of Cognitive Neuropsychology and Artificial Neural Networks. In the concluding segment of this paper, 'Saturation of Threshold Value', the rationale for the freezing of 'Threshold Value' is being discussed. Such thoughtfully and scientifically constructed Android App will be the world's first App, surpassing numerous Computerized CBT Applications. The hallmark of this App will be Personification along with 0% cost associated with it.

II. COMPUTERIZED COGNITIVE BEHAVIORAL THERAPY

There are cognitive behavioral therapy sessions in which the user interacts with computer software (either on a PC, or sometimes via a voice-activated phone service), instead of face to face with a therapist. This can provide an option for patients, especially in light of the fact that there are not always therapists available, or the cost can be prohibitive. For people who are feeling depressed and withdrawn, the prospect of having to speak to someone about their innermost problems can be off-putting. In this respect, computerized CBT / especially if delivered through a Smartphone App can be a good option which will apparently offset the drawbacks of a Computerized CBT.

III. ANDROID-BASED APP FOR CBT WITH KOHONEN'S SOM ALGORITHM

The Kohonen SOM Nets[5] (Kohonen 1988) consists of a single layer of nodes (plus an input layer). Each node receives inputs from the environment and from the other nodes within the layer. When we build a Kohonen network, it is important to properly initialize the weight vectors and input vectors are normalized to a constant (typically unit length). Each node computes by taking the dot product of its weights vector and the input vector. The result reflects their similarity (or distance). Symbolically,

$$O_j = X.\ W_j$$

978-1-5090-5573-9/17 $31.00 © 2017 IEEE
DOI 10.1109/WCCCT.2016.69

where O_j is the activation level of unit j, X is the input vector, and W_j is the weight vector of unit j. Suppose we place all weight vectors in a matrix called a matrix **w**, and let the vector **O** represent the activations of all nodes. Then we obtain

$$O = X.W$$

Next, we examine the functionality of the Kohonen network: clustering, learning, statistical modeling, and topology preservation.

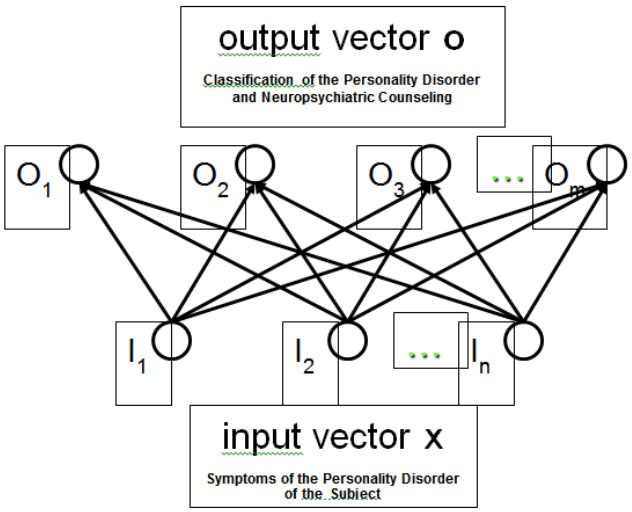

Figure 1.Kohonen's Self-Organizing Algorithm in Android-based App for CBT

Kohonen's Self-Organizing Network (adapted)

- **Weight Initialization**
  - Weights are initialized to small random values.
  - The initial radius of the neighborhood is set properly.
- **Calculation of Activation**
  1. The activation X_i of input unit *i* is determined by the instance presented to the network.
  2. The activation O_j of output unit *j* is calculated by

$$O_j = F_{min}(d_j) = F_{min}\left(\sum_i (X_i - W_{ji})^2\right)$$

where F_{min} is the unity function (returning 1) if unit *j* is the output node with minimum d_j or its neighbor, and the zero function (returning 0) otherwise. (Note that if the weight vectors are normalized to constant length, then we may calculate the inner dot product of the input and the weights to find the node with a maximum value.)

- **Weight Training**
  1. Weight modification is given by

$$\Delta W_{ji} = O_j \eta (X_i - W_{ji})$$

Where is a gain term ($0 < \eta < 1$) that decreases over time. Note that the radius of the neighborhood also does so.

2. Repeat by presenting a new instance, calculating activations, and modifying weights until $\eta = 0$.

IV. PERSONALITY INVENTORY FOR SETTING THE THRESHOLD VAULE

A. Administering of Questionnaire

The admisnistered Questionnaire for the deployment of Kohonen's SOM Network Algorithm in Android-app based CBT embodies **Close-Ended Questions.**

Experimental Design using "Close-ended" Questionnaires with Seven Options such as 'Never', 'Very Rarely', 'Rarely, Sometimes', 'Frequently', 'Very Frequently', and 'Always'. The Seven Options as exercised by the Respondents indicate the Onset, Prevalence and Chronic State of the Personality Disorders[6] and or Neuropsychiatric Disorders. The Questionnaire was administered to the Individuals who are adolescents and are in the adulthood.

V. EXTRACTION OF INFERENCES

The Formulated Questionnaire contains 30 already-predetermined Close-ended Questions. All the 30 Questions have been segmented to probe into the presence / onset of 10 Personality Disorders. Each of the Three Questions in every segment embodies the pathological / diagnostic questions.
Each of the question's options are being provided with an appropriate Weight such as the following:

- Do you prefer to be alone always?
  a) Never b) Very rarely c) Rarely d) Sometimes e) Frequently f) Very Frequently g) Always

This question reveals the fundamental mood type of a subject / person who suffers from Schizoid Personality Disorder.

If the respondent has chosen the option "(g) Always" then a Weight of 10 is being awarded. The Weights are given to the options from "(a) Never" to "(f) Very Frequently" are being awarded with 0, 1, 2, 3, 5, 7 respectively.
Some Questions are constructed with reverse options. Such as the following:

- Do you easily go ahead and express your warmth or love for friends, parents, and the dear-ones?
  a) Never b) Very rarely c) Rarely d) Sometimes e) Frequently f) Very Frequently g) Always

If the respondent has chosen the option "(a) Never" then a Weight of 10 is being awarded. The Weights are given to the options from "(b) *Very rarely*" to "(g) Always" are being awarded with 7, 5, 3, 2, 1, 0 respectively.
Thus, it will be concluded that if a person's / subject has the maximum total in any of the 10 segments (comprising of three

questions, representing a Personality Disorder), then the subject could be suffering from that particular disorder. This signifies the **"Winner Take-All Strategy"** in the Kohonen SOM Neural Networks.

If a subject does not score maximum score in any of the 10 Segments and has scored equal total in few segments, then those segments will be passing on their output level to the next closely associated personality disorder with the equal score. For example, if a subject has scored a total of 15 each for the segments (comprising of three questions) Narcissistic Personality Disorder and Antisocial Personality Disorder; the score for a particular question in the Narcissistic Personality Disorder which is very closely related to Antisocial Personality Disorder could be summed up with the already available total of 15 for the segment of three questions representing Antisocial Personality Disorder. This being done, the proposed Android App-based CBT could conclude that the subject may be suffering from Antisocial Personality Disorder. This establishes the concept of Kohonen's SOM Neural Networks, viz., the output of each node (questions segment for the personality disorder) can act as an inhibitory input to the other nodes. Thus, even though there is only one winner node, more than one node are allowed to change their weights **(Lateral inhibition)**.

Similarly as per Kohonen's recommendation, this inhibitory effect of node can also decrease, if the questions in one node (questions segment for the personality disorder), in no way related to any other node; that is no correlation with any other personality disorder. Thus, whatever segment having the maximum total emerges as the winner and prompts the personality disorder that the patient / subject may be suffering from, with all other nodes being suppressed to **Zero Activation Level**. Once the personality disorder with the subject being identified, appropriate CBT procedure can be initiated using the proposed Android-App based CBT.

VI. ASSUMPTIONS OF THE RESEARCH ENDEAVORED

The following are the various Assumptions of this Research which can also be construed as the limitations:

- It is assumed that the Questionnaire administered contains the right questions with which the symptoms of a Personality Disorder / Onset of a Personality Disorder can be traced effectively.
- It is believed that the Respondents did not answer very casually or without realizing what information is being asked for.
- The scoring method adopted has not been approved by any Clinical Psychiatrist, in which case after finding the symptoms, a through interaction and other pathological methods could be used to actually check whether the conclusion drawn holds good.
- The CBT method proposed is the Comprehensive and the best-one. Furthermore, the CBT may not be effective with all the subjects[7] (persons identified to have Personality Disorder), who can only be cured with medications.

VII. CONCLUSIONS

The suggested Kohonen SOM Neural Network Algorithm can be extended to different facets of Neuropsychology, especially with regard to probing cognitive capacities of a Person and his / her Behavioral Implications such as in selection of pupils for courses in any of specialized fields, in recruiting personnel in sensitive positions that require someone who is emotional stable and has a better outlook without any inclination to Personality Disorders(s), in forming Teams that require highly skilled and coordinated members who will be entrusted with mission critical projects both in the Private and Public Sector / State-owned enterprises. Unlike several hundred remotely-related computerized CBT, which are available at exorbitant price per user, with varying results as they do not stem neither from any universally proven algorithm nor prone to be applicable to all personality disorders; the resultant Android App of this research endeavor will be providing a consistent outcome when used by the people with various personality disorder.

REFERENCES

[1] Behavioral Therapists Market Research Report, Issue Mar 2016 available at http://www.ibisworld.com/industry/behavioral-therapists.html

[2] http://www.apa.org/helpcenter/ understanding-psychotherapy.aspx

[3] Agrawal, G. (2015). Psychology in India: A Career with Uncertain Opportunities. Online Journal of Multidisciplinary Research, 1(2): 1-7.

[4] Peter Kinderman & team (2016), The British Journal of Psychiatry - The feasibility and effectiveness of Catch It, an innovative CBT smartphone app.. BJPsych Open (2016) 2, 204–209. doi: 10.1192/bjpo.bp.115.002436. AppStore Link - http://appstore.liv.ac.uk/catch-it/

[5] A LiMin Fu**,** "Neural Networks in Computer Intelligence", Tata McGraw Hill Publications 2003 Edition.

[6] Mario Maj, Hagop S. Akiskal, Juan E. Mezzich, Ahmed Okasha , " Personality Disorders", WPA Series Evidence and Experience in Psychiatry Volume 8.

[7] Jan Derksen, Cesare Maffei, Herman Groen," Treatment of Personality Disorders".

Synthesis, Structural, Optical and Dielectric Properties of Cadmium Sulfide Nanoparticles as Photocathode for a Solar Cell

Recent Trends in Materials Science and Applications pp 159-170 | Cite as

- F. Michael Raj (1)
- A. Jeya Rajendran (1) Email author (jeyarajendran@yahoo.com)

1. Advanced Materials Research Lab, Department of Chemistry, Loyola College, , Chennai, India

Conference paper
First Online: 04 May 2017

Part of the Springer Proceedings in Physics book series (SPPHY, volume 189)

Abstract

Cadmium sulfide nanoparticles were prepared by chemical co-precipitation method using cadmium acetate, sodium sulfide and tetrabutylammonium bromide (TBAB) as a capping agent. The synthesized nanoparticles were characterized by using UV-Vis spectroscopic analysis, X-ray diffraction analysis (XRD), Field emission scanning electron microscopic analysis (FESEM), Energy dispersive X-ray analysis (EDAX) and BET surface area nitrogen adsorption-desorption analysis. The band gap of capped CdS was calculated by using UV-Vis absorption spectrum as 3.23 eV. The X-ray diffraction pattern

revealed that the synthesized cadmium sulfide nanoparticles were polycrystalline nature with wurtzite hexagonal structure and crystallite size was calculated as 7.2 nm by using Debye Scherer method. The surface area, pore volume and pore size were found to be 93.15 m^2/g, 1.64×10^{-2} cm^3/g and 6.2 Å by BET nitrogen adsorption-desorption analysis. The dielectric constant , dielectric loss and AC conductivities were studied over a range of frequency (50 Hz–5 MHz) and temperature (40–200 °C). Solar cell was fabricated using cadmium sulfide as photocathode, titanium dioxide as photoanode, potassium iodide/iodine as an electrolyte solution, ruthenium dye as a sensitizer and power conversion efficiency was found to be 2.7 %.

Keywords

Dielectric Loss Cadmium Sulfide Tetrabutylammonium Bromide Cadmium Acetate Sodium Sulfide

These keywords were added by machine and not by the authors. This process is experimental and the keywords may be updated as the learning algorithm improves.

Notes

Acknowledgements

The authors gratefully acknowledge the financial support provided by UGC (India) for the project [**F.No. 41-1005/2012 (SR)]**.

References

1. Kandasamy, K., Singh, H.B., Kulshreshtha, S.K.: Synthesis and characterization of CdS and CdSe nanoparticles prepared from novel intramolecularly stabilized single-source precursors. J. Chem. Sci. **121**, 293–296 (2009)

Google Scholar (https://scholar.google.com/scholar?q=Kandasamy%2C%20K.%2C%20Singh%2C%20H.B.%2C%20Kulshreshtha%2C%20S.K.%3A%20Synthesis%20and%20characterization%20of%20CdS%20and%20CdSe%20nanoparticles%20prepared%20from%20novel%20intramolecularly%20stabilized%20single-source%20precursors.%20J.%20Chem.%20Sci.%20121%2C%2093%E2%80%93296%20%282009%29)

2. Ikhmayies, S.J.: Characterization of nanocrystalline CdS thin films prepared by thermal evaporation. J. Mater. Chem. **3**, 28–33 (2013)
Google Scholar (https://scholar.google.com/scholar?q=Ikhmayies%2C%20S.J.%3A%20Characterization%20of%20nanocrystalline%20CdS%20thin%20films%20prepared%20by%20thermal%20evaporation.%20J.%20Mater.%20Chem.%203%2C%2028%E2%80%9333%20%282013%29)

3. Thilagavathi, T., Geetha, D.: Nano ZnO structures synthesized in presence of anionic and cationic surfactant under hydrothermal process. Appl. Nanosci. **4**, 127–132 (2012)
Google Scholar (https://scholar.google.com/scholar?q=Thilagavathi%2C%20T.%2C%20Geetha%2C%20D.%3A%20Nano%20ZnO%20structures%20synthesized%20in%20presence%20of%20anionic%20and%20cationic%20surfactant%20under%20hydrothermal%20process.%20Appl.%20Nanosci.%204%2C%20127%E2%80%93132%20%282012%29)

4. Prabhu, R.R., Abdul Khaddar, M.: Characterization of chemically synthesized CdS nanoparticles. Pramana J. Phys. **65**, 801–807 (2005)
Google Scholar (https://scholar.google.com/scholar?q=Prabhu%2C%20R.R.%2C%20Abdul%20Khaddar%2C%20M.%3A%20Characterization%20of%20chemically%20synthesized%20CdS%20nanoparticles.%20Pramana%20J.%20Phys.%2065%2C%20801%E2%80%93807%20%282005%29)

5. Khiew, P.S., Haung, N.H., Radiman, S., Ahmad, M.S.: Synthesis and characterization of conducting polyaniline-coated cadmium sulphide nanocomposites in reverse microemulsion. Mater. Lett. **58**, 516–521 (2004)
Google Scholar (https://scholar.google.com/scholar?q=Khiew%2C%20P.S.%2C%20Haung%2C%20N.H.%2C%20Radi

man%2C%20S.%2C%20Ahmad%2C%20M.S.%3A%20Synthesis%20and%20characterization%20of%20conducting%20polyaniline-coated%20cadmium%20sulphide%20nanocomposites%20in%20reverse%20microemulsion.%20Mater.%20Lett.%2058%2C%20516%E2%80%93521%20%282004%29)

6. Elango, M., Nataraj, D., Thamilselvan, M.: Synthesis and characterization of nickel doped cadmium sulphide. Mater. Res. Bull. **47**, 1533–1538 (2012)
Google Scholar (https://scholar.google.com/scholar?q=Elango%2C%20M.%2C%20Nataraj%2C%20D.%2C%20Thamilselvan%2C%20M.%3A%20Synthesis%20and%20characterization%20of%20nickel%20doped%20cadmium%20sulphide.%20Mater.%20Res.%20Bull.%2047%2C%201533%E2%80%931538%20%282012%29)

7. Rao, B.S., Kumar, B.R., Reddy, V.R., Rao, T.S.: Preparation and characterization of CdS nanoparticles by chemical co-precipitation technique. Chalcogenide Lett. **8**, 177–185 (2011)
Google Scholar (https://scholar.google.com/scholar?q=Rao%2C%20B.S.%2C%20Kumar%2C%20B.R.%2C%20Reddy%2C%20V.R.%2C%20Rao%2C%20T.S.%3A%20Preparation%20and%20characterization%20of%20CdS%20nanoparticles%20by%20chemical%20co-precipitation%20technique.%20Chalcogenide%20Lett.%208%2C%20177%E2%80%93185%20%282011%29)

8. Meera, J., Sumithra, V., Seethu, R., Prajeshkumar, J.M.: Dielectric properties of Nanocrystalline ZnS. Acad. Rev. **1**, 93–100 (2010)
Google Scholar (https://scholar.google.com/scholar?q=Meera%2C%20J.%2C%20Sumithra%2C%20V.%2C%20Seethu%2C%20R.%2C%20Prajeshkumar%2C%20J.M.%3A%20Dielectric%20properties%20of%20Nanocrystalline%20ZnS.%20Acad.%20Rev.%201%2C%2093%E2%80%93100%20%282010%29)

9. Choubey, S.K., Tiwary, K.P.: Microwave assisted synthesis of CdS nanoparticles for structural and optical characterization. IJIRSET **3**, 10670–10674 (2014)
Google Scholar (https://scholar.google.com/scholar?q=Choubey%2C%20S.K.%2C%20Tiwary%2C%20K.P.%3A%20Microwave%20assisted%20synthesis%20of%20CdS%20nanoparticles%20for%20structural%20and%20optical%20characterization.

%20IJIRSET%203%2C%2010670%E2%80%9310674%20%282014%29)

10. Elango, M., Gopalakrishnan, K., Vairam, S., Thamilselvan, M.: Structural, optical and magnetic studies on non-aqueous synthesized CdS:Mn nanomaterials. J. Alloy. Compd. **538**, 48–55 (2012)
Google Scholar (https://scholar.google.com/scholar?q=Elango%2C%20M.%2C%20Gopalakrishnan%2C%20K.%2C%20Vairam%2C%20S.%2C%20Thamilselvan%2C%20M.%3A%20Structural%2C%20optical%20and%20magnetic%20studies%20on%20non-aqueous%20synthesized%20CdS%3AMn%20nanomaterials.%20J.%20Alloy.%20Compd.%20538%2C%2048%E2%80%9355%20%282012%29)

11. Arellano, I.H.J., Mangadlao, J., Ramiro, I.B., Suazo, K.F.: 3-component low temperature solvothermal synthesis of colloidal cadmium sulfide quantum dot. Mater. Lett. **64**, 785–788 (2010)
Google Scholar (https://scholar.google.com/scholar?q=Arellano%2C%20I.H.J.%2C%20Mangadlao%2C%20J.%2C%20Ramiro%2C%20I.B.%2C%20Suazo%2C%20K.F.%3A%203-component%20low%20temperature%20solvothermal%20synthesis%20of%20colloidal%20cadmium%20sulfide%20quantum%20dot.%20Mater.%20Lett.%2064%2C%20785%E2%80%93788%20%282010%29)

12. Lu, H.Y., Chu, S.Y., Tan, S.S.: The characteristics of low-temperature- synthesized ZnS and ZnO nanoparticles. J. Cryst. Growth. **269**, 385–391 (2004)
Google Scholar (https://scholar.google.com/scholar?q=Lu%2C%20H.Y.%2C%20Chu%2C%20S.Y.%2C%20Tan%2C%20S.S.%3A%20The%20characteristics%20of%20low-temperature-%20synthesized%20ZnS%20and%20ZnO%20nanoparticles.%20J.%20Cryst.%20Growth.%20269%2C%20385%E2%80%93391%20%282004%29)

13. Chou, C.S., Yang, R.Y., Weng, M.H., Yeh, C.H.: Study of the applicability of TiO_2/Dye composite particles for a Dye sensitized Solar Cell. Adv. Powder. Technol. **19**, 541–558 (2007)
Google Scholar (https://scholar.google.com/scholar?q=Chou%2C%20C.S.%2C%20Yang%2C%20R.Y.%2C%20Weng%2C%20M.H.%2C%20Yeh%2C%20C.H.%3A%20Study%20of%20t

he%20applicability%20of%20TiO2%2FDye%20composite%20particles%20for%20a%20Dye%20sensitized%20Solar%20Cell.%20Adv.%20Powder.%20Technol.%2019%2C%20541%E2%80%93558%20%282007%29)

14. Onwudiwe, D.C., Strydom, C.A., Oluwafemi, O.S.: Effect of some nitrogen donar ligands on the optical and structural properties of CdS nanoparticles. New J. Chem. **37**, 834–842 (2013)
Google Scholar (https://scholar.google.com/scholar?q=Onwudiwe%2C%20D.C.%2C%20Strydom%2C%20C.A.%2C%20Oluwafemi%2C%20O.S.%3A%20Effect%20of%20some%20nitrogen%20donar%20ligands%20on%20the%20optical%20and%20structural%20properties%20of%20CdS%20nanoparticles.%20New%20J.%20Chem.%2037%2C%20834%E2%80%93842%20%282013%29)

15. Pathak, C.S., Mandal, M.K., Agarwala, V.: Synthesis and characterization of Zinc sulphide Nanoparticles Prepared by Mechanochemical Route. Superlattices Microstruct. **58**, 135–143 (2013)
Google Scholar (https://scholar.google.com/scholar?q=Pathak%2C%20C.S.%2C%20Mandal%2C%20M.K.%2C%20Agarwala%2C%20V.%3A%20Synthesis%20and%20characterization%20of%20Zinc%20sulphide%20Nanoparticles%20Prepared%20by%20Mechanochemical%20Route.%20Superlattices%20Microstruct.%2058%2C%20135%E2%80%93143%20%282013%29)

16. Khan, Z.R., Zulfequar, M., Khan, M.S.: Chemical synthesis of CdS nanoparticles and their optical and dielectric studies. J. Mater. Sci **46**, 5412–5416 (2011)
Google Scholar (https://scholar.google.com/scholar?q=Khan%2C%20Z.R.%2C%20Zulfequar%2C%20M.%2C%20Khan%2C%20M.S.%3A%20Chemical%20synthesis%20of%20CdS%20nanoparticles%20and%20their%20optical%20and%20dielectric%20studies.%20J.%20Mater.%20Sci%2046%2C%205412%E2%80%935416%20%282011%29)

17. Jeya Rajendran, A., Prabhu, M., Eswara Moorthi, K., Celine Rose, I.R., Santhanaraj, D., Sugandhi, K., Radhika, S.: Dielectric and conductivity studies of stereo-selectively synthesized d- and l-nor- ephedrine. J. Therm. Anal. Calorim. **119**, 369–379 (2015)
Google Scholar (https://scholar.google.com/scholar?q=Jeya%20Rajendran%2C%20A.%2C%20Prabhu%2C%20M.%2C

%20Eswara%20Moorthi%2C%20K.%2C%20Celine%20Rose%2C%20I.R.%2C%20Santhanaraj%2C%20D.%2C%20Sugandhi%2C%20K.%2C%20Radhika%2C%20S.%3A%20Dielectric%20and%20conductivity%20studies%20of%20stereo-selectively%20synthesized%20d-%20and%20l-%20nor-%20ephedrine.%20J.%20Therm.%20Anal.%20Calorim.%20119%2C%20369%E2%80%93379%20%282015%29)

18. Onwudiwe, D.C., Arfin, T., Strydom, C.A.: Synthesis, Characterization and dielectric properties of N-butyl aniline capped CdS nanoparticles. Electrochim. Acta **116**, 217–223 (2014) Google Scholar (https://scholar.google.com/scholar?q=Onwudiwe%2C%20D.C.%2C%20Arfin%2C%20T.%2C%20Strydom%2C%20C.A.%3A%20Synthesis%2C%20Characterization%20and%20dielectric%20properties%20of%20N-butyl%20aniline%20capped%20CdS%20nanoparticles.%20Electrochim.%20Acta%20116%2C%20217%E2%80%93223%20%282014%29)

Copyright information

About this paper

Cite this paper as:

Michael Raj F., Jeya Rajendran A. (2017) Synthesis, Structural, Optical and Dielectric Properties of Cadmium Sulfide Nanoparticles as Photocathode for a Solar Cell. In: Ebenezar J. (eds) Recent Trends in Materials Science and Applications. Springer Proceedings in Physics, vol 189. Springer, Cham

- First Online 04 May 2017
- DOI https://doi.org/10.1007/978-3-319-44890-9_16
- Publisher Name Springer, Cham
- Print ISBN 978-3-319-44889-3
- Online ISBN 978-3-319-44890-9
- eBook Packages Physics and Astronomy

Personalised recommendations

Facile Synthesis, Formation Mechanism and Optical Properties of ZnO Nanostructures

Recent Trends in Materials Science and Applications pp 313-326 | Cite as

- Linu M. Johny (1)
- N. S. Nirmala Jothi (1) Email author (jmjnirmala@yahoo.co.in)
- P. Sagayaraj (1)

1. Department of Physics, Loyola College, , Chennai, India

Conference paper
First Online: 04 May 2017

Part of the Springer Proceedings in Physics book series (SPPHY, volume 189)

Abstract

ZnO is a very promising material because of its wide range of applications in electronics, photonics, optics and as energy storage materials. Zinc oxide nanorods were synthesized using a simple hydrothermal method at lower temperature and nano spheres by solvothermal method. The formation process of ZnO nanorods and nanospheres is discussed. The X-ray diffraction pattern indicates that the nanorods and nanospheres have hexagonal wurtzite structure. The high resolution transmission electron microscopy (HRTEM) images reveal that the synthesized ZnO nanorods grow along 〈001〉 direction. The optical properties were studied by UV visible absorption and photoluminescence spectroscopy.

Keywords

High Resolution Transmission Electron Microscopy
High Resolution Transmission Electron Microscopy Blue Emission
Strong Emission Peak
High Resolution Transmission Electron Microscopy Micrographs
These keywords were added by machine and not by the authors. This process is experimental and the keywords may be updated as the learning algorithm improves.

References

1. Grundmann, M., Wenckstern, H.V., Pickenhain, R., Nobis, Th, Rahm, A., Lorenz, M.: Electrical properties of ZnO thin films and optical properties of ZnO-based nanostructures. Superlattices Microstruct. **38**, 317–328 (2005)
ADS (http://adsabs.harvard.edu/cgi-bin/nph-data_query?link_type=ABSTRACT&bibcode=2005SuMi...38..317G)
CrossRef (https://doi.org/10.1016/j.spmi.2005.08.026)
Google Scholar (http://scholar.google.com/scholar_lookup?title=Electrical%20properties%20of%20ZnO%20thin%20films%20and%20optical%20properties%20of%20ZnO-based%20nanostructures&author=M.%20Grundmann&author=HV.%20Wenckstern&author=R.%20Pickenhain&author=Th.%20Nobis&author=A.%20Rahm&author=M.%20Lorenz&journal=Superlattices%20Microstruct.&volume=38&pages=317-328&publication_year=2005)
2. Xu, Q., Zhou, S., Schmidt, H.: Magnetic properties of ZnO nanopowders. J. Alloys Compd. **487**, 665–667 (2009)
CrossRef (https://doi.org/10.1016/j.jallcom.2009.08.033)
Google Scholar (http://scholar.google.com/scholar_lookup?title=Magnetic%20properties%20of%20ZnO%20nanopowders&author=Q.%20Xu&author=S.%20Zhou&author=H.%20Schmidt&journal=J.%20Alloys%20Compd.&volume=487&pages=665-667&publication_year=2009)

3. Hsu, C.L., Chen, K.C.: Improving piezoelectric nanogenerator comprises ZnO nanowires by bending the flexible PET substrate at low vibration frequency. J. Phys. Chem. C **116**(16), 9351–9355 (2012)
CrossRef (https://doi.org/10.1021/jp301527y)
Google Scholar (http://scholar.google.com/scholar_lookup?title=Improving%20piezoelectric%20nanogenerator%20comprises%20ZnO%20nanowires%20by%20bending%20the%20flexible%20PET%20substrate%20at%20low%20vibration%20frequency&author=CL.%20Hsu&author=KC.%20Chen&journal=J.%20Phys.%20Chem.%20C&volume=116&issue=16&pages=9351-9355&publication_year=2012)

4. Wang, X., Li, W., Liu, J., Wang, F., Kong, J., Qiu, S., Cuizhu, H., Lua, L.: Synthesis of nestlike ZnO hierarchically porous structures and analysis of their gas sensing properties. ACS Appl. Mater. Interfaces **4**, 817–825 (2012)
CrossRef (https://doi.org/10.1021/am201476b)
Google Scholar (http://scholar.google.com/scholar_lookup?title=Synthesis%20of%20nestlike%20ZnO%20hierarchically%20porous%20structures%20and%20analysis%20of%20their%20gas%20sensing%20properties&author=X.%20Wang&author=W.%20Li&author=J.%20Liu&author=F.%20Wang&author=J.%20Kong&author=S.%20Qiu&author=H.%20Cuizhu&author=L.%20Lua&journal=ACS%20Appl.%20Mater.%20Interfaces&volume=4&pages=817-825&publication_year=2012)

5. Barpuzary, D., Banik, A., Panda, A.N., Qureshi, M.: Mimicking heteroleptic dyes for an efficient 1D-ZnO based dye-sensitized solar cell using the homoleptic ruthenium(II) dipyridophenazine complex as a photosensitizer. J. Phys. Chem. C **119**(8), 3892–3902 (2015)
CrossRef (https://doi.org/10.1021/jp510422d)
Google Scholar (http://scholar.google.com/scholar_lookup?title=Mimicking%20heteroleptic%20dyes%20for%20an%20efficient%201D-ZnO%20based%20dye-sensitized%20solar%20cell%20using%20the%20homoleptic%20ruthenium%28II%29%20dipyridophenazine%20complex%20as%20a%20photosensitizer&author=D.%20Barpuzary&author=A.%20Banik&author=AN.%20Panda&author=M.%20Qureshi&journal=J.%20Phys.%20Chem.%20C&volume=119&issue=8&pages=3892-3902&publication_year=2015)

6. Shen, X., Mu, D., Chen, S., Wu, B., Wu, F.: Enhanced electrochemical performance of ZnO-loaded/porous carbon composite as anode materials for lithium ion batteries. Appl. Mater. Interfaces **5**, 3118–3125 (2013)
CrossRef (https://doi.org/10.1021/am400020n)
Google Scholar (http://scholar.google.com/scholar_lookup?title=Enhanced%20electrochemical%20performance%20of%20ZnO-loaded%2Fporous%20carbon%20composite%20as%20anode%20materials%20for%20lithium%20ion%20batteries&author=X.%20Shen&author=D.%20Mu&author=S.%20Chen&author=B.%20Wu&author=F.%20Wu&journal=Appl.%20Mater.%20Interfaces&volume=5&pages=3118-3125&publication_year=2013)

7. Liu, B., Zeng, H.C.: Hydrothermal synthesis of ZnO nanorods in the diameter regime of 50 nm. J. Am. Chem. Soc. **125**(15), 4430–4431 (2003)
CrossRef (https://doi.org/10.1021/ja0299452)
Google Scholar (http://scholar.google.com/scholar_lookup?title=Hydrothermal%20synthesis%20of%20ZnO%20nanorods%20in%20the%20diameter%20regime%20of%2050%20nm&author=B.%20Liu&author=HC.%20Zeng&journal=J.%20Am.%20Chem.%20Soc.&volume=125&issue=15&pages=4430-4431&publication_year=2003)

8. Xu, C., Shin, P., Cao, L., Gao, D.: Preferential growth of long ZnO nanowire array and its application in dye-sensitized solar cells. J. Phys. Chem. C **114**(1), 125–129 (2010)
CrossRef (https://doi.org/10.1021/jp9085415)
Google Scholar (http://scholar.google.com/scholar_lookup?title=Preferential%20growth%20of%20long%20ZnO%20nanowire%20array%20and%20its%20application%20in%20dye-sensitized%20solar%20cells&author=C.%20Xu&author=P.%20Shin&author=L.%20Cao&author=D.%20Gao&journal=J.%20Phys.%20Chem.%20C&volume=114&issue=1&pages=125-129&publication_year=2010)

9. Wang, C., Mao, B., Kang, Z., Tian, C.: Solution synthesis of ZnO nanotubes via a template-free hydrothermal route. Solid State Commun. **141**(11), 620–623 (2007)
ADS (http://adsabs.harvard.edu/cgi-bin/nph-data_query?link_type=ABSTRACT&bibcode=2007SSCom.141..620W)
CrossRef (https://doi.org/10.1016/j.ssc.2006.12.028)

Google Scholar (http://scholar.google.com/scholar_lookup?title=Solution%20synthesis%20of%20ZnO%20nanotubes%20via%20a%20template-free%20hydrothermal%20route&author=C.%20Wang&author=B.%20Mao&author=Z.%20Kang&author=C.%20Tian&journal=Solid%20State%20Commun.&volume=141&issue=11&pages=620-623&publication_year=2007)

10. Wang, X.D., Song, V.Z., Wang, L.: Nanowire and nanobelt arrays of zinc oxide from synthesis to properties and the novel devices. J. Mater. Chem. **17**(8), 711–720 (2007)
CrossRef (https://doi.org/10.1039/b616963p)
Google Scholar (http://scholar.google.com/scholar_lookup?title=Nanowire%20and%20nanobelt%20arrays%20of%20zinc%20oxide%20from%20synthesis%20to%20properties%20and%20the%20novel%20devices&author=XD.%20Wang&author=VZ.%20Song&author=L.%20Wang&journal=J.%20Mater.%20Chem.&volume=17&issue=8&pages=711-720&publication_year=2007)

11. Su,Y., Li, J., Luo, Z., Lua, B., Li, P.: Microstructure, growth process and enhanced photocatalytic activity of flower-like ZnO particles RSC Adv. (2016)
Google Scholar (https://scholar.google.com/scholar?q=Su%2CY.%2C%20Li%2C%20J.%2C%20Luo%2C%20Z.%2C%20Lua%2C%20B.%2C%20Li%2C%20P.%3A%20Microstructure%2C%20growth%20process%20and%20enhanced%20photocatalytic%20activity%20of%20flower-like%20ZnO%20particles%20RSC%20Adv.%20%282016%29)

12. Zhang, Y., Xu, J., Xiang, Q., Li, H., Pan, Q., Xu, P.: Brush-like hierarchical ZnO nanostructures: synthesis, photoluminescence and gas sensor properties. J. Phys. Chem. C **113**, 3430–3435 (2009)
CrossRef (https://doi.org/10.1021/jp8092258)
Google Scholar (http://scholar.google.com/scholar_lookup?title=Brush-like%20hierarchical%20ZnO%20nanostructures%3A%20synthesis%2C%20photoluminescence%20and%20gas%20sensor%20properties&author=Y.%20Zhang&author=J.%20Xu&author=Q.%20Xiang&author=H.%20Li&author=Q.%20Pan&author=P.%20Xu&journal=J.%20Phys.%20Chem.%20C&volume=113&pages=3430-3435&publication_year=2009)

13. Lu, L., Chen, J., Li L., Wang, W.: Direct synthesis of vertically aligned ZnO nanowires on FTO substrates using a CVD method and the improvement of photovoltaic performance .Nanoscale Res Lett. **7**(1), 293 (2012)
Google Scholar (https://scholar.google.com/scholar?q=Lu%2C%20L.%2C%20Chen%2C%20J.%2C%20Li%20L.%2C%20Wang%2C%20W.%3A%20Direct%20synthesis%20of%20vertically%20aligned%20ZnO%20nanowires%20on%20FTO%20substrates%20using%20a%20CVD%20method%20and%20the%20improvement%20of%20photovoltaic%20performance%20.Nanoscale%20Res%20Lett.%207%281%29%2C%20293%20%282012%29)

14. Wang, X., Ding, Y., Yuan, D., Hong, J., Liu, Y., Wong, C.P., Hu, C., Wang. Z.L.: Reshaping the tips of ZnO nanowires by pulsed laser irradiation. Nano Res. **5**(6) (2012)
Google Scholar (https://scholar.google.com/scholar?q=Wang%2C%20X.%2C%20Ding%2C%20Y.%2C%20Yuan%2C%20D.%2C%20Hong%2C%20J.%2C%20Liu%2C%20Y.%2C%20Wong%2C%20C.P.%2C%20Hu%2C%20C.%2C%20Wang.%20Z.L.%3A%20Reshaping%20the%20tips%20of%20ZnO%20nanowires%20by%20pulsed%20laser%20irradiation.%20Nano%20Res.%205%286%29%20%282012%29)

15. Vassieres, L., Keis, K., Lindquist, S.E.: Purpose built anisotropic metal oxide materials: 3D highly oriented arrays of ZnO. J. Phys. Chem. B **105**(17), 3350–3352 (2001)
CrossRef (https://doi.org/10.1021/jp010026s)
Google Scholar (http://scholar.google.com/scholar_lookup?title=Purpose%20built%20anisotropic%20metal%20oxide%20materials%3A%203D%20highly%20oriented%20arrays%20of%20ZnO&author=L.%20Vassieres&author=K.%20Keis&author=SE.%20Lindquist&journal=J.%20Phys.%20Chem.%20B&volume=105&issue=17&pages=3350-3352&publication_year=2001)

16. Hung, C.H., Whang, W.T.: A novel low-temperature growth and characterization of single crystal ZnO nanorods. Mater. Chem. Phys. **82**(3), 705–710 (2003)
CrossRef (https://doi.org/10.1016/S0254-0584(03)00331-6)
Google Scholar (http://scholar.google.com/scholar_lookup?title=A%20novel%20low-temperature%20growth%20and%20characterization%20of%20single%20crystal%20ZnO%20nanorods&author=CH.%20Hung&au

thor=WT.%20Whang&journal=Mater.%20Chem.%20Phys.&volume=82&issue=3&pages=705-710&publication_year=2003)

17. Yu, H.C., Bo, T.C., Chih, K.C., Ying, Y., Chun, T.Y., Heng, L., Tzy, R.L., Chien, C.L., Hao, C.K., Shing, C.W., Tien, C.L.: Ultrastrong mode confinement in ZnO surface plasmon nanolasers. ACS Nano **9**(4), 3978–3983
Google Scholar (https://scholar.google.com/scholar?q=Yu%2C%20H.C.%2C%20Bo%2C%20T.C.%2C%20Chih%2C%20K.C.%2C%20Ying%2C%20Y.%2C%20Chun%2C%20T.Y.%2C%20Heng%2C%20L.%2C%20Tzy%2C%20R.L.%2C%20Chien%2C%20C.L.%2C%20Hao%2C%20C.K.%2C%20Shing%2C%20C.W.%2C%20Tien%2C%20C.L.%3A%20Ultrastrong%20mode%20confinement%20in%20ZnO%20surface%20plasmon%20nanolasers.%20ACS%20Nano%209%284%29%2C%203978%E2%80%933983)

18. Alenezi, M.R., Alshammari, A.S., Alzanki, T.H., Jarowski, P., Henley, S.J., Ravi, S., Silva, P.: ZnO nanodisk based UV detectors with printed electrodes. Langmuir **30**(13), 3913–3921 (2014)
CrossRef (https://doi.org/10.1021/la500143w)
Google Scholar (http://scholar.google.com/scholar_lookup?title=ZnO%20nanodisk%20based%20UV%20detectors%20with%20printed%20electrodes&author=MR.%20Alenezi&author=AS.%20Alshammari&author=TH.%20Alzanki&author=P.%20Jarowski&author=SJ.%20Henley&author=S.%20Ravi&author=P.%20Silva&journal=Langmuir&volume=30&issue=13&pages=3913-3921&publication_year=2014)

19. Li, F., Gong, F., Xiao, Y., Zhang, A., Zhao, J., Fang, S., Jia, D.: ZnO twin-spheres exposed in (001) facets: stepwise self-assembly growth and anisotropic blue emission. Acsnano **7**(12), 10482–10491 (2013)
ADS (http://adsabs.harvard.edu/cgi-bin/nph-data_query?link_type=ABSTRACT&bibcode=2015Nanos...710482L)
Google Scholar (http://scholar.google.com/scholar_lookup?title=ZnO%20twin-spheres%20exposed%20in%20%28001%29%20facets%3A%20stepwise%20self-assembly%20growth%20and%20anisotropic%20blue%20emission&author=F.%20Li&author=F.%20Gong&author=Y.%20Xiao&author=A.%20Zhang&author=J.%20Zhao&author=S.%20Fang&author=D.%20Jia&journal=Acsnano&volume=7&issue=12&pages=10482-10491&publication_year=2013)

20. Alenezi, M.R., Henley, S.J., Emerson, N.G., Ravi, S., Silva, P.: From 1D and 2D ZnO nanostructures to 3D hierarchical structures with enhanced gas sensing properties
Google Scholar (https://scholar.google.com/scholar?q=Alenezi%2C%20M.R.%2C%20Henley%2C%20S.J.%2C%20Emerson%2C%20N.G.%2C%20Ravi%2C%20S.%2C%20Silva%2C%20P.%3A%20From%201D%20and%202D%20ZnO%20nanostructures%20to%203D%20hierarchical%20structures%20with%20enhanced%20gas%20sensing%20properties)

21. Baraneedharan, P., Siva, C., Nehru, K., Sivakumar, M.: Investigations on structural, optical and electrochemical properties of blue luminescence SnO_2 nanoparticles. J. Mater. Sci.: Mater. Electron. **25**, 255–261 (2014)
Google Scholar (http://scholar.google.com/scholar_lookup?title=Investigations%20on%20structural%2C%20optical%20and%20electrochemical%20properties%20of%20blue%20luminescence%20SnO2%20nanoparticles&author=P.%20Baraneedharan&author=C.%20Siva&author=K.%20Nehru&author=M.%20Sivakumar&journal=J.%20Mater.%20Sci.%3A%20Mater.%20Electron.&volume=25&pages=255-261&publication_year=2014)

22. Naveed ul, H.A.: Linköping studies in science and technology. Dissertation No. 1378 luminescence properties of ZnO nanostructures and their implementation as white light emitting diodes (LEDs) by ISBN: 978-91-7393-139-7
Google Scholar (https://scholar.google.com/scholar?q=Naveed%20ul%2C%20H.A.%3A%20Link%C3%B6ping%20studies%20in%20science%20and%20technology.%20Dissertation%20No.%201378%20luminescence%20properties%20of%20ZnO%20nanostructures%20and%20their%20implementation%20as%20white%20light%20emitting%20diodes%20%28LEDs%29%20by%20ISBN%3A%20978-91-7393-139-7)

23. Zeng, H., Duan, G., Li, Y., Yang, S., Xu, X., Cai, W.: Blue luminescence of ZnO nanoparticles based on non-equilibrium processes: defect origins and emission controls. Adv. Funct. Mater. **20**, 561–572 (2010)
CrossRef (https://doi.org/10.1002/adfm.200901884)
Google Scholar (http://scholar.google.com/scholar_lookup?title=Blue%20luminescence%20of%20ZnO%20nanoparticles%20based%20on%20non-equilibrium%20processes%3A%20defect%20origins%20and%20

emission%20controls&author=H.%20Zeng&author=G.%20Duan&author=Y.%20Li&author=S.%20Yang&author=X.%20Xu&author=W.%20Cai&journal=Adv.%20Funct.%20Mater.&volume=20&pages=561-572&publication_year=2010)

24. Cao, B., Teng, X., Heo, S.H., Li, Y., Cho, S.O., Li, G., Cai, W.: Different ZnO nanostructures fabricated by a seed-layer assisted electrochemical route and their photoluminescence and field emission properties. J. Phys. Chem. C **111**(6), 2470–2476 (2007)
CrossRef (https://doi.org/10.1021/jp066661l)
Google Scholar (http://scholar.google.com/scholar_lookup?title=Different%20ZnO%20nanostructures%20fabricated%20by%20a%20seed-layer%20assisted%20electrochemical%20route%20and%20their%20photoluminescence%20and%20field%20emission%20properties&author=B.%20Cao&author=X.%20Teng&author=SH.%20Heo&author=Y.%20Li&author=SO.%20Cho&author=G.%20Li&author=W.%20Cai&journal=J.%20Phys.%20Chem.%20C&volume=111&issue=6&pages=2470-2476&publication_year=2007)

25. Monticone, S., Tufeu, R., Kanaev, A.V.: Complex nature of the UV and visible fluorescence of colloidal ZnO nanoparticles. J. Phys. Chem. B **102**, 2854–2862 (1998)
CrossRef (https://doi.org/10.1021/jp973425p)
Google Scholar (http://scholar.google.com/scholar_lookup?title=Complex%20nature%20of%20the%20UV%20and%20visible%20fluorescence%20of%20colloidal%20ZnO%20nanoparticles&author=S.%20Monticone&author=R.%20Tufeu&author=AV.%20Kanaev&journal=J.%20Phys.%20Chem.%20B&volume=102&pages=2854-2862&publication_year=1998)

Copyright information

About this paper

Cite this paper as:

Johny L.M., Nirmala Jothi N.S., Sagayaraj P. (2017) Facile Synthesis, Formation Mechanism and Optical Properties of ZnO Nanostructures. In: Ebenezar J. (eds) Recent

Trends in Materials Science and Applications. Springer Proceedings in Physics, vol 189. Springer, Cham

- First Online 04 May 2017
- DOI https://doi.org/10.1007/978-3-319-44890-9_29
- Publisher Name Springer, Cham
- Print ISBN 978-3-319-44889-3
- Online ISBN 978-3-319-44890-9
- eBook Packages Physics and Astronomy

Personalised recommendations

Hollow $ZnSnO_3$ Crystallites: Structural, Electrical and Optical Properties

Recent Trends in Materials Science and Applications pp 255-262 | Cite as

- P. Prabakaran (1)
- M. Victor Antony Raj (1)
- Jobin Job Mathen (1)
- S. Prathap (2)
- J. Madhavan (1) Email author (jmadhavang@yahoo.com)

1. Department of Physics, Loyola College, , Chennai, India
2. Department of Physics, Arul Anandar College, , Madurai, India

Conference paper
First Online: 04 May 2017

Part of the Springer Proceedings in Physics book series (SPPHY, volume 189)

Abstract

Zinc stannate ($ZnSnO_3$) hollow cubic crystallites were successfully synthesized by hydrothermal reaction at 120 °C. X-ray diffraction (XRD) and Scanning Electron Microscopy (SEM) studies were employed to characterize the structure and morphology of the as-synthesized $ZnSnO_3$ crystallites and it is found that $ZnSnO_3$ exhibits almost uniform cubic structure. The FT-IR analysis confirmed the functional groups. Dielectric

constant and dielectric loss were found to decrease with increase in frequency. UV and Photoluminescence spectra analysis were also performed.

Keywords

Dielectric Loss Stannic Chloride Dielectric Study
Face Centered Cubic Broad Absorption Peak

These keywords were added by machine and not by the authors. This process is experimental and the keywords may be updated as the learning algorithm improves.

References

1. Shen, Y.S., Zhang, T.S.: Preparation, structure and gas sensing properties of ultramicro $ZnSnO_3$ powder. Sens. Actuators, B **12**, 5–9 (1993)
CrossRef (https://doi.org/10.1016/0925-4005(93)85003-S)
Google Scholar (http://scholar.google.com/scholar_lookup?title=Preparation%2C%20structure%20and%20gas%20sensing%20properties%20of%20ultramicro%20ZnSnO3%20powder&author=YS.%20Shen&author=TS.%20Zhang&journal=Sens.%20Actuators%2C%20B&volume=12&pages=5-9&publication_year=1993)

2. Chen, Y.J., Xue, X.Y., Li, Q.H., Wang, C., Wang, Y.G., Wang, T.H.: Linear ethanol sensing of SnO_2 nanorods with extremely high sensitivity. Appl. Phys. Lett. **88**, 083105 (2006)
ADS (http://adsabs.harvard.edu/cgi-bin/nph-data_query?link_type=ABSTRACT&bibcode=2006ApPhL..88h3105C)
CrossRef (https://doi.org/10.1063/1.2166695)
Google Scholar (http://scholar.google.com/scholar_lookup?title=Linear%20ethanol%20sensing%20of%20SnO2%20nanorods%20with%20extremely%20high%20sensitivity&author=YJ.%20Chen&author=XY.%20Xue&author=QH.%20Li&author=C.%20Wang&author=YG.%20Wang&author=TH.%20Wang&journal=Appl.%20Phys.%20Lett.&volume=88&pages=083105&publication_year=2006)

3. Zhang, T.S., Shen, Y.S., Zhang, R.F.: Ilmenite structure-type beta CdSnO used as on ethonal sensing material. Mater. Lett. **23**, 69–71 (1995)
CrossRef (https://doi.org/10.1016/0167-577X(95)00007-0)
Google Scholar (http://scholar.google.com/scholar_lookup?title=Ilmenite%20structure-type%20beta%20CdSnO%20used%20as%20on%20ethonal%20sensing%20material&author=TS.%20Zhang&author=YS.%20Shen&author=RF.%20Zhang&journal=Mater.%20Lett.&volume=23&pages=69-71&publication_year=1995)

4. Wu, X.H., Wang, Y.D., Li, Y.F., Zhang, Z.L.: Study on $ZnSnO_3$ sensitive material based on combustible gases. Mater. Chem. Phys. **77**, 588–593 (2002)
Google Scholar (http://scholar.google.com/scholar_lookup?title=Study%20on%20ZnSnO3%20sensitive%20material%20based%20on%20combustible%20gases&author=XH.%20Wu&author=YD.%20Wang&author=YF.%20Li&author=ZL.%20Zhang&journal=Mater.%20Chem.%20Phys.&volume=77&pages=588-593&publication_year=2002)

5. Kovacheva, D., Petrov, K.: Preparation of crystalline $ZnSnO_3$ from Li_2SnO_3 by low-temperature ion exchange. Solid State Ionics **109**, 327–332 (1998)
CrossRef (https://doi.org/10.1016/S0167-2738(97)00507-9)
Google Scholar (http://scholar.google.com/scholar_lookup?title=Preparation%20of%20crystalline%20ZnSnO3%20from%20Li2SnO3%20by%20low-temperature%20ion%20exchange&author=D.%20Kovacheva&author=K.%20Petrov&journal=Solid%20State%20Ionics&volume=109&pages=327-332&publication_year=1998)

6. Zeng, Y., Zhang, T., Fan, H.T., Lu, G.Y., Kang, M.H.: Growth and selective acetone detection based on ZnO nanorod arrays. Sen. Actuators B **143**, 449–453 (2009)
CrossRef (https://doi.org/10.1016/j.snb.2009.07.021)
Google Scholar (http://scholar.google.com/scholar_lookup?title=Growth%20and%20selective%20acetone%20detection%20based%20on%20ZnO%20nanorod%20arrays&author=Y.%20Zeng&author=T.%20Zhang&author=HT.%20Fan&author=GY.%20Lu&author=MH.%20Kang&journal=Sen.%20Actuators%20B&volume=143&pages=449-453&publication_year=2009)

7. Zeng, Y., Zhang, T., Fan, H.T., Fu, W.Y., Lu, G.Y, Sui, Y.M., Yang, H.B.: One-pot synthesis and gas-sensing properties of hierarchical $ZnSnO_3$ nanocages. J. Phys. Chem. C. **113**, 1900–1905 (2009)
Google Scholar (https://scholar.google.com/scholar?q=Zeng%2C%20Y.%2C%20Zhang%2C%20T.%2C%20Fan%2C%20H.T.%2C%20Fu%2C%20W.Y.%2C%20Lu%2C%20G.Y%2C%20Sui%2C%20Y.M.%2C%20Yang%2C%20H.B.%3A%20One-pot%20synthesis%20and%20gas-sensing%20properties%20of%20hierarchical%20ZnSnO3%20nanocages.%20J.%20Phys.%20Chem.%20C.%20113%2C%201900%E2%80%931905%20%282009%29)

8. Xu, J.Q., Jia, X.H., Lou, X.D., Shen, J.N.: One-step hydrothermal synthesis and gas sensing property of $ZnSnO_3$ microparticles. Solid State Electron. **50**, 504–508 (2006)
ADS (http://adsabs.harvard.edu/cgi-bin/nph-data_query?link_type=ABSTRACT&bibcode=2006SSEle..50..504X)
CrossRef (https://doi.org/10.1016/j.sse.2006.02.001)
Google Scholar (http://scholar.google.com/scholar_lookup?title=One-step%20hydrothermal%20synthesis%20and%20gas%20sensing%20property%20of%20ZnSnO3%20microparticles&author=JQ.%20Xu&author=XH.%20Jia&author=XD.%20Lou&author=JN.%20Shen&journal=Solid%20State%20Electron.&volume=50&pages=504-508&publication_year=2006)

9. Geng, B.Y., Fang, C.H., Zhan, F.M., Yu, N.: Synthesis of polyhedral $ZnSnO_3$ microcrystals with gas-sensing properties. Small **4**, 1337–1343 (2008)
CrossRef (https://doi.org/10.1002/smll.200701177)
Google Scholar (http://scholar.google.com/scholar_lookup?title=Synthesis%20of%20polyhedral%20ZnSnO3%20microcrystals%20with%20gas-sensing%20properties&author=BY.%20Geng&author=CH.%20Fang&author=FM.%20Zhan&author=N.%20Yu&journal=Small&volume=4&pages=1337-1343&publication_year=2008)

10. Zeng, Y.I., Zhang, K., Wang, X., Sui, Y., Zou, B., Zheng, W., Zou, G.: Rapid and selective H_2S detection of hierarchical $ZnSnO_3$ nanocages. Sens. Actuators B **159**, 245–250 (2011)
CrossRef (https://doi.org/10.1016/j.snb.2011.06.080)
Google Scholar (http://scholar.google.com/scholar_lookup?title=Rapid%20and%20selective%20H2S%20detection%20of%2

0hierarchical%20ZnSnO3%20nanocages&author=YI.%20Zeng&author=K.%20Zhang&author=X.%20Wang&author=Y.%20Sui&author=B.%20Zou&author=W.%20Zheng&author=G.%20Zou&journal=Sens.%20Actuators%20B&volume=159&pages=245-250&publication_year=2011)

11. Fu, X.L., Wang, X.X., Ding, Z.X., Leung, D.Y.C., Zhang, Z.Z., Long, J.L., Zhang, W.X., Li, Z.H., Fu, X.Z.: Hydroxide $ZnSn(OH)_6$: a promising new photocatalyst for benzene degradation. Appl. Catal. B. Environ. **91**, 67–72 (2009)
CrossRef (https://doi.org/10.1016/j.apcatb.2009.05.007)
Google Scholar (http://scholar.google.com/scholar_lookup?title=Hydroxide%20ZnSn%28OH%296%3A%20a%20promising%20new%20photocatalyst%20for%20benzene%20degradation&author=XL.%20Fu&author=XX.%20Wang&author=ZX.%20Ding&author=DYC.%20Leung&author=ZZ.%20Zhang&author=JL.%20Long&author=WX.%20Zhang&author=ZH.%20Li&author=XZ.%20Fu&journal=Appl.%20Catal.%20B.%20Environ.&volume=91&pages=67-72&publication_year=2009)

12. Wu, M.M., Li, X.L., Shen, G.P., Li, J., X, R.R., Proserpio, D.M.: Hydrothermal synthesis and structural characterization of a novel hydroxo stannate: $Sr_2Sn(OH)_8$. J. Solid State Chem. **151**, 56–60 (2000)
ADS (http://adsabs.harvard.edu/cgi-bin/nph-data_query?link_type=ABSTRACT&bibcode=2000JSSCh.151...56W)
CrossRef (https://doi.org/10.1006/jssc.2000.8621)
Google Scholar (http://scholar.google.com/scholar_lookup?title=Hydrothermal%20synthesis%20and%20structural%20characterization%20of%20a%20novel%20hydroxo%20stannate%3A%20Sr2Sn%28OH%298%0A%20%20%20%20%20%20%20%20%20%20%20&author=MM.%20Wu&author=XL.%20Li&author=GP.%20Shen&author=J.%20Li&author=RR.%20X&author=DM.%20Proserpio&journal=J.%20Solid%20State%20Chem.&volume=151&pages=56-60&publication_year=2000)

13. Nehru, L.C., Sanjeeviraja, C.: Microwave-assisted solution combustion synthesis of nanostructured Zn_2SnO_4. Nanosci. Nanotechnol. **3**(1), 10–13 (2013)
Google Scholar (http://scholar.google.com/scholar_lookup?title=Microwave-assisted%20solution%20combustion%20synthesis%20of%20nanostructured%20Zn2SnO4%0A%20%20%20%20%20%20%20%2

0%20%20&author=LC.%20Nehru&author=C.%20Sanjeeviraja&journal=Nanosci.%20Nanotechnol.&volume=3&issue=1&pages=10-13&publication_year=2013)

14. Huang, J., Xiaojuan, X., Cuiping, G., Wang, W., Geng, B., Sun, Y., Liu, J.: Size-controlled synthesis of porous $ZnSnO_3$ cubes and their gas-sensing and photocatalysis properties. Sens. Actuators B **171–172**, 572–579 (2012)
CrossRef (https://doi.org/10.1016/j.snb.2012.05.036)
Google Scholar (http://scholar.google.com/scholar_lookup?title=Size-controlled%20synthesis%20of%20porous%20ZnSnO3%20cubes%20and%20their%20gas-sensing%20and%20photocatalysis%20properties&author=J.%20Huang&author=X.%20Xiaojuan&author=G.%20Cuiping&author=W.%20Wang&author=B.%20Geng&author=Y.%20Sun&author=J.%20Liu&journal=Sens.%20Actuators%20B&volume=171%E2%80%93172&pages=572-579&publication_year=2012)

15. Borhade, A.V., Baste, Y.R.: Study of photocatalytic asset of the $ZnSnO_3$ synthesized by green chemistry. Arab. J. Chem. **25**, 134–139 (2012)
Google Scholar (https://scholar.google.com/scholar?q=Borhade%2C%20A.V.%2C%20Baste%2C%20Y.R.%3A%20Study%20of%20photocatalytic%20asset%20of%20the%20ZnSnO3%20synthesized%20by%20green%20chemistry.%20Arab.%20J.%20Chem.%2025%2C%20134%E2%80%93139%20%282012%29)

16. Dong, S., Sun, J., Li, Y., Yu, C., Li, Y., Sun, J.: $ZnSnO_3$ hollow nanospheres/reduced graphene oxide nanocomposites as high-performance photocatalysts for degradation of metronidazole. Appl. Catal. B **144**, 386–390 (2014)
CrossRef (https://doi.org/10.1016/j.apcatb.2013.07.043)
Google Scholar (http://scholar.google.com/scholar_lookup?title=ZnSnO3%20hollow%20nanospheres%2Freduced%20graphene%20oxide%20nanocomposites%20as%20high-performance%20photocatalysts%20for%20degradation%20of%20metronidazole&author=S.%20Dong&author=J.%20Sun&author=Y.%20Li&author=C.%20Yu&author=Y.%20Li&author=J.%20Sun&journal=Appl.%20Catal.%20B&volume=144&pages=386-390&publication_year=2014)

17. Liu, C., Roder, R., Zhang, L., Ren, Z., Chen, H., Zhang, Z., Ronning, C., Gao, P.X.: Highly efficient visible-light driven photocatalysts: a case of zinc stannate based nanocrystal assemblies. J. Mater. Chem. A **2**, 4157–4159 (2014)
CrossRef (https://doi.org/10.1039/c3ta14611a)
Google Scholar (http://scholar.google.com/scholar_lookup?title=Highly%20efficient%20visible-light%20driven%20photocatalysts%3A%20a%20case%20of%20zinc%20stannate%20based%20nanocrystal%20assemblies&author=C.%20Liu&author=R.%20Roder&author=L.%20Zhang&author=Z.%20Ren&author=H.%20Chen&author=Z.%20Zhang&author=C.%20Ronning&author=PX.%20Gao&journal=J.%20Mater.%20Chem.%20A&volume=2&pages=4157-4159&publication_year=2014)

Copyright information

About this paper

Cite this paper as:

Prabakaran P., Victor Antony Raj M., Mathen J.J., Prathap S., Madhavan J. (2017) Hollow $ZnSnO_3$ Crystallites: Structural, Electrical and Optical Properties. In: Ebenezar J. (eds) Recent Trends in Materials Science and Applications. Springer Proceedings in Physics, vol 189. Springer, Cham

- First Online 04 May 2017
- DOI https://doi.org/10.1007/978-3-319-44890-9_24
- Publisher Name Springer, Cham
- Print ISBN 978-3-319-44889-3
- Online ISBN 978-3-319-44890-9
- eBook Packages Physics and Astronomy

Personalised recommendations

Spinel Ferrite Nanoparticles: Synthesis, Crystal Structure, Properties, and Perspective Applications

International Conference on Nanotechnology and Nanomaterials

NANO 2016: Nanophysics, Nanomaterials, Interface Studies, and Applications pp 305-325 | Cite as

- Tetiana Tatarchuk (1) Email author (tatarchuk.tetyana@gmail.com)
- Mohamed Bououdina (2)
- J. Judith Vijaya (3)
- L. John Kennedy (4)

1. Department of Inorganic and Physical Chemistry, Faculty of Natural Science, Vasyl Stefanyk Precarpathian National University, , Ivano-Frankivsk, Ukraine
2. Department of Physics, College of Science, University of Bahrain, , Southern Governorate, Bahrain
3. Catalysis and Nanomaterials Research Laboratory, Department of Chemistry, Loyola College, , Chennai, India
4. Materials Division, School of Advanced Sciences, Vellore Institute of Technology (VIT) University, Chennai Campus, , Chennai, India

Conference paper
First Online: 10 May 2017

Part of the Springer Proceedings in Physics book series (SPPHY, volume 195)

Abstract

Recent developments show that the exceptional physical, optical, magnetic, and electrical properties of spinel ferrite (SF) nanomaterials have now attracted the attention as high-density data storage materials, catalysts, gas sensors, rechargeable lithium batteries, information storage systems, magnetic bulk cores, adsorbents, magnetic fluids, microwave absorbers, and medical diagnostics. The aim of this review consists on an overview on the methods of preparation, the crystal structure and application of SFs used in technology for the design of new materials and devices. The chapter begins with a review of the different synthesis methods commonly used for the preparation of SFs. Then, the structural features of spinel unit cell, crystal chemical parameters, and extrinsic magnetic and optical properties are described in this chapter. Since the magnetism of SFs depends not only on particle chemistry and phase but also on the particle size and environment, the role of cationic distribution and ion exchange interaction are explored in determining the magnetic properties of the system. In addition, the potential applications of SFs in different fields of technology are also discussed.

Keywords

Spinel structure Ferrite Cation distribution Oxygen parameter Magnetic properties Optical properties Magnetization

References

1. Yan Z, Gao J, Li Y, Zhang M et al (2015) Hydrothermal synthesis and structure evolution of metal-doped magnesium ferrite from saprolite laterite. RSC Adv 5:92778–92787
CrossRef (https://doi.org/10.1039/C5RA17145H)
Google Scholar (http://scholar.google.com/scholar_lookup?title=Hydrothermal%20synthesis%20and%20structure%20evolution%20of%20metal-doped%20magnesium%20ferrite%20from%20saprolite%20laterit

e&author=Z.%20Yan&author=J.%20Gao&author=Y.%20Li&author=M.%20Zhang&journal=RSC%20Adv&volume=5&pages=92778-92787&publication_year=2015)

2. Olsson RT, Salazar-Alvarez G, Hedenqvist SM et al (2005) Controlled synthesis of near-stoichiometric cobalt ferrite nanoparticles. Chem Mater 17:5109–5118
CrossRef (https://doi.org/10.1021/cm0501665)
Google Scholar (http://scholar.google.com/scholar_lookup?title=Controlled%20synthesis%20of%20near-stoichiometric%20cobalt%20ferrite%20nanoparticles&author=RT.%20Olsson&author=G.%20Salazar-Alvarez&author=SM.%20Hedenqvist&journal=Chem%20Mater&volume=17&pages=5109-5118&publication_year=2005)

3. Latham AH, Williams ME (2008) Controlling transport and chemical functionality of magnetic nanoparticles. Acc Chem Res 41:411–420
CrossRef (https://doi.org/10.1021/ar700183b)
Google Scholar (http://scholar.google.com/scholar_lookup?title=Controlling%20transport%20and%20chemical%20functionality%20of%20magnetic%20nanoparticles&author=AH.%20Latham&author=ME.%20Williams&journal=Acc%20Chem%20Res&volume=41&pages=411-420&publication_year=2008)

4. Moussaoui HE, Mahfoud T, Habouti S et al (2016) Synthesis and magnetic properties of tin spinel ferrites doped manganese. J Magn Magn Mater 405:181–186
ADS (http://adsabs.harvard.edu/cgi-bin/nph-data_query?link_type=ABSTRACT&bibcode=2016JMMM..405..181E)
CrossRef (https://doi.org/10.1016/j.jmmm.2015.12.059)
Google Scholar (http://scholar.google.com/scholar_lookup?title=Synthesis%20and%20magnetic%20properties%20of%20tin%20spinel%20ferrites%20doped%20manganese&author=HE.%20Moussaoui&author=T.%20Mahfoud&author=S.%20Habouti&journal=J%20Magn%20Magn%20Mater&volume=405&pages=181-186&publication_year=2016)

5. Mathew DS, Juang R (2007) An overview of the structure and magnetism of spinel ferrite nanoparticles and their synthesis in microemulsions. Chem Eng J 129:51–65
CrossRef (https://doi.org/10.1016/j.cej.2006.11.001)

Google Scholar (http://scholar.google.com/scholar_lookup?title=An%20overview%20of%20the%20structure%20and%20magnetism%20of%20spinel%20ferrite%20nanoparticles%20and%20their%20synthesis%20in%20microemulsions&author=DS.%20Mathew&author=R.%20Juang&journal=Chem%20Eng%20J&volume=129&pages=51-65&publication_year=2007)

6. Carta D, Casula MF, Falqui A et al (2009) A structural and magnetic investigation of the inversion degree in ferrite nanocrystals MFe_2O_4 (M = Mn, Co, Ni). J Phys Chem C 113:8606–8615
CrossRef (https://doi.org/10.1021/jp901077c)
Google Scholar (http://scholar.google.com/scholar_lookup?title=A%20structural%20and%20magnetic%20investigation%20of%20the%20inversion%20degree%20in%20ferrite%20nanocrystals%20MFe2O4%20%28M%20%3D%20Mn%2C%20Co%2C%20Ni%29&author=D.%20Carta&author=MF.%20Casula&author=A.%20Falqui&journal=J%20Phys%20Chem%20C&volume=113&pages=8606-8615&publication_year=2009)

7. Song Q, Ding Y, Wang ZL et al (2007) Tuning the thermal stability of molecular precursors for the nonhydrolytic synthesis of magnetic $MnFe_2O_4$ spinel nanocrystals. Chem Mater 19:4633–4638
CrossRef (https://doi.org/10.1021/cm0709900)
Google Scholar (http://scholar.google.com/scholar_lookup?title=Tuning%20the%20thermal%20stability%20of%20molecular%20precursors%20for%20the%20nonhydrolytic%20synthesis%20of%20magnetic%20MnFe2O4%20spinel%20nanocrystals&author=Q.%20Song&author=Y.%20Ding&author=ZL.%20Wang&journal=Chem%20Mater&volume=19&pages=4633-4638&publication_year=2007)

8. Kefeni KK, Msagati TAM, Mamba BB (2017) Ferrite nanoparticles: synthesis, characterisation and applications in electronic device. Mater Sci Eng B 215:37–55
CrossRef (https://doi.org/10.1016/j.mseb.2016.11.002)
Google Scholar (http://scholar.google.com/scholar_lookup?title=Ferrite%20nanoparticles%3A%20synthesis%2C%20characterisation%20and%20applications%20in%20electronic%20device&author=KK.%20Kefeni&author=TAM.%20Msagati&author=BB.%20Mamba&journal=Mater%20Sci%20Eng%20B&volume=215&pages=37-55&publication_year=2017)

9. Pang YL, Lim S, Ong H et al (2016) Research progress on iron oxide-based magnetic materials: synthesis techniques and photocatalytic applications. Ceram Int 42:9–34
CrossRef (https://doi.org/10.1016/j.ceramint.2015.08.144)
Google Scholar (http://scholar.google.com/scholar_lookup?title=Research%20progress%20on%20iron%20oxide-based%20magnetic%20materials%3A%20synthesis%20techniques%20and%20photocatalytic%20applications&author=YL.%20Pang&author=S.%20Lim&author=H.%20Ong&journal=Ceram%20Int&volume=42&pages=9-34&publication_year=2016)

10. Goswami PP, Choudhury HA, Chakma S et al (2013) Sonochemical synthesis and characterization of manganese ferrite nanoparticles. Ind Eng Chem Res 52:17848–17855
CrossRef (https://doi.org/10.1021/ie401919x)
Google Scholar (http://scholar.google.com/scholar_lookup?title=Sonochemical%20synthesis%20and%20characterization%20of%20manganese%20ferrite%20nanoparticles&author=PP.%20Goswami&author=HA.%20Choudhury&author=S.%20Chakma&journal=Ind%20Eng%20Chem%20Res&volume=52&pages=17848-17855&publication_year=2013)

11. Kurikka JL, Shafi VPM, Ulman A et al (2004) Mixed iron–manganese oxide nanoparticles. J Phys Chem B 108:14876–14883
CrossRef (https://doi.org/10.1021/jp049913w)
Google Scholar (http://scholar.google.com/scholar_lookup?title=Mixed%20iron%E2%88%92manganese%20oxide%20nanoparticles&author=JL.%20Kurikka&author=VPM.%20Shafi&author=A.%20Ulman&journal=J%20Phys%20Chem%20B&volume=108&pages=14876-14883&publication_year=2004)

12. Song Q, Zhang ZJ (2012) Controlled synthesis and magnetic properties of bimagnetic spinel ferrite $CoFe_2O_4$ and $MnFe_2O_4$ nanocrystals with core–shell architecture. J Am Chem Soc 134:10182–10190
CrossRef (https://doi.org/10.1021/ja302856z)
Google Scholar (http://scholar.google.com/scholar_lookup?title=Controlled%20synthesis%20and%20magnetic%20properties%20of%20bimagnetic%20spinel%20ferrite%20CoFe2O4%20and%20MnFe2O4%20nanocrystals%20with%20core%E2%80%93shell%20architecture&author=Q.%20Song&author=ZJ.%20Zhang

&journal=J%20Am%20Chem%20Soc&volume=134&pages=10182-10190&publication_year=2012)

13. Ni D, Lin Z, Xiaoling P et al (2015) Preparation and characterization of nickel-zinc ferrites by a solvothermal method. Rare Metal Mater Eng 44:2126–2131
CrossRef (https://doi.org/10.1016/S1875-5372(16)30010-8)
Google Scholar (http://scholar.google.com/scholar_lookup?title=Preparation%20and%20characterization%20of%20nickel-zinc%20ferrites%20by%20a%20solvothermal%20method&author=D.%20Ni&author=Z.%20Lin&author=P.%20Xiaoling&journal=Rare%20Metal%20Mater%20Eng&volume=44&pages=2126-2131&publication_year=2015)

14. Li Z, Gao K, Han G, Wang R et al (2015) Solvothermal synthesis of $MnFe_2O_4$ colloidal nanocrystal assemblies and their magnetic and electrocatalytic properties. New J Chem 39:361–368
CrossRef (https://doi.org/10.1039/C4NJ01466A)
Google Scholar (http://scholar.google.com/scholar_lookup?title=Solvothermal%20synthesis%20of%20MnFe2O4%20colloidal%20nanocrystal%20assemblies%20and%20their%20magnetic%20and%20electrocatalytic%20properties&author=Z.%20Li&author=K.%20Gao&author=G.%20Han&author=R.%20Wang&journal=New%20J%20Chem&volume=39&pages=361-368&publication_year=2015)

15. Yin Y, Liu W, Huo N et al (2016) Synthesis of vesicle-like $MgFe_2O_4$/Graphene 3D network anode material with enhanced lithium storage performance. ACS Sustain Chem Eng.
doi: 10.1021/acssuschemeng.6b01949
(https://doi.org/10.1021/acssuschemeng.6b01949)
Google Scholar (http://scholar.google.com/scholar_lookup?title=Synthesis%20of%20vesicle-like%20MgFe2O4%2FGraphene%203D%20network%20anode%20material%20with%20enhanced%20lithium%20storage%20performance&author=Y.%20Yin&author=W.%20Liu&author=N.%20Huo&journal=ACS%20Sustain%20Chem%20Eng&publication_year=2016&doi=10.1021%2Facssuschemeng.6b01949)

16. Pereira C, Pereira AM, Fernandes C et al (2012) Superparamagnetic MFe_2O_4 (M = Fe, Co, Mn) nanoparticles: tuning the particle size and magnetic properties through a novel one-step coprecipitation route. Chem Mater 24:1496–1504

CrossRef (https://doi.org/10.1021/cm300301c)
Google Scholar (http://scholar.google.com/scholar_lookup?title=Superparamagnetic%20MFe2O4%20%28M%20%3D%20Fe%2C%20Co%2C%20Mn%29%20nanoparticles%3A%20tuning%20the%20particle%20size%20and%20magnetic%20properties%20through%20a%20novel%20one-step%20coprecipitation%20route&author=C.%20Pereira&author=AM.%20Pereira&author=C.%20Fernandes&journal=Chem%20Mater&volume=24&pages=1496-1504&publication_year=2012)

17. Carta D, Loche D, Mountjoy G et al (2008) $NiFe_2O_4$ nanoparticles dispersed in an aerogel silica matrix: an X-ray absorption study. J Phys Chem C 112:15623–15630
CrossRef (https://doi.org/10.1021/jp803982k)
Google Scholar (http://scholar.google.com/scholar_lookup?title=NiFe2O4%20nanoparticles%20dispersed%20in%20an%20aerogel%20silica%20matrix%3A%20an%20X-ray%20absorption%20study&author=D.%20Carta&author=D.%20Loche&author=G.%20Mountjoy&journal=J%20Phys%20Chem%20C&volume=112&pages=15623-15630&publication_year=2008)

18. Mukhtar MW, Irfan M, Ahmad I et al (2015) Synthesis and properties of Pr-substituted MgZn ferrites for core materials and high frequency applications. J Magn Magn Mater 381:173–178
ADS (http://adsabs.harvard.edu/cgi-bin/nph-data_query?link_type=ABSTRACT&bibcode=2015JMMM..381..173M)
CrossRef (https://doi.org/10.1016/j.jmmm.2014.12.072)
Google Scholar (http://scholar.google.com/scholar_lookup?title=Synthesis%20and%20properties%20of%20Pr-substituted%20MgZn%20ferrites%20for%20core%20materials%20and%20high%20frequency%20applications&author=MW.%20Mukhtar&author=M.%20Irfan&author=I.%20Ahmad&journal=J%20Magn%20Magn%20Mater&volume=381&pages=173-178&publication_year=2015)

19. Sharma R, Bansal S, Singhal S (2015) Tailoring the photo-Fenton activity of spinel ferrites (MFe_2O_4) by incorporating different cations (M = Cu, Zn, Ni and Co) in the structure. RSC Adv 5:6006–6018
CrossRef (https://doi.org/10.1039/C4RA13692F)
Google Scholar (http://scholar.google.com/scholar_lookup?title=Tailoring%20the%20photo-

Fenton%20activity%20of%20spinel%20ferrites%20%28MFe2O4%29%20by%20incorporating%20different%20cations%20%28M%20%3D%20Cu%2C%20Zn%2C%20Ni%20and%20Co%29%20in%20the%20structure&author=R.%20Sharma&author=S.%20Bansal&author=S.%20Singhal&journal=RSC%20Adv&volume=5&pages=6006-6018&publication_year=2015)

20. Jesudoss SK, Vijaya JJ, Kennedy LJ et al (2016) Studies on the efficient dual performance of $Mn_{1-x}Ni_xFe_2O_4$ spinel nanoparticles in photodegradation and antibacterial activity. J Photochem Photobiol B 165:121–132. doi: 10.1016/j.jphotobiol.2016.10.004 (https://doi.org/10.1016/j.jphotobiol.2016.10.004)
CrossRef (https://doi.org/10.1016/j.jphotobiol.2016.10.004)
Google Scholar (http://scholar.google.com/scholar_lookup?title=Studies%20on%20the%20efficient%20dual%20performance%20of%20Mn1%E2%80%93xNixFe2O4%20spinel%20nanoparticles%20in%20photodegradation%20and%20antibacterial%20activity&author=SK.%20Jesudoss&author=JJ.%20Vijaya&author=LJ.%20Kennedy&journal=J%20Photochem%20Photobiol%20B&volume=165&pages=121-132&publication_year=2016&doi=10.1016%2Fj.jphotobiol.2016.10.004)

21. Tadjarodi A, Imani M, Salehi M (2015) $ZnFe_2O_4$ nanoparticles and a clay encapsulated $ZnFe_2O_4$ nanocomposite: synthesis strategy, structural characteristics and the adsorption of dye pollutants in water. RSC Adv 5:56145–56156
CrossRef (https://doi.org/10.1039/C5RA02163D)
Google Scholar (http://scholar.google.com/scholar_lookup?title=ZnFe2O4%20nanoparticles%20and%20a%20clay%20encapsulated%20ZnFe2O4%20nanocomposite%3A%20synthesis%20strategy%2C%20structural%20characteristics%20and%20the%20adsorption%20of%20dye%20pollutants%20in%20water&author=A.%20Tadjarodi&author=M.%20Imani&author=M.%20Salehi&journal=RSC%20Adv&volume=5&pages=56145-56156&publication_year=2015)

22. Marinca TF, Chicinaş I, Isnard O et al (2016) Nanocrystalline/nanosized manganese substituted nickel ferrites – $Ni_{1-x}Mn_xFe_2O_4$ obtained by ceramic-mechanical milling route. Ceram Int 42(4):4754–4763. doi: 10.1016/j.ceramint.2015.11.155 (https://doi.org/10.1016/j.ceramint.2015.11.155)
CrossRef (https://doi.org/10.1016/j.ceramint.2015.11.155)

Google Scholar (http://scholar.google.com/scholar_lookup?title=Nanocrystalline%2Fnanosized%20manganese%20substituted%20nickel%20ferrites%20%E2%80%93%20Ni1%E2%88%92xMnxFe2O4%20obtained%20by%20ceramic-mechanical%20milling%20route&author=TF.%20Marinca&author=I.%20Chicina%C5%9F&author=O.%20Isnard&journal=Ceram%20Int&volume=42&issue=4&pages=4754-4763&publication_year=2016&doi=10.1016%2Fj.ceramint.2015.11.155)

23. Angadi VJ, Rudraswamy B, Sadhana K et al (2016) Effect of Sm^{3+}–Gd^{3+} on structural, electrical and magnetic properties of Mn–Zn ferrites synthesized via combustion route. J Alloys Compd 656:5–12. doi: 10.1016/j.jallcom.2015.09.222 (https://doi.org/10.1016/j.jallcom.2015.09.222)
CrossRef (https://doi.org/10.1016/j.jallcom.2015.09.222)
Google Scholar (http://scholar.google.com/scholar_lookup?title=Effect%20of%20Sm3%2B%E2%80%93Gd3%2B%20on%20structural%2C%20electrical%20and%20magnetic%20properties%20of%20Mn%E2%80%93Zn%20ferrites%20synthesized%20via%20combustion%20route&author=VJ.%20Angadi&author=B.%20Rudraswamy&author=K.%20Sadhana&journal=J%20Alloys%20Compd&volume=656&pages=5-12&publication_year=2016&doi=10.1016%2Fj.jallcom.2015.09.222)

24. Singh C, Jauhar S, Kumar V et al (2015) Synthesis of zinc substituted cobalt ferrites via reverse micelle technique involving in situ template formation: a study on their structural, magnetic, optical and catalytic properties. Mater Chem Phys 156:188–197. doi: 10.1016/j.matchemphys.2015.02.046 (https://doi.org/10.1016/j.matchemphys.2015.02.046)
CrossRef (https://doi.org/10.1016/j.matchemphys.2015.02.046)
Google Scholar (http://scholar.google.com/scholar_lookup?title=Synthesis%20of%20zinc%20substituted%20cobalt%20ferrites%20via%20reverse%20micelle%20technique%20involving%20in%20situ%20template%20formation%3A%20a%20study%20on%20their%20structural%2C%20magnetic%2C%20optical%20and%20catalytic%20properties&author=C.%20Singh&author=S.%20Jauhar&author=V.%20Kumar&journal=Mater%20Chem%20Phys&volume=156&pages=188-

197&publication_year=2015&doi=10.1016%2Fj.matchemphys.2015.02.046)

25. Kotsikau D, Ivanovskaya M, Pankov V et al (2015) Structure and magnetic properties of manganese–zinc-ferrites prepared by spray pyrolysis method. Solid State Sci 39:69–73. doi: 10.1016/j.solidstatesciences.2014.11.013 (https://doi.org/10.1016/j.solidstatesciences.2014.11.013) ADS (http://adsabs.harvard.edu/cgi-bin/nph-data_query?link_type=ABSTRACT&bibcode=2015SSSci..39...69K) CrossRef (https://doi.org/10.1016/j.solidstatesciences.2014.11.013) Google Scholar (http://scholar.google.com/scholar_lookup?title=Structure%20and%20magnetic%20properties%20of%20manganese%E2%80%93zinc-ferrites%20prepared%20by%20spray%20pyrolysis%20method&author=D.%20Kotsikau&author=M.%20Ivanovskaya&author=V.%20Pankov&journal=Solid%20State%20Sci&volume=39&pages=69-73&publication_year=2015&doi=10.1016%2Fj.solidstatesciences.2014.11.013)

26. Cortes MS, Martínez-Luevanos A, García-Cerda LA et al (2015) Nanostructured pure and substituted cobalt ferrites: fabrication by electrospinning and study of their magnetic properties. J Alloys Compd 653:290–297. doi: 10.1016/j.jallcom.2015.08.262 (https://doi.org/10.1016/j.jallcom.2015.08.262) CrossRef (https://doi.org/10.1016/j.jallcom.2015.08.262) Google Scholar (http://scholar.google.com/scholar_lookup?title=Nanostructured%20pure%20and%20substituted%20cobalt%20ferrites%3A%20fabrication%20by%20electrospinning%20and%20study%20of%20their%20magnetic%20properties&author=MS.%20Cortes&author=A.%20Mart%C3%ADnez-Luevanos&author=LA.%20Garc%C3%ADa-Cerda&journal=J%20Alloys%20Compd&volume=653&pages=290-297&publication_year=2015&doi=10.1016%2Fj.jallcom.2015.08.262)

27. Cai X, Wang J, Li B et al (2016) Microwave absorption properties of LiZn ferrites hollow microspheres doped with La and Mg by self-reactive quenching technology. J Alloys Compd 657:608–615.

doi: 10.1016/j.jallcom.2015.10.153
(https://doi.org/10.1016/j.jallcom.2015.10.153)
CrossRef (https://doi.org/10.1016/j.jallcom.2015.10.153)
Google Scholar (http://scholar.google.com/scholar_lookup?title=Microwave%20absorption%20properties%20of%20LiZn%20ferrites%20hollow%20microspheres%20doped%20with%20La%20and%20Mg%20by%20self-reactive%20quenching%20technology&author=X.%20Cai&author=J.%20Wang&author=B.%20Li&journal=J%20Alloys%20Compd&volume=657&pages=608-615&publication_year=2016&doi=10.1016%2Fj.jallcom.2015.10.153)

28. Ishaque M, Khan MA, Ali I et al (2015) Investigations on structural, electrical and dielectric properties of yttrium substituted Mg-ferrites. Ceram Int 41(3):4028–4034.
doi: 10.1016/j.ceramint.2014.11.093
(https://doi.org/10.1016/j.ceramint.2014.11.093)
CrossRef (https://doi.org/10.1016/j.ceramint.2014.11.093)
Google Scholar (http://scholar.google.com/scholar_lookup?title=Investigations%20on%20structural%2C%20electrical%20and%20dielectric%20properties%20of%20yttrium%20substituted%20Mg-ferrites&author=M.%20Ishaque&author=MA.%20Khan&author=I.%20Ali&journal=Ceram%20Int&volume=41&issue=3&pages=4028-4034&publication_year=2015&doi=10.1016%2Fj.ceramint.2014.11.093)

29. Anjum S, Hameed S, Bashir F (2015) Microstructural, structural, magnetic and optical properties of antimony doped cobalt spinel ferrites. Mater Today Proc 2(10):5329–5336.
doi: 10.1016/j.matpr.2015.11.045
(https://doi.org/10.1016/j.matpr.2015.11.045)
CrossRef (https://doi.org/10.1016/j.matpr.2015.11.045)
Google Scholar (http://scholar.google.com/scholar_lookup?title=Microstructural%2C%20structural%2C%20magnetic%20and%20optical%20properties%20of%20antimony%20doped%20cobalt%20spinel%20ferrites&author=S.%20Anjum&author=S.%20Hameed&author=F.%20Bashir&journal=Mater%20Today%20Proc&volume=2&issue=10&pages=5329-

5336&publication_year=2015&doi=10.1016%2Fj.matpr.2015.11.045)

30. Cross WB, Affleck L, Kuznetsov MV et al (1999) Self-propagating high-temperature synthesis of ferrites MFe_2O_4 (M = Mg, Ba, Co, Ni, Cu, Zn); reactions in an external magnetic field. J Mater Chem 9:2545–2552. doi: 10.1039/A904431K (https://doi.org/10.1039/A904431K)
CrossRef (https://doi.org/10.1039/a904431k)
Google Scholar (http://scholar.google.com/scholar_lookup?title=Self-propagating%20high-temperature%20synthesis%20of%20ferrites%20MFe2O4%20%28M%20%3D%20Mg%2C%20Ba%2C%20Co%2C%20Ni%2C%20Cu%2C%20Zn%29%3B%20reactions%20in%20an%20external%20magnetic%20field&author=WB.%20Cross&author=L.%20Affleck&author=MV.%20Kuznetsov&journal=J%20Mater%20Chem&volume=9&pages=2545-2552&publication_year=1999&doi=10.1039%2FA904431K)

31. Peng E, Ding J, Xue JM (2014) Concentration-dependent magnetic hyperthermic response of manganese ferrite-loaded ultrasmall graphene oxide nanocomposites. New J Chem 38:2312–2319. doi: 10.1039/C3NJ01555F (https://doi.org/10.1039/C3NJ01555F)
CrossRef (https://doi.org/10.1039/C3NJ01555F)
Google Scholar (http://scholar.google.com/scholar_lookup?title=Concentration-dependent%20magnetic%20hyperthermic%20response%20of%20manganese%20ferrite-loaded%20ultrasmall%20graphene%20oxide%20nanocomposites&author=E.%20Peng&author=J.%20Ding&author=JM.%20Xue&journal=New%20J%20Chem&volume=38&pages=2312-2319&publication_year=2014&doi=10.1039%2FC3NJ01555F)

32. Leal MP, Rivera-Fernández S, Franco JM et al (2015) Long-circulating PEGylated manganese ferrite nanoparticles for MRI-based molecular imaging. Nanoscale 7:2050–2059. doi: 10.1039/C4NR05781C (https://doi.org/10.1039/C4NR05781C)
ADS (http://adsabs.harvard.edu/cgi-bin/nph-data_query?link_type=ABSTRACT&bibcode=2015Nanos...7.2050P)
CrossRef (https://doi.org/10.1039/C4NR05781C)

Google Scholar (http://scholar.google.com/scholar_lookup?title=Long-circulating%20PEGylated%20manganese%20ferrite%20nanoparticles%20for%20MRI-based%20molecular%20imaging&author=MP.%20Leal&author=S.%20Rivera-Fern%C3%A1ndez&author=JM.%20Franco&journal=Nanoscale&volume=7&pages=2050-2059&publication_year=2015&doi=10.1039%2FC4NR05781C)

33. Kaiser M (2016) Magnetic and electric modulus properties of ln substituted Mg–Mn–Cu ferrites. Mater Res Bull 73:452–458. doi: 10.1016/j.materresbull.2015.09.015 (https://doi.org/10.1016/j.materresbull.2015.09.015)
CrossRef (https://doi.org/10.1016/j.materresbull.2015.09.015)
Google Scholar (http://scholar.google.com/scholar_lookup?title=Magnetic%20and%20electric%20modulus%20properties%20of%20ln%20substituted%20Mg%E2%80%93Mn%E2%80%93Cu%20ferrites&author=M.%20Kaiser&journal=Mater%20Res%20Bull&volume=73&pages=452-458&publication_year=2016&doi=10.1016%2Fj.materresbull.2015.09.015)

34. Kombaiah K, Vijaya JJ, Kennedy LJ, Bououdina M (2017) Optical, magnetic and structural properties of $ZnFe_2O_4$ nanoparticles synthesized by conventional and microwave assisted combustion method: a comparative investigation. Optik Int J Light Electron Optics 129:57–68. doi: 10.1016/j.ijleo.2016.10.058 (https://doi.org/10.1016/j.ijleo.2016.10.058)
CrossRef (https://doi.org/10.1016/j.ijleo.2016.10.058)
Google Scholar (http://scholar.google.com/scholar_lookup?title=Optical%2C%20magnetic%20and%20structural%20properties%20of%20ZnFe2O4%20nanoparticles%20synthesized%20by%20conventional%20and%20microwave%20assisted%20combustion%20method%3A%20a%20comparative%20investigation&author=K.%20Kombaiah&author=JJ.%20Vijaya&author=LJ.%20Kennedy&author=M.%20Bououdina&journal=Optik%20Int%20J%20Light%20Electron%20Optics&volume=129&pages=57-68&publication_year=2017&doi=10.1016%2Fj.ijleo.2016.10.058)

35. Kurta SA, Mykytyn IM, Tatarchuk TR (2014) Structure and the catalysis mechanism of oxidative chlorination in nanostructural layers of a surface of alumina. Nanoscale Res Lett 9:357.

doi: 10.1186/1556-276X-9-357 (https://doi.org/10.1186/1556-276X-9-357)
ADS (http://adsabs.harvard.edu/cgi-bin/nph-data_query?link_type=ABSTRACT&bibcode=2014NRL.....9..357K)
CrossRef (https://doi.org/10.1186/1556-276X-9-357)
Google Scholar (http://scholar.google.com/scholar_lookup?title=Structure%20and%20the%20catalysis%20mechanism%20of%20oxidative%20chlorination%20in%20nanostructural%20layers%20of%20a%20surface%20of%20alumina&author=SA.%20Kurta&author=IM.%20Mykytyn&author=TR.%20Tatarchuk&journal=Nanoscale%20Res%20Lett&volume=9&pages=357&publication_year=2014&doi=10.1186%2F1556-276X-9-357)

36. Tatarchuk T (2014) Catalytic oxidation of carbon monoxide on lithium-zinc ferrites with a spinel structure. Ekologia i Technika 32(2):70–75
Google Scholar (http://scholar.google.com/scholar_lookup?title=%D0%A1atalytic%20oxidation%20of%20carbon%20monoxide%20on%20lithium-zinc%20ferrites%20with%20a%20spinel%20structure&author=T.%20Tatarchuk&journal=Ekologia%20i%20Technika&volume=32&issue=2&pages=70-75&publication_year=2014)

37. Tatarchuk TR, Boyko EV, Yaremiy IP et al (2014) Synthesis crystal chemistry and antistructure modelling of $CoFe_2O_4$ nanoparticles prepared by citrate sol-gel method. Phys Chem Solid State 15(4):792–797
Google Scholar (http://scholar.google.com/scholar_lookup?title=Synthesis%20crystal%20chemistry%20and%20antistructure%20modelling%20of%20CoFe2O4%20nanoparticles%20prepared%20by%20citrate%20sol-gel%20method&author=TR.%20Tatarchuk&author=EV.%20Boyko&author=IP.%20Yaremiy&journal=Phys%20Chem%20Solid%20State&volume=15&issue=4&pages=792-797&publication_year=2014)

38. Sickafus KE, Wills JM, Grimes NW (1999) Structure of spinel. J Am Ceram Soc 82:3279–3292. doi: 10.1111/j.1151-2916.1999.tb02241.x (https://doi.org/10.1111/j.1151-2916.1999.tb02241.x)
CrossRef (https://doi.org/10.1111/j.1151-2916.1999.tb02241.x)
Google Scholar (http://scholar.google.com/scholar_lookup?title=Structure%20of%20spinel&author=KE.%20Sickafus&autho

r=JM.%20Wills&author=NW.%20Grimes&journal=J%20Am%20Ceram%20Soc&volume=82&pages=3279-3292&publication_year=1999&doi=10.1111%2Fj.1151-2916.1999.tb02241.x)

39. Kane SN, Satalkar M (2017) Correlation between magnetic properties and cationic distribution of $Zn_{0.85-x}Ni_xMg_{0.05}Cu_{0.1}Fe_2O_4$ nanospinel ferrite: effect of Ni doping. J Mater Sci 52(6):3467–3477. doi: 10.1007/s10853-016-0636-7 (https://doi.org/10.1007/s10853-016-0636-7)
ADS (http://adsabs.harvard.edu/cgi-bin/nph-data_query?link_type=ABSTRACT&bibcode=2017JMatS..52.3467K)
CrossRef (https://doi.org/10.1007/s10853-016-0636-7)
Google Scholar (http://scholar.google.com/scholar_lookup?title=Correlation%20between%20magnetic%20properties%20and%20cationic%20distribution%20of%20Zn0.85%E2%88%92x%0A%20%20%20%20%20%20%20%20%20%20%20%20Ni%0A%20%20%20%20%20%20%20%20%20%20%20%20%20%20%20%20%20%20%20%20%20%20%20x%0A%20%20%20%20%20%20%20%20%20%20%20%20%20%20%20%20%20%20%20%20Mg0.05Cu0.1Fe2O4%20nanospinel%20ferrite%3A%20effect%20of%20Ni%20doping&author=SN.%20Kane&author=M.%20Satalkar&journal=J%20Mater%20Sci&volume=52&issue=6&pages=3467-3477&publication_year=2017&doi=10.1007%2Fs10853-016-0636-7)

40. Tatarchuk TR, Bououdina M, Paliychuk ND et al (2017) Structural characterization and antistructure modeling of cobalt-substituted zinc ferrites. J Alloys Compd 694(15):777–791. doi: 10.1016/j.jallcom.2016.10.067 (https://doi.org/10.1016/j.jallcom.2016.10.067)
CrossRef (https://doi.org/10.1016/j.jallcom.2016.10.067)
Google Scholar (http://scholar.google.com/scholar_lookup?title=Structural%20characterization%20and%20antistructure%20modeling%20of%20cobalt-substituted%20zinc%20ferrites&author=TR.%20Tatarchuk&author=M.%20Bououdina&author=ND.%20Paliychuk&journal=J%20Alloys%20Compd&volume=694&issue=15&pages=777-791&publication_year=2017&doi=10.1016%2Fj.jallcom.2016.10.067)

41. Angadi VJ, Choudhury L, Sadhana K et al (2017) Structural, electrical and magnetic properties of Sc^{3+} doped Mn-Zn ferrite

nanoparticles. J Magn Magn Mater 424:1–11.
doi: 10.1016/j.jmmm.2016.10.050
(https://doi.org/10.1016/j.jmmm.2016.10.050)
ADS (http://adsabs.harvard.edu/cgi-bin/nph-data_query?link_type=ABSTRACT&bibcode=2017JMMM..424....1A)
CrossRef (https://doi.org/10.1016/j.jmmm.2016.10.050)
Google Scholar (http://scholar.google.com/scholar_lookup?title=Structural%2C%20electrical%20and%20magnetic%20properties%20of%20Sc3%2B%20doped%20Mn-Zn%20ferrite%20nanoparticles&author=VJ.%20Angadi&author=L.%20Choudhury&author=K.%20Sadhana&journal=J%20Magn%20Magn%20Mater&volume=424&pages=1-11&publication_year=2017&doi=10.1016%2Fj.jmmm.2016.10.050)

42. Lemine OM, Bououdina M, Sajieddine M et al (2011) Synthesis, structural, magnetic and optical properties of nanocrystalline $ZnFe_2O_4$. Physica B 406(10):1989–1994.
doi: 10.1016/j.physb.2011.02.072
(https://doi.org/10.1016/j.physb.2011.02.072)
ADS (http://adsabs.harvard.edu/cgi-bin/nph-data_query?link_type=ABSTRACT&bibcode=2011PhyB..406.1989L)
CrossRef (https://doi.org/10.1016/j.physb.2011.02.072)
Google Scholar (http://scholar.google.com/scholar_lookup?title=Synthesis%2C%20structural%2C%20magnetic%20and%20optical%20properties%20of%20nanocrystalline%20ZnFe2O4%0A&author=OM.%20Lemine&author=M.%20Bououdina&author=M.%20Sajieddine&journal=Physica%20B&volume=406&issue=10&pages=1989-1994&publication_year=2011&doi=10.1016%2Fj.physb.2011.02.072)

43. Al-Saie AM, Bououdina M, Jaffar A et al (2011) The effect of annealing on the structure, magnetic properties and AC heating of $CoFe_2O_4$ for biomedical applications. J Alloys Compd 509:S393–S396. doi: 10.1016/j.jallcom.2011.02.024
(https://doi.org/10.1016/j.jallcom.2011.02.024)
CrossRef (https://doi.org/10.1016/j.jallcom.2011.02.024)
Google Scholar (http://scholar.google.com/scholar_lookup?title=The%20effect%20of%20annealing%20on%20the%20structure%2C%20magnetic%20properties%20and%20AC%20heating%20of%20CoFe2O4%20for%20biomedical%20applications&autho

r=AM.%20Al-Saie&author=M.%20Bououdina&author=A.%20Jaffar&journal=J%20Alloys%20Compd&volume=509&pages=S393-S396&publication_year=2011&doi=10.1016%2Fj.jallcom.2011.02.024)

44. Sundararajan M, Sailaja V, Kennedy LJ, Vijaya JJ (2017) Photocatalytic degradation of rhodamine B under visible light using nanostructured zinc doped cobalt ferrite: kinetics and mechanism. Ceram Int 43(1A):540–548. doi: 10.1016/j.ceramint.2016.09.191 (https://doi.org/10.1016/j.ceramint.2016.09.191) CrossRef (https://doi.org/10.1016/j.ceramint.2016.09.191) Google Scholar (http://scholar.google.com/scholar_lookup?title=Photocatalytic%20degradation%20of%20rhodamine%20B%20under%20visible%20light%20using%20nanostructured%20zinc%20doped%20cobalt%20ferrite%3A%20kinetics%20and%20mechanism&author=M.%20Sundararajan&author=V.%20Sailaja&author=LJ.%20Kennedy&author=JJ.%20Vijaya&journal=Ceram%20Int&volume=43&issue=1A&pages=540-548&publication_year=2017&doi=10.1016%2Fj.ceramint.2016.09.191)

45. Angadi VJ, Anupama AV, Choudhary HK et al (2017) Mechanism of γ-irradiation induced phase transformations in nanocrystalline $Mn_{0.5}Zn_{0.5}Fe_2O_4$ ceramics. J Solid State Chem 246:119–124. doi: 10.1016/j.jssc.2016.11.017 (https://doi.org/10.1016/j.jssc.2016.11.017) ADS (http://adsabs.harvard.edu/cgi-bin/nph-data_query?link_type=ABSTRACT&bibcode=2017JSSCh.246..119J) CrossRef (https://doi.org/10.1016/j.jssc.2016.11.017) Google Scholar (http://scholar.google.com/scholar_lookup?title=Mechanism%20of%20%CE%B3-irradiation%20induced%20phase%20transformations%20in%20nanocrystalline%20Mn0.5Zn0.5Fe2O4%20ceramics&author=VJ.%20Angadi&author=AV.%20Anupama&author=HK.%20Choudhary&journal=J%20Solid%20State%20Chem&volume=246&pages=119-124&publication_year=2017&doi=10.1016%2Fj.jssc.2016.11.017)

46. Angadi VJ, Rudraswamy B, Sadhana K et al (2016) Structural and magnetic properties of manganese zinc ferrite nanoparticles prepared by solution combustion method using mixture of fuels. J

Magn Magn Mater 409:111–115.
doi: 10.1016/j.jmmm.2016.02.096
(https://doi.org/10.1016/j.jmmm.2016.02.096)
ADS (http://adsabs.harvard.edu/cgi-bin/nph-data_query?link_type=ABSTRACT&bibcode=2016JMMM..409..111A)
CrossRef (https://doi.org/10.1016/j.jmmm.2016.02.096)
Google Scholar (http://scholar.google.com/scholar_lookup?title=Structural%20and%20magnetic%20properties%20of%20manganese%20zinc%20ferrite%20nanoparticles%20prepared%20by%20solution%20combustion%20method%20using%20mixture%20of%20fuels&author=VJ.%20Angadi&author=B.%20Rudraswamy&author=K.%20Sadhana&journal=J%20Magn%20Magn%20Mater&volume=409&pages=111-115&publication_year=2016&doi=10.1016%2Fj.jmmm.2016.02.096)

47. Gawas SG, Meena SS, Yusuf SM et al (2016) Anisotropy and domain state dependent enhancement of single domain ferrimagnetism in cobalt substituted Ni–Zn ferrites. New J Chem 40:9275–9284. doi: 10.1039/C6NJ02121B
(https://doi.org/10.1039/C6NJ02121B)
CrossRef (https://doi.org/10.1039/C6NJ02121B)
Google Scholar (http://scholar.google.com/scholar_lookup?title=Anisotropy%20and%20domain%20state%20dependent%20enhancement%20of%20single%20domain%20ferrimagnetism%20in%20cobalt%20substituted%20Ni%E2%80%93Zn%20ferrites&author=SG.%20Gawas&author=SS.%20Meena&author=SM.%20Yusuf&journal=New%20J%20Chem&volume=40&pages=9275-9284&publication_year=2016&doi=10.1039%2FC6NJ02121B)

48. Singh SB, Srinivas C, Tirupanyam BV et al (2016) Structural, thermal and magnetic studies of $Mg_xZn_{1-x}Fe_2O_4$ nanoferrites: study of exchange interactions on magnetic anisotropy. Ceram Int 42(16):19179–19186. doi: 10.1016/j.ceramint.2016.09.081
(https://doi.org/10.1016/j.ceramint.2016.09.081)
CrossRef (https://doi.org/10.1016/j.ceramint.2016.09.081)
Google Scholar (http://scholar.google.com/scholar_lookup?title=Structural%2C%20thermal%20and%20magnetic%20studies%20of%20MgxZn1%E2%88%92xFe2O4%20nanoferrites%3A%20study%20of%20exchange%20interactions%20on%20magnetic%20anisotropy&author=SB.%20Singh&author=C.%20Srinivas&author=BV.%20Tirupanyam&journal=Ceram%20Int&volume=42&iss

ue=16&pages=19179-19186&publication_year=2016&doi=10.1016%2Fj.ceramint.2016.09.081)

49. Sundararajan M, Kennedy LJ, Vijaya JJ et al (2015) Microwave combustion synthesis of $Co_{1-x}Zn_xFe_2O_4$ ($0 \leqslant x \leqslant 0.5$): structural, magnetic, optical and vibrational spectroscopic studies. Spectrochim. Acta Part A 140:421–430. doi: 10.1016/j.saa.2014.12.035 (https://doi.org/10.1016/j.saa.2014.12.035) ADS (http://adsabs.harvard.edu/cgi-bin/nph-data_query?link_type=ABSTRACT&bibcode=2015AcSpA.140..421S) CrossRef (https://doi.org/10.1016/j.saa.2014.12.035) Google Scholar (http://scholar.google.com/scholar_lookup?title=Microwave%20combustion%20synthesis%20of%20Co1%E2%88%92xZnxFe2O4%20%280%E2%A9%BDx%E2%A9%BD0.5%29%3A%20structural%2C%20magnetic%2C%20optical%20and%20vibrational%20spectroscopic%20studies&author=M.%20Sundararajan&author=LJ.%20Kennedy&author=JJ.%20Vijaya&journal=Spectrochim.%20Acta%20Part%20A&volume=140&pages=421-430&publication_year=2015&doi=10.1016%2Fj.saa.2014.12.035)

50. Manikandan A, Vijaya JJ, Mary JA et al (2014) Structural, optical and magnetic properties of Fe_3O_4 nanoparticles prepared by a facile microwave combustion method. J Ind Eng Chem 20(4):2077–2085. doi: 10.1016/j.jiec.2013.09.035 (https://doi.org/10.1016/j.jiec.2013.09.035) CrossRef (https://doi.org/10.1016/j.jiec.2013.09.035) Google Scholar (http://scholar.google.com/scholar_lookup?title=Structural%2C%20optical%20and%20magnetic%20properties%20of%20Fe3O4%20nanoparticles%20prepared%20by%20a%20facile%20microwave%20combustion%20method&author=A.%20Manikandan&author=JJ.%20Vijaya&author=JA.%20Mary&journal=J%20Ind%20Eng%20Chem&volume=20&issue=4&pages=2077-2085&publication_year=2014&doi=10.1016%2Fj.jiec.2013.09.035)

51. Lemine OM, Omri K, Zhang B et al (2012) Sol–gel synthesis of 8 nm magnetite (Fe_3O_4) nanoparticles and their magnetic properties. Superlattice Microst 52(4):793–799. doi: 10.1016/j.spmi.2012.07.009 (https://doi.org/10.1016/j.spmi.2012.07.009)

ADS (http://adsabs.harvard.edu/cgi-bin/nph-data_query?link_type=ABSTRACT&bibcode=2012SuMi...52..793L)
CrossRef (https://doi.org/10.1016/j.spmi.2012.07.009)
Google Scholar (http://scholar.google.com/scholar_lookup?title=Sol%E2%80%93gel%20synthesis%20of%208%20nm%20magnetite%20%28Fe3O4%29%20nanoparticles%20and%20their%20magnetic%20properties&author=OM.%20Lemine&author=K.%20Omri&author=B.%20Zhang&journal=Superlattice%20Microst&volume=52&issue=4&pages=793-799&publication_year=2012&doi=10.1016%2Fj.spmi.2012.07.009)

52. Manikandan A, Kennedy LJ, Bououdina M et al (2014) Synthesis, optical and magnetic properties of pure and Co-doped $ZnFe_2O_4$ nanoparticles by microwave combustion method. J Magn Magn Mater 349:249–258. doi: 10.1016/j.jmmm.2013.09.013 (https://doi.org/10.1016/j.jmmm.2013.09.013)
ADS (http://adsabs.harvard.edu/cgi-bin/nph-data_query?link_type=ABSTRACT&bibcode=2014JMMM..349..249M)
CrossRef (https://doi.org/10.1016/j.jmmm.2013.09.013)
Google Scholar (http://scholar.google.com/scholar_lookup?title=Synthesis%2C%20optical%20and%20magnetic%20properties%20of%20pure%20and%20Co-doped%20ZnFe2O4%20nanoparticles%20by%20microwave%20combustion%20method&author=A.%20Manikandan&author=LJ.%20Kennedy&author=M.%20Bououdina&journal=J%20Magn%20Magn%20Mater&volume=349&pages=249-258&publication_year=2014&doi=10.1016%2Fj.jmmm.2013.09.013)

53. Manikandan A, Vijaya JJ, Kennedy LJ et al (2013) Microwave combustion synthesis, structural, optical and magnetic properties of $Zn_{1-x}Sr_xFe_2O_4$ nanoparticles. Ceram Int 39(5):5909–5917. doi: 10.1016/j.ceramint.2013.01.012 (https://doi.org/10.1016/j.ceramint.2013.01.012)
CrossRef (https://doi.org/10.1016/j.ceramint.2013.01.012)
Google Scholar (http://scholar.google.com/scholar_lookup?title=Microwave%20combustion%20synthesis%2C%20structural%2C%20optical%20and%20magnetic%20properties%20of%20Zn1%E2%88%92xSrxFe2O4%20nanoparticles&author=A.%20Manikandan&author=JJ.%20Vijaya&author=LJ.%20Kennedy&journal=Ceram%20Int&volume=39&issue=5&pages=5909-

5917&publication_year=2013&doi=10.1016%2Fj.ceramint.2013.01.012)

54. Manikandan A, Vijaya JJ, Kennedy LJ et al (2013) Structural, optical and magnetic properties of $Zn_{1-x}Cu_xFe_2O_4$ nanoparticles prepared by microwave combustion method. J Mol Struct 1035:332–340. doi: 10.1016/j.molstruc.2012.11.007 (https://doi.org/10.1016/j.molstruc.2012.11.007) ADS (http://adsabs.harvard.edu/cgi-bin/nph-data_query?link_type=ABSTRACT&bibcode=2013JMoSt1035..332M) CrossRef (https://doi.org/10.1016/j.molstruc.2012.11.007) Google Scholar (http://scholar.google.com/scholar_lookup?title=Structural%2C%20optical%20and%20magnetic%20properties%20of%20Zn1%E2%88%92xCuxFe2O4%20nanoparticles%20prepared%20by%20microwave%20combustion%20method&author=A.%20Manikandan&author=JJ.%20Vijaya&author=LJ.%20Kennedy&journal=J%20Mol%20Struct&volume=1035&pages=332-340&publication_year=2013&doi=10.1016%2Fj.molstruc.2012.11.007)

55. Manikandan A, Vijaya JJ, Kennedy LJ (2013) Comparative study of pure and Ni-doped $ZnFe_2O_4$ nanoparticles for structural, optical and magnetic properties. Adv Mater Res 699:524–529 CrossRef (https://doi.org/10.4028/www.scientific.net/AMR.699.524) Google Scholar (http://scholar.google.com/scholar_lookup?title=Comparative%20study%20of%20pure%20and%20Ni-doped%20ZnFe2O4%20nanoparticles%20for%20structural%2C%20optical%20and%20magnetic%20properties&author=A.%20Manikandan&author=JJ.%20Vijaya&author=LJ.%20Kennedy&journal=Adv%20Mater%20Res&volume=699&pages=524-529&publication_year=2013)

56. Panchal S, Raghuvanshi S, Gehlot K et al (2016) Cationic distribution assisted tuning of magnetic properties of $Li_{0.5-x/2}Zn_xFe_{2.5-x/2}O_4$. AIP Adv 6(5):055930. doi: 10.1063/1.4944517 (https://doi.org/10.1063/1.4944517) ADS (http://adsabs.harvard.edu/cgi-bin/nph-data_query?link_type=ABSTRACT&bibcode=2016AIPA....6e5930P) CrossRef (https://doi.org/10.1063/1.4944517) Google Scholar (http://scholar.google.com/scholar_lookup?title=Cationic%20distribution%20assisted%20tuning%20of%20magnetic%20properties%20of%20Li0.5-x%2F2ZnxFe2.5-

x%2F2O4%0A&author=S.%20Panchal&author=S.%20Raghuvanshi&author=K.%20Gehlot&journal=AIP%20Adv&volume=6&issue=5&pages=055930&publication_year=2016&doi=10.1063%2F1.4944517)

57. Khalaf KAM, Al-Rawas AD, Widatallah HM et al (2016) Influence of Zn^{2+} ions on the structural and electrical properties of $Mg_{1-x}Zn_xFeCrO_4$ spinels. J Alloys Compd 657:733–747. doi: 10.1016/j.jallcom.2015.10.157 (https://doi.org/10.1016/j.jallcom.2015.10.157) CrossRef (https://doi.org/10.1016/j.jallcom.2015.10.157) Google Scholar (http://scholar.google.com/scholar_lookup?title=Influence%20of%20Zn2%2B%20ions%20on%20the%20structural%20and%20electrical%20properties%20of%20Mg1%E2%88%92xZnxFeCrO4%20spinels&author=KAM.%20Khalaf&author=AD.%20Al-Rawas&author=HM.%20Widatallah&journal=J%20Alloys%20Compd&volume=657&pages=733-747&publication_year=2016&doi=10.1016%2Fj.jallcom.2015.10.157)

58. Hashim M, Shirsath SE, Meena SS et al (2015) Manganese ferrite prepared using reverse micelle process: structural and magnetic properties characterization. J Alloys Compd 642:70–77. doi: 10.1016/j.jallcom.2015.04.085 (https://doi.org/10.1016/j.jallcom.2015.04.085) CrossRef (https://doi.org/10.1016/j.jallcom.2015.04.085) Google Scholar (http://scholar.google.com/scholar_lookup?title=Manganese%20ferrite%20prepared%20using%20reverse%20micelle%20process%3A%20structural%20and%20magnetic%20properties%20characterization&author=M.%20Hashim&author=SE.%20Shirsath&author=SS.%20Meena&journal=J%20Alloys%20Compd&volume=642&pages=70-77&publication_year=2015&doi=10.1016%2Fj.jallcom.2015.04.085)

59. Heiba ZK, Mohamed MB, Ahmed MA et al (2014) Cation distribution and dielectric properties of nanocrystalline gallium substituted nickel ferrite. J Alloys Compd 586:773–781. doi: 10.1016/j.jallcom.2013.10.137 (https://doi.org/10.1016/j.jallcom.2013.10.137) CrossRef (https://doi.org/10.1016/j.jallcom.2013.10.137)

Google Scholar (http://scholar.google.com/scholar_lookup?title=Cation%20distribution%20and%20dielectric%20properties%20of%20nanocrystalline%20gallium%20substituted%20nickel%20ferrite&author=ZK.%20Heiba&author=MB.%20Mohamed&author=MA.%20Ahmed&journal=J%20Alloys%20Compd&volume=586&pages=773-781&publication_year=2014&doi=10.1016%2Fj.jallcom.2013.10.137)

60. Hemeda OM, Mostafa NY, Abd Elkader OH et al (2014) Solubility limits in Mn–Mg ferrites system under hydrothermal conditions. J Magn Magn Mater 364:39–46. doi: 10.1016/j.jmmm.2014.03.061 (https://doi.org/10.1016/j.jmmm.2014.03.061)
ADS (http://adsabs.harvard.edu/cgi-bin/nph-data_query?link_type=ABSTRACT&bibcode=2014JMMM..364...39H)
CrossRef (https://doi.org/10.1016/j.jmmm.2014.03.061)
Google Scholar (http://scholar.google.com/scholar_lookup?title=Solubility%20limits%20in%20Mn%E2%80%93Mg%20ferrites%20system%20under%20hydrothermal%20conditions&author=OM.%20Hemeda&author=NY.%20Mostafa&author=OH.%20Abd%20Elkader&journal=J%20Magn%20Magn%20Mater&volume=364&pages=39-46&publication_year=2014&doi=10.1016%2Fj.jmmm.2014.03.061)

61. Manikandan A, Vijaya JJ, Sundararajan M et al (2013) Optical and magnetic properties of Mg-doped $ZnFe_2O_4$ nanoparticles prepared by rapid microwave combustion method. Superlattice Microst 64:118–131. doi: 10.1016/j.spmi.2013.09.021 (https://doi.org/10.1016/j.spmi.2013.09.021)
ADS (http://adsabs.harvard.edu/cgi-bin/nph-data_query?link_type=ABSTRACT&bibcode=2013SuMi...64..118M)
CrossRef (https://doi.org/10.1016/j.spmi.2013.09.021)
Google Scholar (http://scholar.google.com/scholar_lookup?title=Optical%20and%20magnetic%20properties%20of%20Mg-doped%20ZnFe2O4%20nanoparticles%20prepared%20by%20rapid%20microwave%20combustion%20method&author=A.%20Manikandan&author=JJ.%20Vijaya&author=M.%20Sundararajan&journal=Superlattice%20Microst&volume=64&pages=118-131&publication_year=2013&doi=10.1016%2Fj.spmi.2013.09.021)

62. Tanaka T, Shimazu R, Nagai H et al (2009) Preparation of spherical and uniform-sized ferrite nanoparticles with diameters between 50 and 150 nm for biomedical applications. J Magn Magn Mater 321:1417–1420
ADS (http://adsabs.harvard.edu/cgi-bin/nph-data_query?link_type=ABSTRACT&bibcode=2009JMMM..321.1417T)
CrossRef (https://doi.org/10.1016/j.jmmm.2009.02.054)
Google Scholar (http://scholar.google.com/scholar_lookup?title=Preparation%20of%20spherical%20and%20uniform-sized%20ferrite%20nanoparticles%20with%20diameters%20between%2050%20and%20150%20nm%20for%20biomedical%20applications&author=T.%20Tanaka&author=R.%20Shimazu&author=H.%20Nagai&journal=J%20Magn%20Magn%20Mater&volume=321&pages=1417-1420&publication_year=2009)

63. Jasso-Terán RA, Cortés-Hernández DA, Sánchez-Fuentes HJ et al (2017) Synthesis, characterization and hemolysis studies of $Zn_{(1-x)}Ca_xFe_2O_4$ ferrites synthesized by sol-gel for hyperthermia treatment applications. J Magn Magn Mater.
doi: 10.1016/j.jmmm.2016.10.099
(https://doi.org/10.1016/j.jmmm.2016.10.099) (in press)
Google Scholar (http://scholar.google.com/scholar_lookup?title=Synthesis%2C%20characterization%20and%20hemolysis%20studies%20of%20Zn%281%E2%88%92x%29CaxFe2O4%20ferrites%20synthesized%20by%20sol-gel%20for%20hyperthermia%20treatment%20applications&author=RA.%20Jasso-Ter%C3%A1n&author=DA.%20Cort%C3%A9s-Hern%C3%A1ndez&author=HJ.%20S%C3%A1nchez-Fuentes&journal=J%20Magn%20Magn%20Mater&publication_year=2017&doi=10.1016%2Fj.jmmm.2016.10.099%20%28in%20press%29)

64. Ruthradevi T, Akbar J, Kumar GS et al (2017) Investigations on nickel ferrite embedded calcium phosphate nanoparticles for biomedical applications. J Alloys Compd 695:3211–3219.
doi: 10.1016/j.jallcom.2016.11.300
(https://doi.org/10.1016/j.jallcom.2016.11.300)
CrossRef (https://doi.org/10.1016/j.jallcom.2016.11.300)
Google Scholar (http://scholar.google.com/scholar_lookup?title=Investigations%20on%20nickel%20ferrite%20embedded%20calcium%20phosphate%20nanoparticles%20for%20biomedical%20applications&author=T.%20Ruthradevi&author=J.%20Akbar

&author=GS.%20Kumar&journal=J%20Alloys%20Compd&volume=695&pages=3211-3219&publication_year=2017&doi=10.1016%2Fj.jallcom.2016.11.300)

65. Latorre-Esteves M, Corte's A, Torres-Lugo M et al (2009) Synthesis and characterization of carboxymethyl dextran-coated Mn/Zn ferrite for biomedical applications. J Magn Magn Mater 321:3061–3066
ADS (http://adsabs.harvard.edu/cgi-bin/nph-data_query?link_type=ABSTRACT&bibcode=2009JMMM..321.3061L)
CrossRef (https://doi.org/10.1016/j.jmmm.2009.05.023)
Google Scholar (http://scholar.google.com/scholar_lookup?title=Synthesis%20and%20characterization%20of%20carboxymethyl%20dextran-coated%20Mn%2FZn%20ferrite%20for%20biomedical%20applications&author=M.%20Latorre-Esteves&author=A.%20Corte%E2%80%99s&author=M.%20Torres-Lugo&journal=J%20Magn%20Magn%20Mater&volume=321&pages=3061-3066&publication_year=2009)

66. Falsafi F, Hashemi B, Mirzaei A et al (2017) Sm-doped cobalt ferrite nanoparticles: a novel sensing material for conductometric hydrogen leak sensor. Ceram Int 43:1029–1037.
doi: 10.1016/j.ceramint.2016.10.035
(https://doi.org/10.1016/j.ceramint.2016.10.035)
CrossRef (https://doi.org/10.1016/j.ceramint.2016.10.035)
Google Scholar (http://scholar.google.com/scholar_lookup?title=Sm-doped%20cobalt%20ferrite%20nanoparticles%3A%20a%20novel%20sensing%20material%20for%20conductometric%20hydrogen%20leak%20sensor&author=F.%20Falsafi&author=B.%20Hashemi&author=A.%20Mirzaei&journal=Ceram%20Int&volume=43&pages=1029-1037&publication_year=2017&doi=10.1016%2Fj.ceramint.2016.10.035)

67. Sandu I, Presmanes L, Alphonse P et al (2006) Nanostructured cobalt manganese ferrite thin films for gas sensor application. Thin Solid Films 495:130–133
ADS (http://adsabs.harvard.edu/cgi-bin/nph-data_query?link_type=ABSTRACT&bibcode=2006TSF...495..130S)

CrossRef (https://doi.org/10.1016/j.tsf.2005.08.318)
Google Scholar (http://scholar.google.com/scholar_lookup?title=Nanostructured%20cobalt%20manganese%20ferrite%20thin%20films%20for%20gas%20sensor%20application&author=I.%20Sandu&author=L.%20Presmanes&author=P.%20Alphonse&journal=Thin%20Solid%20Films&volume=495&pages=130-133&publication_year=2006)

68. Wen T, Zhu W, Xue C et al (2014) Novel electrochemical sensing platform based on magnetic field-induced self-assembly of Fe_3O_4@Polyaniline nanoparticles for clinical detection of creatinine. Biosens Bioelectron 56:180–185
CrossRef (https://doi.org/10.1016/j.bios.2014.01.013)
Google Scholar (http://scholar.google.com/scholar_lookup?title=Novel%20electrochemical%20sensing%20platform%20based%20on%20magnetic%20field-induced%20self-assembly%20of%20Fe3O4%40Polyaniline%20nanoparticles%20for%20clinical%20detection%20of%20creatinine&author=T.%20Wen&author=W.%20Zhu&author=C.%20Xue&journal=Biosens%20Bioelectron&volume=56&pages=180-185&publication_year=2014)

69. Praveena K, Chen H-W, Liu H-L et al (2016) Enhanced magnetic domain relaxation frequency and low power losses in Zn^{2+} substituted manganese ferrites potential for high frequency applications. J Magn Magn Mater 420:129–142
ADS (http://adsabs.harvard.edu/cgi-bin/nph-data_query?link_type=ABSTRACT&bibcode=2016JMMM..420..129P)
CrossRef (https://doi.org/10.1016/j.jmmm.2016.07.011)
Google Scholar (http://scholar.google.com/scholar_lookup?title=Enhanced%20magnetic%20domain%20relaxation%20frequency%20and%20low%20power%20losses%20in%20Zn2%2B%20substituted%20manganese%20ferrites%20potential%20for%20high%20frequency%20applications&author=K.%20Praveena&author=H-W.%20Chen&author=H-L.%20Liu&journal=J%20Magn%20Magn%20Mater&volume=420&pages=129-142&publication_year=2016)

70. Li B, Yue Z-X, Qi X-W et al (2003) High Mn content NiCuZn ferrite for multiplayer chip inductor application. Mater Sci Eng B 99:252–254
CrossRef (https://doi.org/10.1016/S0921-5107(02)00489-0)

Google Scholar (http://scholar.google.com/scholar_lookup?title=High%20Mn%20content%20NiCuZn%20ferrite%20for%20multiplayer%20chip%20inductor%20application&author=B.%20Li&author=Z-X.%20Yue&author=X-W.%20Qi&journal=Mater%20Sci%20Eng%20B&volume=99&pages=252-254&publication_year=2003)

71. Yang Q, Zhang H, Liu Y et al (2009) Microstructure and magnetic properties of microwave sintered M-type barium ferrite, for application in LTCC devices. Mater Lett 63:406–408
CrossRef (https://doi.org/10.1016/j.matlet.2008.10.066)
Google Scholar (http://scholar.google.com/scholar_lookup?title=Microstructure%20and%20magnetic%20properties%20of%20microwave%20sintered%20M-type%20barium%20ferrite%2C%20for%20application%20in%20LTCC%20devices&author=Q.%20Yang&author=H.%20Zhang&author=Y.%20Liu&journal=Mater%20Lett&volume=63&pages=406-408&publication_year=2009)

72. Reddy NR, Ramana MV, Rajitha G et al (2009) Stress insensitive NiCuZn ferrite compositions for microinductor applications. Curr Appl Phys 9:317–323
ADS (http://adsabs.harvard.edu/cgi-bin/nph-data_query?link_type=ABSTRACT&bibcode=2009CAP.....9..317R)
CrossRef (https://doi.org/10.1016/j.cap.2008.02.012)
Google Scholar (http://scholar.google.com/scholar_lookup?title=Stress%20insensitive%20NiCuZn%20ferrite%20compositions%20for%20microinductor%20applications&author=NR.%20Reddy&author=MV.%20Ramana&author=G.%20Rajitha&journal=Curr%20Appl%20Phys&volume=9&pages=317-323&publication_year=2009)

73. Kumbhar VS, Jagadale AD, Shinde NM et al (2012) Chemical synthesis of spinel cobalt ferrite ($CoFe_2O_4$) nano-flakes for supercapacitor application. Appl Surf Sci 259:39–43
ADS (http://adsabs.harvard.edu/cgi-bin/nph-data_query?link_type=ABSTRACT&bibcode=2012ApSS..259...39K)
CrossRef (https://doi.org/10.1016/j.apsusc.2012.06.034)
Google Scholar (http://scholar.google.com/scholar_lookup?title=Chemical%20synthesis%20of%20spinel%20cobalt%20ferrite%20%28CoFe2O4%29%20nano-flakes%20for%20supercapacitor%20application&author=VS.%20Kumbhar&author=AD.%20Jagadale&author=NM.%20Shinde&jo

urnal=Appl%20Surf%20Sci&volume=259&pages=39-43&publication_year=2012)

74. Bashir B, Shaheen W, Asghar M et al (2016) Copper doped manganese ferrites nanoparticles anchored on graphene nano-sheets for high performance energy storage applications. J Alloys Compd 695:881–887. doi: 10.1016/j.jallcom.2016.10.183 (https://doi.org/10.1016/j.jallcom.2016.10.183)
CrossRef (https://doi.org/10.1016/j.jallcom.2016.10.183)
Google Scholar (http://scholar.google.com/scholar_lookup?title=Copper%20doped%20manganese%20ferrites%20nanoparticles%20anchored%20on%20graphene%20nano-sheets%20for%20high%20performance%20energy%20storage%20applications&author=B.%20Bashir&author=W.%20Shaheen&author=M.%20Asghar&journal=J%20Alloys%20Compd&volume=695&pages=881-887&publication_year=2016&doi=10.1016%2Fj.jallcom.2016.10.183)

75. Bindu K, Sridharan K, Ajith KM et al (2016) Microwave assisted growth of stannous ferrite microcubes as electrodes for potentiometric nonenzymatic H_2O_2 sensor and supercapacitor applications. Electrochim Acta 217:139–149
CrossRef (https://doi.org/10.1016/j.electacta.2016.09.083)
Google Scholar (http://scholar.google.com/scholar_lookup?title=Microwave%20assisted%20growth%20of%20stannous%20ferrite%20microcubes%20as%20electrodes%20for%20potentiometric%20nonenzymatic%20H2O2%20sensor%20and%20supercapacitor%20applications&author=K.%20Bindu&author=K.%20Sridharan&author=KM.%20Ajith&journal=Electrochim%20Acta&volume=217&pages=139-149&publication_year=2016)

76. Charalampos AS, Litsardakis G (2016) Y-type hexagonal ferrites for microwave absorber and antenna applications. J Magn Magn Mater 405:54–61
CrossRef (https://doi.org/10.1016/j.jmmm.2015.12.027)
Google Scholar (http://scholar.google.com/scholar_lookup?title=Y-type%20hexagonal%20ferrites%20for%20microwave%20absorber%20and%20antenna%20applications&author=AS.%20Charalampos&author=G.%20Litsardakis&journal=J%20Magn%20Magn%20Mater&volume=405&pages=54-61&publication_year=2016)

77. Dadfar MR, Ebrahimi SAS, Masoudpanah SM (2015) Sol–gel synthesis and characterization of $SrFe_{12}O_{19}/TiO_2$ nanocomposites. J Supercond Nov Magn 28(1):89–94
CrossRef (https://doi.org/10.1007/s10948-014-2802-y)
Google Scholar (http://scholar.google.com/scholar_lookup?title=Sol%E2%80%93gel%20synthesis%20and%20characterization%20of%20SrFe12O19%2FTiO2%20nanocomposites&author=MR.%20Dadfar&author=SAS.%20Ebrahimi&author=SM.%20Masoudpanah&journal=J%20Supercond%20Nov%20Magn&volume=28&issue=1&pages=89-94&publication_year=2015)

78. Meng P, Xiong K, Ju K (2015) Wideband and enhanced microwave absorption performance of doped barium ferrite. J Magn Magn Mater 385:407–411
ADS (http://adsabs.harvard.edu/cgi-bin/nph-data_query?link_type=ABSTRACT&bibcode=2015JMMM..385..407M)
CrossRef (https://doi.org/10.1016/j.jmmm.2015.02.059)
Google Scholar (http://scholar.google.com/scholar_lookup?title=Wideband%20and%20enhanced%20microwave%20absorption%20performance%20of%20doped%20barium%20ferrite&author=P.%20Meng&author=K.%20Xiong&author=K.%20Ju&journal=J%20Magn%20Magn%20Mater&volume=385&pages=407-411&publication_year=2015)

79. Zhang X-J, Wang G-S, Cao W-Q et al (2014) Enhanced microwave absorption property of reduced graphene oxide (RGO)-$MnFe_2O_4$ nanocomposites and polyvinylidene fluoride. ACS Appl Mater Interfaces 6:7471–7478
CrossRef (https://doi.org/10.1021/am500862g)
Google Scholar (http://scholar.google.com/scholar_lookup?title=Enhanced%20microwave%20absorption%20property%20of%20reduced%20graphene%20oxide%20%28RGO%29-MnFe2O4%20nanocomposites%20and%20polyvinylidene%20fluoride&author=X-J.%20Zhang&author=G-S.%20Wang&author=W-Q.%20Cao&journal=ACS%20Appl%20Mater%20Interfaces&volume=6&pages=7471-7478&publication_year=2014)

80. Chang S, Kangning S, Pengfei C (2012) Microwave absorption properties of Ce-substituted M-type barium ferrite. J Magn Magn Mater 324(5):802–805
ADS (http://adsabs.harvard.edu/cgi-bin/nph-data_query?link_type=ABSTRACT&bibcode=2012JMMM..324..802C)

CrossRef (https://doi.org/10.1016/j.jmmm.2011.09.023)
Google Scholar (http://scholar.google.com/scholar_lookup?title=Microwave%20absorption%20properties%20of%20Ce-substituted%20M-type%20barium%20ferrite&author=S.%20Chang&author=S.%20Kangning&author=C.%20Pengfei&journal=J%20Magn%20Magn%20Mater&volume=324&issue=5&pages=802-805&publication_year=2012)

81. Tyagi S, Baskey HB, Agarwala RC et al (2011) Development of hard/soft ferrite nanocomposite for enhanced microwave absorption. Ceram Int 37(7):2631–2641
CrossRef (https://doi.org/10.1016/j.ceramint.2011.04.012)
Google Scholar (http://scholar.google.com/scholar_lookup?title=Development%20of%20hard%2Fsoft%20ferrite%20nanocomposite%20for%20enhanced%20microwave%20absorption&author=S.%20Tyagi&author=HB.%20Baskey&author=RC.%20Agarwala&journal=Ceram%20Int&volume=37&issue=7&pages=2631-2641&publication_year=2011)

82. Casbeer E, Sharma VK, Li X-Z (2012) Synthesis and photocatalytic activity of ferrites under visible light: a review. Sep Purif Technol 87:1–14
CrossRef (https://doi.org/10.1016/j.seppur.2011.11.034)
Google Scholar (http://scholar.google.com/scholar_lookup?title=Synthesis%20and%20photocatalytic%20activity%20of%20ferrites%20under%20visible%20light%3A%20a%20review&author=E.%20Casbeer&author=VK.%20Sharma&author=X-Z.%20Li&journal=Sep%20Purif%20Technol&volume=87&pages=1-14&publication_year=2012)

83. Valero-Luna C, Palomares-Sanchéz SA, Ruíz F (2016) Catalytic activity of the barium hexaferrite with H_2O_2/visible light irradiation for degradation of methylene blue. Catal Today 266:110–119. doi: 10.1016/j.cattod.2015.08.049
(https://doi.org/10.1016/j.cattod.2015.08.049)
CrossRef (https://doi.org/10.1016/j.cattod.2015.08.049)
Google Scholar (http://scholar.google.com/scholar_lookup?title=Catalytic%20activity%20of%20the%20barium%20hexaferrite%20with%20H2O2%2Fvisible%20light%20irradiation%20for%20degradation%20of%20methylene%20blue&author=C.%20Valero-Luna&author=SA.%20Palomares-Sanch%C3%A9z&author=F.%20Ru%C3%ADz&journal=Catal%20

Today&volume=266&pages=110-119&publication_year=2016&doi=10.1016%2Fj.cattod.2015.08.049)

Copyright information

About this paper

Cite this paper as:

Tatarchuk T., Bououdina M., Judith Vijaya J., John Kennedy L. (2017) Spinel Ferrite Nanoparticles: Synthesis, Crystal Structure, Properties, and Perspective Applications. In: Fesenko O., Yatsenko L. (eds) Nanophysics, Nanomaterials, Interface Studies, and Applications. NANO 2016. Springer Proceedings in Physics, vol 195. Springer, Cham

- First Online 10 May 2017
- DOI https://doi.org/10.1007/978-3-319-56422-7_22
- Publisher Name Springer, Cham
- Print ISBN 978-3-319-56244-5
- Online ISBN 978-3-319-56422-7
- eBook Packages Physics and Astronomy

Personalised recommendations

Hierarchical ZSM-5 Zeolite Nanosurfaces with High Porosity—Structural, Morphological and Textural Investigations

Recent Trends in Materials Science and Applications pp 109-118 | Cite as

- S. K. Jesudoss (1)
- J. Judith Vijaya (1) Email author (jjvijaya78@gmail.com)
- A. Anancia Grace (1)
- L. John Kennedy (2)
- S. Sivasanker (3)
- P. Kathirgamanathan (4)

1. Catalysis and Nanomaterials Research Laboratory, Department of Chemistry, Loyola College, , Chennai, India
2. Materials Division, School of Advanced Sciences, Vellore Institute of Technology (VIT) University, , Chennai, India
3. National Centre for Catalysis Research, Indian Institute of Technology Madras, , Chennai, India
4. Organic Electronics, Wolfson Centre, Brunel University, , Uxbridge, UK

Conference paper
First Online: 04 May 2017

Part of the Springer Proceedings in Physics book series (SPPHY, volume 189)

Abstract

The present paper describes the successful synthesis of hierarchical ZSM-5 zeolite nanosurfaces with high porosity from the rice straw ash (RSA) by means of the hydrothermal method at varying time intervals in the presence of small amount of tetrapropylammonium bromide as a single template. The synthesized samples were characterized by X-ray diffraction (XRD), Fourier transform infrared spectroscopy (FT-IR), high resolution scanning electron microscopy (HR-SEM), and nitrogen adsorption–desorption analysis (BET). The XRD pattern confirms the formation of pure ZSM-5 zeolite crystalline phase without any impurity phases. The IR spectrum shows a vibration band at 548 cm^{-1}, which is assigned to the double 5-rings of MFI-type zeolites. The surface area results reveal the formation of additional mesoporosity without destroying the intensive microporosity in a hierarchical ZSM-5 zeolite, which is due to the addition of TPABr during the synthesis. The characterization results conclude that the long time process of hierarchical ZSM-5 zeolite nanosurfaces with high porosity have produced high crystallinity.

Keywords

Rice Straw High Resolution Scanning Electron Microscopy
Zeolite Surface Tetrapropylammonium Bromide
Material Rice Straw
These keywords were added by machine and not by the authors. This process is experimental and the keywords may be updated as the learning algorithm improves.

Notes

Acknowledgements

The authors duly acknowledge the financial support rendered by Loyola college, Tamil Nadu, India through Loyola College-Times of India (LC-TOI) Major Research Project scheme vide (Project Code: 2LCTOI14CHM003, dated 25.11.2014) to the first author.

References

1. Dey, K.P., Ghosh, S., Naskar, M.K.: Organic template-free synthesis of ZSM-5 zeolite particles using rice husk ash as silica source. Ceram. Int. **39**, 2153–2157 (2013)
CrossRef (https://doi.org/10.1016/j.ceramint.2012.07.083)
Google Scholar (http://scholar.google.com/scholar_lookup?title=Organic%20template-free%20synthesis%20of%20ZSM-5%20zeolite%20particles%20using%20rice%20husk%20ash%20as%20silica%20source&author=KP.%20Dey&author=S.%20Ghosh&author=MK.%20Naskar&journal=Ceram.%20Int.&volume=39&pages=2153-2157&publication_year=2013)

2. Jiang, J., Duanmu, C., Yang, Y., Gu, X., Chen, J.: Synthesis and characterization of high siliceous ZSM-5 zeolite from acid-treated palygorskite. Powder Technol. **251**, 9–14 (2014)
CrossRef (https://doi.org/10.1016/j.powtec.2013.10.020)
Google Scholar (http://scholar.google.com/scholar_lookup?title=Synthesis%20and%20characterization%20of%20high%20siliceous%20ZSM-5%20zeolite%20from%20acid-treated%20palygorskite&author=J.%20Jiang&author=C.%20Duanmu&author=Y.%20Yang&author=X.%20Gu&author=J.%20Chen&journal=Powder%20Technol.&volume=251&pages=9-14&publication_year=2014)

3. Motsi, T., Rowson, N.A., Simmons, M.J.H.: Kinetic studies of the removal of heavy metals from acid mine drainage by natural zeolite. Int. J. Miner. Process. **101**, 42–49 (2011)
CrossRef (https://doi.org/10.1016/j.minpro.2011.07.004)
Google Scholar (http://scholar.google.com/scholar_lookup?title=Kinetic%20studies%20of%20the%20removal%20of%20heavy%20metals%20from%20acid%20mine%20drainage%20by%20natural%20zeolite&author=T.%20Motsi&author=NA.%20Rowson&author=MJH.%20Simmons&journal=Int.%20J.%20Miner.%20Process.&volume=101&pages=42-49&publication_year=2011)

4. Egeblad, K., Christensen, C.H., Kustova, M., Christensen, C.H.: Templating mesoporous zeolites. Chem. Mater. **20**, 946–960 (2008)
CrossRef (https://doi.org/10.1021/cm702224p)

Google Scholar (http://scholar.google.com/scholar_lookup?title=Templating%20mesoporous%20zeolites&author=K.%20Egeblad&author=CH.%20Christensen&author=M.%20Kustova&author=CH.%20Christensen&journal=Chem.%20Mater.&volume=20&pages=946-960&publication_year=2008)

5. Argauer, R.J., Landolt G.R.: US Patent 3 702 886 A. (1972)
Google Scholar (https://scholar.google.com/scholar?q=Argauer%2C%20R.J.%2C%20Landolt%20G.R.%3A%20US%20Patent%203%20702%20886%20A.%20%281972%29)

6. Narayanan, S., Vijaya, J.J., Sivasanker, S., Yang, S., Kennedy, L.J.: Hierarchical ZSM-5 catalyst synthesized by a Triton X-100 assisted hydrothermal method. Chinese J. Catal. **35**, 1892–1899 (2014)
CrossRef (https://doi.org/10.1016/S1872-2067(14)60177-7)
Google Scholar (http://scholar.google.com/scholar_lookup?title=Hierarchical%20ZSM-5%20catalyst%20synthesized%20by%20a%20Triton%20X-100%20assisted%20hydrothermal%20method&author=S.%20Narayanan&author=JJ.%20Vijaya&author=S.%20Sivasanker&author=S.%20Yang&author=LJ.%20Kennedy&journal=Chinese%20J.%20Catal.&volume=35&pages=1892-1899&publication_year=2014)

7. Pan, F., Lu, X., Wang, Y., Chen, S., Wang, T., Yan, Y.: Synthesis and crystallization kinetics of ZSM-5 without organic template from coal-series kaolinite. Micropor. Mesopor. Mater. **184**, 134–140 (2014)
CrossRef (https://doi.org/10.1016/j.micromeso.2013.10.013)
Google Scholar (http://scholar.google.com/scholar_lookup?title=Synthesis%20and%20crystallization%20kinetics%20of%20ZSM-5%20without%20organic%20template%20from%20coal-series%20kaolinite&author=F.%20Pan&author=X.%20Lu&author=Y.%20Wang&author=S.%20Chen&author=T.%20Wang&author=Y.%20Yan&journal=Micropor.%20Mesopor.%20Mater.&volume=184&pages=134-140&publication_year=2014)

8. Azizi, S., Yousefpour, M.: Synthesis of zeolites NaA and analcime using rice husk ash as silica source without using organic template. J. Mater. Sci. **45**, 5692–5697 (2010)
ADS (http://adsabs.harvard.edu/cgi-bin/nph-data_query?link_type=ABSTRACT&bibcode=2010JMatS..45.5692A)

CrossRef (https://doi.org/10.1007/s10853-010-4637-7)
Google Scholar (http://scholar.google.com/scholar_lookup?title=Synthesis%20of%20zeolites%20NaA%20and%20analcime%20using%20rice%20husk%20ash%20as%20silica%20source%20without%20using%20organic%20template&author=S.%20Azizi&author=M.%20Yousefpour&journal=J.%20Mater.%20Sci.&volume=45&pages=5692-5697&publication_year=2010)

9. Gadde, B., Menke, C., Wassmann, R.: Rice straw as a renewable energy source in India, Thailand, and the Philippines: overall potential and limitations for energy contribution and greenhouse gas mitigation. Biomass Bioenerg. **33**, 1532–1546 (2009)
CrossRef (https://doi.org/10.1016/j.biombioe.2009.07.018)
Google Scholar (http://scholar.google.com/scholar_lookup?title=Rice%20straw%20as%20a%20renewable%20energy%20source%20in%20India%2C%20Thailand%2C%20and%20the%20Philippines%3A%20overall%20potential%20and%20limitations%20for%20energy%20contribution%20and%20greenhouse%20gas%20mitigation&author=B.%20Gadde&author=C.%20Menke&author=R.%20Wassmann&journal=Biomass%20Bioenerg.&volume=33&pages=1532-1546&publication_year=2009)

10. Hamdan, H., Muhid, M.N.M., Endud, S., Listiorini, E., Ramli, Z.: ^{29}Si MAS NMR, XRD and FESEM studies of rice husk silica for the synthesis of zeolites. J. Non-Cryst. Solids **211**, 126–131 (1997)
ADS (http://adsabs.harvard.edu/cgi-bin/nph-data_query?link_type=ABSTRACT&bibcode=1997JNCS..211..126H)
CrossRef (https://doi.org/10.1016/S0022-3093(96)00611-4)
Google Scholar (http://scholar.google.com/scholar_lookup?title=%0A%20%20%20%20%20%20%20%20%20%20%20%20%209Si%20MAS%20NMR%2C%20XRD%20and%20FESEM%20studies%20of%20rice%20husk%20silica%20for%20the%20synthesis%20of%20zeolites&author=H.%20Hamdan&author=MNM.%20Muhid&author=S.%20Endud&author=E.%20Listiorini&author=Z.%20Ramli&journal=J.%20Non-Cryst.%20Solids&volume=211&pages=126-131&publication_year=1997)

11. Azizi, S.N., Yousefpour, M.: Spectroscopic studies of different kind of rice husk samples grown in North of Iran and the extracted silica by using XRD, XRF, IR, AA and NMR techniques. Eurasian J. Anal. Chem. **3**, 298–306 (2008)

Google Scholar (http://scholar.google.com/scholar_lookup?title=Spectroscopic%20studies%20of%20different%20kind%20of%20rice%20husk%20samples%20grown%20in%20North%20of%20Iran%20and%20the%20extracted%20silica%20by%20using%20XRD%2C%20XRF%2C%20IR%2C%20AA%20and%20NMR%20techniques&author=SN.%20Azizi&author=M.%20Yousefpour&journal=Eurasian%20J.%20Anal.%20Chem.&volume=3&pages=298-306&publication_year=2008)

12. Yusof, A.M., Nizam, N.A., Rashid, N.A.A.: Hydrothermal conversion of rice husk ash to faujasite-types and NaA-type of zeolites. J. Porous Mater. **17**, 39–47 (2010)
CrossRef (https://doi.org/10.1007/s10934-009-9262-y)
Google Scholar (http://scholar.google.com/scholar_lookup?title=Hydrothermal%20conversion%20of%20rice%20husk%20ash%20to%20faujasite-types%20and%20NaA-type%20of%20zeolites&author=AM.%20Yusof&author=NA.%20Nizam&author=NAA.%20Rashid&journal=J.%20Porous%20Mater.&volume=17&pages=39-47&publication_year=2010)

13. Barrer, R.M.: The hydrothermal chemistry of zeolites. Academic Press, London (1982)
Google Scholar (http://scholar.google.com/scholar_lookup?title=The%20hydrothermal%20chemistry%20of%20zeolites&author=RM.%20Barrer&publication_year=1982)

14. Wang, L., Yin, C., Shan, Z., Liu, S., Du, Y., Xiao, F.S.: Bread-template synthesis of hierarchical mesoporous ZSM-5 zeolite with hydrothermally stable mesoporosity. Colloids Surf. A **340**, 126–130 (2009)
CrossRef (https://doi.org/10.1016/j.colsurfa.2009.03.013)
Google Scholar (http://scholar.google.com/scholar_lookup?title=Bread-template%20synthesis%20of%20hierarchical%20mesoporous%20ZSM-5%20zeolite%20with%20hydrothermally%20stable%20mesoporosity&author=L.%20Wang&author=C.%20Yin&author=Z.%20Shan&author=S.%20Liu&author=Y.%20Du&author=FS.%20Xiao&journal=Colloids%20Surf.%20A&volume=340&pages=126-130&publication_year=2009)

15. Becheri, A., Dürr, M., Nostro, P.L., Baglioni, P.: Synthesis and characterization of zinc oxide nanoparticles: Application to

textiles as UV-absorbers. J. Nanopart. Res. **10**, 679–689 (2008)
ADS (http://adsabs.harvard.edu/cgi-bin/nph-data_query?link_type=ABSTRACT&bibcode=2008JNR....10..679B)
CrossRef (https://doi.org/10.1007/s11051-007-9318-3)
Google Scholar (http://scholar.google.com/scholar_lookup?title=Synthesis%20and%20characterization%20of%20zinc%20oxide%20nanoparticles%3A%20Application%20to%20textiles%20as%20UV-absorbers&author=A.%20Becheri&author=M.%20D%C3%BCrr&author=PL.%20Nostro&author=P.%20Baglioni&journal=J.%20Nanopart.%20Res.&volume=10&pages=679-689&publication_year=2008)

16. Guo, Y.P., Wang, H.J., Guo, Y.J., Guo, L.H., Chu, L.F., Guo, C.X.: Fabrication and characterization of hierarchical ZSM-5 zeolites by using organosilanes as additives. Chem. Eng. J. **166**, 391–400 (2011)
CrossRef (https://doi.org/10.1016/j.cej.2010.10.057)
Google Scholar (http://scholar.google.com/scholar_lookup?title=Fabrication%20and%20characterization%20of%20hierarchical%20ZSM-5%20zeolites%20by%20using%20organosilanes%20as%20additives&author=YP.%20Guo&author=HJ.%20Wang&author=YJ.%20Guo&author=LH.%20Guo&author=LF.%20Chu&author=CX.%20Guo&journal=Chem.%20Eng.%20J.&volume=166&pages=391-400&publication_year=2011)

17. Narayanan, S., Vijaya, J.J., Sivasanker, S., Yang, S., Kennedy, L.J.: Hierarchical ZSM-5 catalyst synthesized by a Triton X-100 assisted hydrothermal method. Chinese J. Catal. **35**, 1892–1899 (2014)
CrossRef (https://doi.org/10.1016/S1872-2067(14)60177-7)
Google Scholar (http://scholar.google.com/scholar_lookup?title=Hierarchical%20ZSM-5%20catalyst%20synthesized%20by%20a%20Triton%20X-100%20assisted%20hydrothermal%20method&author=S.%20Narayanan&author=JJ.%20Vijaya&author=S.%20Sivasanker&author=S.%20Yang&author=LJ.%20Kennedy&journal=Chinese%20J.%20Catal.&volume=35&pages=1892-1899&publication_year=2014)

18. Chester, A.W., Derouane, E.G.: Zeolite Characterization and Catalysis: A Tutorial. Springer, (2009)

Google Scholar (https://scholar.google.com/scholar?q=Chester%2C%20A.W.%2C%20Derouane%2C%20E.G.%3A%20Zeolite%20Characterization%20and%20Catalysis%3A%20A%20Tutorial.%20Springer%2C%20%282009%29)

19. Vijaya, J.J., Kennedy, L.J., Sekaran, G., Nagaraja, K.S.: Synthesis, characterization and humidity sensing properties of Cu–Sr–Al mixed metal oxide composites. Mater. Res. Bull. **43**, 473–482 (2008)
CrossRef (https://doi.org/10.1016/j.materresbull.2007.02.030)
Google Scholar (http://scholar.google.com/scholar_lookup?title=Synthesis%2C%20characterization%20and%20humidity%20sensing%20properties%20of%20Cu%E2%80%93Sr%E2%80%93Al%20mixed%20metal%20oxide%20composites&author=JJ.%20Vijaya&author=LJ.%20Kennedy&author=G.%20Sekaran&author=KS.%20Nagaraja&journal=Mater.%20Res.%20Bull.&volume=43&pages=473-482&publication_year=2008)

20. Schmidt, F., Lohe, M.R., Buchner, B., Giordanino, F., Bonino, F., Kaskel, S.: Improved catalytic performance of hierarchical ZSM-5 synthesized by desilication with surfactants. Micropor. Mesopor. Mater. **165**, 148–157 (2013)
CrossRef (https://doi.org/10.1016/j.micromeso.2012.07.045)
Google Scholar (http://scholar.google.com/scholar_lookup?title=Improved%20catalytic%20performance%20of%20hierarchical%20ZSM-5%20synthesized%20by%20desilication%20with%20surfactants&author=F.%20Schmidt&author=MR.%20Lohe&author=B.%20Buchner&author=F.%20Giordanino&author=F.%20Bonino&author=S.%20Kaskel&journal=Micropor.%20Mesopor.%20Mater.&volume=165&pages=148-157&publication_year=2013)

21. Sang, Y., Liu, H., He, S., Li, H., Jiao, Q., Wu, Q., Sun, K.: Catalytic performance of hierarchical H-ZSM-5/MCM-41 for methanol dehydration to dimethyl ether. J. Energy Chem. **22**, 769–777 (2013)
CrossRef (https://doi.org/10.1016/S2095-4956(13)60102-3)
Google Scholar (http://scholar.google.com/scholar_lookup?title=Catalytic%20performance%20of%20hierarchical%20H-ZSM-5%2FMCM-41%20for%20methanol%20dehydration%20to%20dimethyl%20ether&author=Y.%20Sang&author=H.%20Liu&author=S.%20He&author=H.%20Li&author=Q.%20Jiao&author=Q.%20Wu&author

=K.%20Sun&journal=J.%20Energy%20Chem.&volume=22&pages=769-777&publication_year=2013)

22. Wang, Y.Y., Gin, G.Q., Guo, X.Y.: Growth of ZSM-5 coating on biomorphic porous silicon carbide derived from durra. Micropor. Mesopor. Mater. **118**, 302–306 (2009)
CrossRef (https://doi.org/10.1016/j.micromeso.2008.09.001)
Google Scholar (http://scholar.google.com/scholar_lookup?title=Growth%20of%20ZSM-5%20coating%20on%20biomorphic%20porous%20silicon%20carbide%20derived%20from%20durra&author=YY.%20Wang&author=GQ.%20Gin&author=XY.%20Guo&journal=Micropor.%20Mesopor.%20Mater.&volume=118&pages=302-306&publication_year=2009)

23. Fernandez, C., Stan, I., Gilson, J.P., Thomas, K., Vicente, A., Bonilla, A., Ramirez, J.P.: Hierarchical ZSM-5 zeolites in shape-selective xylene isomerization: Role of mesoporosity and acid site speciation. Chem. Eur. J. **16**, 6224–6233 (2010)
CrossRef (https://doi.org/10.1002/chem.200903426)
Google Scholar (http://scholar.google.com/scholar_lookup?title=Hierarchical%20ZSM-5%20zeolites%20in%20shape-selective%20xylene%20isomerization%3A%20Role%20of%20mesoporosity%20and%20acid%20site%20speciation&author=C.%20Fernandez&author=I.%20Stan&author=JP.%20Gilson&author=K.%20Thomas&author=A.%20Vicente&author=A.%20Bonilla&author=JP.%20Ramirez&journal=Chem.%20Eur.%20J.&volume=16&pages=6224-6233&publication_year=2010)

Copyright information

About this paper

Cite this paper as:

Jesudoss S.K., Judith Vijaya J., Anancia Grace A., John Kennedy L., Sivasanker S., Kathirgamanathan P. (2017) Hierarchical ZSM-5 Zeolite Nanosurfaces with High Porosity—Structural, Morphological and Textural Investigations. In: Ebenezar J. (eds) Recent

Trends in Materials Science and Applications. Springer Proceedings in Physics, vol 189. Springer, Cham

- First Online 04 May 2017
- DOI https://doi.org/10.1007/978-3-319-44890-9_11
- Publisher Name Springer, Cham
- Print ISBN 978-3-319-44889-3
- Online ISBN 978-3-319-44890-9
- eBook Packages Physics and Astronomy

Personalised recommendations

Structural and electrical properties of organic stilbazolium single crystal of DSCHS

S. John Sundaram, A. Antony Raj, Jerald V. Ramaclus, and P. Sagayaraj

Citation: AIP Conference Proceedings **1731**, 100004 (2016); doi: 10.1063/1.4948010
View online: http://dx.doi.org/10.1063/1.4948010
View Table of Contents: http://aip.scitation.org/toc/apc/1731/1
Published by the American Institute of Physics

Structural and Electrical Properties of Organic Stilbazolium Single Crystal of DSCHS

S. John Sundaram[a], A. Antony Raj[b], Jerald V. Ramaclus[a], P. Sagayaraj[a]*

[a]*Department of Physics, Loyola College, Chennai – 600034 *e-mail: psagayaraj@hotmail.com*
b Department of Physics, AMET University, Kanathur, Chennai - 603112

Abstract. Organic nonlinear optical crystal 4-N, N-Dimethyl Amino-4'N'-Methyl-Stilbazolium 3-Carboxy-4-Hydroxy benzenesulfonate (DSCHS) has been successfully grown from aqueous methanol solution by adopting slow solvent evaporation technique. Chemical composition of the sample was confirmed by CHN analysis. Powder X-ray diffraction analysis was carried out and it shows that DSCHS crystal belongs to triclinic structure with P1 space group. It is found that this material exhibits positive photoconductivity. Dielectric studies were also carried out for different temperature by varying the frequency.

Keywords: Organic compound; X-ray diffraction; Dielectric; Nonlinear optical materials
PACS: 78.30.jw; 61.05 cp; 77.22.-d

INTRODUCTION

The chrysalis of organic non-centrosymmetric nonlinear optical (NLO) crystals for Terahertz (THz) generation and detection has been an extremely active field of research lately. It is due to their superior NLO properties when compared to other conventional semiconductors and inorganic materials. One of the popular ionic organic crystals, 4-N, N-dimethylamino-4-methyl-stilbazolium tosylate (DAST), is now commercially available as a THz source [1-4]. The development of ionic organic crystals by changing counter anion approach provides ample choice of new derivatives of DAST [4]. One such material, 4-N, N-Dimethyl Amino-4'N'-Methyl-Stilbazolium 3-Carboxy-4-Hydroxy benzenesulfonate (DSCHS) whose counter anion possesses hydroxyl and carboxyl groups, is found to be attractive because it showed a strong SHG activity 30% higher than the well-known organic nonlinear optical crystal DAST [1]. However it was crystallized only in the micrometre range [1]. Therefore we have attempted to increase the size by optimizing the growth conditions and report their structural and electrical properties.

MATERIAL SYNTHESIS

DSCHS was prepared via metathesization by adding 4-N, N-dimethylamino-4-N'-methylstilbazolium iodide (DMSI) cation with sodium salt of 3-Carboxy 4-hydroxy benzenesulfonate anion. The cation DMSI was synthesized from 1, 4-dimethyl pyridinium iodide (10 mmol), and 4N, N-dimethylamino benzaldehyde (10 mmol) in the presence of piperidine (0.2 ml), methanol as a solvent. The purity of DSCHS is further improved by successive re-crystallization from methanol.

Crystal Growth

A mixed solvent of methanol and water (1:1) is taken for the crystal growth of DSCHS because of its unfavorable solubility characteristics in polar and non-polar solvents. Crystal growth experiment is performed by using the slow solvent evaporation method. In 250 ml of mixed solvent, 0.4 g of DSCHS was well dissolved by stirring for many hours, after that it was filtered and kept it in the temperature bath for crystal growth. The temperature was maintained at 35 ˚C for the crystal growth. After 10-15 days of solvent evaporation, crystals of size 1 x 0.5 mm^2 were harvested (Fig.1).

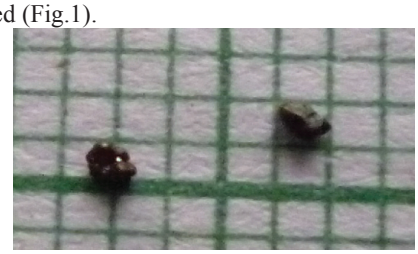

FIGURE 1 Photograph of DSCHS single crystal.

DAE Solid State Physics Symposium 2015
AIP Conf. Proc. 1731, 100004-1–100004-3; doi: 10.1063/1.4948010
Published by AIP Publishing. 978-0-7354-1378-8/$30.00

RESULT AND DISCUSSION

CHN Analysis

Organic compounds are essentially made up of the elements carbon, hydrogen, nitrogen and oxygen. In order to confirm the chemical composition of the synthesized DSCHS material, we carried out CHN analysis using the CHNS analyzer. The percentage of carbon, hydrogen and nitrogen found from CHN analysis are 60.24, 5.44 and 6.22% respectively. Theoretical values of C, H and N calculated from the molecular formula of DSCHS (C23H24N2O6S) are: C= 60.51%, H= 5.30 % and N= 6.14%. The experimental and calculated values of C, H and N are in good agreement with each other. It is also revealed from this study that material was free from any impurities and confirming the formation of DSCHS.

Powder XRD Analysis

Powder X-ray diffraction analysis on the DSCHS crystal was carried out in the range 10 - 50°. The Kα radiations from a copper target (λ = 1.5406 Å) was used. The powdered sample of DSCHS was spread over a square centimeter area and placed in a beam of monochromatic X-rays. The mass of powder was rotated about all possible axes. From the θ value for each peak, the spacing d was obtained. The indexed Powder X-ray diffraction pattern of DSCHS is shown in Figure 2. From the powder X-ray diffraction data, the lattice parameters have been calculated Table 1. It is observed that lattice parameters are in good agreement with the reported values [1]. The crystal belongs to the triclinic structure with noncentrosymmetric group.

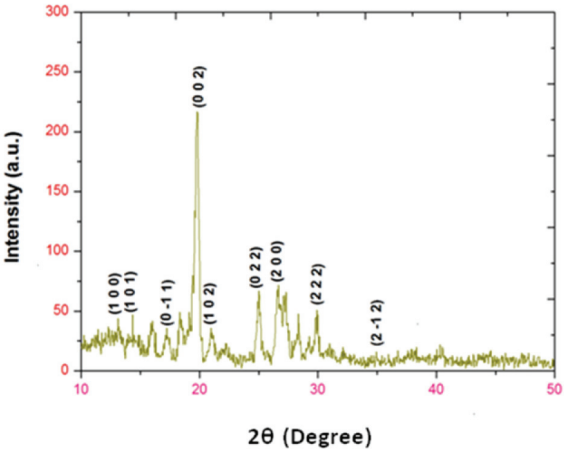

FIGURE 2 Powder XRD pattern for DSCHS crystal.

TABLE 1 XRD data for DSCHS crystal

Parameter	Powder XRD	Single crystal XRD [1]
Formula	$C_{23}H_{24}N_2O_6S$	$C_{23}H_{24}N_2O_6S$
Formula weight	456.50	456.50
Crystal system	Triclinic	Triclinic
Space group	P1	P1
a (Å)	7.139	7.1334
b (Å)	8.637	8.5394
c (Å)	9.936	9.965

Photoconductivity study

The variation of both dark current (Id) and photocurrent (Ip) with applied field is shown in figure. It is seen from the plots that both Id and Ip of the sample increases linearly with applied field. It is further observed from the plot the photocurrent is always higher than the dark current. Hence it can be concluded that DSCHS exhibits positive photoconductivity. This phenomenon can be attributed to the generation of mobile charge carriers caused by the absorption of the photons. This suggests that, the prospect of DSCHS as an organic photoconductive material can also be explored in future.

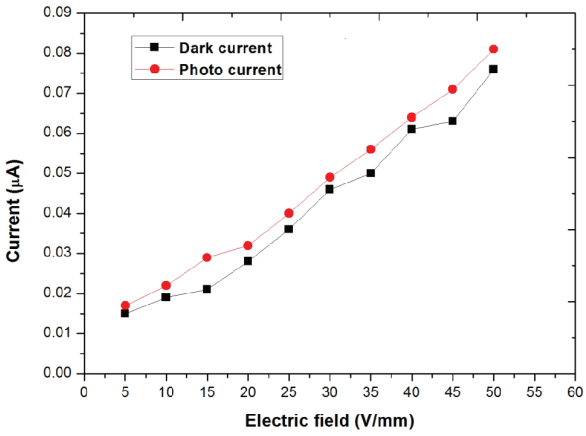

FIGURE 3 Plot of current vs applied electric field for DSCHS crystal

Dielectric study

Dielectric permittivity measurements were carried out on DSCHS crystal. The sample was silver coated and then placed inside a dielectric cell and the capacitance measurements were done by maintaining the temperature at 313 K, 323 K, 333 K, 343 K, 353 and 363 K in the frequency range 50 Hz to 5MHz

using HOIKI 3532-50 LCR Hitester. Figure 4 and 5 show the plot of dielectric constant ε_r as a function of log frequency and the plot of dielectric loss (tan δ) as a function of log frequency for DSCHS crystal respectively [5]. It is observed that both dielectric constant and dielectric loss exhibit similar variation with frequency. The graphs show that dielectric constant and dielectric loss are both inversely proportional to frequency. This is a normal dielectric behaviour that both ε_r and tan δ decrease with increasing frequency. This can be understood on the basis that the mechanism of polarization is similar to that of conduction process. Further, the dielectric constant value of the DSCHS sample is found to increase with increase temperature.

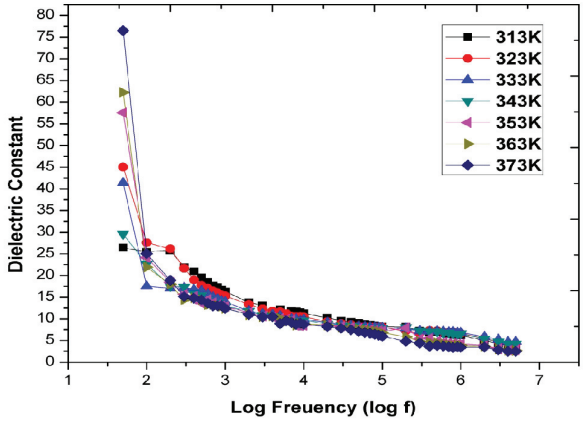

FIGURE 4 Frequency dependence of dielectric constant for DSCHS crystal

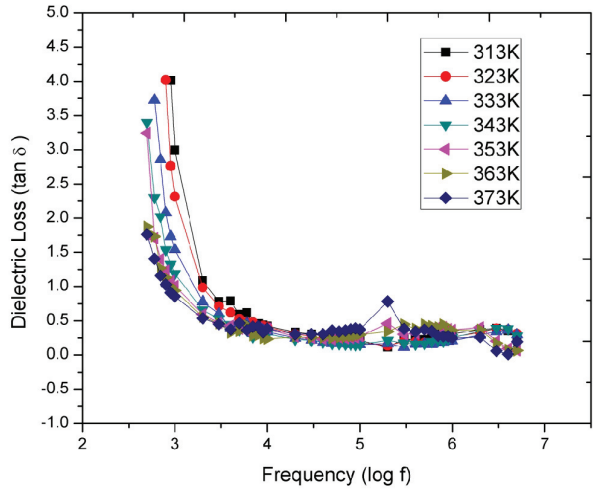

FIGURE 5 Frequency dependence of dielectric loss for DSCHS crystal

CONCLUSION

The size of DSCHS single crystals were improved into a reasonable size by slow solvent evaporation method using methanol-water as solvent. The crystal structure and elemental composition were determined by powder X-ray diffraction and CHN Analyses. Photoconductivity Studies shows that sample exhibit positive photoconductivity. The dielectric constant and dielectric loss were found to be decreasing with increase of frequency. Thus the growth of DSCHS single crystal of good crystalline quality would makes it as a potential candidate for NLO, photonics and THz applications.

ACKNOWLEDGMENTS

The authors acknowledge DST-SERB (SR/S2/LOP-029/2013) India, for funding this research work.

REFERENCES

1. J. Yin, L. Li, Z. Yang, M. Jazbinsek, X. Tao, P. Günter, H. Yang, Dyes and Pigments **94**, 120-126 (2012).
2. R. Jerald Vijay, N. Melikechi, Tina Thomas, R. Gunaseelan, M. Antony Arockiaraj, P. Sagayaraj, Journal of Crystal Growth **338**, 170–176 (2012)
3. A. Antony Raj, S. John Sundaram, R. Gunaseelan, P. Sagayaraj, pectrochimica Acta Part A: Molecular and Biomolecular Spectroscopy, **149**, 957-964 (2015)
4. Z. Yang, S. Aravazhi, A. Schneider, P. Seiler, M. Jazbinsek P. Gunter, Adv. Funct. Mater., **15**, 1072-1076 (2005)
5. R. Jerald Vijay, Tina Thomas, S. Ramesh, P. Sagayaraj, E. A. Michael, CrystEngComm, **16**, 6889-6895 (2014)

Available online at www.sciencedirect.com

ScienceDirect

Materials Today: Proceedings 3 (2016) 1599–1603

materialstoday: PROCEEDINGS

www.materialstoday.com/proceedings

Recent Advances In Nano Science And Technology 2015 (RAINSAT2015)

Effect of hydrothermal synthesis on the particulate characteristics of Nanocrystalline titanium dioxide

Sheeba Anu Jacob, S. Jerome Das*

Department of Physics, Loyola College, Chennai 600 034, India.

Abstract

Nanocrystalline Titanium dioxide particles have been synthesized through hydrothermal method to study the effect of autoclaving temperature and annealing temperature on their particulate characteristics. The nanoparticles have been synthesized using a Titanium alkoxide precursor at two different temperatures 160 °C and 200 °C for 14h and annealed at 450 °C. X-ray diffraction studies were used to ascertain the tetragonal structure and the anatase phase represented by the synthesized samples. The particle size of the synthesized material was derived using the Scherrer formula and it was found to be of the order of 10 - 20 nm. The optical absorption spectrum reveals the absorption-edge to be slightly red-shifted. The band gap of the synthesized materials was evaluated using the Tauc plot and it was determined to be ~ 3.25 ± 0.02eV. The emission spectrum for the sample was recorded at an excitation wavelength of 295 nm and the flat bands were found to depict the inherent defect states. Although the FE-SEM images display a high agglomeration, they reveal the morphology of the particulates to be a spherical one. The HR-TEM images of the sample clearly corroborate with the spherical morphology and the particle size as represented by FESEM and XRD studies respectively.

Selection and Peer-review under responsibility of [Conference Committee Members of Recent Advances In Nano Science and Technology 2015

*Keywords:*Tetragonal anatase TiO_2; red shifted absorption edge; Tauc plot; spherical morphology

* Corresponding author. Tel.+919094139314; fax: +0-000-000-0000 .
E-mail address: jerome@loyolacollege.edu

Selection and Peer-review under responsibility of [Conference Committee Members of Recent Advances In Nano Science and Technology 2015.].

1. Introduction

Nanocrystalline Titanium dioxide has etched a place for itself under the category of promising functional materials due to its multivariant applications[1,2], strong oxidizing power[3], cost effectiveness[2] and stability against photocorrosion[3] and chemical corrosion[3]. The existence of the material in three different phases (i.e. anatase, rutile and brookite) and the excellent properties exhibited by its anatase phase puts it as a frontrunner in the choice of materials. To improve the functional properties of the material, it is important to control its particulate characteristics by tailoring its surface-to-volume ratio and the electronic structure [4]. These can be controlled by a careful selection of the method of fabrication. Among the various synthesis techniques, hydrothermal synthesis finds a unique place due to the various aspects that it can control. Hydrothermal treatment helps to control grain size, particle morphology, phase composition and surface chemical properties by controlling parameters like temperature, pressure, duration, concentration and pH value [5]. In the present work, Titanium dioxide nanoparticles have been synthesized in the anatase phase at an ambient molar ratio of the precursor and solvent in an effort to functionalize its particulate characteristics by controlling its autoclaving and annealing temperature.

2. Experimental

In our present work, Titanium (IV) isopropoxide was used as the precursor and absolute ethanol was used as the solvent. The chemicals purchased from Merck were used without further purification. The alkoxide precursor was added dropwise into the solvent at a molar ratio of 1:2 while stirring. The solution immediately turns turbid and stirring was continued for few hours at a mild temperature of 40°C until a clear and homogenous solution was obtained. The homogenous solution was then transferred into a 150 ml stainless steel Teflon-lined autoclave and maintained at temperatures 160 and 200 °C for 14h. The autoclave was cooled down to room temperature. The white precipitate obtained was then washed several times with double distilled water. The final product thus obtained was dried in an oven at 100 °C for about a day. The powders were then ground well using a ceramic mortar and subjected to annealing at 450 °C for 3h in a furnace. The X-ray diffractograms for the synthesized samples were obtained using Sumens D5000 instrument with Cu Kα radiation (λ=1.540598 Å) in the 2θ range 10 - 70°. The optical absorption spectra were recorded in the wavelength range of 200 – 800 nm on a Varian Cary 500 Spectrophotometer. The room temperature PL measurements were done on a JOBIN YVON FLUROLOG-3-11 SPECTROFLURIMETER with a 450W Xenon Lamp as source. The images of surface morphology were captured at a voltage of 30 kV on a HITACHI SU6600 FESEM instrument. The HR-TEM images were recorded using FEI-TECHNAI, G2-Model T30 High Resolution Transmission Electron microscope (HRTEM) at an accelerating voltage of 250 kV.

3. Results and Discussion

3.1. Structural characteristics

Fig. 1 shown below displays the X-ray diffraction patterns for the samples synthesized at 160 and 200°C respectively. The synthesized material displays a tetragonal structure and all the peaks are indexed to the anatase phase of Titanium dioxide corresponding to the card no. (PCPDF 73-1764). However, as reported by E.P. Melian et.al. [6] a minor peak corresponding to the Brookite phase is also visible.

The Scherrer formula [7] was used to calculate the particle size for the most prominent peak at (101) and it was found to be 10 nm and 14 nm for samples at 160 °C and 200 °C respectively. It can be seen that an increase in autoclaving temperature produces a narrowing of peak width and hence an increase in particle size. Further, the annealing of the sample at 450 °C has resulted in a high degree of crystallinity.

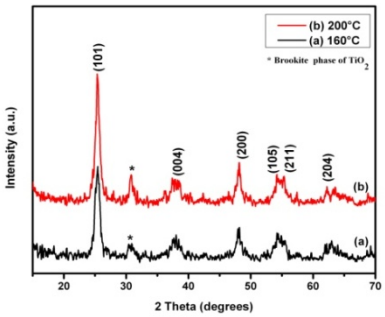

Fig.1. X-ray diffraction patterns for TiO_2 powders annealed at 450

3.2. Optical characteristics

The absorption band gap energy was determined using the Tauc formula [8] given by $(\alpha h\nu)^{1/n} = K(h\nu - E_g)$, where α is the absorption coefficient, hν is the photon energy, K is a constant relative to the material and n is the nature of transition in a semiconductor material. A plot of $(\alpha h\nu)^2$ vs (hν) is used to evaluate the direct optical band gap of the material. Fig. 2b shows the Tauc plot for both the synthesized samples. Extrapolating the linear portion of the curve, the band gap was determined and it was found to be 3.24 eV and 3.20 eV for samples synthesized at 160 °C and 200 °C respectively. The values are much in line with the values reported for anatase TiO_2 [9]. Although there is no significant variation in band gap with change in autoclaving temperature, the minor variations seen can be correlated with the particle size variation in both the samples as discussed through the X-ray diffraction patterns.

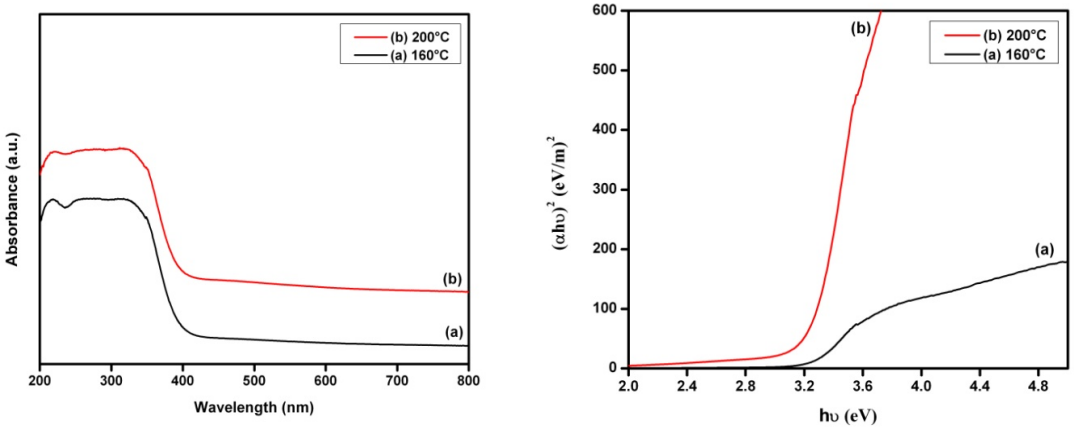

Fig. 2. (a) Absorption Spectrum for annealed TiO_2 powders, (b) Tauc plot for annealed TiO_2 powders

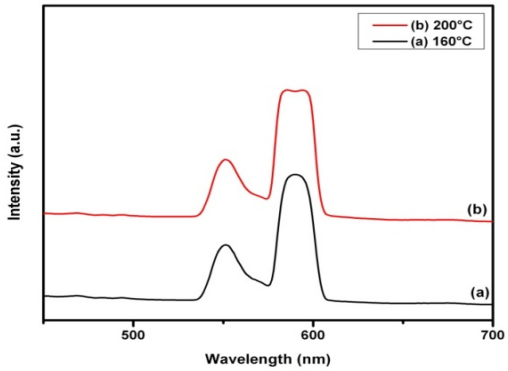

Fig. 3. Photoluminescence spectrum for TiO_2 powders annealed at 450 °C

The room temperature PL measurements were done on a JOBIN YVON FLUROLOG-3-11 SPECTROFLURIMETER with a 450W Xenon Lamp as source. Fig. 3 shows the room temperature PL spectra recorded for samples synthesized at 160 °C and 200 °C for a wavelength range of 250 - 700 nm. The emission peaks were recorded at an excitation wavelength of 295 nm. The spectra shows two emission band centered around 550 nm and 590 nm. It has been reported by Lei et.al [10] that nanostructured titania generally exhibit broad emission band centered at around 360 - 550 nm at room temperature. This could be more because of the surface defects which play a major role in defining the luminescence properties. The band centered around 590 nm can also be assumed to originate from the defect states present [11], which could be because of the oxygen vacancies that arise during annealing at 450 °C.

It has been clearly reported by A. Schuler et.al. [12] that variations in annealing temperature causes a shift in the dominating peak of the PL spectrum and higher annealing temperature results in an increasing mean cluster size. However, in our present work since the annealing temperature is maintained at 450 °C for both samples, the minor dip seen in sample (b) in the band centered at 590 nm could be attributed to the changes in the formation of nanocrystals with the autoclaving temperature being different for both the samples.

3.3. Morphological characteristics

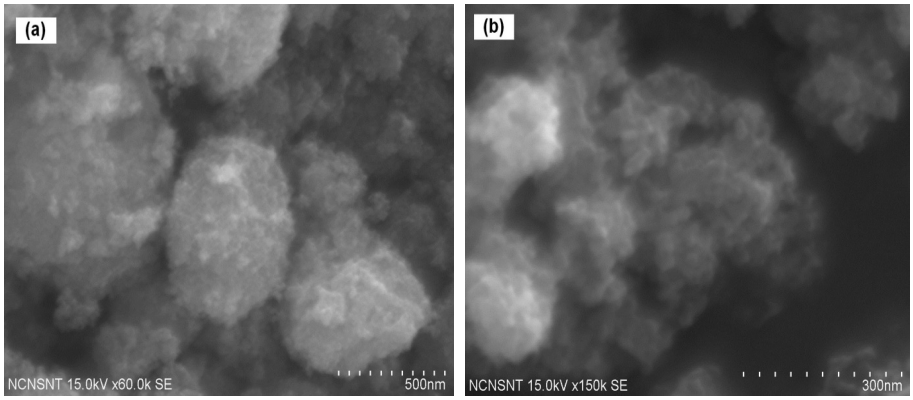

Fig. 4. FE-SEM images for annealed TiO_2 powders synthesized at (a) 160 °C (b) 200 °C

Fig.4a and 4b shows the FE-SEM images for samples synthesized at 160 and 200 ºC for 14h. The FE-SEM image in Fig.4a displays the synthesized powder in the form of polydisperse and roughly spherical particles with their sizes ranging about ~15 nm. It can be seen that the powders are heavily agglomerated. With an increase in temperature to 200 ºC, it exhibits a rearranged nature and the nanocrystallites appear as much more well-defined spheres as in Fig.4b with their size ~ 18-20 nm. This is caused by the restructuring of TiO_2 at a higher temperature [13,14]. The crystallite sizes calculated from the FE-SEM images are found to be in almost good agreement with the XRD results.

The HR-TEM images for samples synthesized at 200 ºC for 14h at two different magnifications is shown in Fig. 5a and 5b. Although the agglomeration is clearly visible, a better picture of the spherical particulates is convincingly displayed. The images reflect numerous primary TiO_2 particles in the form of roughly spherical spheres with crystallite sizes in the range of 10 - 15 nm, which is in good agreement with the XRD results as well as with the FE-SEM images. It can be well explained through these images that at an autoclaving temperature of 200 ºC, the particles attain better uniformity and good crystallinity.

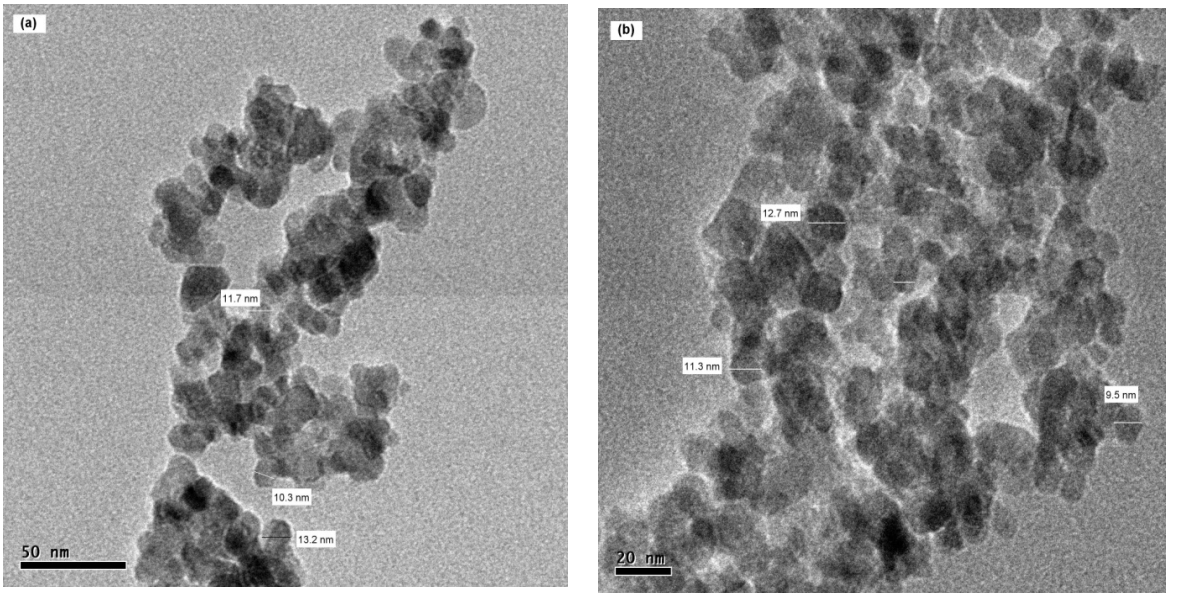

Fig. 5. HR-TEM images for annealed TiO_2 powders synthesized at 200 °C at (a) low magnification (b) high magnification

4. Conclusions

Nanocrystalline anatase TiO_2 particles with tetragonal structure have been synthesized through hydrothermal route and it can be understood that the autoclaving temperature as well as the annealing temperature plays a vital role in defining the characteristics of the particle. While the autoclaving temperature promotes grain growth, annealing causes particle agglomeration, increase in size, while bringing in better crystallinity. Optical analysis brings in a better understanding about the bandgap of the synthesized samples which is related to its particle size variation and hence dependent on both autoclaving and annealing temperature. The quantum of information provided by the PL spectrum elaborates upon the impurity states present and the role of autoclaving temperature is evident in the sample. The morphological presentation provided by the HR-TEM images with a spherical nature gives a tallying insight to the above discussions.

Acknowledgement

The authors gratefully acknowledge the financial assistance from Department of Science and Technology (DST), Government of India through the project [REF: SR/WOS-A/PS-16/2012 (G)] under Women Scientist Scheme (WOS-A).

References

[1] Xia X.H., Luo Y.S., Wang Z., Liang Y., Fan J., Jia Z.J. et al., Mater. Lett 2007; 61: 257-4
[2] Kin I.D., Rothschild A, Lee B.H., Kim D.Y., Jo S.M., Tuller H.L., Nano Lett 2006; 6: 2009-13
[3] M.R. Hoffmann, S.T. Martin, W. Choi, D. W. Bahnemann, Chem. Rev. 95 (1995) 69
[4] M. Tomita, M. Matsuoka, Masahiro, J. Opt. Soc. Am. B 7 (1990) 1198 - 1203
[5] K. Byrappa, M. Yoshimura, Handbook of Hydrothermal Technology, William Andrew Publishing, New York, 2001
[6] E. P. Melian, O.G. Diaz, J.M.D. Rodriguez, G. Colon, J.A. Navio, J. Perez pena, Applied Catalysis A: General 411-412 (2012)153-159.
[7] Yee-Shin Chang, Yen-Hwei Chang, Journal of Crystal growth, 2002, 243(2), 319-326.
[8] J. Tauc, R. Grigorovici, A. Vancu, Phys. Status. Solid. 15 (1966) 627- 637.
[9] X.H. Wang, J.G. Li, H. Kamiyama, M. Katada, N. Ohashi, Y. Moriyoshi, T. Ishigaki, J. Am. Chem. Soc. 127 (2005) 10982.
[10] Y.Lei, D. Zhang, Journal of Materials Research, 16 (2001) 1138.
[11] N. Serpone, D. Lawless, R. Khairutdinov, J. Phys. Chem. 99 (1995) 16646.
[12] A. Schuler, M. Python, M. Valle del Olmo, E. de Chambrier, Solar Energy 81(2007) 1159-1165.
[13] J.D. Ng, B. Lorber, J. Witz, A. Theobald-Dietrich, D. kern, R. Giege, J. Cryst. Growth 168 (1996) 50.
[14] R. Boistelle, J.P. Astier, J. Cryst. Growth 90 (1988) 14.

Available online at www.sciencedirect.com

ScienceDirect

Materials Today: Proceedings 3 (2016) 2008–2017

materialstoday: PROCEEDINGS

www.materialstoday.com/proceedings

Recent Advances In Nano Science And Technology 2015 (RAINSAT2015)

Iron (III)-Salen-Catalyzed H_2O_2Oxidation of Dibenzyl Sulfide in Reverse Micelles

Sweetlin Rajula Rubavathi[a*], Balakumar Subramanian[b], Balakumar Pathakaraimuthu[c]

*Loyola College,Nungambakkam, Chennai-600034

bPSN College of Engineering and Technology,Tirunelveli- 627152

[c]Dr.Sivanthi Aditanar College of Engineering,Tiruchendur.

Abstract

Iron(III)-salen complexes {salen = N,N'bis(salicylidene)ethylenediaminato} efficiently catalyze the H_2O_2 oxidation of organic sulfides. This reaction leads to the formation of sulfoxides as the major product. The spectrophotometric kinetic study shows that the reaction follows Michaelis-Menten kinetics. The reactions are then performed in the presence of anionic reverse micelle AOT to understand the rate changes of the reactions in the reverse micelles. The reactions in the micellar medium are faster than in the pure solvent. Based on the spectral and kinetic studies a suitable electron transfer mechanism is proposed.

Selection and Peer-review under responsibility of [Conference Committee Members of Recent Advances In Nano Science and Technology 2015.].

Keywords: Iron(III)-salen catalyst ;H2O2oxidation; dibenzyl sulfide

1. Introduction

Several surfactants are able to aggregate in non-aqueous solvents to yield reverse micelles in which the polar head group of the surfactant monomers cluster to form a micelle core and are directed towards the centre of the assembly and the hydrophobic tails extend outwards into the bulk organic phase [1-3]. Both experimental and theoretical approaches show that key structural parameter of reverse micelle is the [water]/[surfactant] molar ratio(W_0) which determines the micellar size as well as the unique physicochemical properties of the entrapped water. Among the anionic surfactants that form reverse micelles, the best known are the systems derived from the AOT (sodium 1, 4-bis-2-ethylhexylsulfosuccinate) in different nonpolar media. AOT has a well-known V-shaped geometry, giving rise to stable reverse micelles without co surfactant. AOT has the remarkable ability to solubilize a

* Corresponding author.

E-mail address: dsrrchemistry@gmail.com

Selection and Peer-review under responsibility of [Conference Committee Members of Recent Advances In Nano Science and Technology 2015.].

large amount of water with values of W_0(W_0=[H_2O]/[AOT]),as large as 40-60 depending on the surrounding nonpolar medium, the solute, and the temperature; however the droplets size depends only on the water amount W_0 [4-6]. Several transition metal complexes have been used for studying electron-transfer reactions. Iron is the most prominent transition metal in biological perspective, as many enzymes containing ferrous or ferric ion catalyze various bio-transformations [7-22]. Therefore it is desirable to study the catalytic activities of iron (III) complexes. In this context Rajagopal etal [23] have used iron (III)-salen complexes as enzyme models for the selective oxidation of organic sulfides to sulfoxides using PhIO as the oxygen source. It is advantageous to use H_2O_2 as the oxidant instead of PhIO as H_2O_2 is a safe, readily available and cheap reagent. Further this eco-friendly redox system may serve as peroxidases model and leaves water as the only by product. With this aim of using eco-friendly reagents, six iron(III)-salen complexes are synthesized and used as catalysts. The reaction is facile and organic sulfoxides are the major product of the reaction. The effect of reverse micellar environment on the electron transfer rate has also been examined and is presented.

2. Experimental

2.1. Materials

Salicylaldehyde and the substituted salicylaldehyes (5-methyl, 5-bromo, 5-chloro, 3, 5-di-tert butyl, 5-methoxy) were purchased from Aldrich and used as such. Dibenzyl sulfide purchased from Sigma-Aldrich was used as received. CH_3CN, Isooctane of HPLC grade were purchased and used as such. Sodium bis(2-ethylhexyl)sulfosuccinate (AOT), (99%) purity was purchased from Merck and used as such. All other reagents were of Analar grade. The kinetic study of the reaction was performed after the purities of the reactants and solvents used in the system were confirmed.

2.2. Synthesis of ligands and iron(III)-salen complexes

Various salen ligands were prepared from ethylenediamine and the corresponding salicylaldehyde by standard methods [24-27]. Iron(III)-salen complexes I-VI(eq.1) were synthesized using established procedures [28-30]. The complexes were characterized by IR and UV-Visible absorption spectral techniques.

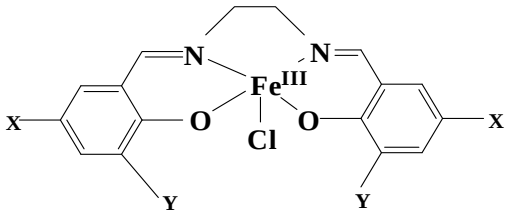

1

I X=Y=H II X=Cl,Y=H
III X=Br,Y IV X=CH_3, Y=H
V X=OCH_3, Y=H VI X=Y=t-butyl

2.3. Procedures

Stock solutions of AOT reverse micelle were prepared by weighing and dilution in isooctane. Stock solutions of 1M surfactant were agitated in a sonicating bath until the reverse micelle was optically clear. The appropriate amount of stock solution to obtain a given concentration of surfactant in the micellar media was transferred into the cell. The addition of water to the corresponding solution was performed using a calibrated microsyringe. The amount of water present in the system is expressed as the molar ratio between water and the surfactant present in the reverse micelle (W_0=[H2O]/[surfactant]). The lowest value of W_0, called W_0=0, corresponds to a system with no addition of water.

2.4. Kinetic studies

The absorption spectra of iron(III)-salen complexes was obtained using a ELICO SL-164 UV- Vis spectrophotometer. The kinetic study of the H_2O_2 oxidation of DBS catalyzed by six iron(III)-salen complexes have been carried out in 100% acetonitrile at 298K under pseudo first order conditions. The rate of the reaction is measured by following the decay of absorbance of iron(III)-salen complex with time at appropriate (λ_{max}) wavelength (Table-1).The pseudo-first-order rate constant(k_1)value for each kinetic run was evaluated from the linear least-square plots of log(absorbance) vs time .

Table .1. λmax values of iron(III)-salen complexes for the kinetic study

Iron(III)-salen complex	λ_{max}, nm
I	470
II	467
III	472
IV	489
V	501
VI	503

3. Results and discussion

3.1. Active Oxidant Species:

The λ_{max} value for the iron(III)-salen complex at 470nm is due to ligand to metal charge transfer $PhO^- \rightarrow$ iron (III), transition (Figure-1). This absorption maximum is influenced by the nature of the substituent in the salen ligand. Addition of H_2O_2 to iron(III)-salen complex leads to substantial changes in the absorption spectrum which help to understand the nature of the active oxidant species. Spectral changes observed for the complex is shown in Figure-2.

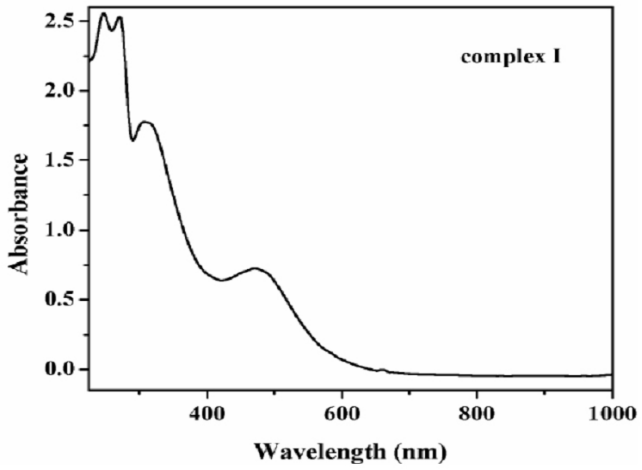

Fig. 1. UV-vis absorption spectrum for iron(III)-salen complex [I] = 2 x 10-4 M.

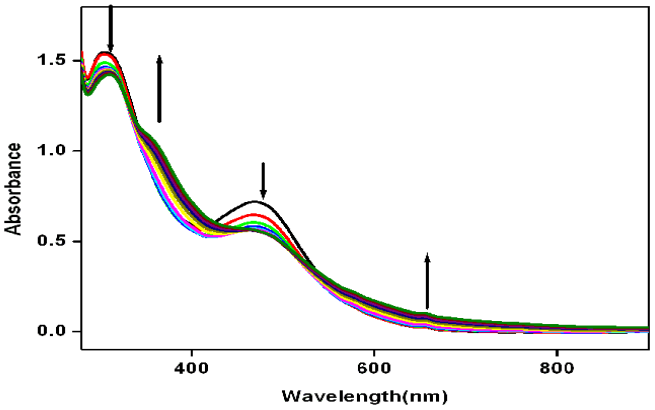

Fig. 2. Change in absorbance of I with time in the presence of H2O2, [I] = 2x 10-4M, [H2O2] = 5x10-3M.

In the presence of H_2O_2 the absorbance of parent $[Fe(III)\text{-salen}]^+$ ion decreases at 350nm and 470nm and increases at 370nm and 640nm. These new features are identical to previously reported spectra for ferric acylperoxo complex $(P)Fe^{III}(O_2COAr)$ that is generated from the reaction of m-CPBA with iron(III)-tetramesitylporphyrin(TMP) [31]. The similarity of these spectral changes indicates the formation of ferric hydroperoxide (Fe^{III}-OOH) in the reaction between iron(III)-salen complex and H_2O_2. Fujii etal [32,33] proposed iron(III)-monophenoxylradical as the active oxidizing species when sterically hindered iron(III)-salen complex was oxidized electrochemically in CH_2Cl_2-ethanol mixture at 203K and oxidized with m-CPBA at 193K.Since the present study is carried out at 298K and the possibility of the formation of monophenoxy radical species is ruled out and $[O=Fe^{IV}(salen)]^{+\bullet}$ is proposed as the active species responsible for the oxidation of substrate. This proposal has a strong literature background as many non-heme iron enzymes in combination with H_2O_2 efficiently catalyze various oxidations. Van Edlick and co-workers [34] have reported that the absorbance changes in the region 550-750nm during the formation of active species for the reaction between Fe(III)-porphyrin complex and m-CPBA. Similar spectral changes are observed in the present system as illustrated in Figure- 3 with the decrease in absorbance at 470nm (curve A) and increase in absorbance at 640nm (curve B).

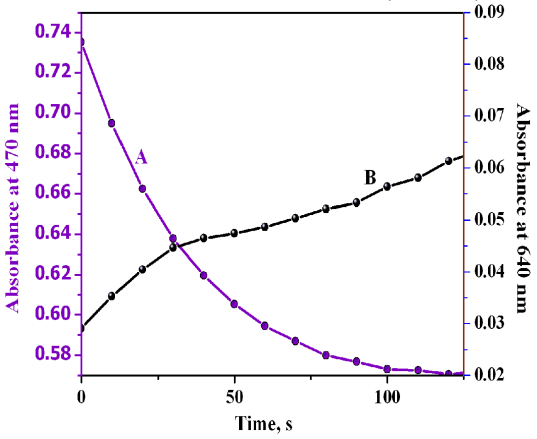

Fig. 3. Spectral details of complex I -H2O2 system with time I = 2 x 10-4 M, [H2O2] = 5 x 10-3 M. Decay at 470 nm (curve A) and simultaneous growth at 640 nm (curve B).

The spectral changes observed in the present work leads to the conclusion that the possible active oxidant is iron oxo species under the present experimental conditions similar to the proposal of VanEdlic and co-workers. The possibility of self-decay of the oxidant in complex I was tested by plotting OD versus time at λ_{max}= 470nm in the

absence of DBS. The decay of the active oxidant species in the presence and absence of DBS is shown in Figure-4. From the Figure -4 it is inferred that the rate of self-decay is negligible (curveA) compared to the rate in the presence of the substrate (curveB). It indicates that the oxidation of organic sulfides by hydrogen peroxide using iron(III)-salen ion as the catalyst is the major reaction in the presence of substrates.

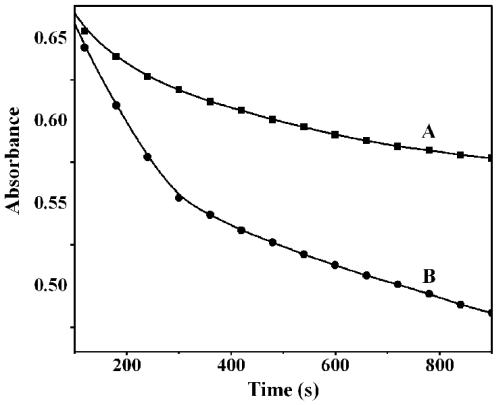

Fig. 4. Change in absorbance with time at λmax = 470nm A.[I] = 2x10-4 M , [H2O2] = 5x10-3 M B.[I] = 2x10-4 M , [H2O2] = 5x10-3 M , [DBS] = 5x10-3 M.

3.2. Kinetic Results

The kinetics of iron(III)- salen ion catalyzed H_2O_2 oxidation of DBS in acetonitrile at 298K has been studied using spectrophotometric technique by measuring the change in OD with time at 470 nm for the parent complex and a sample run is shown in Figure-5. The reaction is found to be first order in the oxidant, which is evident from the linear log (absorbance) Vs time plots. The dependence of the reaction rate on substrate concentration is studied with different substrate concentrations and the kinetic results are shown in Table-2&Figure-6.From figure-6 it is evident that the rate of the reaction increases with increase in substrate concentration but attains saturation in high substrate concentration. The inference from the saturation kinetics is that the substrate binds to the oxidant before the rate controlling step. Thus the reaction proceeds through Michaelis - Menten kinetics.

$$\text{Oxidant + substrate} \rightleftharpoons \text{Complex} \qquad (1)$$

$$\text{Complex} \xrightarrow{k} \text{Products} \qquad (2)$$

Based on Michaelis-Menten formulation, the observed rate constant k_1 is given by the eqn-3 and the rearrangement of eqn-3leads to eqn-4

$$k_1 = k_{obs} = k\,[\text{substrate}] / k_M + [\text{substrate}] \qquad (3)$$

$$z1 / k_1 = 1 / k + k_M / k\,[\text{substrate}] \qquad (4)$$

From the plot of $1/k_1$ vs. 1/ [substrate], the values of k and k_M have been evaluated and are given in Table 3. Here k and k_M are the rate constant for the product formation and Michaelis-Menton constant respectively. From the linear plot of $1/ k_1$Vs 1/ [substrate] the values of k and k_M have been calculated. Both k and $k_m$values are sensitive to the change of substituents in the salen ligand of the catalyst. The low K_M values point out the strong binding nature of the substrate with the active oxidant species of the reaction.

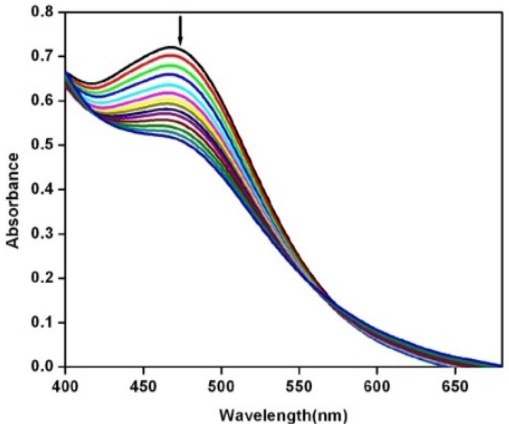

Fig. 5.Change of absorbance of I – H2O2 system with time in the presence of DBS

Table 2. Pseudo first order rate constants 104 k1, s-1 for iron(III)-salen catalyzed H2O2 oxidation of DBS in CH3CN at 298K.

[DBS], M	I	II	III	IV	V	VI
0.001	4.50±0.01	6.00±0.03	6.67±0.06	3.12±0.04	0.77±0.05	0.91±0.07
0.002	5.70±0.04	7.51±0.04	8.80±0.01	3.57±0.04	1.05±0.02	0.95±0.02
0.003	6.85±0.03	8.69±0.08	9.51±0.04	3.90±0.05	1.25±0.07	0.98±0.12
0.004	7.30±0.09	9.40±0.06	10.82±0.02	3 .95±0.09	1.38±0.01	1.01±0.04
0.005	8.60±0.07	10.53±0.03	11.30±0.05	3.98±0.11	1.50±0.02	1.08±0.01
0.006	9.10±0.02	11.81±0.01	12.01±0.02	4.01±0.06	1.77±0.01	1.11 ±0.01
0.007	9.50±0.04	12.00±0.02	12.58±0.04	4.09±0.08	1.92±0.07	1.12±0.04
0.008	10.09±0.03	12.80±0.07	13.45±0.08	4.11±0.01	2.12±0.01	1.13±0.09
0.009	10.41±0.02	12.81±0.01	13.50±0.10	4.13±0.13	2.13±0.10	1.13±0.02
0.01	10.53±0.10	12.82±0.08	13.51±0.09	4.13±0.07	2.13±0.17	1.13±0.07

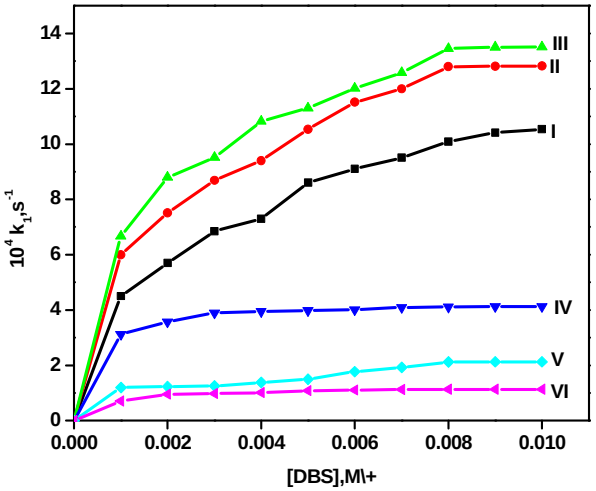

Fig.6.Plot of k1 vs [DBS] for iron(III)-salen complexes catalyzed H2O2 oxidation of DBS

Table 3. Rate Constants and Michaelis-Menten constant for the iron(III)-salen catalyzed H2O2 oxidation of DBS in CH3CN at298K

Complexes	Rate Constant $10^4 s^{-1}$	Michaelis-Menten constant $10^3 K_M$
I	11.59	1.67
II	13.96	1.40
III	14.59	1.24
IV	6.30	0.38
V	4.39	0.24
VI	2.83	0.71

3.3. Substituent effect

The rate of iron(III)-salen ion catalyzed H_2O_2 oxidation of DBS is influenced by the nature of the substituents present in the phenolic part of the salen ligand. The relationship between structure and reactivity of substituted salen complexes can be explained in terms of Hammett equation [35]. When log k is plotted againstσ a straight line is obtained. The slope of the straight line gives the ρ value. The reaction constant value was found to be +0.45 (r = 0.98). The positive ρ value points out that there is a charge separation in the transition state of the reaction. The Hammett plot is shown in Figure-7.

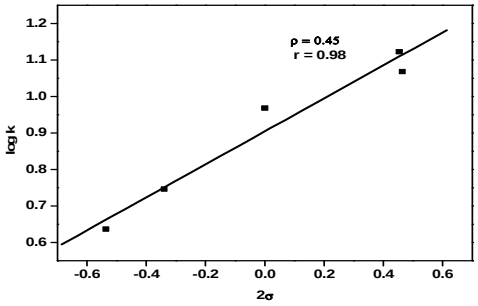

Figure 7. Hammett plot for the oxidation of DBS with H_2O_2 catalyzed by iron(III)-salen complexes I-V.

3.4. Effect of AOT concentration

The kinetics of H_2O_2 oxidation of DBS catalyzed by six iron(III)-salen complexes are studied at different concentrations of surfactant (AOT) keeping the other experimental conditions constant. The results are given in Table 4 and Figure-8. In all the cases the pseudo first order rate constant is greater than that observed in the absence of micelle. This shows that AOT increases the rate of the reaction. As the concentration of AOT increases, the rate of the reaction is also found to increase. For a change in concentration of AOT from 0.1M to 0.4M the rate constant increases from 15.99×10^4,s^{-1} to 17.53×10^4,s^{-1} for complex III and in the absence of micelle the rate constant is only 6.67×10^4,s^{-1} .The general trend observed is that the increase in rate is maximum in the case of complex III and minimum in the case of complex VI .Similar trend has been observed for the complexes in the absence of micelles. The trend has been explained through Hammett plot (Figure-7). Under reverse micellar conditions when AOT is added, the micellar interface increases with increase in AOT concentration. The reactants are bound to the micellar interface and hence the reaction rate is higher than in the absence of micelles. The complexes are positively charged and AOT is negatively charged. The pronounced effect of electrostatic interaction between the two species binds them together causing an increase in the rate of the reaction [36].

Table .4. Pseudo first order rate constants 104 k1, s-1 for iron(III)-salen complexes catalyzed H2O2 oxidation of sulfides at different [AOT] .

[I-VI]-2 ×10-4M; [S]-1×10-3M; W0=10

[AOT], M	I	II	III	IV	V	VI
0	4.50±0.01	6.00±0.03	6.67±0.06	3.12±0.04	0.77±0.05	0.91±0.07
0.1	10.98±0.02	14.28±0.05	15.99±0.03	7.13±0.07	3.25±0.05	2.59±0.04
0.2	12.03±0.05	15.39±0.05	16.39±0.08	8.52±0.10	4.53±0.04	3.98±0.02
0.3	13.10±0.05	16.58±0.06	17.38±0.07	9.21±0.01	5.23±0.09	4.05±0.08
0.4	13.23±0.06	16.90±0.11	17.53±0.08	9.53±0.08	5.72±0.03	4.53±0.19

3.5. Effect of water dispersed

It is of interest to study the rate of the reaction when the amount of water dispersed (W_0) changes from 4 to 20. The results are given in Table 5 and Figure-9.In the reverse micelle the polar head groups are directed towards the inner core forming an aggregate. The reactants are supposed to be present in the micellar phase. In the experiment the rate constant value increases reaches a maximum and then decreases. At very low W_0 values almost all the water molecules are used up to hydrate the surfactant head groups. So the dissolved reactants are in a bound state and have very low mobility. When water is added the polar head groups pointing towards the inner core are solvated. Now the reactants experience greater mobility. Then the reaction is fast. However after a particular W_0 value the rate of the reaction decreases. At high W_0 values the water content is high and it virtually behaves like the bulk water phase. As a result the concentration of the reactants in the micellar phase decreases. Due to the decrease in local concentration of the reactants the rate of the reaction decreases [37].[15]

Table 5. Pseudo first order rate constants $10^4 k_1, s^{-1}$ for iron(III)-salen complexes catalyzed H_2O_2 oxidation of sulfides at different W_0.

[I-VI]-2 X 10^{-4}M; [S]-1X10^{-3}M; [AOT] =0.1M

W_0	I	II	III	IV	V	VI
0	4.50±0.01	6.00±0.03	6.67±0.06	3.12±0.04	0.77±0.05	0.91±0.07
4	7.93±0.05	10.93±0.06	11.11±0.01	5.53±0.03	2.11±0.05	1.03±0.06
6	8.15±0.09	12.39±0.14	12.68±0.04	5.98±0.14	2.98±0.03	1.93±0.02
8	9.13±0.18	13.15±0.17	14.09±0.05	6.11±0.08	3.22±0.07	2.39±0.03
10	10.98±0.01	14.28±0.05	15.99±0.02	7.13±0.07	3.25±0.04	2.59±0.04
13	9.58±0.13	13.54±0.02	13.25±0.18	6.93±0.11	2.95±0.05	2.02±0.02
15	8.33±0.04	12.53±0.09	12.91±0.06	5.25±0.13	2.53 ±0.09	1.83±0.02
20	7.44±0.06	12.05±0.15	12.53±0.11	4.13±0.01	2.45±0.07	1.53±0.12

3.6. Product analysis

A solution containing 5mM DBS, 0.2mM iron(III) – salen complex and 5mM H_2O_2 in 5ml of CH_3CN was stirred at 298K for 1-2 hours. The reaction mixture after the completion of the reaction is extracted with chloroform to recover the products. The product is dried over sodium sulfate and after evaporating the solvent it is subjected to ^{1}H NMR analysis. The ^{1}H NMR spectrum for the products shows distinct peaks at δ2.4 and 2.7 ppm. It is known from the literature [38] the peak at δ2.7 ppm is identified as S (O) stretching frequency which confirms sulfoxide as the product of the reaction. The aromatic region is also informative as the aromatic protons of sulfides and sulfoxides appear as multiplets centered at δvalues 7.2 and 7.3 ppm and at 7.6 and 7.7 ppm respectively [39,40].In the absence

of peaks corresponding to sulfones, ^{1}H NMR study confirms the selective oxidation of sulfides to sulfoxides under the present experimental condition.

3.7. Mechanism

The spectral changes obtained in the present work and comparison of these results with the recent literature on similar systems leads to the conclusion that the possible active species is iron oxo species. The Michaelis-Menten kinetics observed confirms that the reaction proceeds through the complex formation between the oxidant and the substrate. The observed saturation kinetics and low K_M values indicate the strong binding of substrate with the oxidant. Similar type of saturation kinetics is observed in some reactions involving Fe(III) complexes[16,23]. When iron(III)-salen and H_2O_2 are considered as the catalyst and oxidant, the formation of the active oxidant species[Fe^{IV}=O] $^{+\bullet}$ may be formulated via compound 0 formation. The following observations support the above formulation. On adding H_2O_2 to the iron(III)-salen complex, the absorbance is decreased at 350 and 470 nm and increased at 390nm and 640nm (Figure2).These changes observed in the absorption spectrum and comparison of these changes with the published data[12] formulate the nature of the active oxidant species as [Fe^{IV}=O(salen)] $^{+\bullet}$ .Rajagopal etal[23] have proposed the formation of oxo iron species[Fe^{IV}=O(salen)] $^{+\bullet}$ as the active oxidant from the reaction of iron(III)-salen and PhIO and it was characterized by UV-visible, resonance Raman, EPR,ESI-MS and Mossbauer spectral techniques. Mossbauer spectral study reveals that iron is in the +4 oxidation state in the active species [oxo(salen)iron].Bryliakov and Talsi [17] have proposed the reactive species as iron(III)-salen-PhIO adduct at low temperature based on NMR studies. The UV-visible spectral study clearly shows the formation of Fe^{III}-OOH which undergoes heterolytic cleavage resulting in the formation of reactive species[Fe^{IV}=O(salen)] $^{+\bullet}$. The radical cation may form the product through an ET mechanism.

In this mechanism the transfer of one electron first occurs from sulfide to [Fe^{IV}=O (salen)] $^{+\bullet}$ (compound I) to form a sulfide radical cation and [Fe^{IV}=O(salen)] (compound II). The sulfoxide is then formed by transfer of the oxygen atom from[Fe^{IV}=O(salen)] (compound II) to the sulfur radical cation through oxygen rebound step. This mechanism is supported by Oae and coworkers [19]. The linearity of the Hammett plots (Figure7) indicate that the substituent effect is pronounced in these iron(III)-salen complexes. This fact favours the ET mechanism in the reaction between iron(III)-salen complexes and DBS.(Scheme 1). In the presence of reverse micelle the rate constant is maximum for complex III and minimum for complex VI. The same trend has been observed for complexes in the absence of reverse micelle. The products are also the same. Therefore the mechanism proposed for the oxidation in non micellar medium holds good for the reaction catalyzed by AOT.

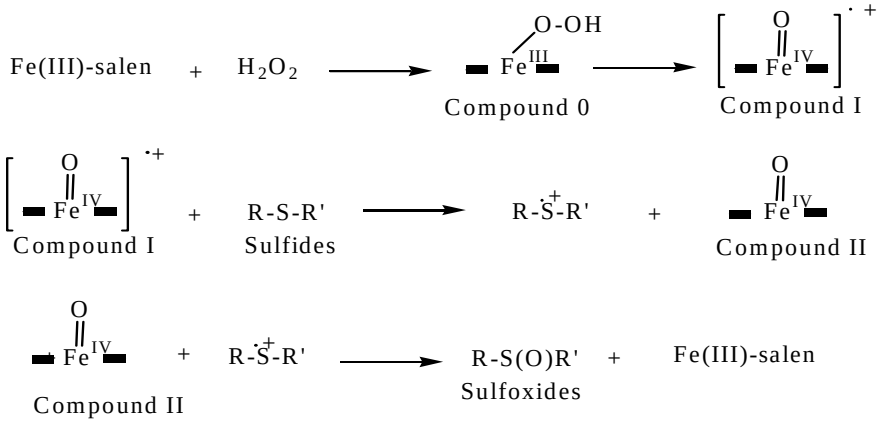

DBS - R ,R'- $C_6H_5CH_2$

Scheme 1.Electron transfer mechanism for the H_2O_2 oxidation of sulfides to sulfoxides in CH_3CN.

4. Conclusion

The oxidation of aromatic sulfides with H_2O_2 catalyzed by iron (III)-salen ions in CH_3CN is an efficient and environmentally benign process. This reaction is facile to produce selectively the corresponding sulfoxides under the experimental conditions. The kinetic studies were performed spectrophotometrically and the characterizations of products were done by ^1H NMR analysis. To account for the experimental observations, an electron transfer mechanism is proposed for this oxidation reaction. The fact that overall rate of the reaction is accelerated in reverse micelle medium with respect to the pure solvent suggests that the reaction occur in the micellar interface.

References

[1] N.M. Correa, E.N. Durantini, J.J. Silber, J.Org.Chem. 6 5, (2000), 6427.
[2] R.D. Falcone,N.M. Correa,M.A. Biasutti,J.J.Silber,Langmuir 18, (2002), 2039.
[3] T.K. De, A. Maitra, Adv. Colloid Interface Sci. 59,(1995), 95.
[4] M.P. Pileni, J. Phys. Chem. 97,(1993), 6961.
[5] L.García-Río, J.R. Leis, E. Iglesias, . J. Phys. Chem.99, (1995), 12318.
[6] I.B.Blagoeva, .;P.Gray, M.F. Ruasse, J. Phys. Chem. 100,(1996), 12638.
[7] R.D.Makote,C.Chatterjee.,Indian.J.Chem,38A,(1999),783.
[8] A.K. Julie, M.B. Lisa, Acc. Chem. Res. 40 (2007) 501.
[9] X. Shan, L. Que Jr., J. Inorg. Biochem. 100 (2006) 421.
[10] Y. Mekmouche, H. Hummel, R.Y.N. Ho, L. Que Jr., V. Schunemann, F. Thomas,A.X. Trautwein, C. Lebrun, K. Gorgy, J.C. Lepretre,M.N. Collomb, A. Eeronzier,M.Fontecave, S. Menage, Chem. Eur. J. 8 (2002) 1196.
[11] E.G. Kovalena, M.B. Neibergall, S. Chakrabarthy, J.D. Lipscomb, Acc. Chem. Res.40 (2007) 475.
[12] M.M. Abu-Omar, A. Loaiza, N. Hontzeas, Chem. Rev. 105 (2005) 2227.
[13].U. Rohde, A. Stubna, E.L. Bominaar, E. Munck, W. Nam, L. Que Jr, Inorg. Chem.45 (2006) 6435.
[14] G.B. Shul'pin, G.V. Nizova, Y.N. Kozlov, L.G. Cuervo, G. Suss-Fink, Adv. Synth.Catal. 346 (2004) 317.
[15] T. Ueno, T. Koshiyama, M. Ohashi, K. Kondo, M. Kono, A. Suzuki, T. Yamane, Y.Watanabe, J. Am. Chem. Soc. 127 (2005) 6556
[16] S. Kobayashi, M..Nakano, T. Goto, T. Kimura, A.P. Scaap, Biochem. Biophys. Res. Commun. 135, (1986),166.
[17] S. Kobayashi, M. Nakano, T. Kimura, A.P. Scaap, Biochemistry, 26,(1987), 5019.
[18] K.P..Bryliakov,E.P.;Talasi, E.P.Angew.Chem.Int.Ed.s 43,(2004), 5228.
[19] K.P Bryliakov, E.P.;Talasi,.Chem. Eur.J. 13,(20070,8045.
[20] J.F. Berry, E. Bill, E. Bothe, F. Neese, K. Wieghardt, J. Am. Chem. Soc. 128 (2006)13515.
[21] S.Oae, Y. Watanabe, k. Fujimori, Tetrahedron Lett. 23,(1982),1189.
[22] H. Natalya, F. Alicja, M. Dominik,W.Wolf-D, R. van Edlic, J. Am. Chem. Soc. 129(2007) 12473.
[23] T. Katsuki, J. Mol. Catal. A: Chem. 113 (1996) 87.
[24] W. Nam, Acc. Chem. Res. 40 (2007) 522.
[25] V.K.Sivasubramanian,M. Ganesan, S. Rajagopal, R. Ramaraj, . J. Org. Chem. 67,(2002),1506
[26] P.Pfeiffer, E. Breith, T. Tsumaki, T. Leibigs. Ann. Chem. 503,(1933) 84.
[27] A.Chellamani, P. Kulanthaipandi, S. Rajagopal, .J. Org. Chem. 64,(1999), 2232.
[28] R.Sevvel, S. Rajagopal, C. Srinivasan, N.M. Alhaji, A. Chellamani, .J. Org. Chem. 65,(2000), 3334.
[29] D.Chen, A. Martell, .Inorg.Chem. , 26,(1987) 1026.
[30] M.Gulloti, L. Casella, A. Pasini, R. Ugo, .J. Chem. Soc.Dalton Trans. 33,1977.
[31] M.Gerloch,J.;Lewis,F.E.Mabbs, R. Richards,. J.Chem.Soc.A 1968,112
[32] A. Bottcher, M.W. Grinstaff, J.A.Labinger, H.B. Gray, J. Mol. Cat. A: Chem. 113,(1996), 1991.
[33] J.D.Soper,S.V.Kryatov,E.V.;Rybak-Akimova, D.G.;Nocera, .J.Am. Chem.Soc.129,(2007),5069
[34] T.Kurahashi, Y. Kobayashi, S. Nagamoto, T. Tosha, T. Kitagawa, H.Fujji, Inorg. chem. 44,(2005), 8156.
[35] T.Kurahashi, K. Oda, M. Sigimoto, T. Ogura, H.. Fujii, . Inorg. chem. 45,(2006), 7709.
[36] H.Natalya, F.Felicja, M.Dominick, D.W. Wolf, .J. Am. Chem. Soc.129, (2007), 12473
[37] J.March Reactions,,Mechanisms and structure,john Wiley&Sons,1992.
[38] N.M.Correa,Biasutti,Silber,J.J.J.Colloidal interface Sci 184,(1996),570
[39] D.Sarkar,P.V.Subharao,G.Begum,K.Ramakrishna,K. J.Colloid.InterfaceSci 288,(2005),591
[40] G.Du, J.H. Espenson, Inorg. Chem. 44,(2005), 2465.
[41] K.John Adaikalasamy, N.S.Venkataramanan, S.Rajagopal,Tetrahedron, 59,(2003), 3613.
[42] I.Smith ,T.S.Pecoraro, .Inorg. Chem. 41,(2002), 6754.

A simple and facile synthesis of MPA capped CdSe and CdSe/CdS core/shell nanoparticles

D. Sukanya and P. Sagayaraj

Citation: **1665**, 050028 (2015); doi: 10.1063/1.4917669
View online: http://dx.doi.org/10.1063/1.4917669
View Table of Contents: http://aip.scitation.org/toc/apc/1665/1
Published by the American Institute of Physics

A Simple and Facile Synthesis of MPA Capped CdSe and CdSe/CdS Core/Shell Nanoparticles

D. Sukanya and P. Sagayaraj*

Department of Physics, Loyola College (Autonomous), Chennai-600034, India
**E-mail: psagayaraj@hotmail.com*

Abstract. II-VI semiconductor nanostructures, in particular, CdSe quantum dots have drawn a lot of attention because of their promising potential applications in biological tagging, photovoltaic, display devices etc. due to their excellent optical properties, high emission quantum yield, size dependent emission wavelength and high photostability. In this paper, we describe the synthesis and properties of mercaptopropionic acid capped CdSe and CdSe/CdS nanoparticles through a simple and efficient co-precipitation method followed by hydrothermal treatment. The growth process, characterization and the optical absorption as a function of wavelength for the synthesized MPA capped CdSe and CdSe/CdS nanoparticles have been determined using X-ray diffraction study (XRD), Ultraviolet-Visible spectroscopy (UV-Vis), Fourier transform infrared spectroscopy (FT-IR) and High Resolution Transmission Electron Microscopy (HRTEM).

Keywords: Nanocrystals, II-VI semiconductors, Quantum dots, Fluorescence, Luminescence
PACS: 61.46.Hk, 81.05Dz, 81.07Ta, 87.64kv, 87.15mq

INTRODUCTION

Colloidal semiconductor nanocrystals, especially II-VI type quantum dots have immense potential for biolabelling and bioimaging applications because of their size dependent photoluminescence (PL), broad absorption spectra and narrow emission spectra, and excellent physical and chemical stability which can be controlled effectively by tuning the sizes, compositions and crystal structures of the nanocrystals[1]. In recent years, considerable efforts have been made to design and fabricate core/shell structured materials as well as hollow structures in physics, chemistry and material science communities due to their specific structures and unique properties [2]. Core/shell nanostructures constitute a very special class of nanomaterials, where a noticeable enhancement in the luminescence and conductive properties is achieved by modifying the core surfaces typically by the process of encapsulation with the shell of desired material [3]. The optical properties of the core only structure are greatly improved when a semiconductor shell is grown on the core. In particular, the growth of a shell on the core nanocrystals enhances their quantum yield and the resistance to photobleaching and reduces fluorescence emission blinking at the single particle level[4]. Hence researchers have concentrated on the passivation of the surface of quantum dots with a wider band gap semiconducting material in order to confine the exciton within the core and enhance the photoluminescence quantum yield.

CdSe is a direct band gap semiconductor with the band gap of 1.74 eV and CdS is a mid band gap semiconductor with the band gap of 2.4 eV. Herein, efforts have been made to synthesize CdSe and CdSe/CdS core/shell nanoparticles directly from an aqueous medium, using mercaptopropionic acid as the capping agent, thus reducing the toxicity of CdSe nanoparticles. The structural and optical properties of the synthesized CdSe and CdSe/CdS nanoparticles have been studied and reported.

MATERIALS AND METHODS

All the reagents are of AR grade and used without further purification. Cadmium oxide (CdO), selenium powder, sodium borohydride ($NaBH_4$), mercaptopropionic acid (MPA), sodium hydroxide (NaOH), ethanol and thiourea were purchased from Merck. Double distilled water was used as a solvent.

Synthesis of MPA capped CdSe nanoparticles: The typical synthesis procedure for CdSe quantum dots is as follows: Solutions of CdO and MPA were mixed and titrated to pH 9 by the dropwise addition of 1.0 M NaOH solution with continuous stirring for about 1 h. In a three necked flask, 10 ml of fresh NaHSe solution

Solid State Physics
AIP Conf. Proc. 1665, 050028-1–050028-3; doi: 10.1063/1.4917669

was prepared from selenium powder through a reduction reaction with $NaBH_4$. All the reactions were carried out in the inert gas atmosphere. The CdO solution was then added into the NaHSe solution for the formation of CdSe nanoparticles. The solution was then transferred into the autoclave and kept in furnace at 160 ˚C for 1 h.

Synthesis of MPA capped CdSe/CdS nanoparticles: The core CdSe nanoparticles were synthesized by the above described procedure and the particles were obtained by centrifugation and the precipitates were resuspended in 5 ml of distilled water, to be used in the next step of synthesis. For the CdS shell synthesis, the Cd^{2+} precursor solution was prepared by dissolving CdO and MPA in 25 ml of distilled water and titrated to pH 11 by the dropwise addition of 1.0 M NaOH solution. Next, the core CdSe nanoparticles resuspended in distilled water and thiourea were added into the CdO solution for the formation of CdSe/CdS nanoparticles, titrated to pH 12 and then transferred into the autoclave and kept in the furnace at 160 ˚C for 1 h.

RESULTS AND DISCUSSION

The powder XRD patterns of both CdSe and CdSe/CdS nanoparticles are presented in Figure 1. Three strong, broad and sharp diffraction peaks have been observed for both the CdSe and CdSe/CdS nanoparticles which corresponds to the (111) (220) and (311) planes which could be indexed to the cubic zinc blende structure with the very slight shift towards larger angles in the case of CdSe/CdS nanoparticles. All the diffraction peaks matches well with JCPDS 19-0191[5]. The broad diffraction peaks indicate the nanocrystalline nature and finite size of the nanoparticles. It can be observed that there is no recognizable difference in the XRD peak positions of CdSe and CdSe/CdS nanoparticles since both CdSe and CdS exhibits the same shape and the emergence of CdS shell is not observed. In addition, the crystallite size of the CdSe and CdSe/CdS nanoparticles were calculated from Debye-Scherer formula and was to be around 11 nm for CdSe and 13 nm for CdSe/CdS nanoparticles.

The UV-Vis absorption spectra of CdSe and CdSe/CdS nanoparticles are shown in Figure 2. An absorption peak was observed at around 281 nm for CdSe nanoparticles with the corresponding band gap of 4.42 eV and around 277 nm for CdSe/CdS nanoparticles with the corresponding band gap of 4.48 eV. The excitonic absorption peaks for both CdSe and CdSe/CdS nanoparticles are found to be blue shifted in comparison with the bulk value indicating the quantum confinement effect[6] and finite size of the nanoparticles.

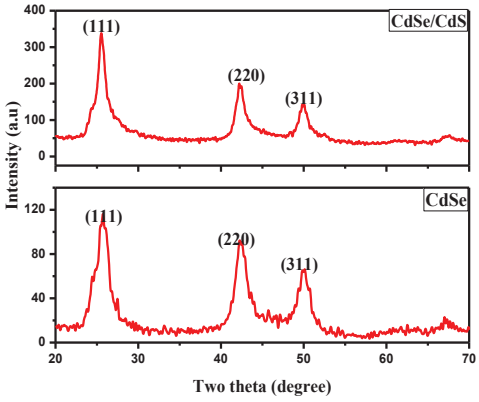

FIGURE 1. Powder XRD patterns of CdSe and CdSe/CdS nanoparticles.

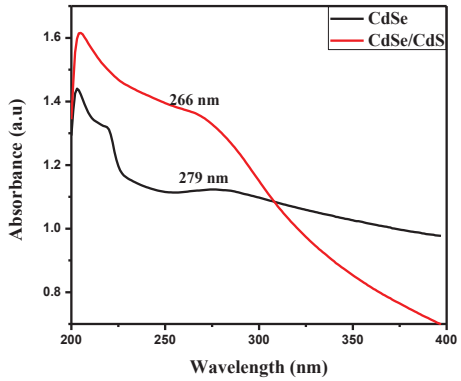

FIGURE 2. Absorption spectra of CdSe and CdSe/CdS nanoparticles.

The FT-IR spectra of MPA capped CdSe and CdSe/CdS nanoparticles are shown in Figure 3. In both cases, there is a most prominent, strong and broad peak around 3500-3000 cm^{-1} O-H bond[7,8]. The peak at 1634 and 1548 cm^{-1} corresponds to C=O stretching, but the peaks are broad and small for CdSe and sharp for CdSe/CdS nanoparticles. The peak at 1387 cm^{-1} shows the C-O stretching vibrations[7]. The peak at 2927 cm^{-1} in the case of CdSe nanoparticles corresponds to $–CH_2$ vibration, whereas this peak is not found in the case of CdSe/CdS nanoparticles. The S-H vibrations are not detectable in the IR spectra. It is well known that MPA are water soluble and their results clearly depicts that CdSe and CdSe/CdS nanoparticles are covered with MPA.

The morphology and the size distribution of the synthesized CdSe and CdSe/CdS nanoparticles were characterized using the HRTEM and their corresponding SAED patterns are shown in Figure 4. The HRTEM images of both CdSe and CdSe/CdS nanoparticles depicts that the particles are monodisperse, spherical in shape and dense with the tendency of agglomeration. In addition, the average diameters of the particles were found to be around 8 nm for CdSe nanoparticles and around 12 nm for CdSe/CdS nanoparticles. The lattice spacing of CdSe and CdSe/CdS nanoparticles can be clearly observed from the HRTEM images.

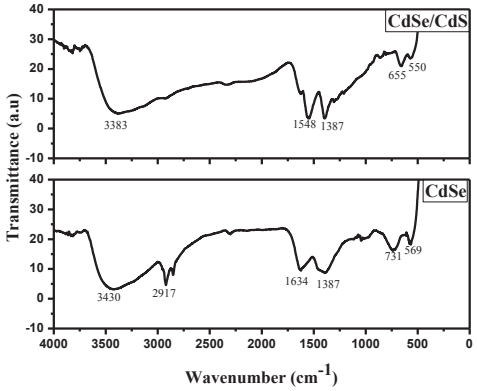

FIGURE 3. FTIR spectra of CdSe and CdSe/CdS nanoparticles.

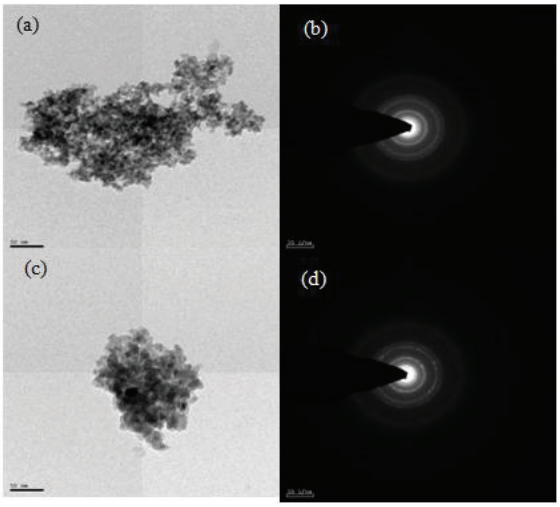

FIGURE 4. HRTEM images and SAED pattern of (a), (b) CdSe and (c), (d) CdSe/CdS nanoparticles.

CONCLUSION

In summary, highly crystalline, monodisperse and spherical shaped mercaptopropionic acid capped CdSe and CdSe/CdS nanoparticles with particle size less than 10 nm have been successfully synthesized via a simple, facile and cost effective co-precipitation method followed by hydrothermal treatment. The XRD studies and TEM images confirm the structure and morphology of the synthesized nanoparticles. The FT-IR measurements confirmed the presence of capping ligand on the surface of the as-synthesized CdSe and CdSe/CdS nanoparticles. These type of nanoparticles synthesized in an aqueous route using environmental friendly precursors are highly suitable for biological and biomedical applications.

ACKNOWLEDGEMENT

The authors acknowledge DST-SERB, India for providing facility through a project (SR/S2/LOP-29/2013).

REFERENCES

1. A. Samanta, Z. Deng and Y. Liu, *Langmuir* **28**, 8205-8215 (2012).
2. X. M. Shuai and W. Z. Shen, *J. Phys. Chem. C* **115**, 6415-6422 (2011).
3. A. Datta, S.K. Panda and S. Chaudhuri, *J. Phys. Chem. C* **111**, 17260-17264 (2007).
4. B. Mahler, B. Nadal C. Bouet, G. Patriarche and B. Dubertret, *J. Am. Chem. Soc.* **134**, 134, 18591-18598 (2012).
5. X. Liu, C. Ma, Y. Yan, G. Yao, Y. Tang, P. Huo, W. Shi and Y. Yan, *Ind. Eng. Chem. Res.* **52**, 15015-15023 (2013).
6. N. Mntungwa, V.S.R. Pullabhotla and N. Revaprasadu, *Colloids Surf., B: Biointerfaces* **101**, 450-456 (2013).
7. F.O. Silva, M.S. Carvalho, R. Mendonça, W.A.A. Macedo, K. Balzuweit, P. Reiss and M.A. Schiavon, *Nanoscale Res. Lett.* **7**, 536 (2012).
8. N. Li, X. Zhang, S. Chen, X. Hou, Y. Liu and X. Zhai, *Mater. Sci. Eng., B* **176**, 688-691 (2011).

Study on synthesis and electrochemical properties of hematite nanotubes for energy storage in supercapacitor

D. Muthu Gnana Theresa Nathan and P. Sagayaraj

Citation: AIP Conference Proceedings **1665**, 050086 (2015); doi: 10.1063/1.4917727
View online: http://dx.doi.org/10.1063/1.4917727
View Table of Contents: http://aip.scitation.org/toc/apc/1665/1
Published by the American Institute of Physics

Study on Synthesis and Electrochemical Properties of Hematite Nanotubes for Energy Storage in Supercapacitor

D. Muthu Gnana Theresa Nathan and P. Sagayaraj*

Department of Physics, Loyola College (Autonomous), Chennai-600034, India
**E-mail: psagayaraj@hotmail.com*

Abstract. Hematite nanotubes (α-Fe_2O_3 NTs) are synthesized via a cost-effective and environmental-friendly hydrothermal technique. Field emission scanning electron microscopy and X-ray powder diffraction analyses reveal the formation of α-Fe_2O_3 NTs with high crystallinity and purity. Optical behavior of α-Fe_2O_3 NTs is studied employing UV-visible spectroscopy. Electrochemical properties of the as-prepared electrode material are investigated by cyclic voltammetry, chronopotentiometry and electrochemical impedance spectroscopy in a three electrode cell. The synthesized α-Fe_2O_3 NTs present enhanced pseudocapacitive performance with high specific capacity of 230 Fg^{-1} at current density of 1 Ag^{-1}. The prepared α-Fe_2O_3 NTs can be utilized as a potential electrode material for electrochemical capacitor applications.

Keywords: Oxides, Nanotubes, Supercapacitors.
PACS: 77.84.Bw, 81.07.De, 88.80.fh

INTRODUCTION

To meet the ever growing energy demand of today, exploration of efficient energy conversion and storage devices are essential. In this scenario, electrochemical supercapacitors (ECs) have emerged as promising energy storage devices, especially in the field of consumer electronics, electric and hybrid electric vehicles due to their high power density and long cycle life[1]. Based on charge storage mechanism, the supercapacitors are broadly categorized into two types. In electric double layer capacitors (EDLCs), the capacitance arises from electrostatic charge separation at electrode/electrolyte interface, whereas in pseudocapacitors, it is due to fast reversible faradaic redox process[2]. Generally, pseudocapacitors exhibit high specific capacitance than that of EDLCs. Carbon-based materials, conducting polymers and transition metal oxides (TMOs) are the three kinds of materials that have been investigated for supercapacitors[3]. Among TMOs, hydrous RuO_2 is a good material with high pseudocapacitance and conductivity. However, high cost, toxic nature and rare availability restrict its practical applications[3,4]. Therefore, design and development of low cost and non-toxic electrode materials are of great importance.

Here, hematite (α-Fe_2O_3), an n-type semiconductor has gained special attention for scientific and industrial applications due to its abundance, low cost, less toxicity and thermal stability. In particular, α-Fe_2O_3 nanostructures have been intensively studied as a negative electrode in various energy storage systems like supercapacitors[5], lithium ion batteries[6] and sodium ion batteries[7]. Further, α-Fe_2O_3 nanoparticles have been found to exhibit size and morphology dependent physical and chemical properties. One dimensional nanostructures can provide short diffusion path to ions and electrons and low contact resistance.

In the present work, hematite nanotubes (α-Fe_2O_3 NTs) were synthesized employing a cost-effective hydrothermal method. The structural, morphological, optical and electrochemical properties of the prepared α-Fe_2O_3 NTs were investigated.

EXPERIMENTAL

A facile hydrothermal route was employed for the preparation of α-Fe_2O_3 NTs. In a typical procedure, aqueous solution of 0.1 M $FeCl_3$, 3 mM NH_4PO_4 and 3 mM Na_2SO_4 were thoroughly mixed under magnetic stirring at ambient temperature. The mixture was filled to 80% capacity of a 150 ml Teflon-lined autoclave and heated at 220 °C for 48 h. After the treatment, the autoclave was allowed to cool naturally to room temperature. Then, the precipitate was separated by centrifugation, washed with deionized water and absolute ethanol, and dried in vacuum at 80 °C for 3 h.

Solid State Physics
AIP Conf. Proc. 1665, 050086-1–050086-3; doi: 10.1063/1.4917727

RESULTS AND DISCUSSION

The crystal structure and phase purity of α-Fe_2O_3 NTs were analyzed by X-ray powder diffraction (XRD) technique. Figure 1 represents XRD pattern of α-Fe_2O_3 NTs. All the reflections with d-spacings and relative intensities corresponding to (104), (110), (113), (024), (116), (018), (214) and (300) planes, were identified for hexagonal phase α-Fe_2O_3 crystal structure with lattice parameters a = 5.034 Å, b = 5.034 Å and c = 13.752 Å (JCPDS card No.33-0664). No peaks were observed other than α-Fe_2O_3, which confirms the phase purity of the sample.

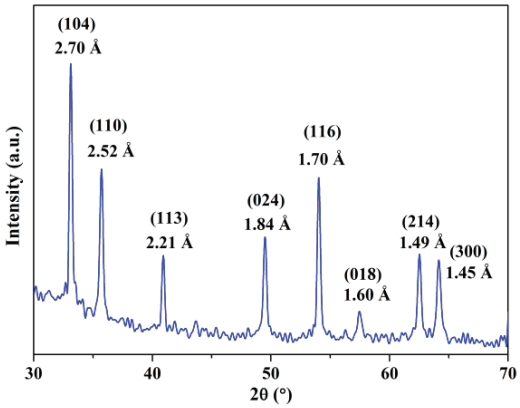

FIGURE 1. XRD pattern of α-Fe_2O_3 NTs.

The surface morphology of α-Fe_2O_3 NTs was examined using a field emission scanning electron microscope (FESEM) and elemental composition by energy dispersive X-ray analysis (EDX). Figure 2 depicts FESEM image of α-Fe_2O_3 NTs. The diameter and length of the α-Fe_2O_3 NTs are found to be in the range of 70-90 nm and 260-300 nm, respectively. The EDX data (not shown here) reveals the presence of only Fe and O, thus confirming high purity of the sample.

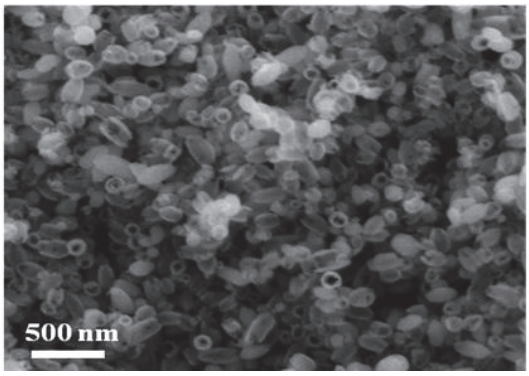

FIGURE 2. FESEM image of α-Fe_2O_3 NTs.

The optical absorption spectrum of α-Fe_2O_3 NTs is illustrated in Figure 3. Two characteristic absorption bands are observed around 380 to 450 nm and 540 to 560 nm. This observation is in line with the earlier reports[6,8]. The absorption in the UV region corresponds to the direct charge transfer transition of O^{2-} 2p → Fe^{3+} 3d, and the absorption in the visible region is due to the Fe^{3+} 3d → 3d indirect transition[8]. The absorption could be modified by tailoring the size and shape of α-Fe_2O_3, which is vital for improving photocatalytic activity.

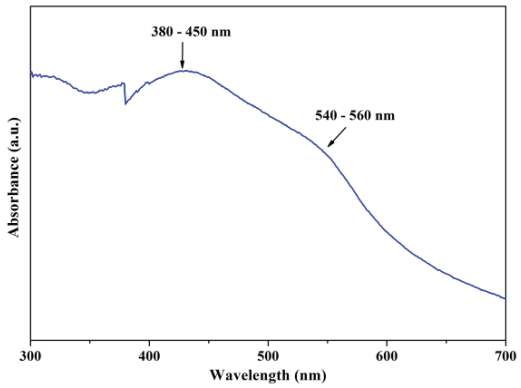

FIGURE 3. Optical absorption spectrum of α-Fe_2O_3 NTs.

Electrochemical Measurements

Cyclic voltammetry (CV), chronopotentiometry (CP) and electrochemical impedance spectroscopy (EIS) were performed using an electrochemical workstation (CHI 661C). The measurements were performed using a standard three electrode cell. The prepared α-Fe_2O_3 was coated on a nickel foil as working electrode, platinum wire as counter electrode and saturated calomel electrode (SCE) as reference electrode. Aqueous 1.0 M KOH solution was used as electrolyte at ambient conditions.

CV was performed in a potential window of 0-0.45 V at various scan rates to study the capacitive behavior of electrode material (Fig. 4). Differing from ideal rectangular shape of electric double layer capacitance, the CV curves exhibit distinct redox peaks during anodic and cathodic sweeps. This suggests that the prominent storage mechanism is pseudocapacitance. The pseudocapacitance arises due to reversible redox between Fe^{2+} and Fe^{3+} accompanied by intercalation of K^+ ions[5]. Specific capacitances (SC) calculated from CV curves are 189, 139, 114 and 99 Fg^{-1} at scan rates of 25, 50, 75 and 100 mVs^{-1}, respectively. The increased area under the

CV curves with increased scan rate reveals the high capacitive performance.

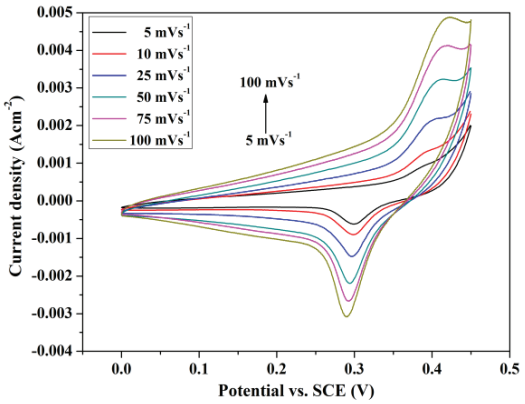

FIGURE 4. Cyclic voltammograms for α-Fe_2O_3 NTs at different scan rates.

Galvanostatic charge-discharge study was done in a potential range of 0-0.4 V at different current densities. Figure 5 depicts the charge-discharge curves. The nonlinear and unsymmetrical shape of discharge curves indicates the pseudocapacitance behavior and this is in line with the CV studies[2]. Highest SC of 230 Fg^{-1} at 1 Ag^{-1} is attributed to high surface area of α-Fe_2O_3 NTs. Further, it could be increased by carefully tuning diameter and length of α-Fe_2O_3 NTs.

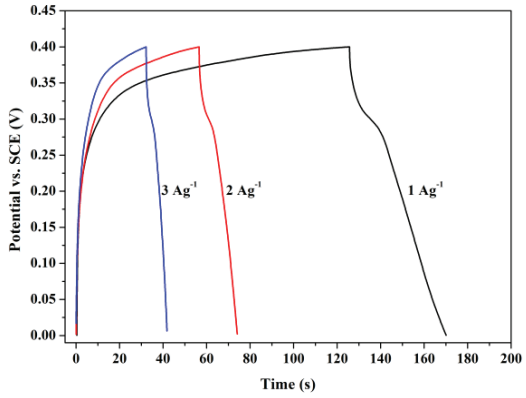

FIGURE 5. Charge-discharge curves for α-Fe_2O_3 NTs at various current densities.

EIS was carried out in a frequency range of 100 kHz to 0.1 Hz. Generally, the intercept at real part (Z') in high frequency region gives equivalent series resistance (ESR). It is a combination of ionic resistance of electrolyte, intrinsic resistance of the oxides and contact resistance between active material and current collector[9]. In Nyquist plot (Fig. 6), the linear part at low frequency is called Warburg resistance (Z_w), which is due to ion diffusion mechanism. The near absence of semicircle at high frequency indicates the low internal resistance of the electrode materials.

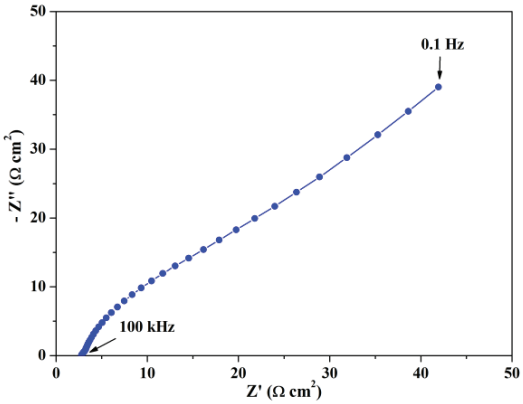

FIGURE 6. Nyquist impedance plot for α-Fe_2O_3 NTs.

CONCLUSION

In summary, α-Fe_2O_3 NTs electrode materials have been synthesized employing a simple and cost-effective hydrothermal route. The as-prepared α-Fe_2O_3 NTs with unique morphology demonstrated good electrochemical behaviors. This suggests that the synthesized material is one of the suitable electrode materials for supercapacitor applications.

ACKNOWLEDGMENTS

Authors thank DST-SERB, India for providing facilities through a project (SR/S2/LOP-29/2013). Support from Mr. Josef Gühmann is greatly appreciated.

REFERENCES

1. D. Wang, Y. Li, Q. Wang and T. Wang, *J. Solid State electrochem.* **16**, 2095-2102 (2012).
2. Z. Wang, C. Ma, H. Wang, Z. Liu and Z. Hao, *J. Alloys Compd.* **552**, 468-491 (2013).
3. M. Zhu, Y. Wang, D. Meng, X. Qin and G. Diao, *J. Phy. Chem. C* **116**, 16276-16285 (2012).
4. J. Du, G. Zhou, H. Zhang, C. Cheng, J. Ma, W. Wei, L. Chen and T. Wang, *ACS Appl. Mater. Interfaces* **5**, 7405-7409 (2013).
5. D. Sarkar, M. Mandal and K. Mandal,, *ACS Appl. Mater. Interfaces* **5**, 11995-12004 (2013).
6. W. Zhu, X. Cui, X. Liu, Y. Zhang, J. Huang, X. Piao and Q. Zhang, *Nanoscale Res. Lett.* **8**, 2 (2013).
7. M. Valvo, F. Lindgren, U. Lafont, F. Bjorefors and K. Edstrom, *J. Power Sources* **245**, 967-978 (2014).
8. G. Y. Zhang, Y. Feng, Y. Y. Xu, D. Z. Gao and Y. Q. Sun, *Mater. Res. Bull.* **47**, 625-630 (2012).
9. A. N. Naveen and S. Selladurai, *Electrochim. Acta* **125**, 404-414 (2014).

Spectroscopic and thermodynamic properties of L-ornithine monohydrochloride

M. Dinesh Raja, C. Maria Ashok Kumar, S. Arulmozhi, and J. Madhavan'

Citation: AIP Conference Proceedings **1665**, 060008 (2015); doi: 10.1063/1.4917843
View online: http://dx.doi.org/10.1063/1.4917843
View Table of Contents: http://aip.scitation.org/toc/apc/1665/1
Published by the American Institute of Physics

Spectroscopic And Thermodynamic Properties Of L-Ornithine Monohydrochloride

M. Dinesh Raja[1], C. Maria Ashok Kumar[2] S.Arulmozhi[2] and J.Madhavan[2,*]

[1]*Department of Physics, Bharath University, Chennai – 600073, India*
[2]*Department of Physics, Loyola College, Chennai – 600034, India*
[*]*E-mail: jmadhavang@yahoo.com*

Abstract. L-Ornithine Monohydrochloride (LOMHCL) has been investigated with the help of B3LYP density functional theory with 6-31 G (d, p) basis set. Fourier transform infrared and Fourier transform Raman spectra is to identify the various functional groups. The theoretical frequencies showed very good agreement with experimental values. On the basis of the thermodynamic properties of the title compound at different temperatures have been calculated, revealing the correlations between standard heat capacities (C) standard entropies (S), and standard enthalpy changes (H) and temperatures. Second harmonic generation (SHG) efficiency of the grown crystal has been studied.

Keywords: LOMHCL, DFT, SHG.
PACS: 05. 05.10.-a

INTRODUCTION

Novel nonlinear optical (NLO) materials have been built from organic–inorganic complexes in which the high optical non-linearity of a organic compound is combined with the favorable properties of inorganic materials [1]. The present work deals with the growth and detailed spectral investigation of LOMHCL.

Synthesis of LOMHCL

LOMHCL was synthesized by dissolving stoichiometric amount of L-Ornithine (Merck 99%) and high purity hydrochloric acid in deionized water, the photograph of the crystal is shown in Figure 1

Computational Details

The optimization of the title compound were calculated using DFT and B3LYP method with 6-31+G(d, p) basis set using GAUSSIAN 03 program package [2]. The molecular structure of LOMHCL was as shown in the Figure 2

FIGURE. 1 Photograph of as grown LOMHCl single crystal

FIGURE. 2 Atomic numbering system adapted for ab initio computations of LOMHCL molecule

FT-IR and FT-Raman Analysis

FT-IR spectrum of the grown crystal was recorded in the range 500 cm^{-1} to 4000 cm^{-1}, using KBr pellet technique on BRUKKER IFS FT-IR Spectrometer. For comparison, the experimental FT-IR and theoretically simulated spectra were presented in Figures 3 and 4. The FT-Raman spectrum (Figure 5) was compared with simulated spectrum (Figure 6).

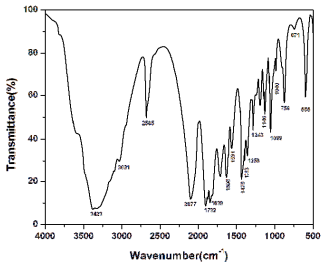

FIGURE. 3 FT-IR of LOMHCL

Solid State Physics
AIP Conf. Proc. 1665, 060008-1–060008-2; doi: 10.1063/1.4917843

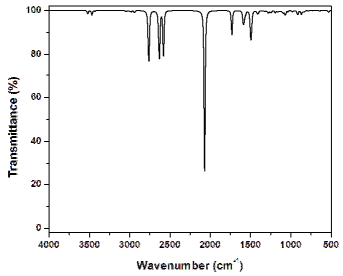

FIGURE 4 FT-IR of LOMHCl by DFT

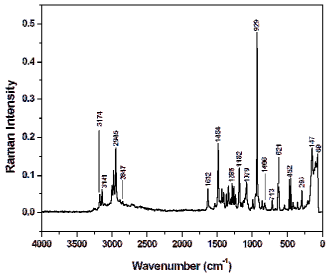

FIGURE.5 FT-Raman of LOMHCL

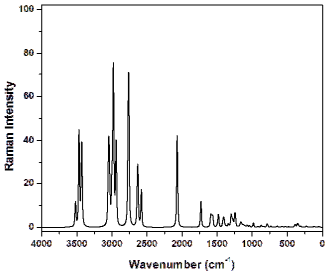

FIGURE.6 FT Raman of LOMHCL by DFT

NH_3^+ group vibration

In LOMHCL, the NH_3^+ asymmetric deformation vibration is observed at 1630 cm^{-1} in IR and as a medium band at 1632 cm^{-1} in Raman.

Carboxylate group vibrations

The asymmetric stretching of COO^- vibration appears in IR and Raman at 1451cm^{-1} and 1432 cm^{-1} respectively. The COO^- deformation coupled with rocking mode appears as a very strong band at 671 cm^{-1} in IR and 635, 1451cm^{-1}in Raman.

C-N Vibrations

The computed frequencies are presented at 1110, 1126, 1147and 1067 cm^{-1} by using B3LYP method. The C-N stretching vibrations were observed at 1099 cm^{-1} and 1079 cm^{-1} for IR and Raman respectively.

CH_2 group vibrations

The strong bands observed in the Raman spectrum at 2950 and 2964 cm^{-1} are assigned to the symmetric stretching mode of the CH_2 group, while the asymmetric mode occurs at 2990 cm^{-1} [3].

Thermo-dynamical properties

The standard statistical thermodynamic functions at B3LYP/631G (d, p) level heat capacity C_P^0m, entropy S^0m and enthalpy changes ΔH^0m for the title compound are obtained from the theoretical wave numbers [4]. The correlation graphs are shown in figure 7 the corresponding fitting equations are as follows.

$C_P^0m = 4.609 + 0.148T - 5.442 \times 10^{-5}T^2$ (R^2=0.9994)

$S^0m = 55.854 + 0.1726T - 3.9275 \times 10^{-5}T^2$ (R^2=0.9998)

$\Delta H^0m = -1.451 + 0.018T + 4.489 \times 10^{-5}T^2$ (R^2=0.99968)

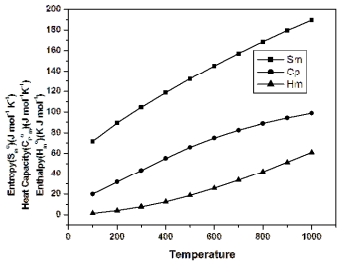

FIGURE.7 Correlation graph of entropy , heat capacity and enthalpy vs temperature of LOMHCL

Nonlinear Optical Properties

The SHG efficiency of LOMHCL was determined by Kurtz and Perry powder technique [5]. The SHG efficiency of LOMHCL is found to be 1.7 times higher than KDP.

CONCLUSION

Optically transparent single crystal of LOMHCL is grown by slow evaporation technique in a period of 40 days. Functional groups present in the grown crystal were identified using FT-IR and Raman spectrum. SHG analysis reveals that the efficiency of this material is about 1.7 times that of KDP.

REFERENCES

1. Sankar D, Vinay Raj Menon, Sagayaraj P and Madhavan J., *Physica B.*, 405 (2010) 192.
2. Frisch, A.B. Nielson, A.J. Holder, *Gaussview User Manual, Gaussian Inc.,Pittsburgh, PA*, 2000.
3. Nabil Elleuch Walid Amamou Ali Ben Ahmed, Younes Abid, Habib Feki *Spectrochimica Acta Part A: Molecular and Biomolecular Spectroscopy* 128 (2014) 781–789
4. Ott J.B., Goates J.B., *Chemical Thermodynamics: Principles and Applications, Academic Press, San Diego*, 2000.
5. Kurtz S.K. and Perry T.T. (1968), *J. Appl. Phys.*, Vol. 39, pp. 3798-3813

Surface characterization of rapidly grown TiO_2 nanotubes assisted by field supporting effect

T. Manovah David, P. Wilson, Shibu Joseph, C. Ramesh, N. Murugesan, and P. Sagayaraj

Citation: AIP Conference Proceedings **1665**, 050191 (2015); doi: 10.1063/1.4917832
View online: http://dx.doi.org/10.1063/1.4917832
View Table of Contents: http://aip.scitation.org/toc/apc/1665/1
Published by the American Institute of Physics

Surface Characterization of Rapidly Grown TiO_2 Nanotubes Assisted by Field Supporting Effect

T. Manovah David[1,2], P. Wilson[1], Shibu Joseph[2], C. Ramesh[3], N. Murugesan[3] and P. Sagayaraj[2]

[1]*Department of Chemistry, Madras Christian College, Chennai – 600059, India*
[2]*Department of Physics, Loyola College, Chennai – 600 034, India*
[3]*MCD, Chemistry Group, Indira Gandhi Centre for Atomic Research, Kalpakkam – 603104, India*
[*]*E-mail:psagayaraj@hotmail.com*

Abstract. This study examines the electrochemical anodization of Ti foils in the presence of oxalic acid and malonic acid as field supporting agents. Notably, these additional electrolyte constituents are found to have a strong influence in the formation of TiO_2 nanotubes. These nanotubes were also found to possess good crystallinity and better surface morphology. Interestingly, the TiO_2 nanotubes grown showed hydrophobic behavior.

Keywords: Titanium dioxide; Nanotubes; Anodic films; FESEM
PACS: 81.05.Dz; 81.07.De; 82.45.Cc; 82.80.Dx

INTRODUCTION

Titania (TiO_2) is a multifunctional material and is used in versatile applications, including photo-splitting of water, biomedicine, photocatalysis, light sensitive materials, sunscreen protection for cosmetics, dye sensitized solar cells and gas-sensing [1]. TiO_2 in nanometer scale has been reported with different morphologies; such as instance nanospheres, nanoparticles, nanorods, nanowires and nanotubes (NTs). Among the morphologies, TiO_2 NTs has attracted the interest of several researchers around the world due to its large surface-to-volume ratio, optical characteristics and electrical properties [2]. Interestingly, fabrication of TiO_2 NTs employing electrochemical anodization has made significant contribution to the increasing attention with its ability to precisely control the NTs architecture [3, 4]. Parameters like voltage, current intensity, time, pH and electrolyte concentration play a vital role in the formation of TiO_2 NTs [5]. In the present work, investigation on the growth of TiO_2 NTs is carried out by altering the electrolyte chemistry by separately adding oxalic or malonic acid to the ethylene glycol based electrolyte solution. Compared to that of electrolyte without these weak organic acids, excellent increase in the length of NTs is observed with the presence of these additional electrolyte constituents. The contact angle measurements are conducted for all the samples and work of adhesion is carried out. Fascinatingly, the results revealed that TiO_2 NTs formed in the presence of malonic acid was comparatively more hydrophobic than samples prepared through oxalic acid.

EXPERIMENTAL SECTION

Highly ordered TiO_2 NTs were synthesized via potentiostatic electrochemical anodization of Ti foil. In a typical procedure, a two electrode system was utilized and the reactions were conducted at 30 V for a constant period of 1 h at room temperature. Degreased Ti foil and Pt mesh were used as anode and cathode respectively. The main constituent of the electrolyte was ethylene glycol along with 0.3 wt% NH_4F and 2 vol% DI H_2O. To this combination 1 wt% of additives, either oxalic or malonic acid was included to study their effect in the growth of the NTs. The TiO_2 NTs samples obtained from these electrolyte combinations were named as OT and MT, respectively. For comparison, one of the samples was formed without the addition of these weak organic acids and thus achieved TiO_2 NTs was named ET. The as-obtained samples were annealed at 450 ^oC for a period of 5 h before characterization. Electrodeposition of Pt was carried out on the using three electrode system for surface functionalization. The crystallinity and structure of the formed TiO_2 NTs were analyzed by

Solid State Physics
AIP Conf. Proc. 1665, 050191-1–050191-3; doi: 10.1063/1.4917832

Rigaku Smart Lab X-ray diffractometer (XRD) with CuKα (λ = 1.54060 Å) radiation. The morphological characterization was investigated with Carl Zeiss Supra 55 Field Emission Scanning Electron Microscope (FESEM) attached with Energy Dispersive X-ray Analysis (EDX) to determine the elemental composition of the samples. Contact angle measurements were done on the samples by slowly depositing DI water over the surfaces by screw syringe. The temperature was maintained at 24 ^{o}C during the measurements.

RESULTS AND DISCUSSION

Figure 1a, b and c illustrate the XRD pattern of the as-anodized TiO_2 NTs with oxalic acid (OT), malonic acid (MT) and bare (ET), respectively. Distinct peaks with planes of the annealed samples are identified to be (101) (004) (200) (211) and (204) confirming the formation of anatase phase in all the three samples, indexed to a standard JCPDS data (21-1272). Peaks (103) (112) (105) are from the Ti foil beneath the TiO_2 NTs indexed to a JCPDS card (44-1294). The results are in line with the reported data [6]. Although all the patterns reveal good crystalline nature, MT (Figure 1b) seems to demonstrate better intensity of peaks compared to its counterpart OT (Figure 1a). However, the sample ET showed much less intensity of the peaks formed. XRD analyses of samples OT, MT and ET reveal that the presence of weak organic acids largely contributes to the formation of highly crystalline TiO_2 NTs.

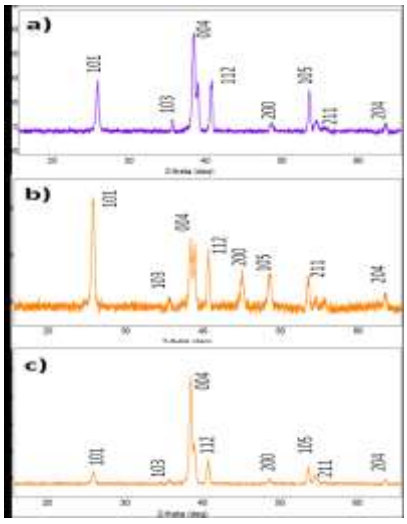

FIGURE 1. XRD pattern of a) OT, b) MT and c) ET.

Figure 2a, b and c illustrates the cross-sectional TiO_2 NTs FESEM images corresponding to the samples OT, MT and ET. The growth rate determining factor, the potential was kept constant so as to study the influence of the additional constituents. Figure 2c is found to possess poor growth of TiO_2 NTs with 4.8 μm/h. On the other hand, efficient growth of the TiO_2 NTs was seen in the samples OT and MT (Figure 2a and b). Both the samples are observed to possess higher growth rate, however MT possessed better growth in length with 12.8 μm/h than OT with 6.9 μm/h. The rapid growth may be attributed to the field supporting effect and the good oxidizing capacity of the weak organic acids. Another study earlier with lactic acid is reported to be the fastest growth in any combination of electrolyte [7]. The report supports the fact related to the present study, that these additional electrolyte components play an important role in the formation and growth of the highly ordered TiO_2 NTs array.

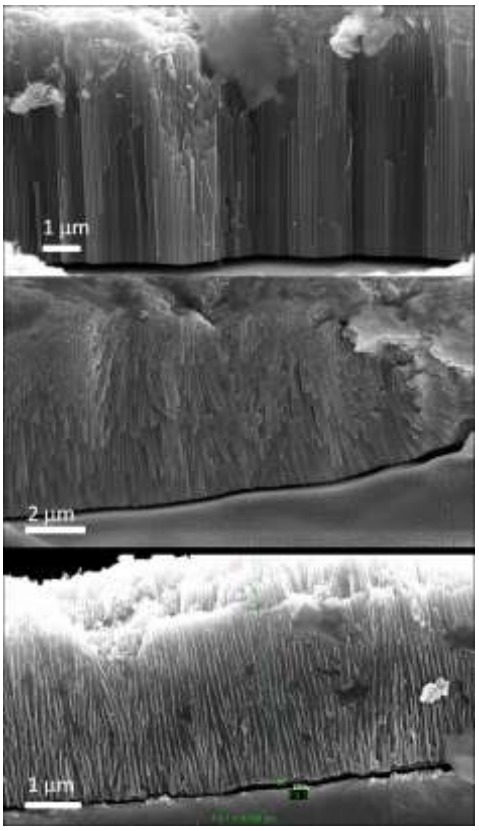

FIGURE 2. Cross-section FESEM images of a) OT, b) MT and c) ET.

Figure 3a, b and c depicts the top surface morphology of the samples OT, MT and ET, respectively. Figure 3d illustrates the back side image of MT. Notably, the accelerated growth in OT and MT has not affected the open tubular morphology of the TiO_2 NTs. Besides, minimal breakdown is observed in the sample ET. Close observation reveals hcp

arrangement in all the samples. However, MT (Figure 3b) depicts better surface morphology than the other two samples. The images of OT and MT further reveal that the architecture comprising of wall thickness and pore size is uniform when compared to ET and earlier reports [4,8,9].

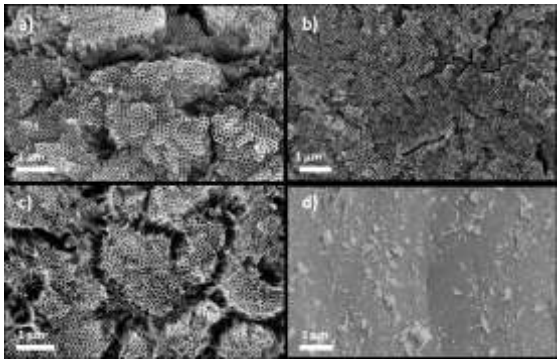

FIGURE 3. Top surface images of a) OT, b) MT and c) ET, and d) Bottom image of MT.

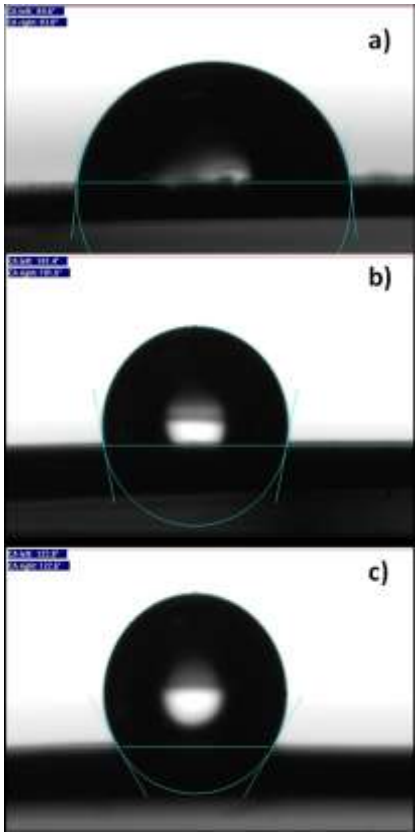

FIGURE 4. Contact angle measurements of a) OT, b) MT and c) ET.

Figure 4a, b and c shows the image of contact angle measurements made on as-prepared TiO_2 NTs OT, MT and ET, respectively. As understood, the samples OT and MT showed hydrophobic nature with contact angles above 90^o. However, the ET sample showed hydrophilicity nature with contact angle less than 90^o. The finding was supported with the fact that ET has high work of adhesion (W_A) according to Young-Dupre equation [10]. W_A was 33. 3, 58.4 and 80.6 mN/m for OT, MT and ET samples, respectively.

In summary, rapid growth is observed in the samples with the addition of oxalic acid and malonic acid. The growth rate has not affected the surface morphology of the samples. Hydrophobic nature is observed in the faster grown samples. Moreover, the study suggests further improvement is possible in the anodic formation of TiO_2 NTs

ACKNOWLEDGMENTS

The authors gratefully acknowledge UGC-DAE CSR (Grant No: CSR-KN/CRS-52/2013-14/651) for funding this research project.

REFERENCES

1. D. Regonini, C.R. Bowen, A. Jaroenworaluck and R. Stevens, Mater. Sci. Eng. R, 74, 377-406, (2013)
2. D. Feng, Z. Rui, Y. Lu and H. Ji, *Chem. Eng. J.* **179**, 363-371 (2012).
3. P. Roy, S. Berger and P. Schmuki, *Angew. Chem. Int. Ed.* **50**, 2904-2939 (2011).
4. Gong D, C.A. Grimes, O.K. Varghese, W. Hu, R.S. Singh, Z. Chen and E.C. Dickey, *J. Mater. Res.* **16**, 3331-3334 (2001).
5. O.K. Varghese, D. Gong, M. Paulose, K.G. Ong, E.C. Dickey and C.A. Grimes, *Adv. Mater.* **15**, 624-628 (2003).
6. Y.R. Smith and V.R. Subramanian, *J. Phys. Chem. C*, **115**, 8376–8385 (2011).
7. S. Seulgi, K. Lee and P. Schmuki, *J. Am. Chem. Soc.* **134**, 11316−11318 (2012).
8. L.K. Tsui, T. Homma and G. Zangar, *J. Phys. Chem. C*, **117,** 6979−6989 (2013).
9. G.D. Sulka, J.K. Kolodziej, A. Brzozka and M. Jaskula, *Electrochim. Acta.* **104**, 526-536 (2013).
10. D.P. Subedi, *The Himalayan Physics*, **2**, 1-4 (2011).

A CETD matrix Approach to analyze the Dimensions of Personality of Person

A.Victor Devadoss
Head & Associate Professor
Department of Mathematics
Loyola College, Chennai-34, INDIA

M. Clement Joe Anand
Ph.D Research Scholars
Department of Mathematics
Loyola College, Chennai-34, INDIA

A. Felix.
Ph.D Research Scholars
Department of Mathematics
Loyola College, Chennai-34, INDIA.

Abatract:- **The objective of this paper is to find out the peak age of person getting anger in Chennai, for that we study the dimensions of personality of person. Personality has been classified in to five factors as Openness, Conscientiousness, Extraversion, Agreeableness and Negative Emotion. Each of these dimensions has six facets. For the first time in 1998 fuzzy matrix theory was developed by W.B. Vasantha and V. Indira to study the passenger transportation. To study this problem, they divided and defined four types of matrices are called Initial Raw Data Matrix, Average Time Dependent Data matrix (ATD Matrix), Refined Time Dependent Data matrix (RTD Matrix) and Combined Effect Time Dependent Data Matrix (CETD Matrix). In the year 2003 the same technique was used by W.B. Vasantha to study the migrant laborers who were affected by HIV/AIDS. In 2012 and 2013, A. Victor Devadoss, M. Clement Joe Anand and A. Felix have studied dimensions of personality of men and women separately using this model. Now we use this model to study the Dimensions of personality of person.**

Keywords- **Personality of Men, Personality of Women, OCEAN, ATD Matrix, RTD Matrix, CETD Matrix.**

INTRODUCTION

This paper has four sections. In the first section we just recall the methods of applications of CETD matrix. In section two we describe the dimensions of personality. The section three we apply the six facets of dimensions of personality of person by using CETD model to find out the peak age of group of OCEAN. In final section we derived conclusions and gives suggestion based on our study.

I. THE METHOD OF APPLICATION OF CETD MATRIX

A. Average Time Dependent (ATD) Matrix

Raw data transform it into a raw time dependent data matrix by taking along the rows the age group and along the columns using the raw data matrix we make it into the Average Time Dependent Data (ATD) matrix(a_{ij}) by dividing each entry of the raw data matrix by the number of years i.e., the time period. This matrix represents a data, which is totally uniform. At the third stage we find the average and Standard Deviation (S.D) of every column in the ATD matrix.

B. Refined Time Dependent (RTD) Matrix

Using the average μ_j of each j^{th} column and σ_j the S.D of the each j^{th} column we chose a parameter α from the interval [0,1] and form the Refined time dependent Matrix (RTD matrix),

Using the formula

If $a_{ij} \le (\mu_j - \alpha * \sigma_j)$ then $e_{ij} = -1$ else

if $a_{ij} \in \left(\mu_j - \alpha * \sigma_j, \mu_j + \alpha * \sigma_j\right)$ then $e_{ij} = 0$ else

if $a_{ij} \ge \left(\mu_j + \alpha * \sigma_j\right)$ then $e_{ij} = 1$.

We redefine the ATD matrix into the Refined time dependent fuzzy matrix for here the entries are =-1,0 or 1. Now the row sum of this matrix gives the maximum age group

C. Combined Effective Time Dependent Data (CETD) Matrix

We also combine the above RTD matrices by varying the $\alpha \in [0,1]$, so that we get the Combined Effective Time Dependent Data (CETD) matrix. The row sum is obtained for CETD matrix and conclusions are derived based on the row sums. All these are represented by graphs and graphs play a vital role in exhibiting the data by the simplest means, which can be even understood by a layman

II. DIMENSIONS OF PERSONALITY

A. Personality

Personality models are needed; since people with different personalities may react differently to same situations. Personality is that that patterns of characteristics thoughts, feelings and behaviors that distinguish one person from another and that persist over time and situation. It is sum biologically based and learnt behavior which makes the person response to environmental stimuli exclusively. In contemporary psychology, personality is specified as a function of thirty attributes-each of which called personality facet. The personality facets are clustered in five groups, each called a personality trait or personality factor. The five personality factors are also referred to as "the big five" [15]. The value of each personality factor is determined by the values of its six facets. The five clusters of personality factors are also referred to by letter designation [1] and [15]. Acton refer to a thing them as the OCEAN model.

In the **OCEAN** model, the letters stands for the following meanings:

O: Openness, culture, Originality, or intellect.
C: Conscientiousness, consolidation, or will to achieve.
E: Extraversion.
A: Agreeableness or accommodation.

978-1-4799-3010-4/14 $31.00 © 2014 IEEE
DOI 10.1109/CSCI.2014.92

N:Need for stability, negative emotionality, or neuroticism

B. Personality Traits

1. *Openness*

"Openness to experience is tendency to be intellectual, interested in the arts, emotionally aware, and liberal" [2].Openness refers to the number of interests to which one is attracted and the depth to which those interests are pursued. It is also referred to culture, originality, or intellect. It is about creativity".

2. Conscientiousness

"Conscientiousness is tendency to set high goals, to accomplish work successfully and to behave dutifully and morally" [1]. Furthermore, "conscience is the awareness of a moral or ethical aspect to one's conduct together with the urge to prefer right over wrong".

3. Extraversion

"Extraversion is trait associated with sociability and positive affect", [1]. "It refers to the number of relationships with which one is comfortable because the distribution of the factor scores is normal and not bimodal, the practice of dichotomizing respondents for example into extraverts and introverts is unjustified. McCrae and Costa prefer speaking of degree of extra version. For convenience's sake, they speak of three level [low, medium, high] in which one might score-extraversion, ambiversion, and introversion.

4. Agreeableness

"Agreeableness is tendency to be a nice person"[1]. It is also referred to as accommodation.

5. Negative Emotion

Negative emotionality, neuroticism, or need for stability is the trait associated with emotional instability and negative affect" [1]. "Negative emotionality refers to the number and strength of stimuli required to elicit negative emotions in a person".

III. DESCRIPTION OF THE PROBLEM

In this research we give an algebraic approach to the dimensions of personality of Person in Chennai. For that we have interviewed 200 people in Chennai. First by the term, each five dimensions have six facets. In which we mainly concentrate the negative emotion among the five dimensions. We approach the dimensions of personality of Person by determining the peak age group. In which they are maximum of being Openness, Conscientiousness, Extraversion, Agreeableness, and Negative Emotion.

We analyze these problems using fuzzy matrix, we call the RTD Matrix as fuzzy matrix for that take their entries from the set {-1, 0, 1}. So the terms of RTD matrix or fuzzy matrix mean one and the same matrix. One of the major and broad its heads of the study negative emotions of Person among the five dimensions.

In this research will discuss six faces of each dimensions of personality of person, which are taken as the columns of the initial row data matrix the age group in years, 10-17, 18-24, 25-29, 30-39, 40-49, 50-59 and 60-75. The estimation of the maximum age group is five-stage process. In the first stage we give the matrix representation of the raw data. Entries corresponding to the intersection of rows and columns are values corresponding to the live network. The 3 x 6 matrix is not uniform i.e. the number of individual years in each interval may not be the same. So in the second stage we in order to obtain an unbiased uniform effect on each and every data so collected, transform this initial matrix into an Average Time Dependent Data (ATD) matrix. To make the calculations easier and simpler we in the third stage using the simple average techniques convert the above average time dependent data matrix in to a matrix with entries $e_{ij} \in \{-1, 0, 1\}$.We name this matrix as the Refined Time Dependent Data Matrix (RTD Matrix) or as the fuzzy matrix. The value of e_{ij} corresponding to each entry is determined in a special way described in section I of this paper. At the fourth stage using the fuzzy matrices we obtain the Combined Effect Time Dependent Data Matrix (CETD Matrix), which gives the cumulative effect of all these entries. In the final stage we obtain the row sums of the CETD matrix. The tables given are self-explanatory at each stage. The graph of the RTD matrix and CETD matrix are given.

A) Estimation of maximum age group of person being Openness by using 7x6 matrix

In this section we apply six facets i.e. O_1-Fantasy, O_2-Aesthetics, O_3-Feelings, O_4- Actions, O_5-Ideas and O_6-Values of Openness of person to the CETD model.

Table 1: Initial raw data matrix of Openness of order 7×6

Age	O_1	O_2	O_3	O_4	O_5	O_6
10-17	22	23	19	25	27	16
18-24	22	24	20	21	18	13
25-29	22	24	24	21	21	24
30-39	17	17	14	19	23	20
40-49	11	20	20	12	23	18
50-59	7	13	14	5	21	13
60-75	4	13	8	4	20	8

Table 2: The ATD matrix of Openness of order 7×6

Age	O_1	O_2	O_3	O_4	O_5	O_6
10-17	2.75	2.88	2.38	3.13	3.38	2.00
18-24	3.14	3.43	2.86	3.00	2.57	1.86
25-29	4.40	4.80	4.80	4.20	4.20	4.80
30-39	1.70	1.70	1.40	1.90	2.30	2.00
40-49	1.10	2.00	2.00	1.20	2.30	1.80
50-59	0.70	1.30	1.40	0.50	2.10	1.30
60-75	0.25	0.81	0.50	0.25	1.25	0.50

Table 3: The Average and Standard deviation of given ATD Matrix

Average	2.01	2.42	2.19	2.03	2.59	2.04
S.D	1.49	1.38	1.38	1.48	0.95	1.33

The RTD matrix for α = 0.2 row sum matrix

$$\begin{bmatrix} 1 & 1 & 0 & 1 & 1 & 0 \\ 1 & 1 & 1 & 1 & 1 & 0 \\ 1 & 1 & 1 & 1 & 1 & 1 \\ -1 & -1 & -1 & 0 & -1 & 0 \\ -1 & -1 & 0 & -1 & -1 & 0 \\ -1 & -1 & -1 & -1 & -1 & -1 \\ -1 & -1 & -1 & -1 & -1 & -1 \end{bmatrix} \quad \begin{bmatrix} 4 \\ 5 \\ 6 \\ -4 \\ -4 \\ -6 \\ -6 \end{bmatrix}$$

Graph 1: Depicting maximum age group of Person being OPENNESS for α = 0.2

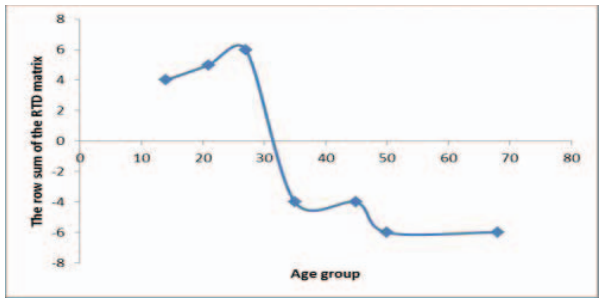

Similarly we can find the RTD matrix for α = 0.32, 0.57 and0.7

The CETD Matrix row sum matrix

$$\begin{bmatrix} 2 & 2 & 0 & 4 & 4 & 0 \\ 4 & 4 & 2 & 4 & 2 & 0 \\ 4 & 4 & 4 & 4 & 4 & 4 \\ -1 & -2 & -2 & 0 & -1 & 0 \\ -2 & -1 & 0 & -2 & -1 & 0 \\ -4 & -4 & -2 & -4 & -2 & -2 \\ -4 & -4 & -4 & -4 & -4 & -4 \end{bmatrix} \quad \begin{bmatrix} 12 \\ 16 \\ 24 \\ -6 \\ -6 \\ -18 \\ -24 \end{bmatrix}$$

Graph:2 Depicting maximum age group of person being OPENNESS

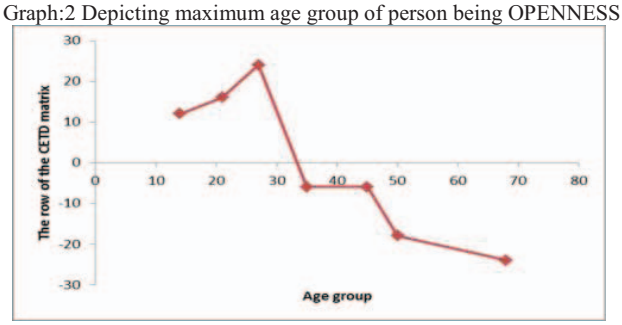

B) Estimation of Maximum age group of person being Conscientiousness by using 7x6 matrix

In this section we apply six facets i.e. In this section we apply six facets i.e. C_1-Competence, C_2-Order, C_3-Dutifulness, C_4-Achievepersont Striving, C_5-Self Discipline and C_6-Deliberation of Conscientiousness of person to the CETD model

Table-4: Initial raw data matrix of Conscientiousness of order 7 × 6

Age	C_1	C_2	C_3	C_4	C_5	C_6
10-17	9	10	8	15	12	5
18-24	14	18	12	20	14	11
25-29	19	25	21	27	20	20
30-39	18	22	20	15	20	23
40-49	14	26	24	20	23	23
50-59	12	22	19	16	17	19
60-75	7	8	6	9	8	13

Table-5: ATD Matrix of Conscientiousness of order 7 × 6

Age	C_1	C_2	C_3	C_4	C_5	C_6
10-17	1.13	1.25	1.00	1.88	1.50	0.63
18-24	2.00	2.57	1.71	2.86	2.00	1.57
25-29	3.80	5.00	4.20	5.40	4.00	4.00
30-39	1.80	2.20	2.00	1.50	2.00	2.30
40-49	1.40	2.60	2.40	2.00	2.30	2.30
50-59	1.20	2.20	1.90	1.60	1.70	1.90
60-75	0.44	0.50	0.38	0.56	0.50	0.81

Table-6: The Average and Standard deviation of given ATD Matrix

Average	1.68	2.33	1.94	2.26	2.00	1.93
S.D	1.06	1.40	1.20	1.55	1.06	1.13

The RTD matrix for α = 0.27 row sum matrix

$$\begin{bmatrix} -1 & -1 & -1 & 0 & 0 & -1 \\ 1 & 0 & 0 & 1 & 0 & 0 \\ 1 & 1 & 1 & 1 & 1 & 1 \\ 0 & 0 & 0 & -1 & 1 & 1 \\ 0 & 0 & 0 & 0 & 1 & 1 \\ -1 & -1 & 0 & -1 & -1 & 0 \\ -1 & -1 & -1 & -1 & -1 & -1 \end{bmatrix} \quad \begin{bmatrix} -4 \\ 2 \\ 6 \\ 0 \\ 2 \\ -4 \\ -6 \end{bmatrix}$$

Graph-3: Depicting maximum age group of Person being CONSCIENTIOUSNESS for α = 0.27

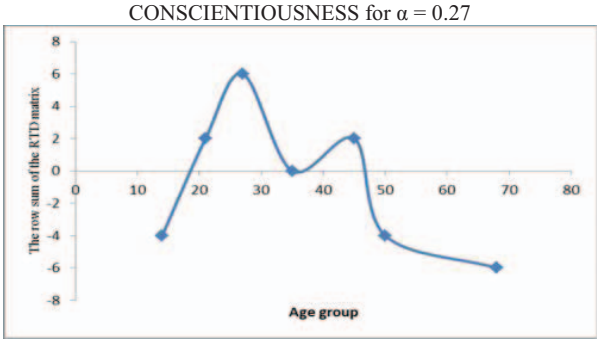

Similarly we can find RTD matrix for α = 0.4, 0.65 and 0.8

The CETD Matrix row sum matrix

$$\begin{bmatrix} -3 & -3 & -1 & 0 & 0 & -4 \\ 1 & 0 & 0 & 1 & 0 & 0 \\ 4 & 4 & 4 & 4 & 4 & 4 \\ 0 & 0 & 0 & -1 & 0 & 1 \\ 0 & 0 & 0 & 0 & 1 & 1 \\ -2 & -1 & 0 & -2 & -1 & 0 \\ -4 & -4 & -4 & -4 & -4 & -4 \end{bmatrix} \quad \begin{bmatrix} -11 \\ 2 \\ 24 \\ 0 \\ 2 \\ -6 \\ -24 \end{bmatrix}$$

Graph-4: Depicting maximum age group of Person being CONSCIENTIOUSNESS for CETD Matrix

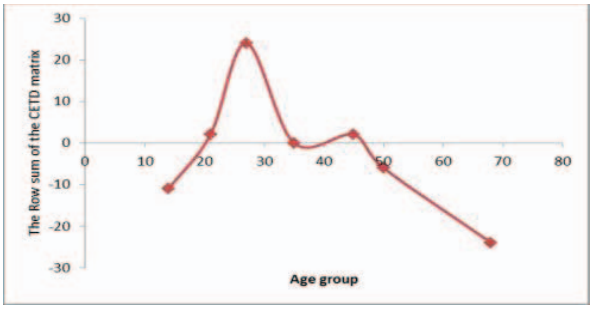

C) Estimation of maximum age group of person being Extraversion by using 7x6 matrix

In this section we apply six facets i.e. E_1-Warmth, E_2-Gregariousness, E_3-Assertiveness, E_4-Activity, E_5-Excitepersont Seeking and E_6-Positive Emotions of Extraversion of person to the CETD model.

Table-7: Initial raw data matrix of Extraversion of order 7 × 6

Age	E_1	E_2	E_3	E_4	E_5	E_6
10-17	9	17	13	26	23	22
18-24	26	22	11	22	23	18
25-29	26	26	20	24	26	19
30-39	20	21	23	25	18	21
40-49	17	22	21	19	15	21
50-59	14	13	17	14	10	21
60-75	5	12	6	6	5	11

Table-8: ATD Matrix of Extraversion of order 7 × 6

Age	E_1	E_2	E_3	E_4	E_5	E_6
10-17	1.13	2.13	1.63	3.25	2.88	2.75
18-24	3.71	3.14	1.57	3.14	3.29	2.57
25-29	5.20	5.20	4.00	4.80	5.20	3.80
30-39	2.00	2.10	2.30	2.50	1.80	2.10
40-49	1.70	2.20	2.10	1.90	1.50	2.10
50-59	1.40	1.30	1.70	1.40	1.00	2.10
60-75	0.31	0.75	0.38	0.38	0.31	0.69

Table-9: The Average and Standard deviation of given ATD Matrix

Average	2.21	2.40	1.95	2.48	2.28	2.30
S.D	1.68	1.45	1.09	1.43	1.65	0.94

The RTD matrix for α = 0.3 row sum matrix

$$\begin{bmatrix} -1 & 0 & 0 & 1 & 1 & 1 \\ 1 & 1 & -1 & 1 & 1 & 0 \\ 1 & 1 & 1 & 1 & 1 & 1 \\ 0 & 0 & 1 & 0 & 0 & 0 \\ 0 & 0 & 0 & -1 & -1 & 0 \\ -1 & -1 & 0 & -1 & -1 & 0 \\ -1 & -1 & -1 & -1 & -1 & -1 \end{bmatrix} \quad \begin{bmatrix} 2 \\ 3 \\ 6 \\ 1 \\ -2 \\ -4 \\ -6 \end{bmatrix}$$

Graph-5: Depicting maximum age group of Person being EXTRAVERSION for α = 0.3

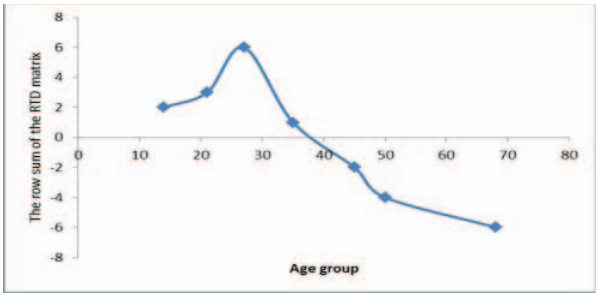

Similarly we can find the RTD matrix for α = 0.42, 0.65 and0.8

The CETD Matrix row sum matrix

$$\begin{bmatrix} -2 & 0 & 0 & 2 & 1 & 2 \\ 4 & 2 & -1 & 2 & 2 & 0 \\ 4 & 4 & 4 & 4 & 4 & 4 \\ 0 & 0 & 1 & 0 & 0 & 0 \\ 0 & 0 & 0 & -1 & -1 & 0 \\ -2 & -3 & 0 & -3 & -3 & 0 \\ -4 & -4 & -4 & -4 & -4 & -4 \end{bmatrix} \quad \begin{bmatrix} 3 \\ 9 \\ 24 \\ 1 \\ 2 \\ -11 \\ -24 \end{bmatrix}$$

Graph-6: Depicting maximum age group of Person being EXTRAVERSION for CETD Matrix

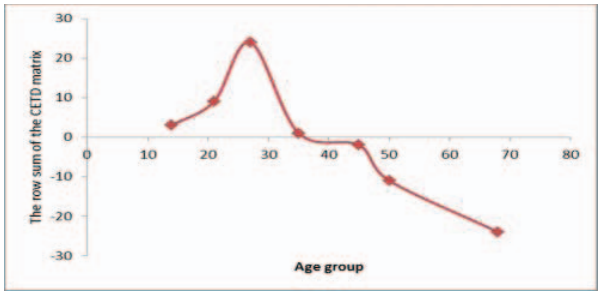

D) Estimation of maximum age group of person being Agreeableness by using 7x6 matrix

In this section we apply six facets i.e. A_1-Trust, A_2-Straight Forwardness, A_3-Altruism, A_4-Compliance, A_5-Modesty and A_6-Tender Mindness of Extraversion of person to the CETD model.

Table-10: Initial raw data matrix of Agreeableness of Order 7 × 6

Age	A_1	A_2	A_3	A_4	A_5	A_6
10-17	25	28	10	21	16	19
18-24	18	17	20	18	27	9
25-29	15	16	21	16	27	12
30-39	18	15	21	18	17	12
40-49	20	23	18	20	14	11
50-59	16	21	22	15	10	15
60-75	5	17	10	11	6	20

Table-11: ATD Matrix of Agreeableness of order 7 × 6

Age	A_1	A_2	A_3	A_4	A_5	A_6
10-17	3.13	3.50	1.25	2.63	2.00	2.38
18-24	2.57	2.43	2.86	2.57	3.86	1.29
25-29	3.00	3.20	4.20	3.20	5.40	2.40
30-39	1.80	1.50	2.10	1.80	1.70	1.20
40-49	2.00	2.30	1.80	2.00	1.40	1.10
50-59	1.60	2.10	2.20	1.50	1.00	1.50
60-75	0.31	1.06	0.63	0.69	0.38	1.25

Table-12: The Average and Standard deviation of given ATD Matrix

Average	2.06	2.30	2.15	2.05	2.25	1.59
S.D	0.97	0.86	1.15	0.83	1.76	0.56

The RTD matrix for α = 0.15 row sum matrix

$$\begin{bmatrix} 1 & 1 & -1 & 1 & 0 & 1 \\ 1 & 0 & 1 & 1 & 1 & -1 \\ 1 & 1 & 1 & 1 & 1 & 1 \\ -1 & -1 & 0 & -1 & -1 & -1 \\ 0 & 0 & -1 & 0 & -1 & -1 \\ -1 & -1 & 0 & -1 & -1 & 0 \\ -1 & -1 & -1 & -1 & -1 & -1 \end{bmatrix} \quad \begin{bmatrix} 3 \\ 3 \\ 6 \\ -5 \\ -3 \\ -4 \\ -6 \end{bmatrix}$$

Graph-8: Depicting maximum age group of Person being AGREABLENESS for α = 0.15

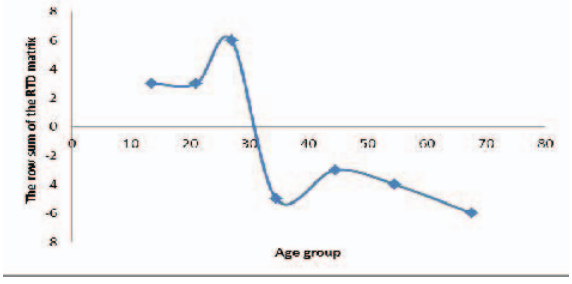

Similarly we can find RTD matrix for α = 0.37, 0.58 and 0.75

The CETD Matrix row sum matrix

$$\begin{bmatrix} 4 & 4 & -4 & 3 & 0 & 4 \\ 2 & 0 & 3 & 3 & 4 & -2 \\ 4 & 4 & 4 & 4 & 4 & 4 \\ -1 & -4 & 0 & -1 & -1 & -3 \\ 0 & 1 & -1 & 0 & -2 & -4 \\ -2 & -1 & 0 & -3 & -3 & 0 \\ -4 & -4 & -4 & -4 & -4 & -3 \end{bmatrix} \quad \begin{bmatrix} 11 \\ 10 \\ 24 \\ -10 \\ -6 \\ -9 \\ -23 \end{bmatrix}$$

Graph-8: Depicting maximum age group of Person being AGREABLENESS for CETD matrix

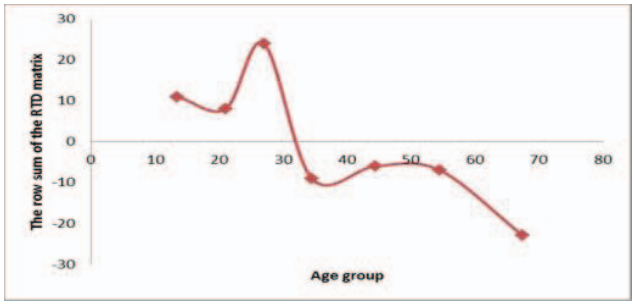

E) Estimation of maximum age group of person being Negative emotion by using 7x6 matrix

In this section we apply six facets i.e. N_1 -Worry, N_2-Anger, N_3-Discouragepersont, N_4-Self Consciousness, N_5-Impulsiveness, and N_6-Vulnerability of negative emotion of person to the CETD model.

Table-13: Initial raw data matrix of Negative Emotion of order 7 × 6

Age	N_1	N_2	N_3	N_4	N_5	N_6
10-17	6	13	17	10	14	13
18-24	18	30	23	23	27	21
25-29	29	29	21	27	28	25
30-39	25	25	22	19	19	12
40-49	24	27	24	22	26	20
50-59	20	18	20	15	11	12
60-75	19	10	14	10	9	12

Table-14: ATD Matrix of Negative Emotion of order 7 × 6

Age	N_1	N_2	N_3	N_4	N_5	N_6
10-17	0.75	1.63	2.13	1.25	1.75	1.63
18-24	2.57	4.29	3.29	3.29	3.86	3.00
25-29	5.80	5.80	4.20	5.40	5.60	5.00
30-39	2.50	2.50	2.20	1.90	1.90	1.20
40-49	2.40	2.70	2.40	2.20	2.60	2.00
50-59	2.00	1.80	2.00	1.50	1.10	1.20
60-75	1.19	0.63	0.88	0.63	0.56	0.75

Table-15: The Average and Standard deviation of given ATD Matrix

Average	2.46	2.76	2.44	2.31	2.48	2.11
S. D	1.63	1.75	1.05	1.60	1.74	1.47

The RTD matrix for α = 0.25 row sum matrix

$$\begin{bmatrix} -1 & -1 & -1 & -1 & -1 & -1 \\ 0 & 1 & 1 & 1 & 1 & 1 \\ 1 & 1 & 1 & 1 & 1 & 1 \\ 0 & 0 & 0 & -1 & -1 & -1 \\ 0 & 0 & 0 & 0 & 0 & 0 \\ -1 & -1 & -1 & -1 & -1 & -1 \\ -1 & -1 & -1 & -1 & -1 & -1 \end{bmatrix} \quad \begin{bmatrix} -6 \\ 5 \\ 6 \\ -3 \\ 0 \\ -6 \\ -6 \end{bmatrix}$$

Graph-9: Depicting maximum age group of Person being NEGATIVE EMOTION for α = 0.25

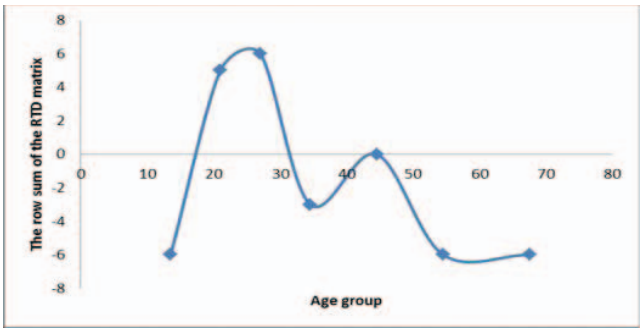

Similarly we can find RTD matrix for α = 0.38, 0.65 and 0.88

The CETD Matrix row sum matrix

$$\begin{bmatrix} -4 & -2 & -1 & -3 & -2 & -1 \\ 0 & 3 & 3 & 2 & 3 & 2 \\ 4 & 4 & 4 & 4 & 4 & 4 \\ 0 & 0 & 0 & -1 & -1 & -2 \\ 0 & 0 & 0 & 0 & 0 & 0 \\ -1 & -2 & -2 & -2 & -3 & -2 \\ -3 & -4 & -4 & -4 & -4 & -4 \end{bmatrix} \quad \begin{bmatrix} -13 \\ 13 \\ 24 \\ -4 \\ 0 \\ -12 \\ -23 \end{bmatrix}$$

Graph-10: Depicting maximum age group of Person being NEGATIVE EMOTION for CETD Matrix

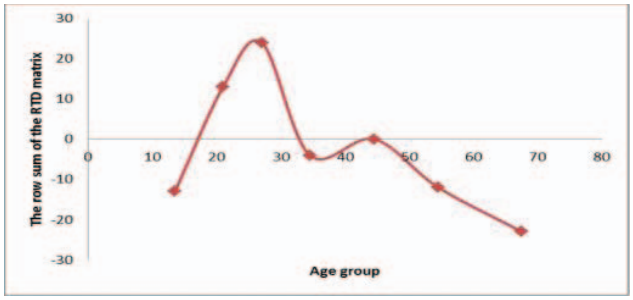

IV. CONCLUSION

A) Openness

The openness starts at the age 14. The maximum age group of person being open are at the age 27 as they have unusual ideas, curiosity, variety of experience, feelings and adventure. The openness decreases after the age 34. When person are not open and when their ideas not accepted, it makes them to get angry.

B) Conscientiousness

The Conscientiousness begins at the age 20. The maximum age group of person being conscientious are at the age 27, because they possess qualities like self-discipline, dutifulness, achievepersonts, striving and expectation in their work. The Conscientiousness gets decreased from the age 47.

C) Extraversion

The person belonging to the age group 15 begin to develop extraversion in them. The maximum age groups of person being extraversion are at the age 27 because they will be compassionate, co-operate, suspicious and antagonistic in all. The extraversion decreases from the age 46.

D) Agreeableness

The Agreeableness starts at the yearly teenage 14. The maximum age group of person being agreeableness are at the age 27 because they will be straight forward, tender mind, trust, tendency to seek stimulate in their work and family. The agreeableness decreases from the age 33.

E) Negative Emotion

Person at the age of 18 begin to develop negative emotion. The peak age of person having negative emotion at 27 because they have discouragepersont, impulsiveness, worry and vulnerability. When they are discouraged in their work and among their friends it makes them angry. The negative emotion decreases from the age 45 and above.

From our research we found out that starting and peak age of dimensions of personality of Person in Chennai and it is projected in the following table16.

We can see from the table that the peak age of a Chennai Person's personality is at 26-28. The negative approach starts after the peak age. So an individual become angry when their personality at the peak.

Table 16: Dimensions of personality of Person

	Dimensions of Personality of Men[23]					Dimensions of Personality of women[22]					Dimensions of Personality of Person				
OCEAN / Ages	**O** For α =0.1, 0.25, 0.3, 0.53	**C** For α =0.11, 0.23, 0.5, 0.6	**E** For α =0.19, 0.23, 0.39, 07 3	**A** For α =0.19, 0.29, 0.34, 0.55	**N** For α =0.2, 0.31, 0.47, 0.62	**O** For α =0.1, 0.25, 0.3, 0.53	**C** For α =0.1, 0.3, 0.5, 0.7	**E** For α =0.1, 0.3, 0.5, 0.7	**A** For α =0.1, 0.3, 0.5, 0.7	**N** For α =0.1, 0.3, 0.5, 0.7	**O** For α =0.2, 0.32, 0.57, 0.7	**C** For α = 0.27, 0.4, 0.65, 0.8	**E** For α = 0.3, 0.42, 0.65, 0.8	**A** For α =0.15, 0.37, 0.58, 0.75	**N** For α =0.25, 0.38, 0.65, 0.88
Starting Age	14	21	15	14	18	14	20	15	14	18	14	20	15	14	18
Peak Age	27	26	28	27	27	27	28	26	27	26	27	27	27	27	27

We did our previous work on dimensions of personality of men and women separately. From that work we have got same result for the personality of both men and women. To justify this we have taken the survey from both men and women and analyzed using CETD matrix and arrived results also same. From the above table 16, we conclude that there is no gender difference of dimensions of personality.

REFERENCES

[1] Acton-Glossary: http://www.personalityresearch.org/glossary.html

[2] A. Bandura, "A social cognitive theory of personality". In L. Pervin and O. John (Eds.), Handbook of personality, New York: Guilford Publications, pp. 154-194, 1999.

[3] A. Victor Devadoss and M. Clement Joe Anand, "Dimensions of Personality of women in Chennai Using CETD matrix" International Journal of Computer Applications. Volume 50 – No.5, 2012.

[4] A. Victor Devadoss and A. Felix, "Dimensions of Personality of men in Chennai Using CETD matrix" Indian Journal of Applied Research, volume 3, Issue 8, 2013.

[5] B. A. Bettencourt, A. Talley and A.J. Benjamin, "Personality and Aggressive Behavior Under Provoking and Neutral Conditions: A Meta-Analytic Review", Psychological Bulletin, 132(5), 751-777, 2006.

[6] "Emotion", Retrieved 15 March, (2009), from http://dictionary.reference.com/browse/emotion?jss=1

[7] G.S. Acton, Five-Factor Model (2000): http://www.personalityresearch.org/

[8] J. Heinstrom, "Five Personality dimensions and their influence on information behavior": Information Research, 9(1). Retrieved March 15, 2009. http://InformationR.net/ir/9-1/paper165.html

[9] L. Malatesta, G. Caridakis, A. Raouzaiou and K.Karpouzis, "Agent Personality traits in virtual environments based on appraisal theory predictions". In Processing of AISB'07: Artificial and Ambient Intelligence, Language, Speech and Gesture for Expressive Characters, Newcastle upon Tyne, UK, 2007.

[10] M.S. El-Nasr and M. Skubic, "A fuzzy emotional agent for decision-making in a mobile robot". In Proceeding of the 1998 International Conference On Fuzzy Systems, Anchorage, Alaska, pp. 135-140, 1998.

[11] M.S. El-Nasr, J. Yen and T. Loerger, "FLAME-A Fuzzy logic Adaptive Model of Emotions", Automous Agents and Multi-agent Systems,3, pp. 219-257, 2000.

[12] N. Ghasem-Aghaee and T.I. Oren, "Towards Fuzzy Agents with Dynamic Personality for Human Behavior Simulation". In proceeding of the 2003 Summer Computer Simulation Conference, Montreal, PQ, Canada, pp. 3-10, 2003.

[13] N. Ghasem-Aghaee and T.I. Oren, "Cognitive complexity and dynamic personality in agent simulation". Computers in Human Behavior, 23(6), 2983-2997, 2007.

[14] N.H. Frijda, "*The emotions".* Cambridge, New York: Cambridge University Press, 1998.

[15] P.J. Howard, "The owner's Manual for the Brain, Second Edition, Bard Press, Atlanta, GA, 2000. www.bradpress.com

[16] P.J. Howard and J.M. Howard, The BIG FIVE Quickstart: An Introduction to the Five-factor model of personality for Human Resource Professionals, Center for Applied Cognitive Studies Charlotte, North Carolina, 2003. www.centacs.com/quickstart.html

[17] T.I. Oren, N. Ghasem - Aghaee, B. Khalesi and M. Kazemifard, "Anger and Aggressive Behavior in Agent Simulation", 2003.

[18] T.I. Oren and N. Ghasem – Aghaee, "Personality Representation Processable n Fuzzy Logic for Human Behavior Simulation". In Proceeding of the 2003 Summer Computer Simulation Conference, Montreal, PQ, Canada, 2003.

[19] W.B.V. Kandasamy, F. Smarandache and Ilanthenral, "*Elementary Fuzzy Matrix Theory and Fuzzy Models for Social Scientists",* Printed in United States of America, 2007.

[20] W.B.V. Kandasamy, F. Smarandache and Ilanthenral, "*Special Fuzzy Matrices For Social Scientists"*, Printed in United States of America, 2007.